Advanced Structured Materials

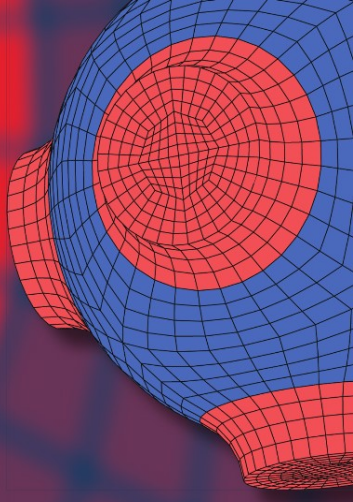

Holm Altenbach
Serge Kruch *Editors*

Advanced Materials Modelling for Structures

Springer

Advanced Structured Materials

Volume 19

Series Editors

Andreas Öchsner
Lucas F. M. da Silva
Holm Altenbach

For further volumes:
http://www.springer.com/series/8611

Holm Altenbach · Serge Kruch
Editors

Advanced Materials Modelling for Structures

Springer

Editors
Holm Altenbach
Lehrstuhl für Technische Mechanik
Institut für Mechanik
Magdeburg
Germany

and

Fakultät für Maschinenbau
Otto-von-Guericke-Universität
Magdeburg
Germany

Serge Kruch
ONERA/DMSM
Chatillon Cedex
France

ISSN 1869-8433 ISSN 1869-8441 (electronic)
ISBN 978-3-642-35166-2 ISBN 978-3-642-35167-9 (eBook)
DOI 10.1007/978-3-642-35167-9
Springer Heidelberg New York Dordrecht London

Library of Congress Control Number: 2012955998

Printed on acid-free paper

Springer is part of Springer Science+Business Media (www.springer.com)

Committees

Scientific Committee

Prof. Holm Altenbach (Otto-von-Guericke-Universität, Magdeburg)
Prof. Andre Dragon (LMPM-ENSMA, Poitiers, France)
Prof. Fionn Dunne (Imperial College London, UK)
Prof. Noel O'Dowd (University of Limerick, Ireland)
Prof. Masamichi Kawai (University of Tsukuba, Japan)
Prof. Nobutada Ohno (University of Nagoya, Japan)
Prof. Jacek Skrzypek (Krakow University of Technology, Krakow, Poland)

Local Organizing Committee

Serge Kruch, Onera (Chair)
Ahmed Benallal, LMT Cachan
Esteban Busso, Ecole des Mines de Paris
Anaïs Gaubert, Onera
Vincent Maurel, Ecole des Mines de Paris
Alexandre Iltchev, Onera
Jean-Briac le Graverend, Onera

Participants

S. Afshan	Imperial College London, UK s.afshan09@imperial.ac.uk
H. Altenbach	Otto-von-Guericke-Universität Magdeburg, Germany holm.altenbach@ovgu.de
R. Barrett	Mechanical and Biomedical Engineering, College of Engineering and Informatics, NUI Galway, Ireland r.barrett2@nuigalway.ie
A. Benallal	LMT-Cachan, France benallal@lmt.ens-cachan.fr
A. Benzerga	Texas A&M University, USA benzerga@tamu.edu
L. Bergers	Eindhoven University of Technology, The Netherlands l.i.j.c.bergers@tue.nl
C. Betts	Imperial College London, UK charles.betts03@imperial.ac.uk
V. Birman	Missouri University of Science and Technology, USA vbirman@mst.edu
J. Boyle	University of Strathclyde, UK jim.boyle@strath.ac.uk
M. Brünig	Institut für Mechanik und Statik, Germany michael.bruenig@unibw.de
E. Busso	Ecoles des Mines de Paris, France esteban.busso@ensmp.fr
J. L. Chaboche	Onera, France jean-louis.chaboche@onera.fr
J. Cormier	Institut Pprime, UPR CNRS 3346—ENSMA, France jonathan.cormier@ensma.fr
C. Davies	Imperial College London, UK catrin.davies@imperial.ac.uk
R. Desmorat	LMT-Cachan, France desmorat@lmt.ens-cachan.fr

J. Dirrenberger	Ecole des Mines de Paris, France justin.dirremberger@ensmp.fr
D. Dunand	Northwestern University, USA dunand@northwestern.edu
F. Dunne	Imperial College London, UK fionn.dunne@imperial.ac.uk
H. Egner	Institute of Applied Mechanics, Cracow University of Technology, Poland halina.egner@pk.edu.pl
B. Fedelich	BAM Division 5.2, Germany bernard.fedelich@bam.de
A. Ganczarski	Institute of Applied Mechanics, Cracow University of Technology, Poland artur.ganczarski@pk.edu.pl
E. Gariboldi	Politecnico di Milano—Dip. Meccanica, Italy elisabetta.gariboldi@polimi.it
A. Gaubert	Onera, France anais.gaubert@onera.fr
P. Geantil	University of Southern California, USA geantil@usc.edu
S. Ghosh	Johns Hopkins University, USA sghosh20@jhu.edu
Y. Gorash	University of Strathclyde, Department of Mechanical Engineering, UK gorash@daad-alumni.de
X. Han	Centre des Matériaux—Mines ParisTech, France xu.han@mines-paristech.fr
S. Holdsworth	EMPA, Switzerland stuart.holdsworth@empa.ch
T. Hyde	University of Nottingham, UK thomas.hyde@nottingham.ac.uk
A. Iltchev	Onera, France alexandre.iltchev@onera.fr
G. Kang	School of Mechanics and Engineering, Southwest Jiaotong University, People's Republic of China guozhengkang@yahoo.com.cn
M. Kawai	University of Tsukuba, Japan mkawai@kz.tsukuba.ac.jp
S. Kruch	Onera, France serge.kruch@onera.fr
T. Langdon	University of Southern California, USA langdon@usc.edu
J. B. le Graverend	Onera, France jean-briac.le-graverend@onera.fr

S. Leen	Mechanical and Biomedical Engineering, College of Engineering and Informatics, NUI Galway, Ireland sean.leen@nuigalway.ie
D. Li	University of Limerick, Ireland dongfeng.li@ul.ie
J. Lin	Imperial College London, UK jianguo.lin@imperial.ac.uk
J. Lu	City University of Hong Kong, China jianlu@cityu.edu.hk
V. Marcadon	Onera, France vincent.marcadon@onera.fr
R. Marull	Laboratoire d'Étude des Microstructures (ONERA/CNRS), France roxane.marull@onera.fr
K. Maruyama	Tohoku University, Graduate School of Engineering, Japan maruyama@material.tohoku.ac.jp
T. Matsuda	University of Tsukuba, Japan matsuda@kz.tsukuba.ac.jp
T. Mayer	Empa—Swiss Federal Laboratories for Materials Science and Technology, Switzerland thomas.mayer@empa.ch
Y. Murata	Department of Materials Science and Engineering, Japan murata@numse.nagoya-u.ac.jp
N. O'Dowd	University of Limerick, Ireland noel.odowd@ul.ie
K. Ohguchi	Akita University, Japan ken@ipc.akita-u.ac.jp
N. Ohno	Nagoya University, Japan ohno@mech.nagoya-u.ac.jp
H. Riedel	Fraunhofer-Institut fuer Werkstoffmechanik, Germany hermann.riedl@iwm.fraunhofer.de
K. Sasaki	Graduate School of Engineering, Hokkaido University, Japan katsu@eng.hokudai.ac.jp
M. Sakane	Ritsumeikan University, Japan sakanem@se.ritsumei.ac.jp
S. Schmauder	IMWF University Stuttgart, Germany siegfried.schmauder@imwf.uni-stuttgart.de
V. Silberschmidt	Loughborough University, UK V.Silberschmidt@lboro.ac.uk
D. Smith	University of Bristol, UK David.Smith@bristol.ac.uk
S. Spigarelli	DIISM, Università Politecnica delle Marche, Italy s.spigarelli@univpm.it

M. Spindler EDF Energy Gloucester, UK
mike.spindler@edf-energy.com
T. Sumigawa Kyoto University, Japan
Y. Takahashi Central Research Institute of Electric Power Industry, Japan
yukio@criepi.denken.or.jp
V. Vorontsov Imperial College London, UK
vassili.vorontsov@googlemail.com
G. Voyiadjis Louisiana State University, USA
voyiadjis@eng.lsu.edu

Final Program

April 23 (Monday)

10:00–10:15 Opening Address—**Serge Kruch**
10:15–11:00 **General Lecture**
(Chairperson: Noel O'Dowd)

Micromechanical studies of deformation, lattice rotation, stress, and crack nucleation in single and polycrystal materials
Fionn Dunne, Mehmet Kartal, and Caoimhe Sweeney

11:00–12:10 **Crystal Plasticity (1)**
(Chairperson: Noel O'Dowd)

Dwell Fatigue Initiation in Polycrystalline Ti Alloys Using Multi-Time Scaling Crystal Plasticity FE Models
Somnath Ghosh
Length scale effects in generalised continuum crystal plasticity
Esteban P. Busso, Nicolas Cordero, and Samuel Forest

13:30–14:15 **General Lecture**
(Chairperson: Fionn Dunne)

Lifetime prediction for low cycle and thermo-mechanical fatigue—cyclic plasticity, microcrack growth, and microstructural evolution
Hermann Riedel

14:15–16:00 **Mechanical Modelling (1)**
(Chairperson: Fionn Dunne)

An exploration of the interaction between residual stress and applied loading of high temperature structures
David Smith, Chris Truman, Yiqiang Wang, and Anil Shirahatti

Modelling of coupled dissipative phenomena in engineering materials
Halina Egner, Władysław Egner
Multiscale Optimization of Joints of Dissimilar Materials in Nature and Lessons for Engineering Applications
Victor Birman, Yanxin Liu, Stavros Thomopoulos, and Guy M. Genin

16:30–18:15 **Mechanical Modelling (2)**
(Chairperson: Victor Birman)

Mechanics of materials for microelectronic components and packages
Vadim V. Silberschmidt
An investigation of the mechanical properties of open cell aluminium foam struts: microtensile testing and modelling
Charles Betts, Jianguo Lin, and Daniel Balint
Viscoplastic Constitutive Model to Divide Inelastic Strain into Time-Independent and Time-Dependent Strains
Ken-ichi Ohguchi and Katsuhiko Sasaki

April 24 (Tuesday)

9:00–9:45 **General Lecture**
(Chairperson: Amine Benzerga)

Microstructural modelling and characterization of deformation in polycrystalline steels
Noel P. O'Dowd, Dong-Feng Li, Catrin M. Davies, and Shu-Yan Zhang

9:45–10:55 **Crystal Plasticity (2)**
(Chairperson: Amine Benzerga)

A microstructure sensitive model to account for the non-isothermal creep behavior of Ni-based single crystal superalloys
Jonathan Cormier, J. Ghighi, J.-B. Le Graverend, T. Link, L. Dirand, Z. Hervier, E. Ostoja-Kuczynski, S. Kruch, F. Gallerneau, J. Mendez, and G. Cailletaud
A cyclic crystal plastic model considering both dislocation slipping and twining for Ti-6Al-4V alloy
Chao Yu and **Guozheng Kang**

11:25–12:35 **Crystal Plasticity (3)**
(Chairperson: Masamichi Kawai)

Advances and open issues about the microscopical and the macroscopical modelling of single crystal superalloys
Bernard Fedelich
A strain rate sensitive formulation to account for the effect of γ' rafting on the high temperature mechanical properties of Ni-based single crystal superalloys
Jean-Briac le Graverend, J. Cormier, S. Kruch, F. Gallerneau, and J. Mendez

13:30–14:15 **General Lecture**
(Chairperson: Nobutada Ohno)

Homogenization based continuum damage mechanics model for monotonic and cyclic damage in 3D composites
Somnath Ghosh

14:15 – 15:25 **Continuum Damage Mechanics (1)**
(Chairperson: Nobutada Ohno)

High-temperature inelastic behavior of the austenitic steel AISI type 316
Yevgen Gorash and Holm Altenbach
Damage deactivation of engineering materials and structures
Artur Ganczarski and Marcin Cegielski

15:55–17:40 **Continuum Damage Mechanics (2)**
(Chairperson: Somnath Ghosh)

Kelvin modes based cubic plasticity and induced anisotropic damage. Application to creep of AM1 single crystal
Roxane Marull and Rodrigue Desmorat
Modelling of microstructural degradation during long-term high-temperature creep of strength enhanced high Cr ferritic steel
Kouichi Maruyama, R. P. Chen, J. Nakamura, and M. Igarashi
Micro-mechanical numerical studies on the stress state dependence of ductile damage
Michael Brünig, Steffen Gerke, and Vanessa Hagenbrock

April 25 (Wednesday)

9:00–9:45 **General Lecture**
(Chairperson: Ahmed Benallal)

Some consequences of stress range-dependent constitutive models in creep
James T. Boyle

9:45–10:55 **Coupled Fields (1)**
(Chairperson: Ahmed Benallal)

Power-law creep from discrete dislocation dynamics simulations
Amine A. Benzerga and S. M. Keralavarma
Modelling the creep threshold stress due to climb of a dislocation in the stress field of a misfitting precipitate
Matthew E. Krug and **David C. Dunand**

11:25–12:35 **Coupled Fields (2)**
(Chairperson: David Dunand)

Phase-field simulation of microstructural evolution in nickel-based superalloys during creep and in low carbon steels during martensite transformation
Yoshinori Murata, Yuhki Tsukada, and Toshiyuki Koyama
Application of the phase field model of dislocations to the study of high-temperature mechanical behavior of Ni-base superalloys.
Vassili A. Vorontsov, R. E. Voskoboinikov, and C. M. F. Rae

13:30–14:15 **General Lecture**
(Chairperson: David Smith)

From reheat cracking to improved creep damage models
Mike W. Spindler

14:15–15:25 **Material Science (1)**
(Chairperson: David Smith)

Dislocation-induced internal stresses
Peter Geantil, Benoit Devincre, Michael E. Kassner
Recent advances in the processing and properties of ultrafine-grained metals using severe plastic deformation
Terence G. Langdon

15:55–17:40 **Material Science (2)**
(Chairperson: Jian Lu)

Microscale Residual Stresses due to Nanoscale Precipitates
Siegfried Schmauder
Enriched digital image correlation for precise characterization of time-dependent metallic microbeam bending
Lambert I. J. C. Bergers, J. P. M. Hoefnagels, J. Neggers, and M. G. D. Geers
Fatigue and Fracture criterion in nano-components
Takayuki Kitamura, **Takashi Sumigawa**, and Takahiro Shimada

April 26 (Thursday)

9:00–9:45 **General Lecture**
(Chairperson: Esteban Busso)

The Effect of Temperature on Interfacial gradient plasticity in Metallic Thin Films
George Z. Voyiadjis and Danial Faghihi

9:45–10:55 **Cyclic Plasticity (1)**
(Chairperson: Esteban Busso)

A masing-type modelling concept for cyclic plasticity at elevated temperature
Thomas Mayer, E. Mazza, and S. R. Holdsworth
On the non saturation of cyclic plasticity law: a power law for kinematic hardening.
Rodrigue Desmorat

11:25–12:35 **Cyclic Plasticity (2)**
(Chairperson: George Voyiadjis)

Multiaxial Low Cycle Fatigue for Ni-base Single Crystal Super Alloy at High Temperature
Masao Sakane, Shengde Zhang, Akira Yoshinari, Noriaki Matsuda, and Nobuhiro Isobe
Finite element modelling of the thermo-mechanical behavior of A 9Cr martensitic steel
Sean B. Leen, Peter E. O'Donoghue, and **Richard A. Barrett**

13:30–14:15 **General Lecture**
(Chairperson: Sean B. Leen)

Effect of orientation on the creep and creep crack growth properties of 2xxx aluminum alloy forgings.
Elisabetta Gariboldi, A. Lo Conte

14:15–15:25 **Creep Modelling and Interactions (1)**
(Chairperson: Sean Leen)

Constitutive models for the description of creep and plasticity of cast and wrought Mg-Al and Mg-Zn alloys
Stefano Spigarelli, and M. El Mehtedi
An overview of small specimen creep testing
Thomas H. Hyde, W. Sun, and C. J. Hyde

15:55–17:40 **Creep Modelling and Interactions (2)**
(Chairperson: Elisabetta Gariboldi)

A Grand Master Curve Approach for off-axis creep rupture behavior of orthotropic polymer matrix composites at different temperatures
Masamichi Kawai
Deformation and failure of various alloys under creep-fatigue loading and their modelling
Yukio Takahashi
Creep crack growth modelling in 316H stainless steel
Catrin M. Davies, A. Mehmanparast, K. M. Nikbin

April 27 (Friday)

9:00–9:45 **General Lecture**
(Chairperson: Holm Altenbach)

Homogenized elastic-viscoplastic behavior of anisotropic open-porous bodies with pore pressure
Nobutada Ohno, Kazutaka Ikenoya, Dai Okumura, and Tetsuya Matsuda

9:45–10:55 **Multiscale Modelling (1)**
(Chairperson: Holm Altenbach)

Micromechanical modelling of void healing
Shireen Afshan, D. Balint, J. Lin, and D. Farrugia
Multiscale mechanics for the study of high strength and high ductility nanomaterials
Jian Lu, L. L. Zhu, H. L. Chan, A. Y. Chen, and H. N. Kou

11:25–13:10 **Multiscale Modelling (2)**
(Chairperson: Jianguo Lin)

Macro/Micro Elastic-Viscoplastic Analysis of Woven Composite Laminates with Misaligned Woven Fabrics
Tetsuya Matsuda, S. Kanamaru, N. Honda, and N. Ohno
Surface viscoelasticity and effective properties of materials and structures
Holm Altenbach and Victor Eremeyev
A Micromechanical model for the mechanical behaviour of irradiated austenitic stainless steels
Xu Han, Jacques Besson, Samuel Forest, and Benoît Tanguy

13:10 Closing Address—**Serge Kruch**

Preface

The IUTAM symposium "Advanced Materials Modelling for Structures", held in Paris in April 23–27, 2012, was co-organised by Onera (The French Aerospace Lab) and the Ecole des Mines de Paris under the auspice of the International Union of Theoretical and Applied Mechanics. The meeting was a new version of the previous IUTAM symposia "Creep in Structures" proposed every 10 years (Stanford, U.S.A., 1960; Gothenburg, Sweden, 1970; Leicester, U.K., 1980; Cracow, Poland, 1990; Nagoya, Japan, 2000) to discuss recent advances and results in this fundamental field of applied mechanics [1–5].

These last years an important progress was observed in testing practice for high temperature behaviour as well as in observation techniques, giving important information on deformation patterns and damage evolutions in interaction with the material microstructure which can be used to propose more physically based constitutive models. At the same time, the research fields in solid mechanics and particularly the modelling of advanced materials have evolved considerably thanks to the development of multiscale approaches. Although some progress has been made in the theoretical field, the application of multi-scale modelling to compute real components subjected to strong thermo-mechanical loads is still at an early stage, with different groups around the world following a wide range of approaches. This is particularly the case for high temperature structures where nonlinear phenomena, like creep, are predominant and drive lifetime.

The aims of the Symposium were not only to consolidate the advance in high temperature materials research, but also to provide a forum to discuss the new horizon placing a particular emphasis on multiscale approaches at several length-scales applied to nonlinear and heterogeneous materials. Discussion of new approaches have been emphasised from various related disciplines, including metal physics, micromechanics, mathematical and computational mechanics.

According to the spirit and following the Rule and Guidelines of IUTAM symposia, this Symposium gathered a group of active scientists and engineers researching within well-defined fields. The single session format conference gave the opportunity for in-depth discussions between delegates and for young doctorate students to interact with seniors. The Symposium brought together some 60

participants from 11 countries. Forty-nine invited oral presentations were divided into relatively long talks (45 min General Lectures and 35 min ordinary ones) in order to encourage interactions and discussions. Lunches taken in a single room during the conference as well as an informal dinner on a boat trip on the river Seine brought in a warm and convivial atmosphere.

A wide range of topics have been discussed during the meeting. Accordingly, the program was divided into the following main fields:

- Crystal Plasticity (3 sessions)
- Mechanical Modelling (2 sessions)
- Continuum Damage Mechanics (2 sessions)
- Coupled Fields (2 sessions)
- Material Science (2 sessions)
- Cyclic Plasticity (2 sessions)
- Creep Modelling and Interactions (2 sessions)
- Multiscale Modelling (2 sessions)

The editors wish to thank all the authors and delegates for their contribution. After reviewing, 32 papers are finally presented in this volume that aims to become a helpful and valuable reference in the field of mechanics for scientists as well as for engineers.

The success of this event is due to the help of many people. We would like to thank the International Scientific Committee, the Organising Committee and the session chairpersons who were really effective in leading discussions. Our special thanks are extended to Prof. David Hayhurst for his encouraging support in the preparation of this conference. We would like to express our thanks to the editorial staff of Springer-Verlag for their co-operation in publishing this volume.

Magdeburg, November 2012 Holm Altenbach
Paris Serge Kruch

References

1. Hoff, N.J. (ed.): Creep in Structures. Springer, Berlin (1962)
2. Hult, J. (ed.): Creep in Structures. Springer, Berlin (1972)
3. Ponter, A.R.S., Hayhurst, D.R. (eds.): Creep in Structures. Springer, Berlin (1981)
4. Zyczkowski, M. (ed.): Creep in Structures. Springer, Berlin (1991)
5. Murakami, S., Ohno, N. (eds): IUTAM Symposium on Creep in Structures. Kluwer, Dordrecht (2001)

Contents

Micromechanical Modelling of Void Healing

Shireen Afshan, Daniel Balint, Jianguo Lin and Didier Farrugia

Abstract Predicting effective consolidation or level of remnant porosity for a range of steel grade (function of solidification regime), billet size, pass schedule/roll design and thermo-mechanical conditions has always been an important issue for steel producers as it will affect the mechanical properties of final products (strength, ductility, etc.). It is known that partial or complete recovery of strength in such porous materials can be obtained by pore closure and diffusive healing processes at elevated temperature. This study investigates the elimination of porosity through two stages of void closure and healing. An Abaqus/UMAT has been developed for the analysis of the material porosity elimination process including two stages of void closure and healing. The model uses the Gurson-Tvergaard (GT) model under compression to predict the void closure. The closure model parameters were calibrated by an optimisation technique using a representative volume element concept. Then a healing model based on a combination of diffusion bonding, creep and plasticity was implemented as a UMAT subroutine and finally the whole behaviour of the material was controlled using a status check method developed in this work.

1 Introduction

High-temperature internal damage healing and microstructurally related processes have been the subject of significant interest and study for many years. Void elimination can be investigated through two stages. The first stage is void closure when the void shrinks to a slit (crack) as a result of compression. At the end of this stage the surfaces of the slit may not be bonded properly and will be separated easily by further

S. Afshan (✉) · D. Balint · J. Lin
Department of Mechanical Engineering, Imperial College London, London SW6 2EP, UK
e-mail: s.afshan09@imperial.ac.uk

D. Farrugia
Swinden Technology Centre, Tata UK Ltd, Moorgate, Rotherham S60 3AR, UK

H. Altenbach and S. Kruch (eds.), *Advanced Materials Modelling for Structures*,
Advanced Structured Materials 19, DOI: 10.1007/978-3-642-35167-9_1,

application of a small tension. A strong bond which has the mechanical properties of the original material is obtained in the second stage when the surfaces of the void are bonded.

The problem of void closure has been studied by many researchers and great progress has been made to identify the parameters that affect the behaviour of voids during hot rolling or forging. Some of these studies generally have dealt with the combination of parameters such as the effects of rolling reduction, die geometry (die shape and size) and the rate of deformation [5, 12, 17, 18, 22]. Other parameters such as pressure, temperature and time have also been investigated [9, 26]. It is well known that void closure is more easily and quickly obtained if plastic deformation takes place under the influence of compressive hydrostatic pressure. Wang et al. [23] found that pore closure occurs at a certain level of hydrostatic pressure and speeds up at high temperatures. It was also shown that the holding period of the pressure in the compressive state affects the degree of healing.

Void healing has been studied as the final stage of crack healing [23, 24] and metal bonding [4, 7]. In crack healing, pore formation is due to crack splitting whereas in metal bonding, voids form as a result of deformation of surface asperities. There have been many attempts to model the void shrinkage process, however these models use different approaches. The discrepancies arise from the varied origins of the models. Some of the models [2, 3, 11] originated from powder sintering models, whereas others [7] were developed from void growth models, where void shrinkage was considered as negative void growth [10, 16].

Attempts to model diffusion bonding of different shapes of voids can be found in the literature. In some cases the original surface has been modelled as a series of long parallel straight-sided ridges [3, 4]. Other works have been carried out based on the assumption that the surfaces to be bonded consisted of parallel, semicircular grooves with unit length and width [14]. Attempts to model diffusive shrinkage of spherical and spheroidal voids have also been made [19, 25], where expressions have been derived for the shrinkage rate as a function of the void spacing, the applied stress, the internal pressure built up by the gas filled in the void as well as relevant material parameters.

This study investigates the applicability of the Gurson-Tvergaard (GT) model [8, 20, 21] to predict void closure under compressive stress states. A FE model is developed which applies the closure model parameters from an automated calibration algorithm [1] and simulates the healing process, predicting the healing extent and the healing time as a function of physical and material properties.

2 Model

An Abaqus/UMAT has been developed for the analysis of the material porosity elimination process including two stages of void closure and healing. The model uses reverse GT to predict void closure, where as a result of compression the void

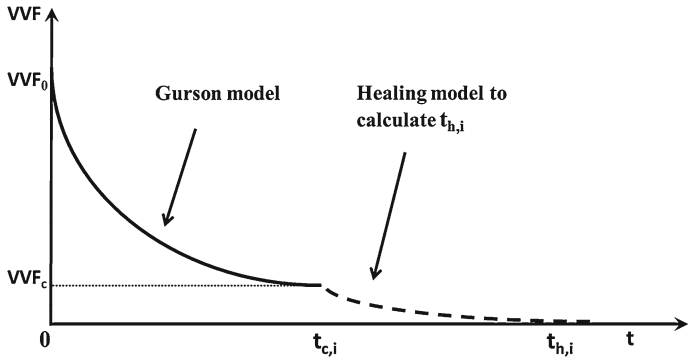

Fig. 1 The change in VVF with time as a result of reverse Gurson and healing model

volume fraction (VVF) of the material reduces to a point, after which it does not decrease any more. This is the point when a void is assumed to be closed (Fig. 1).

In order to estimate the time required for healing, pores are assumed to be small cylinders. This study applies the model proposed by Pilling [13–15] to predict the healing time.

The voids in different positions experience varying stress states and will close at different times and under different pressures. Therefore at each time increment characteristics of each element should be monitored. This requires the definition of an array storing the stress conditions, healing process and finally the element status. Defining I as,

$$I_k^{i,j} = [S^i, t_c^i, t_h^i, \sigma_{e,k}^i, P_k^i]$$

in which i is the element number, j is the number of parameters/properties associated with I (here $j = 5$) and k is the increment number; t_c, is the time at which the void closes, t_h is the time required for healing, σ_e is the equivalent stress of the element (this is required in calculation of the healing time), P is the pressure under which the void closure happens and S represents the status of the element which is defined as follows,

$$S^i = \begin{cases} 0 & \text{if } vvf_k^i < vvf_c \\ 1 & \text{if } vvf_k^i \geq vvf_c \end{cases}$$

The above definition means that the element status is defined as zero for a void which has not yet been closed and as one if the element's void volume fraction (vvf) has reached the void volume fraction at closure (vvf_c).

It is evident that at the initial state (before the process starts), I is empty or in other words, $I_0^{i,j} = 0$. As the compression starts, the void volume fraction of each element would be checked. If an element reaches the vvf_c, additional application of the reverse GT model will not heal the void. For healing to take place the material has to be held at a certain pressure and temperature for some time. A model is therefore

required to predict the bonding time as a function of physical and material properties of the test.

Once an element closes the healing time (t_h) will be calculated for that particular element depending on its stress state. Every time an element heals, the extent of healing (defined as the percentage of the healed elements of the whole FE model) is calculated. However, the load distribution might be such that some elements experience less pressure and consequently remain unclosed; therefore a healing of 100 % might not occur.

While elements are checked for closure status, the stress state of those elements which have already been closed might change from compression to tension. In that case since the elements have not been completely healed they might reopen again. To check this situation the change in *vvf* is monitored at each time increment. A positive change in the *vvf* implies that the element is under tension and the void is growing. In that case if the *vvf* of that element exceeds the vvf_c the element status has to be changed from closed ($S = 1$) to open ($S = 0$). The flow chart in Fig. 2 represents the structure of the model for the void elimination process.

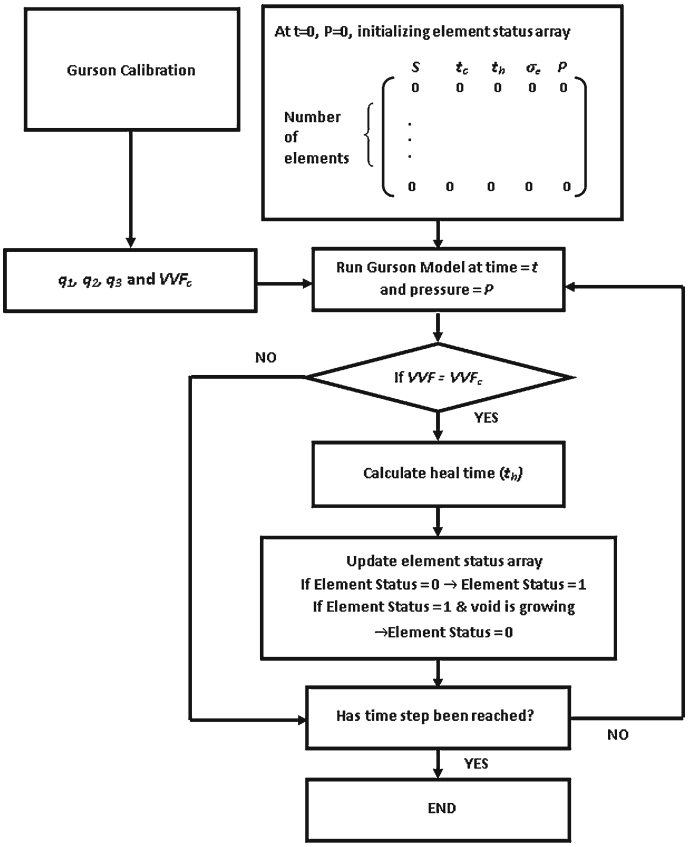

Fig. 2 The developed UMAT structure

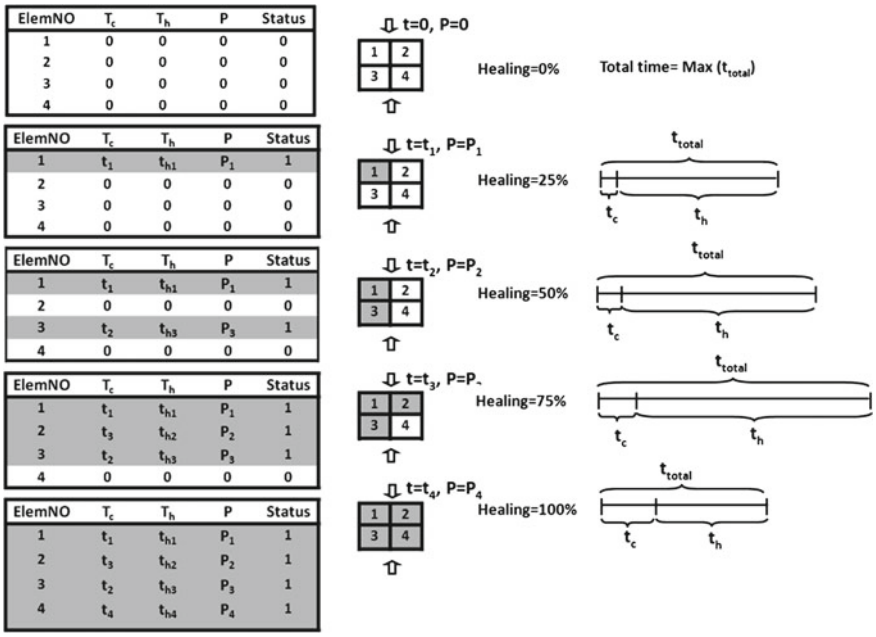

Fig. 3 Illustration of the void healing process

Practically, after each element is closed the bonding time should be implemented for that element. But since the healing times for different elements could be long the problem of simulating real time emerges. To overcome this problem the elements will only be checked for closure. The healing times would then be calculated individually for each element. The total time required for the whole process will then be obtained as the maximum closure and healing time summation. The process has been illustrated in Fig. 3.

3 Results

An axisymmetric model of a cylinder of material with a central porous zone was constructed using Abaqus/Standard, a schematic of which is shown in Fig. 4. The developed UMAT was applied to the porous section and the outer section was given elastic plastic properties of a free cutting steel grade obtained experimentally at 900 °C and $\dot{\varepsilon} = 0.1$ [6]. The cylinder was initially compressed, held under pressure for some time and then stretched. Figure 5 compares the variation in VVF for a model with the developed closure-healing UMAT and the same model with the reverse Gurson (Closure) UMAT.

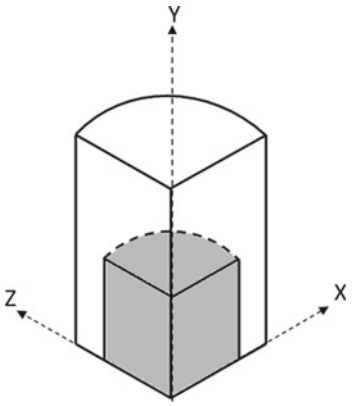

Fig. 4 The cylindrical model with defined central porous zone

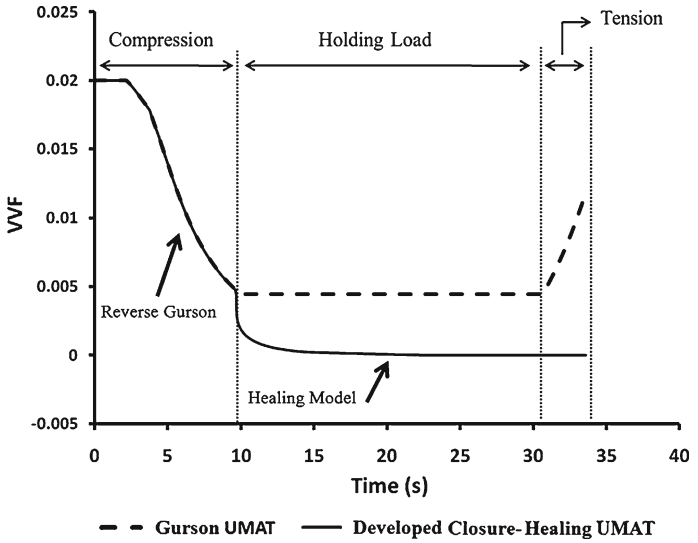

Fig. 5 The comparison of the Gurson UMAT and the developed closure-healing UMAT

As the results show for the Gurson UMAT model, where the void has been only closed and not healed the VVF will increase as a result of tension whereas for the developed closure-healing UMAT the VVF will remain zero, indicating the void healing process has taken place.

The process of void healing is represented in Fig. 6, where the extent of healing is shown at different time increments.

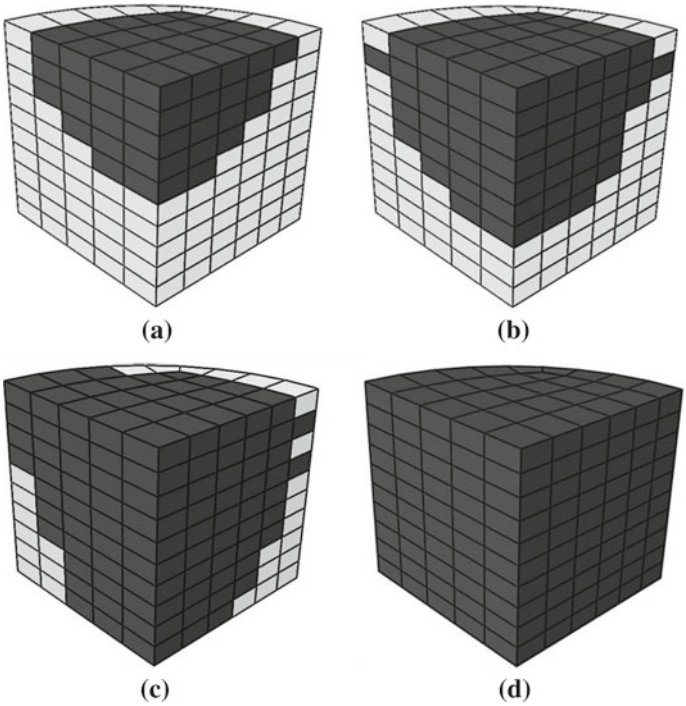

Fig. 6 Extent of healing at **a** t = 9.84 s, **b** t = 9.93 s, **c** t = 9.93 s and **d** t = 10 s

4 Conclusion

An Abaqus/UMAT has been developed for the analysis of the material porosity elimination process. The calibrated q parameters for certain triaxiality and initial VVF are fed into the UMAT to predict Void Closure. Pilling's healing model [13] has been implemented into the UMAT to predict the change in VVF with time as a function of physical conditions and material properties.

References

1. Afshan, S., Balint, D., et al.: Automated calibration of a void closure model for high-temperature deformation. J. Multiscale Model. **3**(1–2), 79–90 (2011)
2. Artz, E., Ashby, M.F., et al.: Practical applications of hotisostatic pressing diagrams: four case studies. Metall. Mater. Trans. A **14**(1), 211–221 (1983)
3. Derby, B., et al.: Theoretical model for diffusion bonding. Metal Sci. **16**(1), 49–56 (1982)
4. Derby, B., Wallach, E.R.: Diffusion bonds in copper. J. Mater. Sci. **19**(10), 3140–3148 (1984)
5. Dudra, S.P., Young-Taek, I.: Analysis of void closure in open-die forging. Int. J. Mach. Tools Manuf. **30**(1), 65–75 (1990)

6. Foster, A.: Ph.D. University of Birmingham, Birmingham (2007)
7. Guo, Z.X., et al.: Modelling of diffusion bonding of metals. Mater. Sci. Technol. **3**(11), 945–953 (1987)
8. Gurson, A.L.: Continuum theory of ductile rupture by void nucleation and growth: part I—yield criteria and flow rules for porous ductile media. J. Eng. Mater. Technol. Trans. ASME **99**, 2–15 (1977)
9. Han, J., Zhao, G., et al.: Internal crack recovery of 20MnMo steel. Sci. China Ser. E Technol. Sci. **40**(2), 164–169 (1997)
10. Hancock, J.W.: Creep cavitation without a vacancy flux. Metal Sci. **10**(9), 319–325 (1976)
11. Hill, A., Wallach, E.R.: Modelling solid-state diffusion bonding. Acta Metall. **37**(9), 2425–2437 (1989)
12. Park, C.Y., Yang, D.Y.: Modelling of void crushing for large-ingot hot forging. J. Mater. Process. Technol. **67**(1–3), 195–200 (1997)
13. Pilling, J.: The kinetics of isostatic diffusion bonding in superplastic materials. Mater. Sci. Eng. **100**, 137–144 (1987)
14. Pilling, J., Ridely, N.: Solid state bonding of superplastic AA 7475. Mater. Sci. Technol. **3**(5), 353–359 (1987)
15. Pilling, J., Ridley, N., et al.: On the modelling of diffusion bonding in materials: superplastic Super Alpha-2. Mater. Sci. Eng. A **205**(1–2), 72–78 (1996)
16. Rimmer, D.: The growth of grain-boundary voids under stress. Philos. Mag. **4**, 673–687 (1959)
17. Stahlberg, U.: Influence of spread and stress on the closure of a central longitudinal hole in the hot rolling of steel. J. Mech. Work. Technol. **13**(1), 65–81 (1986)
18. Stahlberg, U., H. keife, et al.: A study of void closure during plastic deformation. J. Mech. Work. Technol. **4**(1), 51–63 (1980)
19. Sun, J.: A model for shrinkage of a spherical void in the center of a grain: influence of lattice diffusion. J. Mater. Sci. Perform. **11**(3), 322–331 (2002)
20. Tvergaard, V.: Influence of voids on shear band instabilities under plane strain conditions. Int. J. Fract. **17**(4), 389–407 (1981)
21. Tvergaard, V.: On localization in ductile materials containing spherical voids. Int. J. Fract. **18**(4), 237–252 (1982)
22. Wallero, A.: Closing of a central longitudinal pore in hot rolling. J. Mech. Work. Technol. **12**(2), 233–242 (1985)
23. Wang, A., Thomson, P.F., et al.: A study of pore closure and welding in hot rolling process. J. Mater. Process. Technol. **60**, 1996 (1996)
24. Wang, H., Huang, P., et al.: Crack and void healing in metals. In: Zwaag, S.v.d. (ed.) Self Healing Materials, An Alternative Approach to 20 Centuries of Materials Science, vol. 100, pp. 255–277. Springer, Dordrecht (2008)
25. Wang, H., Li, Z.: The three-dimensional analysis for diffusive shrinkage of a grain-boundary void in stressed solid. J. Mater. Sci. **39**(10), 3425–3432 (2004)
26. Wei, D., Han, J., et al.: A study on crack healing in 1045 steel. J. Mater. Process. Technol. **177**(1–3), 233–237 (2006)

Surface Viscoelasticity and Effective Properties of Materials and Structures

Holm Altenbach and Victor A. Eremeyev

Abstract In this paper we discuss the influence of surface viscoelasticity on the effective properties of materials such as effective bending stiffness of plates or shells. Viscoelasticity in the vicinity of the surface can differ from the properties of the bulk material, in general. This difference influences the behavior of nanosized thin elements. In particular, the surface viscoelastic stresses are responsible for the size-depended dissipation of nanosized structures. Extending of the Gurtin-Murdoch model and using the correspondence principle of the linear viscoelasticity we derive the expressions of the stress resultant tensors for shear deformable plates and shells.

1 Introduction

The surface effects play an important role for such nanosized materials as films, nanoporous materials, etc., while in this case the influence of surface is more significant. The mechanics of solids which takes into account explicitly the phenomenon of surface stresses was proposed by Gurtin and Murdoch [1]. Within the framework of the theory of surface stresses an elastic body can be considered as a "usual" elastic body with elastic membrane glued on its surface. Unlike to classical mechanics of materials where the surface stresses can be neglected in most cases, at the micro- and nanoscale the surface stresses play an important role. For example, they influence the effective or apparent properties of very thin specimens and predict the so-called

H. Altenbach (✉) · V. A. Eremeyev
Faculty of Mechanical Engineering, Otto-von-Guericke-University,
39106 Magdeburg, Germany
e-mail: holm.altenbach@ovgu.de

V. A. Eremeyev
South Scientific Center of RASci & South Federal University, Milchakova St. 8a,
Rostov on Don 344090, Russia
e-mail: eremeyev.victor@gmail.com; victor.eremeyev@ovgu.de

H. Altenbach and S. Kruch (eds.), *Advanced Materials Modelling for Structures*,
Advanced Structured Materials 19, DOI: 10.1007/978-3-642-35167-9_2,

size effect, that is dependence of apparent material properties on a specimen size. Hence, the classical continuum mechanics can be extended at the nanoscale taking into account surface stresses acting on the boundary of a nanosized body, see [2, 3]. In the literature are presented various applications of the Gurtin-Murdoch model in nanomechanics, see, for example, the review [4]. In particular, the theory of elasticity with surface stresses is used in the two-dimensional theories of nanosized plates and shells, see [5–13]. Let us note that in most of papers the elastic medium is considered. On the other hand, inelastic behavior analysis is also important in micro- and nanomechanics. Dissipative processes in the vicinity of the surface are related to the higher mobility of molecules, surface imperfections, absorbates, etc., see [14] among others. For the description of surface dissipation of nanosized beams, Ru [15] was proposed one-dimensional constitutive law that is similar to the model of the standard viscoelastic solids but formulated for the two-dimensional surface stresses.

Following [16] in this paper we consider the influence of surface viscoelasticity on the effective or apparent properties of nanosized thin-walled structures. We recall the basic equations of the continuum with surface stresses and use the more general constitutive viscoelastic model for the surface stresses than the proposed by Ru [15]. Using the correspondence principle, we present the governing equations of plates and shells with viscoelastic surface stresses. Here we assume that the bulk material is elastic while the surface has viscoelastic properties. We formulate the two-dimensional (2D) constitutive equations and obtain the 2D relaxation functions for plates and shells. Finally, we compare the proposed model of shells with viscoelastic surface stresses with the model of a sandwich plate with viscoelastic faces.

2 Basic Equations of Linear Elasticity with Viscoelastic Surface Stresses

Let us consider the problem for a deformable body with surface stresses. Let $V \in \mathbb{R}^3$ is the volume of the body with the boundary $\Omega = \partial V$. For quasistatic deformations of solids with surface stresses the boundary-value problem is given by

$$\nabla \cdot \boldsymbol{\sigma} + \rho \mathbf{f} = \mathbf{0}, \quad \mathbf{x} \in V, \tag{1}$$

$$\mathbf{u}|_{\Omega_1} = \mathbf{0}, \quad \mathbf{n} \cdot \boldsymbol{\sigma}|_{\Omega_2} = \mathbf{t}, \quad \mathbf{x} \in \Omega, \tag{2}$$

where $\boldsymbol{\sigma}$ is the stress tensor, $\mathbf{u}$ the displacement vector, ∇ the 3D gradient operator (3D nabla operator), ρ the density, $\mathbf{f}$ the density of the volume forces, and $\mathbf{n}$ the external unit normal to $\Omega = \Omega_1 \bigcup \Omega_2$, $\Omega_1 \bigcup \Omega_2 = \emptyset$. The surface stress vector $\mathbf{t}$ is expressed through a given load $\boldsymbol{\varphi}$ and the stress vector due the surface stresses $\mathbf{t}_S$ by the formula [1, 2, 17]

$$\mathbf{t} = \boldsymbol{\varphi} + \mathbf{t}_S, \quad \mathbf{t}_S = \nabla_S \cdot \boldsymbol{\tau}.$$

Here τ is the surface stress tensor on Ω, ∇_S is the surface nabla operator on Ω given by $\nabla_S = \nabla - \mathbf{n}\partial/\partial z$, where z is the coordinate along the normal to Ω.

For the sake of simplicity, we restrict ourselves to an isotropic material. We also assume that the bulk material is elastic but the surface stresses are viscoelastic. Hence, we have the Hooke law for the bulk material

$$\boldsymbol{\sigma} = 2\mu\boldsymbol{\varepsilon} + \lambda\mathbf{I}\mathrm{tr}\,\boldsymbol{\varepsilon} \quad \text{with} \quad \boldsymbol{\varepsilon} = \boldsymbol{\varepsilon}(\mathbf{u}) \equiv \frac{1}{2}\big(\nabla\mathbf{u} + (\nabla\mathbf{u})^T\big), \tag{3}$$

where $\boldsymbol{\varepsilon}$ is the strain tensor, λ and μ are Lamé's moduli, and $\mathbf{I}$ is the three-dimensional unit tensor, respectively.

For the surface stresses we assume the following constitutive equation

$$\boldsymbol{\tau} = 2\int_{-\infty}^{t} \mu_S(t-\tau)\dot{\mathbf{e}}(\tau)\,d\tau + \int_{-\infty}^{t} \lambda_S(t-\tau)\mathrm{tr}\,\dot{\mathbf{e}}(\tau)\,d\tau\mathbf{A}, \tag{4}$$

$$\mathbf{e} = \mathbf{e}(\mathbf{v}) \equiv \frac{1}{2}\big(\nabla_S\mathbf{v}\cdot\mathbf{A} + \mathbf{A}\cdot(\nabla_S\mathbf{v})^T\big),$$

where $\mathbf{e}$ is the surface strain tensor, $\mathbf{v}$ the displacement of the surface point $\mathbf{x}$ of Ω_2, $\mathbf{A} \equiv \mathbf{I} - \mathbf{n}\otimes\mathbf{n}$ the two-dimensional unit tensors, the overdot denotes differentiation with respect to time t, and λ_S and μ_S are the relaxation functions of the surface film Ω_2, respectively.

Following [1, 17], we state that the displacements of the surface film Ω_2 coincide with the body displacements on the boundary $\mathbf{v} = \mathbf{u}|_{\Omega_2}$.

The integral constitutive law (4) contains the viscoelastic constitutive equation of [15] as the special case. If μ_S and λ_S are constants then (4) reduces to the elastic constitutive equations used in [2].

The system of Eqs. (1)–(4) constitute the boundary-value problem (BVP) for the elastic body with viscoelastic surface stresses. In what follows we use this BVP to derive two-dimensional (2D) equations of shear-deformable shells.

3 Reduction to the Two-Dimensional Theory

In the literature there are known various approaches of derivation of 2D equations of plates and shells using the reduction procedure of the equations of 3D continuum mechanics. Here we apply to the nonclassical BVP (1)–(4) the through-the-thickness integration procedure described, for example, in [18].

In the case of viscoelastic material we use the correspondence principle which establishes that if an elastic solution of the problem is known, the corresponding viscoelastic solution can be obtained by substituting for the elastic quantities the Laplace transform of the unknown functions [19, 20]. In other words, one can use the solution of BVP for elastic material as the solution of BVP for viscoelastic

material but given in terms of Laplace transform. According to this principle we use the results of 3D to 2D reduction procedure for the elastic shell-like body given by [6, 7].

In fact, using the Laplace transform one can write (4) as it follows

$$\overline{\boldsymbol{\tau}} = 2s\overline{\mu}_S(s)\overline{\mathbf{e}} + s\overline{\lambda}_S(s)(\operatorname{tr}\overline{\mathbf{e}})\mathbf{A}, \quad \overline{(\ldots)}(s) = \int_0^\infty (\ldots)(t)e^{-st}\,\mathrm{d}t, \tag{5}$$

which coincides formally with the surface Hooke's law assumed in [6, 7].

The through-the-thickness integration procedure applied to shell-like bodies with surface stresses leads to the following 2D equations, see [16],

$$\nabla_S\cdot\mathbf{T} + \mathbf{q} = \mathbf{0}, \quad \nabla_S\cdot\mathbf{M} + \mathbf{T}_\times + \mathbf{m} = \mathbf{0}, \tag{6}$$

where $\mathbf{T}$ is the stress resultant tensor, $\mathbf{M}$ the couple stress tensor, $\mathbf{T}_\times$ denotes the vectorial invariant of second-order tensor $\mathbf{T}$, see [18], $\mathbf{q}$ and $\mathbf{m}$ are the surface force and couple vector fields defined as in [6, 7].

Tensors $\mathbf{T}$ and $\mathbf{M}$ can be represented each as the sums of two terms, see [5–7, 16],

$$\mathbf{T} = \mathbf{T}_b + \mathbf{T}_s, \quad \mathbf{M} = \mathbf{M}_b + \mathbf{M}_s. \tag{7}$$

Here $\mathbf{T}_b$ and $\mathbf{M}_b$ are the stress and couple stress resultant tensors related to the bulk material while $\mathbf{T}_s$ and $\mathbf{M}_s$ are the stress and couple stress resultant tensors related to the surface stresses. With the accuracy of $O(h/R)$ where h is the shell thickness and R is the maximum of the curvature radius of the shell base surface, one can use the following formulae for $\mathbf{T}_b$, $\mathbf{M}_b$, $\mathbf{T}_s$, and $\mathbf{M}_s$

$$\mathbf{T}_b = \langle \mathbf{A}\cdot\boldsymbol{\sigma}\rangle, \quad \mathbf{M}_b = -\langle \mathbf{A}\cdot z\boldsymbol{\sigma}\times\mathbf{n}\rangle, \qquad \langle(\ldots)\rangle = \int_{-h/2}^{h/2} (\ldots)\,\mathrm{d}z, \tag{8}$$

$$\mathbf{T}_s = \boldsymbol{\tau}_+ + \boldsymbol{\tau}_-, \quad \mathbf{M}_s = -\frac{h}{2}(\boldsymbol{\tau}_+ - \boldsymbol{\tau}_-)\times\mathbf{n}, \tag{9}$$

where $\boldsymbol{\tau}_\pm$ are the surface stresses acting at the shell faces, i.e. $\boldsymbol{\tau}_\pm = \boldsymbol{\tau}\big|_{z=\pm h/2}$. Equation (8) result in the following component representations

$$\mathbf{T}_b = T_{\alpha\beta}\boldsymbol{\rho}^\alpha\otimes\boldsymbol{\rho}^\beta + T_{\alpha 3}\boldsymbol{\rho}^\alpha\otimes\mathbf{n}, \quad \mathbf{M}_b = -M_{\alpha\beta}\boldsymbol{\rho}^\alpha\otimes\boldsymbol{\rho}^\beta\times\mathbf{n}, \qquad \alpha,\beta = 1,2,$$
$$T_{\alpha\beta} = \langle\sigma_{\alpha\beta}\rangle, \quad T_{\alpha 3} = \langle\sigma_{\alpha 3}\rangle, \quad M_{\alpha\beta} = \langle z\sigma_{\alpha\beta}\rangle, \tag{10}$$

where $\sigma_{\alpha\beta} = \boldsymbol{\rho}_\alpha\cdot\boldsymbol{\sigma}\cdot\boldsymbol{\rho}_\beta$, $\sigma_{\alpha 3} = \boldsymbol{\rho}_\alpha\cdot\boldsymbol{\sigma}\cdot\mathbf{n}$, $\boldsymbol{\rho}_\alpha$ and $\boldsymbol{\rho}^\beta$ are the main and reciprocal bases on the shell base surface ω with the unit normal vector $\mathbf{n}$.

In what follows we use the linear approximation of the translation vector $\mathbf{u}$

$$\mathbf{u}(z) = \mathbf{w} - z\boldsymbol{\vartheta}, \quad \mathbf{n}\cdot\boldsymbol{\vartheta} = 0. \tag{11}$$

This approximation is used in the theories of shear-deformable plates and shells, see, e.g., [18], $\mathbf{w}$ is the translation vector of the shell base surface ω and $\boldsymbol{\vartheta}$ is the rotation vector of the shell normal. Both are kinematically independent each other.

For the isotropic shell dependence of $\mathbf{T}_b$ and $\mathbf{M}_b$ on strain measures is given by

$$\begin{gathered}\mathbf{T}_b = C_1\boldsymbol{\varepsilon} + C_2\mathbf{A}\mathrm{tr}\,\boldsymbol{\varepsilon} + \Gamma\boldsymbol{\gamma}\otimes\mathbf{n}, \quad \mathbf{M}_b = -\left[D_1\boldsymbol{\kappa} + D_2\mathbf{A}\mathrm{tr}\,\boldsymbol{\kappa}\right]\times\mathbf{n}, \\ C_1 = 2C_{22}, \quad C_2 = C_{11} - C_{22}, \quad D_1 = 2D_{22}, \quad D_2 = D_{33} - D_{22}.\end{gathered} \tag{12}$$

where $\boldsymbol{\varepsilon}$, $\boldsymbol{\kappa}$, and $\boldsymbol{\gamma}$ are strain measures introduced by

$$\boldsymbol{\varepsilon} = \frac{1}{2}\left(\nabla_S\mathbf{w}\cdot\mathbf{A} + \mathbf{A}\cdot(\nabla_S\mathbf{w})^T\right), \quad \boldsymbol{\kappa} = \frac{1}{2}\left(\nabla_S\boldsymbol{\vartheta}\cdot\mathbf{A} + \mathbf{A}\cdot(\nabla_S\boldsymbol{\vartheta})^T\right),$$
$$\boldsymbol{\gamma} = \nabla_S(\mathbf{w}\cdot\mathbf{n}) - \boldsymbol{\vartheta},$$

and the components C_{11}, C_{22}, D_{22}, D_{33}, and Γ are given by

$$\begin{aligned} C_{11} &= \frac{Eh}{2(1-\nu)}, & C_{22} &= \frac{Eh}{2(1+\nu)}, \\ D_{22} &= \frac{Eh^3}{24(1+\nu)}, & D_{33} &= \frac{Eh^3}{24(1-\nu)}, \quad \Gamma = k\mu h, \\ E &= 2\mu(1+\nu), & \nu &= \frac{\lambda}{2(\lambda+\mu)}, \\ C \equiv C_{11} + C_{22} &= \frac{Eh}{1-\nu^2}, & D \equiv D_{11} + D_{22} &= \frac{Eh^3}{12(1-\nu^2)}, \end{aligned}$$

where E and ν are the Young modulus and Poisson ratio of bulk material. C and D are the tangential and bending stiffness of the shell, Γ is the transverse shear stiffness, and k the transverse shear factor, respectively.

Let us consider the constitutive equations for $\mathbf{T}_s$ and $\mathbf{M}_s$. For simplicity we assume the same viscoelastic behaviour of both shell faces. From (11) it follows the relations

$$\begin{aligned}\boldsymbol{\tau}_\pm = &\int_{-\infty}^{t} \lambda_S(t-\tau)\mathrm{tr}\,\dot{\boldsymbol{\varepsilon}}(\tau)\,d\tau\mathbf{A} + 2\int_{-\infty}^{t}\mu_S(t-\tau)\dot{\boldsymbol{\varepsilon}}(\tau)\,d\tau \\ &\mp\frac{h}{2}\left(\int_{-\infty}^{t}\lambda_S(t-\tau)\mathrm{tr}\,\dot{\boldsymbol{\kappa}}(\tau)\,d\tau\mathbf{A} + \int_{-\infty}^{t} 2\mu_S(t-\tau)\dot{\boldsymbol{\kappa}}(\tau)\,d\tau\right).\end{aligned}$$

Finally we have, see [16],

$$\mathbf{T}_s = \int_{-\infty}^{t} \left[C_1^S(t-\tau)\dot{\boldsymbol{\varepsilon}}(\tau) + C_2^S(t-\tau)\mathbf{A}\mathrm{tr}\,\dot{\boldsymbol{\varepsilon}}(\tau) \right] d\tau, \tag{13}$$

$$\mathbf{M}_s = -\int_{-\infty}^{t} \left[D_1^S(t-\tau)\dot{\boldsymbol{\kappa}}(\tau) + D_2(t-\tau)^S\mathbf{A}\mathrm{tr}\,\dot{\boldsymbol{\kappa}}(\tau) \right] d\tau \times \mathbf{n}, \tag{14}$$

$$C_1^S = 4\mu_S, \quad C_2^S = 2\lambda_S, \quad D_1^S = h^2\mu_S, \quad D_2^S = h^2\lambda_S/2.$$

As a result from (7), (13), and (14) we derive the constitutive equations of the shell with viscoelastic surface stresses in the form

$$\mathbf{T} = \int_{-\infty}^{t} \left[C_1(t-\tau)\dot{\boldsymbol{\varepsilon}}(\tau) + C_2(t-\tau)\mathbf{A}\mathrm{tr}\,\dot{\boldsymbol{\varepsilon}}(\tau) \right] d\tau + \Gamma\boldsymbol{\gamma} \otimes \mathbf{n},$$

$$\mathbf{M} = -\int_{-\infty}^{t} \left[D_1(t-\tau)\dot{\boldsymbol{\kappa}}(\tau) + D_2(t-\tau)\mathbf{A}\mathrm{tr}\,\dot{\boldsymbol{\kappa}}(\tau) \right] d\tau \times \mathbf{n},$$

$$C_1(t) = 2C_{22} + 4\mu_S(t), \quad C_2(t) = C_{11} - C_{22} + 2\lambda_S(t),$$

$$D_1(t) = 2D_{22} + h^2\mu_S(t), \quad D_2(t) = D_{33} - D_{22} + \frac{h^2}{2}\lambda_S(t).$$

The tangential and bending relaxation functions are given by

$$C = \frac{Eh}{1-\nu^2} + 4\mu_S + 2\lambda_S, \quad D = \frac{Eh^3}{12(1-\nu^2)} + \frac{h^2}{2}(2\mu_S + \lambda_S). \tag{15}$$

Let us note that the surface stresses do not influence the transverse shear stiffness.

4 Plate with Surface Stresses as Three-Layered Plate

The presented above model of plates and shells with surface stresses is similar to the theories of three-layered plates and shells that are widely presented in the literature, see [7] for the elastic case and [16] for viscoelastic faces. We consider the symmetric three-layered plate (sandwich plate) with the thickness $h = h_\mathrm{c} + 2h_\mathrm{f}$, where h_c is the thickness of core, h_f the thickness of faces, and $h_\mathrm{c} \gg h_\mathrm{f}$. We assume that the core is made of elastic material with the Young modulus E or the shear modulus μ, and Poisson ratio ν while the faces are viscoelastic with the relaxation function $E_\mathrm{f}(t)$ and the constant Poisson ratio ν_f.

Using the approach suggested in [7, 21], for the viscoelastic sandwich plate we obtain the constitutive equations in the form similar to (13) and (14) but with different expressions for relaxation functions. The tangential and bending relaxation functions of the three-layered plate are given by

$$\widetilde{C} = \widetilde{C}_{11} + \widetilde{C}_{22} = \frac{2E_{\mathrm{f}}h_{\mathrm{f}}}{1-\nu_{\mathrm{f}}^2} + \frac{Eh_{\mathrm{c}}}{1-\nu^2}, \tag{16}$$

$$\widetilde{D} = \widetilde{D}_{22} + \widetilde{D}_{33} = \frac{1}{12}\left[\frac{E_{\mathrm{f}}(h^3-h_{\mathrm{c}}^3)}{1-\nu_{\mathrm{f}}^2} + \frac{E_{\mathrm{c}}h_{\mathrm{c}}^3}{1-\nu_{\mathrm{c}}^2}\right], \tag{17}$$

$$\widetilde{C}_{11} = \frac{1}{2}\left(\frac{2E_{\mathrm{f}}h_{\mathrm{f}}}{1-\nu_{\mathrm{f}}} + \frac{Eh_{\mathrm{c}}}{1-\nu}\right), \quad \widetilde{C}_{22} = \frac{1}{2}\left(\frac{2E_{\mathrm{f}}h_{\mathrm{f}}}{1+\nu_{\mathrm{f}}} + \frac{Eh_{\mathrm{c}}}{1+\nu}\right),$$

$$\widetilde{D}_{22} = \frac{1}{24}\left[\frac{E_{\mathrm{f}}(h^3-h_{\mathrm{c}}^3)}{1+\nu_{\mathrm{f}}} + \frac{Eh_{\mathrm{c}}^3}{1+\nu}\right], \quad \widetilde{D}_{33} = \frac{1}{24}\left[\frac{E_{\mathrm{f}}(h^3-h_{\mathrm{c}}^3)}{1-\nu_{\mathrm{f}}} + \frac{Eh_{\mathrm{c}}^3}{1-\nu}\right]$$

Comparing (16) with $(15)_1$ we conclude that the surface relaxation functions λ_S and μ_S can be expressed through the relaxation function of faces E_{f}, Poisson ratio ν_{f}, and the thickness h_{f}. With accuracy of $O(h_{\mathrm{f}}^2)$ we obtain that

$$\mu_S \approx \frac{E_{\mathrm{f}}h_{\mathrm{f}}}{2(1+\nu_{\mathrm{f}})} \equiv \mu_{\mathrm{f}}h_{\mathrm{f}}, \quad \lambda_S \approx \frac{\nu_{\mathrm{f}}E_{\mathrm{f}}h_{\mathrm{f}}}{1-\nu_{\mathrm{f}}^2} \equiv \lambda_{\mathrm{f}}h_{\mathrm{f}}\frac{1-2\nu_{\mathrm{f}}}{1-\nu_{\mathrm{f}}}, \tag{18}$$

where λ_{f} is the second relaxation function of faces. Let us note that the comparison of $(15)_2$ with (17) results in the same formulae. Hence, we get

$$\mu_S = \lim_{h_{\mathrm{f}}\to 0}\mu_{\mathrm{f}}h_{\mathrm{f}}, \quad \lambda_S = \lim_{h_{\mathrm{f}}\to 0}\lambda_{\mathrm{f}}\frac{1-2\nu_{\mathrm{f}}}{1-\nu_{\mathrm{f}}}h_{\mathrm{f}}. \tag{19}$$

The latter equations give us the interpretation of the surface viscoelastic functions μ_S and λ_S through the relaxation functions of plate faces and their thickness.

5 Conclusions

Here we discuss the extension of the constitutive relations of elastic thin-walled structures with surface stresses taking into account the surface viscoelasticity. As in the Gurtin-Murdoch model of surface elasticity the linear surface viscoelasticity contains the surface stresses which depend on the surface the prehistory of strains. In the linear isotropic case these dependencies are given by the relation (4). Using the correspondence principle and the through-the-thickness integration technique of reduction of 3D equations to 2D ones we derive the constitutive equations for stress resultants and analyzed the dependence of the effective properties on bulk and surface material behaviour.

Acknowledgments The second author was supported by the DFG with the grant No. AL 341/33-1 and by the RFBR with the grant No. 12-01-00038.

References

1. Gurtin, M.E., Murdoch, A.I.: A continuum theory of elastic material surfaces. Arch. Ration. Mech. Anal. **57**(4), 291–323 (1975)
2. Duan, H.L., Wang, J., Karihaloo, B.L.: Theory of elasticity at the nanoscale. Adv. Appl. Mech. **42**, 1–68 (2008)
3. Wang, J., Duan, H.L., Huang, Z.P., Karihaloo, B.L.: A scaling law for properties of nano-structured materials. Proc. Royal Soc. Lond. A **462**(2069), 1355–1363 (2006)
4. Wang, J., Huang, Z., Duan, H., Yu, S., Feng, X., Wang, G., Zhang, W., Wang, T.: Surface stress effect in mechanics of nanostructured materials. Acta Mechanica Solida Sinica **24**(1), 52–82 (2011)
5. Altenbach, H., Eremeyev, V.A.: On the shell theory on the nanoscale with surface stresses. Int. J. Eng. Sci. **49**(12), 1294–1301 (2011)
6. Altenbach, H., Eremeyev, V.A., Morozov, N.F.: Linear theory of shells taking into account surface stresses. Doklady Phys. **54**(12), 531–535 (2009)
7. Altenbach, H., Eremeyev, V.A., Morozov, N.F.: On equations of the linear theory of shells with surface stresses taken into account. Mech. Solids **45**(3), 331–342 (2010)
8. Dahmen, K., Lehwald, S., Ibach, H.: Bending of crystalline plates under the influence of surface stress—a finite element analysis. Surf. Sci. **446**(1–2), 161–173 (2000)
9. Eremeyev, V.A., Altenbach, H., Morozov, N.F.: The influence of surface tension on the effective stiffness of nanosize plates. Doklady Phys. **54**(2), 98–100 (2009)
10. Huang, D.W.: Size-dependent response of ultra-thin films with surface effects. Int. J. Solids Struct. **45**(2), 568–579 (2008)
11. Lu, P., He, L.H., Lee, H.P., Lu, C.: Thin plate theory including surface effects. Int. J. Solids Struct. **43**(16), 4631–4647 (2006)
12. Wang, Z.Q., Zhao, Y.P.: Self-instabilityand bending behaviors of nano plates. Acta Mechanica Solida Sinica **22**(6), 630–643 (2009)
13. Zhu, H.X., Wang, J.X., Karihaloo, B.: Effects of surface and initial stresses on the bending stiffness of trilayer plates and nanofilms. J. Mech. Mat. Struct. **4**(3), 589–604 (2009)
14. Seoánez, C., Guinea, F., Castro Neto, A.H.: Surface dissipation in nanoelectromechanical systems: unified description with the standard tunneling model and effects of metallic electrodes. Phys. Rev. B **77**(12), 125107 (2008)
15. Ru, C.Q.: Size effect of dissipative surface stress on quality factor of microbeams. Appl. Phys. Lett. **94**, 051905-1–051905-3 (2009)
16. Altenbach, H., Eremeyev, V.A., Morozov, N.F.: Surface viscoelasticity and effective properties of thin-walled structures at the nanoscale. Int. J. Eng. Sci. **59**, 83–89 (2012)
17. Povstenko, Y.Z.: Theoretical investigation of phenomena caused by heterogeneous surface tension in solids. J. Mech. Phys. Solids **41**(9), 1499–1514 (1993)
18. Lebedev, L.P., Cloud, M.J., Eremeyev, V.A.: Tensor Analysis with Applications in Mechanics. World Scientific, New Jersey (2010)
19. Christensen, R.M.: Theory of Viscoelasticity. An Introduction. Academic Press, New York (1971)
20. Tschoegl, N.W.: The Phenomenological Theory of Linear Viscoelastic Behavior. An Introduction. Springer, Berlin (1989)
21. Altenbach, H., Eremeyev, V.A.: On the bending of viscoelastic plates made of polymer foams. Acta Mechanica **204**(3–4), 137–154 (2009)

High-Temperature Inelastic Behavior of the Austenitic Steel AISI Type 316

Holm Altenbach and Yevgen Gorash

Abstract A conventional material model is extended to taking into account of varying thermo-mechanical loading conditions in a wide stress range. The developed model basis is a creep constitutive law in the form of the hyperbolic sine stress response function originally proposed by Nadai. The extension is done by incorporation of two additional inner variables reflecting hardening and recovery effects under cyclic loading conditions. The first one is presented by the relatively fast saturating back-stress K describing the kinematic hardening. The second one is presented by the relatively slow saturating parameter H describing the isotropic hardening. Evolution equations for K and H originally proposed by Chaboche are formulated in a modified form and based on the Frederick-Armstrong concept. The uniaxial modelling results are compared with cyclic stress-strain diagrams and alternative experimental data in the form of creep curves, tensile stress-strain diagrams, relaxation curves, etc. for the austenitic steel AISI type 316 at 600 °C in a wide stress range.

1 Introduction

The review of failures in fossil-fired steam power plants [5] indicate that 81 % of the failures are mechanical in nature, and that the remainder occurs due to corrosion. Considering the mechanical failures, 65 % are classified as short-time, elevated-temperature failures. Only 9 % are due to creep, with the rest being due to fatigue,

H. Altenbach (✉)
Department of Engineering Mechanics, Otto-von-Guericke University Magdeburg, Universitätsplatz 2, 39106 Magdeburg, Germany
e-mail: holm.altenbach@ovgu.de

Y. Gorash
Department of Mechanical and Aerospace Engineering, University of Strathclyde, 75 Montrose Street, Glasgow G1 1XJ, UK
e-mail: yevgen.gorash@strath.ac.uk

H. Altenbach and S. Kruch (eds.), *Advanced Materials Modelling for Structures*, Advanced Structured Materials 19, DOI: 10.1007/978-3-642-35167-9_3,

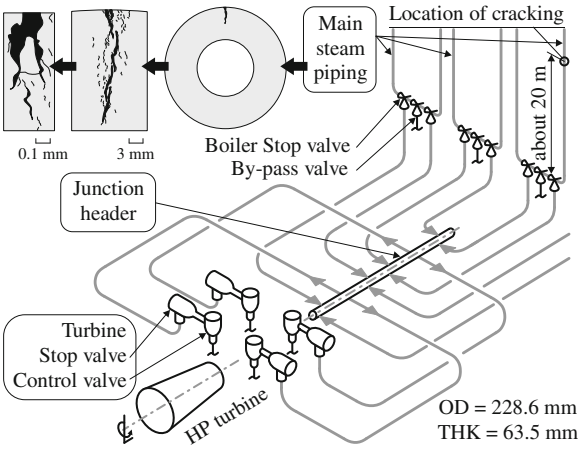

Fig. 1 Failure of the steel AISI type 316 components at Eddystone unit no. 1 power station, after [20]

weld failures, erosion, etc. Thus, failure occurs due to the complex interaction of creep deformation mechanisms and other material behavior processes, which lead to an acceleration of the material degradation. Therefore, for the purpose of correct simulation of a creep failure case study (CFCS), appropriate life time assessment and precise prediction of failure location, it is necessary to apply unified material behavior models. They have to describe various creep deformation mechanisms, the accompanying processes like damage, strain hardening/softening, recovery, stress relaxation, the processes evolving independently like plasticity, LCF, oxidation, corrosion, embrittlement, etc. In order to simulate the CFCS of Eddystone unit no. 1 components (see Fig. 1) it is necessary to develop a unified material model, which is able to describe the inelastic behavior of the steel AISI type 316 for the temperatures up to 650 °C. Due to the details of CFCS [8, 20], the model has to include such phenomena as creep, plasticity, LCF resulting into creep-fatigue interaction and evolution of corresponding damage parameters to assess the time of failure.

Inelastic material behavior of the austenitic steel AISI type 316 has been comprehensively studied experimentally in the 1990s by several material research laboratories [11, 12, 17–19]. The uniaxial creep tests were force-controlled and conducted for a wide range of constant stress values from 50 to 350 MPa and for the temperature range 500–750 °C. One of the material property, which was also measured individually for each creep curve under defined stress and temperature, was the instantaneous (or initial) strain ε^{ins}. Figure 2 shows the comparison of ε^{ins} values obtained from creep experiments [17–19] in the stress range 60–330 MPa at temperature 600 °C with elastic strain ε^{el} derived from the Hooke's law $\varepsilon^{\text{el}} = \sigma/E$, where Young's modulus was $E = 150$ GPa, see [9]. It illustrates the fact that certain initial plastic strain ε^{pl} for the steel AISI type 316 at 600 °C is induced even for moderate stress values. This observation also coincides with the value of the experimental yield limit

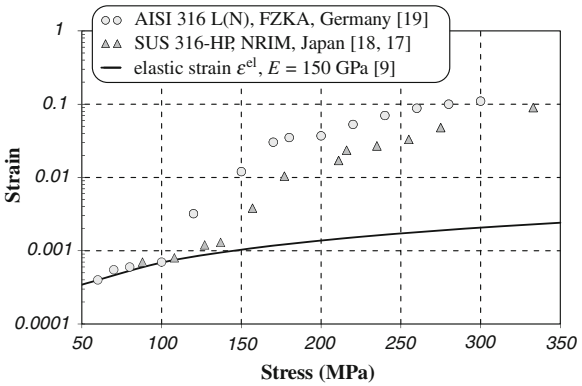

Fig. 2 Instantaneous strain of the steel AISI type 316 at 600 °C from experiments [17–19]

$\sigma_y = 114$ MPa corresponding to the temperature 600 °C [9]. Thus, at high temperatures the material behavior of the steel AISI type 316 is viscous and requires the accounting of the significant amount of plastic strain ε^{pl}.

The steel AISI type 316 steel has been used within the power-generating industry, e.g. superheater pressurized tubing exposed to temperatures of 650 °C or higher. Comparing to martensitic and ferritic steels, austenitic grades including ASTM 316 have a lower yield strength σ_y, but excellent ductility. Their long-term ductility can vary from below 10 % to over 100 % also depending on the temperature. All basic thermal and mechanical properties of the steel AISI type 316 show significant temperature dependence [9]. For more detailed description we refer to [8].

2 Creep Constitutive Equation

The deformation mechanism map of steel AISI type 316 [11] shows the requirement to take into account both main creep mechanisms during the creep modelling: power-law creep, which includes generally the high stress range, and linear or viscous creep, which includes generally moderate and low stress ranges. The industrial application conditions lay mostly in the "viscous creep" region, close to the transition boundary, which provides relatively better creep resistance. On the other hand, the laboratory testing conditions lay mostly in the power-law region, so its results have limited validity for the industrial use of the steel. The temperature range for the steel AISI type 316 relevant to the engineering practice lays in the range 500–700 °C.

Within the phenomenological approach to creep modelling one usually starts with the formulation of a constitutive equation. Figure 3 illustrates collected experimental data [12, 17–19] for the steel AISI type 316, presenting the dependence of the minimum creep rate $\dot{\varepsilon}^{cr}_{min}$ on the applied stress σ in the ranges of "moderate" and

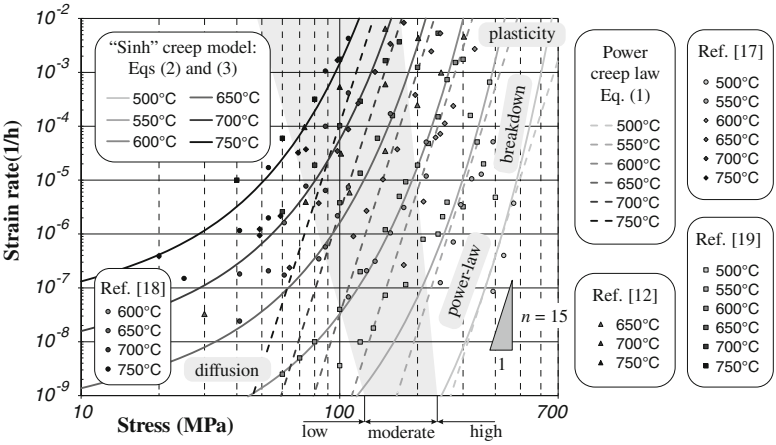

Fig. 3 Fitting of creep constitutive Eqs. (1) and (2) to creep experiments [12, 17–19]

"high" stress levels. The conventional stress-response function proposed by Norton and Bailey is usually extended with the Arrhenius-type function to describe creep behavior in "power-law" area at different temperatures:

$$\dot{\varepsilon}^{\mathrm{cr}} = g\,(\sigma, T) = c\ \exp\left[-Q_{\mathrm{cr}}/RT\right]\sigma^{n}, \tag{1}$$

where the creep exponent $n = 15$, creep material parameter $c = 10^{-11}\,\mathrm{h}^{-1}$ and creep activation energy $Q_{\mathrm{cr}} = 330000\ \mathrm{J/mol}$ are defined fitting the experimental data [12, 17–19] within only high stress range, as illustrated on Fig. 3.

Similarly to the approach in [16] employed for X20CrMoV12-1 steel, the hyperbolic sine stress response function originally proposed by Nadai [14] is selected as the basis for constitutive model due to satisfactory fitting of experimental data for the complete stress range and the temperature range 500–750 °C:

$$\dot{\varepsilon}^{\mathrm{cr}} = f\,(\sigma, T) = A\,(T)\ \sinh\left[B\,(T)\ \sigma\right], \tag{2}$$

where the temperature-dependent creep material parameters $A(T)$ and $B(T)$ are Arrhenius-type temperature-response functions:

$$A(T) = a\ \exp\left[-Q_{\mathrm{ln}}/RT\right] \quad \text{and} \quad B(T) = b\ \exp\left[-Q_{\mathrm{pw}}/RT\right]. \tag{3}$$

In Eqs. (2) and (3) all the necessary secondary creep material parameters of the steel AISI type 316 are identified by fitting the available experimental points [12, 17–19] at the general diagram Fig. 3 corresponding to several temperatures simultaneously: $a = 75776\,\mathrm{h}^{-1}$, $Q_{\mathrm{ln}} = 170000\,\mathrm{J/mol}$, $b = 0.7\,\mathrm{MPa}^{-1}$ and $Q_{\mathrm{pw}} = 12000\,\mathrm{J/mol}$.

3 Phenomenological Approach

Referring to [15] the phenomenological approach to the development of a unified material model is based on the mathematical description of experimental creep curves obtained from uniaxial creep tests under constant loading, since creep is the dominant material behavior at high temperatures. The best way to illustrate the developed technique is to explain processes affecting the shape of an idealized creep curve in Fig. 4 and to propose some phenomenological description for them. According to mechanical properties of the steel AISI type 316 [9] explained in Fig. 2, the values of the normal stress σ in the specimen, corresponding to moderate axial loading, may exceed the yield limit of the material $\sigma_y \approx 100-120$ MPa. The instantaneous inelastic material response is therefore elasto-plastic at high temperatures:

$$\varepsilon^{\text{ins}} = \varepsilon^{\text{el}} + \varepsilon^{\text{pl}}, \tag{4}$$

where ε^{ins}, ε^{el} and ε^{pl} are the instantaneous, the elastic and the plastic strains, respectively. The elastic strain ε^{el} is characterized by the temperature dependent Young's modulus E. A portion of ε^{pl} is defined by the hardening processes, which induce the evolution of both hardening parameters—relatively slow saturating isotropic H and relatively fast saturating kinematic K. The contribution of each parameter on ε^{pl} is dependent on the stress level, i.e. at high stresses mainly by H and at low stresses mainly by K.

The time-dependent inelastic response is the slow increase of the creep strain ε^{cr} with a variable creep strain rate $\dot{\varepsilon}^{\text{cr}}$. Depending on the character of creep strain acceleration $\ddot{\varepsilon}^{\text{cr}}$, three stages can be considered in a typical creep curve as illustrated in Fig. 4: the first stage (primary or reduced creep), the second stage (secondary or stationary creep) and the third stage (tertiary or accelerated creep). Moreover, referring to [21] the shape of the creep curve is determined by following competing reactions or processes, as explained in Fig. 4:

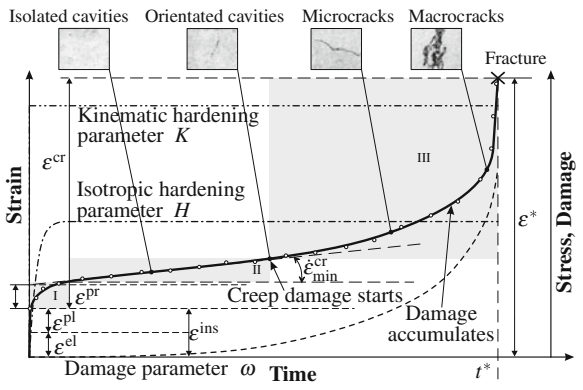

Fig. 4 Idealized creep curve with illustration of internal state variables evolution

(a) creep strain hardening;
(b) softening processes such as recovery, recrystallization, strain softening, and precipitate overaging;
(c) damaging processes characterized by the damage parameter ω resulting in cavities initiation and cracking.

One of these three factors—creep strain hardening (a)—tends to decrease the creep rate $\dot{\varepsilon}^{\mathrm{cr}}$, whereas the two factors—(b, c)—tend to increase the creep rate $\dot{\varepsilon}^{\mathrm{cr}}$. The balance among these factors determines the creep curve shape. During the primary creep stage the decreasing slope of the creep curve is attributed to strain hardening, which decreases the creep rate to a certain value (minimum creep rate $\dot{\varepsilon}^{\mathrm{cr}}_{\mathrm{min}}$). A part of creep strain $\varepsilon^{\mathrm{pr}}$ accumulated during the primary creep stage is defined by the evolution of both hardening parameters K and H, as in the case of $\varepsilon^{\mathrm{pl}}$. The contribution of each parameter on $\varepsilon^{\mathrm{pr}}$ depends on the stress level. A number of creep material properties can be deduced from the uniaxial creep curve. The most important of them are the duration of each of the creep stages, the value of the minimum creep rate $\dot{\varepsilon}^{\mathrm{cr}}_{\mathrm{min}}$, the time to fracture t^* and the strain value at fracture ε^*:

$$\varepsilon^* = \varepsilon^{\mathrm{ins}} + \varepsilon^{\mathrm{cr}} = \varepsilon^{\mathrm{el}} + \varepsilon^{\mathrm{pl}} + \varepsilon^{\mathrm{cr}}, \tag{5}$$

As the first iteration in the unified model development, it is formulated for a defined temperature. The temperature 600 °C is chosen as the basic for the definition of creep material parameters for the steel AISI type 316, since this value is close to the mean service temperature of the power plant components from Eddystone unit no. 1. For the purpose to adjust the basic creep law, two experimental sets of creep curves at 600 °C are employed for the creep parameters identification. The first set includes 6 creep curves in the stress range 60–170 MPa [19]. The second set includes 6 creep curves in the stress range 200–300 MPa [2]. Each curve from the both sets is differentiated numerically with respect to time in order to identify corresponding minimum creep rate values $\dot{\varepsilon}^{\mathrm{cr}}_{\mathrm{min}}$. The result of this identification is illustrated in Fig. 5 with unfilled and filed points. Both sets of $\dot{\varepsilon}^{\mathrm{cr}}_{\mathrm{min}}$ are fitted numerically by Eqs. (1) and (2) using the weighted Levenberg-Marquardt algorithm as illustrated in Fig. 5 with solid and dashed lines, providing the following values of material parameters: $n = 7.515$ and $C = 5.647 \cdot 10^{-23}$ 1/h, $A = 2.335 \cdot 10^{-10}$ 1/h and $B = 0.053$ 1/MPa. Applying a strain-controlled loading to Sinh creep model with a fixed value of the total strain $\Delta\varepsilon_{\mathrm{t}}$, than one can obtain a perfect stress response, i.e. the model provides irreversible deformation without any increase in stresses reaching a certain stress level. One gets a stable closed hysteresis loop as shown in Fig. 5.

Following [10] depending on the form of stress response under cyclic strain-controlled loading all metals for high-temperature application are usually divided into cyclic (or isotropic) stable and instable. Typical examples of stable metals are medium-carbon steels, which have the width of elasto-plastic hysteresis loop almost not dependent on the number of loading cycles. Instable metals are subdivided into isotropic hardening and softening, while their instability is usually associated with microstructure transformations undergoing cyclic or significant inelastic

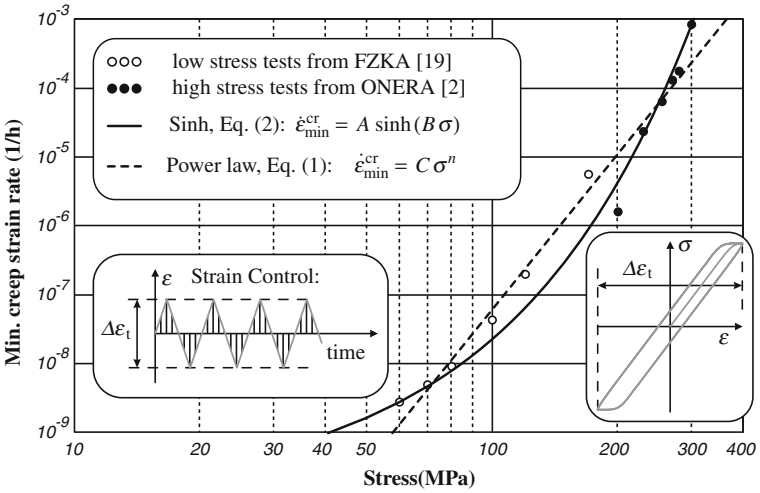

Fig. 5 Modelling of minimum creep strain rate using experimental creep curves for the steel AISI type 316 at 600 °C [2, 19]

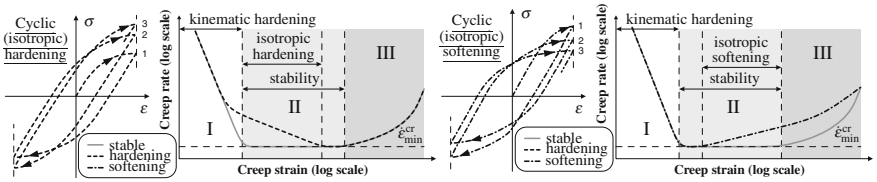

Fig. 6 Schematic representations of idealized creep strain rate versus creep strain dependence

deformations, see Fig. 6. Isotropic softening metals are characterized by the gradient narrowing of elasto-plastic hysteresis loop observable after first loading cycle. Such type of metals is usually presented by high-strength heat-resistant steels, e.g. martensite steel X20CrMoV12-1 described in [16] with a combined model for hardening, softening and damage processes. Isotropic hardening metals are characterized by the gradient expansion of the elasto-plastic hysteresis loop observable after first loading cycle. Such type is usually presented by ductile stainless steels, e.g. austenitic steel AISI type 316, which cyclic plasticity behavior is described in [6] for a wide temperature range with the Chaboche unified visco-plasticity model [2].

One can make the assumption that the plastic strain ε^{pl} and the strain accumulated during primary creep stage ε^{pr} for stable metals are defined only by kinematic hardening, which provides the shift of the initial yield surface. In the case of softening metals this assumption is also correct, but the softening phenomenon additionally influences ε^{pl}, providing the reduction of the initial yield surface, and the second creep stage. The steady-state segment almost vanishes due to the creep acceleration caused by material transformation towards softer microstructure and followed by damage accumulation on the tertiary stage, see Fig. 6 and for explanation [16]. In the

case of hardening the strains $\varepsilon^{\mathrm{pl}}$ and $\varepsilon^{\mathrm{pr}}$ are defined by both kinematic and isotropic hardening, which provides an additional growth of the initial yield surface. The influence of the hardening reduces the creep strain deceleration on the second part of primary stage, thus also the vanishing steady-state segment of the second stage. Such a behavior is caused by material transformation towards harder microstructure and followed by damage accumulation on the tertiary stage, see Fig. 6. Therefore, for the adequate description of inelastic material behavior of the steel AISI type 316, it is necessary to formulate such a phenomenological model, which is able to reflect all the features of hardening specified above.

4 Formulation of the Unified Model

The constitutive Eq. (2) based on the Sinh stress-response function is taken as a basis of the proposed unified visco-plasticity model for the steel AISI type 316. It will be extended below in order to take into account both the kinematic and the isotropic hardening effects. Therefore, the model is formulated not for $\dot{\varepsilon}^{\mathrm{cr}}$, but for the inelastic strain rate $\dot{\varepsilon}^{\mathrm{in}}$. Note that the values of the creep parameters A and B for Eq. (2) remain the same as they are defined in Sect. 3 by fitting the available experimental creep curves at 600 °C. Thus, the extension consists in replacement of the value of applied stress σ by the value of viscous stress σ_{v}, which is initially significantly higher than the value of σ, but saturates towards it under a constant loading after a certain time depending on the applied stress and loading rate:

$$\sigma_{\mathrm{v}} = \sigma/(1 - h + H) + \sigma_0 \operatorname{sign}(\sigma - K) - K, \tag{6}$$

where σ_0 and h are material parameters for the steel AISI type 316 at 600 °C, which present the saturation values for the kinematic backstress K and the isotropic hardening variable H, respectively. The influence of additional material state variables (K and H) and corresponding saturation values σ_0 and h results in so-called overstress $X = \sigma_{\mathrm{v}} - \sigma$, which saturates towards zero under a constant loading after a certain time. The value of the overstress in the initial moment of time before the elastic response of material considering the finite loading rate is following:

$$X = \sigma\ h\ /(1 - h) + \sigma_0. \tag{7}$$

In the case of the following form for viscous stress

$$\sigma_{\mathrm{v}} = \sigma/(1 - H) + \sigma_0 \operatorname{sign}(\sigma - K) - K \tag{8}$$

the model provides kinematic hardening combined with isotropic softening.

The evolution equations for hardening state variables (K and H) are taken in the same form as implemented in [6, 16] using the Frederick-Armstrong concept [4]. The evolution equation for the isotropic hardening parameter H is as it follows:

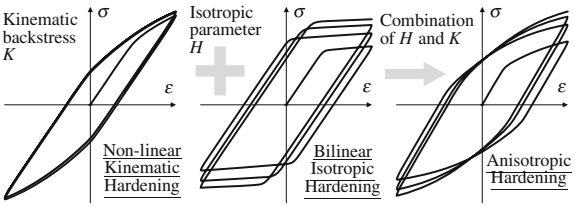

Fig. 7 Schematic representations of hardening material behavior with idealized hysteresis loops

$$\dot{H} = C_1 \, (h - H) \, |\dot{\varepsilon}^{\text{in}}|, \tag{9}$$

where the value of the saturation parameter h varies from 0 to 1, specifying the initial yield stress σ_{y} on the first 0.25 hysteresis loop of the tensile stress-strain diagram. Parameters C_1 define the rate of saturation for parameter H towards the value of h, thus providing the stabilization of hysteresis loops and reaching the conventional value of the ultimate stress σ_{u} on the tensile stress-strain diagram.

The evolution equation for kinematic hardening backstress K is following:

$$\dot{K} = C_2 \left[\sigma_0 \, \text{sign} \, (\sigma - K) - K \right] |\dot{\varepsilon}^{\text{in}}|, \tag{10}$$

which is very close to the conventional form [2, 4], and provides the same effect of kinematic shift under application of reverse loading and positive value of σ, because the sign of $\dot{\varepsilon}^{\text{in}}$ is defined by the difference between σ and K. In Eq. (10) σ_0 presents some kinematic shift of the initial yield surface, and C_2 defines the rate of this shift, thus providing the graduate transition from the elastic slope to plastic on tensile stress-strain diagram and the initial strain rate on primary creep stage.

In addition, the relation between the elastic ε^{el} and the inelastic strain ε^{in} for a strain-controlled test is formulated in the following form:

$$\dot{\sigma} = E(\dot{\varepsilon}^{\text{t}} - \dot{\varepsilon}^{\text{in}}), \tag{11}$$

where E is the elasticity modulus and ε^{t} is the applied total strain.

The unified visco-plasticity model (2), (6), (9)–(11) provides all the required features of material behavior under constant and monotonic loading, as illustrated in Figs. 4 and 6, and hardening behavior under cyclic loading, as illustrated in Fig. 7. The resulting hysteresis loop illustrating anisotropic hardening can be decomposed on two idealized hysteresis loops presenting the separate influence of kinematic backstress K and isotropic parameter H on the constitutive model (2).

5 Verification of the Model by Uniaxial Tests

Referring to [13] for a qualitative analysis, several characteristic tests have to be performed to describe the phenomenology of visco-plastic materials at high temperature. The classical tests are essentially conducted in simple tension or tension-compression

at constant temperature. The specimen is subjected to an axial load (force or displacement) which produces a uniform state of stress or strain within the whole useful volume of the specimen. The most general types of uniaxial tests required to characterize a material and to verify a corresponding material model are creep, relaxation, hardening and cyclic tests. These types of tests can be conducted in different combinations with different duration for the complex investigation of material behavior. If the tests, with the exception of relaxation, are conducted during undefined period of time, than the fracture of the specimen is achieved and the durability characteristics of the material can be obtained, including fracture stress and strain, time, number of cycles to fracture and energy dissipated in fracture.

Therefore, simulation results obtained by the proposed model (2), (6), (9)–(11) with appropriate creep parameters have to be compared with all mentioned above types of uniaxial experimental data for the steel AISI type 316 at 600 °C. The values of creep parameters $A = 2.335 \cdot 10^{-10}$ 1/h and $B = 0.053$ 1/MPa for constitutive Eq. (2) are defined in Sect. 3 by fitting the available creep curves [2, 19]. The values of hardening material parameters $C_1 = 20$, $h = 0.35$ in Eq. (9) and $C_2 = 1100$, $\sigma_0 = 170$ MPa in Eq. (10) are defined in the first iteration by fitting of the first 1.25 loop from the experiment [6], conducted under 0.3 % of ε^{t} amplitude with strain rate $\dot{\varepsilon}^{\mathrm{t}} = 2.66 \cdot 10^{-4}$ 1/s. The experimental data in [6] are fitted by the Chaboche viscoplasticity model with the set of 10 corresponding material parameters also provided in [6], as shown in Fig. 8. The comparison of the cyclic simulation results for two unified models in Fig. 8 shows that the Chaboche model provides much better results for cyclic stress response and form of saturated loop after 50 cycles.

However, for the experimental data of relaxation [3] and hardening tests [1] the proposed model provides much more preferable simulation results, than the Chaboche model. The explanation for this is that the material parameters provided from [6] have been identified using only the cyclic tests. Moreover, in [2] the capacity of the Chaboche model to reproduce relaxation tests was demonstrated. The relaxation curve obtained by the proposed model, corresponding to the value of total strain

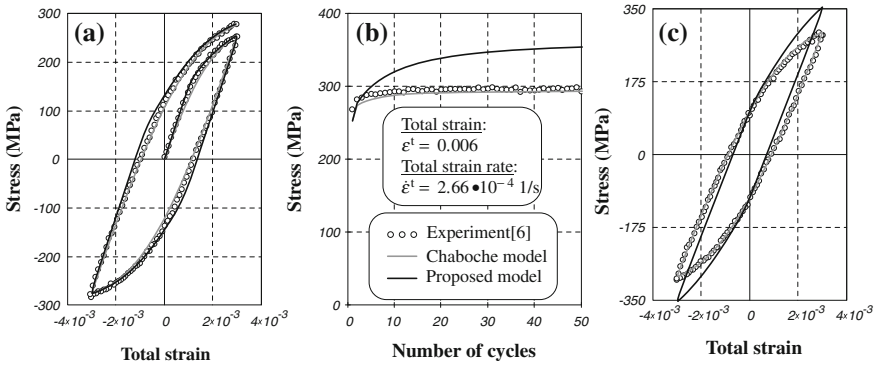

Fig. 8 Fitting of the proposed model (2), (6), (9–11) to the uniaxial strain-controlled cyclic experiment [6]: **a** first 1.25 loop, **b** cyclic stress response and **c** saturated loop

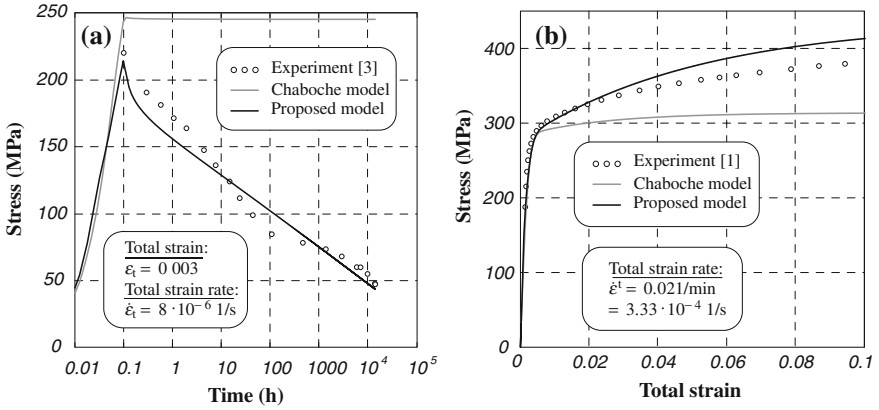

Fig. 9 Comparison of the models simulation results for: **a** relaxation experiment [3] and **b** hardening experiment [1]

$\varepsilon^t = 0.003$ achieved with the strain rate $\dot{\varepsilon}_t = 8 \cdot 10^{-6}$ 1/s, provides the necessary rate of stress decrease, which coincides with experimental relaxation curve [3], as shown in Fig. 9a. The stress-strain diagram obtained by the proposed model, corresponding to the strain rate $\dot{\varepsilon}^t = 0.02$ 1/min $= 3.33 \cdot 10^{-4}$ 1/s selected regarding the EN 10002-5 standard, provides the necessary level of yield stress σ_y and hardening slope of the experimental stress-strain diagram [1], as shown in Fig. 9b.

Finally, the creep test simulation results obtained by the both models are compared with experimental strain rate versus strain dependencies extracted from two sets of experimental creep curves. The first set includes creep curves in low stress range (60–170 MPa) provided by [19] and shown in Fig. 10, and the second set includes creep curves in high stress range (200–300 MPa) provided by [2] and shown in Fig. 11. The Chaboche model with corresponding material constants does not provide any reasonable creep simulation results for the both sets of creep curves. Creep simulation results presented on Figs. 10 and 11 provided by the proposed model are far from the optimal matching of experiments. The simulated inelastic strains ε^{in} overestimate the experimental strains before reaching $\dot{\varepsilon}^{cr}_{min}$ for low stresses and underestimate the experimental strains for high stresses.

The positive features of obtained simulation results include two facts observed on Figs. 10 and 11. First, the required values of $\dot{\varepsilon}^{cr}_{min}$ are reached for the complete stress range with the exception of some moderate stresses. Second, the simulation curves for the low stress range demonstrate the separate influence of kinematic and isotropic hardening resulting in smooth changing of the curves' slope before reaching $\dot{\varepsilon}^{cr}_{min}$, as it is assumed in Sect. 3 in Fig. 6. This assumption is confirmed by the experimental curve shape corresponding to 200 MPa on Fig. 11, which demonstrate the influence of different hardening types. Therefore, the creep simulation results may be improved by setting the saturation parameters σ_0 and h corresponding to kinematic backstress K and isotropic parameter H as functions depending on σ. Then, these functions can be separately fitted to corresponding segments of experimental creep curves.

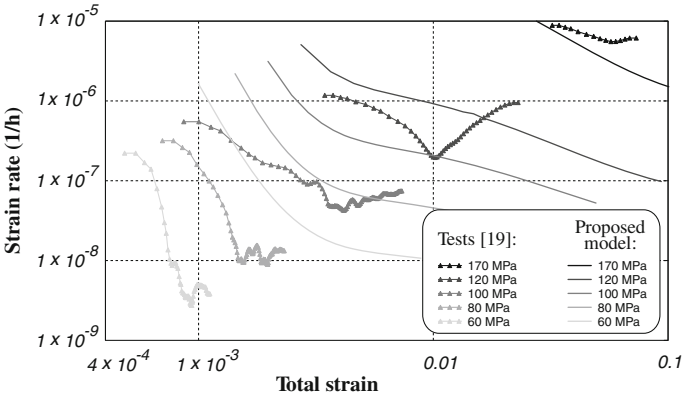

Fig. 10 Comparison of the model simulation results for the strain rate from creep tests conducted at low stresses [19]

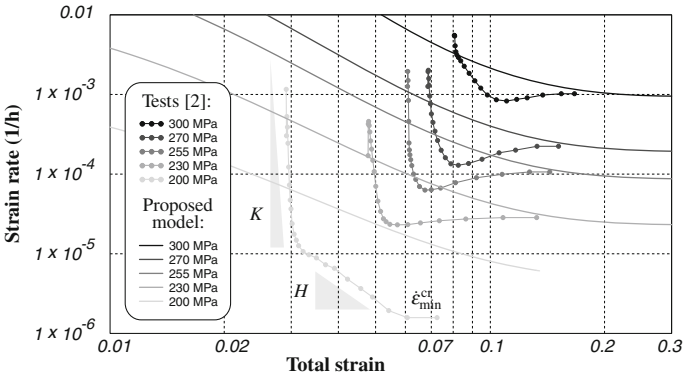

Fig. 11 Comparison of the model simulation results for the strain rate from creep tests conducted at high stresses [2]

6 Conclusions

The results of a numerical life-time assessment for the main steam piping (MSP) from Eddystone unit no. 1 power station applying conventional creep-fatigue model [7, 8] in ABAQUS comply with a conservative locus on creep-fatigue damage interaction diagram. In order to improve the simulation results, a conventional sinh-based creep model for the steel AISI type 316 has been extended by the introduction of two additional hardening state variables (K and H). The uniaxial simulation results of the proposed unified model satisfactory comply with cyclic stress response, creep curves, stress-strain diagram and relaxation curve at 600 °C. In comparison to the unified Chaboche model, the proposed model has less number of material constants (7 vs. 10) and provides better results in modelling of creep and relaxation. The

constitutive Eq. (2) of the proposed model, analogically to conventional model [7, 8], can be coupled with evolution equations for creep damage ω_{cr} and fatigue damage ω_f parameters. In case of constant loading, ω_{cr} influences the accumulation of inelastic strain ε^{in} resulting in tertiary creep stage on creep curve. In case of variable loading, the influence of ω_f on ε^{in} results in the fast narrowing of last hysteresis loops before the fracture. However, the proposed model is less accurate regarding the cyclic behavior, therefore it requires some significant improvements, such as introduction of stress and temperature dependence for hardening material constants. In order to provide better fitting of experimental data a numerical optimization procedure has to be developed for material parameters identification.

References

1. Brnic, J., Niu, J., Canadija, M., Turkalj, G., Lanc, D.: Behavior of AISI 316L steel subjected to uniaxial state of stress at elevated temperatures. J. Mater. Sci. Technol. **25**(2), 175–180 (2009)
2. Chaboche, J.L.: Constitutive equations for cyclic plasticity and cyclic viscoplasticity. Int. J. Plast. **5**, 247–302 (1989)
3. Douglas, J., Spindler, M., Dennis, R.: Development of an advanced creep model for type 316 stainless steel. In: Proceedings of CREEP8: 8th International Conference on Creep and Fatigue at Elevated Temperatures, CREEP2007-26152, pp. 399–418. ASME, San Antonio (2007)
4. Frederick, C.O., Armstrong, P.J.: A mathematical representation of the multiaxial bauschinger effect. Mater. High Temp. **24**(1), 1–26 (2007)
5. French, D.N.: Metallurgical Failures in Fossil Fired Boilers. Wiley, New York (1993)
6. Gong, Y.P., Hyde, C.J., Sun, W., Hyde, T.H.: Determination of material properties in the Chaboche unified viscoplasticity model. J. Mater. Des. Appl. **224**(1), 19–29 (2010)
7. Gorash, Y., Altenbach, H.: Creep-fatigue analysis of the steel AISI type 316 component failure. Proc. Appl. Math. Mech. **11**, 373–374 (2011). doi:10.1002/pamm.201110178
8. Gorash, Y., Altenbach, H., Lvov, G.: Modelling of high-temperature inelastic behaviour of the austenitic steel AISI type 316 using a continuum damage mechanics approach. J. Strain Anal. **47**(4), 229–243 (2012)
9. Karditsas, P.J., Baptiste, M.J.: Thermal and structural properties of fusion related materials. ARIES Properties Archive: UKAEA FUS 294, Euratom/UKAEA Fusion Association, San Diego (1995)
10. Khazhinskiy, G.M.: Models of Deformation and Fracture of Metals (in Russian). Nauchnyy Mir, Moscow (2011)
11. Kloc, L., Fiala, J.: Viscous creep in metals at intermediate temperatures. Kovové Materiály **43**(2), 105–112 (2005)
12. Kloc, L., Sklenička, V., Ventruba, J.: Comparison of low creep properties of ferritic and austenitic creep resistant steels. Mater. Sci. Eng. A **319–321**, 774–778 (2001)
13. Lemaitre, J., Chaboche, J.L.: Mechanics of Solid Materials. Cambridge University Press, Cambridge (1994)
14. Nadai, A.: The influence of time upon creep. The hyperbolic sine creep law. In: J.M. Lessells, J.P. Den Hartog, G.B. Karelitz, R.E. Peterson, H.M. Westergaard (eds.) Stephen Timoshenko 60th Anniversary Volume, pp. 155–170. The Macmillan Co., New York (1938)
15. Naumenko, K., Altenbach, H.: Modelling of Creep for Structural Analysis. Springer, Berlin (2007)
16. Naumenko, K., Altenbach, H., Kutschke, A.: A combined model for hardening, softening, and damage processes in advanced heat resistant steels at elevated temperature. Int. J. Damage Mech. **20**(4), 578–597 (2011)

17. Okada, M. et al.: Data sheets on the elevated-temperature stress relaxation properties of 18Cr-12Ni-Mo hot rolled stainless steel plate (SUS 316-HP). NRIM Creep Data Sheet No. 42, National Research Institute for Metals, Tsukuba (1996)
18. Okada, M. et al.: Data sheets on the elevated-temperature properties of 18Cr-12Ni-Mo stainless steel tubes for boilers and heat exchangers (SUS 316H TB). NRIM Creep Data Sheet No. 6B, National Research Institute for Metals, Tsukuba (2000)
19. Rieth, M., Falkenstein, A., Graf, P., Heger, S., Jäntsch, U., Klimiankou, M., Materna-Morris, E., Zimmermann, H.: Creep of the austenitic steel AISI 316 L(N): experiments and models. Technical Report: FZKA 7065, Forschungszentrum Karlsruhe GmbH, Karlsruhe (2004)
20. Skelton, R.P.: Creep-fatigue interactions (crack initiation). In: Milne, I., Ritchie, R.O., Karihaloo, B. (eds.) Creep and High-Temperature Failure, Comprehensive Structural Integrity, vol. 5, pp. 25–112. Elsevier, Amsterdam (2003)
21. Viswanathan, R.: Damage Mechanisms and Life Assessment of High-Temperature Components. ASM International, Metals Park (1989)

Finite Element Modelling of the Thermo-Mechanical Behaviour of a 9Cr Martensitic Steel

R. A. Barrett, P. E. O'Donoghue and S. B. Leen

Abstract A multi-axial, unified sinh viscoplastic material model has been developed to model the behaviour of advanced materials subjected to high temperature cyclic loading. The material model accounts for rate-dependent effects related to high temperature creep and cyclic plasticity effects such as isotropic and kinematic hardening. The material model, which is capable of simulating both isothermal and anisothermal loading conditions, is implemented in multi-axial form in a material user subroutine and validated against uniaxial test data. The results validate the implementation for both isothermal and anisothermal uniaxial loading conditions for as-new P91 steel.

1 Introduction

Next generation power plants are faced with the need to facilitate an ever increasing growth in renewable energy technologies. The unpredictable nature of renewable sources of energy, attempts to minimise CO_2 emissions and more widespread use of flexible combined cycle gas power plant, results in the need for fossil-fuel based power plant to operate with increased flexibility. Such a load-following mode of operation results in potentially large cyclic thermal gradients, which in turn, lead to

R. A. Barrett (✉) · S. B. Leen
Mechanical and Biomedical Engineering, College of Engineering and Informatics, NUI, Galway, Ireland
e-mail: r.barrett2@nuigalway.ie

S. B. Leen
e-mail: sean.leen@nuigalway.ie

P. E. O'Donoghue
Civil Engineering, College of Engineering and Informatics, NUI, Galway, Ireland
e-mail: padraic.odonoghue@nuigalway.ie

R. A. Barrett · P. E. O'Donoghue · S. B. Leen
Ryan Institute for Environmental, Marine and Energy Research, NUI, Galway, Ireland

H. Altenbach and S. Kruch (eds.), *Advanced Materials Modelling for Structures*, Advanced Structured Materials 19, DOI: 10.1007/978-3-642-35167-9_4,

increased thermo-mechanical fatigue (TMF) of plant components and a reduction in component life. Coupled with this increased TMF is the requirement to improve overall plant efficiency and hence reduce the level of CO_2 emissions. This may be achieved through the use of an ultra-supercritical (USC) cycle, with plant components subjected to increased steam pressure and temperature. With Type IV cracking already observed in plant components operating under a subcritical cycle [17], there is a need for the development of accurate life prediction methods for power plant components. To achieve this, effective and efficient computational methods are required to predict the life of plant components. This, in turn, requires material models which can accurately describe the constitutive behaviour of candidate materials, such as 9Cr steels, under high temperature loading.

The material model must have the capability to simulate, on the one hand, the rate-dependent effects associated with high temperature creep, while also maintaining the ability to model phenomena related to cyclic loading conditions, such as the Bauschinger effect and isotropic hardening. Thus, a unified approach is required to model the creep-fatigue interaction observed in 9Cr steels. A number of models capable of dealing with the high temperature creep-fatigue interaction have been proposed, such as uniaxial implementations of the Chaboche power law model [3, 9, 10, 15, 20, 21], the two layer viscoplasticity model [6] and the MATMOD model [13]. The model proposed in the current study is a multi-axial sinh formulation. The sinh formulation is beneficial for a number of reasons. Firstly, as 9Cr steels display a linear stress-strain rate relationship at low stresses and strain rates and an exponential relationship at higher values, the sinh formulation allows for reliable interpolation and extrapolation beyond the limited experimental data available. Secondly, the mechanisms which dominate deformation vary from diffusion based creep at low stresses and high temperature to dislocation based creep at higher stresses [8]. As the low stress regime corresponds to Nabarro-Herring creep with an exponent of unity and the higher stress regimes are represented by power law creep with an exponent of up to 11 [18], the use of a sinh formulation allows for smooth transition from one phenomena to another.

The sinh material model is implemented in both uniaxial and multi-axial form. The multi-axial implementation is developed in a user material subroutine, for use with the commercial finite element (FE) code Abaqus. This study presents the first step in assessing the performance of the multi-axial material model by validating against uniaxial isothermal fatigue data [10] and uniaxial TMF test data [15] available in the literature.

2 Material Model

The sinh unified viscoplastic material model described in this study allows for accurate modelling of the isotropic and kinematic hardening phenomena associated with cyclic loading and the creep effects related to high temperature loading. This is achieved through the use of the following constitutive equation for the effective

accumulated plastic strain rate:

$$\dot{p} = \alpha \sinh \beta \left(\mathrm{J}(\boldsymbol{\sigma} - \boldsymbol{\chi}) - \mathrm{R} - \mathrm{k}\right) \tag{2.1}$$

where $\mathrm{J}(\boldsymbol{\sigma} - \boldsymbol{\chi})$ is the von Mises effective stress function, R is the isotropic hardening parameter, k is the initial yield stress, $\boldsymbol{\chi}$ is the back-stress tensor and α and β are temperature-dependent, viscoplastic material parameters. The material model uses an implicit integration scheme to evaluate the increment of effective plastic strain. The nature of the implicit scheme used in this model dictates that a trial stress is used to check for viscoplastic behaviour. This allows for the dissipation potential to be evaluated at the current timestep and the use of a radial return method [4] applies plastic correction to the value of trial stress obtained.

2.1 Material Model Development

Assuming only small strains apply, classical additive decomposition of strain gives the following equation for the total strain, $\boldsymbol{\varepsilon}$:

$$\boldsymbol{\varepsilon} = \boldsymbol{\varepsilon}^{\mathrm{el}} + \boldsymbol{\varepsilon}^{\mathrm{pl}} + \boldsymbol{\varepsilon}^{\mathrm{th}} \tag{2.2}$$

where $\boldsymbol{\varepsilon}^{\mathrm{el}}$ corresponds to the elastic strain, $\boldsymbol{\varepsilon}^{\mathrm{pl}}$ is the plastic strain and $\boldsymbol{\varepsilon}^{\mathrm{th}}$ is the thermal strain. The increment in stress, $\Delta\boldsymbol{\sigma}$, is calculated using the multi-axial form of Hooke's law, coupled with Eq. (2.2) written in terms of the elastic strain:

$$\Delta\boldsymbol{\sigma} = 2\mu\left(\Delta\boldsymbol{\varepsilon} - \Delta\boldsymbol{\varepsilon}^{\mathrm{th}}\right) + \lambda \mathrm{Tr}\left(\Delta\boldsymbol{\varepsilon} - \Delta\boldsymbol{\varepsilon}^{\mathrm{th}}\right) I - 2\mu\Delta\boldsymbol{\varepsilon}^{\mathrm{pl}} \tag{2.3}$$

where λ and μ are Lamé's constants. In Eq. (2.3), the first two terms on the right hand side give the trial stress and the final term corresponds to the applied plastic correction. The increment of plastic strain, $\Delta\boldsymbol{\varepsilon}^{\mathrm{pl}}$, is determined by the flow rule:

$$\Delta\boldsymbol{\varepsilon}^{\mathrm{pl}} = \Delta p \mathbf{n} \tag{2.4}$$

where $\mathbf{n}$ represents the tensor normal and Δp corresponds to the increment in effective plastic strain. For a von Mises material, the tensor normal is defined by the following equation:

$$\mathbf{n} = \frac{\partial f}{\partial \boldsymbol{\sigma}} = \frac{3}{2}\frac{\mathbf{s} - \boldsymbol{\chi}}{\mathrm{J}\left(\mathbf{s} - \boldsymbol{\chi}\right)} \tag{2.5}$$

In Eq. (2.5), $\mathbf{s}$ is deviatoric stress and f defines the viscous stress if $f > 0$ and the elastic domain if $f \leq 0$. For the current model, f is defined as:

$$f = \mathrm{J}\left(\boldsymbol{\sigma} - \boldsymbol{\chi}\right) - \mathrm{R} - \mathrm{k} \tag{2.6}$$

Nonlinear kinematic hardening, which accounts for translation of the centre of the elastic domain in 3D stress space, is described by a summation of Armstrong-Frederick type back-stress tensors [2, 11]:

$$\boldsymbol{\chi} = \boldsymbol{\chi}_1 + \boldsymbol{\chi}_2 \tag{2.7}$$

$$\dot{\boldsymbol{\chi}}_i = \frac{2}{3} C_i \dot{\boldsymbol{\varepsilon}}^{\mathrm{pl}} - \gamma_i \boldsymbol{\chi}_i \dot{p} + \frac{1}{C_i} \frac{\partial C_i}{\partial T} \boldsymbol{\chi}_i \dot{T} \tag{2.8}$$

where T is temperature and C_i and γ_i are temperature-dependent material parameters. The three terms in Eq. (2.8) correspond to (i) a linear kinematic hardening term, (ii) a recall term and (iii) a temperature rate term, respectively. $\boldsymbol{\chi}_1$ accounts for the kinematic behaviour at lower strain hardening levels and $\boldsymbol{\chi}_2$ for higher levels of strain hardening. The variable R takes into account the expansion/contraction of the elastic domain and is given by the following relationship [11, 22]:

$$\dot{R} = b\,(Q - R)\,\dot{p} + \left(\frac{1}{b} \frac{\partial b}{\partial T} + \frac{1}{Q} \frac{\partial Q}{\partial T} \right) R \dot{T} \tag{2.9}$$

where b and Q are temperature-dependent material parameters representing the decay rate and the saturation value of R respectively. In Eqs. (2.8) and (2.9), the temperature-rate terms account for the effects of anisothermal loading conditions and the variations of the material parameters b, Q and C_{i} as functions of temperature.

The sinh formulation defined above has been implemented in uniaxial form in a stand-alone computer program and also in multi-axial form within a user material (UMAT) subroutine in the general-purpose, non-linear FE code Abaqus. Figure 1 depicts a flowchart of the main processes involved in the subroutine. Once the equivalent trial stress has been obtained, a check for viscoplastic behaviour on the current timestep is conducted. Viscoplastic behaviour is implemented ($\dot{\boldsymbol{\varepsilon}}^{\mathrm{pl}} \neq 0$) if the following criterion is met:

$$\Omega > 0 \quad \text{and} \quad \frac{\partial \Omega}{\partial \boldsymbol{\sigma}} : \dot{\boldsymbol{\sigma}} > 0 \tag{2.10}$$

where Ω is the dissipation potential, defined for the hyperbolic sine model as:

$$\Omega = \frac{\alpha}{\beta} \cosh(\beta f)\, \mathrm{sgn}(\beta f) \tag{2.11}$$

If viscoplastic behaviour is observed, a Newton iterative method is employed to obtain a converged increment in effective plastic strain and the increments of the plastic strain tensor are evaluated using the flow rule, described by Eq. (2.4). The increment of stress is then calculated using the simple constitutive equation:

$$\Delta\boldsymbol{\sigma} = \boldsymbol{\Lambda} : (\Delta\boldsymbol{\varepsilon} - \Delta\boldsymbol{\varepsilon}^{\mathrm{pl}} - \Delta\boldsymbol{\varepsilon}^{\mathrm{th}}) \tag{2.12}$$

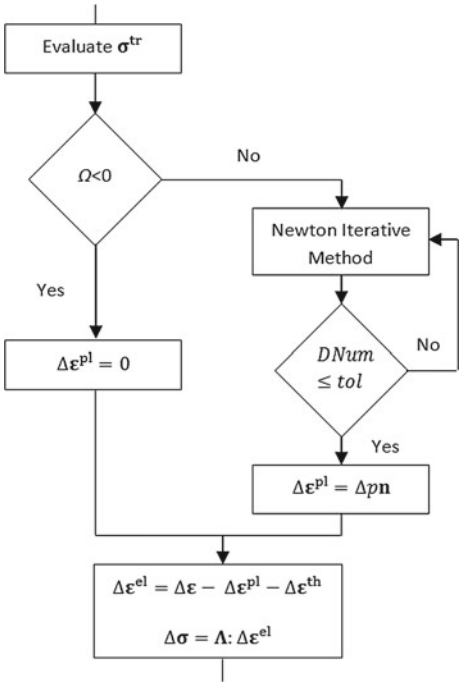

Fig. 1 Flowchart of the material user subroutine process

where $\boldsymbol{\Lambda}$ is the standard elasticity matrix.

2.2 Material Model Parameters

This paper is primarily concerned with the multi-axial implementation of a hyperbolic sine unified viscoplasticity model for cyclic stress-strain rate dependence and with preliminary identification of the salient hyperbolic material parameters, α and β, for the TMF behaviour of as-new P91. To this end, the published stress relaxation data of Koo et al. [10] for temperatures of 500 and 600 °C and the isothermal cyclic data of Saad et al. [15] for P91 steel, between 400 and 600 °C are employed. The experimental cyclic data of Saad et al. [15] is obtained at a strain rate of 0.1 %/s and a strain range of ±0.5 %. The first step is calibration of the material parameters. This is achieved using the stand-alone uniaxial code. Three sets of constants are identified, namely (i) elastic constants, Young's modulus (E), Poisson's ratio (ν, taken as 0.3 throughout), initial yield stress (k) and the coefficient of thermal expansion (α_{COE}), (ii) kinematic and isotropic hardening parameters and (iii) the cyclic viscoplastic parameters. For P91 steel, the temperature-dependent parameters for (i) are published by ASME [1] and are given in Table 1. The present model is essentially a generlisation of the unified

Table 1 Published temperature-dependent values of Young's modulus and coefficient of thermal expansion for as-new P91 steel [1]

Temperature (°C)	E (GPa)	α_{COE} (/°C)
400	184	12.95×10^{-6}
500	163	13.31×10^{-6}
600	142	13.59×10^{-6}

Table 2 Isotropic and kinematic hardening parameters for as-new P91 steel [15]

T (°C)	k (MPa)	Q (MPa)	b	C_1 (MPa)	γ_1	C_2 (MPa)	γ_2
400	96	−55.0	0.45	352500.0	2350.0	48600.00	405.0
500	90	−60.0	0.60	215872.6	2191.6	48235.29	460.7
600	43	−75.4	1.00	106860.0	2055.0	31159.90	463.0

Table 3 Temperature-dependent hyperbolic material parameters for as-new P91 steel

Temperature (°C)	α (s^{-1})	β (MPa^{-1})
400	8×10^{-07}	0.07
500	4×10^{-07}	0.064
600	1×10^{-07}	0.055

Chaboche power law model, with (i) a hyperbolic viscoplasticity function replacing the power-law function and (ii) inclusion of additional temperature-rate terms for the isotropic and kinematic hardening functions, but otherwise with similar isotropic and kinematic hardening evolution functions. Hence, for the current study, the kinematic and isotropic hardening parameters of [15] are adopted in general. Note that the initial yield stress value, k, at 600 °C is however, lower than that of [15], as calibration of the relaxation data of Koo et al. [10] led to a modified value of 43 MPa for this. As it is well documented that P91 steel undergoes cyclic softening behaviour due to coarsening of the microstructure [7, 15, 16], the isotropic hardening parameter Q has a negative value (Table 2).

From this initial material data, an iterative process is undertaken within the uniaxial code, whereby preliminary values of the cyclic viscoplastic parameters, α and β, are obtained by comparison with stress relaxation data [10] and isothermal cyclic data [15]. The resulting temperature-dependent values are listed in Table 3. Piece-wise linear interpolation is used to evaluate the material constants for the anisothermal cases.

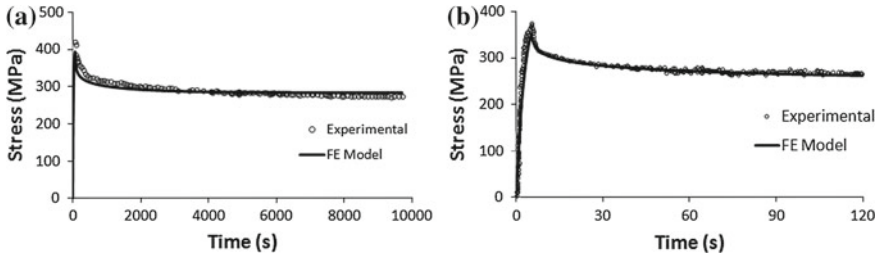

Fig. 2 Stress relaxation tests at 500 °C for **a** calibration of the hyperbolic viscoplastic parameters from the data of Koo et al. [10] and **b** validation against data of Saad et al. [15]

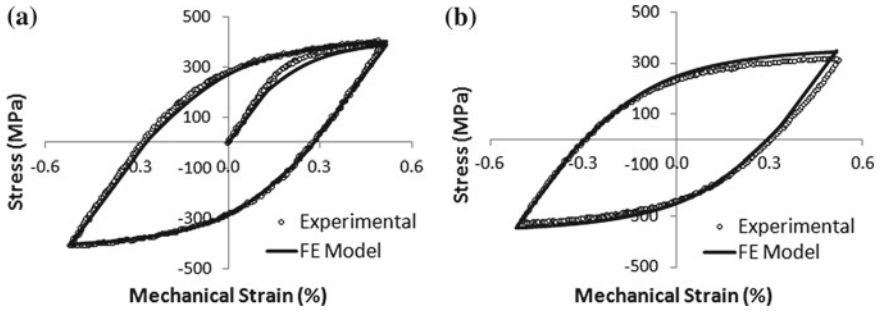

Fig. 3 Calibration of the material parameters from the experimental data of Saad et al. [15] at 500 °C and a strain rate of 0.1 %/s for **a** the initial cycle and **b** after 600 cycles

3 Results

The uniaxial code has been successfully calibrated against the previously published experimental results of [10, 15] and the multi-axial UMAT implementation has, in turn, been successfully validated against (i.e. gave identical results to) the uniaxial stand-alone code. The details are not shown here for compactness. The results of the calibration process are illustrated in Figs. 2a, 3 and 4. Following calibration using the

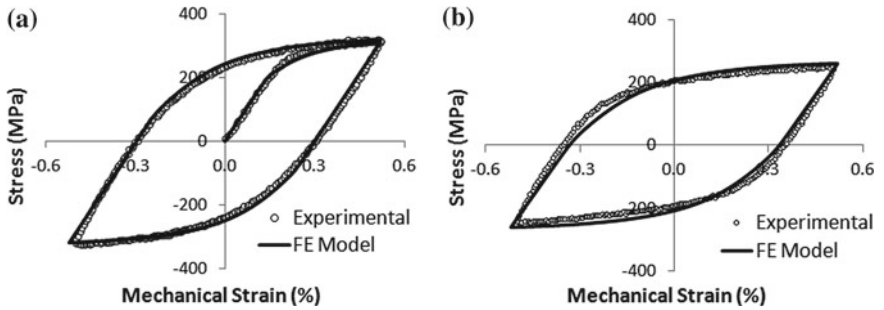

Fig. 4 Calibration of the material parameters from the experimental data of Saad et al. [15] at 600 °C and a strain rate of 0.1 %/s for **a** the initial cycle and **b** after 300 cycles

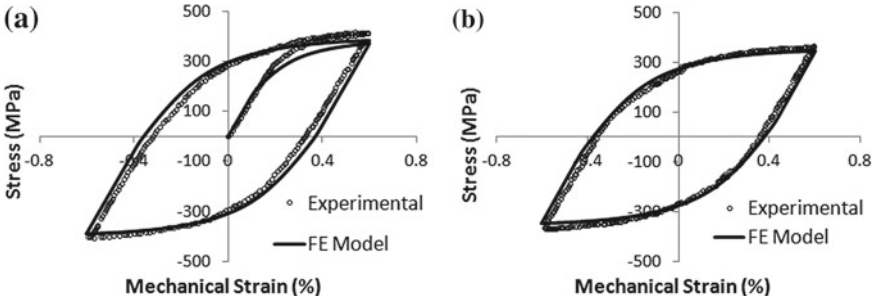

Fig. 5 Validation comparison of FE-predicted and the experimental data of Koo et al. [10] at 500 °C and a strain rate of 0.01 %/s for **a** the initial cycle and **b** after 130 cycles

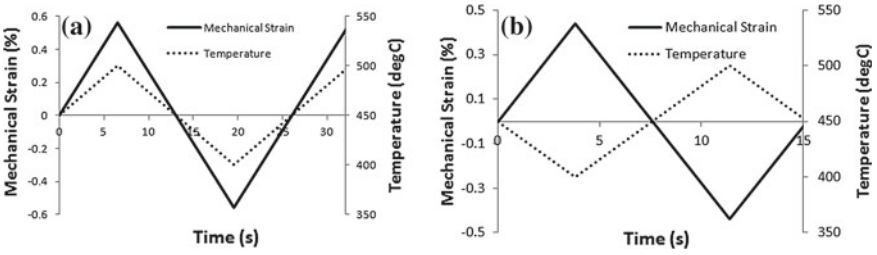

Fig. 6 Loading conditions for **a** TMF-IP loading and **b** TMF-OP loading

uniaxial code, the next steps are (i) validation of the multi-axial FE-implementation for isothermal (uniaxial) strain-controlled test conditions for P91 steel, and (ii) investigation of the validity of the isothermally-identified parameters for anisothermal (TMF) test conditions for P91 steel, including initial assessment of the effects of the additional temperature-rate terms over the range of test conditions from [10, 15]. Validation of the performance of the multi-axial material model for uniaxial isothermal cyclic loading conditions is conducted against data available in the literature [10, 15]. Figure 2b depicts the results obtained for a stress relaxation test at a temperature of 500 °C for the conditions tested in [15] and Fig. 5 illustrates the isothermal cyclic results obtained at a temperature of 500 °C for a different strain rate of 0.01 %/s, where excellent agreement with the experimental data is obtained. A similar quality of correlation is achieved for isothermal modelling at 400 °C. As expected, P91 steel exhibits considerable cyclic softening, with a 22 % reduction in the stress range for isothermal loading at 600 °C, for example.

Figure 6 shows the in-phase (IP) and out-of-phase (OP) anisothermal loading conditions simulated within the present study. Figure 7 illustrates that excellent correlation is achieved between the FE and measured [15] stress-strain responses for IP loading in the 400–500 °C range. Similar results are obtained for the 400–600 °C IP case, as shown in Fig. 8, although the model over-predicts stress range by about 5 %,

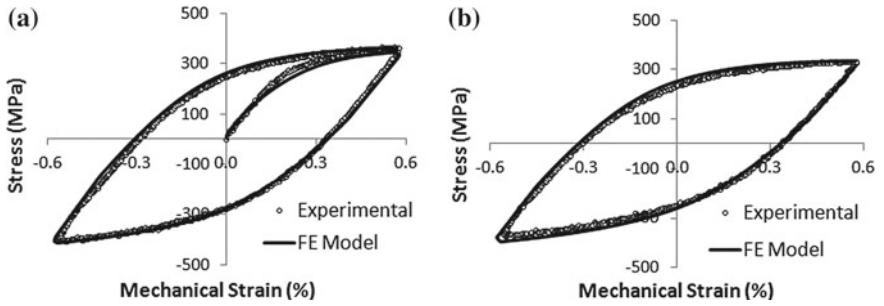

Fig. 7 Comparison of FE-predicted and measured [15] hysteresis loops for 400−500 °C TMF-IP loading, for **a** the initial loop and **b** after 100 cycles

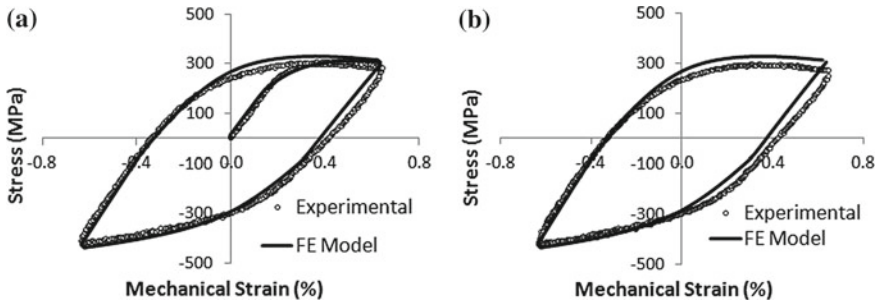

Fig. 8 Comparison of FE-predicted and measured [15] hysteresis loops for 400−600 °C TMF-IP loading, for **a** the initial loop and **b** after 3 cycles

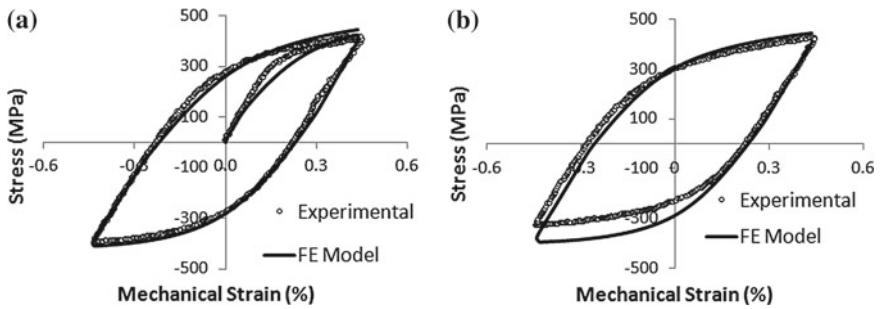

Fig. 9 Comparison of FE-predicted and measured [15] hysteresis loops for 400−500 °C TMF-OP loading, for **a** the initial loop and **b** after 100 cycles

at the tensile side, for later cycles. Figure 9 shows that the model performs well for the early cycles for the 400–500 °C OP case; however, it slightly over-predicts stress range (∼10 %) for later cycles, but still captures the tensile peak accurately.

4 Discussion and Conclusions

For the strain rates and strain ranges considered, the FE implementation of a multi-axial hyperbolic sine material model results in good correlation with both the experimental data and the unified Chaboche model implementations of [10, 15]. For the isothermal conditions simulated from 500 to 600 °C, the results show excellent agreement with the experimental data; discrepancies within the results may be attributable to non-optimised material parameters.

It has been argued (e.g. [5, 14]) that the hyperbolic sine viscoplasticity function, as compared to the power-law function of the unified Chaboche model, is (i) more representative of the mechanisms of deformation for martensitic-ferritic steels at high temperature, spanning a range of loading levels, e.g. cyclic loading, and (ii) therefore, has potential benefits for interpolation and extrapolation from the limited test conditions, typically employed for constitutive parameter identification, to the broader range of stress, strain-rate and temperature conditions experienced by real-plant components, as particularly required for ever-more flexible plant operation. This benefit has been alluded to within the present study by the ability of the hyperbolic sine material model to simulate the behaviour of P91 steel at different strain rates (e.g. see Figs. 3 and 5). Further validation of the multi-axial capability of the material model is required in future work, for example, by comparison with notched specimen data, e.g. see [19]. The ultimate aim is for application to realistic plant operating conditions for identification of representative TMF conditions for testing, e.g. see [6] and life prediction.

For the case of anisothermal loading conditions, the predicted results, which are also similar to those of the unified Chaboche model [15], suggest that the isothermal identification of material parameters is a reasonable basis for subsequent anisothermal behaviour prediction. The IP predictions are superior to the OP predictions, particularly for later OP cycles. The additional temperature-rate terms (i.e. the temperature derivative terms on the right hand side of Eqs. 2.8 and 2.9) have been found, for the conditions studied here, to lead to a relatively small effect on stress range, typically about 6 %. It is proposed that the use of a global optimisation technique, such as in [12], in future work will allow more detailed identification of the material parameters.

Acknowledgments This publication has emanated from research conducted with the financial support of Science Foundation Ireland under Grant Number SFI/10/IN.1/I3015. SBL gratefully acknowledges receipt of a Millennium Travel Grant from NUI Galway.

References

1. ASME Boiler and Pressure Vessel Code, 1998. Section II, Part D, ASME, New York (1998)
2. Chaboche, J.L.: A review of some plasticity and viscoplasticity constitutive theories. Int. J. Plast. **24**, 1642–1693 (2008)

3. Chaboche, J.L., Rousselier, G.: On the plastic and viscoplastic constitutive equations-part I: rules developed with internal variable concept. J. Press. Vessel Tech. **105**, 153–158 (1983)
4. Dunne, F., Petrinic, N.: Introduction to Computational Plasticity. Oxford University Press, Oxford (2007)
5. Dyson, B.F., Osgerby, S.: Modelling and analysis of creep deformation and fracture in a 1Cr1/2Mo ferritic steel. NPL Report DMM(A) 116, 1993
6. Farragher, T.P., Scully, S., O'Dowd, N.P., Leen, S.B.: Thermomechanical Analysis of a Pressurised Pipe Under Plant Conditions. Int. J. Press. Vessel Tech. (2012, in press)
7. Fournier, B., Sauzay, M., Barcelo, F., Rauch, E., Renault, A., Cozzika, T., Dupuy, L., Pineau, A.: Creep-Fatigue Interactions in a 9 Pct Cr-1 Pct Mo Martensitic Steel: Part II. Microstructural evolutions. Metall. Mater. Trans. A **40**, 330–341 (2009)
8. Hertzberg, R.W.: Deformation and Fracture Mechanics of Engineering Materials. Wiley, New York (1996)
9. Hyde, C.J., Sun, W., Leen, S.B.: Cyclic thermo-mechanical material modelling and testing of 316 stainless steel. Int. J. Press. Vessel. Pip. **87**, 29–33 (2010)
10. Koo, G.H., Kwon, J.H.: Identification of inelastic material parameters for modified 9Cr–1Mo steel applicable to the plastic and viscoplastic constitutive equations. Int. J. Press. Vessel. Pip. **88**, 26–33 (2011)
11. Lemaitre, J., Chaboche, J.L.: Mechanics of Solid Materials. Cambridge University Press, Cambridge (2000)
12. Mahmoudi, A.H., Pezeshki-Najafabadi, S.M., Badnava, H.: Parameter determination of Chaboche kinematic hardening model using a multi objective genetic algorithm. Comput. Mater. Sci. **50**, 1114–1122 (2011)
13. Miller, A.K.: The MATMOD equations, In: Miller, A.K. Unified Constitutive Equations for Creep and Plasticity, pp. 139–220. Elsevier Applied Science, London (1987)
14. Perrin, I.J., Hayhurst, D.R.: Creep constitutive equations for a 0.5Cr–0.5Mo–0.25V ferritic steel in the temperature range 600–675°C. J. Strain Anal. **31**, 299–314 (1996)
15. Saad, A.A., Hyde, C.J., Sun, W., Hyde, T.H.: Thermal-mechanical fatigue simulation of a P91 steel in a temperature range of 400–600°C. Mater. High Temp. **28**(3), 212–218 (2011)
16. Saad, A.A., Sun, W., Hyde, T.H., Tanner, D.W.J.: Tanner, Cyclic softening behaviour of a P91 steel under low cycle fatigue at high temperature. Procedia Eng. **10**, 1103–1108 (2011)
17. Scully, S.: ESB Energy International, personal communication (2012)
18. Shrestha, T., Basirat, M., Charit, I., Potirniche, G.P., Rink, K.K., Sahaym, U.: Creep deformation mechanisms in modified 9Cr–1Mo steel. J. Nucl. Mater. **423**, 110–119 (2012)
19. Tanner, D.W.J., Sun. W., Hyde, T.H.: FE analysis of a notched bar under thermomechanical fatigue using a unified viscoplasticity model, Procedia Engineering. Procedia Eng. **10**, 1081–1086 (2011)
20. Tong, J., Vermeulen, B.: The description of cyclic plasticity and viscoplasticity of Waspaloy using unified constitutive equations. Int. J. Fatigue **25**, 413–420 (2003)
21. Zhan, Z.: A study of creep-fatigue interaction in a new nickel-based superalloy. PhD thesis, University of Portsmouth (2004)
22. Zhang, Z., Delagnes, D., Bernhart, G.: Anisothermal cyclic plasticity modelling of martensitic steels. Int. J. Fatigue **24**, 635–648 (2002)

Enhanced Global Digital Image Correlation for Accurate Measurement of Microbeam Bending

L. I. J. C. Bergers, J. Neggers, M. G. D. Geers and J. P. M. Hoefnagels

1 Introduction

Microbeams are simple on-chip test structures used for thin film and MEMS materials characterization [3], see Fig. 1. Optical profilometry techniques are typically used for the measurement of deformations [8, 10]. Profilometry can be combined with Euler-Bernoulli (EB) beam theory to extract material parameters, like the E-modulus or creep parameters. The latter requires characterization of time-dependent microbeam bending, though non-trivial, as it involves long term sub-microscale measurements. On the one hand environmental instabilities directly hinder accurate long term measurements. On the other hand microfabrication limitations often affect the ideal fixed-end geometrical boundary condition [2]. This requires attention, because a non-ideal fixed-end, e.g. a compliant anchor, introduces errors when using the microbeam *deflection* with EB-theory [6]. Hence, the problem is attaining sufficient accuracy and precision in these measurements.

A first step towards precise microbeam bending experiments is the careful design and construction of the setup and proper control of the profilometer's environment [1]. In [1] we presented a simple image correlation based methodology to correct the rigid body motions, e.g. due to drift, of the deformed specimen on the $xy\theta_x\theta_y$-positioning stage. The difference between the reference profile and this deformed profile yielded the tip deflection. However, this correlation based correction has a drawback: the correction is extrapolated to the entire beam profile based on a limited

L. I. J. C. Bergers · J. Neggers · M. G. D. Geers · J. P. M. Hoefnagels (✉)
Department of Mechanical Engineering, Materials Technology,
Eindhoven University of Technology, P.O. Box 513, 5600 MB Eindhoven, The Netherlands
e-mail: j.p.m.hoefnagels@tue.nl

L. I. J. C. Bergers
Foundation for Fundamental Research on Matter, P.O. Box 3021, 3502 GA Utrecht,
The Netherlands

L. I. J. C. Bergers
Materials innovation institute M2i, P.O. Box 5008, 2600 GA Delft, The Netherlands

H. Altenbach and S. Kruch (eds.), *Advanced Materials Modelling for Structures*,
Advanced Structured Materials 19, DOI: 10.1007/978-3-642-35167-9_5,

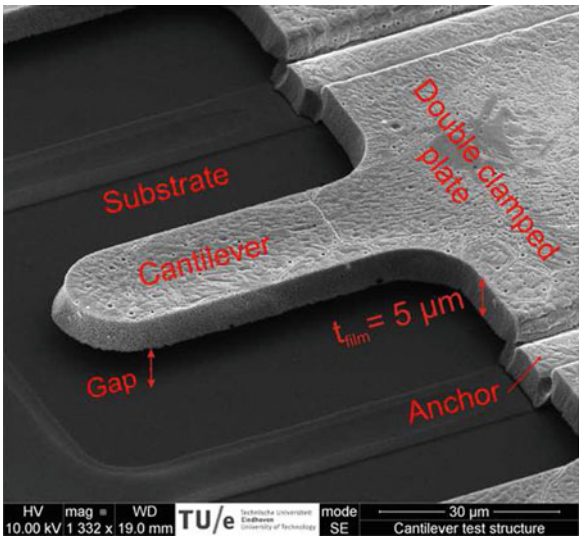

Fig. 1 Scanning electron micrograph of a typical on-chip microbeam attached to a free-standing double clamped plate that is anchored to the substrate

reference area on the anchor. As the beam lies in the extended direction of the anchor, the resulting tip deflection is sensitive to an extrapolation error.

Following Neggers et al. [7], we here present an improved approach for microbeam bending analysis. The approach in [7] extracts curvature from profilometry data of bulged membranes through enhanced global digital image correlation (GDIC). The key point is the use of the deformation kinematics as degrees of freedom to be solved in the minimization problem formulated for DIC as demonstrated by Hild and Roux [4, 5]. Therefore, in the approach presented here we combine the drift and beam bending kinematics and directly correlate on the beam, eliminating any extrapolation errors. The correlation procedure yields the displacement fields. This does not directly yield the beam *deflection*, because the position of the anchor is not resolved. However, the *curvature* field of the beam can be directly extracted from this displacement field, because a C2-continuous basis for the degrees of freedom is chosen. This effectively filters measurement noise, overcoming issues when taking derivatives to calculate the curvature. In short, this improved approach yields an accurate curvature field, in stead of beam deflection, that serves equally well in analyzing microbeam bending mechanics.

In this work, we describe the kinematics involved followed by the implementation into the GDIC procedure through which the curvature is determined. To asses the accuracy of this new procedure a numerical experiment is performed of which the implementation and results are discussed.

2 Principle of Global Digital Image Correlation and Curvature Measurement

In the solid mechanics community DIC has become an established method to measure deformation fields at various length scales both in 2D and 3D geometries [9]. For the 2D case one records an image of an undeformed, reference situation of an object and of its the deformed situation. Parts of the image with a unique pattern can then be correlated from one image to the next, allowing one to extract the displacements between the two instances. Traditionally, one applies a pattern with sufficient detail and variation to obtain uniqueness for the correlation procedure.

The correlation procedure in 2D is based on the principle of optical flow conservation. It states that the reference image, represented by the intensity field $f(\mathbf{x})$, is related to the deformed image, $g(\mathbf{x})$ through the in-plane displacement field $\mathbf{u}_{xy}(\mathbf{x})$ and measurement noise $n_0(\mathbf{x})$:

$$g(\mathbf{x} + \mathbf{u}_{xy}(\mathbf{x})) = f(\mathbf{x}) + n_0(\mathbf{x}). \tag{1}$$

In the case of optical profilometer data, the intensity is in fact a height, and can also vary due to e.g. deformations. This quasi 3D nature can be exploited by relaxing the optical flow conservation:

$$g(\mathbf{x} + \mathbf{u}_{xy}(\mathbf{x})) = f(\mathbf{x}) + u_z(\mathbf{x}) + n_0(\mathbf{x}). \tag{2}$$

The unknown displacement fields $\mathbf{u}(\mathbf{x})$ are found through minimizing the global residual η of the weak form of Eq. (2) over the considered domain

$$\eta^2 = \int [(f(\mathbf{x}) - g(\mathbf{x} + \mathbf{u}_{xy}(\mathbf{x})) + u_z(\mathbf{x})]^2 d\mathbf{x} = \int r(\mathbf{x})^2 d\mathbf{x}, \tag{3}$$

where $r(\mathbf{x})$ is the residual field. The displacement field is parameterized and interpolated using a set of basis functions $\phi_n(\mathbf{x})$ acting globally over the entire domain and weighted with a discrete set of degrees of freedom u_n

$$\mathbf{u}(\mathbf{x}) = u_x(\mathbf{x})\mathbf{e}_x + u_y(\mathbf{x})\mathbf{e}_y + u_z(\mathbf{x})\mathbf{e}_z = \sum_n u_n \phi_n(\mathbf{x})\mathbf{e}_i, \tag{4}$$

where $i = [x, y, z]$ and the basis functions $\phi_n(\mathbf{x})$ are polynomial functions depending on $\mathbf{x} = x\mathbf{e}_x + y\mathbf{e}_y$

$$\phi_n = x^{\alpha(n)} y^{\beta(n)}. \tag{5}$$

The choice for this parametrization has the benefit that it allows one to introduce degrees of freedom suitable for describing the deformation kinematics, whilst maintaining a continuously differentiable solution. This aspect is important, because the strain and, particularly for microbeam bending, curvature fields are (higher order)

derivatives of the displacement fields. Furthermore when the order of the polynomials are limited, measurement noise is effectively filtered, yielding a robust curvature measurement: the smooth continuously differentiable displacement fields and not the measurement data serve as input for differentiation.

The introduction of the degrees of freedom and the appropriate basis functions can be based on prior knowledge of the deformation kinematics. For example, a uniaxial strain in x, ϵ_{xx}, could be described by adding a basis function of degree $[\alpha, \beta] = [1, 0]$ in x-direction: $\phi_{10} = x^1 y^0$. Adding this basis function to the z-direction would describe a constant tilt. One should however be aware that superfluous degrees of freedom will not necessarily yield the correct solution for the displacement fields, because of the measurement noise. On the other hand residual fields showing systematic deviations from zero might indicate insufficient kinematic degrees of freedom. Therefore, the prior knowledge allows a sufficient choice of degrees of freedom that will describe the kinematics, but limit inaccuracies due to noise.

As the curvature field is the desired measurand from the microbeam bending experiment, we consider all rigid body displacements, rotations about the x- and y-axis, resulting from drift of the $xy\theta_x\theta_y$-platform, and the end-loaded bending of the single clamped microbeam. The bending results in a gradient in curvature, involving a third order displacement derivative along the beam's axis, which is taken along the x-direction. Hence the parametrization of the displacement fields takes the following form:

$$u(x) = (u_{x,00})\mathbf{e}_x + (u_{y,00})\mathbf{e}_y + (u_{z,00} + u_{z,10}x + u_{z,01}y + u_{z,20}x^2 + u_{z,30}x^3)\mathbf{e}_z. \quad (6)$$

From the displacement fields resulting from the GDIC procedure, the curvature field tangent to the beam's surface in x-direction, $\kappa_{xx}(\mathbf{x})$, can be derived. First the curvature tensor is constructed as the dyadic product of the gradient operator and the surface normal:

$$\kappa = \nabla \otimes \mathbf{n}, \quad (7)$$

where the gradient operator is defined as

$$\nabla = \mathbf{e}_x \frac{\partial}{\partial x} + \mathbf{e}_y \frac{\partial}{\partial y} + \mathbf{e}_z \frac{\partial}{\partial z}. \quad (8)$$

The normal vector is calculated from the position field of the deformed microbeam $z(x, y)$, obtained by applying the resulting displacement fields to the reference profile:

$$\mathbf{n} = \frac{\nabla z(\mathbf{x})}{||\nabla z(\mathbf{x})||}. \quad (9)$$

Finally the curvature field in a given tangent direction is calculated by

$$\kappa_{\mathbf{t}}(\mathbf{x}) = \mathbf{t} \cdot \kappa \cdot \mathbf{t} \quad (10)$$

where the unit tangent vector, $\mathbf{t}(\boldsymbol{\tau})$, along an in-plane unit vector $\boldsymbol{\tau}(\mathbf{x}) = \tau_x \mathbf{e}_x + \tau_y \mathbf{e}_y$ is

$$\mathbf{t} = \frac{\tau_x \mathbf{e}_x + \tau_y \mathbf{e}_y + (\nabla f) \cdot \boldsymbol{\tau} \otimes \mathbf{e}_z}{\sqrt{\tau_x{}^2 + \tau_y{}^2 + [(\nabla f) \cdot \boldsymbol{\tau}]^2}} \tag{11}$$

and $\boldsymbol{\tau} \otimes \mathbf{e}_z$ is the dyadic product of the two vectors. In the processing applied, the curvature is measured along the tangent in-plane unit vector $\boldsymbol{\tau} = 1\mathbf{e}_x$.

3 Evaluation of Accuracy

In order to evaluate the accuracy of the GDIC approach a numerical microbeam bending experiment is conducted. A linear elastic finite element model of a representative microbeam ($l = 100$ µm, $w = 20$ µm, $t = 5$ µm) is modeled in Marc/Mentat using quadratic thick shell elements, see Fig. 2. Only half of the microbeam is modeled due to symmetry. It is deflected at the end by 2 µm. The surface topography of a physical microbeam is measured using a Sensofar Plu2300 confocal optical profilometer, see Fig. 3a and [1] for details. A corresponding part of this topography, see ROI_f in Fig. 3b, is deformed with the numerically generated displacement fields. An additional constant in-plane displacement $\mathbf{u}_{xy}(\mathbf{x}) = 1,162\mathbf{e}_x - 0,830\mathbf{e}_y$ µm as well as an out-of-plane tilt $\mathbf{u}_z(\mathbf{x}) = (0,0005x - 0,0006y)\mathbf{e}_z$ µm simulate drift, see ROI_g in Fig. 3b. These values are selected as uneven half-pixel multiples, where the pixel size is $0,332 \times 0,332$ µm^2, serving as a worst case, because this leads to the poorest DIC accuracy [4]. The deformed and displaced topography serves as input for the GDIC procedure with the natural surface features serving as the pattern. Subsequently the curvature is calculated based on the GDIC output and compared to the numerically prescribed curvature calculated from the nodal displacements and rotations of the FEM output.

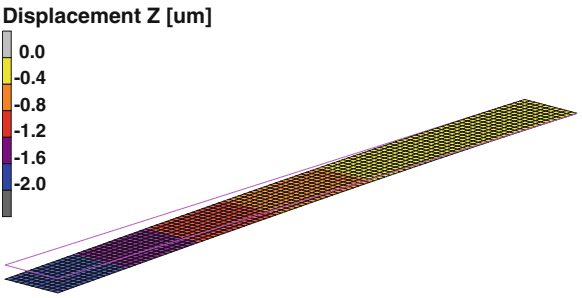

Fig. 2 The FEM model in deformed state used for generating the displacement fields. The left end is deflected, whilst the right end is clamped

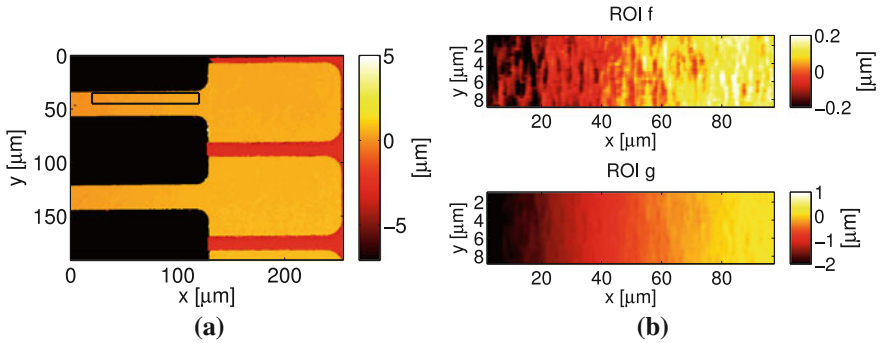

Fig. 3 **a** A contour plot of two actual microbeams. The box on the top beam's surface indicates the part used for GDIC as shown in **b**: ROIs of the undeformed **f** and deformed **g** selection from the beam

To minimize numerical artifacts when doing this numerical evaluation there are some issues to address. First, the computational mesh and discrete surface topography will have a different discretization. This is overcome by interpolating both surfaces with C1- or C2-continuous interpolation functions to finer and equal grids and excluding pixels adjacent to the border of the region of interest. Second, the prescribed curvature fields calculated from interpolated nodal displacement fields will show artifacts, because the nodal displacements are not C1-continuous between elements. Although nodal rotations strictly speaking also suffer the same discontinuity, they effectively do form a C1-continuous gradient of the displacement field for the curvature calculation. Hence the nodal rotations θ_i are interpolated and used in the curvature calculation through the following definition of $\mathbf{n}$:

$$\mathbf{n} = \frac{\tan(\theta_y(\mathbf{x}))\mathbf{e}_x + \tan(\theta_x(\mathbf{x}))\mathbf{e}_y + \mathbf{e}_z}{\sqrt{\tan(\theta_x(\mathbf{x}))^2 + \tan(\theta_y(\mathbf{x}))^2 + 1}}. \tag{12}$$

4 Results

The results of the GDIC at different levels of deflection are judged by the displacement fields obtained in x-, y- and z-direction and the residual field. The resulting displacement fields show good agreement with the prescribed displacement fields, see Fig. 4. For the in-plane displacements an accuracy of <13 nm is observed, which corresponds to $\sim$0, 04 pixels for a 332 nm pixel size. The accuracy of the z displacement field is <2 nm, whilst its field reveals a systematic error. This might be caused by a slight curvature in y-direction that is not covered by the admitted degrees of freedom.

When regarding the residual field and comparing to the undeformed pattern, see Fig. 5, no systematic features are observed, indicating the correlation has reached the

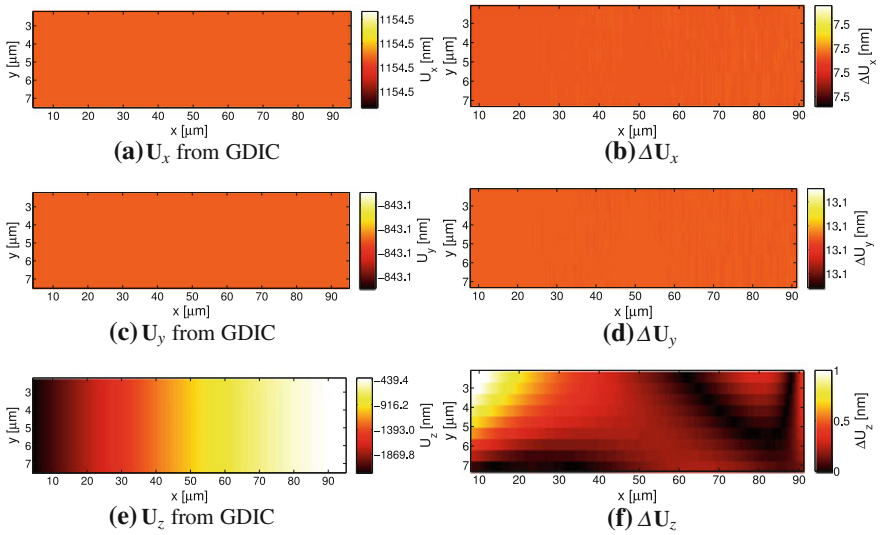

Fig. 4 Resulting displacement fields including drift at 2 µm deflection obtained through GDIC. **a, c, e** are the GDIC obtained displacement fields and **b, d, f** are the difference fields between the GDIC and FEM displacement fields

global minimum. Further, the amplitude of the residual field is relatively large, about 10 % of the undeformed pattern. If the global minimum is obtained, this amplitude can only be attributed to the limited number of pixels, being $\sim 20 \times 190$, and the effect of interpolating the surface pattern within the correlation algorithm. Improving this requires a smoother surface pattern and higher spatial sampling. Nonetheless, the results are adequate compared to local DIC approaches where typically facets of 15×15 pixels are employed to resolve displacement fields with similar accuracy.

The curvature fields κ_{xx} obtained through the GDIC at 1 and 2 µm deflection and the difference between these and the simulated κ_{xx} reveal a good measurement of κ_{xx}, see Fig. 6. The expected gradient in κ_{xx} is visible, approaching 0 at the tip of the beam (left hand side of images) and reaching a maximum at the clamped end (right hand side of images). The difference shows a limited error, caused by the limited choice of degrees of freedom and required interpolation during correlation.

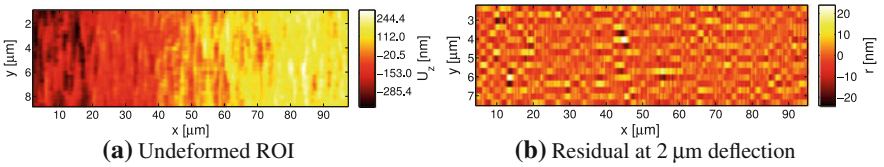

Fig. 5 Comparison of the amplitude in the pattern and the resulting residuals showing a relatively low residual

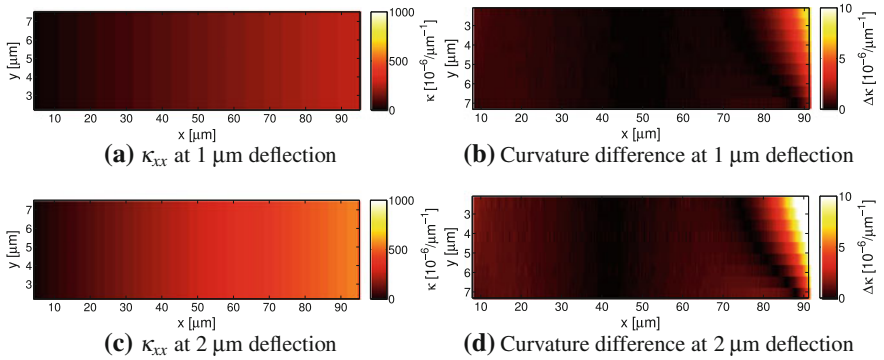

(a) κ_{xx} at 1 µm deflection **(b)** Curvature difference at 1 µm deflection

(c) κ_{xx} at 2 µm deflection **(d)** Curvature difference at 2 µm deflection

Fig. 6 Curvature fields κ_{xx} at 1 and 2 µm deflection reveal the expected gradient, whilst the differences with the numerically prescribed fields show a good accuracy

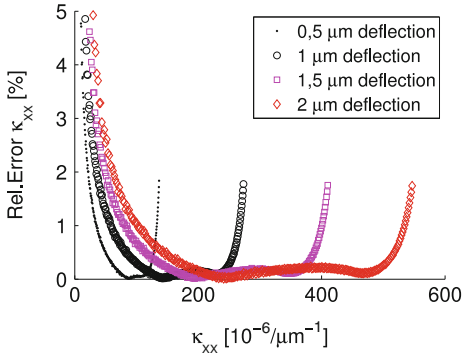

Fig. 7 The accuracy of κ_{xx} obtained is good for the part of the ROI that is not near the loaded end or the clamped end

Within the probed range of κ_{xx} the accuracy of the measurement is $<1\,\%$ for most of the ROI, see Fig. 7. The accuracy, defined as the relative error $(\kappa_{xx,GDIC} - \kappa_{xx,FEM})/\kappa_{xx,FEM}$, increases near the clamped end due to the additional κ_{yy} and at the loaded end due to the definition of the accuracy. Naturally one can opt not to measure data near these regions.

5 Conclusion

We presented an enhanced digital image correlation approach to extract beam curvature from full-field deformation data of microbeam bending experiments. A limited yet sufficient amount of degrees of freedom in the GDIC described the bending kinematics as well as possible rigid body motions that might be caused due to drift in actual experiments. A numerical analysis of the accuracy based on FEM revealed that the proposed GDIC accurately resolved the bending kinematics: an accuracy in the κ_{xx}-measurement of $<1\,\%$ for parts of the beam away from the clamped and free

ends. The presented numeric analysis can also be extended to simulate the influence of measurement artifacts, e.g. noise or pattern quality. This GDIC methodology thus enables the precise measurement of beam curvature required for time-dependent microbeam bending experiments. It might also find application in other microbeam bending analyses, e.g. stress measurements of deflecting structural parts of microdevices in case of known material parameters.

Acknowledgments This research was carried out under Project number M62.2.08SDMP12 in the framework of the Industrial Partnership Program on Size Dependent Material Properties of the Materials innovation institute M2i (http://www.m2i.nl) and the Foundation of Fundamental Research on Matter (FOM), which is part of the Netherlands Organization for Scientific Research (NWO).

References

1. Bergers, L.I.J.C., Hoefnagels, J.P.M., Delhey, N.K.R., Geers, M.G.D.: Measuring time-dependent deformations in metallic MEMS. Microelectron. Reliab. **51**, 1054–1059 (2011)
2. Gill, J.J.Y., Ngo, L.V., Nelson, P.R., Kim, C.J.: Elimination of extra spring effect at the step-up anchor of surface-micromachined structure. J. Microelectromech. Syst. **7**, 114–121 (1998)
3. Guckel, H., Burns, D., Rutigliano, C., Lovell, E., Choi, B.: Diagnostic microstructures for the measurement of intrinsic strain in thin films. J. Micromech. Microeng. **2**, 86–95 (1992)
4. Hild, F., Roux, S.: Digital image correlation: from displacement measurement to identification of elastic properties—A review. Strain **2**, 69–80 (2006)
5. Hild, F., Roux, S.: Comparison of local and global approaches to digital image correlation. Exp. Mech. **52**(9), 1503–1519 (2012). doi:10.1007/s1134001296037
6. Menčík, J., Quandt, E.: Determination of elastic modulus of thin films and small specimens using beam bending methods. J. Mater. Res. **14**, 2152–2161 (1999)
7. Neggers, J., Hoefnagels, J.P.M., Hild, F., Roux, S., Geers, M.G.D.: A Global Digital Image Correlation enhanced full-field bulge test method. Proc. IUTAM. **4**, 73–81 (2012)
8. O'Mahony, C., Hill, M., Brunet, M., Duane, R., Mathewson, A.: Characterization of micromechanical structures using white-light interferometry. Meas. Sci. Tech. **14**, 1807–1814 (2003)
9. Sutton, M.A., Orteu, J., Schreier, H.W.: Image Correlation for Shape. Motion and Deformation Measurements. Springer, New York (2009)
10. Van Spengen, W.M., Puers, R., Mertens, R., De Wolf, I.: Characterization and failure analysis of MEMS: high resolution optical investigation of small out-of-plane movements and fast vibrations. Microsyst. Technol. **10**, 89–96 (2004)

An Investigation of the Mechanical Properties of Open Cell Aluminium Foam Struts: Microtensile Testing and Modelling

Charles Betts, Daniel Balint and Jianguo Lin

Abstract A microtensile test procedure has been developed to directly determine the mechanical properties of individual metal foam struts. The results reveal that the measured strut properties display a considerable reduction in elastic stiffness compared to the typical value of 70 GPa for aluminium alloys. A realistic finite element modelling procedure of the as-tested struts has been established, using X-ray microtomography scans of the undeformed struts, to assess the reasons for this reduction in stiffness. The material model in the FE simulations was established using a damage model that comprises of a set of continuum mechanics-based viscoplastic damage constitutive equations. The equations were calibrated with the microtensile test data and implemented into ABAQUS through the user defined subroutine VUMAT. The prime factor in the recorded reduction in stiffness was found to be slippage between the grips and the strut during testing.

1 Introduction

Metal foams are a relatively new class of materials that show good potential for lightweight structures, energy absorption, and thermal management [1–3]. They can combine low density with good bending stiffness and strength [2]. They can also be made with integral skins [4]. They display a densification stage when subjected to a compressive stress, where the stress rises rapidly with strain as the foam cells crush—this has the implication that the integrity of a metal foam core sandwich panel

C. Betts (✉) · D. Balint · J. Lin
Department of Mechanical Engineering, Imperial College London,
South Kensington Campus, London SW7 2AZ, UK
e-mail: charles.betts03@imperial.ac.uk

D. Balint
e-mail: d.balint@imperial.ac.uk

J. Lin
e-mail: jianguo.lin@imperial.ac.uk

H. Altenbach and S. Kruch (eds.), *Advanced Materials Modelling for Structures*,
Advanced Structured Materials 19, DOI: 10.1007/978-3-642-35167-9_6,

is not necessarily compromised when subjected to impacts. Open cell foams do not trap moisture (i.e. they are less susceptible to corrosion than honeycomb cores) [5].

Efforts have been made to accurately assess the mechanical properties of metal foams. The important length scale in metal foams is cell size or strut length. The unit cell of cellular/lattice materials is in the order of millimetres or micrometres, allowing them to be treated both as structures and materials. The lattices can be studied using traditional methods of mechanics, but one must also treat the lattice as a 'material' in its own right, with its own set of effective properties that allows a direct comparison with fully dense materials [6, 7]. Analytical methods to determine the basic properties of metal foams have been extensively studied—see e.g. [8]. From these models it is apparent that the foam strength is strongly dependant on the individual cell strut properties. Typically, the material properties of the bulk alloy from which the foam is made are used to predict the foam properties. However, due to the foaming process and length scale of the struts, there can be notable differences between the mechanical properties of the bulk alloy and the individual struts due to differences in both composition and microstructure.

Few studies have been previously done to assess the mechanical properties of individual metal foam struts, especially with regards to their direct measurement [9–12]. This paper aims to further this work by developing a novel microtensile testing technique to measure the tensile properties of metal foam struts. X-ray micro-tomography (XMT) is employed as a means to accurately measure the strut cross-sections prior to deformation, so as to enable the experimental force readings to be converted to stress. A set of continuum mechanics-based viscoplastic damage constitutive equations are used to model the material behaviour of the struts. The equations are calibrated with the microtensile test data and implemented into ABAQUS through the user defined subroutine VUMAT. Realistic finite element (FE) simulations of the as-tested struts are then conducted, using the XMT scans for the part geometry. The FE simulations are used to evaluate any experimental errors in the microtensile test set-up.

2 Characterisation of Metal Foam Samples

2.1 Ageing of Metal Foam Samples and Chemical Composition

The metal foam was acquired from BPE International, Germany. It is a metal matrix composite with TiC particles fabricated from an Al-Zn-Mg-Cu (7xxx series) alloy and has an open cell structure. To achieve peak strength, the T6 heat treatment process, detailed below, was applied to the as-cast metal foam. The T6 ageing condition does not significantly impair the ductility of the struts.

1. The foam was solution heat treated at 480 °C and subsequently quenched in cold water;
2. The foam was then aged by heating to 120 °C for 4 h;
3. The foam was then left to cool slowly at room temperature.

Table 1 Chemical composition of Al-Zn-Mg-Cu-TiC alloy metal foam strut (in weight percent)

Element	Mg	Al	Si	Ti	Cu	Zn
Average	1.09	Balance	0.68	6.49	1.46	4.18

Average based on 8 readings from 2 separate samples

The chemical composition of the metal foam was determined using energy-dispersive X-ray spectroscopy (EDX) and is shown in Table 1.

3 Experimental Procedures

3.1 Microtensile Test Set-up

The Gatan Microtest 300 rig was used for microtensile testing of the metal foam struts in the scanning electron microscope (SEM). Figure 1 shows the test set-up. The struts were clamped with parallel, flat-surface steel grips. The tests were conducted at a speed of 0.5 mm/min, with a sampling time of 500 ms.

3.2 Determination of Stress and Strain

To convert the force readings from the test software into engineering stress, the undeformed cross-sectional area of the struts is required. Each strut was scanned using XMT prior to testing. The 3D render was imported into the analysis software Avizo, where cross-sectional slices of the strut could be exported at specific increments (between 15.79 and 18.25 μm, depending on the scan).

Thirty cross-sectional slices were taken along the central region of each strut and their area was measured using the imaging software ImageJ. The force readings

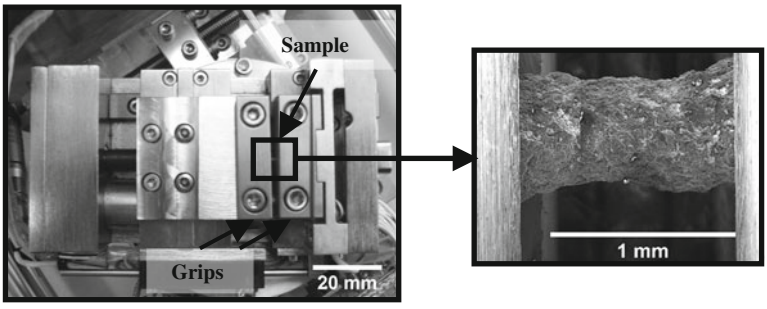

Fig. 1 Photograph of the microtensile testing set-up showing Gatan Microtest rig

were converted to stress by dividing each value by the average area of the thirty cross-sectional slices.

Engineering strain was determined from the test rig crosshead displacement.

4 Microtensile Test Results

4.1 Microtensile Properties of the Struts

Ten metal foam struts were heat treated as outlined in Sect. 2.1. The struts were scanned using XMT and microtensile tested. Six specimens fractured at the grips and were thus excluded from the analysis. Figure 2a gives the experimental stress-strain graphs for the four struts that did not fracture at the grips.

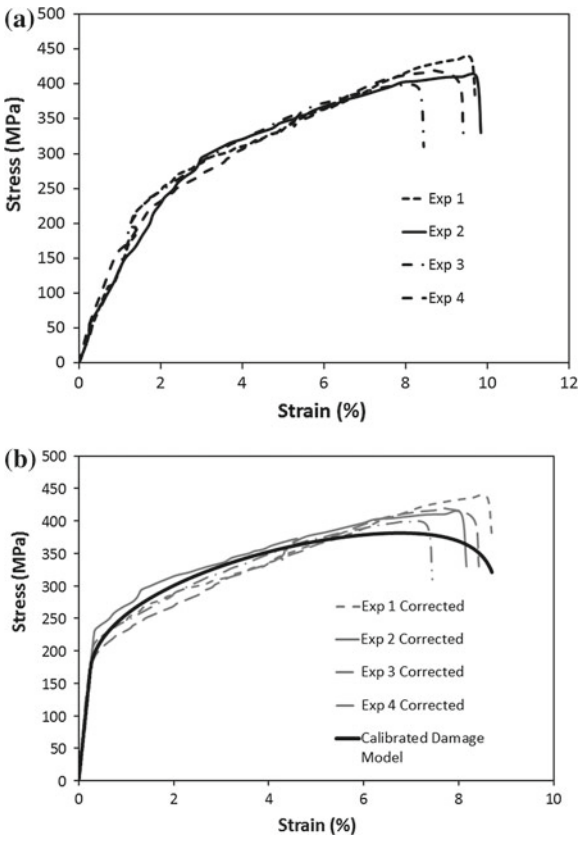

Fig. 2 **a** Experimental microtensile test stress-strain graphs for the metal foam struts aged at 120 °C for 4 h. Four repeats were carried out under the same conditions. **b** Corrected stress-strain graphs adjusted to address the observed significant reduction in strut stiffness seen in **a**. The calibrated damage model is also shown

Figure 2a shows that the gradient of the initial elastic region of the stress-strain plots is much lower than the ballpark figure of 70 GPa for corresponding aluminium alloys. The average gradient measured from the experiment results is 14 GPa. The reasons for this disparity are discussed in Sect. 6. The tested struts show decent repeatability in the results, with the UTS varying from 398 to 435 MPa and the failure strain varying from 8.4 to 9.8 %.

4.2 Corrected Stress-Strain Graphs of the Struts

From the observed test results in Fig. 2a, it is clear that the elastic behaviour of the struts was not correctly measured. Previous work [12] has suggested this may be due to the initial curvature of the struts, which may reduce the strut stiffness. This proposal is further assessed in Sect. 5.2. Strut slippage effects are discussed in Sect. 6.

It is proposed that at the onset of yielding, the struts are subjected to uniaxial tensile testing conditions and slippage effects are significantly reduced. The stress-strain plots of Fig. 2a have consequently been modified as follows:

1. The elastic region of the plots has been modified so that the Young's modulus is equal to 70 GPa;
2. The displacement due to slippage effects has been subtracted from the total measured displacement so as to correct the reported strain values.

The validity of this approach is investigated in Sect. 6. Figure 2b shows the corrected stress-strain graphs.

5 Damage Modelling

5.1 Unified Viscoplastic Damage Constitutive Law and Calibration

A series of constitutive equations for viscoplastic damage have been previously developed [13–15]. These equations capture the effect of various time-dependant phenomena such as dislocation-associated hardening and damage. When implemented into an FE model, this approach can validate results and facilitates the extrapolation to new loading states. The multi-axial constitutive equation set presented in [16] is proposed to describe the damage behaviour of the metal foam struts:

$$\dot{\varepsilon}_e^P = \left(\frac{\bar{\sigma}_e - k - R}{K}\right)^n \tag{1}$$

$$\dot{\bar{\rho}} = A_1(1 - \bar{\rho})\dot{\varepsilon}_e^P \tag{2}$$

$$R = B\bar{\rho}^{\frac{1}{m}} \tag{3}$$

$$\dot{\omega} = \frac{\alpha C \dot{\varepsilon}_e^P}{(1-\omega)^{n_0}} \tag{4}$$

$$\sigma_{ij} = 2G\varepsilon_{ij}^e + \lambda\delta_{ij}\varepsilon_{kk}^e \tag{5}$$

$$\varepsilon_{ij}^e = \varepsilon_{ij}^t - \varepsilon_{ij}^p \tag{6}$$

$$\tilde{\sigma_{ij}} = \frac{\sigma_{ij}}{(1-\omega)} \tag{7}$$

$$\dot{\varepsilon}_{kl}^P = \frac{3}{2}\frac{S_{kl}}{\sigma_e}\dot{\varepsilon}_e^P \tag{8}$$

where $\dot{\varepsilon}_e^P$ is the effective viscoplastic strain rate. $\dot{\varepsilon}_e^P = \left(\frac{\tilde{\sigma_e} - k - R}{K}\right)^n$ when $\tilde{\sigma_e} - k - R \geq 0$ and $\dot{\varepsilon}_e^P = 0$ when $\tilde{\sigma_e} - k - R < 0$. $\dot{\tilde{\rho}}$ is the rate of normalised dislocation density and R describes the hardening caused by dislocations within the material. ω is damage and varies from 0 (no damage) to 1 (full damage). $\alpha = 1$ when $\sigma_{kk} = \sigma_{11} + \sigma_{22} + \sigma_{33} \geq 0$ or $\alpha = 0$ when $\sigma_{kk} = \sigma_{11} + \sigma_{22} + \sigma_{33} < 0$ which ensures damage is only included in the constitutive equation set when loading is in tension.

ε_{ij}^e is the elastic strain and is determined from the total strain, ε_{ij}^t subtracted from the plastic strain, ε_{ij}^p. k is the material yielding stress and K is the drag stress. G and λ are the Lamé parameters (where G is the shear modulus). The von Mises stress is given by $\sigma_e = \sqrt{\frac{3}{2}S_{ij}S_{ij}}$. The deviatoric stress is given by $S_{ij} = \sigma_{ij} - \frac{1}{3}\sigma_{kk}\delta_{ij}$. $\tilde{(\ )}$ denotes effective tensors in terms of damage, such as in Eq. (7). δ_{ij} is the Kronecker delta, equal to 1 when $i = j$ and equal to 0 when $i \neq j$. All indices—i, j, k, l—follow the usual tensor conventions. n, A_1, B, m, C, and n_0 are material constants.

The material constants associated with the equation set were determined by calibrating the damage model using the corrected test results presented in Sect. 4.2. Table 2 gives the set of parameters used for the tested struts. Figure 2b shows the calibrated damaged model superimposed on the corrected test stress-strain plots.

5.2 FE Model of As-Tested Struts

FE modelling of the as-tested metal foam struts has been conducted using the software ABAQUS 6.9-1. The models consist of a 3D meshed geometry of identical dimensions to the as-tested struts. This has been achieved by importing the XMT scans into the analysis software Avizo, where the geometry was meshed with a 4-node tetrahedral grid. The mesh was imported into ABAQUS with element type C3D4 selected.

Table 2 Constants used in the multi-axial constitutive equation set for the metal foam struts

E (GPa)	υ	k (MPa)	K (MPa)	n	A1	B (MPa)	C	m	n_0
70	0.33	180	100	1.4	0.55	1450	0.8	2	6

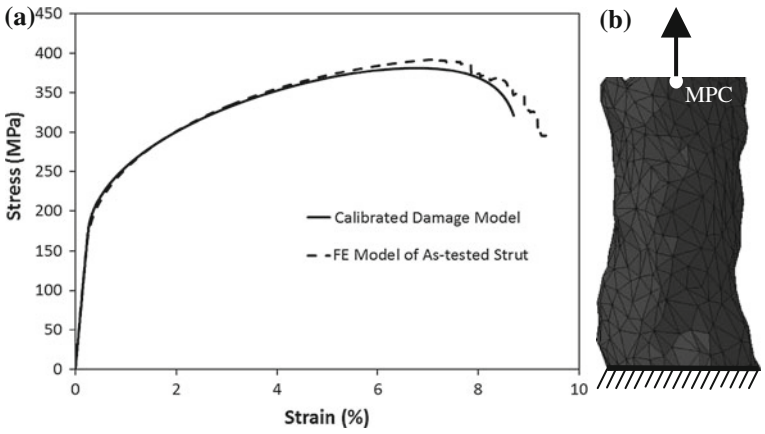

Fig. 3 **a** Comparison of stress-strain graphs for the calibrated damage model and the FE model of the as-tested strut. **b** FE model of as-tested metal foam strut with calibrated damage model set as material definition

The applied boundary conditions are shown in Fig. 3b. The bottom face of the strut was constrained in all degrees of freedom. A uniform tensile load was modelled by applying a multi-point constraint (MPC) along the top face of the strut, whereby all nodes along that face were tied to the central node. Load versus displacement plots were obtained by moving this central node in the vertical direction under a controlled, linear displacement. The viscoplastic damage constitutive equation set presented in [16] was implemented into the ABAQUS model through the user defined subroutine VUMAT.

5.3 FE Results of As-Tested Struts

Figure 3a shows a comparison of the stress-strain graphs for the calibrated damage model of Sect. 5.2 and the FE model of one of the as-tested struts. There is good agreement between the two curves, indicating that the damage model has been successfully implemented into ABAQUS, and that any effect of the struts straightening from an initially curved shape by bending before uniaxial tension has minimal impact on the force versus displacement readings.

The large reduction in the gradient of the initial elastic region of the experimental stress-strain plots in relation to that for corresponding aluminium alloys is therefore due primarily to another factor. The effect of slippage between the tested struts and the grips has been considered in Sect. 6.

6 FE Analysis of Slippage Effects

An FE model has been constructed to capture the effect of slippage between the grips and the tested strut to establish the reasons for the reduction in measured stiffness. The strut geometry was constructed as described in Sect. 5.2. The grips were modelled as rigid bodies.

6.1 Applied Boundary Conditions, Loads and Material Model

For the first time step of the analysis, the grips were brought together by applying a vertical displacement to a reference point on each of the grips. All other degrees of freedom were constrained. In the second step, the left pair of grips was constrained in all degrees of freedom and a horizontal displacement was applied to the right pair of grips with all other degrees of freedom constrained so as to model the test conditions. The material model is as per that used in Sect. 5.2.

6.2 Surface Interactions

To model the effect of slippage between the grips and the strut, the tangential surface interaction between the grips and strut was assigned a penalty friction formulation, with a constant coefficient of friction, $\mu_f = 0.25$. This value was selected through trial and error so as to achieve the best fit with the experimental data, and lies within the typical range for aluminium/steel surface interactions—see e.g. [17]. The effect of varying μ_f is discussed in Sect. 6.3.

6.3 FE Results of Slippage Effects

Figure 4 shows a comparison, for one tested strut, of the stress-strain graphs for the FE model with slippage for three different values of coefficient of friction, $\mu_f = 0.15$, 0.25 and 0.40, and the experimental microtensile test result of the same strut. The best agreement is achieved in the observed stiffness between the FE model with slippage and the experiment result when $\mu_f = 0.25$. Figure 4 indicates that slippage between the strut and grips is the prime cause for the measured reduction in strut stiffness during microtensile testing. As expected, a lower value of μ_f reduces the observed stiffness in the FE model with slippage and a higher value of μ_f increases it.

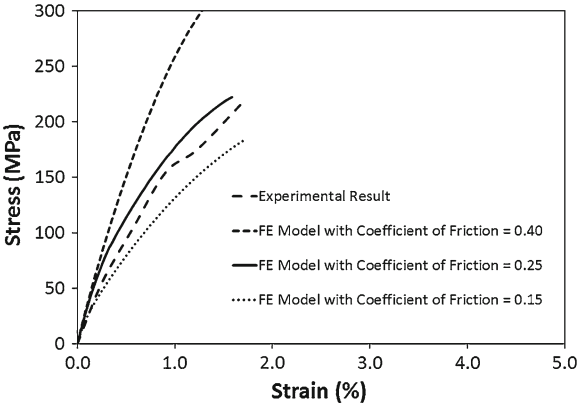

Fig. 4 Comparison of elastic region of stress-strain graphs for the FE model with slip with $\mu_r = 0.15$, $\mu_r = 0.25$, and $\mu_r = 0.40$ and the microtensile experimental result of same strut

Figure 5 compares the strain field along the same longitudinal strut cross-section between the FE model with slip (with $\mu_f = 0.15$, 0.25 and 0.40) and the FE model with no slip for a displacement of 0.00211 mm. It can be seen from Fig. 5 that the effective gauge length (defined as the region where appreciable strain is observed) is greater for the FE model with slip (equal to 2×0.86 mm for $\mu_f = 0.15$) than that with no slip (equal to 2×0.58 mm). This furthers the explanation for the reduction in observed strut stiffness. Increasing the coefficient of friction in the model with slip reduces the effective gauge length and the measured strains increase and tend towards that for the case with no slip, as observed in Fig. 6a, b.

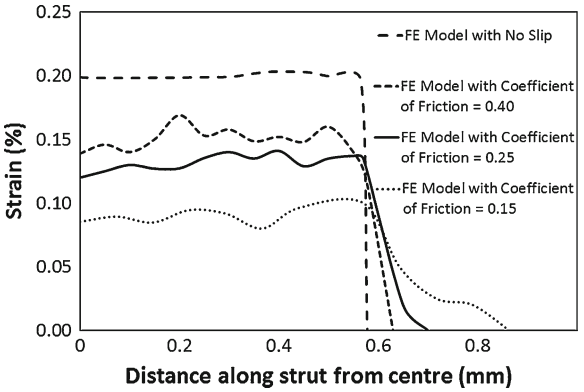

Fig. 5 Comparison of strain field along the same longitudinal strut cross-section between the FE model with slip with $\mu_r = 0.15$, $\mu_r = 0.25$, and $\mu_r = 0.40$ and the FE model with no slip for a displacement of 0.00211 mm

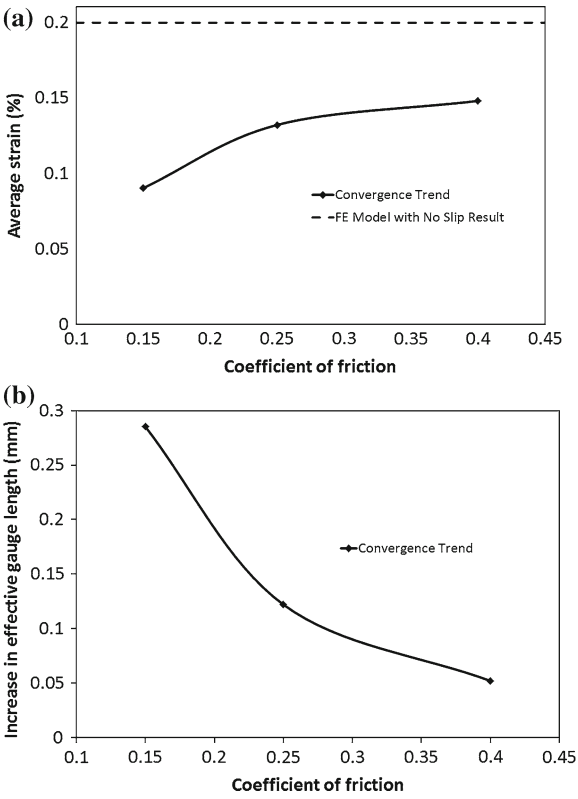

Fig. 6 Convergence of FE model with slip with increasing μ_f towards the FE model with no slip for (**a**) average strain across the gauge length; and (**b**) effective gauge length

7 Conclusions

A microtensile test procedure has been developed to directly determine the mechanical properties of individual metal foam struts. The conversion of the force data to stress has been achieved using XMT scans of the undeformed struts.

The measured strut properties showed a significant reduction in elastic stiffness compared to the typical value of 70 GPa for aluminium alloys. The reasons for this have been investigated via realistic FE modelling of the as-tested struts. The material model in the FE simulations was established using a set of continuum mechanics-based viscoplastic damage constitutive equations. The equations were calibrated with the microtensile test data and implemented into ABAQUS through the user defined subroutine VUMAT. The calibrated damage model is used in forthcoming FE studies to determine the extent of structural damage in a foam for different loading scenarios.

It has been established that, for the metal foam material investigated in this paper, strut curvature has a minimal impact on the measured strut stiffness. Slippage between the grips and the strut during microtensile testing appears to be the chief factor in the recorded reduction in stiffness.

The microtensile test procedure and ability to ascertain the mechanical properties of individual metal foam struts is valuable as there can be notable differences between the mechanical properties of the bulk alloy and the individual struts due to variances in both composition and microstructure.

References

1. Banhart, J.: Manufacture, characterisation, and application of cellular materials and metal foams. Prog. Mat. Sci. **46**, 559–632 (2001)
2. Ashby, M.F., Evans, A., Fleck, N.A., Gibson, L.J., Hutchinson, J.W., Wadley, H.N.G.: Metal Foams: A Design Guide. 1st edn. Butterworth-Heinemann, Boston (2000)
3. Evans, A.G. et al.: The topological design of multifunctional cellular metals. Prog. Mater. Sci. **46**, 309–327 (2001)
4. McCormack, T.M. et al.: Failure of sandwich beams with metallic foam cores. Int. J Solid Struct. **38**, 4901–4920 (2001)
5. Sypeck, D.: Cellular truss core sandwich structures. Appl. Compos. Mater. **12**, 229–246 (2005)
6. Ramamurty, U., Paul, A.: Variability in mechanical properties of a metal foam. Acta Mater. **52**, 869–876 (2004)
7. Ashby, M.F.: The properties of foams and lattices. Phil. Trans. R. Soc. **364**, 15–30 (2006)
8. Ashby, M.F., Gibson, L.J., Cellular Solids Structure and Properties. 1st edn. Pergamon Press, Cambridge (1988)
9. Markaki, A.E., Clyne, T.W.: The effect of cell wall microstructure on the deformation and fracture of aluminium-based foams. Acta Mater. **49**(6), 1677–1686 (2001)
10. Simone, A.E., Gibson, L.J.: Aluminum foams produced by liquid-state processes. Acta Mater. **46**(9), 3109–3123 (1998)
11. Zhou, J., Allameh, S., Soboyejo, W.O.: An investigation of the microstructure and strength of open-cell 6101 aluminum foam. Metall. Mater. Trans. **33**, 1413–1427 (2002)
12. Zhou, J., Allameh, S., Soboyejo, W.O.: Microscale testing of the strut in open cell aluminium foams. J. Mater. Sci. **40**, 429–439 (2005)
13. Lin, J., Dean, T.A.: Modelling of microstructure evolution in hot forming using unified constitutive equations. J. Mater. Process. Technol. **167**(2–3), 354–362 (2005)
14. Lin, J.: Selection of material models for predicting necking in superplastic forming. Int. J. Plast. **19**(4), 469–481 (2003)
15. Lin, J., Liu, Y., Dean, T.A.: A review on damage mechanisms, models and calibration methods under various deformation conditions. Int. J. Damage Mech. **14**(4), 299–319 (2005)
16. Wang, S., Lin, J., Balint, D.: Modelling of failure features for TiN Coatings with different substrate materials. J. Multiscale Model. **3**(1–2), 49–64 (2011)
17. Chaplin, R.L., Chilson, P.B.: The coefficient of kinetic friction for aluminum. Wear **107**(3), 213–225 (1986)

Multiscale Optimization of Joints of Dissimilar Materials in Nature and Lessons for Engineering Applications

Victor Birman, Yanxin Liu, Stavros Thomopoulos and Guy M. Genin

Abstract In this chapter we review various aspects of biological attachments of dissimilar materials, concentrating on the example of tendon-to-bone attachment, a composite made up of compliant collagen fibers and stiff mineral platelets. The natural optimization of this attachment occurs on several scales, including macroscopic morphology and interdigitation. Macroscopically, interdigitation is analogous to z-pinning in composite joints. Microscopically, functional grading occurs for both the orientation of collagen fibers and the distribution of mineral. Nanoscopic optimization involves the sequencing of mineral deposition within and around the collagen fibrils. The lessons from the tendon-to-bone attachment are pertinent to the attachments of dissimilar materials in engineering. A discussion on possible applications of these lessons in engineering attachments is included in the concluding section of the chapter.

1 Introduction

Engineering science increasingly relies on lessons available from biology. Natural biological systems invariably demonstrate superior adaptability to loads encountered during their life cycle. In particular, attachments and joints of dissimilar materials

V. Birman (✉)
Missouri University of Science and Technology, St. Louis, MO 63131, USA
e-mail: vbirman@mst.edu

Y. Liu · S. Thomopoulos · G. M. Genin
Washington University in St. Louis, St. Louis, MO 63130, USA
e-mail: yanxinliu@go.wustl.edu

S. Thomopoulos
e-mail: thomopouloss@wudosis.wustl.edu

G. M. Genin
e-mail: genin@wustl.edu

H. Altenbach and S. Kruch (eds.), *Advanced Materials Modelling for Structures*,
Advanced Structured Materials 19, DOI: 10.1007/978-3-642-35167-9_7,

in biology represent an excellent example of such sophistication that can provide lessons applicable to engineering materials and structures.

Typical examples of attachments of dissimilar materials in biology include:

- Joints between the tooth and alveolar bone [1], which exhibit two interfaces with graded variations in their stiffnesses. These interfaces are between the alveolar bone and cementum and between cementum and root dentin.
- Joints between tendon and bone, i.e., the so-called tendon-to-bone insertion site. This joint is discussed in this chapter; here, the stiffness changes by almost two orders of magnitude over a short distance (1 mm or less).

Attachments of dissimilar materials in engineering have attracted significant interest due to an ever-increasing application of advanced and novel structural and material systems. Examples of such attachments include joints between a composite wing or control surface and an aluminum fuselage, chip-substrate packages in electronics, a joint between the composite superstructure and the steel hull in naval architecture, etc. Multiple problems in such assemblies are caused by a mismatch between the properties of connected materials that is sometimes addressed through functional grading.

In this chapter, we outline the results of our recent studies on mechanics of the tendon-to-bone insertion site. This natural biological site possesses high resilience and toughness, while the regenerated site upon healing is highly vulnerable, exhibiting failure rates up to 94 % [2]. The analysis of the regenerated insertion site, as compared to the natural site, points to the reason for such a striking difference. While the natural site is characterized by multiscale grading, orthotropic properties and an optimum gross morphology, the regenerated site is filled with scar tissue that is homogeneous and isotropic. We demonstrate some of the mechanisms responsible for the resilience and toughness of the natural tendon-to-bone insertion site and suggest methodologies and solutions for engineering materials, utilizing the lessons learned from our biomechanical research.

2 Optimization Through Multiscale Functional Grading and Interface Morphology

Functional grading in engineering applications is often conducted on a single scale [3]. For example, macromechanical grading of the fiber orientation around a hole was suggested as a method of reduction of stress concentrations [4]. Functionally graded architectures developed in the eighties to enhance thermomechanical properties of ceramic-metal space plane structures exposed to an elevated temperature were characterized by through-the thickness microscale grading of ceramic and metal constituents [5]. In comparison, natural functional grading often occurs across several scales. A typical example of a multiscale biological attachment is the tendon-to-bone joint, where two materials with a nearly two-order of magnitude property mismatch (the modulus of elasticity of bone and the longitudinal modulus of tendon are of

the order of 20 GPa [6] and 450 MPa [7], respectively) are joined through a transitional region that is less than 1 mm long. The tendon-to-bone insertion represents a continuous functionally graded material where the grading occurs on the nanometer scale as well as on the micrometer scale. The insertion site consists of collagen fibers and mineral inclusions. While the orientation of collagen fibers varies from nearly uniaxial in the tendon to a less organized distribution at the insertion, the content of mineral increases nearly linearly from the front of the partially mineralized region of the insertion to the bone [8]. The deposition of mineral on and within collagen fibrils as its concentration increases from the front of the partially mineralized region to the bone may follow several scenarios, differing in the sequence by which mineral is deposited in the gaps between collagen molecules and/or on the surface of each fibril.

Optimum stress and stiffness distributions across the insertion site are achieved through four mechanisms:

1. Nanometer scale gradation: (a) Distribution of bioapatite (mineral) on and within partially mineralized collagen fibrils; (b) Nanoscale architecture facilitating the formation of a compliant bond between the tendon and bone.

It is necessary to first explain the structure of a partially mineralized tendon-to-bone insertion region. Collagen is formed of triple-helix molecules organized in a twisted quasi-triclinic packing [9]. In turn, collagen molecules are arranged in fibril of several hundred nanometers diameter, forming a periodic staggered structure. Collagen fibers are formed from an assembly of fibrils. Fibers assemble to form fascicles and fascicles then assemble to form the tendon.

We investigated five different scenarios of bioapatite accumulation in the graded region, from the bone to the outer radius of mineralization (Fig. 1). The difference in the scenarios was related to the sequence of deposition of the mineral in the gap regions of the fibril, between collagen molecules forming the fibril, and within the intermolecular space. For example, the "gap-nucleated" scenario implies mineral first filling the gaps between the collagen molecules, following with the extrafibrillar mineralization of gaps and subsequently, mineralization of the entire surface of the fibril. The "nucleation-inhibited" scenario assumes that mineral first fills of the gaps between collagen molecules, followed with the formation of an extrafibrillar sheet originating at one location and eventually encompassing the entire fibril. Other scenarios covered all possible sequences of the mineral accumulation between collagen molecules and on the surface of the fibril.

As was shown in our study, all five scenarios demonstrate a local drop in the stiffness, close to the boundary of the mineralization radius. Previous experimental studies confirmed that this drop in stiffness exists at the physiologic insertion [2]; furthermore, experimental measures were even larger than those predicted by our nanoscale modelling. We concluded, based on the qualitative confirmation of experimental data, that a local reduction in the stiffness may serve to facilitate stress transfer at the insertion.

2. Micrometer scale gradation [10–12]**:** (a) Variable orientation of collagen fibers along the insertion length; (b) Graded distribution of mineral from bone to tendon.

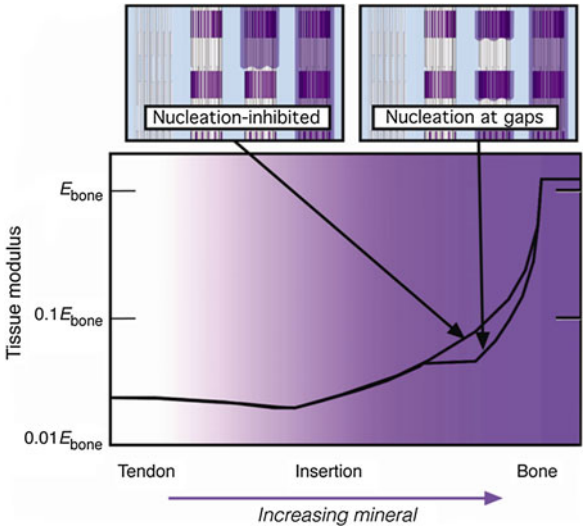

Fig. 1 Variation of the longitudinal modulus along the tendon-to-bone insertion site. The volume fraction of mineral is identified by the intensity of color. There is a small dip in the stiffness close to the front of the mineralized region due to fiber misalignment. The increase of the modulus from the front of the mineralized region to bone is governed by the nanoscale mechanism of mineral accumulation (e.g., "nucleation-inhibited" versus "nucleation at gaps" models) [13]

Two mechanisms, i.e., a variable orientation distribution of collagen fibers along the insertion site combined with a graded distribution of bioapatite (mineral) at the microscopic scale, combine to enhance the attachment strength and toughness and reduce stress concentrations. These gradients are involved in the process of microscopic optimization. The orientation of collagen fibers at the insertion site varies beginning with the predominantly uniaxial organization in the tendon. As the fibers become less organized approaching the bone, the stiffness of the tendon can be expected to drop. However, the second gradient, that of the increasing concentration of mineral, reverses the initial drop in the stiffness. The distribution of mineral gradually (nearly linearly) increases from the front of partially mineralized tissue to fully mineralized bone, as reflected in Fig. 1. The combination of these gradients results in a presumably optimum distribution of stiffness, toughness, and strength throughout the insertion site.

Further investigation [11] focused on spatial stiffness optimization aimed at a reduction of the stress concentration factor in an axisymmetric model resembling a rotator cuff (Fig. 2a). We used Bezier curves to approximate a distribution of the longitudinal and transverse moduli as well as the main Poisson ratio along the insertion site. The dimensions chosen in the analysis were representative of those in a human humeral head. The optimum distribution of properties that enables the complete elimination of the stress concentration is shown in Fig. 2b. Note that the dip in the stiffness found in this study and producing the optimum outcome was larger

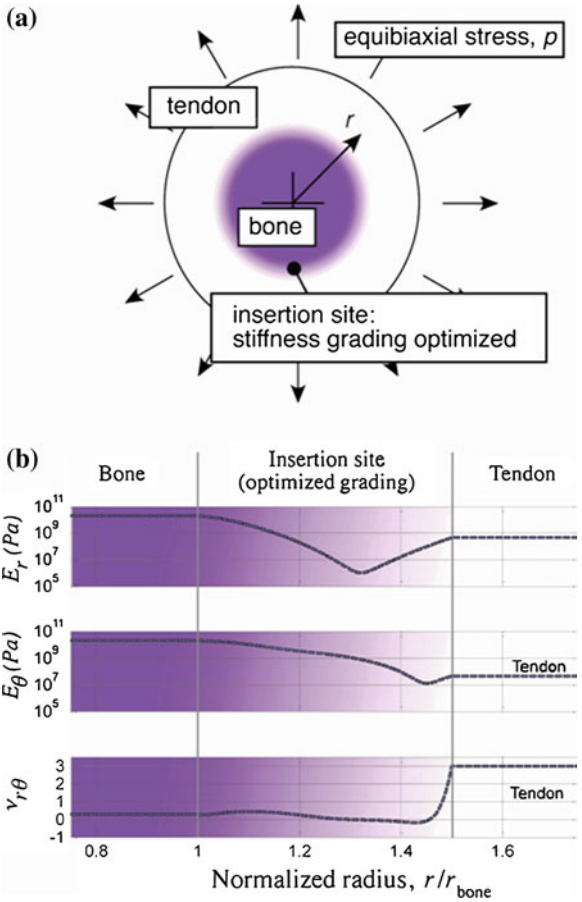

Fig. 2 Idealized axisymmetric model of the functionally graded tendon-to-bone insertion site **a**. The results of optimization aimed at a minimum stress concentration **b**. As follows from these results, a dip in the stiffness is beneficial for reduced stress concentration

than that predicted in the nanoscale investigation (Fig. 1). This discrepancy may be related to specifics of mineral accumulation in the partially mineralized section of the insertion site that are still not entirely clear. However, the qualitative agreement between nanoscale and microscale modelling that is also in agreement with experimental data is instructive. The optimum insertion site between dissimilar materials in nature, and extrapolating from this, the optimum attachment of dissimilar materials in engineering, involves a compliant region that should be graded to produce the most desirable combination of strength, stiffness, and toughness.

3. Macroscale interface grading: Interdigitation of the insertion site, including Sharpey fibers [14] extending from the tendon into the bone [10].

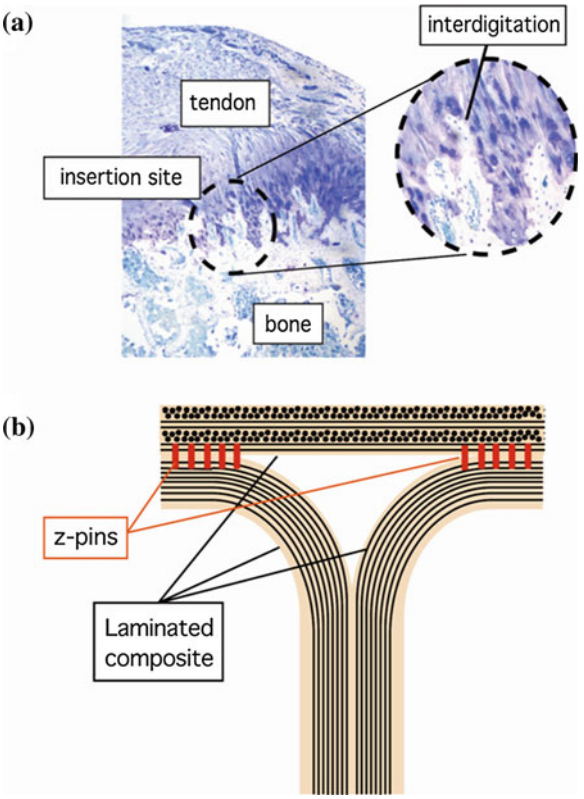

Fig. 3 Interdigitation along the interface between dissimilar materials in nature (**a**) and engineering (**b**). The presence of mineral gradually decreases from bone to tendon (**a**). In composite interfaces, z-pins representing small-diameter rods embedded in the material are employed to avoid or delay delamination (**b**). So-called "Sharpey fibers" resembling z-pins orthogonal to the interface were observed in biological attachments (not shown)

Interdigitation may improve the stress distribution at the junction between the compliant tendon and stiff bone. In engineering, a similar concept was developed to improve toughness along the interfaces of composite laminates. Ultimately, interdigitation may serve both functions: improvement of toughness and reduction of the interfacial stresses.

An example of interdigitation at the tendon-to-bone insertion site is shown in Fig. 3a. Although Sharpey fibers are not observed in this figure, their presence in other biological attachments has been documented (e.g., [15]). Even in the absence of observable Sharpey fibers, the interface in Fig. 3a clearly demonstrates the zone where the materials of predominantly collagen (tendon) and predominantly mineral (bone) coexist. The function of gradients in these materials along the insertion site is discussed in the previous sections of this chapter. The schematics of a z-pinned interface in a composite T-joint is shown in Fig. 3b. The function of such joint is usually an enhancement of toughness, while in-plane strength is unavoidably sacrificed.

The z-pinning concept originated in the aerospace industry, where z-pins represent high-strength small-diameter (usually, less than 1.0 mm) cylindrical rods oriented perpendicular or at an angle to the interface between the layers. Typically, z-pins are inserted prior to curing using an ultrasonic gun [16]. Adding just 1.9 % volume fraction of carbon z-pin fibers can increase the fracture toughness of a composite laminate by a factor of 18, without a noticeable reduction in in-plane tensile strength [17, 18]. The effectiveness of z-pins in the enhancement of the delamination resistance of composites was also demonstrated in [19], where it was suggested that roughening the surface of z-pins may be beneficial for their performance. The effect of z-pins on fracture toughness of composite laminates was further studied by Byrd and Birman [20–22] using the example of a standard double cantilever (DCB) test. It was shown that adding z-pins constituting between 1 and 1.5 % volume fraction of the DCB can result in the arrest of delamination cracks. Furthermore, it was suggested that the effectiveness of z-pins could be enhanced by designing their surface in a manner improving the "grasp" between the z-pin and adjacent material (e.g., woven z-pins with a naturally rough surface). A comprehensive review of z-pinning in composite laminates was published by Mouritz [23], outlining the manufacturing process and discussing advantages and disadvantages of z-pinning. Although quantitative guidance of engineering design based upon the physiologic analog of z-pinning at the tendon-to-bone insertion sites is premature, the existence of an analog to z-pinning in nature suggests that the strategy is well grounded.

4. Morphology of the insertion: Geometric shaping across the insertion site contributes to nonuniformity "employed" to achieve a desirable reduction of the stress concentration [10].

We studied the effect of the shape of the regenerated upon healing insertion site on the stress concentration, varying the shape of the site and employing the properties typical for bone, tendon and insertion scar tissue (Fig. 4a). In this problem, we considered peak principal stresses, based on the assumption that the tendon-to-bone insertion site is optimized for effective load transfer. The optimization resulted in the shape depicted in Fig. 4b, where we show the initial shape on the left and the optimum, somewhat counterintuitive shape, on the right. The stress concentration factor in the optimum shape was reduced to 1.05. This outcome may be instructive for reparative surgery; modern surgical reattachment often involves suturing the tendon to the bone [24]. Outcomes may be improved through a reduction of the stress concentration utilizing morphological studies aimed at an optimum stress concentration.

3 Comment on Multifunctional Optimization of the Attachment of Dissimilar Materials

While the previous discussion outlines studies that were mostly concerned with a reduction of stresses at the tendon-to-bone insertion site, such outcomes are not the only possible reason for the multiscale grading discussed above. A resilient

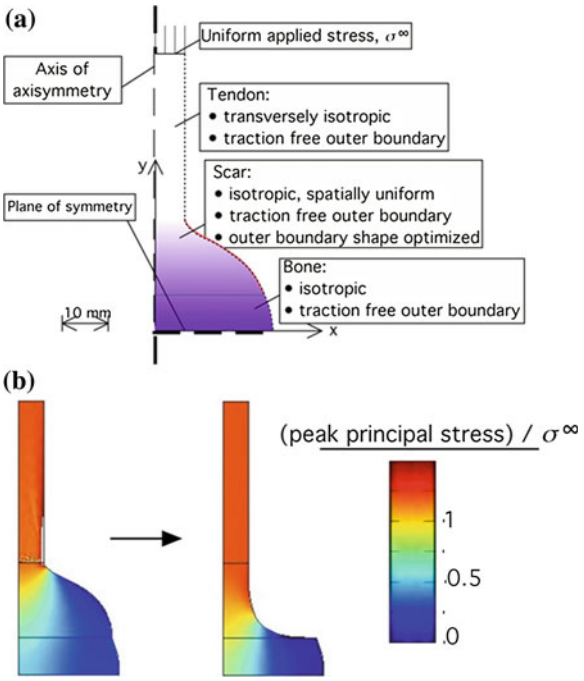

Fig. 4 Morphological optimization of the regenerated tendon-to-bone insertion site **a**. The stress concentration (peak principal stress normalized with respect to the applied tendon stress) can be eliminated by proper shaping of the fillet **b**

and reliable biological attachment should also possess high toughness. It has been established that high toughness is not necessarily related to the high stiffness of biological or engineering materials [25, 26]. We presume that, at the tendon-to-bone insertion, a drop in the stiffness is beneficial for a reduction of stresses but may also produce a desirable enhancement in toughness.

A second observation is that reduction of stresses may not necessarily improve the strength of the attachment, as a stress analysis should also be accompanied by an analysis of strength. For example, the Tsai-Hill criterion for a unidirectional graded composite material in the state of plane stress is

$$\frac{\sigma_1^2(\mathbf{X})}{s_L^2(\mathbf{X})} - \frac{\sigma_1(\mathbf{X})\,\sigma_2(\mathbf{X})}{s_L^2(\mathbf{X})} + \frac{\sigma_2^2(\mathbf{X})}{s_T^2(\mathbf{X})} + \frac{\tau_{12}^2(\mathbf{X})}{s_{LT}^2(\mathbf{X})} = 1 \tag{1}$$

where $\mathbf{X}$ is a position vector, σ_1 and σ_2 are the stresses along and across the fiber direction, respectively, τ_{12} is a shear stress, and s_L, s_T and s_{LT} are the strengths in the longitudinal and transverse directions, and the in-plane shear strength, respectively. Evidently, grading the material with the sole goal of reducing the stresses may actually weaken it, if the stress reduction is accompanied with the decrease of the strength.

A third issue arising in the process of the optimization of the attachment between dissimilar materials and related to toughness is the effect of grading on the fracture toughness of the interface. As was shown in our previous study [10], the order of singularity along the bondline between dissimilar materials is affected by the property mismatch. While the property mismatch may be optimized for a reduction of stresses, there is no guarantee that it will eliminate (or even minimize) the order of singularity.

Therefore, an analysis of attachment should account for all aspects of the material and structural behavior, including the stress distribution and concentration, the local strength, and the toughness. This conclusion is applicable to the majority of engineering materials, though the list of realistic optimization tools may be limited by availability and cost. The complexity of multifunctional optimization employing grading, morphology, and interdigitation that is successfully resolved in natural biological attachments is significant. It is therefore not surprising that engineers often limit the scope of the problem, concentrating on what are assumed to be essential aspects (e.g., minimization of peeling and transverse shear stresses in bonded joints).

4 Conclusions and Lessons for Engineering Applications

Studies of the insertion site demonstrate the presence of a multiscale grading of material distribution and organization. Both the experimental evidence as well as the optimization modelling indicate the presence of a counterintuitive dip in insertion stiffness compared to the stiffness of either bone or tendon [2]. As is shown in our research, one function of this dip is to minimize stress concentrations. It can also be argued that the dip enhances toughness of the attachment, although this has yet to be proven. Other factors that benefit the attachments of dissimilar materials, including the tendon-to-bone insertion site, are interdigitation and shape optimization of the interfacial region.

Both natural and engineering attachments serve multiple functions. Accordingly, the desirable outcome of multiscale grading, interdigitation, and shape optimization is a multifunctional optimization, including stiffening, strengthening, and toughening of the attachment. The achievement of such a comprehensive goal, while demonstrated in biology, is seldom achievable in engineering.

Research presented in this article may lead to the development of biomimetic engineering materials and structures employing multiscale grading for multifunctional optimization. In particular, some possible methods applicable to attachments of dissimilar materials in engineering include:

- Nonuniformly distributed inclusions in the interfacial layer, enhancing its toughness and strength;
- Functionally graded z-pinned interfaces (e.g., concentrating z-pins close to the edges of lapped joints may alleviate three-dimensional stresses leading to fracture);
- Wavy or interdigitated interfaces resembling biological attachments;

– Fibrous interfaces enhanced by addition of nanoparticles whose volume fraction is functionally graded.

References

1. Ho, S.P., Marshall, S.J., Ryder, M.I., Marshall, G.W.: The tooth attachment mechanism defined by structure, chemical composition and mechanical properties of collagen fibers in the periodontium. Biomaterials **28**(35), 5238–5245 (2007)
2. Thomopoulos, S., Williams, G.R., Gimbel, J.A., Favata, M., Soslowsky, L.J.: Variation of biomechanical, structural, and compositional properties along the tendon to bone insertion site. J. Orthop. Res. **21**(3), 413–419 (2003)
3. Birman, V., Byrd, L.W.: Modelling and analysis of functionally graded materials and structures. Appl. Mech. Rev. **60**, 195–216 (2007)
4. Cho, H.K., Rowlands, R.E.: Optimizing fiber direction in perforated orthotropic media to reduce stress concentration. J. Compos. Mater. **43**(10), 1177–1198 (2009)
5. Noda, N.: Thermal stresses in functionally graded materials. J. Therm. Stresses **22**, 477–512 (1999)
6. Bostrom, M.P.G., Boskey, A., Kauffman, J.K., Einhorn, T.A.: Form and function of bone. In: Buckwalter, J.A., Einhorn, T.A., Simon, S.R. (eds.) Orthopaedic Basic Science. 2 edn. pp. 319–370. AAOS, Aurora (2000)
7. Maganaris, C.N., Paul, J.P.: In vivo human tendon mechanical properties. J. Physiol. **521**(Pt 1), 307–313 (1999)
8. Genin, G.M., Kent, A., Birman, V., Wopenka, B., Pasteris, J.D., Marquez, P.J., Thomopoulos, S.: Functional grading of mineral and collagen in the attachment of tendon to bone. Biophys. J. **97**(4), 976–985 (2009)
9. Fratzl, P., Weinkamper, R.: Nature's hierarchical materials. Prog. Mater. Sci. **52**, 1263–1334 (2007)
10. Liu, Y., Birman, V., Chen, C., Thomopoulos, S., Genin, G.M.: Mechanisms of bimaterial attachment at the interface of tendon to bone. J. Eng. Mater. Technol. Trans. ASME **133**(1), 011006 (2011)
11. Liu, Y.X., Thomopoulos, S., Birman, V., Li, J.S., Genin, G.M.: Bi-material attachment through a compliant interfacial system at the tendon-to-bone insertion site. Mech. Mater. **44**, 83–92 (2012)
12. Thomopoulos, S., Marquez, J.P., Weinberger, B., Birman, V., Genin, G.M.: Collagen fiber orientation at the tendon to bone insertion and its influence on stress concentrations. J. Biomech. **39**(10), 1842–1851 (2006)
13. Liu, Y.: The mechanics of bimaterial attachment at the tendon-to-bone insertion site. PhD thesis. Washington University, St. Louis, Missouri (2012)
14. Quain, J.: Elements of Anatomy. 6th edn. Walton and Maberly, London (1856)
15. Liberman, D.E.: Life history variables preserved in dental cementum microstructure. Science **261**(5125), 1162–1164 (1993)
16. Greenhalgh, E., Hiley, M.: The assessment of novel materials and processes for the impact tolerant design of stiffened composite aerospace structures. Compos. Part A Appl. Sci. Manufact. **34**, 151–161 (2003)
17. Freitas, G., Magee, C., Dardzinski, P., Fusco, T.: Fiber insertion process for improved damage tolerance in aircraft laminates. J. Adv. Mater. (USA) **25**(4), 36–43 (1994)
18. Freitas, G., Fusco, T., Campbell, T., Harris, J., Rosenberg, S.: Z-Fiber Technology and Products for Enhancing Composite Design. In: AGARD Conference Proceedings, pp. 17.1–17.8 (1997)
19. Rugg, K.L., Cox, B.N., Ward, K.E., Sherrick, G.O.: Damage mechanisms for aligned through-thickness rod reinforcement in carbon-epoxy laminates. Compos. Part A Appl. Sci. Manufact. **29**, 1603–1613 (1998)

20. Birman, V., Byrd, L.W.: Effect of z-Pins on fracture in composite cocured double cantilever beams. J. Aerosp. Eng. **18**(1), 51–59 (2005)
21. Byrd, L.W., Birman, V.: The estimate of the effect of Z-pins on the strain release rate, fracture and fatigue in a composite co-cured Z-pinned double cantilever beam. Compos. Struct. **68**(1), 53–63 (2005)
22. Byrd, L.W., Birman, V.: Effectiveness of z-pins in preventing delamination of co-cured composite joints on the example of a double cantilever test. Compos. Part B **37**(4–5), 365–378 (2006)
23. Mouritz, A.P.: Review of z-pinned composite laminates. Compos. Part A Appl. Sci. Manufact. **38**, 2383–2397 (2007)
24. Dines, J.S., Bedi, A., Elattrache, N.S., Dines, D.M.: Single-row versus double-row rotator cuff repair: techniques and outcomes. J. Am. Acad. Orthop. Surg. **18**(2), 83–93 (2010)
25. Ashby, M., Gibson, L.J., Wegst, U., Olive, R. The mechanical properties of natural materials. I. Property charts. Proc. Math. Phys. Sci. **450**(1938), 123–140 (1995)
26. Fratzl, P., Gupta, H.S., Paschalis, E.P., Roschger, P.: Structure and mechanical quality of the collagen-mineral nano-composite in bone. J. Mater. Chem. **14**(14), 2115–2123 (2004)

Some Consequences of Stress Range Dependent Constitutive Models in Creep

James T. Boyle

Abstract Detailed procedures for high temperature design remain elusive, even though advanced material models for creep have been developed over several decades and (some) employed in detailed inelastic finite element analysis. The simplified design approaches which are available have in general been developed on the basis of simple power-law creep models, but most have not been re-assessed if more advanced creep models are adopted. Over many years fairly simple alternatives to the power-law have been available but few have been similarly assessed in the design context. These simple alternatives have usually focussed on the problem of stress range dependency: the form of the constitutive model, even for secondary creep, changes as the stress increases from low through moderate to high stress. In this paper some simplified design approaches are initially re-assessed for such creep laws using two simple structures.

1 Introduction

Studies of the behaviour of structural components at high temperature subject to creep have a long history and their behavioural characteristics, certainly for constant and cyclic load, well established. However, the majority of these studies have been based on relatively simple constitutive models in particular time- or strain-hardening for primary creep with a basic power-law model for secondary creep. These basic models can be enhanced to include tertiary creep with the introduction of well-known damage models of the Kachanov-Rabotnov type. Over the past decade, the modelling of advanced high temperature materials has improved considerably and, coupled with advances in computational modelling of real-world components, has

J. T. Boyle (✉)
Department of Mechanical and Aerospace Engineering,
University of Strathclyde, Glasgow, Scotland, UK
e-mail: jim.boyle@strath.ac.uk

H. Altenbach and S. Kruch (eds.), *Advanced Materials Modelling for Structures*,
Advanced Structured Materials 19, DOI: 10.1007/978-3-642-35167-9_8,

allowed a much more realistic and detailed representation of structural behaviour at high temperature subject to precise thermo-mechanical load histories. This can be seen in a comparison between reviews of the state of the art of creep analysis in the early 1980s [7] and the late 2000s [11].

Nevertheless, most design rules for high temperature have been developed based on an understanding of creep behaviour with the simple constitutive models, which remain the most widely used even in design and assessment approaches using detailed nonlinear finite element analysis. To be useful for design purposes, modern advanced material models need to be able to make reference to conventional understanding of the behavioural characteristics of structures subject to creep. Yet this can often be problematic, not due to imprecision in the advanced models, but rather deficiencies in the simple models. Recent studies [2–5, 12] of the behaviour of structures using simple creep models, but ones which are stress range dependent (that is, the form of the constitutive model, even for secondary creep, changes as the stress increases from low through moderate to high stress) have shown that under some types of loading creep behaviour of structures is significantly altered, while for others familiar design concepts can remain valid. Simple stress range dependent constitutive models have been around for well over 60 years but have been rarely used: the power-law has been favoured since it is simple to use and has some desirable features which have led to robust simplified methods for creep design.

The examples used in this paper are intentionally *simple*. Arguably, detailed numerical simulations of complex structures subject to creep using advanced materials modelling may only be confirmed through experimental verification, which is usually prohibitively expensive and time consuming. For example, for many years it was not well understood that for some load conditions in creep, for example where there was significant constraint, that conventional finite element analysis gave poorly converged results [8]. Confidence in such material models, together with an appreciation of their possible limitations and use in nonlinear finite element analysis, must come from investigations of simple structures. On the other hand, this must be balanced with the need for design procedures for creep to be simple, justifiable and transparent. This requires the characteristic behaviour of structures subject to creep, even with advanced material models, to be well understood. This always begins with detailed studies of simple structures in order to develop such design rules, which can then hopefully be verified for more complex structures.

2 Stress Range Dependent Creep Laws

With the assumption that the mechanism of creep is the same for both primary and secondary phases of creep, the majority of approaches to material modelling start with the nonlinear secondary phase where strain rate is constant (‘steady creep’) with simple modifications to include primary creep. In the common time- hardening or strain- hardening models, a function of time or a function of strain respectively pre-multiply the steady state model. The most common creep laws which have been used

for design and analysis purposes have been based on the power-law. Over stress ranges where the creep strain rate is high, and at constant temperature, the relation between creep strain rate, $\dot{\varepsilon}_c$, and stress, σ, can be well represented by a power-law relation

$$\dot{\varepsilon}_c = B\sigma^n \tag{1}$$

where B and n are material constants. The stress exponent, n, represents the gradient of a plot of log(stress) against log(creep strain rate). Nevertheless, the power law is only valid over a certain stress range: it has long been known that the stress exponent can change as stress ranges from low, through medium to high values, depending on the material. An alternative to the power law, suggested by Prandtl and Nadai amongst others, took the hyperbolic sine form

$$\dot{\varepsilon}_c = B\sinh(A\sigma) \tag{2}$$

with A & B material constants. This model recognised that at low stress the relationship between creep strain rate and stress was sensibly linear viscous, while remaining nonlinear at high stress. Garofalo later combined the power- and Prandtl- laws in the form

$$\dot{\varepsilon}_c = B(\sinh(A\sigma))^n \tag{3}$$

A more recent attempt to develop a material model which can represent linear viscous behaviour at low stress as well as power-law behaviour at high stress has been given in [12] as

$$\frac{\dot{\varepsilon}_c}{\dot{\varepsilon}_0} = \frac{\sigma}{\sigma_0} + \left(\frac{\sigma}{\sigma_0}\right)^n \tag{4}$$

where $\dot{\varepsilon}_0$ and σ_0 are material constants. This will be referred to as a modified power-law. Figure 1, taken from the data in [12], shows a plot of creep strain rate against stress for the steady creep of 9 % Cr steel at 600 °C. The transition from linear behaviour to power-law behaviour can be easily seen.

In the following, the behaviour of two simple structures using these varied material models will be examined.

3 Steady Creep of a Two-Bar (Parallel) Structure

Consider two bars of length L_1 and L_2 with the same cross sectional area, A, in parallel. It is assumed that the bars are fixed at their top and rigidly attached to a horizontal bar under a tension Q [7], Fig. 2.

If the material undergoes steady creep according to the modified power-law, Eq. 4, then it can be shown that, if we take $L_2 \geq L_1$, then the maximum stress, σ_1, occurs in bar no.1 and is the solution of the nonlinear equation

$$\beta((\alpha - S) + (\alpha - S)^n) = S + S^n \tag{5}$$

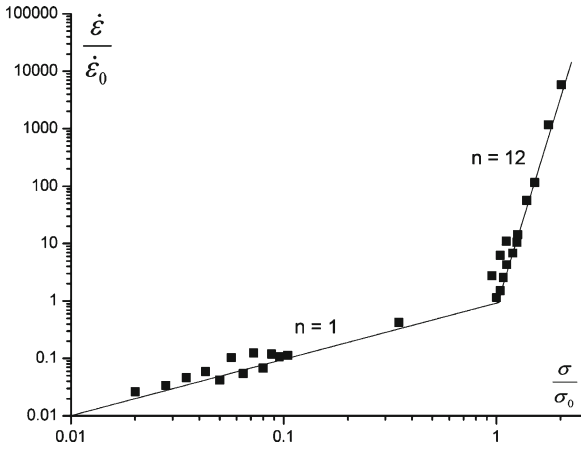

Fig. 1 Steady creep of 9 % Cr steel at 600 °C from [12]

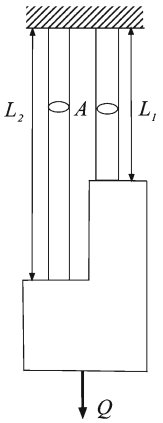

Fig. 2 Two-bar (parallel) structure

on defining the normalised quantities

$$\alpha = \frac{Q}{A\sigma_0} \quad \beta = \frac{L_2}{L_1} \quad S = \frac{\sigma_1}{\sigma_0} \tag{6}$$

The parameter, α, may be considered a 'load factor, since it gives the ratio of nominal stress Q/A to the transition stress σ_0. In the case of a pure power law the maximum normalised stress can be written in a form which is independent of the load factor, but this is not possible here. The parameter, β, may be considered a 'geometry factor'.

Two characteristics of the behaviour of structures subject to steady power-law creep have emerged over the past forty years as being useful for design. In the first it has been observed (see [7] for example) that the maximum stress is almost linear with the reciprocal of the power exponent, n. The steady creep of some basic structures—a

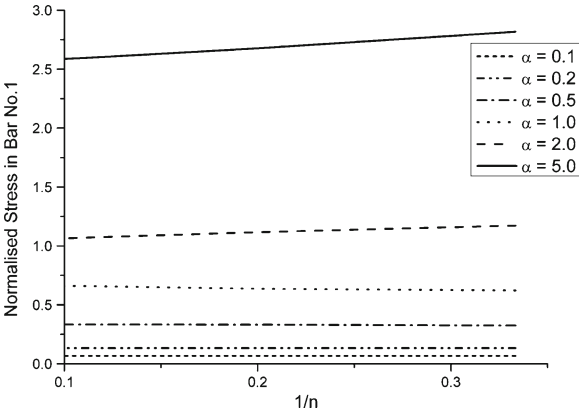

Fig. 3 Variation of maximum normalised stress in the two-bar (parallel) structure with *1/n*

beam in bending and a pressurised thick cylinder—subject to the modified power law were investigated in [12]. These basic problems were re-analysed in [2] and it was shown that the linearity with respect to *1/n* was approximately maintained for the modified power-law for most values of the load factor α. This can be verified for the current two-bar structure from a solution of Eq. 5, shown in Fig. 3:

In the case of this particular structure, the variation is not large. For larger values of the load factor the maximum normalised stress increases with *1/n*, as is normally found [7]. For smaller values of the load factor, where linear viscous behaviour would dominate, the maximum normalised stress slightly decreases—for a purely linear viscous material the maximum normalised stress would simply be proportional to the load factor.

The second characteristic structural behaviour found for power-law creep is the existence of a 'reference stress'. In the reference stress method some measure of deformation (strain or displacement) can be written in the form of a scaling factor multiplied by the result of a uniaxial test held at the reference stress [7]. Both the scaling factor and the reference stress are approximately independent of the material properties. The reference stress concept was reviewed in the IUTAM *Creep in Structures* symposiums in 1970 [10], then in the 1980 [1] and last in 2000 [6].

In the present problem, the vertical downward deflection rate of each bar, $\dot{q}$, is written in the form [7]

$$\dot{q} = \delta \times \dot{\varepsilon}(\sigma_R) \tag{7}$$

where δ is the scaling factor and σ_R the reference stress. For steady power-law creep the scaling factor is in fact a function of the reference stress and the power exponent n. However it can be shown that provided

$$\sigma_R = \frac{1}{2}\frac{Q}{A} \tag{8}$$

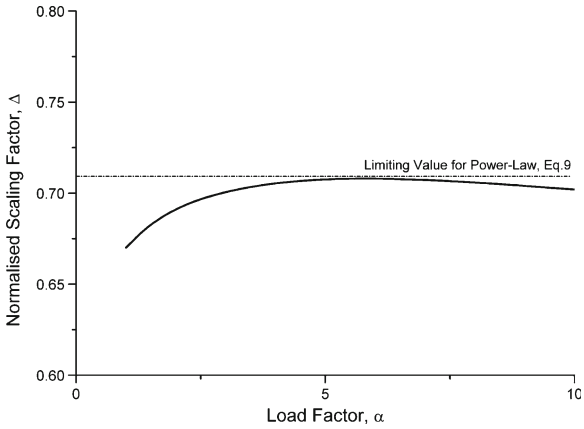

Fig. 4 Variation of scaling factor with load factor for Prandtl's law

Then in the limit

$$\Delta = \frac{\delta(n \to \infty)}{L_2} \to \sqrt{\frac{1}{\beta}} \tag{9}$$

The scaling factor corresponding to $n = 1$ is about 10 % below this value and as n increases the scaling factor approaches the limiting value given by Eq. 9.

The concept of the reference stress and scaling factor was extended to other creep laws, for example the Prandtl law, Eq. 2, in [9]. The Prandtl law was examined for the current problem in [7]. It was found that the scaling factor for the Prandtl law depended not only on the material parameter (A in Eq. 2) but also on the load factor, α. In the case of the power-law the scaling factor is independent of the load factor. Nevertheless it was shown that the scaling factor was relatively insensitive to the load factor over a wide range of values of the load factor, and further that the limiting value found for the power-law, Eq. 9, was approximately an upper bound; this can be seen in Fig. 4 for $\beta = 2$.

Similar behaviour can be seen if the use of a modified power-law for this structure is examined. It can be shown that the normalised scaling factor, Δ, in Eq. 9 is given by

$$\Delta = \frac{1}{\beta}\left(\frac{S + S^n}{\frac{\sigma_R}{\sigma_0} + \left(\frac{\sigma_R}{\sigma_0}\right)^n}\right) \tag{10}$$

where S is the solution of Eq. 5. The normalised scaling factor depends on the material parameters n, σ_0 and the load factor (through S) as for Prandtl's law. However, if we choose the same reference stress as in the case of the power-law, Eq. 8, then in Eq. 10

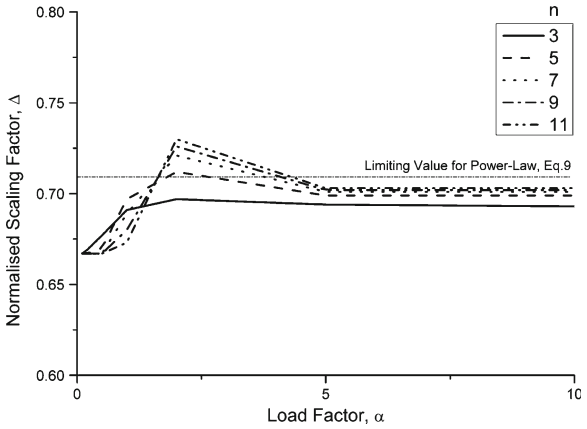

Fig. 5 Variation of scaling factor with load factor for modified power law

$$\frac{\sigma_R}{\sigma_0} = \frac{1}{2}\alpha \tag{11}$$

The variation of the normalised scaling factor with n and load factor is shown in Fig. 5 for $\beta = 2$. As in the case of Prandtl's law, Fig. 4, the scaling factor is almost independent of these, and approximately bounded by the limiting value of scaling factor from the power law.

In conclusion, two of the more familiar simplified methods derived from the power-law—approximate linear variation of maximum stress with the reciprocal of the power-exponent—are also applicable using a modified power-law.

4 Relaxation of a Two-Bar (Series) Structure

Consider two bars with cross sectional areas, A_1 and A_2, but of the same length, L, attached in parallel. It is assumed that the bars are fixed at the end of the first bar and subject to an applied displacement, q, at the end of the second bar, Fig. 6.

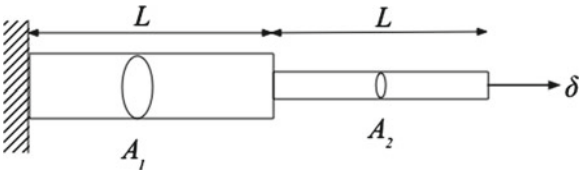

Fig. 6 Two-bar (series) structure

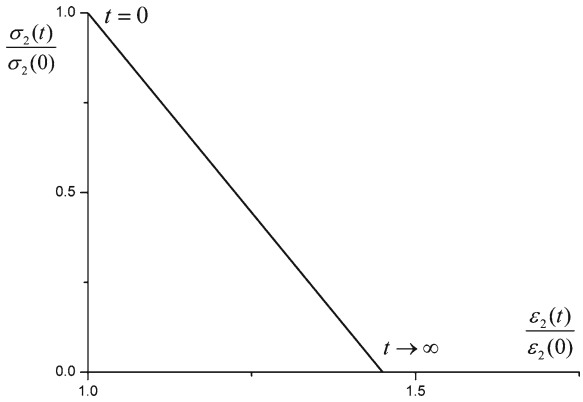

Fig. 7 Stress-strain trajectory in bar no.2 for a power law

This problem has been discussed at length in [3–5] in the context of the design problem of 'elastic follow-up' for a range of stress range dependent creep laws. Under relaxation conditions it would be expected for the stresses to relax to zero, while the deformation remained almost constant. However in some structural configurations it is known that predominantly elastic behaviour in one part slows down the relaxation of stress in another part, with a resultant localised accumulation of strain. The design problem has been to estimate the localised maximum inelastic strain without detailed inelastic analysis. (Elastic follow-up is a particular problem in high temperature piping systems where detailed analysis is expensive).

In the case of a power law it has been found that a plot of the variation of maximum stress with strain (called an isochronous stress-strain trajectory) is almost linear and approximately independent of the power exponent. The trajectory for the current problem is shown in Fig. 7, taken from [3, 4]. The maximum stress and strain occur in bar no.2—Fig. 7 shows the trajectory for the normalised stress and strain, in bar no.2 with respect to their initial (elastic) values for $n = 5$ and $\beta = 2$. The normalised strain tends to a limiting value

$$\lambda = \frac{1+\beta}{1+\beta^n} \tag{12}$$

where $\beta = A_2/A_1$. This is nearly independent of the power exponent for $n > 5$ such that $\lambda \to 1+\beta$ as $n \to \infty$. It is also independent of any load factor. This characteristic behaviour, linearity of the stress-strain trajectory and near independence of the power exponent, has been used as the basis for several simplified approaches used in design.

In [3, 4] this problem was re-analysed for several stress range dependent creep laws: results for the Prandtl and modified power laws are shown for $n = 5$ and $\beta = 2$ in Figs. 8 and 9.

In conclusion, the basis of a common design approach used to estimate elastic follow-up, derived from studies of structures subject to a power-law are *not* applicable using stress range dependent creep laws.

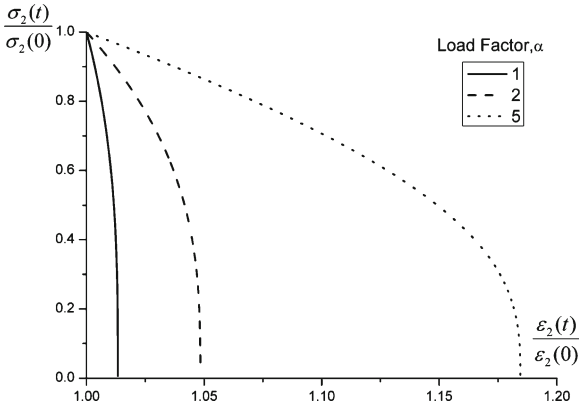

Fig. 8 Stress-strain trajectory in bar no.2 for Prandtl's law

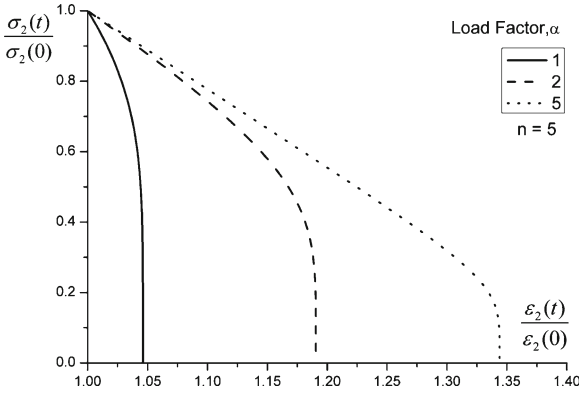

Fig. 9 Stress-strain trajectory in bar no.2 for a modified power law

5 Conclusions

Two simple structures have been examined here: in the first a two-bar (parallel) structure under steady creep has been used to show that familiar, simplified approximate methods remain applicable to stress range dependent creep laws. In the second, relaxation in a two-bar (series) structure shows that simplified methods for estimating the real design problem of elastic follow-up are not applicable to stress range dependent creep laws. The latter result is new and perhaps surprising since such creep laws have been around for many years but not studied in the context of this problem. To the author, it is a clear demonstration of the need to ensure current design approaches are compatible with advanced material models, and vice versa.

References

1. Anderson, R.G.: Some observations on reference stresses, skeletal points, limit loads and finite elements. In: Proceedings of the IUTAM Symposium on Creep in Structures, Leicester, UK (1980)
2. Boyle, J.T.: The creep behaviour of simple structures with a stress-range dependent constitutive model. Arch. Appl. Mech. **82**, 495–514 (2012)
3. Boyle, J.T.: Stress relaxation and elastic follow-up using a stress range dependent constitutive model. Proc. IMechE, Part C: J. Mech. Eng. Sci. **226**, 1472–1483 (2012)
4. Boyle, J.T. : The effect of material models on elastic follow-up. Trans ASME J. Press. Vess. Techn. **134**, 061210-1–061210-2 (2012)
5. Boyle, J.T.: A re-assessment of elastic follow-up in high temperature piping. In: Proceedings of 13th International Conference On Pressure Vessel Technology, London (2012)
6. Boyle, J.T., Seshadri, R.: The reference stress method in creep design : a thirty year retrospective. In: Proceedings of the IUTAM Symposium on Creep in Structures, Nagoya (2000)
7. Boyle, J.T., Spence, J.: Stress Analysis for Creep. Butterworths, London (1983)
8. Guerrerio, J.N.C., Loula, A.F.D., Boyle, J.T.: Finite element methods in stress analysis for creep. In: Proceedings of the IUTAM Symposium on Creep in Structures, Cracow (1990)
9. Johnsson, A.: Reference stress for structures obeying the Prandtl and Dorn creep laws. J. Mech. Eng. Sci. **16**, 298–305 (1974)
10. Marriott, D.L.: A review of reference stress methods for estimating creep deformations. In: Proceedings of the IUTAM Symposium on Creep in Structures, Gothenburg (1970)
11. Naumenko, K., Altenbach, H.: Modelling of Creep for Structural Analysis. Springer, Berlin (2007)
12. Naumenko, K., Altenbach, H., Gorash, Y.: Creep analysis with a stress range dependent constitutive model. Arch. Appl. Mech. **79**, 619–63 (2009)

Micro-Mechanical Numerical Studies on the Stress State Dependence of Ductile Damage

Michael Brünig, Steffen Gerke and Vanessa Hagenbrock

Abstract The paper discusses the effect of stress state on ductile damage behavior. The continuum model has been generalized to take into account stress state dependence of the damage criterion with branches corresponding to different damage mechanisms depending on the stress triaxiality and the Lode parameter. Experiments with differently notched tension and shear specimens taken from aluminum sheets are used to identify basic material parameters. Additional series of micro-mechanical numerical analyses of void containing unit cells have been performed to be able to get more insight in the complex damage and failure behavior of ductile metals. These calculations cover a wide range of stress triaxialities and Lode parameters. The numerical results are used to show general trends, to develop equations for the damage criterion, and to identify material parameters of the continuum model.

1 Introduction

Accurate modelling of inelastic behavior of ductile metals is evident in structural mechanics and corresponding numerical analyses. In the literature, various continuum approaches predicting elastic-plastic behavior as well as material softening caused by damage and failure processes have been discussed. In this context, phenomenological damage models have been developed motivated by experimental observations or numerical analyses on the micro-scale. They are based on internal scalar or tensorial damage variables whose increase is governed by evolution laws.

It is now well known that stress intensity, stress triaxiality and the Lode parameter are important factors controlling initiation and evolution of ductile damage and failure. These dependencies can be studied by performing experiments and

M. Brünig (✉) · S. Gerke · V. Hagenbrock
Institut für Mechanik und Statik, Universität der Bundeswehr München,
Werner-Heisenberg-Weg 39, 85579 Neubiberg, Germany
e-mail: michael.bruenig@unibw.de

H. Altenbach and S. Kruch (eds.), *Advanced Materials Modelling for Structures*,
Advanced Structured Materials 19, DOI: 10.1007/978-3-642-35167-9_9,

corresponding numerical simulations of a series of tests with carefully designed and differently loaded specimens experiencing a wide range of stress states [1–8]. However, this procedure on the macro-level detects several interesting effects but do not allow to predict general trends. To overcome this problem and to be able to detect additional features on the scale of the micro-defects, micro-mechanical numerical analyses can be carried out solving boundary-value problems of representative volume elements with micro-structural details to reliably predict the constitutive response at the macro-level. Thus, three-dimensional finite element calculations of microscopic void-containing cell models have been discussed [9–13] to get more insight in damage and failure mechanisms of ductile solids and to understand stress-state-dependent behavior of micro-defect growth and corresponding ductile damage and failure mechanisms. The numerical results show that the micro-defect growth and their coalescence as well as the macroscopic deformation behavior of the unit cells and the critical failure strain remarkably depend on the value of both the stress triaxiality and of the Lode parameter.

Nearly all published papers deal with void growth and coalescence in regions with high hydrostatic stress states. Thus, their results can only be used in moderate or high stress triaxiality domains where the effect of the Lode parameter on damage and failure behavior has been shown to be marginal [5]. Therefore, further numerical calculations have to be performed to get detailed information on damage and failure mechanisms in ductile solids for a wide range of stress triaxialities and Lode parameters even in the shear and compression ranges. In this context, the present paper discusses results of numerical unit-cell simulations on the micro-scale covering a wide range of three-dimensional stress states. They are used to develop and to verify stress-state-dependent damage criteria taking into account different branches corresponding to various damage modes.

2 Continuum Model

A continuum model is used to predict the inelastic deformations as well as the damage and failure behavior taking into account information of microscopic mechanisms of individual micro-defects and their interaction. Brünig et al. [6, 7] proposed a phenomenological framework to model inelastic deformation behavior of ductile materials including anisotropic damage caused by micro-defects. This approach takes into account different damage mechanisms depending on the amount of the stress triaxiality (Fig. 1): evolution of micro-shear-cracks for negative stress triaxialities, void growth for large positive stress triaxialities and mixed behavior for lower positive stress triaxialities. In the hydrostatic pressure regime a cut-off value of stress triaxiality [14] is taken into account below which damage does not occur. This stress-triaxiality-dependent concept will be generalized to be able to take also into account the effect of the Lode parameter on damage behavior.

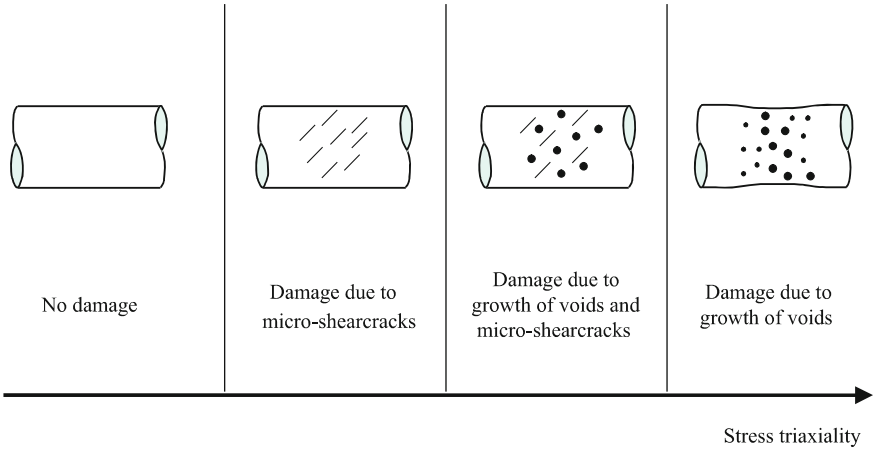

Fig. 1 Damage mechanisms

In particular, the onset of damage is assumed to be governed by the damage condition

$$f^{\mathrm{da}} = \alpha I_1 + \beta\sqrt{J_2} - \sigma = 0 \tag{1}$$

where I_1 and J_2 denote the first and second deviatoric stress invariants, σ is the damage threshold and α and β represent the damage mode parameters taking into account the different branches depending on the stress triaxiality

$$\eta = \sigma_{\mathrm{m}}/\sigma_{\mathrm{eq}} = I_1/(3\sqrt{3J_2}) \tag{2}$$

defined as the ratio of the mean stress σ_{m} and the von Mises equivalent stress σ_{eq} as well as on the Lode parameter

$$\omega = \frac{2\tilde{T}_2 - \tilde{T}_1 - \tilde{T}_3}{\tilde{T}_1 - \tilde{T}_3} \quad \text{with} \quad \tilde{T}_1 \geq \tilde{T}_2 \geq \tilde{T}_3 \tag{3}$$

expressed in terms of the principal stress components $\tilde{T}_1$, $\tilde{T}_2$ and $\tilde{T}_3$.

3 Experiments and Numerical Simulations

Experiments and corresponding numerical simulations on the macro-scale have to be performed to be able to identify material parameters appearing in the constitutive equations. However, since it is not possible to uniquely identify all material parameters appearing in equations modelling inelastic deformation as well as damage

and failure behavior of ductile metals, numerical simulations on the micro-level considering parts of micro-defect containing materials have been performed.

3.1 Experiments and Numerical Simulations on the Macro-Scale

Basic material parameters are taken from tension tests with smooth specimens. Furthermore, stress-state-dependent constitutive parameters can be identified by comparison of experimental data from various tests with differently notched tension and shear specimens taken from aluminum sheets [15, 16] with corresponding numerical simulations [7, 17]. Two- and three-dimensional analyses have been performed to be able to identify the stress state dependence of the damage mode parameter β. However, the experiments with flat specimens did not show remarkable three-dimensional effects and, therefore, it was not possible to study in detail the effect of the Lode parameter on damage behavior.

Due to the lack of information on the influence of the Lode parameter on damage of aluminum sheets by experimental procedures, application of an alternative method is proposed to study the effect of stress state on the damage and failure behavior of ductile metals. Additional numerical simulations on the micro-scale will be performed to be able to study in detail the dissipative and deteriorating mechanisms on the microscopic level.

3.2 Numerical Simulations on the Micro-Scale

To be able to develop damage evolution equations and to identify corresponding material parameters in micro-mechanically motivated constitutive relations the deformation behavior of three-dimensional unit cell models undergoing various loading conditions is studied in detail. The initial void volume fraction is assumed to be 3 % and symmetry boundary conditions are taken into account which simulate periodic distributions of micro-defects. The analysis of this prototype problem is motivated by the observation that nucleation, growth and coalescence of micro-voids and micro-shear-cracks are the most important mechanisms on the micro-level leading to deterioration of material properties on the macro-scale as well as to failure in ductile metals.

It should be noted that the three-dimensional unit cells do not exactly deform like pre-damaged solids with different distributions of micro-defects. However, interaction of these defects on the micro-level can approximately be taken into account due to symmetry boundary conditions of the unit cells under investigation. Interpretation of the numerical results of the unit cell calculations will give information on micro-level-mechanisms like changes in size and shape of single defects as well as

formation and localization of plastic zones. This will provide data for the development of damage and failure criteria as well as of damage evolution equations on the macroscopic level.

Three-dimensional numerical unit-cell calculations have been carried out using the finite element program ANSYS. The analyses are based on different loading conditions covering a wide range of Lode parameters $\omega = -1, -1/2, 0, 1/2, 1$ and of stress triaxiality coefficients $\eta = -1, -2/3, -1/3, 0, 1/3, 2/3, 1$.

During the entire loading history of the unit cells the stress triaxiality coefficient (2) and the Lode parameter (3) are kept constant in all numerical simulations discussed in the present paper. This allows detailed studies of their effect on damage and failure behavior. In particular, to be able to guarantee always constant parameters, the unit cells have to be loaded by the principal stresses

$$\tilde{T}_2(\tilde{T}_1, \omega, \eta) = \frac{\left(-6\omega + 27\eta^2 + 9\omega^2\eta^2 + 2\omega^2 \pm 9\sqrt{\eta^2\hat{\omega}}\right)\tilde{T}_1}{-9 + 6\omega - \omega^2 + 27\eta^2 + 9\omega^2\eta^2}$$
$$\text{with} \quad \hat{\omega} = (-6\omega - 2\omega^3 + 4\omega^2 + \omega^4 + 3) \tag{4}$$

and

$$\tilde{T}_3(\tilde{T}_1, \omega, \eta) = \frac{\left(27\eta^2 + 9 + 9\omega^2\eta^2 - \omega^2 \pm 18\sqrt{\eta^2(3 + \omega^2)}\right)\tilde{T}_1}{-9 + 6\omega - \omega^2 + 27\eta^2 + 9\omega^2\eta^2}. \tag{5}$$

In Eqs. (4) and (5), the first principal stress component $\tilde{T}_1$ characterizes the load intensity. In addition, the initially plane surfaces of the unit cell models have to remain plane during the loading process. Then, these always plane surfaces can be taken as symmetry boundaries. This allows interpretation that the unit cell model is a part of a pre-damaged solid with regular distribution of initially spherical voids.

Figure 2 demonstrates the effect of stress state on damage. For different ratios of the principal stress components $\tilde{T}_1{:}\tilde{T}_2{:}\tilde{T}_3$ corresponding to different amounts of stress triaxiality η and Lode parameter ω Fig. 2 shows the initial (contours) and deformed (grey) shapes of one eighth of the initially spherical voids. In particular, for the high stress triaxiality value $\eta = 1$ the effect of the Lode parameter ω on deformation of micro-defects is marginal. During the entire loading process the initially spherical void nearly remains spherical and only its size increases. This means that isotropic void growth is the predominant microscopic damage mechanism in the high stress triaxiality regime and damaged induced anisotropy does not play a significant role. However, the numerical cell model calculations predict an increase in the effect of the Lode parameter on micro-defect deformation with decreasing stress triaxialities $\eta \leq 1/3$. For example, the evolution of prolate elliptical pores with one elongated principal direction is observed for the negative Lode parameter $\omega = -1$ whereas the formation of oblate elliptical voids with two equally stretched principal directions is numerically predicted for the positive Lode parameter $\omega = 1$. On the other hand, the size of the micro-defects decreases in the high negative stress triaxiality regime

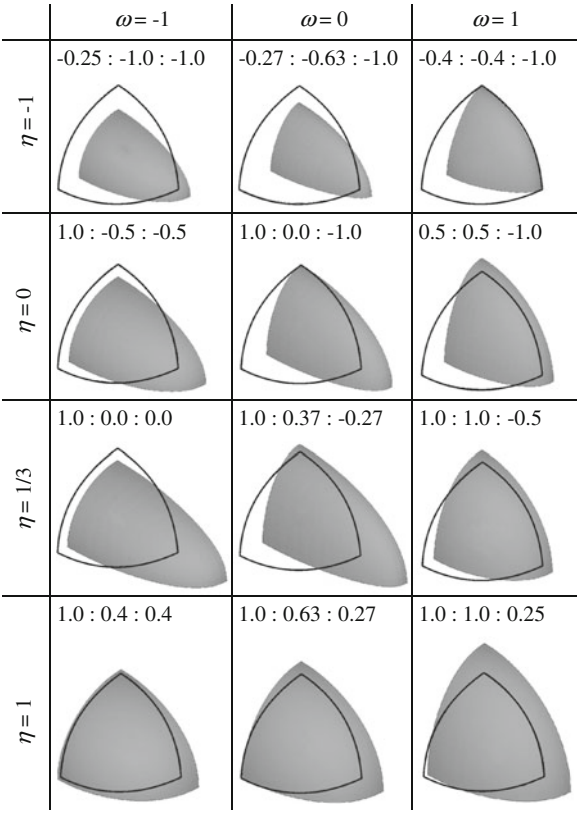

Fig. 2 Deformation of voids depending on stress triaxiality η and on Lode parameter ω

($\eta = -1$). This means that no further damage occurs under high compression loading conditions and the material behavior can be described by an elastic-plastic model.

In the proposed continuum damage model [6] the formation of damage is characterized by the damage strain rate tensor $\dot{\mathbf{H}}^{da}$. In this context, the amount of damage is taken to be quantified by the scalar-valued equivalent damage strain measure

$$\varepsilon_{\mathrm{v}}^{\mathrm{da}} = \int \dot{\varepsilon}_{\mathrm{v}}^{\mathrm{da}} \mathrm{d}t \tag{6}$$

with

$$\dot{\varepsilon}_{\mathrm{v}}^{\mathrm{da}} = \sqrt{\frac{2}{3}\dot{\mathbf{H}}^{\mathrm{da}} \cdot \dot{\mathbf{H}}^{\mathrm{da}}}. \tag{7}$$

Figure 3 shows the increase in equivalent damage strain with increasing loading of the unit cells. In particular, for high positive stress triaxialities larger equivalent

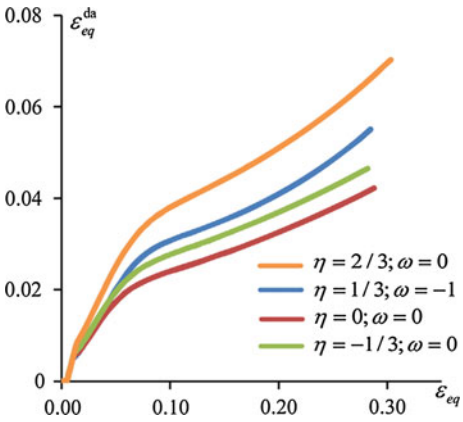

Fig. 3 Equivalent damage strain versus equivalent strain

damage strain measures are numerically predicted whereas they are smaller for shear loading conditions ($\eta = 0$). However, remarkable equivalent damage strains may be seen even for negative stress triaxialities where decrease in volume of the micro-defects has been observed (see Fig. 2) indicating that no further damage occurs. Hence, the equivalent damage strain measure (6, 7) alone is not able to characterize the occurrence of damage and to quantify its amount.

To overcome this problem, the formation of the void volume fraction f is also taken into account. In the present analyses, it is directly computed from the current geometry of the initially spherical void in the unit cell model. Figure 4 shows the formation of the volume of the micro-defects with increasing loading of the one-pore material sample for different stress states. In particular, in the high stress triaxiality regime an increase in porosity is observed while for shear loading ($\eta = 0$) no remarkable change in void volume fraction is numerically predicted indicating isochoric deformation behavior. On the other hand, decrease in volume of micro-defects can be seen in Fig. 4 for negative stress triaxiality. This means that no further damage occurs. This observation based on unit cell model calculations agrees well with the introduction of a cut-off value [14] based on experiments. Thus, to be able to decide

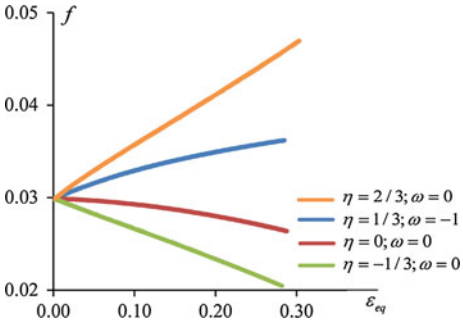

Fig. 4 Void volume fraction versus equivalent strain

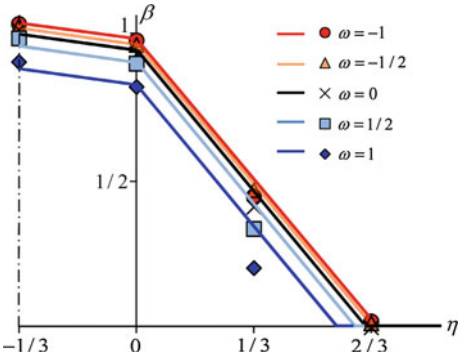

Fig. 5 Damage mode parameter versus stress triaxiality

whether damage occurs in a loaded solid or not, the numerically predicted formation of the void volume fraction f is considered. In this context, non-marginal decrease in volume of initial micro-defects means that no damage takes place during loading of ductile solids.

Comparison of macroscopic experimental-numerical results discussed above and numerical results taken from unit cells with 3 % initial void volume fraction and from undamaged cubes with the same volume of the elastic-plastic matrix material allow identification of the macroscopic stress at the onset of damage. In this point, for each macroscopic stress state the first and second deviatoric stress invariants are determined to be able to compute with Eq. (1) the damage mode parameter β shown in Fig. 5.

For different Lode parameters ω and stress triaxiality coefficients η the damage mode parameters obtained from micro-mechanical numerical analyses described above (different points in Figs. 5 and 6) are used to propose the non-negative function

$$\beta(\eta, \omega) = \beta_0(\eta, \omega = 0) + \beta_\omega \geq 0 \tag{8}$$

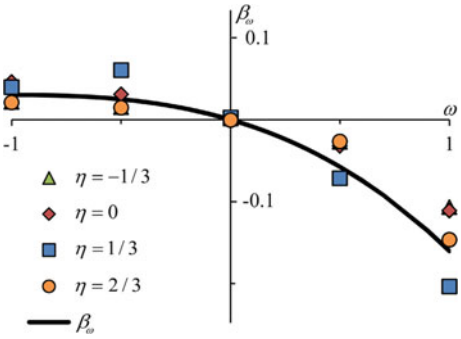

Fig. 6 Damage mode parameter β_ω versus Lode parameter

and to identify the associated material parameters

$$\beta_0 = \begin{cases} -0.45\eta + 0.85 \text{ for } -1/3 \leq \eta \leq 0 \\ -1.28\eta + 0.85 \text{ for } \eta > 0 \end{cases} \tag{9}$$

and

$$\beta_\omega = -0.017\omega^3 - 0.065\omega^2 - 0.078\omega \tag{10}$$

by curve fitting, see Figs. 5 and 6. It can be seen that in the negative stress triaxiality regime $-1/3 \leq \eta \leq 0$ the damage mode parameter is large indicating remarkable influence of J_2 on damage behavior. This corresponds to dominant micro-shear-mechanisms whereas the negative hydrostatic stress is small and does not remarkably affect the damage behavior. On the other hand, for high stress triaxiality coefficients, $\beta = 0$ and only the first stress invariant I_1 is assumed to characterize the onset of damage caused by nearly isotropic void growth mechanisms. Based on the numerical calculations presented here, the amount of stress triaxiality determining the transition from void growth mode to the mixed damage mechanism depends on the Lode parameter and is not a material constant. In particular, for positive Lode parameters ($\omega > 0$) the void growth mechanisms are more dominant than for negative ones ($\omega < 0$).

4 Conclusions

The effect of stress state on damage has been discussed and quantified for the onset of damage. It has been shown that it is not possible to validate the effect of the stress triaxiality and the Lode parameter only by experiments with differently notched tension and shear specimens and corresponding numerical simulations on the macro-scale. To overcome this problem, additional numerical 3D calculations on the micro-level have been performed considering pre-damaged unit cubes with spherical voids under different loading conditions. Details of functions describing occurrence of damage have been detected taking into account a wide range of stress triaxialities and Lode parameters. Based on this procedure, it is possible to quantify the stress-state-dependent damage criterion with different branches corresponding to different damage and failure mechanisms on the micro-scale. Therefore, the combination of experiments with macroscopic numerical simulations and numerical calculations on the micro-scale may be seen as an efficient tool to obtain data to validate stress state dependence of damage and failure criteria in phenomenological continuum models.

Acknowledgments Financial support from the Deutsche Forschungsgemeinschaft (German Research Foundation, BR1793/12-1) is gratefully acknowledged.

References

1. Borvik, T., Hopperstad, O.S., Berstad, T.: On the influence of stress triaxiality and strain rate on the behavior of a structural steel. Part II. Numerical study. Eur. J. Mech. A/Solids **22**, 15–32 (2003)
2. Bao, Y., Wierzbicki, T.: On fracture locus in the equivalent strain and stress triaxiality space. Int. J. Mech. Sci. **46**, 81–98 (2004)
3. Bonora, N., Gentile, D., Pirondi, A., Newaz, G.: Ductile damage evolution under triaxial state of stress: theory and experiment. Int. J. Plast. **21**, 981–1007 (2005)
4. Oh, C.K., Kim, Y.J., Park, J.M., Baek, J.H., Kim, W.S.: Development of stress-modified fracture strain for ductile failure of API X65 steel. Int. J. Fract. **143**, 119–133 (2007)
5. Bai, Y., Wierzbicki, T.: A new model of metal plasticity and fracture with pressure and Lode dependence. Int. J. Plast. **24**, 1071–1096 (2008)
6. Brünig, M.: An anisotropic ductile damage model based on irreversible thermodynamics. Int. J. Plast. **19**, 1679–1713 (2003)
7. Brünig, M., Albrecht, D., Gerke, S.: Numerical analyses of stress-triaxiality-dependent inelastic deformation behavior of aluminum alloys. Int. J. Damage Mech. **20**, 299–317 (2011)
8. Gao, X., Zhang, T., Hayden, M., Roe, C.: Effects of the stress state on plasticity and ductile failure of an aluminum 5083 alloy. Int. J. Plast **25**, 2366–2382 (2009)
9. Kuna, M., Sun, D.Z.: Three-dimensional cell model analyses of void growth in ductile metals. Int. J. Fract. **81**, 235–258 (1996)
10. Zhang, K.S., Bai, J.B., Francois, D.: Numerical analysis of the influence of the Lode parameter on void growth. Int. J. Solids Struct. **38**, 5847–5856 (2001)
11. Kim, J., Gao, X., Srivtsan, T.S.: Modelling of crack growth in ductile solids: a three-dimensional analysis. Int. J. Solids Struct. **40**, 7357–7374 (2003)
12. Gao, X., Wang, T., Kim, J.: On ductile fracture initiation toughness: effects of void volume fraction, void shape and void distribution. Int. J. Solids Struct. **42**, 5097–5117 (2005)
13. Gao, X., Zhang, G., Roe, C.: A study on the effect of the stress state on ductile fracture. Int. J. Damage Mech. **19**, 75–94 (2010)
14. Bao, Y., Wierzbicki, T.: On the cut-off value of negative triaxiality for fracture. Eng. Fract. Mech. **72**, 1049–1069 (2005)
15. Brünig, M., Chyra, O., Albrecht, D., Driemeier, L., Alves, M.: A ductile damage criterion at various stress triaxialities. Int. J. Plast. **24**, 1731–1755 (2008)
16. Driemeier, L., Brünig, M., Micheli, G., Alves, M.: Experiments on stress-triaxiality dependence of material behavior of aluminum alloys. Mech. Mater. **42**, 207–217 (2010)
17. Brünig, M., Albrecht, D., Gerke, S.: Modelling of ductile damage and fracture behavior based on different micro-mechanisms. Int. J. Damage Mech. **20**, 558–577 (2011)

Characterization of Load Sensitive Fatigue Crack Initiation in Ti-Alloys Using Crystal Plasticity Based FE Simulations

P. Chakraborty and S. Ghosh

Abstract Fatigue life in near α Ti-alloys shows large variation with characteristics of applied load and is due to the microstructurally dependent deformation behavior in these alloys. In the present work, the load sensitive fatigue crack nucleation behavior is investigated using a physically motivated crack initiation law and cyclic crystal plasticity based finite element (CPFE) simulations of statistically equivalent image based microstructures. Since cyclic CPFE simulation for large number of cycles using conventional time integration schemes is computationally prohibitive, a wavelet transformation based multi-time scale (WATMUS) method developed in [1, 2] is used in the present work to perform accelerated simulations. To predict cycles to nucleation, a physically motivated crack nucleation model based on crystal plasticity variables developed in [3] has been used in this work. The nucleation model is calibrated and validated with experiments. The sensitivity of crack nucleation to the characteristics of the applied load is studied by performing WATMUS method based CPFE simulations for different cyclic load profiles on a statistically equivalent microstructure.

1 Introduction

Cycles to crack initiation in near α Ti-alloys at room temperature shows large variation with characteristics of applied load. This scatter is attributed to strong influence of underlying microstructure on the deformation and fatigue behavior in these

P. Chakraborty (✉)
The Ohio State University, Columbus OH-43201, USA
e-mail: chakraborty.11@osu.edu

S. Ghosh
Johns Hopkins University, Baltimore MD-21218, USA
e-mail: sghosh20@jhu.edu

H. Altenbach and S. Kruch (eds.), *Advanced Materials Modelling for Structures*,
Advanced Structured Materials 19, DOI: 10.1007/978-3-642-35167-9_10,

alloys [4–6]. A mechanistic approach is pursued in the present work to incorporate this microstructural influence on crack initiation. Similar methodology has been used in [7–12] where CPFE simulations of polycrystalline microstructures are performed and fatigue life models are developed based on crystal plasticity variables. Such a mechanistic approach is more accurate than conventional lifing methods where microstructural influences on fatigue life is accommodated through shifts in data curves obtained from extensive testing [13].

At room temperature, inelastic deformation in Ti-alloys predominantly happens due to slip on different slip systems in individual grains in the microstructure and is strongly size and orientation dependent. Depending on the orientation of a grain with respect to loading axis, it can have large plastic deformation (soft grain) or little or no plasticity (hard grain). Such heterogeneous plastic deformation in the polycrystalline microstructure results in stress concentration at grain interfaces and is conceived as the driver for microstructurally dependent crack nucleation in near α Ti-alloys [4, 14]. A size and rate dependent CPFE model for near α Ti-alloys developed in [15–17] captures this microstructurally dependent stress rise accurately and has been used in the present work. The morphological and crystallographical features of the polycrystalline alloys are statistically represented in the CPFE models [18, 19]. The use of such a statistical description not only reduces the number of grains in the FE simulations but also captures some of the key microstructural features that affect its macroscopic and microscopic responses.

Although CPFE simulations accurately capture the deformation behavior of polycrystalline alloys, they require very fine time steps at large applied stresses and strains when conventional time integration schemes are used. This lead to exorbitant computational requirements when fatigue analysis is performed for large number of cycles, since such reduced time steps are required in every cycle of the loading process. To resolve this computational prohibitiveness, fatigue life predictions have been performed in [7, 20, 21] by extrapolating the results based on CPFE simulations performed for few number of cycles. However extrapolation can lead to considerable error in the evolution of local microstructural variables and cause inaccurate fatigue life estimates based on these variables. Hence for accurate prediction, it is desirable to perform cyclic CPFE simulations till the failure event e.g. crack nucleation.

The dual-time behavior exhibited by the crystal plasticity variables under cyclic loading conditions allows the use of multi-time scale methods to perform accelerated FE simulations. In these methods the low and high frequency responses are decoupled and the low frequency evolution is integrated with coarser time steps to obtain computational benefit. WATMUS method developed in [1, 2] is used to perform accelerated cyclic CPFE simulations in the present work. This method is distinctly advantageous over other multi-time scale schemes such as the method of separation of motions [22, 23], asymptotic expansion based methods [24–26] or almost periodic temporal homogenization operator based method [27, 28] where inherent scale separation and local periodicity or almost periodicity in temporal evolution is assumed. Such assumptions are invalid for crystal plasticity variables which show strong non-periodic evolution and spatio-temporal localization. In WATMUS

method assumptions on characteristics of evolution are not made and hence proves suitable for decoupling the dual-time response of crystal plasticity variables.
A non-local crack nucleation model developed in [3] based on CPFE variables has been used in the present work to study load dependent crack initiation in these alloys. The nucleation criterion is based on stress concentration and dislocation pile up at interface of soft and hard grains. The model is calibrated and validated with fatigue experiments performed on samples of Ti-6242. WATMUS method based cyclic CPFE simulations of statistically equivalent image based microstructures in conjunction with the non-local crack nucleation model is used to characterize the load dependent fatigue crack initiation in near α Ti-alloys. An overview of the CPFE model and WATMUS method to perform accelerated CPFE simulations is presented in Sects. 2 and 3 respectively. The crack nucleation model developed in [3] has been extended in the present work and is discussed in Sect. 4. A detailed numerical study of the variations in number of cycles to crack nucleation and characteristics of applied load is presented in Sect. 5.

2 Size and Rate Dependent CPFE Model for Near α Ti-Alloys

In crystal plasticity based models, the evolution of inelastic deformation in polycrystalline alloys happens due to slip on different slip systems [29, 30]. The slip rate on the individual slip systems depend on the orientation of grains to which they belong and their resistance to slip. Hence through proper representation of orientations of grains in the underlying microstructure and slip system properties, the macroscopic and microscopic deformation behavior of polycrystalline alloys can be accurately captured through crystal plasticity based models. The morphological and crystallographical features of the microstructure are represented statistically from distributions of orientation, misorientation, size, shape of grains and microtexture, obtained from OIM scans of samples of these alloys [18, 19]. In the present work, the crystal plasticity based model and the associated parameters for near α Ti-alloys reported in [15–17] has been used.
The ability of CPFE simulations of statistically equivalent material coupon to capture microstructurally driven local event causing failure motivated the development of a crack nucleation model based on crystal plasticity variables in [3]. However fatigue life predictions using such an approach usually involve cyclic CPFE simulations of statistically equivalent microstructures for large number of cycles. Such simulations can be computationally unachievable using conventional integration schemes. Hence WATMUS method is used to improve the efficiency of cyclic CPFE simulations till crack nucleation and is described below.

3 Wavelet Transformation Based Multi-Time Scale Method for Accelerated Cyclic CPFE Simulations

Under cyclic loading, CPFE variables exhibit dual-time behavior characterized by high frequency oscillations due to applied load and low frequency monotonic response due to material relaxation that evolve with cycles. In the WATMUS method [1], decoupling of high and low frequency responses is achieved through a wavelet based transformation as shown below.

$$v^{\zeta}(t) = v(N,\tau) = \sum_{k=1}^{n} v_k(N)\psi_k(\tau) \quad \text{where} \quad \tau \in [0,T] \tag{1a}$$

$$v_k(N) = \frac{1}{T}\int_0^T v(N,\tau)\psi_k(\tau)d\tau \tag{1b}$$

where $v^{\zeta}(t)$ is single time scale variable, $v(N,\tau)$ is the corresponding dual-scale representation, $\psi_k(\tau)$ are wavelet basis functions that capture high frequency oscillation within each cycle, n is the number of basis functions required for accurate representation of the waveform, $v_k(N)$ are the corresponding coefficients that evolve monotonically with cycles and T is time period of applied load. This transformation allows integration of CPFE equations in the coarse scale with time steps of cycles and provides computational benefit.

The compact support, multi-resolution and orthogonality properties of the wavelets allow significant reduction in the number of basis functions required for accurate representation of arbitrary waveforms and hence used in the method. They also eliminate spurious oscillations that arise due to considering finite number of terms from the set formed by infinitely supported basis functions like Fourier series.

In the WATMUS method, the FE weak form for quasi-static problems is transformed in terms of wavelet basis functions

$$\begin{aligned} R^{\alpha}_{i,k}(N) &= \frac{1}{T}\int_0^T R^{\alpha}_i(N,\tau)\psi_k d\tau \\ &= \sum_e \int_{V_{0,e}} \frac{1}{T}\int_0^T \frac{\partial P^{\alpha}}{\partial x_j}\sigma_{ji} J_e \psi_k d\tau dV_{0,e} \\ &\quad - \sum_{S_T}\int_{S_0} \frac{1}{T}\int_0^T P^{\alpha} t_i J_A \psi_k d\tau dS_0 = 0 \end{aligned} \tag{2}$$

where P^{α} are the polynomial shape functions in every element e, S_T are the surfaces on which tractions are applied, α are the nodes of the discretized domain, $V_{0,e}$ and S_0 are the element volumes and surfaces in the reference configuration respectively and σ_{ji} are the stresses at integration points in the spatially discretized domain. The modified weak form shown in Eq. 2 is solved at discrete cyclic increments by using a Quasi-Newton scheme to obtain the wavelet coefficients of nodal displacements $C^{\alpha}_{i,k}$ where

$$C^{\alpha}_{i,k}(N) = \frac{1}{T}\int_0^T u^{\alpha}_i(N,\tau)\psi_k(\tau)d\tau \tag{3}$$

and u^{α}_i are the nodal displacement degrees of freedom of the conventional FE model. The oscillatory stress $\sigma_{ji}(N,\tau)$ in Eq. 2 depends on the oscillatory deformation gradient $F_{ij}(N,\tau)$ and internal variables $y_m(N,\tau)$. $F_{ij}(N,\tau)$ is obtained from the coefficients of nodal displacements and the oscillatory evolution of $y_m(N,\tau)$ in any cycle is obtained from

$$y_m(N,\tau) = y_{m0}(N) + \int_0^{\tau} f_m(y_m, F_{ij}, N, \tau)d\tau \tag{4}$$

where $y_{m0}(N) = y_m(N,\tau = 0)$ are the internal variables at the start of a cycle. The initial values of internal variables y_{m0} have a monotonic evolution with cycles and form the cycle scale internal variables. Cycle scale rate equations are numerically defined for y_{m0} and is shown below.

$$\frac{\partial y_{m0}}{\partial N} = y_{m0}(N+1) - y_{m0}(N) = y_m(N,T) - y_{m0}(N) \tag{5}$$

where

$$y_m(N,T) = y_{m0}(N) + \int_0^{T} f_m(y_m, F_{ij}, N, \tau)d\tau \tag{6}$$

Since f_m are non-linear functions, numerical integration using backward Euler scheme is used in Eq. 6. The cycle scale internal variables are integrated using second order backward difference formula as shown below.

$$y_{m0}(N) = \beta_1 y_{m0}(N-\Delta N) - \beta_2 y_{m0}(N-\Delta N-\Delta N_p) + \beta_3 \frac{\partial y_{m0}}{\partial N}\Big|_N \Delta N$$

$$\text{where} \quad \beta_1 = \frac{(r+1)^2}{(r+1)^2-1} \quad \beta_2 = \frac{1}{(r+1)^2-1} \quad \beta_3 = \frac{(r+1)^2-(r+1)}{(r+1)^2-1}$$

$$\text{and} \quad r = \frac{\Delta N_p}{\Delta N} \tag{7}$$

A Newton-Raphson scheme is used to integrate Eq. 7.
To reduce the number of global degrees of freedom, only the evolving wavelet coefficients of nodal displacements are solved at any cyclic increment from the cycle scale weak form shown in Eq. 2. These coefficients are selected based on criterion developed in [1]. The evolution of CPFE variables saturates with advancing load and integration of the coarse variables can be performed with larger cycle jumps. Hence, prediction of cycle jumps are made based on an upper bound on the error in truncation of Taylor series in second order backward difference formula in Eq. 7. The use of these adaptive criteria significantly enhances the performance of WATMUS method to perform cyclic CPFE simulations.

4 Non-Local Crack Initiation Model for Near α Ti-Alloys

In the present work, fatigue crack nucleation studies are made using the model developed in [3]. The model is motivated from experimental observations of failed Ti-6242 samples under fatigue loading with maximum stress at 90–95 % of yield strength and stress ratio $\sigma_{min}/\sigma_{max} = 0$. Detailed experimental investigations performed at failure sites suggest that regions with hard grains surrounded by soft grains are susceptible to initiate sub-surface cracks in near α Ti-alloys [31, 32].
In the presence of soft grains with large plastic deformation adjacent to hard grains, large stresses develop in the hard grains to satisfy strain compatibility condition. Additionally, dislocation motions causing plastic deformation in soft grains are prevented at hard-soft grain interfaces which results in piling up of these dislocations at the interface. In the crack nucleation model both these aspects are considered. It is hypothesized that the pile up of dislocation at the interface cause micro crack formation in hard grains. These micro cracks experience large stresses in hard grains and propagate to form macroscopic crack nucleation sites. A stress intensity factor R is defined for the growth of micro cracks as shown below

$$R = T_{eff}\sqrt{c} \quad \text{and} \quad T_{eff} = \sqrt{\langle T_n \rangle^2 + \beta T_t^2} \tag{8}$$

where c is the micro-crack length and T_{eff} is the effective traction on crack plane. Both shear T_t and normal T_n component of traction are considered. Since compressive nature of normal traction T_n cause crack closure, a Macaulay bracket is used implying compressive normal traction has no effect on the stress intensity factor R.
The micro crack length c is related to dislocation pile up length B in adjacent soft grain using the relation proposed in [33]. In the formula, the equilibrated wedge shaped micro-crack length c is given by

$$c = \frac{G}{8\pi(1-\nu)\gamma_s} B^2 \tag{9}$$

where G is the shear modulus and γ_s is the surface energy. The dislocation pile length $\mathbf{B}$ is evaluated from closure failure around any burgers circuit due to inhomogeneous plastic deformation as shown below

$$\mathbf{B} = \oint_{\Gamma} d\bar{\mathbf{x}} = \oint_{\Gamma} \mathbf{F}^p d\mathbf{X} = \int_{\Omega} \boldsymbol{\Lambda}.\mathbf{n} d\Omega \tag{10}$$

where $\mathbf{n}$ is normal to surface Ω in which the burger's circuit is considered and $\boldsymbol{\Lambda}$ is Nye's dislocation tensor which depends on curl of $\mathbf{F}^p$

$$\boldsymbol{\Lambda} = \boldsymbol{\nabla}^T \times \mathbf{F}^p \tag{11}$$

The stress intensity factor R evolves with increasing cycles of applied load. Macroscopic crack nucleation is considered to happen when R at any material point on the interfaces of hard soft grains in the microstructure exceeds the critical stress intensity factor R_c. The critical stress intensity factor R_c is a material constant for a given alloy and is calibrated from experiments.

In the present work, load sensitive fatigue life of Ti-6242 is investigated. Hence, R_c is evaluated for this alloy from WATMUS based cyclic CPFE simulations and dwell fatigue experiments. A detailed description of the calibration procedure is provided in [3]. The procedure is extended in the present work by considering the basal plane as the plane of crack nucleation to determine R. Using in situ surface acoustic wave techniques and dwell fatigue experiments performed on different samples of Ti-6242, it has been observed that crack initiation happens at 80–85 % of total number of cycles to failure [34]. Based on this observation, a lower and upper bound on R_c is determined and these are

$$\begin{aligned} &\text{Crack nucleation at 80 \% of total life} \quad R_{c(80\,\%)} = 6.54\ \text{MPa}\sqrt{\mu m} \\ &\text{Crack nucleation at 85 \% of total life} \quad R_{c(85\,\%)} = 6.80\ \text{MPa}\sqrt{\mu m} \end{aligned}$$

5 Sensitivity of Cycles to Crack Nucleation to Characteristics of Applied Load

A statistically equivalent microstructure of Ti-6242 is considered to correlate cycles to crack nucleation and characteristics of applied load. Two separate studies has been performed. In the first study, comparisons between dwell load, normal cyclic load and maximum stress levels are performed. In the second study, the effect of hold-time in the dwell load on cycles to crack nucleation has been studied.

5.1 Comparison Between Dwell and Normal Cyclic Load

In this sensitivity study the statistically equivalent microstructure is subjected to 4 different types of load as shown below:

- Case A: $\sigma_{max} = 894\,\text{MPa}$, $\sigma_r = 0$, $T_{load} = T_{unload} = 1\,\text{s}$ and $T_{hold} = 120\,\text{s}$
- Case B: $\sigma_{max} = 847\,\text{MPa}$, $\sigma_r = 0$, $T_{load} = T_{unload} = 1\,\text{s}$ and $T_{hold} = 120\,\text{s}$
- Case C: $\sigma_{max} = 894\,\text{MPa}$, $\sigma_r = 0$, $T_{load} = T_{unload} = 61\,\text{s}$ and $T_{hold} = 0\,\text{s}$
- Case D: $\sigma_{max} = 894\,\text{MPa}$, $\sigma_r = 0$, $T_{load} = T_{unload} = 1\,\text{s}$ and $T_{hold} = 0\,\text{s}$

Maximum applied stress (σ_{max}) is 95 % of yield strength in cases A, C and D and is 90 % of the yield strength in case B. Dwell load with 2 min hold is applied in cases A and B. Triangular load with time periods $T = 122$ and $T = 2\,\text{s}$ is applied in cases C and D respectively. WATMUS method is used to perform cyclic CPFE simulations and stress intensity factor R is evaluated at nodes situated at grain interfaces. In a cycle, R is evaluated at start of unloading and corresponds to $\tau = 121\,\text{s}$ in cases A and B, $\tau = 61\,\text{s}$ in case C and $\tau = 1\,\text{s}$ in case D. The evolution R at the node where crack nucleation is predicted using calibrated R_c is shown in Fig. 1.

The number of cycles to crack initiation based on calibrated R_c values at 80 and 85 % of total life is summarized in Table 1. As can be observed from the table, the microstructure has a shorter fatigue initiation life when subjected to dwell load (cases A and B) as compared to normal cyclic loading (cases C and D). The number of cycles to crack nucleation for dwell (case A) and normal fatigue (case D) at 95 % of yield strength shows the same trend as observed experimentally [4–6]. In the normal cyclic loading cases, the decrease in frequency of the load deteriorates the life of the microstructure as can observed from cases C and D. Also it can be observed from this study that an increased maximum stress in normal cyclic loading (cases C and

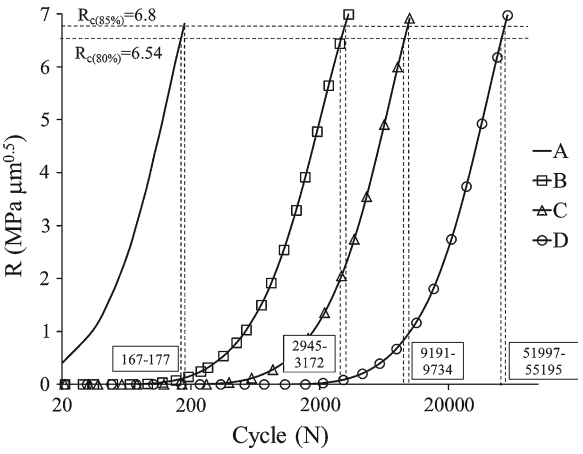

Fig. 1 Evolution of R with cycles at the predicted crack initiation site for 4 different fatigue load cases *A,B,C* and *D*

Table 1 Comparison of number of cycles to crack initiation for different cyclic load forms

Case No.	Cycles to crack nucleation	
	80 % of life	85 % of life
A	167	177
B	2945	3172
C	9191	9734
D	51997	55195

D) is less detrimental than the hold at a lower maximum stress under dwell loading (case B).

5.2 *Comparison Between Different Hold Times for Dwell Load*

The number of cycles to crack nucleation for different hold time and same time period of dwell with maximum applied stress at 95 % of yield strength, is also compared for this statistically equivalent microstructure. WATMUS based CPFE simulations are performed for three different load cases shown below:

- Case E: $T_{load} = T_{unload} = 16$ s and $T_{hold} = 90$ s
- Case F: $T_{load} = T_{unload} = 31$ s and $T_{hold} = 60$ s
- Case G: $T_{load} = T_{unload} = 46$ s and $T_{hold} = 30$ s

The number of cycles to initiate a crack is evaluated from non-local crack nucleation model described in Sect. 4. The evolution of R at the crack initiation site is

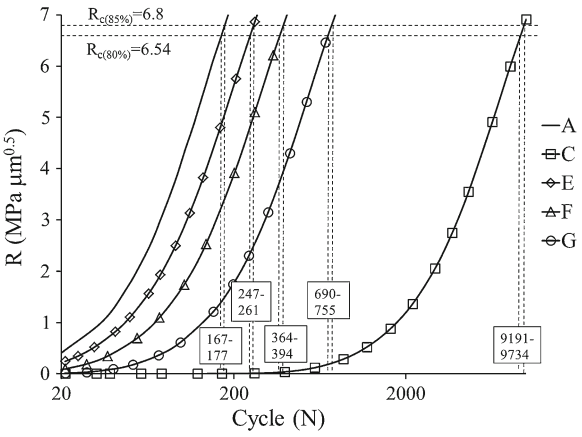

Fig. 2 Evolution of R with Cycles for 5 different fatigue load cases *A,E,F,G* and *C*

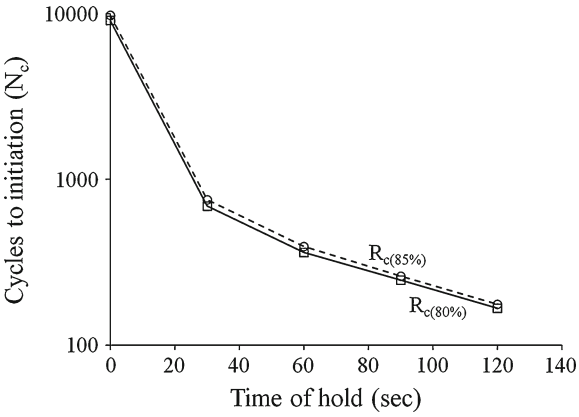

Fig. 3 Comparison of number of cycles to crack initiation for different hold time at maximum stress

shown in Fig. 2. A plot of number of cycles to crack initiation versus hold time is shown in Fig. 3. A definite trend in life to initiation with hold time can be observed.

6 Conclusion

Fatigue crack nucleation in near α Ti-alloys is strongly influenced by its underlying microstructure and a mechanistic approach based on CPFE simulations of statistically equivalent microstructures in conjunction with a physically motivated crack nucleation model is pursued in the present work to accurately predict this behavior. WATMUS method is used to perform accelerated cyclic CPFE simulations which is otherwise infeasible. A non-local crack nucleation model based on micro-crack growth under the influence of local stresses at hard soft grain interfaces is used to predict initiation. A critical stress intensity factor is defined that dictates crack nucleation and is calibrated from dwell fatigue experiments performed on samples of Ti-6242. A statistically equivalent microstructure is subjected to different cyclic load patterns and cycles to crack nucleation is predicted from the proposed model. From the predictions, a trend in cycles to crack initiation and hold, loading, unloading time and maximum applied stress level can be observed.

In the present work the workability of the proposed integrated computational and experimental approach to quantify scatter in fatigue crack nucleation in near α Ti-alloys has been demonstrated. The methodology can be extended to other polycrystalline alloy systems for accurate fatigue life predictions and is considered as a future work.

References

1. Joseph, D.S., Chakraborty, P., Ghosh, S.: Comp. Methods. App. Mech. Engg. **199**, 2177 (2010)
2. Chakraborty, P., Joseph, D.S., Ghosh, S.: Finite Elem. Ana. Des. **47**, 610 (2011)
3. Anahid, M., Samal, M.K., Ghosh, S.: J. Mech. Phys. Solids **59**(10), 2157 (2011)
4. Bache, M.R.: Int. J. Fatigue **25**, 1079 (2003)
5. Bache, M.R., Cope, M., Davies, H.M., Evans, E.J., Harrison, G.: Int. J. Fatigue **19**(93), 83 (1997)
6. Sinha, V., Mills, M.J., Williams, J.C.: Metall. Mat. Trans. A **35**, 3141 (2004)
7. Sinha, S., Ghosh, S.: Int. J. Fatigue **28**, 1690 (2006)
8. Goh, C.H., Wallace, J.M., Neu, R.W., McDowell, D.L.: Int. J. Fatigue **23**, 5423 (2001)
9. Sackett, E., Germain, L., Bache, M.: Int. J. Fatigue **29**, 2015 (2007)
10. Bridiera, F., McDowell, D.L., Villechaisea, P., Mendeza, J.: Int. J. Plasticity **25**, 1066 (2009)
11. Mineur, M., Villechaise, P., Mendez J.: Mater. Sci. Engg. A **286**, 257—268 (2000)
12. McDowell, D., Dunne, F.P.E.: Int. J. Fatigue **32**, 1521 (2010)
13. Suresh, S.: Fatigue of Materials. Cambridge University Press, Cambridge (1998)
14. Lutjering, G., Williams, J.C.: Titanium. Springer-Verlag, Berlin-Heidelberg (2007)
15. Hasija, V., Ghosh, S., Mills, M.J., Joseph, D.S.: Acta Mater. **51**, 4533 (2003)
16. Deka, D., Joseph, D.S., Ghosh, S., Mills, M.J.: Metall. Trans. A. **37**(5), 1371 (2006)
17. Venkatramani, G., Ghosh, S., Mills, M.J.: Acta Mater. **55**, 3971 (2007)
18. Groeber, M., Ghosh, S., Uchic, M.D., Dimiduk, D.M.: Acta. Mat. **56**, 1257 (2008)
19. Groeber, M., Ghosh, S., Uchic, M.D., Dimiduk, D.M.: Acta. Mat. **56**, 1274 (2008)
20. Bennett, V.P., McDowell, D.L.: Int. J. Fatigue **25**, 27 (2003)
21. Turkmen, H.S., Loge, R.E., Dawson, P.R., Miller, M.: Int. J. Fatigue **25**, 267 (2003)
22. Blekhman I.I.: Vibrational mechanics. World Scientific, Singapore (2000)
23. Thomsen, J.J.: Vibrations and stability: theory, analysis and tools, 2nd edn. Springer-Verlag, Berlin (2004)
24. Yu, Q., Fish, J.: Comput. Mech. **29**, 199 (2002)
25. Manchiraju, S., Asai, M., Ghosh, S., Strain Anal, J.: Engg. Des. **42**, 183 (2007)
26. Manchiraju, S., Kirane, K., Ghosh, S.: J. Comp. Aid. Mater. Des. **14**, 47 (2008)
27. Oskay, C., Fish, J.: Int. J. Multiscale. Comput. Engg. **2**, 1 (2004)
28. Oskay, C., Fish, J.: Int. J. Num. Methods Engg. **61**, 329 (2004)
29. Anand, L., Kothari, M.: J. Mech. Phys. Solids **44**(4), 525 (1996)
30. Kalidindi, S.R., Bronkhorst, C.A., Anand, L.: J. Mech. Phys. Solids **40**, 537 (1992)
31. Sinha, V., Spowart, J.E., Mills, M.J., Williams, J.C.: Metall. Mat. Trans. A **37**, 1507 (2006)
32. Sinha, V., Mills, M.J., Williams, J.C.: Metall. Mat. Trans. A **37**, 2015 (2006)
33. Stroh, A.N.: Proc. R. Soc. Lond. Ser. A **223**, 404 (1954)
34. Rokhlin, S., Kim, J.Y., Zoofan, B.: unpublished research. The Ohio State University, Columbus (2005)

Creep Crack Growth Modelling in 316H Stainless Steel

Catrin M. Davies and Ali Mehmanparast

Abstract It has been realised that plasticity has a significant effect on the creep ductility of Austenitic Type 316H stainless steel at 550 °C. Recently a model has been produced to estimate the creep ductility and strain rate as a function of the plastic strain levels in the material. A variable creep ductility model, incorporating stress dependent strain rate effects, has therefore been implemented in a finite element (FE) analysis to predict creep crack growth (CCG) in 316H stainless steel at 550 °C. Recent experimental results have shown that material pre-compression to 8 % plastic strain at room temperature accelerates the creeping rate and significantly reduces the creep ductility of 316H stainless steel at 550 °C. In addition pre-compression significantly hardens the material and thus the levels of plasticity on specimen loading in tension are reduced. As a result, accelerated cracking rates are observed in pre-compressed (PC) materials compared to as-received (AR) (non-compressed) materials. The variable creep ductility FE CCG model has been employed to predict the CCG behaviour of AR and PC materials and to analyse their differences. Comparisons are also made to FE and analytical constant creep ductility models.

1 Introduction

The creep crack growth (CCG) behaviour of 316H stainless steel is of significant concern, particularly in relation to its use in the UK's advanced gas cooled reactors (AGRs). A considerable amount of uniaxial creep and CCG tests have been performed

C. M. Davies (✉) · A. Mehmanparast
Department of Mechanical Engineering,
Imperial College London, South Kensington Campus,
London SW7 2AZ, UK
e-mail: catrin.davies@imperial.ac.uk

A. Mehmanparast
e-mail: ali.mehmanparast@imperial.ac.uk

H. Altenbach and S. Kruch (eds.), *Advanced Materials Modelling for Structures*,
Advanced Structured Materials 19, DOI: 10.1007/978-3-642-35167-9_11,

on Type 316H stainless steel, taken from ex-service steam headers, and tested at 550 °C (see e.g. [1–3]). Recently, significant interest has been developed in pre-compressed (PC) 316H of up to 8 % plastic strain at room temperature [4–6]. It has been found that pre-compression generally hardens the material, reduces the creep rupture times, reduces creep ductility and subsequently increases the CCG rate compared to that of AR material [4–6]. The CCG behaviour of PC material has also been found similar to long term (low load) CCG tests on AR material [6].

Predicting CCG is fundamentally important in high temperature components life-time assessments. Finite element (FE) analysis provides a tool to enable CCG predictions to be performed and the sensitivity of key parameters to be studied. FE analysis is therefore a beneficial aid for understanding CCG behaviour. In this work CCG predictions are obtained for AR and PC materials. Previous studies (e.g. [7, 8]) have assumed the material has a constant creep ductility, ε_f. However recent studies show that the creep ductility of 316H at 550 °C is influenced by the levels of plastic strain in the material [4, 5, 9]. In [9] the applied stress was normalised by the temperature dependent 0.2 % proof stress of the material, $\sigma/\sigma_{0.2}$, to examine plasticity effects on creep failure behaviour. A stress dependent creep ductility model has therefore been incorporated into FE analyses to predict CCG and the results compared to short and long term experimental data on AR and PC materials.

2 Deformation, Damage and Fracture Models

The tensile and creep deformation behaviour of 8 % PC and AR materials at 550 °C have previously been compared in [4, 5], and their CCG behaviour compared in [6]. A summary of the key features relevant to this work is given below, following which the creep failure and CCG models employed are presented.

2.1 Tensile and Creep Deformation

A comparison of the AR and PC materials tensile response at 550 °C is shown in Fig. 1. The material exhibits significant hardening due to the prior plastic compressive strain. Subsequently the 0.2 % proof stress of the PC material is 50 % higher (260 MPa) than that of the AR material (170 MPa). The elastic moduli are however similar at 140 GPa.

Creep deformation is considered to be composed of three regimes—primary, secondary and tertiary creep. The use of an average creep rate, obtained directly from creep rupture data, has been proposed to account for all three stages of creep. This average creep rate, $\dot{\varepsilon}_A$, is defined as

$$\dot{\varepsilon}_A = \varepsilon_f / t_r = \dot{\varepsilon}_o (\sigma/\sigma_0)^n = A\sigma^n \tag{1}$$

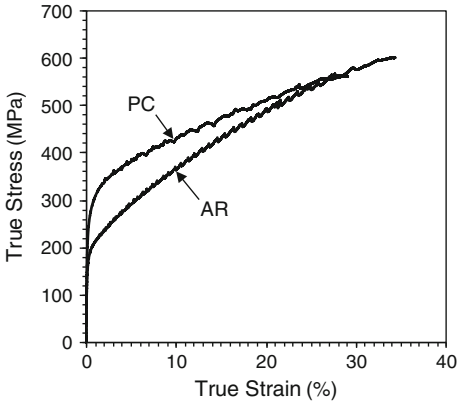

Fig. 1 Tensile response of AR and PC materials at 500 °C

where ε_f is the uniaxial failure strain, t_r is the time to rupture and σ is the equivalent (Mises) stress. The variables, σ_0, A and n in Eq. (1) are generally taken as temperature dependent material constants. The value of n and subsequently A may vary over a wide stress range. Results for AR 316H stainless steel at 550 °C shown in [9] indicate that for $\sigma/\sigma_{0.2} \geq 1.035$, $A = 1.24 \times 10^{-23}$ MPam^{-n}h^{-1} and $n = 7.5$, and for $\sigma/\sigma_{0.2} < 1.035$, $A = 6.56 \times 10^{-12}$ MPam^{-n}h^{-1} and $n = 2.3$. Similar average creep properties have been found between AR and PC material [5, 9], thus the same values of A and n are used in this work for both material conditions. The transition between high/low A and n are also considered to occur at the same normalised stress level for both AR and PC materials.

2.2 Creep Ductility

The trends in the uniaxial creep ductility for 316H stainless steel over a wide range of stresses have recently been examined in [9]. Three regions of creep ductility have been identified. These consist of an upper shelf ($\sigma/\sigma_{0.2} > 1.32$) and lower shelf ($\sigma/\sigma_{0.2} < 0.84$) region with a stress dependent transition region in between, as illustrated in Fig. 2 for 550 °C. Note that the upper shelf value shown, 13.6 %, is the average value of the data set available and the trends for $\sigma/\sigma_{0.2} < 1.32$ have been estimated based on trends identified in data at higher temperatures [9]. Preliminary results have shown that when plotted against, $\sigma/\sigma_{0.2}$, the PC creep ductility data falls upon the AR trends lines [9], hence the trend shown in Fig. 2 may be used for both AR and PC material.

2.3 Creep Damage Model

The creep ductility exhaustion approach has been used to model creep damage accumulation. The damage parameter, ω, is defined such that $0 \leq \omega \leq 1$ and failure

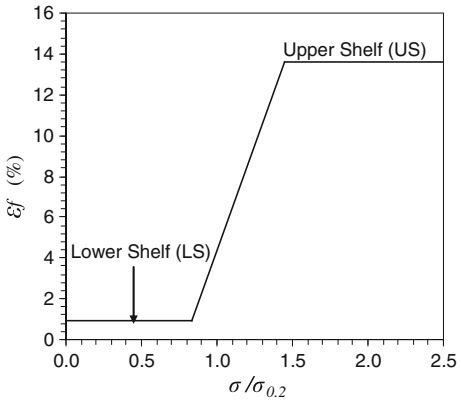

Fig. 2 Stress dependent creep ductility

occurs when ω approaches 1. The rate of damage accumulation, $\dot{\omega}$, is related to the equivalent creep strain rate and multiaxial creep ductility, by the relationship,

$$\dot{\omega} = \dot{\varepsilon}^c / \varepsilon_f^* \tag{2}$$

and the total damage at any instant is the integral of the damage rate in Eq. (2), thus given by

$$\omega = \int_0^t \dot{\omega}\, dt \tag{3}$$

In the vicinity of the crack tip the local (multiaxial) creep ductility, ε_f^*, may be obtained for the material under study from the Cocks and Ashby [10] model. The model describes the ratio of the multiaxial to uniaxial failure strain, $\varepsilon_f^*/\varepsilon_f$, as

$$\frac{\varepsilon_f^*}{\varepsilon_f} = sinh\left[\frac{2}{3}\left(\frac{n-1/2}{n+1/2}\right)\right] \Big/ sinh\left[2\left(\frac{n-1/2}{n+1/2}\right)\frac{\sigma_m}{\sigma_e}\right] \tag{4}$$

where σ_m/σ_e is the ratio between the mean (hydrostatic) stress and equivalent (von Mises) stress, which is often referred to as triaxiality.

2.4 Creep Fracture Parameters

At long times, where a steady state of creep deformation and damage has developed at a crack tip, the CCG rate, $\dot{a}$, may be described by the crack tip parameter C^* according to the power law relationship,

$$\dot{a} = DC^{*\phi} \tag{5}$$

where D and ϕ are material constants, which are temperature and stress state dependent [11]. Under steady state conditions $\dot{a}$ versus C^* data appear as a straight line when plotted on log-log axes [11]. Prior to steady state conditions being achieved, these data points will appear as a 'tail'.

The C^* parameter may be determined experimentally in CCG tests from the load line displacement rate measurements, $\dot{\Delta}$, using the relation [12]

$$C^* = \frac{P\dot{\Delta}}{B_n(W-a)}H\eta \tag{6}$$

where P is the applied load, B_n is the net specimen thickness between the side-grooves and W is the specimen width. In Eq. (6), H and η are geometry dependent constants. For a C(T) specimen $H = n/(n+1)$ and $\eta = 2.2$ [12]. Validity criteria are specified in [13] for the use of the C^* parameter to describe creep crack initiation and growth (see e.g. [1]).

2.5 Creep Crack Growth Models

The NSW model [14], which is based on a ductility exhaustion approach, predicts the steady state creep crack growth rate, $\dot{a}$, using

$$\dot{a} = (n+1)/\varepsilon_f^*(C^*/I_n)^{n/(n+1)}(Ar_c)^{1/(n+1)} \tag{7}$$

where ε_f^* is the critical multiaxial failure strain appropriate to the crack tip stress state and I_n is a nondimensional function of n, values for which are tabulated in [15] for both plane stress and plane strain conditions. In [16] it is recommended that ε_f^* is taken to be the uniaxial failure strain, ε_f, under plane stress conditions.

3 Finite Element Model

Finite element analyses were conducted on a two dimensional FE model of a compact tension, C(T), specimen of width, $W = 50$ mm, thickness $B = 25$ mm and normalised crack length $a/W = 0.5$ using ABAQUS v6.11. Half of the specimen has been modelled and symmetry conditions employed. Previous work has demonstrated that plane strain analyses are consistent with full 3D analyses [7]. In the region of the crack path regular square elements of size 20 μm, have been used. The influence of mesh sensitivity has previously been examined (see e.g. [7, 8]). A small geometry change analysis has been performed employing four noded continuum elements for plane stress analyses (CPS4) and 'hybrid' elements (CPE4H) for plane strain analyses. Three loading cases have been considered using both AR and PC material properties, as described in Table 1, under both plane stress (PS) and plane

Table 1 Summary of C(T) specimens modelled and loading details

ID	P (kN)	$K(a_0)$ (MPa$\sqrt{}$m)	$\sigma_{ref}/\sigma_{0.2}$ PS	$\sigma_{ref}/\sigma_{0.2}$ PE
AR1	10.0	17.3	0.53	0.37
AR2	14.5	25.0	0.77	0.53
AR3	19.5	33.6	1.03	0.71
PC1	10.0	17.3	0.35	0.24
PC2	14.5	25.0	0.50	0.35
PC3	19.5	33.6	0.67	0.46

strain (PE) conditions. Note that the normalised reference stress, $\sigma_{ref}/\sigma_{0.2}$, shown in Table 1 can be used as an indicator of the levels of plasticity at the crack tip on loading.

3.1 Creep Damage and Crack Growth Simulation

Following the approach in [7], crack growth is simulated by reducing an element's load carrying capacity when the damage parameter, ω, attains a critical value. To avoid numerical difficulty, the stress (at a gauss point) in a damaged element is limited to a small value by switching its material response to elastic-perfectly plastic behaviour with a yield stress of 1 MPa. This is done using a user defined field (USDFLD) subroutine in ABAQUS where the creep damage parameter is also evaluated [17]. The USDFLD subroutine was also used to switch the values of A and n depending on the normalised stress value as described in Sect. 2.1. When the damage at the centroid of the element attains $\omega = 1.0$ then that element is considered fully damaged and the crack advances. The analyses were run until terminated by the program when numerical difficulties were encountered. Therefore various crack extensions have been achieved in each simulation.

4 Comparison of CCG Predictions and Experimental Data

CCG data have previously been reported on AR and PC material on the C(T) geometry at a range of load levels [1, 6, 18]. These data are shown in Fig. 3, where long and short term AR data are distinguished. Mean, upper bound (UB) and lower bound (LB) fits have been made to each data set. As can be seen, the CCG rate of the PC material is around a factor of 7 higher than that of the short term (ST) AR material, for a given C^*. Higher CCG rates are also observed in the long-term (LT) AR tests, which follow the same trend lines as the PC material. These results have been discussed in terms of loss of specimen constraint due to plasticity effects in short term (high load) tests and the reduction of creep ductility and retention of specimen constraint in the long term AR and PC data [1, 6, 18]. Note that the slopes of the trends lines to the PC and AR material are similar, as detailed in [18]. This also indicates that the creep stress exponent, n, is similar in both materials.

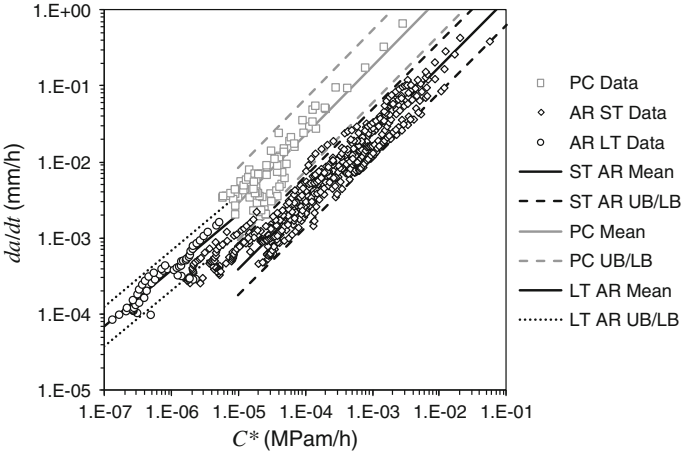

Fig. 3 Comparison of experimental CCG data on short and long term AR and PC material

4.1 Comparison of Predictions to CCG Models

The FE predictions are compared to the NSW model's predictions in Fig. 4, for the AR data assuming plane stress (PS) conditions. Note that three data sets are shown for each load considered. Firstly predictions have been obtained assuming constant creep ductility and creep strain rate properties, corresponding to the upper shelf (US) creep ductility, and similarly corresponding to the lower shelf (LS) creep ductility values, see Fig. 2. The third data set for a given load has been obtained using the

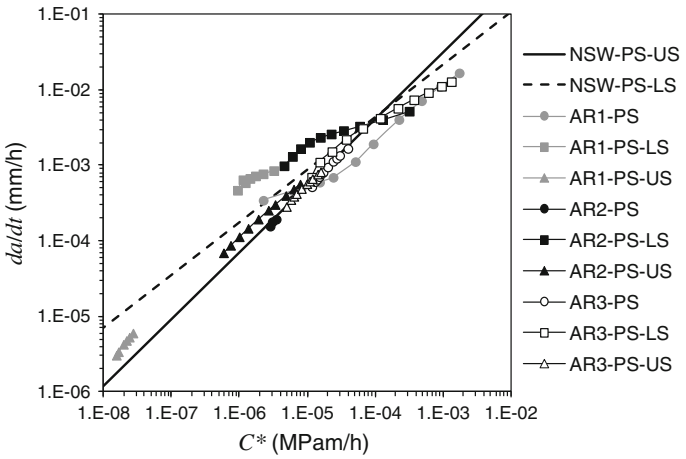

Fig. 4 Comparison of CCG predictions from the FE and NSW model on AR material for plane stress conditions

stress dependent creep ductility and strain rate model described in Sects. 2.1 and 2.2. As expected the US data fall close to or upon the NSW-US model's prediction. Note that although the ASTM validity criteria for $\dot{a}$ versus C^* have been applied to all the predictions, some tails may remain in the FE data as also observed in the experimental data. The LS FE and NSW-LS predictions generally follow the same trend, however the AR1-LS and AR2-LS data generally fall above the NSW-LS prediction which may be attributed to transient creep effects and small variations in the crack tip angle. The initial data for AR3-LS are coincident with the NSW-LS model prediction. As the crack extends and subsequently C^* increases, the levels of crack tip plasticity also increases, leading to a loss of specimen constraint and hence lower CCG rates. This may explain why the latter half of the AR3-LS data fall below the NSW-LS prediction. The AR2 and AR3 data from the stress dependent model fall exactly on the NSW-US model because the normalised reference stress, $\sigma_{ref}/\sigma_{0.2}$, for these valid points are relatively low. The AR1 data shown start at the NSW-LS prediction, but then fall towards and below the NSW-US prediction and data. Though not shown, the crack extension achieved in the simulation for AR1 was significantly higher than that of AR2 and AR3. Therefore, even though the applied load in specimens AR2 and AR3 were higher than that of AR1-PS, the $\sigma_{ref}/\sigma_{0.2}$ values corresponding to the data points shown are higher in AR1-PS, and significantly greater than unity for the majority of the data shown. This again leads to high crack tip plasticity, loss of specimen constraint and hence a reduction of CCG rate with crack extension. Note also that due to the various crack extensions achieved for the three loads examined for a given condition, the C^* values shown may not increase in proportion to the applied load, as in the case of AR1-PS, AR2-PS and AR3-PS.

4.2 Comparison of Predictions to Experimental Data

The plane stress (PS) FE predictions shown in Fig. 4 are compared to plane strain (PE) predictions in Fig. 5. Also included in Fig. 5 are the mean (solid line) and upper bound (UB) and lower bound (LB) (shown as dashed lines) fits to the short and long term AR experimental data. Though not shown, the mean fit to the short term AR experimental data falls very closely to the NSW-US prediction described above. Though the data at high C^* values fell below the NSW-US prediction (which assumes high constraint) these FE predictions fall upon the lower bound fit to the short term AR experimental data. All FE predictions in Fig. 5 fall between the UB fit to the long term data and the LB fit to the short term data. Also there is a general trend of increasing CCG rates as C^* decreases, at relatively low C^* values, as also seen in the experimental data, except for the AR-PS-US data which follows the short term AR material trends, as expected. The amount of crack extensions achieved in the PE simulations were limited, however some data is shown in Fig. 5. The AR1-PE-US and AR2-PE data, which are at relatively small C^* values, fall on the UB to the long term AR data. The AR3-PE-US, AR2-PE-US and AR1-PE data fall close to the LB long term trend line, which is also close to the UB short term trend line. Note that

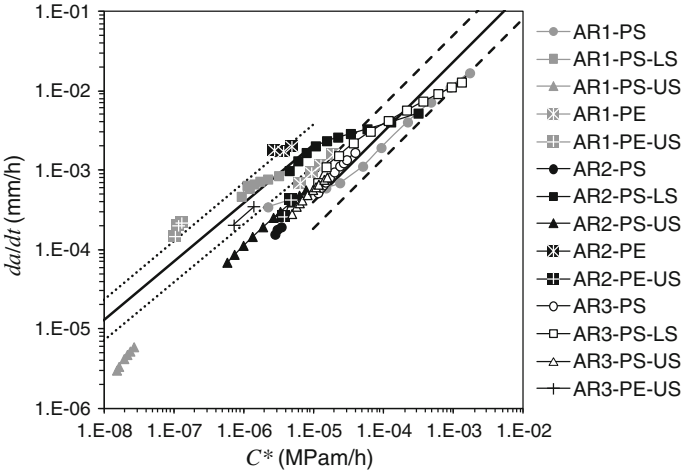

Fig. 5 Comparison of CCG predictions and experimental data for AR material

the CCG rate of the AR2-PE data is higher than that of AR1-PE, for a given C^*, due to the high values of $\sigma_{ref}/\sigma_{0.2}$ in the valid data available for AR1-PE.

In Fig. 6 the PC predictions are compared to the AR and PC trend lines fitted to the experimental data (as shown in Fig. 3). All FE predictions shown fall within the UB and LB trends lines on the PC data. The CCG rate predictions from the stress dependent creep and ductility model decrease as C^* increases, and tends from the upper bound fit to the PC data (if extrapolated) to the LB fit to the PC data. The PS data for the three loads considered is approximately coincident for C^* ranging between 1×10^{-5} to 1×10^{-4} MPamh^{-1}, with the small differences corresponding

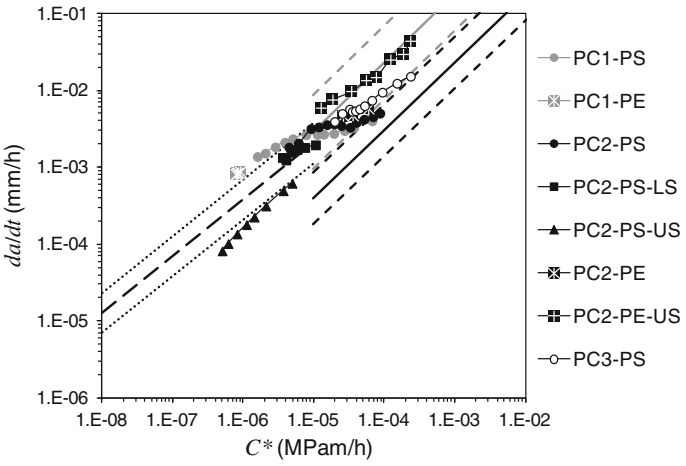

Fig. 6 Comparison of CCG predictions and experimental data for PC material

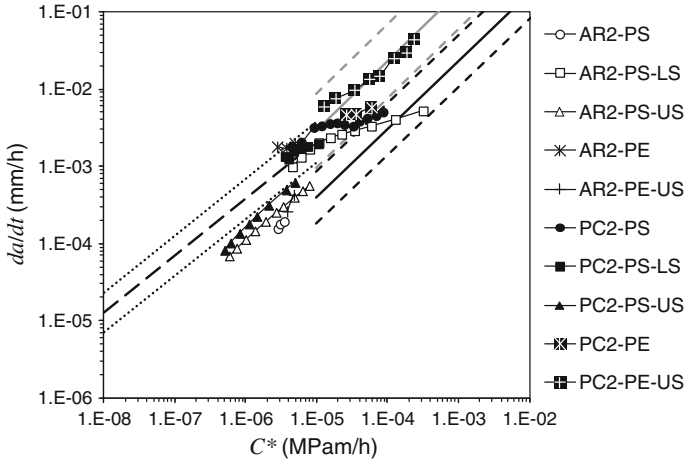

Fig. 7 Comparison of CCG predictions for AR and PC material for a given load

to the relative $\sigma/\sigma_{0.2}$ values of the FE data at these C^* values. For this range of C^*, the PE CCG predictions are effectively the same as the PS predictions, indicating a balance between the increase in CCG rate due to higher triaxiality in PE and a decrease in CCG due to the relatively high $\sigma_{ref}/\sigma_{0.2}$ for this data. Data for PC1-PE however have relatively low $\sigma/\sigma_{0.2}$ values, and hence the CCG rate falls along the UB fit to the PC data. Data for PC2-PE-US have a relatively low $\sigma_{ref}/\sigma_{0.2}$ value and the CCG rate predictions fall upon the mean fit to the experimental PC data. Also note, as may be expected, the lower shelf constant creep ductility predictions, PC2-PS-LS data, fall close to the low load (and $\sigma_{ref}/\sigma_{0.2}$) predictions from the stress dependent model for C^* values from 1×10^{-6} to 1×10^{-5} MPamh^{-1}.

A comparison of the AR and PC data is shown for example at the load of 14.5 kN in Fig. 7. The influence of plasticity alone on the CCG rate may be seen by comparing AR2-PS-US and PC2-PS-US, where a marginally higher CCG rate for a given C^* is observed for the PC material which has lower $\sigma_{ref}/\sigma_{0.2}$ values. Similar trends are seen between AR2-PS-LS and PC2-PS-LS. Limited data is available from the stress dependent model for AR material at this load. However it can be seen that, for a given C^*, the CCG rate of the PC material is around 7 times faster than the AR, which is consistent with the experimental observations. This factor between the CCG rate of AR and PC materials may be reduced for plane strain conditions. However there are insufficient data available at present to deduce such trends.

5 Conclusions

Finite element models have been developed to predict the CCG rate of AR and PC materials, using a novel stress dependent creep strain rate and ductility model. Good agreement has been found between the CCG rate versus C^* predictions and

experimental data. The new stress dependent model has enabled the transition from high CCG rates to lower CCG rates at low and high C^* values, respectively, to be predicted as seen in the experimental data. By comparing the results of the stress dependent and a constant creep ductility model's predictions, the influence of both crack tip plasticity and creep ductility on the CCG rate has been determined. The accelerated CCG rate in PC compared to AR material observed experimentally has been successfully predicted by the FE model. This model is a valuable tool to predict the CCG rate of AR and PC materials at a range of loads and temperatures.

Acknowledgments The authors wish to acknowledge discussions with Prof. Y-J Kim, Dr C-S Oh and Mr N-H Kim from Korea University. This work has been supported by EDF Energy Nuclear Generation and EPSRC under grant EP/I004351/1.

References

1. Davies, C.M., Mueller, F., Nikbin, K.M., O'Dowd, N.P., Webster, G.A.: Analysis of creep crack initiation and growth in different geometries for 316H and carbon manganese steels. J. ASTM Int. 3(2), (2006). doi:10.1520/JAI13223
2. Dean, D.W., Gladwin, D.N.: Creep crack growth behaviour of type 316H steels and proposed modifications to standard testing and analysis methods. Int. J. Press. Vessels Pip. **84**(6), 378–395 (2007)
3. Spindler, M.W.: The multiaxial creep ductility of austenitic stainless steels. Fatigue Fract. Eng. Mater. Struct. **27**(4), 273–282 (2004)
4. Mehmanparast, A., Davies, C.M., Dean, D.W., Nikbin, K.M.: The influence of cold pre-compression on high temperature deformation and fracture behaviour of 316H stainless steel. In: ESIA11: Design, Fabrication, Operation and Disposal, EMAS, Manchester, 24–25 May 2011
5. Davies, C.M., Dean, D.W., Nikbin, K.M.: The influence of compressive plastic pre-strain on the creep deformation and damage behaviour of 316H stainless steel. In: Proceedings of the International Conference on Engineering Structural Integrity Assessment—Its Contribution to the Sustainable Economy, Manchester, EMAS Publishing, UK, 19–20 May 2009
6. Davies, C.M., Dean, D.W., Mehmanparast, A., Nikbin, K.M.: Compressive pre-strain effects on creep and crack growth behaviour of 316H stainless steel. In: ASME 2010 Pressure Vessels and Piping Division/K-PVP Conference, ASME, PVP2010-25044, Bellevue, Washington, USA, 18–22 July 2010
7. Oh, C.-S., Kim, N.-H., Kim, Y.-J., Baek, J.-H., Kim, Y.-P., Kim, W.-S.: A finite element ductile failure simulation method using stress-modified fracture strain model. Eng. Fract. Mech. **78**(1), 124–137 (2011). doi:10.1016/j.engfracmech.2010.10.004
8. Yatomi, M., Nikbin, K.M., O'Dowd, N.P.: Creep crack growth prediction using a damage-based approach. Int. J. Press. Vessels Pip. **80**(7–8), 573–583 (2003)
9. Mehmanparast, A.: Influence of inelastic damage on creep, fatigue and fracture toughness. Ph.D. Thesis, Department of Mechanical Engineering, Imperial College London, 2012
10. Cocks, A.C.F., Ashby, M.F.: On creep fracture by void growth. Prog. Mater. Sci. **27**, 189–244 (1982)
11. Webster, G.A., Ainsworth, R.A.: High Temperature Component Life Assessment, 1st edn. Chapman and Hall, London (1994)
12. Davies, C.M., Kourmpetis, M., O'Dowd, N.P., Nikbin, K.M.: Experimental evaluation of the J or C* parameter for a range of cracked geometries. J. ASTM Int. 3(4), 2006. doi:10.1520/JAI13220

13. ASTM, E1457–07: Measurement of creep crack growth times in metals. In: Annual Book of ASTM Standards, Vol. 03.01. ASTM International, 2007, pp. 1012–1035
14. Nikbin, K.M., Smith, D.J., Webster, G.A.: Prediction of creep crack growth from uniaxial creep data. Proc. Royal Soc. A **396**, 183–197 (1984)
15. Shih, C.F.: Tables of Hutchinson-Rice-Rosengren singular field quantities, MRL E-Providence, Ri, Brown University Technical Report, MRL E-147, June, 1983
16. Tan, M., Célard, N.J.C., Nikbin, K.M., Webster, G.A.: Comparison of creep crack initiation and growth in four steels tested in HIDA. Int. J. Press. Vessels Pip. **78**(12), 737–747 (2001)
17. Davies, C.M., O'Dowd, N.P., Nikbin, K.M., Webster, G.A.: An analytical and computational study of crack initiation under transient creep conditions. Int. J. Solids Struct. **44**, 1823–1843 (2007). doi:10.1016/j.ijsolstr.2006.08.036
18. Mehmanparast, A., Davies, C.M., Dean, D.W., Nikbin, K.M.: Material pre-conditioning effects on the creep behaviour of 316H stainless steel. In: 13th International Conference on Pressure Vessel Technology ICPVT-13, London, 2012

On the Non Saturation of Cyclic Plasticity Law: A Power Law for Kinematic Hardening

Rodrigue Desmorat

Abstract To compensate the drawback of most kinematic hardening rules that exhibit hardening saturation, a solution is proposed by replacing the accumulated plastic strain rate in the springback term by a rate related to the kinematic hardening variable itself. The proposed approach defines a power-law counterpart to the linear (Prager) and exponential (Armstrong-Frederick) laws.

1 Introduction

Most modern nonlinear kinematic hardening rules in metals plasticity have the generic form

$$\dot{\mathbf{X}} = \frac{2}{3} C \dot{\boldsymbol{\varepsilon}}^p - \mathscr{B}(\mathbf{X}, p, \boldsymbol{\sigma}) \dot{\mathscr{P}}(\mathbf{X}, \boldsymbol{\sigma}, \dot{\boldsymbol{\varepsilon}}^p) \tag{1}$$

with $\mathbf{X}$ the kinematic hardening, p the accumulated plastic strain, $\boldsymbol{\sigma}$ the stress, $\dot{\boldsymbol{\varepsilon}}^p$ the plastic strain rate, C a material parameter, and where the springback term $\mathscr{B}\dot{\mathscr{P}}$ is sometimes replaced by a sum $\sum \mathscr{B}_k \dot{\mathscr{P}}_k$. The scalar function $\dot{\mathscr{P}}$ (as $\dot{\mathscr{P}}_k$) is a homogeneous function of degree 1 in $\dot{\boldsymbol{\varepsilon}}^p$, such as $\dot{\mathscr{P}}(\mathbf{X}, \boldsymbol{\sigma}, \lambda \dot{\boldsymbol{\varepsilon}}^p) = \lambda \dot{\mathscr{P}}(\mathbf{X}, \boldsymbol{\sigma}, \dot{\boldsymbol{\varepsilon}}^p)$ $\forall \lambda \geq 0$. The tensorial function $\mathscr{B}$ has usually the sign of $\mathbf{X}$ and $\|\mathscr{B}\|$ increases when the loading increases (in norm). This last feature gives back the concave shape of stress-strain curves for metals.

For instance, this is the form of Armstrong-Frederick rule [1],

$$\dot{\mathbf{X}} = \frac{2}{3} C \dot{\boldsymbol{\varepsilon}}^p - \gamma \mathbf{X} \dot{p} \tag{2}$$

R. Desmorat (✉)
LMT-Cachan, ENS Cachan/UPMC/CNRS/PRES UniverSud Paris, 61 avenue du Président Wilson, Cachan Cedex 94235, France
e-mail: desmorat@lmt.ens-cachan.fr

H. Altenbach and S. Kruch (eds.), *Advanced Materials Modelling for Structures*, Advanced Structured Materials 19, DOI: 10.1007/978-3-642-35167-9_12,

with γ a material parameter, but also of Burlet-Cailletaud rule [2], of Chaboche rule [3] and of Ohno-Wang rule [9]. The normal $\mathbf{n} = \frac{\partial f}{\partial \boldsymbol{\sigma}}$ of the yield surface $f = 0$ is used in some models,[1] it is a function of the stress $\boldsymbol{\sigma}$ and of the kinematic hardening $\mathbf{X}$, the plastic strain rate reading then $\dot{\boldsymbol{\varepsilon}}^p = \dot{p}\,\mathbf{n}(\boldsymbol{\sigma}, \mathbf{X})$.

In uniaxial monotonic tension the generic law (1) simplifies in $\dot{X} = (C - B)\dot{\varepsilon}_p$, with B a positive increasing nonlinear function, rate independent. One observes then that a saturation $\dot{X} = 0$, $X = X_\infty = Const$, is reached for all rules ensuring $B \to C$ at high loading.

Different possibilities to avoid such a saturation of the kinematic hardening exist: make $\gamma = \gamma(p)$ a decreasing (to zero) function of the accumulated plastic strain as in [8], make C dependent of the plastic strain amplitude, through an index function written in the strain space, as in [6]. None recover the power law shape at high plastic strains. Simple ways to naturally gain the non saturation of the kinematic hardening have been proposed in [5]. They allows to define for kinematic hardening a power law counterpart to the usual exponential law.

2 A First Family of Non Saturating Kinematic Hardening Rules

Kinematic hardening $\mathbf{X}$ is a thermodynamics force associated with a tensorial internal state variable denoted $\boldsymbol{\alpha}$, homogeneous to a strain. It is often derived from a quadratic thermodynamics potential as [7]

$$\mathbf{X} = \frac{2}{3} C(T)\boldsymbol{\alpha} \tag{3}$$

where C is the hardening parameter previously introduced, temperature dependent. Initially isotropic and plastically incompressible materials are considered next, with then the expression $p = \int (\frac{2}{3}\dot{\boldsymbol{\varepsilon}}^p : \dot{\boldsymbol{\varepsilon}}^p)^{1/2} \mathrm{d}t$ for the accumulated plastic strain and with $\boldsymbol{\varepsilon}^p = \boldsymbol{\varepsilon}^{p\prime}$ the deviatoric plastic strain rate. In Prager law of linear hardening the internal variable $\boldsymbol{\alpha}$ is equal to $\boldsymbol{\varepsilon}^p$. In case of (anisothermal) Armstrong-Frederick rule it is given by the evolution law $\dot{\boldsymbol{\alpha}} = \dot{\boldsymbol{\varepsilon}}^p - \gamma \boldsymbol{\alpha}\dot{p}$. It is almost equal to the plastic strain either when γ is small or when the plastic strain remains limited.

Among others, a rule avoiding kinematic hardening saturation is the following, valid for anisothermal cases (see Sect. 4 for thermodynamics considerations),

$$\dot{\boldsymbol{\alpha}} = \dot{\boldsymbol{\varepsilon}}^p - \frac{3\Gamma}{2}\mathbf{X}\,\dot{a} \qquad \dot{a} = \sqrt{\frac{2}{3}\dot{\boldsymbol{\alpha}} : \dot{\boldsymbol{\alpha}}} \tag{4}$$

[1] Often $f = (\boldsymbol{\sigma} - \mathbf{X})_{eq} - R - \sigma_y$ in von Mises plasticity, with R the isotropic hardening and σ_y the yield stress.

in which the back stress is now governed by von Mises norm $\dot{a}$ of the rate $\dot{\boldsymbol{\alpha}}$ and with Γ as material parameter.

In case of isothermal loading, C is constant, and Eq. (4) can be rewritten as

$$\dot{\mathbf{X}} = \frac{2}{3} C \dot{\boldsymbol{\varepsilon}}^p - \Gamma \mathbf{X} \dot{x} \qquad \dot{x} = \sqrt{\frac{3}{2} \dot{\mathbf{X}} : \dot{\mathbf{X}}} \tag{5}$$

and leads to a non vanishing rate $\dot{\mathbf{X}}$ solution of the separate variables differential equation $\dot{\mathbf{X}} + \Gamma \mathbf{X} \dot{x} = \frac{2}{3} C \dot{\boldsymbol{\varepsilon}}^p$.

In order to recover a power-law like reponse in monotonic loading, Eq. (4) can be generalized as

$$\dot{\boldsymbol{\alpha}} = \dot{\boldsymbol{\varepsilon}}^p - \frac{3\Gamma}{2} X_{eq}^{M-2} \mathbf{X} \dot{a} \qquad X_{eq} = \sqrt{\frac{3}{2} \mathbf{X} : \mathbf{X}} \tag{6}$$

or (isothermal case):

$$\dot{\mathbf{X}} = \frac{2}{3} C \dot{\boldsymbol{\varepsilon}}^p - \Gamma X_{eq}^{M-2} \mathbf{X} \dot{x} \tag{7}$$

with $M \geq 2$ an additional parameter (already introduced in [3] in another context).

In uniaxial tension-compression (along 1), $\boldsymbol{\varepsilon}^p = diag[\varepsilon_p, -\frac{1}{2}\varepsilon_p, -\frac{1}{2}\varepsilon_p]$, $\mathbf{X} = diag[\frac{2}{3}X, -\frac{1}{3}X, -\frac{1}{3}X]$ so that $X_{eq} = |X|$, $\dot{x} = |\dot{X}|$. Such a first proposal reduces to the scalar expression

$$\dot{X} + \Gamma |X|^{M-2} X \, |\dot{X}| = C \dot{\varepsilon}_p \qquad \text{(1D)} \tag{8}$$

- *In case of monotonic tension,* X and $\dot{X}$ are positive and Eq. (8) reduces to $\left(1 + \Gamma X^{M-1}\right) \dot{X} = C \dot{\varepsilon}_p$ therefore to the kinematic hardening solution of

$$X + \frac{1}{M} \Gamma X^M = C \varepsilon_p \tag{9}$$

At large plastic strains X is unbounded and behaves in $\varepsilon_p^{1/M}$

$$X \approx K \varepsilon_p^{1/M} \qquad K = \left(\frac{MC}{\Gamma}\right)^{1/M} \tag{10}$$

- *In case of symmetric cyclic loading,* X ranges between X_{Max} and $X_{min} = -X_{Max}$, the same calculation with now $\dot{X} > 0$ in tension and $\dot{X} < 0$ in compression ends up to cycle stabilization and to the maximum kinematic hardening solution of

$$X_{Max} + \frac{1}{M} \Gamma X_{Max}^M = C \frac{\Delta \varepsilon_p}{2} \tag{11}$$

and then to a cyclic hardening law[2] $\frac{\Delta\sigma}{2} = k + X_{Max}$ linear in plastic strain amplitude at small $\Delta\varepsilon_p$ and asymptotically a power function at large $\Delta\varepsilon_p$ with then

$$X_{Max} \approx K \left(\frac{\Delta\varepsilon_p}{2}\right)^{1/M} \tag{12}$$

Again it is unbounded and no saturation is reached.

The tensile responses obtained for different sets of parameters are given in Fig. 1. Young's modulus is taken as $E = 200000\,\text{MPa}$ and $k = 400\,\text{MPa}$ is set. For the comparison with Prager and Armstrong-Frederick rules (Fig. 1a), the same constant $C = 20000\,\text{MPa}$ is used for all models and the chosen value for $\Gamma(M = 2)$ is $2.5 \times 10^{-3}\,\text{MPa}^{-1}$ and corresponds to the same first $\frac{d\sigma}{d\varepsilon}$ and second $\frac{d^2\sigma}{d\varepsilon^2}$ derivatives at yielding onset than with Armstrong-Frederick rule (for which $C = 20000\,\text{MPa}$ still and $\gamma = 50$). Parameters Γ for other M are chosen such as all the curves meet at point ($\varepsilon = 0.02$, $\sigma = 655\,\text{MPa}$).

Figure 1b shows a feature specific to the present law: the possibility with large modulus C ($10^6\,\text{MPa}$ in the example) to model very steep stress increase at low plastic strain. In the figure all stress-strain curves are plotted with the same value for modulus K, i.e. for the same power law limit at large plastic strains.

In cyclic loading a (classical) modelling flaw is encountered if the value of the kinematic hardening obtained in tension reaches the critical value $X_{Max} = \Gamma^{\frac{1}{1-M}}$. For $X_{Max} = \Gamma^{\frac{1}{1-M}}$, the slope $\frac{dX}{d\varepsilon_p}$ becomes negative (!) right after load reversal. Such a flaw has been pointed out and solved in [9] simply by making linear the kinematic hardening after load reversal. The law proposed next uses this remedy.

3 Proposal of a Non Saturating Kinematic Hardening Rule

In order to avoid kinematic hardening saturation, one proposes instead of Eq. (6) the following law, *this time with no flaw at large plastic strain amplitudes,*

$$\begin{cases} \mathbf{X} = \frac{2}{3}C\boldsymbol{\alpha} \\ \dot{\boldsymbol{\alpha}} = \dot{\boldsymbol{e}}^p - \frac{3\Gamma}{2C} X_{eq}^{M-2}\mathbf{X}\,\langle \dot{X}_{eq}\rangle \end{cases} \text{or (isothermal)} \quad \dot{\mathbf{X}} = \frac{2}{3}C\dot{\boldsymbol{e}}^p - \Gamma X_{eq}^{M-2}\mathbf{X}\,\langle \dot{X}_{eq}\rangle \tag{13}$$

where $\langle . \rangle$ stands for positive part, i.e. $\langle \dot{X}_{eq}\rangle = \dot{X}_{eq} = \frac{d}{dt}(\frac{3}{2}\mathbf{X} : \mathbf{X})^{1/2}$ when positive, $\langle \dot{X}_{eq}\rangle = 0$ else. The tensile response is unchanged compared to previous law. But a linear kinematic hardening is now obtained in the cycle parts at decreasing (in norm)

[2] The constant $k = \sigma_y + R_\infty$ is the sum of the yield stress and of the (assumed) saturated isotropic hardening R_∞.

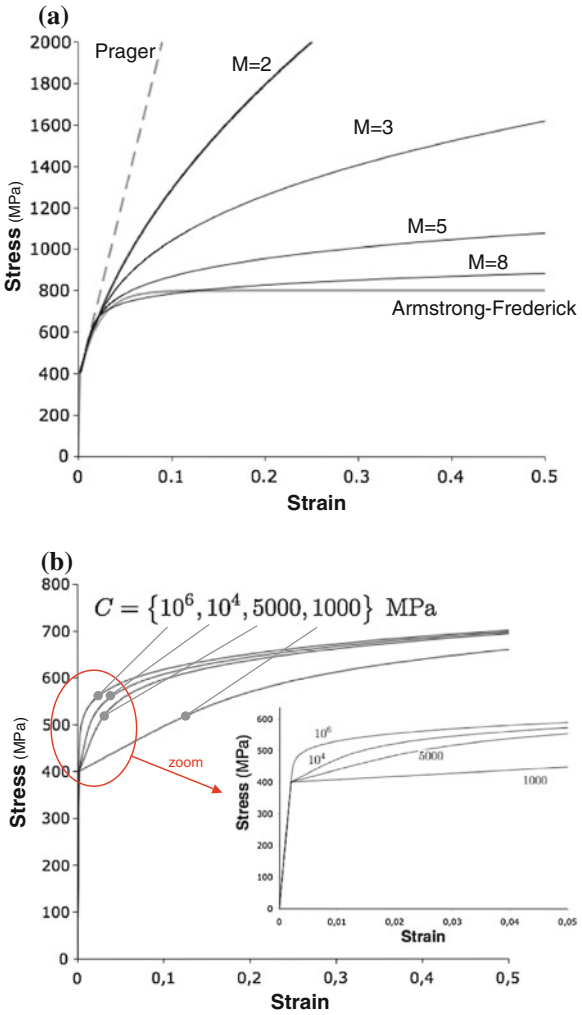

Fig. 1 Tensile stress-strain response from proposed non saturating kinematic hardening rule: (**a**) compared to linear Prager law and Armstrong-Frederick saturating law ($C = 20000$ MPa, $\gamma = 50$) at given C for different exponents M, (**b**) at given $K = (MC/\Gamma)^{1/M}$ and M for different values of parameter C ($K = 347$ MPa, $M = 5$)

kinematic hardening, i.e. at re-yielding just after load reversal (note that this feature is encountered in Ohno-Wang model). Both the monotonic and cyclic features of the new kinematic hardening rule (13) are illustrated in Fig. 1 (again with constant isotropic hardening), still with $E = 200000$ MPa and $k = 400$ MPa.

Cycle stabilization is obtained in case of symmetric (immediate, Fig. 2) and of non symmetric periodic applied strains (cyclic softening up to stabilization, see [5]).

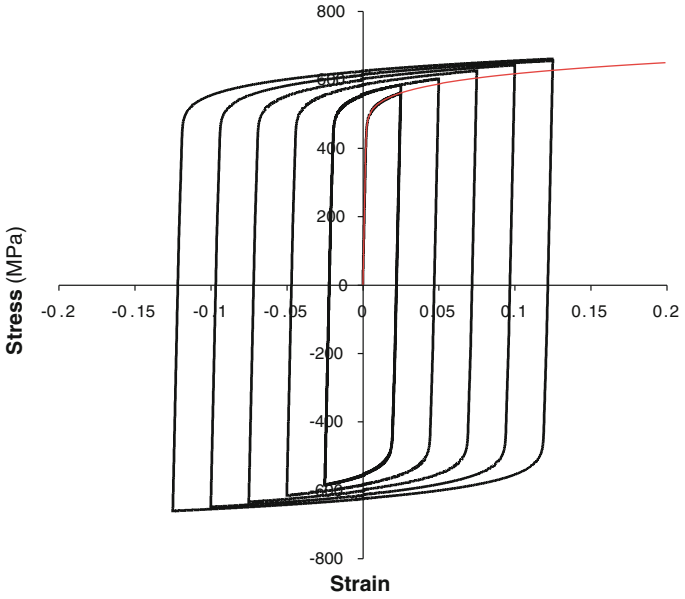

Fig. 2 Cyclic response obtained for increasing stress amplitudes (with $k = 400\,\text{MPa}$, $C = 5 \times 10^5\,\text{MPa}$, $M = 5$, $\Gamma = 5 \times 10^{-7}\,\text{MPa}^{1-M}$): $\Delta\varepsilon = 0.05,\ 0.1,\ 0.15,\ 0.2,\ 0.25$

Figure 2 illustrates the main model feature for large values of C: the possibility to represent very steep stress increase at the onset of plasticity (with no visible elasticity/plasticity slope discontinuity), also then in case of cyclic loading. The stress-amplitude is increased after each two cycles (starting from $\Delta\varepsilon = 5 \times 10^{-2}$). Such a smooth shape of cyclic strain-stress curves, very steep just out from elasticity domain and decreasing rapidly when yielding (but with no saturation), cannot be represented by means of a single Armstrong-Frederick law. As the value for C is large, the linear part after load reversal is barely noticeable. The monotonic tensile model response is reported in the figures.

The monotonic stress strain response is still given by Eq. (11) so that

$$\begin{cases} \sigma = \sigma_y + R(\varepsilon_p(X)) + X \\ \varepsilon_p = \frac{1}{C}\left(X + \frac{1}{M}\Gamma X^M\right) \end{cases} \tag{14}$$

or at constant isotropic hardening and setting still $k = \sigma_y + R_\infty$, $K = (MC/\Gamma)^{1/M}$,

$$\varepsilon_p = \left\langle \frac{\sigma - k}{C} \right\rangle + \left\langle \frac{\sigma - k}{K} \right\rangle^M \tag{15}$$

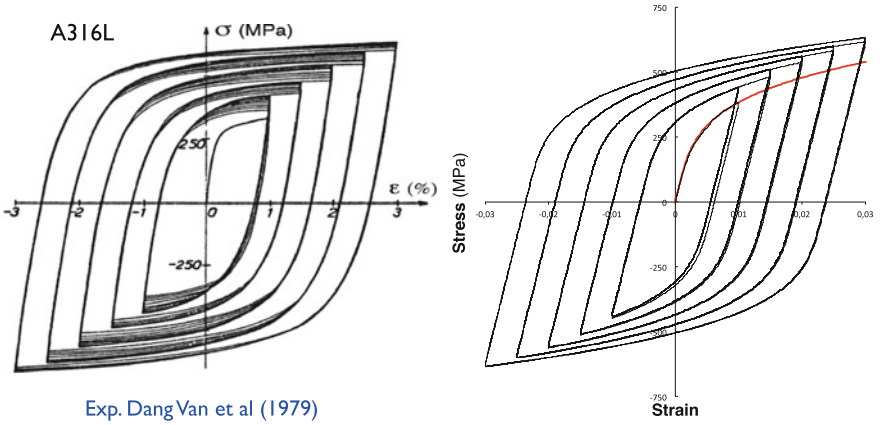

Fig. 3 Modelling of cyclic behavior of 316L by proposed non saturating kinematic hardening rule with constant isotropic hardening (*left*: exp. from [4], *right*: model, Eq. (13))

The cyclic plasticity response (at saturated hardening) is given by

$$\begin{cases} \frac{\Delta\sigma}{2} = k + X_{Max} \\ \frac{\Delta\varepsilon_p}{2} = \frac{1}{C}\left(X_{Max} + \frac{\Gamma}{2M} X_{Max}^M\right) \end{cases} \tag{16}$$

or

$$\frac{\Delta\varepsilon_p}{2} = \left\langle \frac{\frac{\Delta\sigma}{2} - k}{C} \right\rangle + \frac{1}{2}\left\langle \frac{\frac{\Delta\sigma}{2} - k}{K} \right\rangle^M \tag{17}$$

An illustration of the ability the proposed kinematic rule to model cyclic plasticity is given for a material usually quite complex to model (the 316L stainless steel) in Figs. 3 (hysteresis loops) and 4 (cyclic plasticity law, Eq. 17). Note that no modelling at all of the isotropic hardening is introduced ($k = const$) (Fig. 5).

Other examples of identifications are given in Fig. 6 for different materials. The corresponding material parameters are (setting $K_c = \left(\frac{2MC}{\Gamma}\right)^n = 2^n K$ with $n = 1/M$:

The ratcheting behavior with the new rule is found at given C intermediate between linear Prager Modelling (no ratcheting at all) and Armstrong-Frederick modelling (which usually overestimates ratcheting). The ratchet step—i.e. the plastic strain increment over an hysteresis loop—for a stress varying cyclically between $\sigma_{min} > -k$ and $\sigma_{Max} > k$ (with $\sigma_{Max} - \sigma_{min} > 2k$) is gained in a closed form as

$$\delta\varepsilon_p = \frac{(\sigma_{Max} - k)^M - (\sigma_{min} + k)^M}{K^M} \tag{18}$$

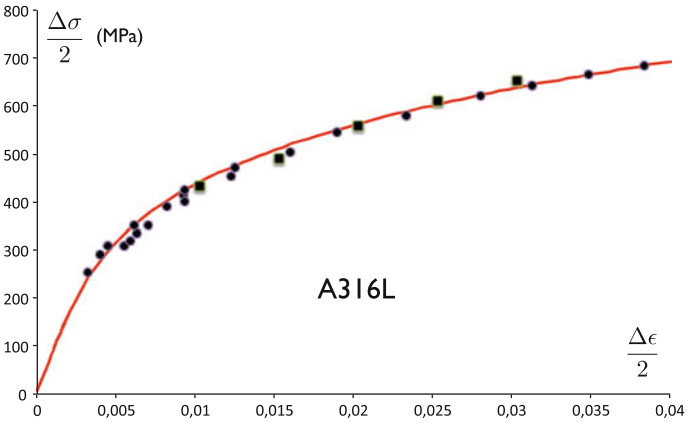

Fig. 4 Cyclic plasticity law of 316L by proposed non saturating kinematic hardening rule with constant isotropic hardening (*left*: exp. from [4], *right*: model, Eq. (13))

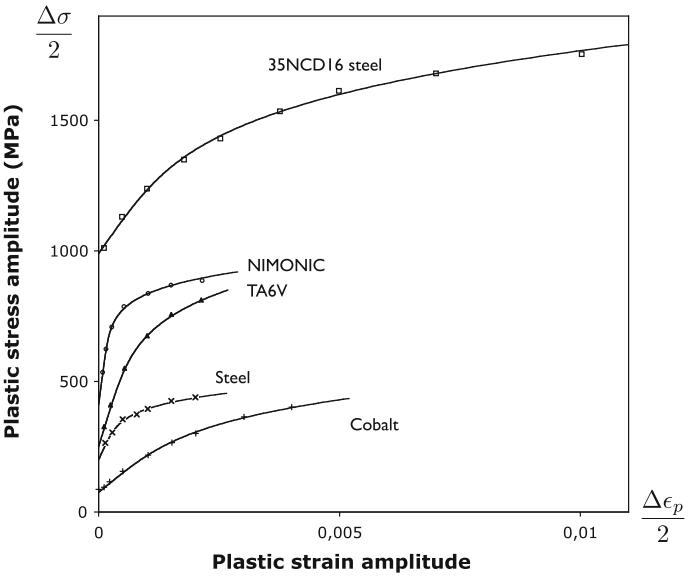

Fig. 5 Cyclic plasticity curves (experiments from Lemaitre and Chaboche, 1985, model from Eq. (17))

It is found constant—at saturated isotropic hardening—and related to the value of exponent M and modulus K governing the non saturation of the kinematic hardening (and to the size of elasticity domain through k). Note that ratcheting is often modeled by the introduction of several kinematic hardening variables $\mathbf{X}_i$, setting $\mathbf{X} = \sum \mathbf{X}_i$ and taking for k a relatively small value. According to the corresponding different plasticity mechanisms at the microscopic scale, it seems judicious to consider

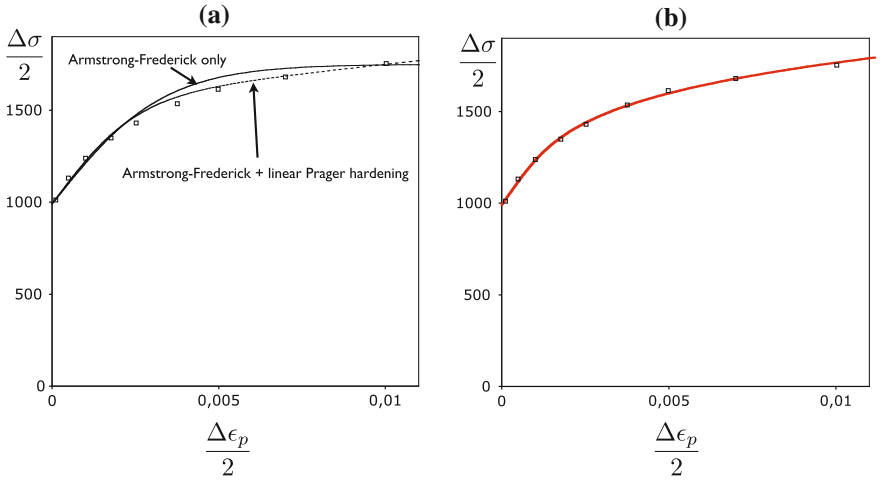

Fig. 6 Comparison of identifications for 35NCD16 steel (stresses in MPa)

Table 1 Material parameters

Material	k (MPa)	C (MPa)	Γ (MPa^{1-M})	M	K (MPa)	K_c (MPa)
35NCD16	990	260000	4×10^{-8}	4	2258	2685
Cobalt	75	150000	2×10^{-7}	4	1316	1565
NIMONIC	410	1400000	5.5×10^{-15}	7	1086	1199
Steel	200	400000	7.5×10^{-9}	5	768	882
TA6V	250	600000	1.3×10^{-10}	5	1873	2152
316L	10	200000	2.5×10^{-7}	4	1337	1591

different laws, i.e. laws of different nature, of different mathematical expression for each $\mathbf{X}_i$, including rules of Armstrong-Frederick type, including rule (13) (Table 1).

Let us end this section by a remark indirectly related to the implementation in a finite element code: the form given by Eq. (13) is implicit since the rate of $\boldsymbol{\alpha}$ (therefore of $\mathbf{X}$) depends on the rate of X_{eq}. Recalling the definition of von Mises norm gives $\langle \dot{X}_{eq} \rangle = \frac{3}{2} \langle \mathbf{X} : \dot{\mathbf{X}} \rangle / X_{eq}$. Altogether with Eq. (13), this allows to show that $\mathbf{X} : \dot{\mathbf{X}}$ is of same sign than $\mathbf{X} : \dot{\boldsymbol{\varepsilon}}^p$, at least in the isothermal case. After some algebraic work, the following alternative (nevertheless fully equivalent) expression for $\dot{\mathbf{X}}$ to isothermal law (13) is derived,

$$\dot{\mathbf{X}} = \frac{2}{3} C \dot{\boldsymbol{\varepsilon}}^p - \frac{C \Gamma X_{eq}^{M-3}}{1 + \Gamma X_{eq}^{M-1}} \left\langle \mathbf{X} : \dot{\boldsymbol{\varepsilon}}^p \right\rangle \mathbf{X} \tag{19}$$

more classical to implement.

4 Positivity of the Intrinsic Dissipation

A full plasticity model using the proposed kinematic hardening laws is a non standard model, the new springback terms not deriving from an evolution potential. One must then prove the positivity of the intrinsic dissipation $\mathscr{D} = \boldsymbol{\sigma} : \dot{\boldsymbol{\varepsilon}}^p - R\dot{p} - \mathbf{X} : \dot{\boldsymbol{\alpha}}$ [7]. Isotropic hardening is introduced as the couple of variables (R, p). The criterion function is the classical $f = (\boldsymbol{\sigma} - \mathbf{X})_{eq} - R - \sigma_y$ such as $f < 0 \rightarrow$ elasticity. Also classically, the plastic strain rate is derived by normality: $\dot{\boldsymbol{\varepsilon}}^p = \dot{p}\frac{3}{2}\frac{\boldsymbol{\sigma}' - \mathbf{X}}{(\boldsymbol{\sigma} - \mathbf{X})_{eq}}$. Plasticity is incompressible ($\mathrm{tr}\,\dot{\boldsymbol{\varepsilon}}^p = 0$) and kinematic hardening is deviatoric ($\mathbf{X} = \mathbf{X}'$), as announced.

After some algebraic work, the dissipation takes the form

$$\begin{aligned}
\text{Law (4):} \quad & \mathscr{D} = \left[(\boldsymbol{\sigma} - \mathbf{X})_{eq} - R\right]\dot{p} + \frac{3\Gamma}{2}\mathbf{X} : \mathbf{X}\,\dot{a} = \sigma_y \dot{p} + \Gamma X_{eq}^2\,\dot{a} \geq 0 \\
\text{Law (6):} \quad & \mathscr{D} = \left[(\boldsymbol{\sigma} - \mathbf{X})_{eq} - R\right]\dot{p} + \frac{3\Gamma}{2}X_{eq}^{M-2}\mathbf{X} : \mathbf{X}\,\dot{a} = \sigma_y \dot{p} + \Gamma X_{eq}^M\,\dot{a} \geq 0 \\
\text{Law (13):} \quad & \mathscr{D} = \left[(\boldsymbol{\sigma} - \mathbf{X})_{eq} - R\right]\dot{p} + \frac{3\Gamma}{2C}X_{eq}^{M-2}\mathbf{X} : \mathbf{X}\,\langle \dot{X}_{eq}\rangle \\
& \quad = \sigma_y \dot{p} + \frac{\Gamma}{C}X_{eq}^M\,\langle \dot{X}_{eq}\rangle \geq 0
\end{aligned} \tag{20}$$

and is therefore positive for any loading, proportional or not, isothermal or not ($\dot{p}$, $\dot{a}$ and $\langle \dot{X}_{eq}\rangle$ are positive by definition).

5 Conclusion

Families of non saturating kinematic hardening laws have been proposed. In order to gain non saturation of the kinematic hardening, the springback term $\mathscr{B}\dot{\mathscr{P}}$ in Eq. (1) is not assumed linear in $\dot{p}$ anymore but in $\dot{a} = (\frac{2}{3}\dot{\boldsymbol{\alpha}} : \dot{\boldsymbol{\alpha}})^{1/2}$ or, better, in the positive part $\langle \dot{X}_{eq}\rangle$, with X_{eq} the von Mises norm of kinematic hardening $\mathbf{X}$. By use of this replacement, any existing rule $\dot{\mathbf{X}} = \frac{2}{3}C\dot{\boldsymbol{\varepsilon}}^p - \mathscr{B}\dot{p}$ can then easily gain the non saturation property by changing it into $\dot{\mathbf{X}} = \frac{2}{3}C\dot{\boldsymbol{\varepsilon}}^p - \mathscr{B}\,\langle \dot{X}_{eq}\rangle$. As examples:

- Burlet-Cailletaud rule [2] made non saturating,

$$\dot{\mathbf{X}} = \frac{2}{3}C\dot{\varepsilon}^p - \Gamma\, X_{eq}^{M-2}(\mathbf{X} : \mathbf{n})\,\mathbf{n}\,\langle \dot{X}_{eq}\rangle \qquad \text{normal } \mathbf{n} = \frac{\partial f}{\partial \boldsymbol{\sigma}} \text{ such as } \dot{\varepsilon}^p = \mathbf{n}\,\dot{p} \tag{21}$$

- Ohno-Wang rule [9] made non saturating

$$\dot{\mathbf{X}} = \frac{2}{3}C\dot{\varepsilon}^p - \Gamma\, X_{eq}^{M-2}\langle \mathbf{k} : \mathbf{n}\rangle\,\mathbf{X}\,\langle \dot{X}_{eq}\rangle \qquad \mathbf{k} = \frac{\mathbf{X}}{X_{eq}} \tag{22}$$

- Chaboche kinematic hardening rule [3], with threshold X_{th}, made non saturating

$$\dot{\mathbf{X}} = \frac{2}{3} C \dot{\varepsilon}^p - \Gamma \langle X_{eq} - X_{th} \rangle^{M-1} \mathbf{k} \langle \dot{X}_{eq} \rangle \tag{23}$$

Proposed rule (13) is the power-law counterpart for kinematic hardening, fully complementary to Armstrong-Frederick saturating rule. Its properties have been illustrated on qualitative examples.

General plasticity modelling, including ratcheting, often introduces several kinematic hardening variables $\mathbf{X}_i$. Considering rules of different nature for each $\mathbf{X}_i$ can help to extend the validity domain of the plasticity models, setting for example $\mathbf{X} = \mathbf{X}_{\text{Prager}} + \mathbf{X}_{\text{AF}} + \mathbf{X}_{\text{NSat}} + \cdots$, with $\mathbf{X}_{\text{Prager}} = \frac{2}{3} C_\ell \varepsilon^p$ linear, with $\mathbf{X}_{\text{AF}}$ following Armstrong-Frederick rule (2), and with $\mathbf{X}_{\text{NSat}}$ following the non saturating rule (13) or any of the extension (21)–(23).

References

1. Armstrong, P.J., Frederick, C.O.: A mathematical representation of the multiaxial Bauschinger effect, CEGB report RD/B/N731. Berkeley Nuclear Laboratories, Berkeley, UK (1966)
2. Burlet, H., Cailletaud, G.: Modelling of cyclic plasticity in finite element codes. In: Desai, C.S., Krempl, E., Kiousis, P.D., et al. (eds.) International Conference on Constitutive Laws for Engineering Materials: Theory and Applications, pp. 1157–1164. Tucson, Arizona (1987)
3. Chaboche, J.L.: On some modifications of kinematic hardening to improve the description of ratcheting effects. Int. J. Plast. **7**, 661–678 (1991)
4. Chaboche, J.L., Dang Van, K., Cordier, G.: Modelization of the strain memory effect on the cyclic hardening of 316 stainless steel. SMIRT-5, Division L Berlin (1979)
5. Desmorat, R.: Non-saturating nonlinear kinematic hardening laws. C.R. Mec. **338**, 146–151 (2010)
6. Delobelle, P., Robinet, P., Bocher, L.: Experimental study and phenomenological modelization of ratchet under uniaxial and biaxial loading on an austenitic stainless steel. Int. J. Plast. **11**, 295–330 (1995)
7. Lemaitre, J., Chaboche, J.-L., Benallal, A.: Desmorat. R, Mécanique des matériaux solides, Dunod (2009)
8. Marquis, D.: Phénoménologie et thermodynamique: couplages entre thermoélasticité, plasticité, vieillissement et endommagement. Thèse de Doctorat d'état, Université Paris 6 (1989)
9. Ohno, N., Wang, J.D.: Kinematic hardening rules with critical state of dynamic recovery. Int. J. Plast. **9**, 375–403 (1993)

Micromechanical Studies of Deformation, Stress and Crack Nucleation in Polycrystal Materials

F. P. E. Dunne and C. Sweeney

Abstract Crystal plasticity analyses of fatigue crack nucleation in an fcc nickel alloy and bcc ferritic steel have been carried out. Three and four-point bend tests respectively carried out on the nickel alloy and steel samples are analysed using a direct representation of the observed microstructures and crystallographic orientations obtained by EBSD. In so doing, direct comparisons of predicted stress, accumulated plastic strain and the independent slip system accumulated slips have been assessed in relation to the location of fatigue crack nucleation. Regions of accumulated plastic strain are found to be precursors to the experimentally observed sites of crack nucleation and propagation in the fcc nickel polycrystal, but for nucleation only in the bcc ferritic steel. For the latter, a decomposition of the accumulated plastic strain in to the major contributors from the independent slip systems show close coincidence of the crack nucleation site with both {110} and {112} slip and that it is not the case that a single slip system type dominates.

1 Introduction

It is becoming increasingly desirable to calculate strain and stress response at progressively smaller length scales. Major drivers for this are in, for example, development of understanding of deformation and fatigue crack nucleation [1, 2]. Length scales of order grain size are relevant to polycrystalline materials for which there is significant interest in slip transfer, slip localization, grain boundary sliding, twinning, fatigue crack nucleation, and micro-texture [3–11]. Also of great interest is the ability to calculate accurately the evolving densities of dislocations, be they geometrically

F. P. E. Dunne (✉) · C. Sweeney
Department of Engineering Science, Oxford University, Oxford, UK
e-mail: fionn.dunne@eng.ox.ac.uk; fionn.dunne@imperial.ac.uk

C. Sweeney
e-mail: c.sweeney4@nuigalway.ie

H. Altenbach and S. Kruch (eds.), *Advanced Materials Modelling for Structures*,
Advanced Structured Materials 19, DOI: 10.1007/978-3-642-35167-9_13,

necessary (GND) or statistically stored (SSD), because of the potential roles played in latent hardening, initiation of recrystallisation and nucleation of fatigue, for example. There are now many modelling techniques available in crystal plasticity finite element analysis [12] and for the determination of GND density and their inclusion in modelling studies related to indentation size effects [13, 14], facet fatigue [7–10] and micro-deformation [1, 15–17] for example, is widespread. However, what is currently less clear is how well current modelling techniques, and in particular, crystal plasticity finite element methods, properly and accurately capture independent experimentally observed behaviour; that is, at the level of individual grains, the strain and stress distributions, the lattice rotations and the densities of GNDs. Hence the primary aim of this paper is to present a summary of length-scale–enhanced crystal plasticity calculation and high resolution EBSD measurement in the context particularly of fatigue crack nucleation.

Our approach in the present paper is to attempt to enable as close as possible a tie-up between the experimental model and that used in gradient-enhanced CPFE analyses. We choose an fcc nickel polycrystal and a bcc ferritic steel and in the latter, investigate fatigue crack nucleation in notched, four-point bend test samples in which the grain size is not dissimilar to the notch radius. In this way, crack nucleation can be related directly to microstructural features local to the notch including grain boundaries, triple points, crystallographic orientation, and the elastic anisotropy. Firstly, we briefly summarize the gradient-enhanced crystal model employed here and go on to address fatigue crack nucleation, and FIPs, in a polycrystal fcc nickel alloy and then in the ferritic steel polycrystal notched samples addressing particularly the role of elastic anisotropy.

2 Crystal Plasticity Model

Crystal plasticity kinematics rely on the deformation gradient $\boldsymbol{F}$, which is usually multiplicatively decomposed into elastic and plastic parts and where

$$\dot{\boldsymbol{F}}^p = \boldsymbol{L}^p \boldsymbol{F}^p \text{ and } \boldsymbol{L}^p = \sum_{i=1}^{n} \dot{\gamma}^i \boldsymbol{s}^i \otimes \boldsymbol{n}^i \tag{1}$$

where the plastic part of the velocity gradient $\boldsymbol{L}^p$ incorporates the crystallographic slip from the active slip systems i, with normal vector $\boldsymbol{n}^i$ and slip direction vector $\boldsymbol{s}^i$, and $\dot{\gamma}^i$ is computed according to a slip rule. The slip rule used here was developed by Dunne et al. [18], and is used in the following form:

$$\dot{\gamma}^i = \rho_S^m {b^i}^2 \nu \exp\left(-\frac{\Delta F}{kT}\right) \sinh\left(\frac{(\tau^i - \tau_c^i)\gamma_0 \Delta V^i}{kT}\right) \tag{2}$$

with $\Delta V^i = l{b^i}^2$ where $l = \frac{1}{\sqrt{\psi(\rho_S^s + \rho_G)}}$

where ρ_S^m and ρ_S^s are the mobile and sessile SSD densities respectively, ρ_G is the overall GND density, n the frequency of attempts (successful or otherwise) by dislocations to jump the energy barrier, b^i the Burger's vector magnitude for slip system i, DF the Helmholtz free energy, k the Boltzman constant, T the temperature in Kelvin (K), t^i the resolved shear stress, τ_c^i the critical resolved shear stress (a slip system is considered active when $\tau^i \geq \tau_c^i$), g_0 the shear strain that is work conjugate to the resolved shear stress, DV the activation volume, l the pinning distance, and y is a coefficient that indicates that not all sessile dislocations (SSDs or GNDs) necessarily act as pinning points. The subsequent implicit integration of constitutive equations and the determination of the consistent elastic—plastic tangent stiffness are also detailed in [18].

2.1 GND Development

The determination of the GND density has been discussed by many authors and here we equate the closure failure (Nye, 1953) written in terms of density of GNDs and the cumulative Burger's vector given with respect to the deformed configuration to give

$$\sum_i \left(\boldsymbol{b}^i \otimes \boldsymbol{\rho}_G^i \right) = \left(\mathrm{curl} \boldsymbol{F}^{e^{-1}} \right)^T \tag{3}$$

in which $\boldsymbol{F}^e$ is the elastic deformation gradient, the summation is over all active slip systems.

In crystals with high degrees of symmetry, the geometric constraints on dislocation density, imposed by the plastic slip gradient field, can be satisfied with many different dislocation configurations. This is the well-acknowledged non-uniqueness problem. In crystals of such symmetry the number of distinct dislocation types may exceed the nine independent components of the Nye tensor, hence a unique solution for the dislocation density may not be possible. Therefore, the GND density may be obtained only by solving Eq. (3) with an imposed constraint such as minimization of stored energy or dislocation line length, for example. In the next section, we firstly summarize an investigation of the FIP accumulated plastic strain in a nickel polycrystal and go on to address fatigue crack nucleation in ferritic polycrystal steel notched, four-point bend samples.

3 Microstructure-Sensitive Fatigue Crack Nucleation in fcc Nickel

Polycrystal samples were developed containing out-of-plane columnar grain structure, hence generating a repeatable model 'two-dimensional' material. An example sample free surface is shown in Fig. 1a in which EBSD has been employed to identify

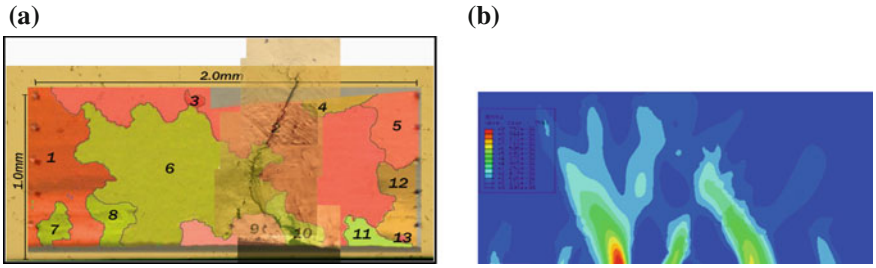

Fig. 1 **a** Microstructure and fatigue crack nucleation and growth in the fcc nickel polycrystal sample subjected to three-point cyclic loading together with **b** the corresponding crystal plasticity model predictions showing accumulated plastic strain after one complete loading cycle

grains and their boundaries together with the crystallographic orientations (which here are approximately uniform through the depth of the sample. Three-point bend tests were carried out on the samples using cylindrical supports generating fully-reversed downward displacement leading to the preferential nucleation of fatigue cracks in gauge region of the test samples, shown in Fig. 1a. The figure also shows the experimentally observed fatigue crack nucleation and growth in the gauge region. A crystal plasticity finite element model of the test sample was also developed and subjected, in principle, to loading conditions identical to those in the experiments, and the resulting distribution of accumulated plastic slip after one cycle of cyclic plasticity is shown in Fig. 1b. Bands of intense slip are predicted to develop, emanating from the sample free surface at locations within a grain and at the boundary between two grains. Grain boundaries appear to be important in the development of the highest levels of plastic slip.

Comparison of the slip band locations with the experimentally observed sites of crack nucleation on the (plane stress) free surfaces shows that the cracks which are seen to nucleate and grow have done so within the predicted bands of persistent slip. The directions of the propagating cracks also match those of the predicted slip. However, no crack nucleation was observed experimentally in the right-most predicted slip band, and this clearly raises the appropriateness or otherwise of the accumulated plastic strain as a FIP. We investigate this further by consideration of crack nucleation in a bcc ferritic steel.

3.1 Elastic Anisotropy in Crack Nucleation in Polycrystal Ferritic Steel

Figure 2 shows a schematic for the four-point bend test set up and identifies the region of the sample containing a notch which has been fully characterised using EBSD in order to identify grain boundaries and crystallographic orientations. The inset figure

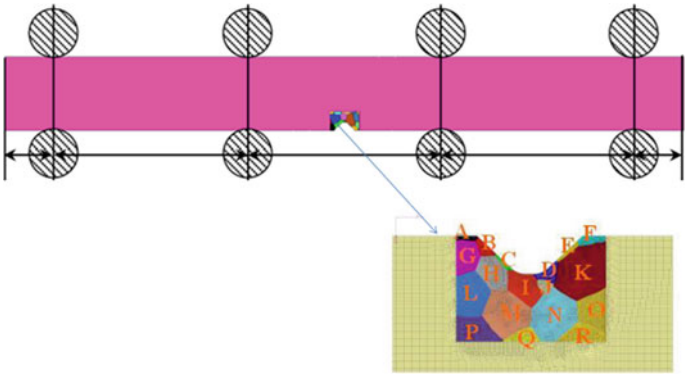

Fig. 2 Schematic diagram showing the notched, four-point bend test sample together with a representation of the fully characterised region (inset)

shows the corresponding crystal plasticity model setup in which each grain identified in the test sample is explicitly represented in the model.

Material properties (critical resolved shear stress and hardening coefficients) were determined from simple shear tests carried out on polycrystal samples in the same material. The regions of the material removed from the notch area, shown simply as a finite element mesh in the inset figure, are simply assumed to deform elastically given that the loading applied was specified to be representative for high cycle fatigue such that localised plasticity only occurs in the region close to the notch, and even then at highly localised locations (see later). Figure 3 shows the sample microstructure close to the notch and the location of observed fatigue crack nucleation (at about 300 k cycles) and growth (at about 1100 k cycles). Also shown are the axial (bending) stresses predicted by the corresponding crystal plasticity model together with the accumulated plastic strain at first yield (according to the crystal model) and at the peak load in the first cycle. The experimentally observed crack development is superimposed on the crystal plasticity calculations showing close coincidence of the nucleation site with both the highest axial (bending) stress and accumulated plastic strain at first and subsequent yield. However, crack nucleation occurs at a free-surface triple point and propagates transgranularly, and the propagation can be seen not to coincide with the clear predicted directions of the slip bands which can be associated with grain boundaries. Figure 4 shows the accumulated slip developing on (a number of) the {110} and {112} slip systems showing the decomposition of the accumulated plastic strain. Both slip system types can be seen to be contributing at the precise site of the observed crack nucleation, but then diverge from the direction of crack propagation.

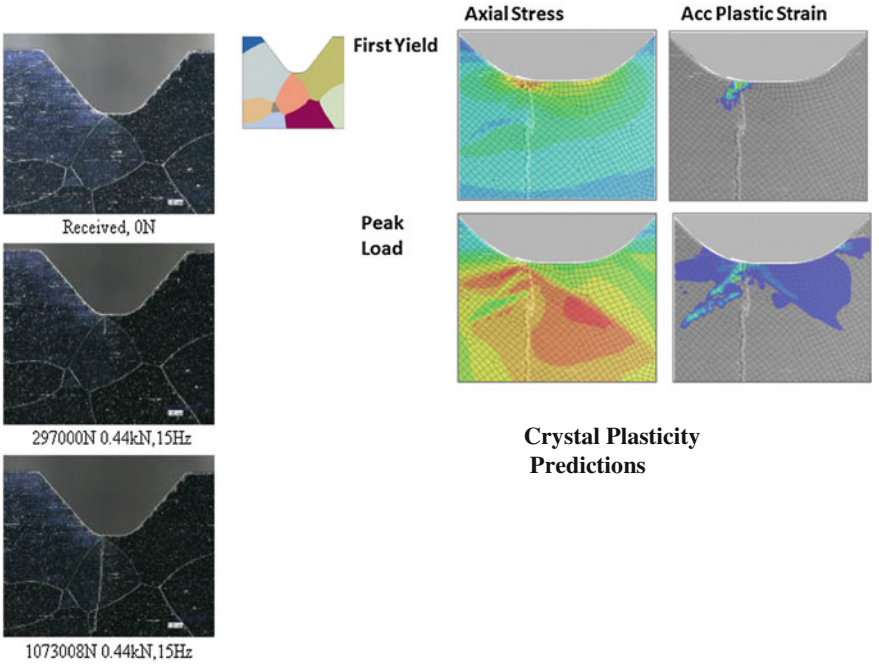

Fig. 3 Notched sample microstructure and fatigue crack nucleation (∼300 k cycles) and propagation (at ∼1100 k cycles) together with the predicted axial (bending) stresses and accumulated plastic strain at first yield and peak load in the first loading cycle. The experimentally observed crack development is superimposed onto the crystal plasticity predictions showing close overlap with the site of highest axial stress and accumulated plastic strain close to first yield

4 Conclusions

The results of bend tests on characterised fcc nickel and bcc ferritic steel samples have been compared with detailed crystal plasticity finite element representations of the sample geometries and microstructures. Regions of accumulated plastic strain are found to be precursors to the experimentally observed sites of crack nucleation and propagation in the fcc nickel polycrystal, but for nucleation only in the bcc ferritic steel. For the latter, a decomposition of the accumulated plastic strain in to the major contributors from the independent slip systems show close coincidence of the crack nucleation site with both {110} and {112} slip and that it is not the case that a single slip system type dominates.

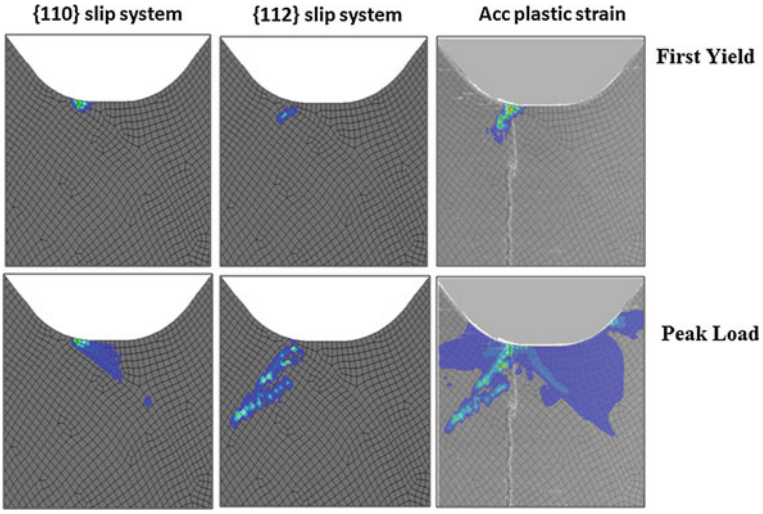

Fig. 4 Predicted accumulated slip on the {110} and {112} slip systems and comparison with the accumulated plastic strain at first yield and peak load in the first cycle

References

1. Dunne, F.P.E., Kiwanuka, R., Wilkinson, A.: Proc. R. Soc. Lond. **468**, 2509–2531 (2012). doi:10.1098/rspa.2012.0050
2. Rugg, D., Dixon, M., Dunne, F.P.E.: **42**(4), 269–279 (2007)
3. Wang, I., Yang, Y., Eisenlohr, P., et al.: Metall. Mater. Trans. A **41A**(2), 421–430 (2010)
4. Gong, J., Wilkinson, A.J.: Acta Mater. **57**(19), 5693–5705 (2009)
5. Rust, M., Todd, R.I.: Materialwissenschaft und Werkstofftechnik **39**(4–5), 289–292 (2008)
6. Korsunsky, A.M., Dini, D., Dunne, F.P.E., Walsh, M.J.: Intl. J. Fatigue **29**(9–11), 1990–1995 (2007)
7. Dunne, F.P.E., Rugg, D.: Fatigue Fract. Eng. Mater. Struct. **31**, 949–958 (2008)
8. McDowell, D.L., Dunne, F.P.E.: Intl. J. Fatigue **32**(9), 1521–1542 (2010)
9. Bache, M.R., Dunne, F.P.E.: Jnl. Strain Anal. **45**, 391–399 (2010)
10. Dunne, F.P.E., Walker, A., Rugg, D.: Proc. R. Soc. Lond. **463**(2082), 1467–1489 (2007)
11. Zhao, L.G., Busso, E.P., O'Dowd, N.P.: Mater. Sci. Tech. **23**(12), 1433–1438 (2007)
12. Roters, F., Eisenlohr, P., Hantcherli, L., et al.: Acta Mater. **58**(4), 1152–1211 (2010)
13. Wilkinson, A.J., Randman, D.: Philos. Mag. **90**(9), 1159–1177 (2010)
14. Britton, T.B., Liang, H., Dunne, F.P.E., Wilkinson, A.J.: Proc. R. Soc. Lond. (2010) **466**(2115), 695–719
15. Cheong, K.S., Busso, E.P.: J. Mech. Phys. Solids **54**(4), 671–689 (2006)
16. Cheong, K.S., Busso, E.P., Arsenlis, A.: Int. J. Plast. **21**(9), 1797–1814 (2005)
17. Kalidindi, S.R., Bhattacharyya, A., Doherty, R.D: Proc. Roy. Soc. Lond. **A460**(2047), 1935–1956 (2004)
18. Dunne, F.P.E., Rugg, D., Walker, A.: Intl. J. Plast. **23**(6), 1061–1083 (2007)

Modelling of Coupled Dissipative Phenomena in Engineering Materials

Halina Egner and Władysław Egner

Abstract In the present paper a general phenomenological model, based on the irreversible thermodynamics, is formulated and used to describe the multi-dissipative material. Two examples are presented: (1) Thermo-elastic-plastic-damage material accounting for coupling between heating rate and two dissipative phenomena: plasticity and damage; (2) 2M1C (2 mechanisms—1 yield criterion) model derived by Cailletaud and Sai [3] and identified by Velay et al. [13] to describe the elasto-viscoplastic behaviour of AISI L6 steel at different (but constant) temperatures, is extended to account for the effect of temperature change.

1 Introduction

The increasing demands for high performance materials require the adequate constitutive modelling, as well as the appropriate predictions of the overall failure mechanisms under complex thermo-mechanical loading.

When engineering materials classified as elastic-plastic are subjected to external loading, the material degradation connected with slip rearrangements of crystallographic planes through dislocation motion is observed at the macro-scale as plastic behaviour (cf. [5]).

Another dissipative phenomenon is the development of micro-cracks and micro-voids [1, 9]. The nucleation, growth and interaction of these micro-defects under external loads result in a deterioration process on the macro-scale and, as a consequence, change of the constitutive properties of the material.

H. Egner (✉) · W. Egner
Institute of Applied Mechanics, Cracow University of Technology, Al. Jana Pawła II 37, Kraków, Poland
e-mail: halina.egner@pk.edu.pl

W. Egner
e-mail: wladyslaw.egner@pk.edu.pl

H. Altenbach and S. Kruch (eds.), *Advanced Materials Modelling for Structures*, Advanced Structured Materials 19, DOI: 10.1007/978-3-642-35167-9_14,

If the elastic-plastic-damage material is loaded so that not only inelastic strains develop, but also the temperature is changed, then thermo-elasticity, thermo-plasticity and thermo-damage are encountered. The experimental results [2] proved that not only the temperature itself but also the heating rate makes a significant impact on parameters that determine carrying capacity at elevated temperatures. In [5] the discussion is made for the necessity of temperature rate terms in the context of hardening rules.

2 General Model of Dissipative Materials Based on Irreversible Thermodynamics

Continuum mechanics approach, applied in the present work, provides the constitutive and damage evolution equations in the framework of thermodynamics of irreversible processes. The material heterogeneity (on the micro- and meso-scale) is smeared out over the representative volume element (RVE) of the piece-wise discontinuous material. The true distribution of micro-changes within the RVE, and the correlation between them are measured by the change of the effective constitutive properties. The micro-structural rearrangements are defined by the set of state variables of scalar, vectorial or tensorial nature.

2.1 Basic Assumptions

In the case of infinitesimal deformation the total strain $\boldsymbol{\varepsilon}$ can be expressed as the sum of the elastic, ($\boldsymbol{\varepsilon}^E$), inelastic ($\boldsymbol{\varepsilon}^I$), and thermal strain ($\boldsymbol{\varepsilon}^\theta$).

The irreversible rearrangements of the internal structure can be represented by a group of state variables describing the current state of material microstructure: $\{\Lambda^k\}, k = p, d, ph, \ldots$ (p meaning plastic, d—damage, ph—phase change etc), where Λ^k may be scalars, vectors or even rank tensors. For example, for damage description, in the case where the damaged material remains isotropic, the current state of damage is often represented by the scalar variable Λ^d denoting the volume fraction of cracks and voids in the total volume, while damage acquired orthotropy requires a second order tensor, for example the classical Murakami-Ohno [11] tensor $\boldsymbol{\Lambda}^d$.

Another group of state variables consists of internal (hidden) variables corresponding to the modifications of loading surfaces: $\left\{h^k\right\} = \left\{r^k, \alpha^k_{ij}, l^k_{ijpq}, g^k_{ijpqmn}\right\}, k = p, d, ph, \ldots$ where r^k is related to isotropic expansion of the loading surface, α^k_{ij} affects translatoric displacements of the loading surface, l^k_{ijpq} is a hardening tensor which includes varying lengths of axes and rotation of the loading surface, and g^k_{ijpqmn} describes changes of the curvature of the loading surface (distortion) related to k-th dissipative phenomenon (cf. [8]). The complete set of state variables

$\{V_{st}\}$ reflecting the current state of the thermodynamic system consists of observable variables: elastic strain tensor ε_{ij}^{E} and absolute temperature θ, and two groups of microstructural $\{\Lambda^k\}$ and hardening $\{h^k\}$ state variables:

$$\{V_{st}\} = \{\varepsilon_{ij}^{E}, \theta; \Lambda^k; h^k\}, k = p, d, ph, \ldots \tag{1}$$

2.2 Equations of the Model

By the use of state variables (1) the Helmholtz' free energy of the material can be written as a sum of elastic (e), plastic (p), damage (d), phase change (ph) etc. terms (cf. [1, 10]):

$$\rho\psi = \rho\psi(V_{st}) = \sum_{j=1}^{n} \rho\psi^j, \; j = e, p, d, ph, \ldots \tag{2}$$

The following state equations express the thermodynamic forces conjugated to state variables (1):

$$\sigma_{ij} = \frac{\partial(\rho\psi)}{\partial\varepsilon_{ij}^{E}}, s = -\frac{\partial\psi}{\partial\theta}, \quad -Y^k = \frac{\partial(\rho\psi)}{\partial\Lambda^k}, H^k = \frac{\partial(\rho\psi)}{\partial h^k} \tag{3}$$

In the above equations ρ is mass density, s is specific entropy, Y^k stand for thermodynamic forces conjugated to microstructural state variables Λ^k , whereas H^k are hardening forces conjugated to hidden state variables h^k.

To derive the kinetic equations the existence of several dissipation potentials F^k is assumed, corresponding to each k-th microstructural rearrangement (due to plastic flow F^p , damage growth F^d , phase change F^{ph} etc.) and defined independently but partly coupled (weak dissipation coupling, [4]).

The kinetic equations for state variables are obtained by the use of the generalized normality rule [4, 6]:

$$\dot{\varepsilon}_{ij}^{I} = \sum_{k=1}^{n} \dot{\lambda}^k \frac{\partial F^k}{\partial\sigma_{ij}} = \underbrace{\dot{\lambda}^p \frac{\partial F^p}{\partial\sigma_{ij}}}_{\dot{\varepsilon}_{ij}^{p}} + \underbrace{\dot{\lambda}^d \frac{\partial F^d}{\partial\sigma_{ij}}}_{\dot{\varepsilon}_{ij}^{Id}} + \underbrace{\dot{\lambda}^{ph} \frac{\partial F^{ph}}{\partial\sigma_{ij}}}_{\dot{\varepsilon}_{ij}^{ph}} + \ldots \tag{4}$$

$$\dot{\Lambda}^k = \sum_{i=1}^{n} \dot{\lambda}^i \frac{\partial F^i}{\partial Y^k} = \underbrace{\dot{\lambda}^p \frac{\partial F^p}{\partial Y^k}}_{\dot{\Lambda}^{pk}} + \underbrace{\dot{\lambda}^d \frac{\partial F^d}{\partial Y^k}}_{\dot{\Lambda}^{dk}} + \underbrace{\dot{\lambda}^{ph} \frac{\partial F^{ph}}{\partial Y^k}}_{\dot{\Lambda}^{phk}} + \ldots \tag{5}$$

$$-\dot{h}^k = \sum_{i=1}^{n} \dot{\lambda}^i \frac{\partial F^i}{\partial H^k} = -\left(\underbrace{\dot{\lambda}^p \frac{\partial F^p}{\partial H^k}}_{\dot{h}^{pk}} + \underbrace{\dot{\lambda}^d \frac{\partial F^d}{\partial H^k}}_{\dot{h}^{dk}} + \underbrace{\dot{\lambda}^{ph} \frac{\partial F^{ph}}{\partial H^k}}_{\dot{h}^{phk}} + \ldots \right) \tag{6}$$

where $\dot{\lambda}^i$ are non-negative consistency multipliers and n is a number of dissipative phenomena, like plastic flow, damage growth, phase change etc., taking place in the material. For rate-independent problems the consistency multipliers may be calculated from the consistency conditions $\dot{f}^k = 0, k = 1, 2, \ldots, n$.

The parameters $\dot{\lambda}^i$ are assumed to obey the classical Kuhn-Tucker loading/unloading conditions.

3 Modelling of Coupling Between Dissipative Phenomena in Engineering Materials

3.1 Coupling Between Thermo-Plasticity and Thermo-Damage

In view of the experimental observations it seems justified to extend the common formulations for coupled thermo-elastic-plastic-damage behaviour, accounting not only for damage effect on the elastic modules but also on plastic and thermal characteristics. Additionally, the effect of both temperature and damage rates has to be included (cf. [7]).

The following form of the state potential, which is here the Helmholtz free energy (2), decomposed into thermo-elastic ($\rho\psi^{te}$), thermo-plastic ($\rho\psi^{tp}$) and thermo-damage ($\rho\psi^{td}$) terms, is assumed after [1]:

$$\rho\psi^{te} = \rho h(\theta) + \frac{1}{2}\varepsilon^E_{ij} E_{ijkl}(\theta, \mathbf{D})\varepsilon^E_{kl} - \beta_{ij}(\theta, \mathbf{D})\varepsilon^E_{ij}(\theta - \theta_0) \tag{7}$$

$$\beta_{ij}(\theta, \mathbf{D}) = E_{ijkl}(\theta, \mathbf{D})\alpha^\theta_{kl}(\theta, \mathbf{D}) \tag{8}$$

$$\rho\psi^{tp} = \frac{1}{3}C^p(\theta, \mathbf{D})\alpha^p_{ij}\alpha^p_{ij} + R^p_\infty(\theta, \mathbf{D})\left[r^p + \frac{e^{-b^p(\theta,\mathbf{D})r^p}}{b^p(\theta, \mathbf{D})} \right] \tag{9}$$

$$\rho\psi^{td} = \frac{1}{2}C^d(\theta, \mathbf{D})\alpha^d_{ij}\alpha^d_{ij} + R^d_\infty(\theta, \mathbf{D})\left[r^d + \frac{e^{-b^d(\theta,\mathbf{D})r^d}}{b^d(\theta, \mathbf{D})} \right] \tag{10}$$

In Eqs. (7)–(10) $h(\theta)$ is the function of temperature, $\boldsymbol{\alpha}^\theta(\theta, \mathbf{D})$ is the thermal expansion tensor; $\mathbf{E}(\theta, \mathbf{D})$ is the elastic stiffness tensor; $C^p(\theta, \mathbf{D})$, $C^d(\theta, \mathbf{D})$, $R^p_\infty(\theta, \mathbf{D})$, $R^d_\infty(\theta, \mathbf{D})$, $b^p(\theta, \mathbf{D})$, $b^d(\theta, \mathbf{D})$ are material parameters, which in general may be temperature and damage ($\mathbf{D}$) dependent. Symbols α^k_{ij} and r^k, $k = p, d$ denote state

variables related to kinematic and isotropic hardening, respectively. Symbol θ_0 stands for the reference temperature at which no thermal strains exists.

State equations can be written by the use of Eq. (3). Note that the damage driving force Y_{ij}^d in the presence of coupling between thermo-elasticity, thermo-plasticity and thermo-damage in the state potential (2), consists of three terms: $Y_{ij}^{ed}(\boldsymbol{\sigma}; \theta, \mathbf{D})$, $Y_{ij}^{pd}(\mathbf{X}^p, R^p; \theta, \mathbf{D})$, $Y_{ij}^{dd}(\mathbf{X}^d, R^d; \theta, \mathbf{D})$ which stand for the elastic, plastic and damage strain energy release rates, respectively, as the extension of commonly used definitions of the elastic strain energy release rate only [6, 9]. Here X_{ij}^k and R^k stand for thermodynamic forces conjugated to hardening variables α_{ij}^k and r^k.

The rates of state variables can be obtained by the use of the generalized normality rule, Eqs. (4)–(6) (cf. [6]). The evolution equations for thermodynamic conjugate forces are derived taking the time rate of state Eq. (3), see Table 1. By taking into account the temperature and damage dependence of material characteristics additional terms appear in rate equations of thermodynamic forces, which may play a significant role when solving high temperature and/or damage rate problems, such as fire conditions or thermal shock problems.

Since the thermodynamic conjugate forces are functions of temperature and damage, the consistency relations for development of plasticity and damage may be transformed to the following form:

$$\dot{f}^p = \frac{\partial f^p}{\partial \sigma_{ij}} E_{ijkl}\, \dot{\varepsilon}_{kl} - \dot{\lambda}^p h_{11} - \dot{\lambda}^d h_{12} + S^p \dot{\theta} = 0 \tag{11}$$

$$\dot{f}^d = \frac{\partial f^d}{\partial \sigma_{ij}} E_{ijkl}\, \dot{\varepsilon}_{kl} - \dot{\lambda}^p h_{21} - \dot{\lambda}^d h_{22} + S^d \dot{\theta} = 0 \tag{12}$$

The quantities h_{11}, h_{12}, h_{21} and h_{22} are the generalized hardening moduli (cf. [12]) which are shown in details in [6]. The temperature sensitivity parameters S^p and S^d express how the yield and damage surfaces change with temperature.

To obtain the general loading/unloading criteria let us first observe that for $f^p < 0$ and $f^d < 0$ a thermo-elastic response occurs. Thermo-plasticity requires $f^p = 0$ and $\dot{\lambda}^p \geq 0$, while thermo-damage demands $f^d = 0$ and $\dot{\lambda}^d \geq 0$. Taking into account (11)–(12) we have $\dot{\lambda}^p = (A_{ij}^p E_{ijkl}\dot{\varepsilon}_{kl} + \bar{S}^p\dot{\theta})/w$ and $\dot{\lambda}^d = (A_{ij}^d E_{ijkl}\dot{\varepsilon}_{kl} + \bar{S}^d\dot{\theta})/w$, where $w = h_{11}h_{22} - h_{21}h_{12} > 0$, $A_{ij}^p = h_{22}\partial f^p/\partial\sigma_{ij} - h_{12}\partial f^d/\partial\sigma_{ij}$, $A_{ij}^d = -h_{21}\partial f^p/\partial\sigma_{ij} + h_{11}\partial f^d/\partial\sigma_{ij}$, $\bar{S}^p = h_{22}S^p - h_{12}S^d$ and $\bar{S}^d = h_{11}S^d - h_{21}S^p$. Therefore, for coupled thermo-plasticity and thermo-damage we arrive at the following loading/unloading criteria:

$$f^k = 0 \text{ and } \begin{cases} A_{ij}^k E_{ijmn}\dot{\varepsilon}_{mn} + \bar{S}^k\dot{\theta} > 0 \Rightarrow \text{active loading} \\ A_{ij}^k E_{ijmn}\dot{\varepsilon}_{mn} + \bar{S}^k\dot{\theta} = 0 \Rightarrow \text{neutral loading} \\ A_{ij}^k E_{ijmn}\dot{\varepsilon}_{mn} + \bar{S}^k\dot{\theta} < 0 \Rightarrow \text{elastic unloading} \end{cases}, k = p, d \tag{13}$$

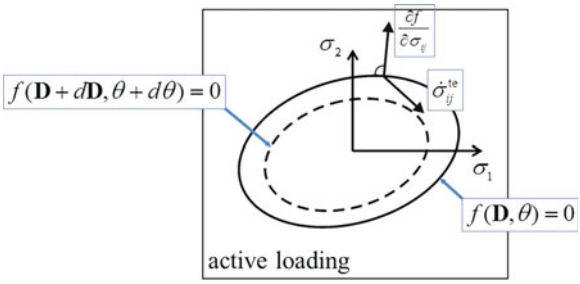

Fig. 1 Illustration of loading/unloading conditions for coupled thermo/plastic/damage process: loading surface contracting with increasing temperature and damage

It should be noticed here that conditions (11)–(12), in the presence of the full thermo-plasticity and thermo-damage coupling, are different from corresponding conditions for uncoupled isothermal case (see Fig. 1). Namely, if we consider purely thermo-elastic behaviour, where $\dot{\lambda}^p = 0$ and $\dot{\lambda}^d = 0$, we obtain the thermo-elastic stress rate which results for a given total strain rate $\dot{\varepsilon}_{kl}$ and a given temperature rate $\dot{\theta}$ provided that the material responds thermo-elastically [12], see Table 1:

$$\dot{\sigma}_{ij}^{te} = E_{ijkl}\dot{\varepsilon}_{kl} + [(\partial E_{ijkl}/\partial\theta)\varepsilon_{kl}^{E} - (\partial\beta_{ij}/\partial\theta)(\theta-\theta_0) + \beta_{ij}]\dot{\theta} \tag{14}$$

Now if the considered loading surface contracts with increasing temperature and/or damage, then even if $(\partial f^p/\partial\sigma_{ij})\dot{\sigma}_{ij}^{te} < 0$ active plastic loading may occur (see Fig. 1), and even if $(\partial f^d/\partial\sigma_{ij})\dot{\sigma}_{ij}^{te} < 0$ active damage loading may take place.

In the case of thermo-elastic-plastic-damage material the general coupled heat equation takes the following form:

$$\begin{aligned}\rho c_\varepsilon^\theta\dot{\theta} = {} & (k_{ij}\theta_{,j})_{,i} + r + \rho\theta\frac{\partial^2\psi}{\partial\varepsilon_{ij}\partial\theta}(\dot{\varepsilon}_{ij} - \dot{\varepsilon}_{ij}^I) + \rho\frac{\partial\psi}{\partial\varepsilon_{ij}}\dot{\varepsilon}_{ij}^I + (\sigma_{ij} - \rho\frac{\partial\psi}{\partial\varepsilon_{ij}})\dot{\varepsilon}_{ij} + \\ & -\rho\left(\frac{\partial\psi}{\partial D_{ij}} - \theta\frac{\partial^2\psi}{\partial\theta\partial D_{ij}}\right)\dot{D}_{ij} - \rho\left(\frac{\partial\psi}{\partial r^p} - \theta\frac{\partial^2\psi}{\partial\theta\partial r^p}\right)\dot{r}^p - \rho\left(\frac{\partial\psi}{\partial\alpha_{ij}^p} - \theta\frac{\partial^2\psi}{\partial\theta\partial\alpha_{ij}^p}\right)\dot{\alpha}_{ij}^p \\ & -\rho\left(\frac{\partial\psi}{\partial r^d} - \theta\frac{\partial^2\psi}{\partial\theta\partial r^d}\right)\dot{r}^d - \rho\left(\frac{\partial\psi}{\partial\alpha_{ij}^d} - \theta\frac{\partial^2\psi}{\partial\theta\partial\alpha_{ij}^d}\right)\dot{\alpha}_{ij}^d\end{aligned} \tag{15}$$

which is nonlinear and fully coupled to mechanical problem.

3.2 Extended 2M1C (2 Mechanisms—1 Yield Criterion) Model

In this analysis the 2M1C model derived by Cailletaud and Sai [3] and identified by Velay et al. [13] to describe the elasto-viscoplastic behaviour of AISI L6 steel at different (but constant) temperatures, is extended to account for the effect of temperature

Table 1 Evolution equations for thermodynamic conjugate forces with additional terms resulted from coupling with damage and temperature

No coupling	Coupling with damage	Coupling with temperature
$\dot{\sigma}_{ij} = E_{ijkl}\dot{\varepsilon}^E_{kl}$	$+\Big[\dfrac{\partial E_{ijpq}}{\partial D_{kl}}\varepsilon^E_{pq} - \dfrac{\partial \beta_{ij}}{\partial D_{kl}}(\theta-\theta_0)\Big]\dot{D}_{kl}$	$+\Big[\dfrac{\partial E_{ijkl}}{\partial \theta}\varepsilon^E_{kl} - \dfrac{\partial \beta_{ij}}{\partial \theta}(\theta-\theta_0)+\beta_{ij}\Big]\dot{\theta}$
$\dot{X}^p_{ij} = \frac{2}{3}C^p\dot{\alpha}^p_{ij}$	$+\dfrac{X^p_{ij}}{C^p}\dfrac{\partial C^p}{\partial D_{kl}}\dot{D}_{kl}$	$+\dfrac{X^p_{ij}}{C^p}\dfrac{\partial C^p}{\partial \theta}\dot{\theta}$
	$+\Big[\dfrac{R^p}{R^p_\infty}\dfrac{\partial R^p_\infty}{\partial D_{ij}}+$	$+\Big[\dfrac{R^p}{R^p_\infty}\dfrac{\partial R^p_\infty}{\partial \theta}+$
$\dot{R}^p = R^p_\infty b^p e^{-b^p r^p}\dot{r}^p$		
	$+\dfrac{(R^p_\infty - R^p)}{b^p}\dfrac{\partial b^p}{\partial D_{ij}}\ln\Big(\dfrac{R^p_\infty}{R^p_\infty - R^p}\Big)\Big]\dot{D}_{ij}$	$+\dfrac{(R^p_\infty - R^p)}{b^p}\dfrac{\partial b^p}{\partial \theta}\ln\Big(\dfrac{R^p_\infty}{R^p_\infty - R^p}\Big)\Big]\dot{\theta}$
$\dot{X}^d_{ij} = C^d\dot{\alpha}^d_{ij}$	$+\dfrac{X^d_{ij}}{C^d}\dfrac{\partial C^d}{\partial D_{kl}}\dot{D}_{kl}$	$+\dfrac{X^d_{ij}}{C^d}\dfrac{\partial C^d}{\partial \theta}\dot{\theta}$
	$+\Big[\dfrac{R^d}{R^d_\infty}\dfrac{\partial R^d_\infty}{\partial D_{ij}}+$	$+\Big[\dfrac{R^d}{R^d_\infty}\dfrac{\partial R^d_\infty}{\partial \theta}+$
$\dot{R}^d = R^d_\infty b^d e^{-b^d r^d}\dot{r}^d$		
	$+\dfrac{(R^d_\infty - R^d)}{b^d}\dfrac{\partial b^d}{\partial D_{ij}}\ln\Big(\dfrac{R^d_\infty}{R^d_\infty - R^d}\Big)\Big]\dot{D}_{ij}$	$+\dfrac{(R^d_\infty - R^d)}{b^d}\dfrac{\partial b^d}{\partial \theta}\ln\Big(\dfrac{R^d_\infty}{R^d_\infty - R^d}\Big)\Big]\dot{\theta}$

Table 2 State variables and thermodynamic forces for 2M1C model

State variable	Conjugated force
ε_{ij}^{E} (elastic strain)	$\sigma_{ij} = E_{ijkl}(\theta)\varepsilon_{kl}^{E}$
θ (temperature)	s
$\alpha_{ij}^{(1)}$ (kinematic hardening)	$X_{ij}^{(1)} = \frac{2}{3}(C_{11}(\theta)\alpha_{ij}^{(1)} + C_{12}(\theta)\alpha_{ij}^{(2)})$
$\alpha_{ij}^{(2)}$ (kinematic hardening)	$X_{ij}^{(2)} = \frac{2}{3}(C_{22}(\theta)\alpha_{ij}^{(2)} + C_{12}(\theta)\alpha_{ij}^{(1)})$
$r^{(1)}$ (isotropic hardening)	$R^{(1)} = b_1(\theta)Q_1(\theta)r^{(1)}$
$r^{(2)}$ (isotropic hardening)	$R^{(2)} = b_2(\theta)Q_2(\theta)r^{(2)}$

change (nonisothermal conditions). The set of state variables and corresponding thermodynamic conjugated forces is given in Table 2.
The model material parameters are contained in Table 3.
Total strain is partitioned into an elastic, inelastic and thermal components: $\varepsilon_{ij} = \varepsilon_{ij}^{E} + \varepsilon_{ij}^{I} + \varepsilon_{ij}^{\theta}$ while inelastic strain can be partitioned itself in two different strain mechanisms: $\varepsilon_{ij}^{I} = A_1(\theta)\varepsilon_{ij}^{(1)} + A_2(\theta)\varepsilon_{ij}^{(2)}$.
The equations of the 2M1C model for isothermal case are in details presented in [13] and therefore will not be repeated here. However, in nonisothermal conditions additional terms appear in the evolution equations for thermodynamic conjugate forces, due to temperature-dependence of the material characteristics ($k = 1, 2$; $l = 1, 2$; $k \neq l$):

$$\dot{\sigma}_{ij} = (\dot{\sigma}_{ij})_{\dot{\theta}=0} - \left[-\frac{\partial E_{ijpq}}{\partial \theta}(\varepsilon_{pq} - \varepsilon_{pq}^{I}) + \frac{\partial \beta_{ij}}{\partial \theta}(\theta - \theta_0) + \beta_{ij} \right] \dot{\theta} \tag{16}$$

$$\dot{X}_{ij}^{(k)} = (\dot{X}_{ij}^{(k)})_{\dot{\theta}=0} + \frac{2}{3}\left(\frac{\partial C_{kk}}{\partial \theta}\alpha_{ij}^{(k)} + \frac{\partial C_{kl}}{\partial \theta}\alpha_{ij}^{(l)} \right) \dot{\theta} \tag{17}$$

$$\dot{R}^{(1)} = (\dot{R}^{(1)})_{\dot{\theta}=0} + \left(\frac{\partial b_1}{\partial \theta} Q_{1\infty} + b_1 \frac{\partial Q_{1\infty}}{\partial \theta} \right) (1 - e^{-2\mu p^*}) r^{(1)} \dot{\theta} \tag{18}$$

$$\dot{R}^{(2)} = (\dot{R}^{(2)})_{\dot{\theta}=0} + \left(\frac{\partial b_2}{\partial \theta} Q_2 + b_2 \frac{\partial Q_2}{\partial \theta} \right) r^{(2)} \dot{\theta} \tag{19}$$

Taking into account the above equations the heat balance law may be written in the following form:

Table 3 2M1C Model coefficients

$E(\theta)$, $R_0(\theta)$	Young modulus and yield stress
$K(\theta)$, $n(\theta)$	Viscous coefficients
$C_{11}(\theta)$, $C_{22}(\theta)$, C_{12}	Parameters of kinematic part
$A_1(\theta)$, $A_2(\theta)$	Localisation coefficients of strain mechanisms
$M_1(\theta)$, $M_2(\theta)$, $m_1(\theta)$, $m_2(\theta)$	Static recovery terms
$Q_{1\infty}(\theta)$, $Q_2(\theta)$, $b_1(\theta)$, $b_2(\theta)$	Parameters of isotropic part

$$\begin{aligned}\rho c_\varepsilon^\theta \dot{\theta} = &-q_{i,i} + r - \theta P_{ij}(\dot{\varepsilon}_{ij} - \dot{\varepsilon}_{ij}^I) + \sigma_{ij}\dot{\varepsilon}_{ij}^I - \left(R^{(1)} - \theta \frac{\partial R^{(1)}}{\partial \theta}\right)\dot{r}^{(1)} \\ &- \left(X_{ij}^{(1)} - \theta \frac{\partial X_{ij}^{(1)}}{\partial \theta}\right)\dot{\alpha}_{ij}^{(1)} + \\ &- \left(R^{(2)} - \theta \frac{\partial R^{(2)}}{\partial \theta}\right)\dot{r}^{(2)} - \left(X_{ij}^{(2)} - \theta \frac{\partial X_{ij}^{(2)}}{\partial \theta}\right)\dot{\alpha}_{ij}^{(2)}\end{aligned} \tag{20}$$

4 Numerical Calculations

The generalized mid-point rule will be used in which the linear interpolation between two points is performed. The fully implicit backward Euler scheme is chosen, which is always stable and very accurate. Adopting the Newton-Raphson method, the iterative solution procedure is defined as $\Delta\mathbf{S}^{(k+1)} = \Delta\mathbf{S}^{(k)} - \left[\mathbf{J}^{(k)}\right]^{-1}\mathbf{R}^{(k)}$ where $\Delta\mathbf{S} = \{\Delta\lambda, \Delta\mathbf{V}_\alpha\}^T$ is the vector containing the increments of unknowns, $[\mathbf{J}] = \frac{\partial \mathbf{R}}{\partial \Delta \mathbf{S}}$ is a Jacobian matrix and $\mathbf{R} = \{R_\lambda, R_V\}^T$ is a residual vector, containing the components $\mathbf{R}_{S_i} = \Delta S_i - \Delta\hat{S}_i$, where ΔS_i is a variable while $\Delta\hat{S}_i$ denotes the function resulting from the evolution rule for i-th variable S_i. The condition $\mathbf{R}(\Delta\mathbf{S}) = \mathbf{0}$ defines the solution. If we expand this condition into a Taylor series, we obtain the following solution for $\Delta\mathbf{S}$: $\Delta\mathbf{S}^{n+1} = \Delta\mathbf{S}^n - \left[\left(\frac{\partial \mathbf{R}}{\partial \Delta \mathbf{S}}\right)^n\right]^{-1}\mathbf{R}^n$.
The iteration procedure is stopped when the norm of $\mathbf{R}$ is sufficiently small.

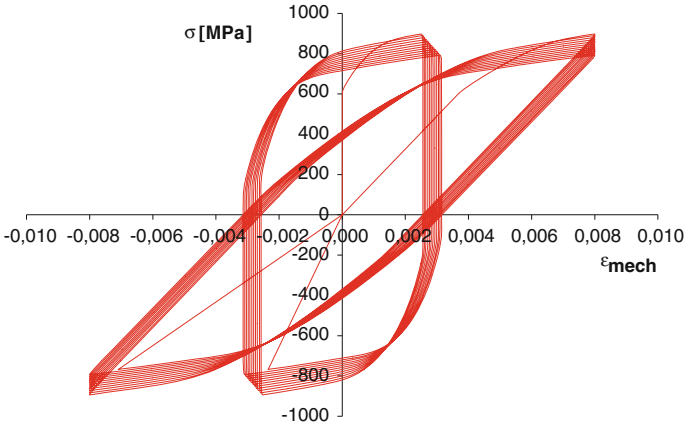

Fig. 2 Numerical simulation of cyclic loading in temperature 500 °C

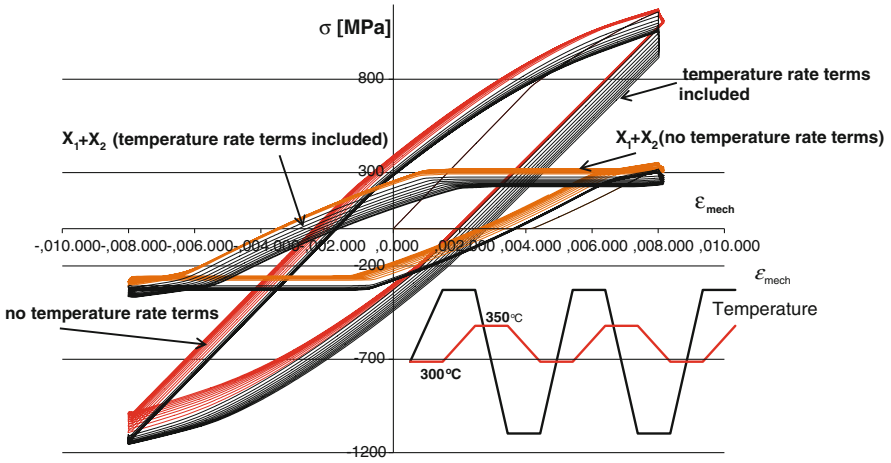

Fig. 3 Effect of temperature rate terms on stress-strain curve

4.1 Numerical Results

The numerical results are shown in Figs. 2 and 3. Figure 2 presents the numerical simulation of cyclic loading of 55NiCrMoV7 tempered martensitic hot work tool steel, performed in temperature 500 °C, which shows a satisfactory agreement with the results given in [13]. In Fig. 3 the effect of temperature rate terms is visible. Namely, in the absence of temperature rate terms the hysteresis loops shift unreasonably in stress, see [5].
The results presented above need to be completed with further simulations to investigate the effect of temperature rate in more detail.

5 Conclusions

The presented paper concerns the modelling of coupling between dissipative phenomena in engineering materials. A special attention is paid to complete and consistent incorporation of temperature and damage softening into the kinetic equations, which results in additional, temperature and damage rate dependent terms, most often neglected in the existing models. However, for high temperature and/or damage rates these terms may play a significant role. It is indicated, that in the case of plastic and/or damage softening the classical loading/unloading conditions have to be extended with additional terms accounting for thermal-plastic-damage coupling, otherwise the recognition of active/neutral/passive processes may be false. The numerical simulations of the influence of temperature rate terms on the hysteresis loops for extended 2M1C model performed so far show unreasonable shift in stress in the absence of temperature rate terms. Further simulations will be done to investigate

the problem in more detail. However, the application of the presented considerations to a general dissipative material requires better experimental recognition of the influence of different dissipative phenomena (like damage, phase transformations etc.) on the material characteristics.

Acknowledgments The Grant No. 2285/B/T02/2011/40 from the Polish Ministry of Science and Higher Education is gratefully acknowledged.

References

1. Abu Al-Rub, R.K., Voyiadjis, G.Z.: On the coupling of anisotropic damage and plasticity models for ductile materials. Int. J. Solids Struct. **40**, 2611–2643 (2003)
2. Bednarek, Z., Kamocka, R.: The heating rate impact on parameters characteristic of steel behaviour under fire conditions. J. Civ. Eng. Manage. **12**(4), 269–275 (2006)
3. Cailletaud, G., Sai, K.: Study of plastic/viscoplastic models with various inelastic mechanisms. Int. J. Plast **11**, 991–1005 (1995)
4. Chaboche, J.L.: Thermodynamic formulation of constitutive equations and application to the viscoplasticity and viscoelasticity of metals and polymers. Int. J. Solids Struct. **34**(18), 2239–2254 (1997)
5. Chaboche, J.L.: A review of some plasticity and viscoplasticity constitutive theories. Int. J. Plast **24**, 1642–1693 (2008)
6. Egner, H.: On the full coupling between thermo-plasticity and thermo-damage in thermodynamic modelling of dissipative materials. Int. J. Solids Struct. **49**, 279–288 (2012)
7. Ganczarski, A., Skrzypek, J.: A study on coupled thermo-elasto-plastic-damage dissipative phenomena: models and application to some innovative materials. J. Therm. Stresses **32**, 698–751 (2009)
8. Kowalsky, U., Ahrens, H., Dinkler, D.: Distorted yield surfaces-modelling by higher order anisotropic hardening tensors. Comput. Mater. Sci. **16**, 81–88 (1999)
9. Lemaitre, J.: A course on damage mechanics. Springer, Berlin (1992)
10. Lemaitre, J., Chaboche, J.L.: Mechanics of solid materials. Cambridge University Press, London (1990)
11. Murakami, S., Ohno, N.: A continuum theory of creep and creep damage. In: Ponter, A.R.S., Hayhurst, D.R. (eds.) Creep in Structures, 3rd IUTAM Symposium on Creep in Structures, pp. 422–444. Springer, Berlin (1980)
12. Ottosen, N.S., Ristinmaa, M.: The mechanics of constitutive modelling. Elsevier, Amsterdam (2005)
13. Velay, V., Bernhart, G., Penazzi, L.: Cyclic behavior modelling of a tempered martensitic hot work tool steel. Int. J. Plast **22**, 459–496 (2006)

Damage Deactivation of Engineering Materials and Structures

Artur Ganczarski and Marcin Cegielski

Abstract When a material is subjected to a cyclic loading at high values of stress or strain, damage develops together with cyclic plastic strain. This process is often accompanied by damage deactivation characterized by actual state of microcracks, which are generally active under tension and passive under compression. In classical formulation damage deactivation occurs instantly when loading changes sign and consequently leads to non smooth path separating both load ranges. The real materials, however, do not exhibit such bilinear paths. Therefore, the more realistic model based on continuous damage deactivation is proposed, in which microcracks close gradually. In the present paper several applications of continuous damage deactivation in modelling of cycle fatigue of engineering materials such as: aluminum alloy Al-2024 and ferritic steel 20MnMoNi55 are demonstrated and compared with experimental results. Detail quantitative and qualitative analysis of obtained solutions confirms necessity and correctness of proposed approach.

1 Introduction

In the case of cycle fatigue, when the stress level is larger than the yield stress, damage develops together with the cyclic plastic strain, after the incubation period that precedes the nucleation and growth of micro-defects is met. In the most frequent approach to the cycle fatigue, in case when a loading is the periodic strain-controlled of constant amplitude, the following assumptions are made: the material becomes perfectly plastic during first cycle, the variation of damage is neglected for

A. Ganczarski (✉) · M. Cegielski
Institute of Applied Mechanics, Cracow University of Technology,
Al. Jana Pawła II 37, 31-864 Kraków, Poland
e-mail: artur@cut1.mech.pk.edu.pl

M. Cegielski
e-mail: morf1@o2.pl

H. Altenbach and S. Kruch (eds.), *Advanced Materials Modelling for Structures*,
Advanced Structured Materials 19, DOI: 10.1007/978-3-642-35167-9_15,

the integration over one cycle and the strain-damage relations are identical both for tension and compression. These allow to simplify calculations of damage cumulation per one cycle and give linear dependency of damage with number of cycles, finally leading to the Manson-Coffin law of low cycle fatigue [18, 23].

On the other hand, the more refined approaches to cycle fatigue [2, 17], based on the kinetic theory of damage evolution and the Gurson-Tvergaard-Needleman model of damage incorporating isotropic hardening, respectively, are able to predict some qualitative phenomena of damage accumulation, crack initiation and fracture only approximately, since they do not account for the unilateral damage.

The phenomenon of the unilateral damage, also called the damage deactivation or the crack closure/opening effect is typical for materials subjected to reverse tension-compression cycles. In the simplest one-dimensional case, if the loading is reversed from tension to compression, the cracks will completely close such that the material behaves as uncracked, or in other words, its initial stiffness is recovered. The mathematical description of unilateral damage is based on the decomposition of the stress or strain into the positive and negative projections [14, 16, 19, 20]. In the simplest case the damage modified stress or strain are used, based on the concept of the Heaviside function, where the negative principal components are ruled out. This means that the negative principal strain or stress components become completely inactive in further damage process as long as the loading condition can again render them active [19]. In a more general approach, both positive and weighted negative eigenvalues of strain or stress tensors influence damage evolution [12, 21]. The positive parts of the strain or stress can also be expressed by the use of the fourth-order positive projection operators written in terms of their eigenvectors [11, 14]. The limitations of the consistent unilateral damage condition applied to the continuum damage theories have been discussed in [4–6]. Authors showed that in the existing theories developed in [13, 15, 22] either non-symmetries of the elastic stiffness or non-realistic discontinuities of the stress-strain response may occur for general multiaxial non-proportional loading conditions. It is easy to show that if the unilateral condition does affect both the diagonal and the off-diagonal terms of the stiffness or compliance tensor, a stress discontinuity takes place when one of principal strains changes sign and the other remain unchanged [24]. In the model proposed in [5] only the diagonal components corresponding to negative normal strains are replaced by the initial (undamaged) values. The consistent description of the unilateral effect was recently developed in [9, 10]. Authors introduced a new fourth-rank damage parameter built upon the eigenvectors of second-order damage tensor that controls the crack closure effect with the continuity requirement of the stress-strain response fulfilled.

2 Concept of Continuous Damage Deactivation

In case of uniaxial state of stress and scalar damage, micro-cracks remain open under tension and almost entirely close under compression, hence the effective stress and the appropriate effective modulus of elasticity are defined in [17] as follows

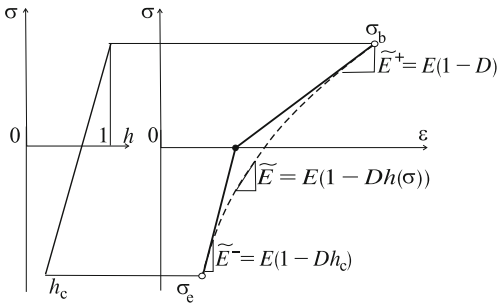

Fig. 1 Concept of the continuous damage deactivation

$$\widetilde{\sigma} = \begin{cases} \sigma/(1-D) \\ \sigma/(1-Dh) \end{cases} \qquad \widetilde{E} = \begin{cases} E\,(1-D) & \text{if} \quad \sigma > 0 \\ E\,(1-Dh) & \text{if} \quad \sigma < 0 \end{cases} \tag{1}$$

Above formulas contain the crack closure parameter h $(0 \leq h \leq 1)$, that depends on a material and loading, however, in practice it is considered to be constant $h = h_c = 0.2$. Application of this model for description of unloading path leads to linear relation between the stress decrease and the strain decrease given by $\widetilde{E}^{+}$. Entering the compression range the material switches to the path characterized by the modulus of elasticity which is equal to $\widetilde{E}^{-}$ (solid line in Fig. 1). The real materials do not exhibit such bilinear unloading paths, therefore the concept of continuous crack closure that allows to eliminate mentioned switch between $\widetilde{E}^{+}$ and $\widetilde{E}^{-}$ is introduced. It consists in the replacement of parameter h by a function $h(\sigma)$, being linear in the simplest case, such that

$$h\,(\sigma) = h_c + (1-h_c)\,(\sigma - \sigma_e)/(\sigma_b - \sigma_e) \tag{2}$$

According to above relation function $h(\sigma)$ is equal to 1 when $\sigma = \sigma_b$ and h_c when $\sigma = \sigma_e$, see Fig. 1.

Three-dimensional generalization of the continuous damage deactivation requires distinction between tension and compression. When the stress tensor is given by its eigenvalues the following decomposition proposed in [17] is applied

$$\boldsymbol{\sigma} = \text{diag}\,\{\sigma_1, \sigma_2, \sigma_3\} = \langle \boldsymbol{\sigma} \rangle - \langle -\boldsymbol{\sigma} \rangle \tag{3}$$

In case of isotropic damage and application of the principle of strain equivalence the general form of effective stress proposed in [17] is as follows

$$\widetilde{\boldsymbol{\sigma}} = \pm \frac{\langle \pm \boldsymbol{\sigma} \rangle}{1-Dh} \pm \frac{\nu}{1-2\nu} \frac{[\text{Tr}\,\langle \pm \boldsymbol{\sigma} \rangle - \langle \pm \text{Tr}(\boldsymbol{\sigma}) \rangle]\mathbf{1}}{(1-Dh)} \tag{4}$$

Terms associated to the factor $\nu/(1-2\nu)$, introducing coupling, disappear if all eigenvalues of stress are of the same sign and in such case simplified effective stresses and the corresponding elastic modules take the form

$$\widetilde{\boldsymbol{\sigma}} = \begin{cases} \langle \boldsymbol{\sigma} \rangle / (1 - D) \\ -\langle -\boldsymbol{\sigma} \rangle / (1 - Dh) \end{cases} \qquad \widetilde{\mathbf{E}} = \begin{cases} \mathbf{E}(1 - D) & \text{“tension”} \\ \mathbf{E}(1 - Dh) & \text{“compression”} \end{cases} \tag{5}$$

Application of the concept of continuous crack closure needs additional hypothesis that introduces the relation between the crack closure magnitude and a scalar function of the stress tensor

$$h(\boldsymbol{\sigma}) = h_{\mathrm{c}} + (1 - h_{\mathrm{c}})[\chi(\boldsymbol{\sigma}) - \chi(\boldsymbol{\sigma}_{\mathrm{e}})]/[\chi(\boldsymbol{\sigma}_{\mathrm{b}}) - \chi(\boldsymbol{\sigma}_{\mathrm{e}})] \tag{6}$$

here the known Hayhurst function

$$\chi(\boldsymbol{\sigma}) = \beta \mathrm{Tr}(\boldsymbol{\sigma}) + (1 - \beta) J_2(\boldsymbol{\sigma}) \tag{7}$$

3 Examples

3.1 Low Cycle Fatigue of Aluminum Alloy Al-2024

The objective of this example is the modelling of damage deactivation concept in the aluminum alloy Al-2024 in order to describe the phenomenon of non-symmetric hysteresis loop evolution due to different damage growth under tension and compression observed in experiment [1], see Fig. 2a. Detailed analysis of the subsequent strain-stress loops, obtained in uniaxial tension-compression test at the constant strain amplitude $\Delta\varepsilon = \pm 1\,\%$, confirms an elasto-plastic behavior of the material and strong influence of the unilateral damage effect. During the initial cycles the material exhibits plastic hardening leading to the stabilized cycle and, then asymmetric drop

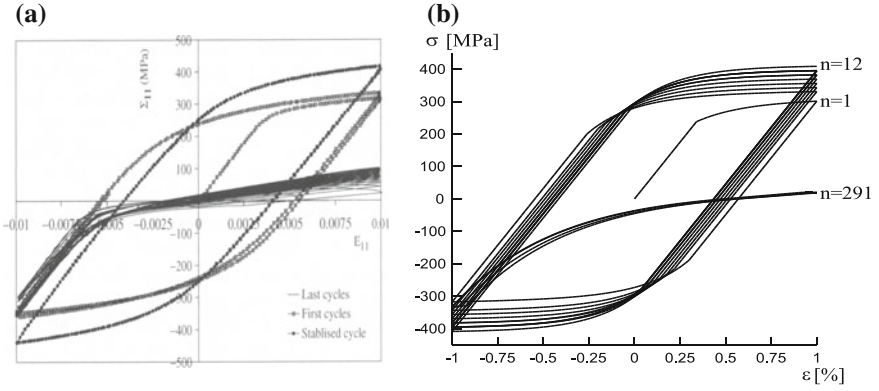

Fig. 2 Cycle fatigue for aluminum alloy Al-2024: **a** tension-compression test [1], **b** numerical simulation with model of continuous damage deactivation [8]

of both the stress amplitude and the modulus of elasticity reveals following damage growth. This process is accompanied by a gradual decrease of the hysteresis area and a change of shape of subsequent hysteresis loops, associated with a formation of the characteristic inflection point on their lower branches. Description of plastic flow including degradation of material properties by damage, able to model experiment is based on the kinetic of damage evolution [17, 18]. In case of uniaxial stress state the dissipation potential being a sum of the plastic and damage potentials is assumed in simplified form

$$F = |\widetilde{\sigma} - X| - R - \sigma_{\mathrm{y}} + 0.75X^2/X_{\infty} + Y^2H(p - p^{\mathrm{D}})/2S(1 - Dh) \quad (8)$$

where elastic strain energy density release rate is equal to $Y = \widetilde{\sigma}^2/2E$. Application of the formalism of associated plasticity leads to the following evolution equations [8]

$$\begin{aligned}
&\mathrm{d}\sigma/\mathrm{d}\varepsilon = E\,(1 - Dh) && \text{elastic range}\\
&\mathrm{d}\sigma/\mathrm{d}p = (1 - Dh)^2\left\{\left[X_{\infty}\gamma + b\,(R_{\infty} - R)\right]\mathrm{sgn}\,(\widetilde{\sigma} - X) - \gamma X\right\} && \text{plastic range}\\
&\qquad\quad -\widetilde{\sigma}^3 H(p - p^{\mathrm{D}})/2ES\\
&\mathrm{d}R/\mathrm{d}p = b\,(R_{\infty} - R)\,(1 - Dh)\\
&\mathrm{d}X/\mathrm{d}p = \gamma\left[X_{\infty}\mathrm{sgn}\,(\mathrm{d}\varepsilon^{\mathrm{p}}) - X\right](1 - Dh)\\
&\mathrm{d}D/\mathrm{d}p = \sigma^2 H\left(p - p^{\mathrm{D}}\right)/2ES\,(1 - Dh)^2
\end{aligned} \quad (9)$$

The effect of continuous damage deactivation describe by Eq. (2) is limited by the additional assumption that the stress referring to the beginning of damage deactivation is equal to $\sigma_{\mathrm{b}} = 0$. Magnitudes of all material constants defining model are given in Table 1. Numerical integration of system of evolution equations (9) for constant strain range $\Delta\varepsilon = \pm 1\,\%$ is done by use of the fourth-order Runge-Kutta technique with the adaptive stepsize control. Model under consideration properly maps unilateral nature of damage softening, in this sense that the dead center ordinates of subsequent hysteresis loops coincide exactly with the appropriate points on experimental curves, see Fig. 2b. Additionally, a gradually decreasing area of the subsequent hysteresis loops and accompanying change of curvature at their unloading branch, are well mapped.

Table 1 Material data for alloy Al-2024

E [GPa]	σ_{y} [MPa]	b	R_{∞} [MPa]	γ	X_{∞} [MPa]	S [MPa]	p^{D}
70	230	0.1	120	4.0	60	3500	0.248

3.2 Yield Surface Affected by Damage

Damage evolution equations presented in the previous example are derived on the basis of kinetic law of damage evolution [17, 18]. Key point of this theory is the

potential of dissipation taken as a sum of the plastic potential referring to theory of associated plasticity and a damage dissipation potential. In the simplest case of isotropic damage and absence of both kinematic and isotropic hardening, it is assumed that the kinetic coupling acts only by the effective stress deviator and this corresponds to the following yield function

$$f(\boldsymbol{\sigma}, Dh) = 0 \tag{10}$$

Simultaneously, it is postulated that the yield function f is a scalar continuous or partly continuous (having at most finite set of corner points) and convex function. Form of yield function is strictly associated with magnitude of damage deactivation parameter h in Eq. (10) and consequently essentially differs in case of tension when damage is active than in case of compression when damage remains inactive. In case of the plane stress state and under assumption that damage is active if only one of stress components is positive ($\sigma_1 > 0$ or $\sigma_2 > 0$) or in other words $h = 1$ if $\mathrm{Tr}\,\langle\boldsymbol{\sigma}\rangle$ is positive, yield potential takes following form

$$\sigma_1^2 - \sigma_1\sigma_2 + \sigma_2^2 = \begin{cases} \sigma_y^2 (1-D)^2 & 1^{\mathrm{st}}, 2^{\mathrm{nd}}, 4^{\mathrm{th}} \text{ quarter} \\ \sigma_y^2 & 3^{\mathrm{rd}} \text{ quarter} \end{cases} \tag{11}$$

and turns out to be non-smooth and non-convex (Fig. 3a). The above mentioned defect of yield potential may be successfully removed by introducing continuous damage deactivation, when micro-cracks do not close instantaneously but gradually Eq. (6). Restricting considerations to the simplified case when $\chi(\boldsymbol{\sigma})$ in Eq. (7) depends only on positive value of the first invariant of stress tensor ($\beta = 1$ and $\mathrm{Tr}(\boldsymbol{\sigma}) = \mathrm{Tr}\,\langle\boldsymbol{\sigma}\rangle$). Assuming further that micro-cracks are fully open under maximum tension $\sigma_b = 2(1-D)\sigma_y/\sqrt{3}$ and close completely under compression ($h_c = 0$) the yield function is given by formulas

$$\sigma_1^2 - \sigma_1\sigma_2 + \sigma_2^2 = \begin{cases} \sigma_y^2 (1-D)^2 & \text{arc } C_1C_2 \\ \sigma_y^2 \left(1 - \frac{D}{1-D}\frac{\sqrt{3}}{2}\frac{\sigma_{2/1}}{\sigma_y}\right)^2 & \text{arcs } C_1A_2 \text{ or } C_2B_2 \\ \sigma_y^2 & \text{arc } A_2B_2 \end{cases} \tag{12}$$

Now yield function is composed of two ellipses and two hyperbolas and its convexity and smoothness are recovered (Fig. 3b). Subsequent stages of damage affected yield function versus experimental investigations (isochronous creep curves) [19] are shown in Fig. 3c, d.

3.3 Low Cycle Fatigue of Notch Specimen Made of Ferritic Steel

Success in modelling of low cycle fatigue of alloy Al-2024 as well as recovery of both convexity and smoothness of yield function allow to consider more advanced

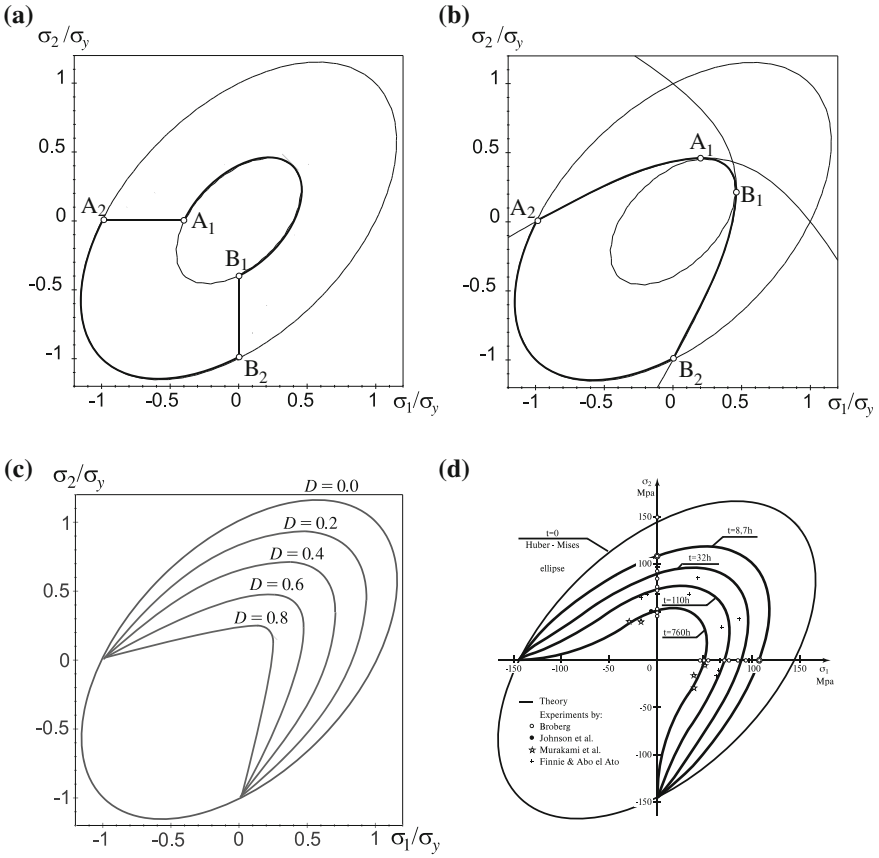

Fig. 3 Yield function affected by damage: **a** non-smooth and non-convex case corresponding to discontinuous damage deactivation ($D = 0.6$), **b** smooth and convex after application of continuous damage deactivation ($D = 0.6$), **c** subsequent yield functions [7], **d** experimental investigations [19]

3D problem. Cyclic test with elongation controlled amplitudes $\Delta l = \pm 0.1$ mm of notched specimens made of ferritic steel 20MnMoNi55 was done in [2]. Subsequent elongation-cyclic load curves, exhibiting Bauschinger-like continuously softening effect are shown in Fig. 4a. A crack initiates at the notch root and extends through the specimen diameter. The test was stopped after 83 cycles to examine the damage evolution.

Analogously to the previous example, inelastic deformation is described in framework of kinetic law of damage evolution [17, 18] generalized for the case of finite deformation. The dissipation potential is assumed in following form

$$F = J_2(\widetilde{\mathbf{S}}' - \mathbf{X}') - R - \sigma_{\mathrm{y}} + 0.75\mathbf{X}' : \mathbf{X}'/X_\infty + F^{\mathrm{D}}(Y, D) \tag{13}$$

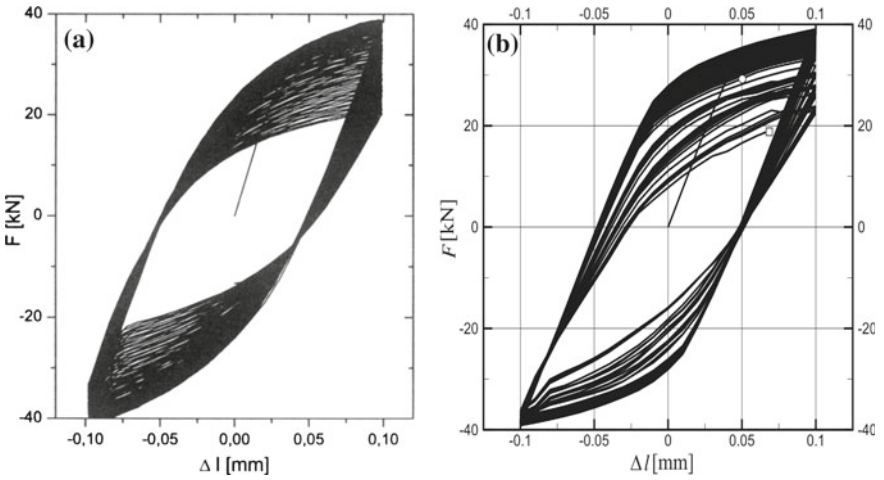

Fig. 4 Cyclic load versus elongation of specimen made of ferritic steel 20MnMoNi55: **a** test result [2], **b** simulation with finite element model [3]

The elastic deformation is described by Hooke's law in which the effective elastic tensor $\widetilde{\mathbf{E}}$ is given by Eq. (5). The associated flow rule defines plastic deformation

$$\mathrm{d}\mathbf{e}^{\mathrm{p}} = 1.5(\widetilde{\mathbf{S}}' - \mathbf{X}')\mathrm{d}\lambda/[J_2(\widetilde{\mathbf{S}}' - \mathbf{X}')(1 - Dh)] \tag{14}$$

whereas the cumulative plastic strain is equal

$$\mathrm{d}p = \sqrt{2\mathrm{d}\mathbf{e}^{\mathrm{p}} : \mathrm{d}\mathbf{e}^{\mathrm{p}}/3} = \mathrm{d}\lambda/(1 - Dh) \tag{15}$$

Application of formalism of associated plasticity yields following evolution equations for isotropic and kinematic hardening

$$\mathrm{d}R/\mathrm{d}\lambda = b(R_\infty - R) \qquad \mathrm{d}\mathbf{X}'/\mathrm{d}\lambda = \gamma[2X_\infty \mathrm{d}\boldsymbol{\varepsilon}^{\mathrm{p}}(1 - Dh)/3\mathrm{d}\lambda - \mathbf{X}'] \tag{16}$$

both dependent on plastic multiplier which is to satisfy the consistency condition

$$\partial F/\partial \mathbf{S}' : \mathrm{d}\mathbf{S}' + \partial F/\partial \mathbf{X}' : \mathrm{d}\mathbf{X}' + \partial F/\partial R : \mathrm{d}R = 0 \tag{17}$$

The strain energy density release rate based on Eq. (13) is equal to

$$Y = 0.5\mathbf{E}^{-1} : \widetilde{\mathbf{S}} : \widetilde{\mathbf{S}} \tag{18}$$

hence damage evolution equation takes the following form

$$\mathrm{d}D/\mathrm{d}p = \mathbf{E}^{-1} : \mathbf{S} : \mathbf{S}\, H(p - p^{\mathrm{D}})/[2S(1 - Dh)^2] \tag{19}$$

Described formalism referring to the total Lagrangian formulation is implemented into finite element code for quadrilateral axisymmetric elements. Magnitudes of material constants, identified by Brocks and Steglich [2], are demonstrated in Table 2. The numerical simulation exhibits all quantitative phenomena of decreasing load due to damage evolution with damage localization starting at the notch root, see Fig. 4b, as in the experiment. Value of damage parameter $D \geq 0.87$ indicates complete loss of stress carrying capacity of the respective element and hence cracking. The number of cycles to failure is equal to about one half when compare to experiment. Further analysis associated with propagation of damage front inside the material is possible if one of special techniques, referring to numerical solution of singular boundary value problem, is applied. Application of classical methods based on Gaussian elimination or LU decomposition is possible as long as system of equations or global stiffness matrix remain nonsingular in mathematical or numerical sense. In other words, this means that critical magnitude of damage $D = 1.0$ is attainable only with certain tolerance since appropriate effective stress Eq. (5) approaches infinity whereas effective stiffness Eq. (5) tends to zero. In all such cases, when global stiffness matrix becomes singular the special techniques of FEM, based on turning off completely damaged elements or substituting by elements of zero or negligible stiffness, turn out to be very attractive. Simultaneously, it is worth to mention here the singular value decomposition as a potentially attractive algorithm which seems to be the most general and effective tool for solving this kind of problems. In the problem under consideration however, the direction of damage front propagation is easy to predict since it begins at the notch bottom and goes towards a symmetry axis, in other words along appropriate edge of finite element mesh. Above observation is a basis for application simplified technique in which subsequent boundary conditions are released following damage parameter D, reaching critical magnitude 0.9 in subsequent Gaussian points. Results of damage analysis done in such a way are shown in Fig. 4b. In subsequent hysteresis loops one can observe further difference in drop of stress amplitude between tension and compression as well as appearance of characteristic inflection point at hysteresis brunch referring to compressive range. This effect is strictly associated with contact of both edges of completely damaged element, next damage deactivation as a result of compression and consequently recovery of initial stiffness.

Table 2 Material constants of ferritic steel 20MnMoNi55

E [GPa]	ν	σ_{y} [MPa]	b	R_∞ [MPa]	X_∞ [MPa]	γ	S [MPa]
210	0.3	470	75	8.0	7500	70	5.0

4 Conclusions

Application of continuous damage deactivation gives both quantitative and qualitative good agreement with experimental data and confirms necessity and correctness of this approach in modelling of low cycle fatigue aluminum alloy Al-2024 and ferritic steel 20MnMoNi55.

Continuous damage deactivation concept applied to model of damage affected plastic potential recovers its convexity and smoothness, simultaneously allowing to avoid physically unjustified discontinuities.

References

1. Abdul-Latif, A., Chadli, M.: Modelling of the heterogeneous damage evolution at the granular scale in polycrystals under complex cyclic loadings. Int. J. Damage Mech. **16**(2), 133–158 (2007)
2. Brocks, W., Steglich, D.: Damage models for cyclic plasticity. In: Buchholtz, F.-G., Richard, H.A., Aliabadi, M.H. (eds) Advances in Fracture and Damage Mechanics. Trans Tech Publ, Zürich (2003)
3. Cegielski, M.: Effect of continuous damage deactivation in CDM. Ph.D. Thesis, Cracow University of Technology (2012)
4. Chaboche, J.-L.: Damage induced anisotropy: on the difficulties associated with the active/passive unilateral condition. Int. J. Damage Mech. **1**(2), 148–171 (1992)
5. Chaboche, J.-L.: Development of continuum damage mechanics for elastic solids sustaining anisotropic and unilateral damage. Int. J. Damage Mech. **2**, 311–329 (1993)
6. Chaboche, J.-L., et al.: Continuum damage mechanics, anisotropy and damage deactivation for brittle materials like concrete and ceramic composites. Int. J. Damage Mech. **4**, 5–21 (1995)
7. Cegielski, M., Ganczarski, A.: Effect of continuous damage deactivation on yield and failure surfaces. Acta Mech. Automatica **1**(2), 11–14 (2007)
8. Ganczarski, A., Cegielski, M.: Application of the continuous damage deactivation to a modelling of low cycle fatigue of aluminum alloy Al-2024. Czas Tech. **5**(105), 61–70 (2008)
9. Halm, D., Dragon, A.: A model of anisotropic damage by mesocrack growth; unilateral effect. Int. J. Damage Mech. **5**, 384–402 (1996)
10. Halm, D., Dragon, A.: An anisotropic model of damage and frictional sliding for brittle materials. Eur. J. Mech. A. Solids **17**(3), 439–460 (1998)
11. Hansen, N.R., Schreyer, H.L.: Damage deactivation. Trans. ASME **62**, 450–458 (1995)
12. Hayakawa, K., Murakami, S.: Thermodynamical modelling of elastic-plastic damage and experimental validation of damage potential. Int. J. Damage Mech. **6**, 333–363 (1997)
13. Ju, J.W.: On energy based coupled elastoplastic damage theories: constitutive modelling and computational aspects. Int. J. Solids Struct. **25**(7), 803–833 (1989)
14. Krajcinovic, D.: Damage mechanics. Elsevier, Amsterdam (1996)
15. Krajcinovic, D., Fonseka, G.U.: The continuous damage theory of brittle materials, part I and II. J. Appl. Mech. ASME **18**, 809–824 (1981)
16. Ladeveze, P., Lemaitre, J.: Damage effective stress in quasi-unilateral conditions. Proc IUTAM Congr Lyngby, Denmark (1984)
17. Lemaitre, J.: A course on damage mechanics. Springer, Berlin (1992)
18. Lemaitre, J., Chaboche, J.-L.: Mécanique des matériaux solides. Bordas, Paris (1985)
19. Litewka, A.: Creep damage and creep rupture of metals. Wyd Polit Poznańskiej (1991)
20. Mazars, J.: A model of unilateral elastic damageable material and its application to concrete. In: Wittmann, F.H. (ed) Energy Toughness and Fracture Energy of Concrete. Elsevier, Amsterdam (1986)

21. Murakami, S., Kamiya, K.: Constitutive and damage evolution equations of elastic-brittle materials based on irreversible thermodynamics. Int. J. Solids Struc. **39**(4), 473–486 (1997)
22. Ramtani, S.: Contribution á la modelisation du comportement multiaxial du beton endommagé avec description du caractere unilateral. Ph.D. Thesis, Univ Paris VI (1990)
23. Skrzypek, J.J., Ganczarski, A.: Modelling of material damage and failure of structures. Springer, Berlin (1999)
24. Skrzypek, J.J., Kuna-Ciskał, H.: Anisotropic elastic-brittle-damage and fracture models based on irreversible thermodynamic. In: Skrzypek, J.J., Ganczarski, A. (eds) Anisotropic Behaviour of Damaged Materials. Springer, Berlin (2003)

Effect of Orientation and Overaging on the Creep and Creep Crack Growth Properties of 2xxx Aluminium Alloy Forgings

Elisabetta Gariboldi and Antonietta Lo Conte

Abstract Long-term high temperature properties of aluminium alloy forgings are widely affected by the extent and direction of plastic flow as well as by the heat treatment and exposure causing overaging processes. The classical creep crack propagation models, for which the material is often considered as isotropic and microstructurally stable, must be adapted to take into account the effects of crystal orientation and of overaging. After presenting the creep behaviour of 2014 and of 2016 Al alloy forgings in different sampling directions and overaging conditions, FE simulations of the crack propagation of CT specimens sampled in different directions were carried out. The possibility to account for the progressive overaging of the material was also taken into account in the model.

1 Introduction

Aluminium-alloy forgings are currently used to manufacture structural components of relatively large and complex shape. The plastic deformations imparted to the material significantly affects its microstructure, which can be roughly described by the effects of grain size and crystal orientations, as well as distribution of intermetallic particles, typically fragmented along the plastic flow direction. Additionally, in heat treatable Al alloys, submicrometer particles formed during the solution treatment and ageing steps can evolve during service at relatively high temperature. Thus, long-term high temperature properties of aluminium alloy forgings are widely affected by the extent and direction of plastic flow as well as by the heat treatment and exposure leading to overaging processes [1, 2]. The above features should also be considered when predicting the propagation of cracks originated from process- or service-induced defects in a progressively overaging material. The classical creep-crack propagation models for which the material is often considered as isotropic and

E. Gariboldi (✉) · A. Lo Conte
Dipartimento di Meccanica, Politecnico di Milano, Via La Masa 1, 20156 Milano, Italy
e-mail: elisabetta.gariboldi@polimi.it

H. Altenbach and S. Kruch (eds.), *Advanced Materials Modelling for Structures*, Advanced Structured Materials 19, DOI: 10.1007/978-3-642-35167-9_16,

microstructurally stable must be adapted to take into account the effects of orientation and of overaging.

The aims of the present paper are to investigate the effects of orientation and overaging on the creep behaviour in age-hardenable 2xxx Al alloy forgings and to explore the possibility to predict the growth of cracks by means of a combination of a material description taking into account the more widely available and accessible uniaxial tension and creep data and of a FE model describing crack propagation by means of a procedure that allows the release of nodes when a critical damage level is locally reached.

2 Materials and Experimental Procedures

Two forgings were experimentally investigated. The first was made of a Al-4.4 Cu-0.5Mg-0.9Si-0.8Mn alloy (IADS AA 2014 grade), axysimmetrically forged from a previously extruded bar into the shape of a cave cylinder 230 mm high, with an outer diameter of about 190 mm. The forging was supplied in peak aged (T6) condition (ST at 505 °C, WQ, aging at 160 °C for 16 h). In the second forging, the hot work process was carried out on an axysimmetric as-cast cylinder of Al-4Cu-0.5M-0.6Si-0.5Ag-Zr (AA 2016) alloy, leading to its final size of 180 mm in height and of 270 mm in outer diameter. The alloy was then heat treated to peak hardness condition by an heat treatment cycle corresponding to that of 2014 alloy.

Two sets of $20 \times 20 \times 100\ mm^3$ bars were sampled longitudinally or tangentially to the cylinder (referred as L and T directions, respectively). Tension tests were carried out at temperatures within the range 20–200 °C. Constant tension load creep tests were performed in the temperature range 130–200 °C, with rupture times ranging from 1 to 10000 h. In the case of 2014 alloy, tension and creep tests were also performed on small sets of L and T specimens previously aged at 170 °C for times up to 1000 h (exposures A, C and D, details given in [3]).

The material characterization was completed by creep crack growth (CCG) tests at 150 °C on CT specimens sampled in CR and CL directions (details of sampling in [4]). The experimental plan for CCG tests, to be carried out at 150 °C according ASTM 1457-07 standard on side-grooved and fatigue precracked CT 1/2″ specimens included tests at initial K_I of 15 and 22 $MPa\sqrt{m}$. During the tests, the crack opening displacement was monitored by means of an extensometric system and the crack length was indirectly measured by means of a DC PD method using the procedure and calibration curve described in [5].

3 Experimental Results and Analyses

The different process routes and alloy compositions led to different microstructural features of the alloy. They can be observed in Fig. 1, where metallographic sections display the microstructures in L-T planes. The 2014 alloy was characterized by the

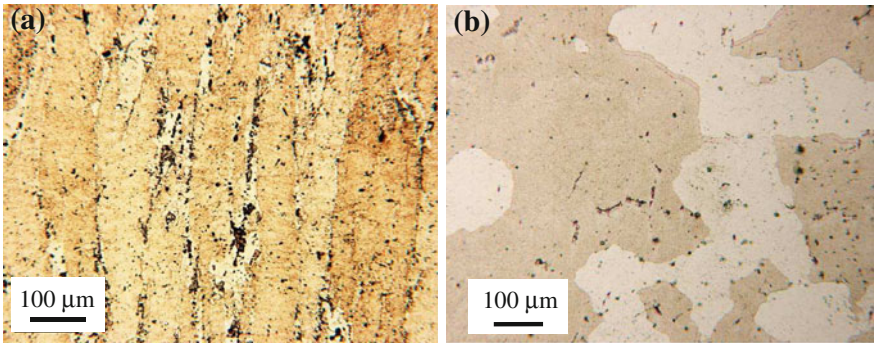

Fig. 1 Metallographic sections of 2014 and 2016 forgings (**a** and **b**, respectively). L direction is vertical, T direction horizontal in the micrographs

extensive plastic flow in the longitudinal direction, along which grains were elongated and bounded by two kinds of coarse secondary particles, most of a quaternary Fe-Mn-Si-Cu phase (dark particles in Fig. 1a) and some globular Al_2Cu particles. In the case of the 2016 alloy forging, the plastic deformation slightly modified the as-cast structure characterized by radially elongated grains, that were slightly flattened. Also in this case, secondary Al_2Cu particles were located preferentially at grain boundaries. The amount of secondary phases was in any case lower than that in 2014 alloy forging.

It is well-known that in these age hardenable Al alloys, the above mentioned second phases, rather coarse and typically located at grain boundaries, are not responsible of the significant strengthening of the material. This is mainly induced by the presence of the much finer intragranular phases that evolve on aging following one or more precipitation sequences, depending on the alloy composition. Previous studies carried out on the alloys here taken into account [6–8] confirmed that the strengthening phases are mainly produced by the sequence (SSSS $\rightarrow$ GPZ $\rightarrow$ θ'' $\rightarrow$ θ' $\rightarrow$ $\theta(Al_2Cu)$). It is also confirmed that after some hours of exposure, the formation of θ' in forgings was completed. Further exposure led to a progressive θ' coarsening and to a corresponding loss in material strength. Since coarsening is controlled by diffusion of Cu in Al, an equivalent time spent at a reference temperature T can be defined as:

$$t_{T,tot} = e^{(-Q_{Cu}/R^*T)} * \sum_{i=1}^{k} t_i * e^{(Q_{Cu}/RT_i)} \quad (1)$$

where t_i is the i^{th} time interval spent at temperature T_i, R the gas constant and Q_{Cu} is the activation energy for the diffusion of Cu in Al, 133.9 kJ/mol [9]. This equivalent time, is proportional to an alternative time-temperature parameter (the normalized time t_{norm}) used in previous studies [3, 6]. With respect to t_{norm}, $t_{T,tot}$ can be more easily handled in cases were the material behaviour at a single temperature can be described and used to model the behaviour of components operating in

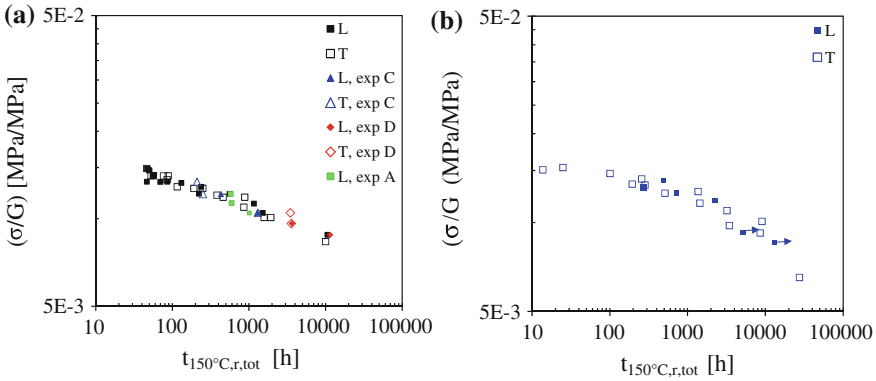

Fig. 2 σ/G versus $t_{150\,^{\circ}C,\,r,\,tot}$ for 2014 (**a**) and 2016 (**b**) alloys tested in T and L directions

isothermal conditions. The total equivalent time ($t_{T,tot}$) in age-hardenable alloys can be considered as a sum of an equivalent aging time up to T6 temper ($t_{T,aging}$), of a exposure equivalent time ($t_{T,exp}$, related to further exposure in single and/or more time/temperature steps) and finally to the equivalent creep time ($t_{T,creep}$), as follows

$$t_{T,tot} = t_{T,aging} + t_{T,exp} + t_{T,creep} \tag{2}$$

In case rupture times are taken into account, $t_{T,tot}$ and $t_{T,creep}$ can be replaced by $t_{T,r,tot}$ and $t_{T,r,creep}$. Neglecting the possible effects of applied stress on overaging processes [2, 10], the creep strength to shear modulus ratio (σ /G) can be correlated to $t_{T,r,tot}$. Figure 2 shows the results of creep tests carried out at different test temperatures and at different previous exposure times for the two investigated forgings in L and T directions in stress-$t_{T,r,tot}$ plots. Here the temperature of 150 °C has been considered as a reference, as usually done for Al alloys. The substitution of $t_{150\,^{\circ}C,r,tot}$ to the simple time to rupture (t_r) leads to a 'master curve' describing the creep strength of the alloys in a wide range of equivalent times at 150 °C. It can be observed that 2014 forging displays the higher creep strength (and correspondingly, the longer creep lives) in the longitudinal direction, while no significant difference exists between L and T orientations in the 2016 alloy. Lastly, for both materials, the experimental data lay on downward-curved rather than on straight lines, and this prevents the use of a single power-law equation correlating stress to $t_{150\,^{\circ}C,r,tot}$ over extended stress ranges.

Experimental creep data were also analysed in terms of (minimum) creep strain rate, using an Arrhenius-type temperature dependence to 'normalize' data at different test temperature to an equivalent strain rate at 150 °C. Figure 3 shows the correlation between the strain rate and the ratio between applied stress and shear modulus. Experimental points lay on a master curve clearly showing a change of slope at about 10^{-5} 1/h, corresponding to the Sherby Dorn threshold strain rate for the Power Law Breakdown. Below this limit the experimental data can be fitted by the classical

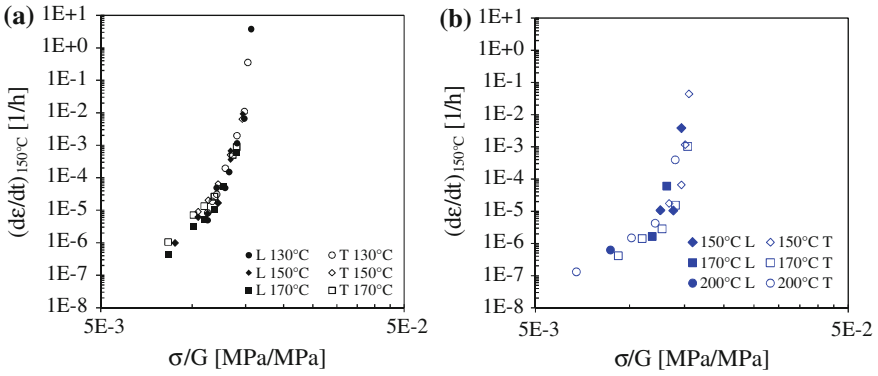

Fig. 3 Equivalent strain rates at 150 °C as function of the applied stress for 2014 and 2016 alloys (**a** and **b**, respectively) in L and T sampling directions

Norton's power-law equation. As Fig. 3a shows, in this stress range the Norton's indexes of 2014 alloy were close to 9 for both sampling directions. The strain rate in T direction was about 2.5 times higher than that in L direction. In the case of 2016 alloy (Fig. 3b), no significant difference of strain rates with sampling orientation was revealed. In the low-stress range, a single fitting equation with Norton's index slightly higher than 5 could be used. The existence of the Monkman-Grant correlation between the minimum strain rate and times to rupture, a useful tool to predict times to rupture of tests interrupted after reaching the minimum strain rate, was checked. For both forgings the relationship was substantially the same for the two orientations, as here presented in Fig. 4a for 2014 alloy.

The creep ductility of the forgings was significantly affected by their microstructural features. Ductility will be here given in terms of reduction of area (RA) at

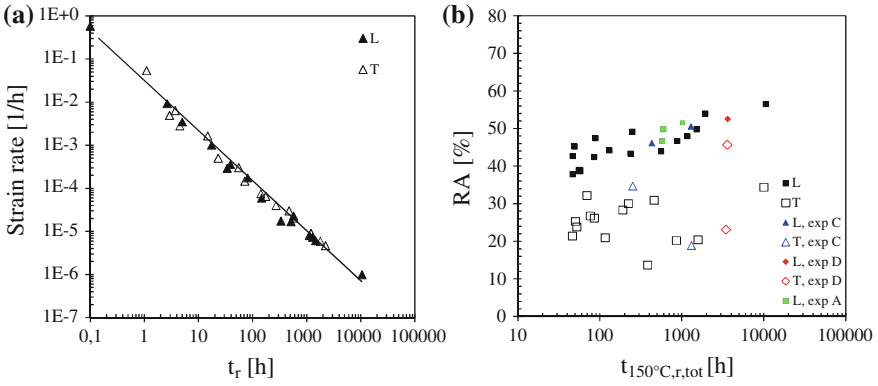

Fig. 4 Strain rate versus time to rupture (**a**) and reduction of area versus $t_{150\,°C,tot}$ (**b**) for 2014 alloy in different sampling directions and exposure times before creep tests

rupture. In short- and long-time tests the 2014 alloy displayed the highest ductility in L direction. Microstructural observations on crept specimens [3, 10] revealed that creep damage leading to the final fracture of these specimens began with the formation of cavities at the coarse intermetallic particles. These linked first longitudinally and then transversally, leading to final separation of specimens by a ductile fracture mode. The role played by the matrix on the creep fracture mechanism suggested to correlate RA to $t_{150\,^\circ C,tot}$, describing matrix softening (see Fig. 4b). A clear trend to increased RA for longer exposure times can be noticed for data in L direction. Notwithstanding the higher experimental scatter and lower RA levels, a similar trend is also suggested for T specimens, where linkage of cavities is favoured.

In the case of 2016 alloy, the RA in both sampling directions was relatively high scattered. Microstructural observation revealed a creep fracture mechanisms similar to that of 2014 alloy, with low ductility values related to the presence of irregularly oriented microstructures or of some residual casting defects. Average RA of 19 and 57 % were considered for 2016 alloy in L and T directions, respectively.

4 Modelling the Crack Propagation in a 2XXX Al Alloy Forgings

The possibility to link uniaxial creep behaviour and crack growth propagation is of wide interest to predict the behaviour of components containing defects (cracks) by means of FEM simulations and has often been proposed in literature (see for example the recent paper [11]). A further advantage would be the possibility to develop models requiring only the time to failure and creep ductility parameters (elongation at rupture or reduction of cross-sectional area) that can be derived from stress-rupture creep tests. In the Nickbin-Smith-Webstrer (NSW) model [12, 13], the uniaxial material creep behaviour up to final fracture is accounted by means of an average creep rate defined as the ratio between the uniaxial creep rupture strain, (ε_r) and the time to rupture (t_r).

In the present case, the crack propagation has been simulated by a two-dimensional FE model corresponding to the CT specimen used for experimental tests. Symmetry reasons led to model the only upper half of the specimen. Four-noded plane-strain isoparametric elements were used with decreasing size, becoming square-shaped elements towards the crack growth zone. In this zone the element size was approximately 0.050 mm, roughly corresponding to the grain size in T and R directions of 2014 alloy forging and to 1/2 and 1/3 of the grain size in the L and T direction of 2016 alloy forging, respectively. The load was applied to a rigid pin in contact with the hole of the CT specimen. A rigid surface was considered along the specimen symmetry plane, containing the initial crack and within which the crack was assumed to grow. The nodes on the crack plane ahead the crack tip were constrained to the rigid surface and were allowed to slide along it until they were involved in the crack growth. When critical conditions for material fracture were reached (see below), the nodes were released. Both the critical condition and the technique for node release

were implemented in a dedicated Fortran subroutine coupled with the ABAQUS 6.9 code for FE simulation [14].

Calculations were performed using elastic-plastic creep behavior. Elastic behavior was considered as symmetric isotropic. The plastic response was assumed to be governed by a Von Mises flow rule with isotropic hardening. The post yield strain was treated as piecewise linear up to the rupture load (σ_r), beyond which no strain hardening occurred. The material creep response was described by a secondary creep law using the average creep rate defined above. Following the approach proposed in the NSW model [12, 13] a ductility exhaustion approach was chosen as the critical condition for the material ahead of a growing crack: the local damage parameter ω approached 1 at the crack tip when the local equivalent accumulated strain (ε_c) reached the local multiaxial strain ($\varepsilon_{r,m}$). At each temporal step of the FE simulation, the damage rate ($\dot{\omega}$) was computed in the four– integration points of each element as the ratio between the equivalent creep strain rate ($\dot{\varepsilon}_c$) and the multiaxial failure strain rate ($\dot{\varepsilon}_{r,m}$). The Cocks and Ashby model [15], already combined to NSW model in literature [12, 13], was here used to describe ($\varepsilon_{r,m}$), accounting for the constrain effect at the crack tip, assuming that creep damage was mainly related to the formation of voids. The critical condition for the release of a node along the crack path was defined as a local damage (obtained by integrating local damage rate) exceeding 0.99 in at least two integration points of each finite element.

The whole method proposed above was re-arranged to model the creep behavior and crack propagation in Al forgings at 150 °C, considered as a reference temperature for this alloy class. The elastic behavior was kept as symmetric isotropic, as in the base-model previously explained, while the uniaxial plastic and creep properties of the material in the direction perpendicular to the crack plane were considered. In this case the directions L and T for which uniaxial tension and creep data were available, were taken into account. In the first extension of the model, for which the results are here proposed, overaging effects on the advancing crack were neglected, considering uniaxial local creep rupture strain (ε_r) independent on the exposure time, but only related to the alloy and to the uniaxial specimen orientation (i.e. $\varepsilon_{rL} \neq \varepsilon_{rT}$). In the case of 2016 alloy ε_{rL} and ε_{rT} were set as 0.19 and 0.57, respectively, while in 2014 alloy forging, they were fixed as 0.44 and 0.28, respectively. The value of time to rupture (t_r) to be inserted in the equation of average strain rate was derived for both alloys by combining the power-law description of the minimum strain rate to the Monkman-Grant correlation, thus obtaining in all cases a power-law correlation between t_r and the applied stress σ. The $t_r - \sigma$ correlation was the same for uniaxial creep data in L and T direction of 2016 alloy forging. In 2014 alloy forging the $t_r - \sigma$ correlations in L and T directions were characterized by the same power-law index, but at the same stress level, t_r in L direction was 2.5 times longer than in T direction.

The above descriptions of the material properties were used to simulate the behavior of the CT specimens in creep crack growth tests. Simulations were repeated varying material, specimen orientation and applied load. Figure 5 shows the results for the cases of constant loads corresponding to initial K_I of 15, 18 and 20 MPa$\sqrt{m}$. The initiation time ($t_{initiation}$), assumed as the time at which the crack length increases of 0.2 mm, are also plotted in the case of the 2016 alloy.

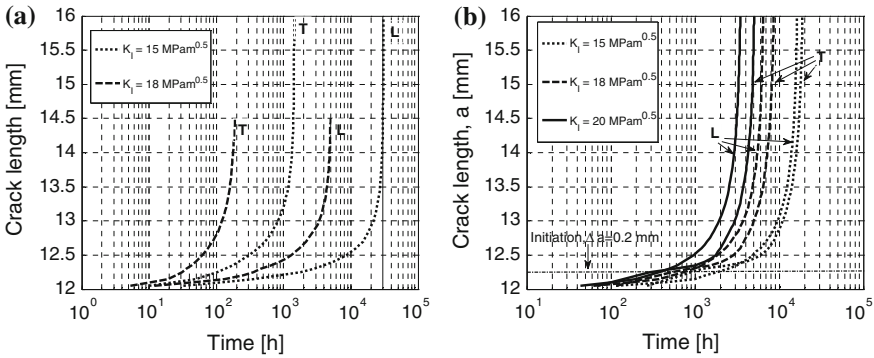

Fig. 5 Simulated crack propagation at 150 °C in planes perpendicular to the T or L directions of the forgings in CT specimens of 2014 (**a**) and 2016 (**b**) alloys. Curves corresponding to different initial K_I values are shown

The creep crack propagation behavior of the two forgings is significantly different, as could be reasonably expected on the basis of short- and long-term data. In 2014 alloy forging, propagation was significantly faster for cracks laying perpendicularly to T direction. On the contrary, only small differences are predicted for similar cracks propagating in the 2016 alloy forging. Further, in this case cracks advanced more easily when developing in a plane perpendicular to the L direction.

At present no creep crack growth test was concluded and these curves cannot be validated experimentally. Nevertheless, for the ongoing test, carried out on CR specimen (crack plane perpendicular to T direction) at initial $K_I = 15\,\mathrm{MPa}\sqrt{\mathrm{m}}$, the use of a potential drop calibration curve supplied a rough estimation of the crack length on the basis of its assumed initial length (to be properly measured at the end of the test) led to an initiation time close to 1000 h.

5 Including Overaging and Other Orientation Effects in the Model

The analyses of experimental creep data on 2014 alloy forgings demonstrated that both the creep strength and the creep ductility at relatively high stress levels, such as those experienced by the material zone ahead the tip of a propagating crack, are strongly affected by the time previously spent at high temperature. These experimental observations can be used to adapt the model to the more general case of age hardenable alloys, taking into account overaging effects. The idea is to substitute the uniaxial local creep rupture strain (ε_r) and time to rupture (t_t) (the ratio of which defines the average creep strain rate) with their correlations to equivalent times spent at the reference temperature. Taking into account (ε_r), Fig. 4b suggests the power-law correlation to the total equivalent time to rupture ($t_{T,r,tot}$): $\varepsilon_r = C(t_{T,r,tot})^m$. Further,

the effects of material ovaraging on ε_r can be taken into account by simply considering $t_{T,r,tot}$ as the sum of a part related to the time spent at high temperature by the component during its life (or by the CT specimen during the test, $t_{T,test}$) and of a constant contribution related to the initial heat treatment ($t_{T,aging}$). The description of equivalent creep rupture times of an overaged material can be obtained combining the power-law equation $t_{T,r,tot} = D^*(\sigma)^{-q}$, fitting experimental data in Fig. 2, to Eq. (2), where $t_{T,tot}$ and $t_{T,creep}$ are substituted by $t_{T,r,tot}$ and $t_{T,r,creep}$:

$$t_{T,r,creep} = t_{T,r,tot} - t_{T,aging} - t_{T,\exp} = D^*(\sigma)^{-q} - t_{T,aging} - t_{T,\exp} \tag{3}$$

The average strain rate of overaging Al alloys thus becomes:

$$\dot{\varepsilon}_A = \frac{\varepsilon_r}{t_r} = \left(\frac{C(t_{T,test} + t_{T,aging})^m}{D^*(\sigma)^{-q} - t_{T,aging} - t_{T,\exp}} \right) \tag{4}$$

where D, C, q and m are constants related to the material and to the specimen orientation.

Focusing on the case of the crack containing CT specimen tested at 150 °C directly after aging, $t_{T,aging}$ is a constant and $t_{T,test}$ simply corresponds to the test time, the identification in it of a time considered as of pure exposure at high temperature ($t_{T,exp}$) and of a second period where creep phenomena occur ($t_{T,creep}$) is not straightforward. Even considering that in points laying on the crack path the applied stress will progressively increases up to the final fracture, fixing a threshold stress or strain above which creep takes place seems not suitable to identify the exposure time, since material strength and ductility depend on the exposure time itself. The idea is to fix a limit to the sum of $t_{T,aging}$ and $t_{T,exp}$ in terms of the fraction f (for example f equal to 1/100, 1/1000…) of the total equivalent time leading to creep fracture under a given stress value (σ_{exp}). This corresponds to the definition of the following correlation between the limit exposure time and σ_{exp}:

$$t_{T,aging} + t_{T,\exp,\lim} = f^* D^*(\sigma_{\exp})^{-q} \tag{5}$$

In a specific point ahead of the crack tip, $t_{T,test}$ will be equal to $t_{T,exp}$ until the (increasing) stress level in that point reaches the σ_{exp} for the actual $t_{T,exp} = t_{T,exp,lim}$. Once this condition has been reached in this point, $t_{T,exp}$ will be kept at $t_{T,exp,lim}$ and $t_{T,test} = t_{T,exp,lim} + t_{T,creep}$. Points laying along the crack path will be characterized by progressively increasing $t_{T,exp,lim}$ and decreasing σ_{exp}. The above method to account for the overaging effects can be relatively easily implemented in the FEM simulation of the crack propagation by means of a user subroutine.

Another extension of the above model can be introduced to take into account different situations that can occur in axysimmetrical forging components within which a crack grows. The above mentioned model links the crack propagation behaviour to uniaxial plastic and creep properties normally to the crack plane. While the simulation can predict widely different situations of cracks advancing in the R-T or R-L planes (see Fig. 4), no difference would be found for cracks growing in different

directions within the same crack plane, such as for example in the case of CR- and CL-oriented CT specimens, where crack develops in the same plane along R and L directions, respectively. As explained before, no experimental data on the creep crack propagation are presently available to check differences in the propagation behaviour and mechanisms in differently oriented cracks. Nevertheless, previous fracture toughness tests and related microstructural investigations carried out at room temperature and at 130 °C on the same forged materials revealed that the distance between second phases along the crack path was the main microstructural feature affecting the crack propagation properties of the material [4]. Together with the plastic behavior of the matrix, these latter are significantly affected by test temperature and overaging.

A similar behavior is expected for the case of creep crack propagation. The microstructural feature affecting the crack propagation along different directions in the same crack plane can be here taken into account by means of growth direction-dependent multiaxial strain factor (MSF_{dir}) correlating the value of multiaxial failure strain to the uniaxial failure strain i.e. $\varepsilon_{r,m} = MSF^{*}_{dir}\,\varepsilon_r$. The form of the MSF_{dir} may be estimated using an appropriate model for void growth and coalescence in anisotropic material.

6 Conclusions

Experimental data on 2014 and 2016 alloy forgings confirmed significant effects of orientation and overaging on their creep behaviour. Data analyses in terms of equivalent times at a reference temperature allowed to describe the effects of prior exposure on the creep strength and ductility. The above data were included in a FE simulation of crack growth in differently oriented planes, characterized by a procedure based on the release of nodes when a critical damage level is locally reached. The proposed method can be slightly rearranged to include overaging effects and crack propagation along different directions within the same crack plane.

Acknowledgments The authors would like to acknowledge P. Bassani, D. Ripamonti, G. Vimercati, A. Fumagalli, M. Grandi and P. De Maria for their contribution in the experimental work.

References

1. Robinson, J.S., Cudd, R.L., Evans, J.T.: Mater. Sci. Techn. **19**, 143–155 (2003)
2. Djakovic, A., Basoalto, H.C., Dyson, B.F., McLean, M.: SIMS, Association of Metallurgical Engineers of Serbia **11**(4), 267–272 (2005)
3. Gariboldi, E.: In: Hirsch, J., Skrotsky, B., Gottstein, G. (eds.) Aluminium Alloys. vol. 2, pp. 1599–1606 (2008)
4. Gariboldi, E., Ripamonti, D., Signorelli, L., Vimercati, G., Casaro, F.: Metallur. Sci. Techn. **25**(1), 3–11 (2007)
5. Belloni, G., Gariboldi, E., Lo Conte, A., Tono, M., Speranzoso, P.: J. Testing Eval. **30**, 1–9 (2002)

6. Angella, G., Bassani, P., Gariboldi, E., Ripamonti, D.: In: Hirsch, J., Skrotsky, B., Gottstein, G. (eds.) Aluminium Alloys. vol. 1, pp. 1092–1067 (2008)
7. Bassani, P., Gariboldi, E., Ripamonti, D.: J. Therm. Anal. Cal. **91**, 29–35 (2008)
8. Bassani, P., Gariboldi, E., Ripamonti, D.: J. Therm. Anal. Cal. **87**, 247–253 (2007)
9. Du, Y., Chang, Y.A., Huang, B., Gong, W., Jin, Z., Xu, H., Yuan, Z., Liu, Y., He, Y., Xie, F.-Y.: Mater. Sci. Eng. **A363**, 140–151 (2003)
10. Casaro, F., Gariboldi, E.: Mater. Sci. Eng. **A462**, 384–388 (2007)
11. Hyde, C.J., Hyde, T.H., Sun, W., Becker, A.A.: Eng. Fract. Mech. **77**, 2385–2402 (2010)
12. Yatomi, M., Nikbin, K.M., Dowd, N.P.O.: Press. Vess. Piping **80**, 573–383 (2003)
13. Nikbin, K.: Mat. Sci. Eng. **A365**, 107–113 (2004)
14. Lo Conte, A.: In: Proceedings of ICF11, paper 5428, http://www.icf11.com/proceeding
15. Cocks, A.C.F., Ashby, M.F.: Metal Sci. **14**, 395–402 (1980)

Dislocation-Induced Internal Stresses

Peter Geantil, Benoit Devincre and Michael E. Kassner

Abstract Long-range internal stresses (LRIS) are widely suggested to exist in plastically deformed materials as a result of dislocation distribution heterogeneity and polarization. Important examples of plastically induced dislocation microstructures are cell and subgrain walls in monotonically deformed materials and edge-dislocation dipole bundles and walls in cyclically deformed materials. Evidence for internal stresses in dislocation microstructures was observed early and the existence of LRIS is commonly supposed responsible for important properties such as the Bauschinger effect in reversed and cyclic deformation. On the other side, other experiments including dipole separation observations and convergent beam electron diffraction experiments are less supportive of LRIS. This is why we recently revisited the question of LRIS using X-ray microbeam diffraction experiments for oriented monotonically and cyclically deformed Cu single crystals. From synchrotron radiation at the Advanced Photon Source it was possible to determine elastic strains in very small volumes within the dislocation cell interiors, and most recently, within the cell walls. These experiments clearly show the existence of LRIS in the dislocation cell structure albeit, at modest levels. The magnitude and statistical variation of these stresses are detailed, and further explored using dislocation dynamics simulations. Our new results are placed in the context of earlier experiments.

P. Geantil (✉) · M. E. Kassner
University of Southern California, Los Angeles, CA, USA
e-mail: geantil@usc.edu

B. Devincre
LEM, CNRS / ONERA, 29 avenue de la division Leclerc,
Chatillon Cedex 72 92322, BP, France
e-mail: devincre@onera.fr

M. E. Kassner
Office of Naval Research,Washington, DC, USA
e-mail: kassner@usc.edu

H. Altenbach and S. Kruch (eds.), *Advanced Materials Modelling for Structures*,
Advanced Structured Materials 19, DOI: 10.1007/978-3-642-35167-9_17,

1 Introduction

Plastic deformation in crystalline metallic materials is controlled at low and intermediate temperatures by dislocation glide. As dislocations move in their slip planes, they strongly interact with each other through stress fields and contact reactions. These long and short-range interactions (including thermally activated processes like cross-slip) cause the development of complex dislocation microstructures made of regions with high and low dislocation densities. In monotonic deformation, when multiple slip systems are active, the dislocation microstructure takes the from of low dislocation density volumes surrounded by dislocation dense walls. This structure is cellular in nature and fairly uniform in space. In single slip deformation, a different microstructure develops consisting of elongated clusters of dislocations. These clusters, made up of primarily edge dislocation dipoles and multipoles loops, result in bundles and braids and ultimately in persistent slip bands if the crystal is cyclically deformed.

What has long been discussed is the existence of long range internal stresses (LRIS) in parallel to dislocation patterning, and the influence of LRIS on the material mechanical properties. In this debate, a composite model was proposed by Mughrabi [1] and Pedersen et al. [2]. They presented the simple case where hard (high dislocation density walls) and soft (low dislocation density channels, or cell interiors) are compatibly deformed. Each component yields plastically at a different stress depending on the dislocation density and arrangement.

Figure 1 illustrates a simplified two dimensional dislocation cell. The crosshatched lines represent the simplified slip system consisting of two active slip planes. Dislocations present on these slip planes in the left panel accumulate at the walls. Some dislocations pass through the walls, while others are deposited onto the wall. The middle panel shows the effective sum of the dislocations gliding and being deposited onto the wall. The final structure allows for two things: The material deforms compatibly between the walls and cell interior, and the sum of the dislocations provide a tensile internal stress in the dislocation dense walls, and a compressive stress in the cell interiors.

In the past years, a number of experiments have been done in an attempt to measure the existence of LRIS:

- In-situ *TEM* experiments have been performed attempting to evaluate the existence of LRIS and resulting magnitudes. Morris and Martin [4] quenched a creep-deformed solid solution Al-Zn alloy. When cooling to ambient temperature, precipitates form that pin dislocations (and dislocation loops) in place. A comparison between dislocation curvature and the line tension bowing equation was applied and suggested enormous LRIS near dislocation walls, at 20 times the applied stress. Two influential experiments were conducted by Mughrabi [1] and Lepinoux and Kubin [5]. Internal stresses were assessed by measuring dislocation loop radii as a function of position within persistent slip band channels in cyclically deformed Cu single crystal. Observations confirmed that the dislocations were bowed more drastically near the dislocation walls than in the center of the channels and LRIS

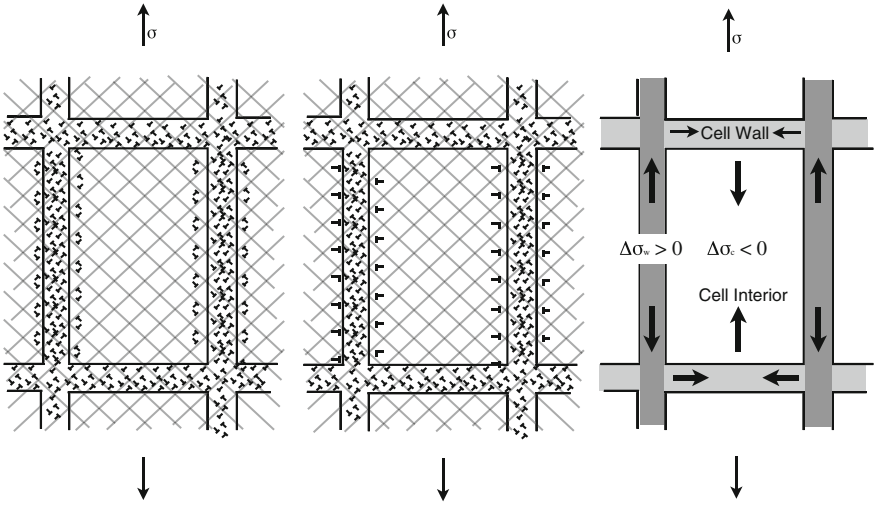

Fig. 1 The *left* diagram shows the accumulation of dislocations inside the walls as well as at the interface. The *second panel* shows the sum of the dislocations, allowing for compatible deformation of the walls and cell interiors, as well as a source of internal stress. The *third panel* shows the resulting internal stresses present in the microstructure [3]

were calculated at up to three times the applied stress near dipole walls. Corrections were later made by Mughrabi and Pschenitzka [6] reducing the value of LRIS to 1.3 times the applied stress.

- *CBED measurements.* Lattice parameters were measured in creep deformed samples. The subgrain boundaries of an aluminum sample and the subgrain cell walls of a copper poly-crystal were inspected using convergent-beam electron diffraction (CBED) [7]. Measurements of the lattice parameters showed no evidence of residual stress within the uncertainty of ±8 MPa (applied creep stress was 7 MPa) for the Al sample, and ±30 MPa (applied creep stress of 20 and 40 MPa) for the Cu sample. Internal stresses may not be resolved in such experiments if they are of the same order or less than the applied stress. Finally the areas where measurements were taken were thin, and surface relaxation effects may exist.
- *Dipole height measurements.* Cyclic deformation experiments on Al and Cu single crystals (oriented for single slip) deformed to about half the saturation stress by Kassner et al. [8] showed the average dipole heights in the presaturation microstructure are approximately independent of location, being equal in the dipole bundles and channels. This may suggest a uniform stress state across the microstructure, which means no significant LRIS exist. Small LRIS cannot be excluded from this as the stress to separate the widest dipoles in Cu is 2–3 times the applied stress. [8, 9]. CBED in the cyclically deformed Cu also showed no evidence of LRIS.
- *X-Ray line profile asymmetry.* During plastic deformation, the diffraction line profile of a crystalline material broadens and develops an asymmetric shape. In agreement with the composite model, this asymmetric peak is considered the sum of two

separate diffraction peaks. In the original Ungar et al. study [10], the sub-profiles were assumed symmetric, and values for the volume fraction of cell interiors and cell walls was obtained using TEM. The larger amplitude and narrower full-width half-maximum (FWHM) peak comes from the dislocation cell interiors, while the shorter, broader peak is a result of the cell walls. The average lattice parameter of each region was deduced from these sub-peaks. In a correction to the previous experiment, Ungar et al. [11] suggested values of $0.1\sigma_a$ in the cell interior and $0.4\sigma_a$ in the cell wall of the deformed copper single crystals.

2 X-Ray Microbeam Measurements

Recently, the development of a specialized micro-diffraction tool by Larson et al. [12] has been extremely important in the effort to characterize LRIS within deformed materials. It was used in a previously discussed experiment by Levine et al. [13] which provided valuable and novel insight into the nature of LRIS. The micro-diffraction setup has the ability to probe materials non-destructively with sub-micron spatial resolution, and measure lattice parameters in sub-micron sized volumes. Jakobsen et al. [14, 15] have also performed influential work with a transmission X-ray setup, measuring cell strains in polycrystalline pure Cu and looking at subgrain evolution in in-situ deformed single crystal Cu.

2.1 Methodology

The X-ray microbeam used here is focused down to roughly 0.5×0.5 microns using a Kirkpatrick-Baez (KB) setup. The setup consists of two parabolic orthogonal X-ray mirrors set at grazing incidence to the X-ray beam. The mirrors focus the beam in the x and y directions independently. A platinum wire is scanned in half micron steps across the sample, blocking diffracting beams with each step. Subtracting subsequent images allows for back solving of the spatial location of the diffracting material and provides the third dimension of resolution.

As an effect of plastic distortion heterogeneity, dislocation channels (in cyclically deformed) and cells (in monotonically deformed) in deformed samples diffract in many directions. Using a monochromatic beam, only cells meeting the Bragg condition will diffract, meaning they must have a specific orientation. To avoid this complication the experiment requires stepping the monochromator, selecting discrete values of λ in 2–3 eV (electron-Volt) steps over a range of 1–2 keV. Using this methodology, the Bragg condition will be met for each section of the dislocation microstructure and all crystallographic orientations will provide diffraction information.

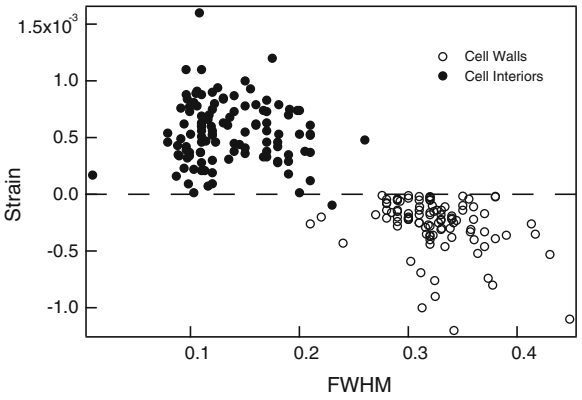

Fig. 2 Strain measurements associated with various dislocation cell wall and cell interior X-ray line profiles. The two groupings are clearly from dislocation cell interior and cell wall measurements

2.2 Results

A series of energy-wire scans were performed on 99.999 % pure, single crystal Cu, deformed in compression $\varepsilon = 0.28$ with a final flow stress of 210 MPa. All measurements were done using the axial 006 reflection. To obtain diffraction from each cell interior the energy was scanned over approximately 1 keV. With the setup, an uncertainty in measurements was calculated as $\Delta q/q = 1 \times 10^{-4}$. For copper, this leads to a maximum uncertainty in stress measurements of 7 MPa.

Once scans were completed, a total of 387 peaks and walls were analyzed. The data displayed in Fig. 2 compares the resulting strain measurements versus the FWHM. There are clearly two groupings of measurements: One relating to cell interiors under a tensile stress, and the other to cell walls under a compressive stress. The volume average internal stress in the walls is $0.1\sigma_a$, and $-0.1\sigma_a$ in the cell interiors.

Possible effects of the free surface in our measurements were also investigated. Over the range of depths probed (roughly 10 microns), no discernible trend in the internal stresses is observed. The stresses maintain the same range of values, when going deeper into the sample.

The strain data clearly have a large range of values. This tells us the strain variations within the cell walls and interiors is quite large, ranging from approximately -100 to 100 MPa. This spread of 200 MPa is comparable to the final applied flow stress of 210 MPa. Along with the strain information, we have the integrated intensities of the X-ray line profiles which, in the kinematic scattering regime [16], is proportional to the volume of diffracting material. We can therefore make calculations as to the statistical distribution of stresses and the volume averaged stresses within the sample. These data were reported recently in Levine et al. [16] and Fig. 3 shows a histogram of the distribution of strains found within the material.

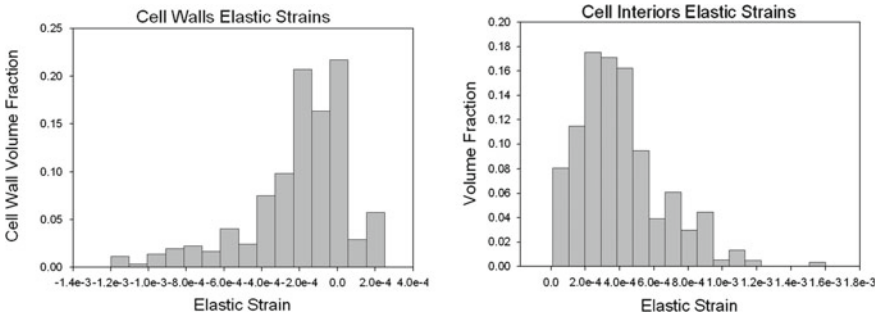

Fig. 3 Normalized histograms of the cell interior and wall stresses measured in the Cu single crystal sample. The volume averages of the internal stresses are roughly $0.1\sigma_a$ in the cell walls, and $-0.1\sigma_a$ in the cell interiors

TEM analysis of the cellular structure in the studied sample gives an estimation of wall material to cell interior material of 55 % to 45 % (±10 %) respectively. Using these numbers, and the measured strains, we found the integrated stress of the bulk measured volume to be 4 MPa. Given that our uncertainty in stress calculation is 7 MPa this cell interior versus wall partition is not surprising and consistent with mechanical equilibrium.

3 Dislocation Dynamics Simulation

Efforts to model the LRIS induced by the dislocation microstructure present in f.c.c. materials in multi-slip deformation has been successfully done in earlier studies [17, 18]. In these studies, dislocation dynamics (DD) simulations were used to reproduce the genesis of the dislocation microstructures at small plastic strain. Dislocation patterning is a systematic tendency observed in DD simulations and is produced by the short-distance and contact interactions between dislocations [19, 20]. Surprisingly, if LRIS do not necessarily contribute to the formation of dislocation patterning, they were found to automatically appear from structures like the dislocation cells. In the latter case, LRIS have been found in qualitative agreement with the composite model predictions [18].

The new simulations presented in this paper were performed using the DD code microMegas. Details regarding the basic principles of these three-dimensional simulations can be found in Devincre et al. [21, 22]. For the present calculations original shortcut procedures have been made to quickly develop a copper dislocation cell structure as close as possible to the one discussed in the previous section. The cell structure was then deformed at a flow stress of roughly 150 MPa, similar to that used in the microbeam measurements. During deformation, the structure was analyzed to examine plastic strain and internal stress.

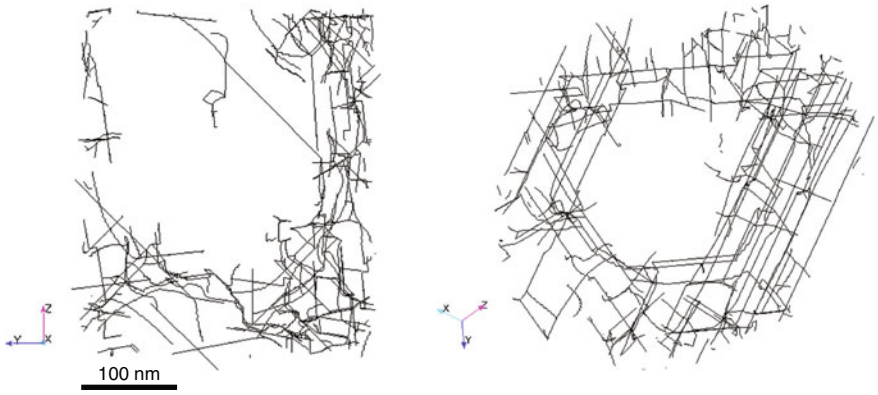

Fig. 4 Slices of the initial dislocation cell structure. The first is viewed along the [100] axis, and second along the [111] axis. Due to the periodic boundary conditions, the walls are only required to be on one side of the simulation box in each direction. A clearly defined cell interior is present

3.1 Methodology

The simulated copper volume element is roughly one cell volume with dimensions $0.4\,\mu\text{m} \times 0.3\,\mu\text{m} \times 0.33\,\mu\text{m}$ and periodic boundary conditions. This volume is first seeded with dislocation prismatic loops on four active slip systems with an initial density of $4 \times 10^{14}\,\text{m}^{-2}$. Then, to quickly generate a starting cell structure, a tensile load of 200 MPa is applied to only a section of the total simulation volume. During this step, dislocation interactions were 'turned off' in the loaded region, thus allowing the dislocations to glide out and form dislocation cell walls on its borders (where junctions and interactions occurred). Once a cell structure is formed, all interactions in the simulated volume are turned on and the dislocation microstructure is relaxed at zero applied stress to check the stability of the 3D dislocation network formed. At this step the total dislocation density has increased to $1 \times 10^{15}\,\text{m}^{-2}$. The microstructure resulting from this initial shortcut is shown in Fig. 4.

The following results were obtained after significant deformation of the Fig. 4 microstructure at a constant strain-rate, imposing approximately a tensile flow stress of 150–200 MPa (as dislocation density increased). During this simulation, the cell structure was stable and the dislocation density in the cell walls was continuously increasing.

3.2 Results

As deformation proceeds with the developed cell structure, a first observation is the emission of mobile dislocations from the cell walls. These dislocations travel through the cell interior, and are deposited on the opposite side, either at the wall interface, or

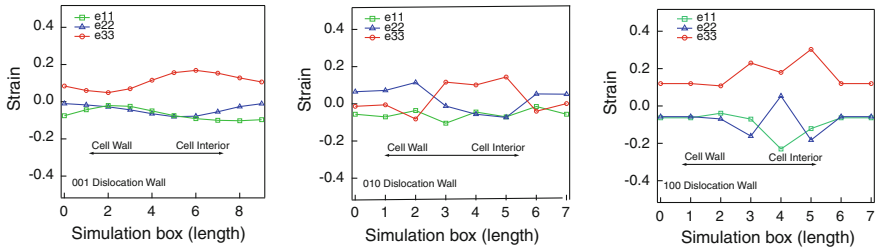

Fig. 5 Strain measurements for the e11, e22, and e33 strain tensor components evaluated in the cell walls and cell interior. The x-axis is spatial, with the dislocation walls being between roughly 0 and 3 (and due to the periodic boundary conditions 7 as well), and the remaining strain measurements coming from the cell interiors

inside the wall. Occasionally a dislocation may pass through the wall as well. Plastic deformation of this nature would, in principle, cause more plastic deformation in the cell interiors.

To measure the strains occurring in the cell interior relative to the cell walls, the simulated volume was first subdivided into $7 \times 7 \times 9$ boxes. The strain tensor was calculated for each box, and this information was used to look at the average strains in the cell walls and interior. Adjacent columns of boxes which went through one dislocation wall and the cell interior were averaged together and plotted. These plots are shown in Fig. 5. It's apparent that there is generally more plastic strain occurring in the cell interiors along the strain axis (the e33 component of the strain tensor) than in the cell walls. This finding is consistent with the composite model predictions.

In addition, the internal stresses were calculated within the microstructure. In the present calculations, the calculated LRIS is formed as the system moved toward equilibrium during the initial microstructure formation. Once a constant strain rate is imposed, the internal stresses fluctuated and gradually relaxed. Fig. 6 shows the internal stress calculation of a plane within the simulation cell after $\sim$0.5 % strain. The average stress in the cell interior region was roughly 10 % of the applied stress, in the opposite direction. The magnitude and sign of this stress is in accordance with the composite model, and microbeam measurements reported previously. This value was calculated considering all the dislocations in the simulated volume and one additional slice of dislocation replicas in the periodic crystal (i.e. a total volume of 27 simulation boxes). Increasing the periodicity further to account for more dislocation replicas did not alter the calculated stress.

4 Concluding Remarks

All of the microbeam measurements and DD simulation results confirm many of the assumptions and results of the composite model. The dislocation wall and interior stresses are of the correct sign, and the volume averaged stresses are in accordance

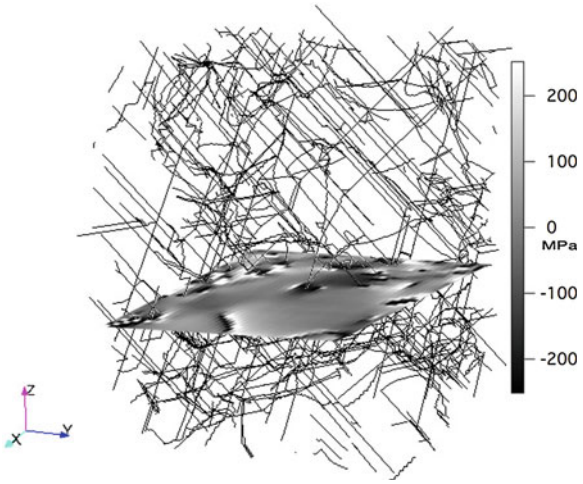

Fig. 6 The dislocation cell simulation volume with a contour showing the calculated LRIS perpendicular to the plane along the strain axis. The average internal stress of the cell interior in this slice is -19 MPa, which is roughly $-0.1\sigma_a$. This value is analgous to the volume averaged back stress measured in microbeam experiments

with the volume fraction of wall and interior material as seen in TEM images. Additionally, there does not appear to be a measurable surface effect on the internal stresses.

The movement and deposition of dislocations across the cell interior assumed in the composite model, appears to be confirmed by DD simulations. It allows for the cell interior to experience more plastic strain than the cell walls. This fact was further explored in Fig. 5, and shows all three walls experiencing smaller strains than the cell interior.

An important note mentioned previously, is the stability of the simulated structure. Through the entire simulation, the cell structure remained stable without any artificial pinning or constraints. The simulated dislocation structure was able to create LRIS similar to those measured by microbeam. This value is significantly smaller than those found in previous experiments.

Acknowledgments Two of the authors wish to acknowledge support from the NSF under OISE-0932413 and DMR-901838. Support from the LEM computing facilities at CNRS/ONERA is also acknowledged.

References

1. Mughrabi, H.: Dislocation wall and cell structures and long-range internal stresses in deformed metal crystals. Acta Metallurgica **31**(9), 1367–1379 (1983)

2. Pedersen, O.B., Brown, L.M., Stobbs, W.M.: The bauschinger effect in copper. Acta Metallurgica **29**(11), 1843–1850 (1981)
3. Mughrabi, H.: A two-parameter description of heterogeneous dislocation distributions in deformed metal crystals. Mater. Sci. Eng. **85**, 15–31 (1987)
4. Morris, M.A., Martin, J.L.: Evolution of internal stresses and substructure during creep at intermediate temperatures. Acta Metallurgica **32**, 1609–1623 (1984)
5. Lepinoux, J., Kubin, L.P.: In situ tem observations of the cyclic dislocation behaviour in persistent slip bands of copper single crystals. Philos. Mag. A **51**(5), 675–696 (1985)
6. Mughrabi, H., Pschenitzka, F.: Constrained glide and interaction of bowed-out screw dislocations in confined channels. Philos. Mag. **85**(26–27), 3029–3045 (2005)
7. Kassner, M.E., Perez-Prado, M.-T., Long, M., Vecchio, K.S.: Dislocation microstructure and internal-stress measurements by convergent-beam electron diffraction on creep-deformed cu and al. Metall. Mater. Trans. A **33**, 311–318 (2002)
8. Kassner, M.E., Wall, M.A.: Microstructure and mechanisms of cyclic deformation in aluminum single crystals at 77 k: Part ii. Metall. Mater. Trans. A **A(30)**, 777–779 (1999)
9. Kassner, M.E., Perez-Prado, M.-T., Vecchio, K.S., Wall, M.A.: Determination of internal stresses in cyclically deformed cu single crystals using cbed and dislocation dipole separation measurements. Acta Mater. **48**, 4247–4254 (2000)
10. Ungar, T., Mughrabi, H., Rönnpagel, D., Wilkens, M.: X-ray line-broadening study of the dislocation cell structure in deformed [001]-orientated copper single crystals. Acta Metall. **32**(3), 333–342 (1984)
11. Ungar, T., Mughrabi, H., Wilkens, M., Hilscher, A.: Long-range internal stresses and asymmetric x-ray line-broadening in tensile-deformed [001]-oriented copper single crystals: The correction of an erratum. Philos. Mag. A **64**(2), 495–496 (1991)
12. Larson, B.C., Yang, W., Ice, G.E., Budai, J.D., Tischler, J.Z.: Three-dimensional x-ray structural microscopy with submicrometre resolution. Nature **415**(6874), 887–890 (2002)
13. Levine, L.E., Larson, B.C., Yang, W., Kassner, M.E., Tischler, J.Z., Delos-Reyes, M.A., Fields, R.J., Liu, W.: X-ray microbeam measurements of individual dislocation cell elastic strains in deformed single-crystal copper. Nat. Mater. **5**(8), 619–622 (2006)
14. Jakobsen, B., Lienert, U., Almer, J., Poulsen, H.F., Pantleon, W.: Direct observation of strain in bulk subgrains and dislocation walls by high angular resolution three-dimensional x-ray diffraction. Mater. Sci. Eng. A **483**–**484**(0), 641–643 (2008). 14th International Conference on the Strength of Materials
15. Jakobsen, B., Poulsen, H.F., Lienert, U., Almer, J., Shastri, S.D., Sorensen, H.O., Gundlach, C., Pantleon, W.: Formation and subdivision of deformation structures during plastic deformation. Science **312**(5775), 889–892 (2006)
16. Levine, Lyle E., Geantil, Peter, Larson, Bennett C., Tischler, Jonathan Z., Kassner, Michael E., Liu, Wenjun, Stoudt, Mark R., Tavazza, Francesca: Disordered long-range internal stresses in deformed copper and the mechanisms underlying plastic deformation. Acta Mater. **59**(14), 5803–5811 (2011)
17. Devincre, B., Kubin, L.P.: Mesoscopic simulations of dislocations and plasticity. Mater. Sci. Eng. **A234–236**, 8–14 (1997)
18. Madec, R., Devincre, B., Kubin, L.P.: Simulation of dislocation patterns in multislip. Scr. Mater. **47**(10), 689–695 2002
19. Devincre, B., Kubin, L.P., Lemarchand, C., Madec, R.: Mesoscopic simulations of plastic deformation. Mater. Sci. Eng. A **309–310**, 211–219 (2001)
20. Gomez-Garcia, D., Devincre, B., Kubin, L.P.: Dislocation patterns and the similitude principle: 2.5d mesoscale simulations. Phys. Rev. Lett. **96**(12), 125503 (2006)

21. Devincre, B., Kubin, L.P., Lemarchand, C., Madec, R.: Mesoscopic simulations of plastic deformation. Mat. Sci. Eng. A **309–310**, 211–219 (2001)
22. Devincre, B., Madec, R., Monnet, G., Queyreau, S., Gatti, R., Kubin, L.P.: Mechanics of Nano-objects, chapter Modelling crystal plasticity with dislocation dynamics simulations: the 'microMegas' code. Presses de l'Ecole des Mines, de Paris (2011)

A Strain Rate Sensitive Formulation to Account for the Effect of γ' Rafting on the High Temperature Mechanical Properties of Ni-Based Single Crystal Superalloys

Jean-Briac le Graverend, Jonathan Cormier, Serge Kruch, Franck Gallerneau and José Mendez

Abstract The **Polystar** model was recently developed to fulfill the effects of possible fast microstructure evolutions occurring upon high temperature non-isothermal loadings. New internal variables were introduced in a crystal plasticity framework to take into account microstructure evolutions such as γ' dissolution/precipitation and dislocation recovery processes, and their effects on the creep behavior and creep life. Nevertheless, this model does not take into account one of the main microstructural evolutions occurring specifically at high temperature, the γ' directional coarsening. Fedelich and Tinga have already proposed models respectively based on a modification of the kinematic hardening and on the level of the von Mises stress. Nevertheless, if the Fedelich's model is implicitly strain rate sensitive, improvements have to be performed for strain controlled tests under fast conditions for which such a model may overestimates the γ channel width evolutions. A new formulation has been proposed to explicitly account for such a strain rate sensitivity and was successfully implemented in the **Polystar** model. The effect

J.-B. le Graverend (✉) · S. Kruch · F. Gallerneau
Onera, 29 avenue de la Division Leclerc, BP 72, 92322 Châtillon, France
e-mail: jean-briac.le_graverend@onera.fr

S. Kruch
e-mail: serger.kruch@onera.fr

F. Gallerneau
e-mail: franck.gallerneau@onera.fr

J.-B. le Graverend · J. Cormier · J. Mendez
Institut P', CNRS-ENSMA-Université de Poitiers, UPR CNRS 3346, ENSMA-Téléport 2, 1 avenue Clément Ader, BP 40109, 86961 Futuroscope Chasseneuil Cedex, France

J. Cormier
e-mail: jonathan.cormier@ensma.fr

J. Mendez
e-mail: jose.mendez@ensma.fr

H. Altenbach and S. Kruch (eds.), *Advanced Materials Modelling for Structures*, Advanced Structured Materials 19, DOI: 10.1007/978-3-642-35167-9_18,

of γ' rafting on the mechanical behavior is well reproduced for both cyclic and monotonic tension tests.

1 Introduction

Monocrystalline nickel base superalloys are widely used in the hottest parts of aero-engines or industrial gas turbines [1]. Blades made of these alloys operate for thousands of hours at temperatures as high as 1373 K (1100 °C) [2]. These alloys are chosen for their superior mechanical performances at high temperatures, in particular their creep resistance for uncooled components such as high pressure turbine blades of turboshaft engines for helicopters or small industrial gas turbines. These interesting properties result from the precipitation of a high volume fraction (close to 70 %) of the long-range ordered $L1_2$ γ' phase which appears as cubes coherently embedded in a face-centered cubic (fcc) solid solution γ matrix.

The recent development of "microstructure sensitive models" (i.e. in which internal variables representing microstructure are added) has been motivated by need to obtain a better predictivity of the mechanical behavior under conditions where microstructure is likely to evolve during the thermomechanical loading. Indeed, under such conditions, classical constitutive modelling approaches where temperature dependence is only taken into account by the temperature dependence of the material's parameters fails to predict transient mechanical responses of the alloy during thermomechanical loading [3]. For example, such a modelling approach is undertaken to account for the impact of the γ' morphology evolution under directional coarsening conditions on the mechanical properties of Ni-based single crystal superalloys [4, 5]. Indeed, when a single crystal superalloy has a negative γ/γ' misfit (coherency stress due to the difference between the lattice parameters of the γ phase and the γ' phase), a directional coarsening of the γ' precipitates occurs perpendicularly to the applied stress axis (see Fig. 1). This morphological evolution, more widely known under the "γ' rafting" denomination, usually takes place during the primary creep stage when the γ' phase has entirely coalesced and the γ channels become wider along the applied stress axis (see Fig. 1) [6–8].

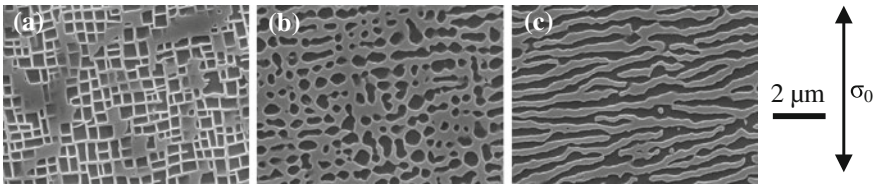

Fig. 1 γ' rafting during a creep test at 1050 °C/160 MPa: γ/γ' microstructure at the beginning of the experiment (**a**), after 4.7 h (during primary creep stage) (**b**) and after 9.4 h (beginning of secondary creep stage) (**c**). Note that the γ' phase appear in *dark*

In this article, a set of constitutive equations that is able to account for the rafting kinetics under isothermal and non-isothermal loading without requiring a computationally intensive microstructural analysis will be detailed. The **Polystar** model recently developed under a crystal plasticity framework was used to implement new evolution laws to account for a strain rate sensitivity of the γ' rafting [9].

2 Model Presentation

The **Polystar** model has been developed under a crystal viscoplasticity framework using the Méric & Cailletaud model as a basis [10]. It only considers the activity of octahedral slip systems since no experimental evidences of cube slip support the use of such systems [11]. A full description of the **Polystar** model is available elsewhere [9]. Only the equations devoted to account for the impact of γ' rafting will be discussed in the present article.

In this model first devoted to the creep behavior modelling, only non-linear isotropic hardening was considered for the evolution of internal stresses. The impact of γ' microstructural evolutions was taken into account using an Orowan stress which was introduced in the isotropic hardening using the following formulation:

$$r^s = \tau_0^s + b \times (Q + Q^*) \times \sum_j h_{sj} \rho^j + \sqrt{\frac{2}{3}} \frac{Gb}{w_{001}} \tag{1}$$

The Orowan stress is the last term of Eq. (1) while the first and the second terms of this equation represent respectively the initial critical resolved shear stress on each octahedral slip systems and the dislocation hardening through the isotropic state variable ρ^s and cross hardening by means of the interaction matrix [h]. Q is a temperature dependent material parameter which depends on the temperature and which corresponds to a steady-state dislocation hardening. Q^* is a transient hardening which is time and temperature dependent through the evolution of an associated internal variable a^* [9].

The initial expression of the γ-channel width along a [001] direction (w_{001}) was the following one:

$$w_{001} = \frac{a_0}{\delta} \times (f_l^{ml} - dtp \times f_s) \tag{2}$$

f_l and f_s represent respectively the volume fractions of large and hyperfine γ' precipitates of a bimodal distribution of γ' particles. dtp, a_0 and δ are model parameters.

It was decided to modify this equation to take into account the γ' microstructure degradation occurring at high temperature. This microstructure degradation basically consists in a homothetic particle growth due to Ostwald ripening ($w_{isotropic}$ in Eq. (3))

and in a directional coarsening (i.e. γ' rafting, see e.g. Fig. 1) under the action of mechanical applied stress ($w_{mechanic}$ in Eq. (3)).

Thus, a new expression of the γ-channel width evolution is proposed which both satisfy γ channels widening under pure isothermal conditions and during non-isothermal solicitations:

$$w_{001} = w_0 \times w_{thermic} \times (1 + w_{mechanic} + w_{isotropic}) \tag{3}$$

$w_{thermic}$ keeps the formulation proposed by Cormier and Cailletaud, as defined in their model [9]:

$$w_{thermic} = f_l^{ml} - dtp \times f_s \tag{4}$$

Moreover, the yield criterion was modified to take into account the kinematic hardening:

$$f = \left|\tau^s\right| - r^s \rightarrow f = \left|\tau^s - x^s\right| - r^s \tag{5}$$

2.1 Homothetic Growth

The driving force for isotropic coarsening is the reduction of the internal γ/γ' interfacial energy. For this reason, the $w_{\text{isotropic}}$ variable will only be time and temperature dependent and not deformation/stress state dependent.

Contrary to what has been proposed by Fedelich et al. [5], it was decided to use a cube root with a temperature dependent model parameter:

$$w_{isotropic} = \sqrt[3]{1 + \chi_0 e^{\frac{-U_t}{RT}} t} \tag{6}$$

In this equation, T is the temperature in Kelvin, U_t an activation energy, R the perfect gas constant and χ_0 a model parameter independent of the temperature.

Indeed, according to the Lifschitz-Slyozov-Walter (LSW) theory, particles coarsening controlled by diffusion processes is cube root dependent on time when the precipitate volume fraction is small [12]. This theory was developed for a binary system and for spherical particles which is not the case for single crystal superalloy. However, Ardell and Nicholson [13] have shown that the assumption of a diffusion-controlled growth stayed available in Ni-based single crystal superalloys. Moreover, Brailsford and Wynblatt [14] have shown that this type of particle growth led to an exponent equal to 3 in the LSW theory.

2.2 Directional Coarsening

Matan et al. have shown that a creep strain threshold was necessary to be overcome so that the γ' rafting process become significant and can proceeds, still in absence of any applied stress [15]. This threshold is equal to 0.10 ± 0.03 % at 950 °C for CMSX-4® alloy. Indeed, as Embury et al. [16] have shown, dislocations enhance the diffusion processes by pipe-line diffusion. Thus, once a given dislocation density at the γ/γ' interfaces is reached (corresponding to the relaxation of coherency stresses), the γ' rafting process occurs.

For this reason, it was chosen to develop a set of constitutive equations to account for γ' rafting dependence on the accumulated viscoplastic strain. Indeed, using the accumulated viscoplastic strain (v) as the internal variable driving the γ' rafting in Eq. (7), rafting will continue at high temperature even if the external load is removed.

Moreover, in case of tests with large viscoplastic strain amplitudes or fast thermomechanical solicitations, it was necessary to consider a strain rate dependence to be able to reproduce all types of test (i.e. cyclic loading. stress relaxation, tension tests, etc.). w_{mechanic} was hence given the following expression depending on the new internal variable (ξ) accounting for the strain rate sensitivity (Eq. (8)).

$$w_{mechanic} = \frac{K_0 \times \left(1 - e^{-\frac{t}{\tau_{diffusion}}}\right) \times \sqrt[3]{v}}{1 + \sinh^{-1}(\xi \times v_0)} \tag{7}$$

$$\dot{\xi} = \left(\frac{\dot{v}^2}{\xi_0} - \xi\right) \times \dot{v} - \left(\frac{\xi}{M}\right)^m \tag{8}$$

In these equations, M, m, ξ_0, v_0 and K_0 are temperature dependent model parameters.

The first term of Eq. (8) allows to smooth evolutions of $w_{mechanic}$ during fast strain controlled tests ($\dot{\varepsilon} \geq 10^{-4}\,\text{s}^{-1}$): the faster the test is, the higher ξ is, leading to a decrease of $w_{mechanic}$. The second term of Eq. (8) allows obtaining a recovery effect in case of mechanical tests for which a large strain rate range can be encountered.

$$\tau_{diffusion} = \frac{d^2}{2 \times D_{Al}^{\gamma'}(T)} \tag{9}$$

For the specific time of diffusion (Eq. (9)), it was chosen to consider the diffusion of aluminium in the γ' phase since it was observed that the rate limiting factor of γ' rafting is the diffusion of γ' elements in the γ' phase [17]. Hence, $D_{Al}^{\gamma'}$ is the diffusion coefficient of aluminium in the γ' phase (unit in m^2/s) and d is the diffusion mean free path for diffusion (unit in m) (see [18] and [19] for more details).

3 Results

3.1 Channel Width Calibrations

The parameters involved in the γ channel width evolutions given through Eqs. (6)–(9) were calibrated using interrupted creep tests and subsequent image analyses for several conditions of stress and temperature. Two examples of these evolutions at 1050 °C under 140 MPa and 1200 °C under 67 MPa are given in Fig. 2 for MC2 alloy.

It can be observed a rather good representation of the γ channel width evolution, within the scatter of the experimental results. Thus, the new formulation proposed to account for the γ' microstructure degradation through the increase in the γ channel width has been calibrated using creep tests under different temperature/stress conditions and is subsequently used to account for the impact of γ' coarsening on high temperature tensile or LCF properties.

3.2 Mechanical Behavior

The aim of the strain rate formulation is to obtain an evolution of γ channel width which allows to account for the impact of the (long term) γ' degradation on the mechanical properties. Indeed, the γ channel width does not evolve during fast tests and a minimum time (or plastic deformation) is required to trigger the γ' rafting. Thus, the predictivity of the modified version of the **Polystar** model including kinematic hardening and the microstructure degradation equations (Eq. (6)–(9)) was assessed using different mechanical tests.

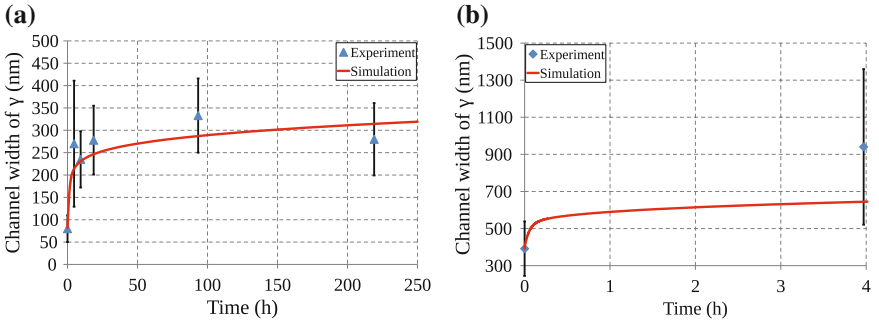

Fig. 2 Experimental evolutions of the γ channel width during creep tests at 1050 °C/160 MPa (**a**) and at 1200 °C/67 MPa (**b**) compared with the **Polystar** calibrations

3.2.1 Creep Tests

To get a first estimation of the potential benefits of this modified version of the **Polystar** model, three isothermal creep tests were studied (see Fig. 3).

To only consider the impact of the microstructure degradation on the mechanical behavior (i.e. primary and secondary creep stages), the damage equations of the **Polystar** model were inactivated. It can be observed in Fig. 3 that the longer the creep test, the better the predictability of the modified **Polystar** model. Indeed, it is observed a better prediction of the secondary creep strain rate for longer creep tests where the γ' rafting is the most pronounced.

Moreover, the strain rate formulation used for the γ channel width evolution gives an evolution of the Orowan stress in good agreement with Fedelich's results [5] (see Fig. 4. However, the plastic strain threshold observed by Matan et al. [18] equal to 0.1 ± 0.03 % necessary to trigger γ' rafting (and hence, the Orowan stress decrease) is not captured by our model, as for the Fedelich one.

The new formulation of the **Polystar** model was also validated using complex non-isothermal experiments. As an example, the predictivity of the model was assessed using a non-isothermal creep test including first an isothermal part at 1050 °C/120 MPa for 24 h and then a thermal cycling under 120 MPa which consists in 15 min/1050 °C–1 min/1100 °C–15 min/1050 °C–1 min/1150 °C repeated four

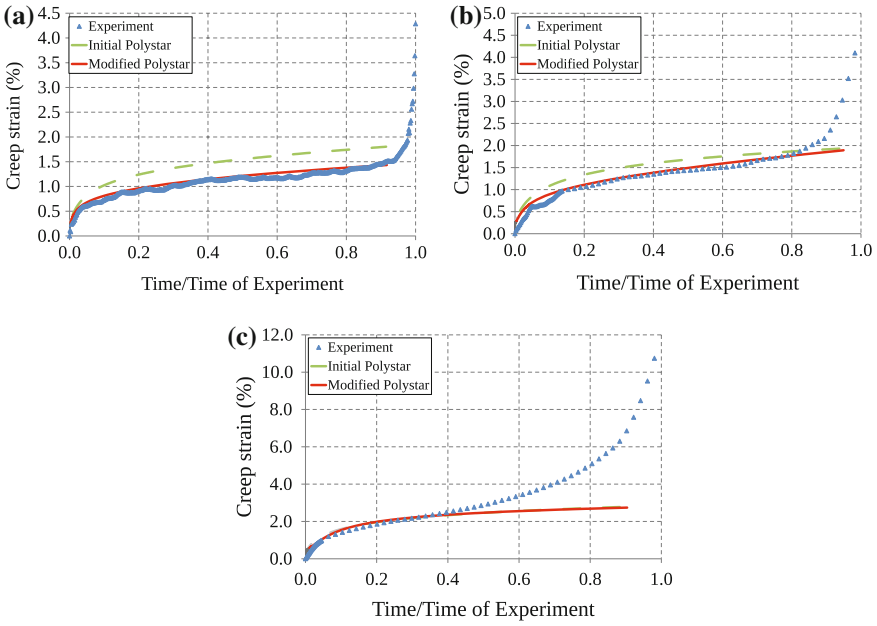

Fig. 3 Comparison between experiments and simulations for creep tests at 1050 °C/160 MPa (**a**), 1050 °C/180 MPa (**b**) and 1050 °C/230 MPa (**c**)

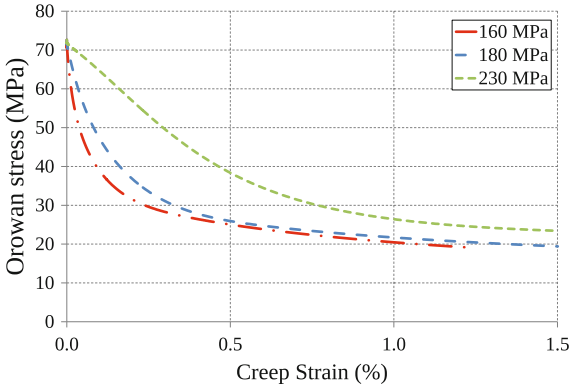

Fig. 4 Evolution of the Orowan stress as a function of creep strain for three different applied stresses at 1050 °C

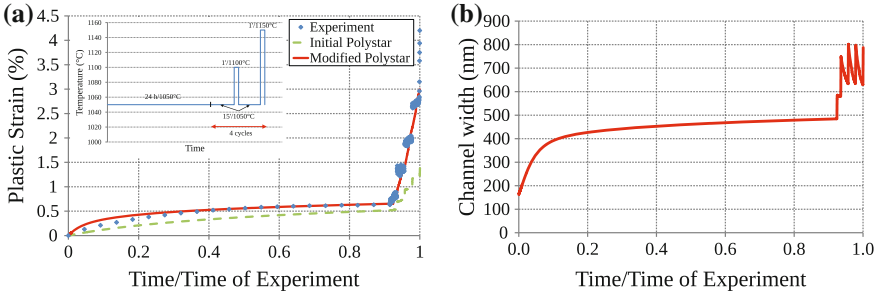

Fig. 5 Comparison between simulations and experiment during a non-isothermal creep test whose reference level is 1050 °C/120 MPa. The thermal and stress loading appears as insert in **a** while **b** shows the numerical evolution of the γ channel width during test

times (see Fig. 5). The modified ***Polystar*** model gives a better simulation especially for strain jumps during the non-isothermal section of the test (Fig. 5a). Indeed, it was evidenced that during such kind of non-isothermal experiments, the γ' rafting is very detrimental to the creep strain rate and life [20]. Such an impact is well captured by the present version of the model.

3.2.2 Cyclic Tests

Figure 6 shows the comparison between the experiments and simulations performed with the original and modified version of the model. Even if the stress levels do not corresponds perfectly with the experimental ones, the numerical evolutions of γ channel width are in good agreement with what has been observed experimentally. Indeed, as shown by Gaubert [21] for the AM1 alloy at 950 °C, a slow cyclic test ($\mathrm{d}\varepsilon/\mathrm{dt} \leq 10^{-5}\,\mathrm{s}^{-1}$) with a fully reversed strain cycling leads to microstructural

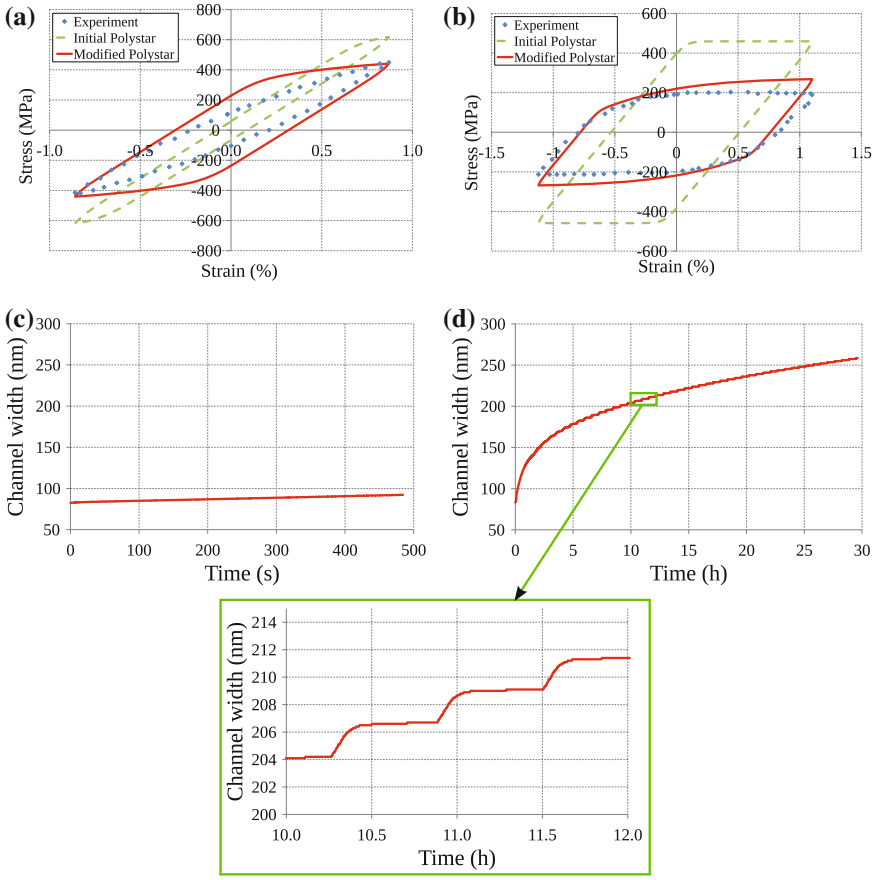

Fig. 6 Comparison between experiments and simulations for two LCF conditions using different strain rates and strain amplitudes at 1050 °C: 14th cycles at 10^{-3} s^{-1} (**a**) and 24th cycles at 10^{-5} s^{-1} (**b**). **c** and **d** represent respectively the numerical evolution of γ channel width presented in **a** and **b**

evolutions characterized by a 45° orientation of the γ' rafting with respects to the tension/compression axis. Hence, for a same number of LCF cycles, the γ channel width will be smaller in case of a fast mechanical cycling test compared to a slow cycling one.

3.2.3 Tensile Tests

Two strain rates were also investigated for tensile tests (10^{-3} and 10^{-5} s^{-1}) to analyze the model sensitivity to the strain rate (see Fig. 7).

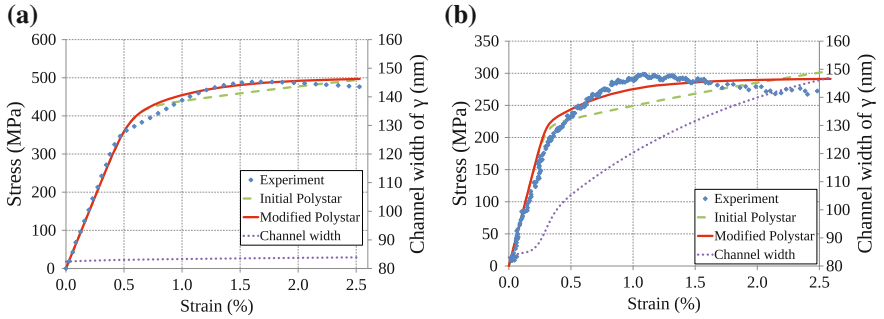

Fig. 7 Comparison between experiments and simulations during tensile tests at 1050 °C:10^{-3} s^{-1} (**a**) and 10^{-5} s^{-1} (**b**). *Purple curves* represent the evolution of γ channel width during simulations

Modifications bring to the model slightly improve the modelling of the tensile behavior.

Moreover, a comparison between experiment and simulations for a tensile test under variable strain rate shows that the modified version of the **Polystar** model provides a better description of the viscoplastic part. When the strain rate decreases from 10^{-3} to 10^{-5} s^{-1}, the experimental decrease of stress is equal to 145 MPa whereas the initial **Polystar** and the modified **Polystar** gives respectively 195 and 175 MPa.

4 Conclusion

The strain rate sensitive formulation developed to account for the effect of γ' rafting on the high-temperature mechanical properties of Ni-based single crystal superalloys gives results in good agreement with experiments over a wide range of strain rate: from 10^{-3} to 10^{-8} s^{-1}.

The consideration of microstructural evolutions was successful in the prediction of the non-isothermal creep behavior after a γ' microstructure degradation.

Thus, this new formulation is an advanced modelling tool for the prediction of both microstructural evolutions at high-temperature for Ni-based single crystal superalloys and their impact on the mechanical properties.

Acknowledgments The authors are particularly grateful to Turbomeca-SAFRAN group for providing the material and to the DPAC (Direction des Programmes Aéronautiques et de la Coopération) for its financial support. This work is conducted under a French program involving Snecma-SAFRAN group, Turbomeca-SAFRAN group, ONERA, CNRS laboratories (Mines Paris Tech, Institut P'-ENSMA, LMT-Cachan, LMS-X, CIRIMAT-ENSIACET) and CEAT.

J.-B. le Graverend is also grateful to D. Pacou, V. Bonnand and R. Degeilh for stimulating discussions.

References

1. Caron, P., Khan, T.: Mater. Sci. Eng. **61**, 173–184 (1983)
2. Reed, R.C.: The Superalloys: Fundamentals and Applications. Cambridge University Press, Cambridge (2006)
3. Cailletaud, G.: Doctoral Thesis. Université Pierre et Marie Curie, France (1979)
4. Tinga, T., Brekelmans, W.A.M., Geers, M.G.D.: Comp. Mater. Sci. **47**, 471–481 (2009)
5. Fedelich, B., Künecke, G., Epishin, A., Link, T., Portella, P.: Mater. Sci. Eng. A **510–511**, 273–277 (2009)
6. Henderson, P., Berglin, L., Jansson, C.: Scripta Mater. **40**, 229–234 (1999)
7. Sass, V., Glatzel, U., Feller-Kniepmeier, M.: Acta Mater. **44**, 1967–1977 (1996)
8. Shui, J., Tian, S., Jao, T., Hu, Z.: Mat. Sci. Eng. A **418**, 229–235 (2006)
9. Cormier, J., Cailletaud, G.: Mater. Sci. Eng. A **527**, 6300–6312 (2010)
10. Méric, L., Poubanne, P., Cailletaud, G.: J. Eng. Mater. Technol. **113**, 162–171 (1991)
11. Vattré, A., Devincre, B., Roos, A.: Acta Mater. **58**, 1938–1951 (2010)
12. Lifshitz, I.M., Slyozov, V.V.: J. Phys. Chem. Solids **19**, 35–50 (1961)
13. Ardell, A.J., Nicholson, R.B.: J. Phys. Chem. Solids **27**, 1793–1804 (1966)
14. Brailsford, A.D., Wynblatt, P.: Acta Metall. **27**, 489–497 (1979)
15. Matan, N., Cox, D.C., Rae, C.M.F., Reed, R.C.: Acta Mater. **47**, 2031–2045 (1999)
16. Embury, J.D., Deschamps, A., Brechet, Y.: Scripta Mater. **49**, 927–932 (2003)
17. Reed, R.C., Cox, D.C., Rae, C.M.F.: Mater. Sci. Tech. **23**, 893–902 (2007)
18. Matan, N., Winand, H.M.A., Carter, P., Karunaratne, M., Bogdanoff, P.D., Reed, R.C.: Acta. Mater. **46**, 4587–4600 (1998)
19. le Graverend, J.-B., Cormier, J., Gallerneau, F., Paulmier, P.: Adv. Mater. Res. **278**, 31–36 (2011)
20. Cormier, J., Jouiad, M., Hamon, F., Villechaise, P., Milhet, X.: Phil. Mag. Lett. **90**, 611–620 (2010)
21. Gaubert, A.: Ph.D. Thesis. Mines Paris-Tech., France (2009)

An Overview of Small Specimen Creep Testing

T. H. Hyde, W. Sun and C. J. Hyde

Abstract In this paper, some commonly used small specimen creep testing methods, including sub-sized uniaxial creep testing, impression creep testing, small punch creep testing, small ring creep testing and small two bar creep testing, are briefly reviewed. Firstly, the reference stress method and the concept of equivalent gauge length (EGL) are described; these form the basis for processing and interpreting the data from small specimen creep tests. Then, the performance and capability of each of these small specimen creep test techniques are discussed and their relative advantages and limitations, for specific practical applications, are assessed. In particular, the suitability of each of the methods for determining "bulk" material properties is described and it is shown that an appropriate test type can be chosen for each particular case. Typical examples of the application of the small specimen creep test methods, in determining creep deformation and rupture life data, are given. Finally, the future possibilities for the exploitation of small specimen creep test techniques are briefly considered.

1 Introduction

Power plants and chemical plants may operate at elevated temperatures for extended periods of time, e.g. more than 30 years. During this time, the material used in the construction of the plants degrades and the creep strength of the material reduces. NDT and small specimen test techniques are used to sample and test the material. For this reason, various small or miniature specimen test methods have been developed and used (e.g. [1]). For example, small punch tests (e.g. [2, 3]), which can be performed at room and elevated temperatures, have been used to obtain the elastic-plastic and creep behaviour of some materials. Alternatively, test methods such as the impression creep test and the small ring creep test methods [4–7], the latter of

T. H. Hyde (✉) · W. Sun · C. J. Hyde
The University of Nottingham, Nottingham, UK
e-mail: thomas.hyde@nottingham.ac.uk

H. Altenbach and S. Kruch (eds.), *Advanced Materials Modelling for Structures*,
Advanced Structured Materials 19, DOI: 10.1007/978-3-642-35167-9_19,

which is suitable for testing highly creep resistant materials [7], have been developed and used to determine the secondary creep behaviour of materials. The latest work on small specimen creep testing involves the development of specimen types which are suitable for obtaining creep rupture data (e.g. [8]). The small test specimens used for these types of tests can be obtained from small button-shaped (scoop) samples (~25 mm in diameter and 2–4 mm in thickness), which are removed, for example, by a non-destructive sampling technique [9].

Small specimen creep testing has become increasingly attractive because some power plant components are now operating beyond their original design life, and economic, "non-invasive" and reliable testing techniques are required when performing remaining life evaluations (e.g. [10, 11]). The ability to measure creep properties from a small volume of material has the potential to, rapidly and economically, support the development of new high temperature, exotic alloys (e.g. [12]). Also, data from small volumes of materials have a direct input into remaining life and ranking studies [5, 13], thereby improving the accuracy of plant/component life prediction. Such data can be used to generate creep constitutive laws for weld materials and for local structures generated during the welding process (e.g. [14, 15]). However, each of the specimen types has its own unique advantages and disadvantages and it may not always be obvious which one is the most appropriate test method to be used for a specific application.

This paper contains an overview of small specimen creep testing methods, their practical applications and the requirements for future development of small specimen creep testing techniques.

2 Theoretical Basis for Data Correction

2.1 Creep Deformation and Reference Stress Method (RSM)

In general, the principle of converting the non-conventional, small specimen creep test data to the corresponding uniaxial data is based on the inverse application of the reference stress method. For some components and loading modes, it is possible to obtain analytical expressions for steady-state creep deformation rate, (e.g. [16–18]). For components made from a material obeying Norton's power law, i.e., the general form of the solution is:

$$\dot{\Delta}_{ss} = f_1(n) f_2(dimensions) B \sigma_{nom}{}^{n} \tag{1}$$

where $f_1(n)$ is a function of the stress index, n, f_2(dimensions) is a function of the component dimensions and σ_{nom} is a conveniently determined nominal stress for the component and loading.

$$\dot{\Delta}_{ss} = \frac{f_1(n)}{\alpha^n} f_2(dimensions) B(\alpha\sigma_{nom})^n \tag{2}$$

Choosing α $(= \eta)$ so that $f_1(n)/(\eta)^n$ is independent (or approximately independent) of n, then Eq. (2) can be further simplified to:-

$$\dot{\Delta}_{ss} \approx D\dot{\varepsilon}^c(\sigma_R) \tag{3}$$

where D is the so-called reference multiplier [$D = (f1(n)/(\eta)^n)f_2(\text{dimensions})$] and $\dot{\varepsilon}^c(\sigma_R)$ is the creep strain rate obtained from a uniaxial creep test at the so-called reference stress, σ_R $(= \eta\sigma_{nom})$. The reference multiplier, D, has units of length, and can generally be defined by $D = \beta d$, where d is a conveniently chosen "characteristic" component dimension. Therefore, if the values of η and β are known, for the known loading mode and component dimensions, the corresponding equivalent uniaxial stress can be obtained from the expression $\sigma_R (= \eta\sigma_{nom})$, and the corresponding.

2.2 Determination of Reference Parameters

If an analytical solution can be obtained, substituting two values of n into the expression $f_1(n)/\eta^n$ and equating the two resulting expressions allows the value of η to be determined. Hence, σ_R $(= \eta\sigma_{nom})$ and D can be obtained. This approach was proposed by MacKenzie [19]. However, analytical solutions only exist for a small number of, usually, relatively simple components and loadings.

If, for example, computed solutions, using the finite element method, are obtained for a creep problem, for several n values, but keeping all other material properties, loading and component dimensions the same, then σ_R can be obtained. This is done by guessing several values of α, normalising the steady-state value of displacement rate, $\dot{\Delta}_{ss}$, with respect to $B(\alpha\sigma_{nom})^n$ and hence finding the value of α which renders $[\dot{\Delta}_{ss}/(B(\alpha\,\sigma_{nom})^n)]$ independent of n (i.e. $\alpha = \sigma_R = \eta$). This process is most easily visualised by plotting $\log[\dot{\Delta}_{ss}/(B(\alpha\sigma_{nom})^n)]$ against n, for various values of α, as illustrated in Fig. 1. It can be seen that the straight lines produced, using all of the α values, have approximately the same intercept on the log axis. This intercept is equal to the logarithm of the reference multiplier, D.

2.3 Equivalent Gauge Length (EGL)

For a conventional uniaxial creep test, the creep strain at a given time is usually determined from the deformation of the gauge length (GL). If the gauge length elongation is Δ^c and the elastic portion is neglected, then

$$\varepsilon^c \approx \frac{\Delta^c}{GL} \tag{4a}$$

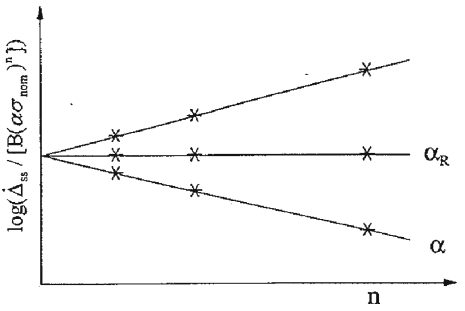

Fig. 1 Schematic diagram illustrating a method which can be used to obtain reference parameters from FE analysis

For non-conventional small specimen creep tests, an equivalent gauge length (EGL) [6, 7] can be defined, if the measured creep deformation can be related to an equivalent uniaxial creep strain, in the same form as that of Eq. (4a), i.e.

$$\varepsilon^c \approx \frac{\Delta^c}{EGL} \tag{4b}$$

The EGL is related to the dimensions of the specimen and in some cases may be related to the time-dependent deformation of the test specimen. The creep strain and creep deformation given in Eq. (4b) may be presented in a form related to the reference stress, σ_R, i.e.

$$\varepsilon^c(\sigma_R) \approx \frac{\Delta^c}{D} \tag{5}$$

in which D ($=\beta$d) is the reference multiplier, which is, in fact, the EGL for the test. In some cases, the geometric changes, which occurs due to the time-dependent deformation of the component, are small (e.g. for impression creep tests), and in such cases, the effects of geometric changes on D (EGL) can be neglected.

3 Small Specimen Creep Testing Methods

3.1 Sub-Sized Uniaxial Creep Test

"Conventional", sub-sized, "uniaxial" specimens (e.g. [20]), Figs. 2a and 3a, have been used for creep testing. Small cylindrical specimens, typically 1.2–3 mm in diameter, were electron beam welded onto conventional end pieces. Data obtained were compared with those of conventional full size creep tests; the two sets of data compared very favourably. Provided grain sizes are not too large, specimen diameters as small as 1 mm can be used to produce "bulk" material creep properties. Small

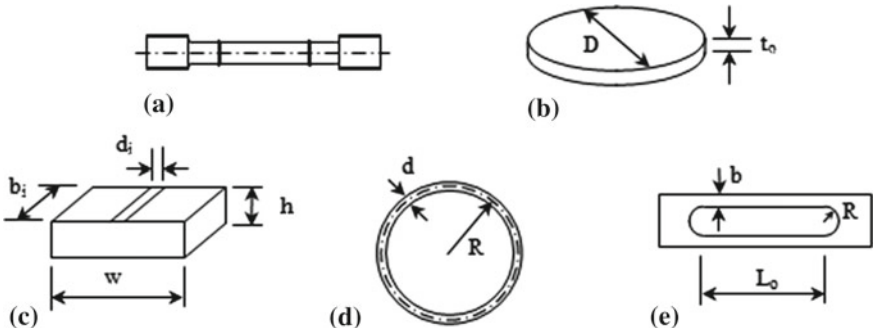

Fig. 2 Small creep test specimens: **a** Sub-size uniaxial specimen (GL ≈ 5–12 mm; d_{GL} ≈ 1–3 mm); **b** SPT specimen (D ≈ 8 mm; t_o ≈ 0.5 mm); **c** ICT specimen (w = b_i ≈ 10 mm; d_i ≈ 1 mm; h ≈ 2.5 mm); **d** SRT specimen (R ≈ 5 mm, d ≈ 1 mm and depth b_o ≈ 2 mm); and **e** TBT specimen (L_o ≈ 5–10 mm; b ≈ 1–2 mm; R ≈ 2–3 mm; thickness d ≈ 1–2 mm)

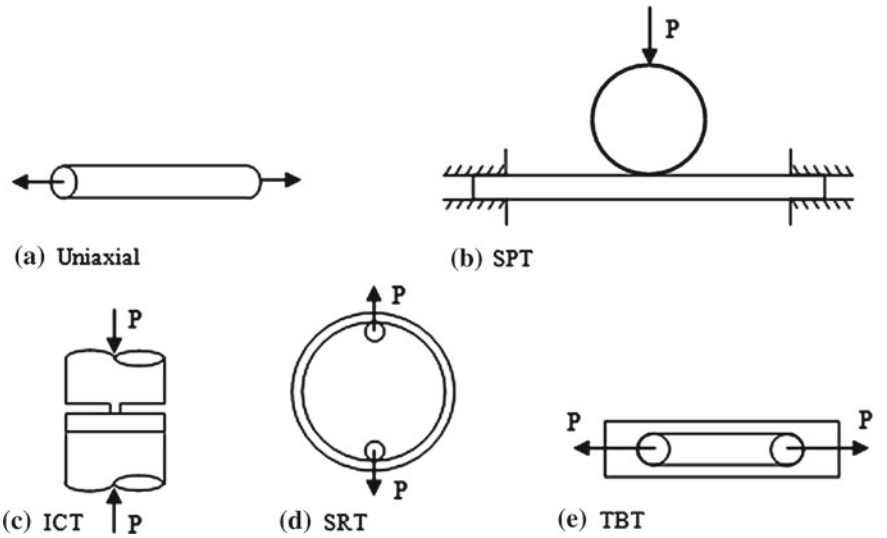

Fig. 3 Schematics diagrams showing the small specimen loading arrangements: **a** Uniaxial; **b** SPT; **c** ICT; **d** SRT; and **e** TBT

gauge lengths (<10 mm) can significantly reduce strain measurement sensitivities compared to conventional creep test specimens and can make strain measurements sensitive to relatively small temperature variations. The effects of specimen misalignment are greater when specimen diameters are small. In addition, specimen manufacture could be more complicated and more expensive than for conventional "full size" specimens.

3.2 Impression Creep Test (ICT)

The impression creep testing technique involves the application of a steady load to a flat-ended rectangular indenter, Figs. 2c and 3c, placed on the surface of a material at elevated temperature, and the small load-line displacement is measured. The displacement-time record from such a test is related to the creep properties of a relatively small volume of material in the immediate vicinity of the indenter. Tests are usually performed with a constant load level, at a fixed temperature. For the rectangular indenters, the reference stress approach has been used as the basis [4] for determining the corresponding equivalent uniaxial stress, σ, and creep strain, ε^c. These are related to the mean indenter pressure, $\bar{p}$, and creep displacement, Δ^c, via relationships [4]:-

$$\sigma = \eta \bar{p} \tag{6a}$$

$$\varepsilon^c = \frac{\Delta^c}{\beta d_i} \tag{6b}$$

The η and β in Eq. (6) are non-dimensional conversion factors. The η and β values for the recommended geometry ($w \times b_i \times h = 10 \times 10 \times 2.5$ mm) are $\eta \approx 0.4$ and $\beta \approx 2$ [4], for an indenter width of $d_i = 1$ mm. These are independent of material properties and do not vary with impression depth provided Δ^c is relatively small compared to the specimen thickness, h. The technique has been used for a wide range of materials (e.g. low alloy ferritic CrMoV steels, stainless steels, high chromium martensitic steels such as P91 and T91 [21], and P92). A typical set of data obtained from such tests for a 1/2 CrMoV steel is shown in Fig. 4. The slight fluctuations in the data are mainly caused by temperature variations within the furnace and within the laboratory. However, it can be seen that these variations are typically well within $\pm 1 \mu$m.

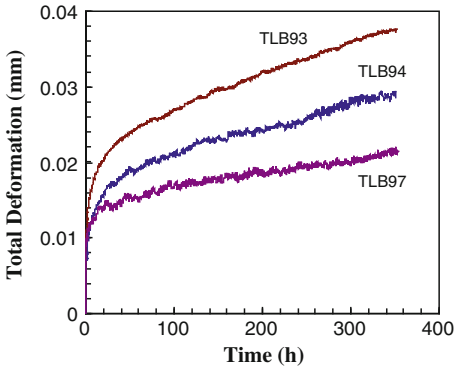

Fig. 4 Impression deformations with time at 90 MPa and 600 °C obtained from ex-service 1/2CrMoV steam pipe samples

3.3 Small Punch Creep Test (SPT)

The small punch creep test involves the application of a central load, through a spherical punch or a ball, to a thin disc, at high temperatures. A typical small punch test specimen and experimental set-up are shown in Figs. 2b and 3b, respectively; typical specimens measure 8 mm in diameter and 0.5 mm in thickness (e.g. [2]). The test involves the measurement of relatively large deformations, producing a deformation curve leading to fracture. The fact that fracture occurs is a particularly attractive feature of this type of test as the possibility of estimating the creep rupture data for the material exists. Empirical relationships between the applied load, P, the "membrane stress", σ, the equivalent strain at the edge of contact, ε, and the total deformation, Δ, have been obtained. For the case of $a_p = 2.0$ mm and $R_s = 1.25$ mm, the P/σ ratio and the strain, ε, for $\Delta > 0.8$ mm, are given by [15, 22]:-

$$P/\sigma = 1.72476\Delta - 0.05638\Delta^2 - 0.17688\Delta^3 \tag{7a}$$

$$\varepsilon = 0.17959\Delta + 0.09357\Delta^2 + 0.00440\Delta^3 \tag{7b}$$

The variation of the maximum P/σ, with a_p, R_{sp} and t_o, for $\Delta > 0.8$ mm, has been obtained and this leads to an expression for σ of the form:-

$$\sigma = \frac{0.3}{K_{sp}} \frac{{Pa_p}^{0.2}}{R_s^{1.2} t_o} \tag{8}$$

where a_p, R_s and t_o are the radius of the unclamped region of the disc between the supports, the radius of the punch and the initial thickness of the disc, respectively; K_{sp} is a non-dimensional correlation factor, which is determined empirically for the particular material. The units for Eqs. (7b) and (8) are: dimensions and deformation in mm, stress in MPa and force in N. Typical creep deformation versus time curves are shown in Fig. 5, which exhibits similar behaviour to that of typical uniaxial curves,

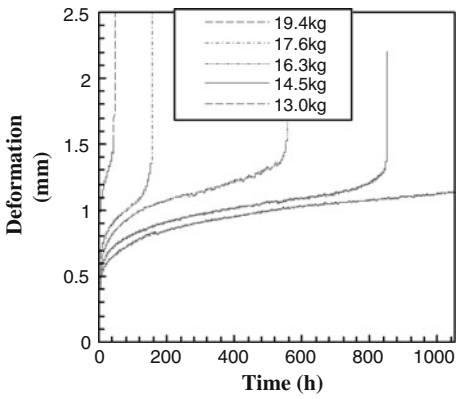

Fig. 5 Typical small punch test data for a P91 steel at 650 °C

i.e. there appears to be "primary", "secondary" and "tertiary" regions. However, a high level of local plasticity occurs at the start of the test, which could have a significant effect on the material, and therefore, the subsequent "creep dominant" deformation.

3.4 Small Ring Creep Test (SRT)

This small specimen type (patent application PCT/GB2008/001547) is an elliptical ring (a particular case of which is that of a circular ring), diametrically loaded in tension, as illustrated in Figs. 2d and 3d. Load-line deformation versus time curves are obtained during the test. It is designed to be "flexible" to enable small strains to be related to relatively large deformations. However, the deformations do not significantly affect the conversion parameters, i.e. η and β, which enables highly accurate secondary creep properties to be obtained.
The steady-state creep solution for the load-line deformation rate, $\dot{\Delta}_V$, of an elliptical ring, obeying a Norton's law ($\dot{\varepsilon}^c = B\sigma^n$), has been obtained, based on the principles of virtual complimentary work and stationary complimentary energy. The conversion relationships (η and β) for a range of geometries have been obtained by use of the reference stress approach. Detailed analytical procedures have been reported [6]. The main relationships are:

$$\dot{\varepsilon}^c(\sigma_{ref}) = \frac{d}{4ab\beta}\dot{\Delta}_V \tag{9a}$$

$$\sigma_{ref} = \eta\frac{Pa}{b_o d^2} \tag{9b}$$

For a circular ring (a = b = R), Eq. (9) become:-

$$\dot{\varepsilon}^c(\sigma_{ref}) = \frac{d}{4R^2\beta}\dot{\Delta}_V \tag{10a}$$

$$\sigma_{ref} = \eta\frac{PR}{b_o d^2} \tag{10b}$$

The test results for circular (a/b = 1) and elliptical (a/b = 2) rings, with R/d = 5, for a P91 steel at 650 °C, with a range of equivalent uniaxial stresses, are shown in Fig. 6.

3.5 Small Two-Bar Specimen Creep Test

A new small specimen test type, suitable for use in obtaining both uniaxial creep strain rate data and creep rupture life data, is shown in Figs. 2e and 3e [8]. The specimen has a simple geometry and can be conveniently machined and loaded

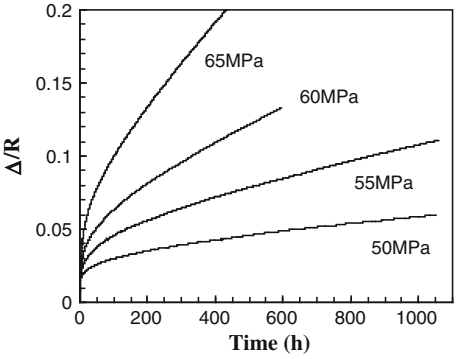

Fig. 6 Deformation (Δ/R) versus time curves obtained from circular rings for a P91 steel at 650 °C

(through pin-connections) for testing. Conversion relationships between the applied load and the corresponding uniaxial stress, and between the measured load-line (pins) deformation, and the corresponding uniaxial minimum creep strain rate, have been obtained, based on the reference stress method. The η-value (≈1) is found to be practically independent of dimension ratios, and the β-value varies with dimension ratios, and for $L_o/b = 4.5$ and $R/b = 1.25$, $\beta = 1.46$ [8]. Test results obtained from the two-bar specimens, for a P91 steel, at 600 °C, Fig. 7, have been used to validate the test method. It can be seen that the deformation curves obtained from the two bar test specimens are the same as those for a typical uniaxial specimens.

4 Application of Small Specimen Creep Testing

4.1 Some Practical Aspects of Small Specimen Creep Testing

Production of test specimens involves extraction of material samples (using the scoop technique, for example) and machining them to make the specimens. Depending on

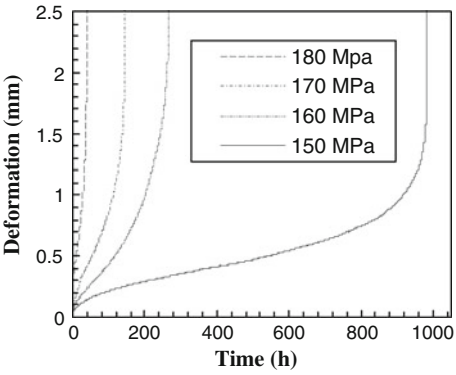

Fig. 7 Deformation versus time curves obtained from two bar specimens for a P91 steel at 600 °C

the accessibility of the site from which the sample is to be extracted, etc., and the production of specimens can be a costly process. However, the overall production costs of the ICT, SRT and SPT specimens are comparable to the costs associated with the production of standard uniaxial creep test specimens; sub-size uniaxial specimens may involve electron beam welding as well as machining processes and hence these specimens are likely to be more expensive [20].

Dead-weight machines are often used for standard uniaxial creep tests and the test equipment is therefore relatively inexpensive; the small specimen testing is recommended to be carried out on servo-electric screw thread machines [21], which may be more expensive to operate than dead-weight machines.

Conventional sub-sized uniaxial creep test specimens, Fig. 2a, have cross-sectional areas and "test volumes" which are large enough to ensure that bulk material properties are obtained, provided the grain sizes or other significant metallurgical features are small compared with the test volumes and cross-sectional areas. Practical experience indicates that the "test volumes" of the other small specimens are generally large enough to produce accurate bulk material data.

4.2 Choice of Small Specimen Test Types

Various factors can influence the choice of which small specimen test type is to be used for a particular application; these factors include the type of data required, e.g. creep strain rate data or creep rupture data, the material to be tested, etc. The test conditions may also be important factors in specimen type selection. Apart from the sub-size uniaxial specimen type, of the other methods described in this paper, only the SPT and TBT methods are capable of producing, directly, creep rupture data. If the temperatures and the test environment for these specimens do not produce excessive oxidation, then it would be acceptable to use these methods. However, research is ongoing into the interpretation of the SPT data, to obtain corresponding uniaxial data, and a generally accepted approach has not yet been developed (e.g. [22]).

The ICT method can be used to obtain creep strain data, but this requires the use of an indenter made from a material which has a creep strength which is two to three orders of magnitude greater than that of the material to be tested. For example [7], a Ni-base superalloy indenter has been used successfully to test P91, P92 and 316 stainless steel specimens. It is also necessary to avoid the possibility of environmental effects by use of an inert gas or a vacuum, if necessary.

The SRT method can also be used to obtain creep strain data, but unlike the ICT method, which required the indenter material to have very high creep strength, the loading pins for the ICT tests can have a creep strength which is even lower than that of the material to be tested. Hence, Ni-base superalloy materials can also be tested and the tests will produce accurate data. Which of the ICT and SRT specimen types is chosen to be used will depend on the strain magnitudes for which data is required.

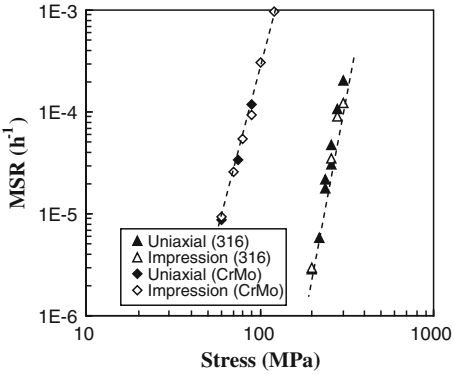

Fig. 8 Minimum creep strain rate (MSR) data for 316 stainless steel at 600 °C and 2-1/4Cr1Mo weld metal at 640 °C, obtained from uniaxial and impression creep tests

4.3 Determination of Creep Data from Small Specimen Tests

4.3.1 Minimum Creep Strain Rate Data

Minimum creep strain rate data obtained from ICT specimen tests carried out on 0.5CrMoV steel, at 640 °C, and on a 316 stainless steel, at 600 °C, are given in Fig. 8 [5]. Also shown in Fig. 8 are the corresponding uniaxial creep test data. It can be seen that, in all cases, excellent agreement exists between the uniaxial creep test data and the corresponding ICT data. Figure 9a shows the results obtained from uniaxial creep data and the corresponding SRT data for a P91 steel, at 650 °C. It can be seen that the two sets of results agree very well. It should be noted that the stress levels for which the ring test results were obtained produced easily measurable deformations with high accuracy. These types of results would be at the limit of what would be achievable, with acceptable accuracy and sensitivity of measurement, from impression creep tests. Figure 9b shows the uniaxial and SRT test data for an Inco718 Ni-base superally, at 800 °C. It can be seen that use of the SRT method, even for a highly creep resistant material (Ni-base), produces very good agreement between the SRT and uniaxial data.

4.3.2 Creep Rupture Life Data

For SPTs, using the empirical relationship (Eq. (8)) for the stress, σ, which relates to the corresponding stress in a uniaxial creep rupture test, the uniaxial rupture lifetimes can be estimated by using a suitable K_s value. Taking the value of K_s to be 1.275, creep rupture data, based on small punch tests of P91, at 650 °C has been obtained, see Fig. 10, as compared with the corresponding uniaxial data. The agreement between the two sets of data, on the log (σ) verses log (t_f) plots, is good.

Creep deformation curves obtained from two-bar specimen tests are shown in Fig. 7 for a P91 steel at 600 °C. The creep rupture data obtained from these tests

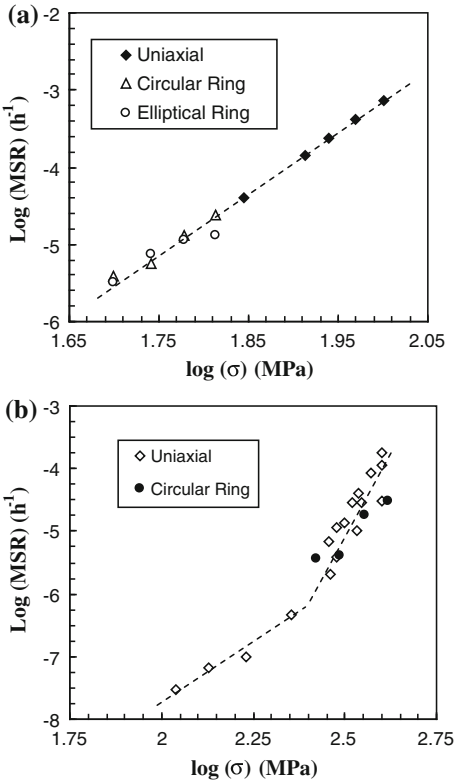

Fig. 9 **a** Minimum creep strain rate data for a P91 steel at 650 °C obtained from uniaxial and ring tests. **b** Minimum creep strain rate data for a Nickel base superalloy at 800 °C obtained from uniaxial and ring tests

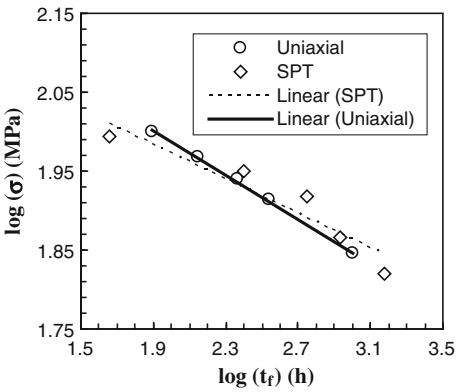

Fig. 10 Converted creep rupture data (using Eq. (8), with $K_s = 1.275$) obtained from a SPT on a P91 steel at 650 °C, compared with corresponding uniaxial data

are compared with the corresponding uniaxial data in Fig. 11. The results given in Figs. 7 and 11 clearly show that the two-bar specimen type is capable of producing the full uniaxial creep strain curve. Specific considerations have also been given to the design and dimension ratio ranges to be used for these specimens; this will be reported in a future paper.

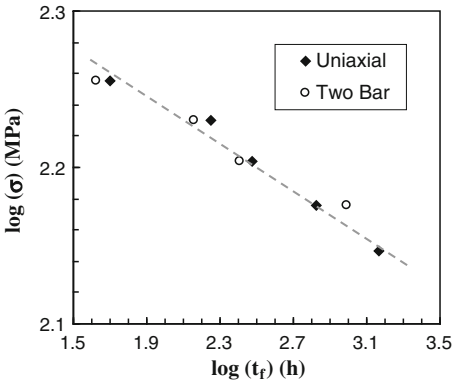

Fig. 11 Creep rupture data obtained from two bar and uniaxial specimens for a P91 steel at 600 °C

5 Discussion

The material extraction process and small specimen manufacture is, in general, more costly than is the manufacture of conventional uniaxial creep test specimens, but not prohibitively so. Test equipment for standard creep testing has been in existence for many decades and compared to the servo-electric types of test machines recommended by the authors [21], the cost is less. Testing, data recording and data processing for the small specimen and conventional specimen types of test are of similar complexity. Hence, although obtaining small specimen results is more costly compared with uniaxial tests, this should not prohibit the use of small specimens, especially as it may be the only practical and reliable method available to obtain some types of creep data.

It has been shown that all of the small specimen test types described in this paper are capable of providing very accurate data. In the case of two of the methods (SPT and ICT) a great deal of test data and test experience exists and there is growing confidence in the use of such methods for practical proposes. The SRT method is relatively new and hence less data is available, but the results of the testing of a Ni-base material (Fig. 9b) are particularly encouraging.

The concept of EGL (equivalent gauge length) is very useful for assessing the relative sensitivities of the small specimen test methods. The EGLs of SPT and ICT specimens are low whereas the SRT specimens have very high EGL which are of the same order of magnitude as the gauge lengths of conventional uniaxial specimens. These can be seen in Table 1.

Provided care is taken, there is no reason why oxidation effects (or the question of whether bulk properties are being obtained) should cause a problem. Also, by performing stepped load or stepped temperature tests, additional information such as the creep stress exponent or the activation energy can be obtained [5, 23].

At this relatively early stage in the development of small specimen creep test methods, there would be considerable benefit to be gained by collaborating with

Table 1 Summary of correlation formulae

Specimen	σ_{nom}	η	β	βL_{nom} (EGL)
Uniaxial	$\frac{4P}{\pi d_{GL}{}^2}$	1	1	GL
ICT [4]	$\frac{P}{b_i d_i}$	~0.4	~2.0	$\sim 2d_i$
SRT (elliptical) [6]	$\frac{Pa}{b_o d^2}$	0.892	~0.3–0.7	$\frac{4ab\beta}{d}$
SRT (circular) [6]	$\frac{PR}{b_o d^2}$	0.892	0.448	$\frac{4R^2\beta}{d}$
SPT* [22]	$\frac{P}{2\pi R_s t_o}$	$\frac{0.6\pi}{K_s}\left(\frac{a_p}{R_s}\right)^{0.2}$	–	–
Two-Bar [8]	$\frac{P}{2bd}$	~1	~1.4	βL_o

*Large deformation effects and complex geometry and deformation behaviour for the SPT make it difficult to define material and deformation independent parameters

a view to producing codes of practice for performing small specimen tests, for all specimen types.

6 Concluding Remarks and Future Work

Impression creep testing is suitable for determining minimum creep strain rate data, particularly at relatively high stresses. It has been extensively used as a "ranking test" and for determining creep properties for HAZs. Sophisticated measurement systems, capable of measuring very small deformations, and high accuracy of temperature control, are required. The potential effects of the impression deformation on the conversion relationships may need to be considered.

The small punch technique involves the measurement of relatively large deformations. Significant local plasticity and complicated deformation modes occur during the test. At present, there is no sound mechanics-based method which is universally accepted for data interpretation. However, it is believed that creep rupture properties could be related to small punch test results and the test method and the results could be very useful for power plant material ranking assessment. Future research into the understanding of the effects of the large initial plastic deformation and hardening on the subsequent creep process is necessary.

The small, ring-type specimen test involves relatively large deformation in relation to its' overall dimensions, which is associated with relatively low strains. The method is suitable for determining minimum creep strain rate data, particularly at relatively low equivalent uniaxial stresses. A unique application of this test type is for obtaining data for highly creep resistant materials. Future developments involve

the establishment of time-dependent geometric correction functions to compensate for the effects of geometry changes during the deformation process.

The creep test data obtained from the small two bar specimen tests, for a P91 steel, have shown good correlation with corresponding uniaxial test data. This indicates that this specimen type is capable of producing full uniaxial creep curves. Further experimental data and validation are necessary; research is currently being undertaken in order to provide the necessary data and validation.

Acknowledgments The authors wish to thank Brian Webster and Shane Maskill at the University of Nottingham for their assistance with the experimental work.

References

1. Hyde, T.H., Sun, W., Williams, J.A.: The requirements for and the use of miniature test specimens to provide mechanical and creep properties of materials: - a review. Int. Mater. Rev. **52**(4), 213–255 (2007)
2. Parker, J.D., James, J.D.: Creep behaviour of miniature disc specimens of low alloy steel, ASME, PVP **279**, Developments in a Progressing Technology, pp. 167–172 (1994)
3. Sturm, R., Jenjo, M., Ule, B., Solar, M.: Small-punch testing of smart weld materials. In: Proceedings of the 2nd International Conference on Structural Integrity of High Temperature Welds, pp. 269–278. IOM^3 Communications, London (2003)
4. Hyde, T.H., Sun, W., Becker, A.A.: Analysis of the impression creep test method using a rectangular indenter for determining the creep properties in welds. Int. J. Mech. Sci. **38**, 1089–1102 (1996)
5. Sun, W., Hyde, T.H., Brett, S.J.: Application of impression creep data in life assessment of power plan materials at high temperatures. J. Mater. Des. Appl. **222**, 175–182 (2008)
6. Hyde, T.H., Sun, W.: A novel, high sensitivity, small specimen creep test. J. Strain Anal. **44**(3), 171–185 (2009)
7. Hyde, T.H., Hyde, C.J., Sun, W.: A basis for selecting the most appropriate small specimen creep test type. ASME 2012 Pressure Vessel & Piping Conference. pp. 15–19. Toronto, Canada (2012)
8. Hyde T.H., Sun, W., Balhassn, A.: A small creep test specimen for use in determining uniaxial creep rupture data. In: 2nd International Conference on Determination of Mechanical Properties of Materials by Small Punch and Other Miniature Testing Techniques, pp. 2–4. Ostrava, Czech Republic, Europe (2012)
9. Parker, J.D., Purmensky, J.: Assessment of performance by monitoring in service changes in material properties. In: 9th European Conference on Fracture, Reliability and Structural Integrity of Advanced Materials, Varna, Bulgaria (1992)
10. Brett, S.J.: UK Experience with modified 9Cr (Grade 91) steel. In: Baltica VII: International Conference on Life Management & Maintenance for Power Plants, pp. 48–60. Helsinki-Stockholm-Helsinki (2007)
11. Garzillo, A., Guardamagna, C., Moscotti, L., Ranzani, A.: Technique for residual life assessment of high temperature components based on creep rupture testing on welded miniature specimens. Int. J. Press. Vess. Piping **66**, 223–232 (1996)
12. Dorner, D., Röller, K., Skrotzki, B., Stöckhert, B., Eggler, G.: Creep of a TiAl alloy: comparison of indentation and tensile testing. Mats. Sci. Eng. A **237**(1–2), 346–354 (2003)
13. Hyde, T.H., Sun, W., Brett, S.J.: Application of impression creep test data for the assessment of service-exposed power plant components. Metall. J. **LXIII**, 138–145 (2010)

14. Hyde, T.H., Sun, W., Becker, A.A., Williams, J.A.: Creep behaviour and failure assessment of new and fully repaired P91 pipe welds at 923 K. Proc. Instn. Mech. Eng. Part L J. Mater. Des. Appl. **218**, 211–222 (2004)
15. Li, Y.Z., Sturm, R.: Determination of Norton creep law and rupture time dependence from small punch test. In: Proceedings of 3rd International Conference on Integrity of High Temperature Welds, pp. 433–449. IoM Communications, London (2007)
16. Anderson, R.G., Gardener, L.R.T., Hodgkins, W.R.: Deformation of uniformly loaded beams obeying complex creep laws. J. Mech. Eng. Sci. **5**, 238–244 (1963)
17. Johnsson, A.: An alternative definition of reference stress for creep. IMechE. Conf. Pub. **13**, 205.1–205.7 (1973)
18. Hyde, T.H., Yehia, K., Sun, W.: Observation on the creep of two-material structures. J. Strain Anal. **31**(6), 441–461 (1996)
19. MacKenzie, A.C.: On the use of a single uniaxial test to estimate deformation rates in some structures undergoing creep. Int. J. Mech. Sci. **10**, 441–453 (1968)
20. Askins, M.C., Marchant, K.D.: Estimating the remanent life of boiler pressure parts, EPRI Contract RP2253-1, Part 2, Miniature specimen creep testing in tension, CEGB Report., TPRD/3099/R86, CEGB, UK (1987)
21. Hyde, T.H., Sun, W., Brett, S.J.: Some recommendations on standardization of impression creep testing. In: Proceedings of ECCC Conference on Creep and Fracture in High Temperature Components—Design and Life Assessment, pp. 1079–1087. Dübendorf, Switzerland (2009)
22. CEN CWA 15627 Workshop Agreement: Small punch test method for metallic materials (Part A). December 2006, European Committee for Standardisation
23. Hyde, T.H., Sun, W.: Multi-step load impression creep tests for a 1/2CrMoV steel at 565 °C. Strain **37**, 99–103 (2001)

Kelvin Modes Based Cubic Plasticity and Induced Anisotropic Damage: Application to Creep of AM1 Single Crystal

Roxane Marull and Rodrigue Desmorat

Abstract Modelling the anisotropic elasto-visco-plastic and damage behavior of FCC single crystal superalloys is a crucial issue, especially in the aircraft engines industry that widely uses such alloys for parts such as turbine blades. If micro-scale written models based on the theory of crystal plasticity and developed at the slip system level have already proved efficient in several loading cases, it is also possible to propose a novel meso-scale model based on Kelvin decomposition of Hooke elasticity tensor which is here applied to the initial cubic symmetry of these superalloys. Three modes (and three corresponding stresses) are then highlighted and used to build a yield criterion which is extended to plasticity and then to visco-plasticity; this fully defined model is identified and validated on different loading cases. The Kelvin modes decomposition also enables the full construction of an anisotropic damage model (described by a second order tensor damage variable), from the definition of a cubic effective stress ensuring the coupling of elasto-visco-plasticity (micro- or meso-scale written) with damage, to the incremental damage law. Coupling is here detailed and carried out at 950 °C for ⟨001⟩, ⟨111⟩ and ⟨011⟩ oriented creep (primary to tertiary) of AM1 single crystal, thus validating the proposed visco-plastic and damage models and corresponding parameters sets that are easily identified thanks to the decoupling of Kelvin modes in crystalline orientations ⟨001⟩ and ⟨111⟩.

R. Marull (✉)
Laboratoire d'Étude des Microstructures, ONERA/CNRS, BP72,
29 Avenue de la Division Leclerc, 92322Chatillon Cedex, France
e-mail: roxane.marull@gmail.com

R. Marull · R. Desmorat
LMT-Cachan, ENS Cachan/UPMC/CNRS/PRES UniverSud Paris,
61 Avenue du Président Wilson, 94235Cachan Cedex, France
e-mail: desmorat@lmt.ens-cachan.fr

H. Altenbach and S. Kruch (eds.), *Advanced Materials Modelling for Structures*,
Advanced Structured Materials 19, DOI: 10.1007/978-3-642-35167-9_20,

1 Introduction

Modelling the (visco-)plastic behavior of anisotropic materials such as single crystal superalloys is often a thorny but crucial issue. Different approaches that are written at different scales were proposed at this aim, from mesoscopic models [1, 17] to cristallographic-phenomenologic [2, 15, 24] or dislocation dynamics descriptive [6] micro-scale models based on Schmid criterion. If micro-scale (visco-)plasticity models that rely on the FCC crystallographic structure of considered alloys have proved efficient to describe the anisotropic behavior of this material class, mesoscopic models are usually insufficient for they do not take the specific cubic symmetry of FCC single crystals into account. The authors have proposed in a previous work a yield criterion based on Kelvin modes decomposition [22, 23] that accounts for cubic symmetry and that was successfully applied to different loading cases for CMSX2 single crystal superalloy [5]. This yield criterion can be extended to plasticity and viscoplasticity what is the aim of present paper. After having proposed a (visco-)plastic model and having validated it in tension and in (primary and secondary) creep on AM1 single crystal superalloy, we here once again use Kelvin modes decomposition for cubic symmetry in order to define an effective stress and an anisotropic incremental damage law extending Lemaitre law [10] and thanks to which anisotropic tertiary creep of AM1 can be modeled.

2 Kelvin Decomposition for Cubic Material Symmetry

Kelvin decomposition [7, 19, 21–23] consists in the spectral decomposition of Hooke fourth-order elasticity tensor $\mathbb{E}$ into eigenvalues $\Lambda^{(I)}$ and eigentensors $\mathbf{e}^{(I)}$ so that $\mathbb{E} : \mathbf{e}^{(I)} = \Lambda^{(I)}\mathbf{e}^{(I)}$. Eigentensors that are associated to a same eigenvalue Λ^K are grouped to define a projector

$$\mathbb{P}^K = \sum_{I/\Lambda^{(I)}=\Lambda^K} \mathbf{e}^{(I)} \otimes \mathbf{e}^{(I)} \tag{1}$$

and the projection of Cauchy stress $\boldsymbol{\sigma}$ on the K^{th} mode defines in a unique and objective manner the associated Kelvin stress by $\boldsymbol{\sigma}^K = \mathbb{P}^K : \boldsymbol{\sigma}$. There are up to six Kelvin modes depending on considered material symmetry.

Kelvin decomposition applied to cubic symmetry exhibits three eigenvalues (or Kelvin moduli) : $\Lambda^{K=1} = 3K = E/(1-2\nu)$, $\Lambda^{K=2} = E/(1+\nu)$ and $\Lambda^{K=3} = 2G$, with E the Young modulus, ν the Poisson ratio and G the shear modulus. Kelvin stresses $\boldsymbol{\sigma}^K = \mathbb{P}^K : \boldsymbol{\sigma}$, obtained by projection of the stress tensor thanks to Kelvin projectors that are detailed for cubic symmetry in [5, 7], are in fact easily gained:

- $\boldsymbol{\sigma}^{K=1} = \boldsymbol{\sigma}^H$ is the hydrostatic stress $\frac{1}{3}\mathrm{tr}\boldsymbol{\sigma}\,\mathbf{1}$ (associated to the Kelvin modulus $3K$),

- $\boldsymbol{\sigma}^{K=2} = \boldsymbol{\sigma}^{d}$ is the diagonal part of the deviatoric stress *in the natural anisotropy basis* (associated to the Kelvin modulus $E/(1+\nu)$),
- $\boldsymbol{\sigma}^{K=3} = \boldsymbol{\sigma}^{\overline{d}}$ is the out of diagonal deviatoric tensor *in this same basis* (associated to the Kelvin modulus $2G$).

Two deviatoric stresses, $\boldsymbol{\sigma}^{d}$ and $\boldsymbol{\sigma}^{\overline{d}}$, are then naturally introduced from Kelvin analysis with $\boldsymbol{\sigma}' = \boldsymbol{\sigma}^{d} + \boldsymbol{\sigma}^{\overline{d}}$ and $\boldsymbol{\sigma} = \boldsymbol{\sigma}' + \boldsymbol{\sigma}^{H}$. Three modes ($d$, $\overline{d}$ and H) associated with objectively defined projectors $\mathbb{P}^{d}$, $\mathbb{P}^{\overline{d}}$ and $\mathbb{P}^{H}$ have then been highlighted in the case of initial cubic symmetry. Corresponding Kelvin stresses are the base for a novel yield criterion.

3 Plasticity Model for FCC Single Crystals

3.1 Yield Function

A yield criterion usually defines the elasticity domain by $f = f(\boldsymbol{\sigma}) < 0$. In the case of cubic material symmetry, f can then be expressed as $f = f(\boldsymbol{\sigma}^{d}, \boldsymbol{\sigma}^{\overline{d}}, \boldsymbol{\sigma}^{H}) < 0$. Incompressible plasticity being often assessed for metallic materials, the hydrostatic mode can be excluded from the criterion. Hosford [8] besides points out the weaknesses of quadratic criteria regarding to cystallographic considerations. A non-quadratic criterion is then proposed [5]

$$f = \left(\frac{\sigma_{eq}^{d}}{\sigma_{y}}\right)^{n} + \frac{\sigma_{eq}^{\overline{d}}}{\overline{\sigma}_{y}} - 1 \tag{2}$$

denoting $(.)_{eq} = \sqrt{\frac{3}{2}(.)' : (.)'}$ the von Mises norm and where σ_y, $\overline{\sigma}_y$ and n are the three material parameters involved in the yield function. Their identification is easily carried out by plotting for each temperature all available data (experimental points and reliable modellings) in a novel and unique diagram with set of axes $(\sigma_{eq}^{d}, \sigma_{eq}^{\overline{d}})$. The locus of experimental points and/or of reliable criteria (such as Schmid criterion for example) can be approximated by a degree n polynomial and σ_y (resp. $\overline{\sigma}_y$) is the value of σ_{eq}^{d} (resp. $\sigma_{eq}^{\overline{d}}$) when $\sigma_{eq}^{\overline{d}} = 0$ (resp. $\sigma_{eq}^{d} = 0$), as illustrated in Fig. 1 in the case of CMSX2 tension-shearing at room temperature.

This novel Kelvin modes based yield criterion has been successfully applied to oriented tension (yield stress *vs.* solliciation orientation between $\langle 001 \rangle$ and $\langle 011 \rangle$ orientations) and tension-shearing of CMSX2 FCC superalloy [5].

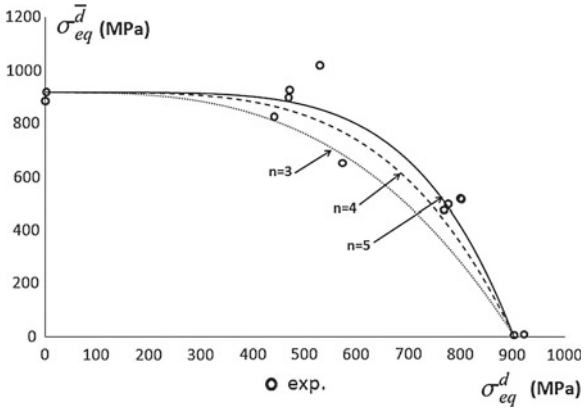

Fig. 1 Yield surface experimental data and proposed Kelvin modes based yield criterion plotted in the $\sigma_{eq}^{\overline{d}}$ versus σ_{eq}^{d} diagram (CMSX2 at room temperature, experimental data after [18])

3.2 Introduction of Isotropic Hardening

Previously defined and validated Kelvin modes based yield criterion is naturally the basis for a full plasticity model that can be built by normality, firstly by introducing isotropic hardening. Two isotropic hardening variables homogeneous to a strain, r and $\overline{r}$, associated to hardenings R and $\overline{R}$ are then defined in the thermodynamic framework [13] so that the hardening laws are $R = R(r)$ and $\overline{R} = \overline{R}(\overline{r})$. A yield function that accounts for hardening is

$$f = \left(\frac{\sigma_{eq}^{d}}{\sigma_y + R} \right)^n + \frac{\sigma_{eq}^{\overline{d}}}{\overline{\sigma}_y + \overline{R}} - 1 \tag{3}$$

and plastic multiplier $\dot{\lambda}$ is related to the rates of the internal variables r and $\overline{r}$ by the generalized normality rule (associated plasticity model)

$$\dot{r} = -\dot{\lambda} \frac{\partial f}{\partial R} \qquad \text{and} \qquad \dot{\overline{r}} = -\dot{\lambda} \frac{\partial f}{\partial \overline{R}} \tag{4}$$

It can be noticed here that the yield criterion is dimensionless, the plastic multiplier being homogeneous to MPa/s. It is determined in the plasticity modelling by the consistency condition $f = 0$ and $\dot{f} = 0$ and will be obtained in the visco-plasticity modelling from a viscosity law $f = f_v(\dot{r}, \dot{\overline{r}}) > 0$. The plastic strain rate is also derived by normality

$$\dot{\boldsymbol{\varepsilon}}^p = \dot{\lambda} \frac{\partial f}{\partial \boldsymbol{\sigma}} = \frac{3}{2} \dot{\lambda} n \frac{(\sigma_{eq}^{d})^{n-1}}{(\sigma_y + R)^n} \frac{\boldsymbol{\sigma}^d}{\sigma_{eq}^{d}} + \frac{3}{2} \dot{\lambda} \frac{1}{(\overline{\sigma}_y + \overline{R})} \frac{\boldsymbol{\sigma}^{\overline{d}}}{\sigma_{eq}^{\overline{d}}} = \dot{\boldsymbol{\varepsilon}}^{pd} + \dot{\boldsymbol{\varepsilon}}^{p\overline{d}} \tag{5}$$

and is naturally parted into a "diagonal deviatoric" $\dot{\boldsymbol{\varepsilon}}^{pd} = \mathbb{P}^{d} : \dot{\boldsymbol{\varepsilon}}^{p}$ and a "non-diagonal deviatoric" $\dot{\boldsymbol{\varepsilon}}^{p\overline{d}} = \mathbb{P}^{\overline{d}} : \dot{\boldsymbol{\varepsilon}}^{p\overline{d}}$ part in the natural anisotropy basis.

In order to take the interaction between hardenings relative to different Kelvin modes into account (following the modelling proposed by [15] where an interaction between the hardenings relative to different slip systems is introduced), an interaction function $g = g(p^d\, p^{\overline{d}}) = g_\infty(1 - e^{-b_{inter}\sqrt{p^d\, p^{\overline{d}}}})$ that is equal to zero for sheer d and $\overline{d}$ modes (i.e. $\langle 001\rangle$ and $\langle 111\rangle$ sollicitations) can finally complete the modelling:

$$f = \left(\frac{\sigma^d_{eq}}{\sigma_y + R}\right)^n + \frac{\sigma^{\overline{d}}_{eq}}{\overline{\sigma}_y + \overline{R}} - 1 - g \tag{6}$$

$$\text{with} \qquad \dot{p}^d = \sqrt{\frac{2}{3}\dot{\boldsymbol{\varepsilon}}^{pd} : \dot{\boldsymbol{\varepsilon}}^{pd}} \qquad \text{and} \qquad \dot{p}^{\overline{d}} = \sqrt{\frac{2}{3}\dot{\boldsymbol{\varepsilon}}^{p\overline{d}} : \dot{\boldsymbol{\varepsilon}}^{p\overline{d}}} \tag{7}$$

It is interesting to notice that $\langle 001\rangle$ and $\langle 111\rangle$ oriented tensions exhibit a full decoupling of deviatoric modes d and $\overline{d}$. In these very cases, the yield function easily reads

$$f^{\langle 001\rangle} = \left(\frac{\sigma^d_{eq}}{\sigma_y + R}\right)^n - 1 \qquad \text{in } \langle 001\rangle \qquad \text{since } \sigma^{\overline{d}}_{eq} = 0 \tag{8}$$

$$f^{\langle 111\rangle} = \frac{\sigma^{\overline{d}}_{eq}}{\overline{\sigma}_y + \overline{R}} - 1 \qquad \text{in } \langle 111\rangle \qquad \text{since } \sigma^{d}_{eq} = 0 \tag{9}$$

This decoupling allows an easy identification of hardenings R and $\overline{R}$. This identification has been led for AM1 superalloy for which tensile curves are given by [20] at 950 °C. Although experimental curves result from tensile tests at $\dot{\epsilon} = 16.6\times10^{-5}\text{s}^{-1}$, we will here consider in a first approach a plastic (without viscosity) model identification ($f = 0$).

For $\langle 001\rangle$ oriented tension, i.e. when $\boldsymbol{\sigma}^{\overline{d}} = 0$, we have from (6) $\sigma^d_{eq} = \sigma_y + R = \sigma$. From the $\langle 001\rangle$ tensile curve saturating shape, isotropic hardening R is chosen equal to $R = R_\infty\left(1 - e^{-br}\right)$. Plastic strain rate is easily found equal to $\dot{\varepsilon}^{p\langle 001\rangle} = \dot{r}$ in this uniaxial case so that

$$\sigma = \sigma_y + R_\infty\left(1 - e^{-b\varepsilon^p}\right) \quad \text{for } \langle 001\rangle \text{ oriented sollicitation} \tag{10}$$

what enables an analytical plotting of corresponding curve ($\langle 001\rangle$ full line of Fig. 2) by identifying parameters σ_y, R_∞ and b on the experimental curve (pink circle symbols, Fig. 2). A similar process for $\langle 111\rangle$ oriented tension, i.e. for $\boldsymbol{\sigma}^{d} = 0$ leads to

$$\sigma = \overline{\sigma}_y + \overline{R}_\infty\left(1 - e^{-\overline{b}\varepsilon^p}\right) \quad \text{for } \langle 111\rangle \text{ oriented sollicitation} \tag{11}$$

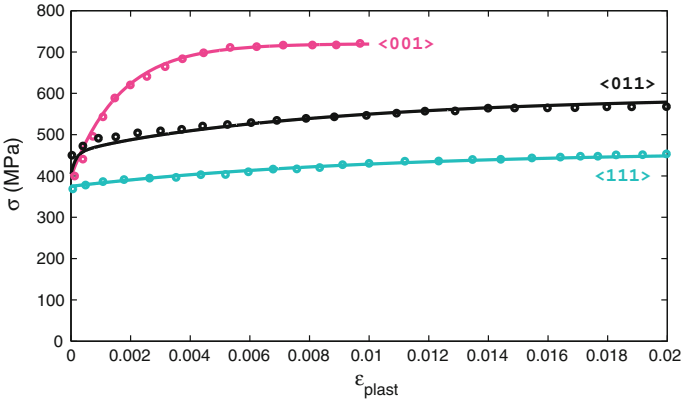

Fig. 2 Experimental (*circle symbols*) and modeled (*full lines*) tensile curves of ⟨001⟩ (*pink*), ⟨111⟩ (*blue*) and ⟨011⟩ (*black*) oriented AM1 superalloy at 950 °C

and corresponding curve is then analytically plotted (⟨111⟩ full line of Fig. 2) by identifying parameters $\overline{\sigma}_y$, $\overline{R}_\infty$ and $\overline{b}$ on the experimental curve (blue circle symbols, Fig. 2).

The model response for ⟨011⟩ oriented tension fits the experimental curve (respectively black full line and circle symbols, Fig. 2) by adjusting the parameters involved in the interaction function g. Table 1 provides the value of the model parameters.

The proposed Modelling appears to fit very well experimental data and allows to represent the plastic anisotropy of AM1 superalloy.

4 Extension to Visco-Plasticity

Visco-plasticity is characterized by condition $f = f_v > 0$ where f is the yield criterion defined at Eq. 3 and f_v is the viscosity function that is here dimensionless and defined as

$$f_v = \left[1 + \left(\frac{\dot{p}^d}{\dot{\varepsilon}_0}\right)^{1/N}\right]^n - 1 + \left(\frac{\dot{p}^{\overline{d}}}{\dot{\overline{\varepsilon}}_0}\right)^{1/\overline{N}} - 2k_i \left(\frac{\dot{p}^d}{\dot{\varepsilon}_0}\right)^{\frac{n}{2N}} \left(\frac{\dot{p}^{\overline{d}}}{\dot{\overline{\varepsilon}}_0}\right)^{\frac{1}{2\overline{N}}} \tag{12}$$

where $\dot{p}^d$ and $\dot{p}^{\overline{d}}$ are defined by Eq. 7. Such a function is equivalent, for pure tension oriented ⟨001⟩ and ⟨111⟩ (resp. modes d and $\overline{d}$) to Lemaitre- [11] or

Table 1 Parameters for Kelvin modes based plasticity model at 950 °C for AM1 superalloy

Temperature (°C)	σ_y (MPa)	R_∞ (MPa)	b	$\overline{\sigma}_y$ (MPa)	$\overline{R}_\infty$ (MPa)	$\overline{b}$	n	g_∞	b_{inter}
950	400	320	600	375	85	100	4	0.4	10000

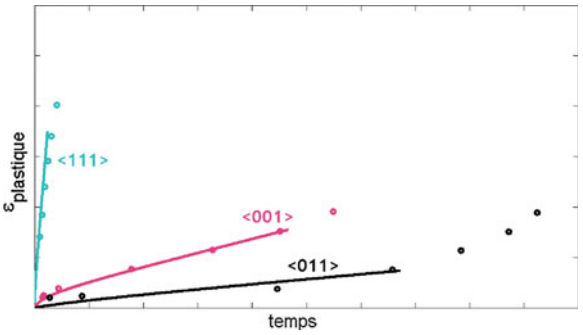

Fig. 3 Experimental (*circle symbols*) and modeled (*full lines*) primary and secondary creep curves of ⟨001⟩ (*pink*), ⟨111⟩ (*blue*) and ⟨011⟩ (*black*) oriented AM1 superalloy at 950 °C

Johnson-Cook-type [9] multiplicative hardening-viscosity law. Here again, an interaction between modes is proposed so that parameter k_i allows a better modelling of secondary creep for mixed modes. Five new viscosity parameters have been introduced ($\dot{\varepsilon}_0$, $\dot{\overline{\varepsilon}}_0$, N, $\overline{N}$ and k_i) that can be easily identified, once again thanks to the decoupling of modes d and $\overline{d}$.

The full visco-plasticity model is validated on AM1 creep at 950° C for a 300 MPa applied stress. All involved parameters (except n and k_i) can be deduced, thanks to the deviatoric modes decoupling, from already known parameters of isotropic or crystallographic-phenomenologic models. We have then chosen here to use as much as possible these previously identified parameters [3] and to compare experimental results from this reference to the modelling we propose. The interaction of hardenings through function g is here neglected (as the interaction between slip systems was also neglected for the micro-scale model identification) but the interaction in the viscosity law is kept and used to better model ⟨011⟩ creep. Resulting curves are shown in Fig. 3.

Here again, modelling is quite satisfying. The creep response for orientation ⟨011⟩ could be better reproduced by modelling the primary creep with the consideration of the hardening interaction function g. Tertiary creep is not yet modeled and it is the subject of next section which introduces the concept of anisotropic continuous damage.

5 An Anisotropic Damage Model for Initially Cubic Materials

Coupling of visco-plasticity with damage is defined by the principle of strain equivalence [10]

$$\boldsymbol{\sigma} = \tilde{\mathbb{E}} : \boldsymbol{\varepsilon}^e \quad \Longleftrightarrow \quad \tilde{\boldsymbol{\sigma}} = \mathbb{E} : \boldsymbol{\varepsilon}^e = \mathbb{E} : (\boldsymbol{\varepsilon} - \boldsymbol{\varepsilon}^p) \tag{13}$$

with the elasticity law deriving from the free enthalpy $\boldsymbol{\varepsilon} - \boldsymbol{\varepsilon}^p = \boldsymbol{\varepsilon}^e = \rho \frac{\partial \psi_e^*}{\partial \boldsymbol{\sigma}}$ and the damage variable $\boldsymbol{D}$ being a second order tensor allowing an anisotropic description of induced damage [16]. A delicate issue of this study is the definition of an effective stress for anisotropic damage that is pertinent to cubic symmetry. The Kelvin modes based effective stress proposed in reference [4] seems satisfying but improvable so that we here propose

$$\tilde{\boldsymbol{\sigma}} = \left(\boldsymbol{H}\boldsymbol{\sigma}^d\boldsymbol{H}\right)^d + \left(\overline{\boldsymbol{H}}\boldsymbol{\sigma}^{\overline{d}}\overline{\boldsymbol{H}}\right)^{\overline{d}} + \left[\frac{\langle\sigma_H\rangle_+}{1-\eta_H D_H} + \langle\sigma_H\rangle_-\right]\mathbf{1} \tag{14}$$

$$= \tilde{\boldsymbol{\sigma}}^d + \tilde{\boldsymbol{\sigma}}^{\overline{d}} + \tilde{\boldsymbol{\sigma}}^H \tag{15}$$

$$\text{with} \quad \boldsymbol{H} = (\mathbf{1}-\boldsymbol{D})^{-\frac{1}{2}} \qquad \text{and} \qquad \overline{\boldsymbol{H}} = (\mathbf{1}-\overline{\eta}\boldsymbol{D})^{-\frac{1}{2}} \tag{16}$$

where $\sigma_H = \frac{1}{3}\text{tr}\boldsymbol{\sigma}$, $D_H = \frac{1}{3}\text{tr}\mathbf{D}$ and where η_H and $\overline{\eta}$ are respectively hydrostatic sensibility and orientation sensibility parameters. This thus defined effective stress derive form a thermodynamic state potential [4], is symmetric and independent from elasticity parameters and enables an easy coupling of plasticity and damage by injecting $\tilde{\boldsymbol{\sigma}}$ instead of the stress tensor $\boldsymbol{\sigma}$ into the chosen plasticity criterion, here the Kelvin modes based one,

$$f = \left[\frac{(\tilde{\boldsymbol{\sigma}})^d_{eq}}{\sigma_y + R}\right]^n + \frac{(\tilde{\boldsymbol{\sigma}})^{\overline{d}}_{eq}}{\overline{\sigma}_y + \overline{R}} - 1 - g \tag{17}$$

and the full coupled model is then built by normality. Positive and negative parts of the trace of stress tensor $< tr\boldsymbol{\sigma} >_+ = \max(tr\boldsymbol{\sigma}, 0)$ and $< tr\boldsymbol{\sigma} >_- = \min(tr\boldsymbol{\sigma}, 0)$ are used instead of classical term $\frac{tr\boldsymbol{\sigma}}{1-\eta_H D_H}$ of [12] to model a damage that is weaker in compression (in negative stress triaxiality cases) than in tension (in positive stress triaxiality cases).

A rate form anisotropic damage law accounting for the stress triaxiality effect and respectful of the material initial cubic symmetry is proposed [14]

$$\dot{\boldsymbol{D}} = \left[(1+\nu)\frac{\left(\tilde{\boldsymbol{\sigma}}^d\right)^2}{2ES} + \frac{\left(\tilde{\boldsymbol{\sigma}}^{\overline{d}}\right)^2}{4G\overline{S}} + \frac{\langle\tilde{\sigma}_H\rangle_+^2\mathbf{1}}{6KS_H}\right]^s \dot{p}_{cub} \tag{18}$$

where $\dot{p}_{cub} = \sqrt{\frac{2}{3}(\dot{\boldsymbol{\varepsilon}}^{pd} : \dot{\boldsymbol{\varepsilon}}^{pd} + c\,\dot{\boldsymbol{\varepsilon}}^{p\overline{d}} : \dot{\boldsymbol{\varepsilon}}^{p\overline{d}})}$ is a cubic plastic strain rate, with parameter c weighting the respective contributions of modes d, and $\overline{d}$ and where s, S, $\overline{S}$ and S_H are the damage parameters. This formulation involves elasticity parameters E, ν and G in such a manner that a $\text{tr}\dot{\boldsymbol{D}}$ is, in the isotropic particular case with exponent $s = 1$, equal to $\dot{D}$ defined by Lemaitre law $\dot{D} = \left(\frac{Y}{S}\right)\dot{p}$ when only one deviatroric mode d or $\overline{d}$ is activated.

This damage model is here validated for creep of AM1 superalloy at 950 °C. The coupling with visco-plasticity indeed allows to complete the creep curves shown

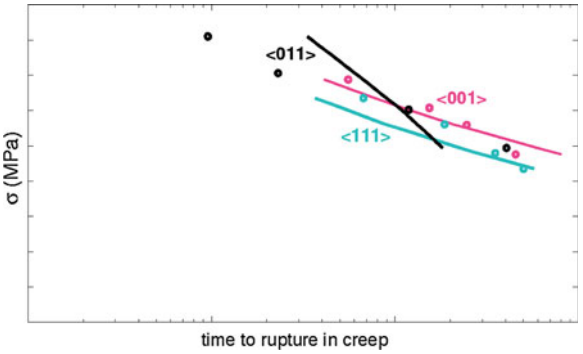

Fig. 4 Experimental (*circle symbols*) and modeled (*full lines*) creep lifetime curves of ⟨001⟩ (*pink*), ⟨111⟩ (*blue*) and ⟨011⟩ (*black*) oriented AM1 superalloy at 950 °C

Fig. 3 by adding the tertiary creep part. For such a monotonic loading, the damage threshold can be defined in terms of plastic strain ε_{p_D}. It is identified from experimental creep curves [3]. A parameters set for damage is identified thanks to creep lifetime curves for orientations ⟨001⟩, ⟨111⟩ et ⟨011⟩ (see Fig. 4), parameters S and S_H (here chosen equal to S) identified with ⟨001⟩ oriented lifetime curve and $\overline{S}$ identified thanks to ⟨111⟩ oriented lifetime curve. Parameters $\overline{\eta}$ and c are adjusted to fit the ⟨011⟩ lifetime data. Finally, coupling visco-plasticity and damage enables the obtention of full creep curves shown Fig. 5, the fracture occuring when damage D_I reaches the critical value D_c, i.e. when the maximum principal value of the damage tensor reaches a critical value.

Figures 4 and 5 present respectively the lifetime (rupture defined by $D = D_c$) for different stress levels and full creep curves at 300 MPa and give a satisfying modelling of the three oriented creep curves. Let us recall that considered lifetime corresponds to the instant where the maximum damage principal value reaches the

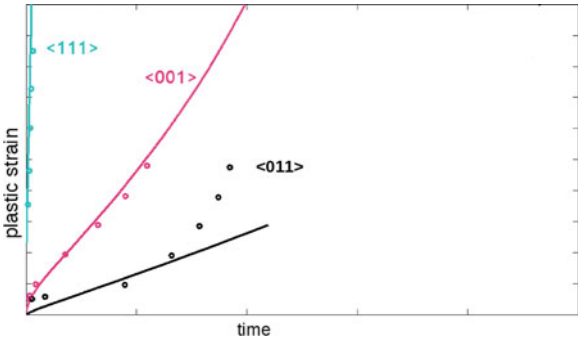

Fig. 5 Experimental (*circle symbols*) and modeled (*full lines*) full creep curves of ⟨001⟩ (*pink*), ⟨111⟩ (*blue*) and ⟨011⟩ (*black*) oriented AM1 superalloy at 950 °C

critical value $D = D_c$ which is here taken equal to $D_c = 0.2$ whatever the loading direction. It appears that simulated curves are in good agreement with experimental creep lifetimes and creep curves at 300 MPa.

6 Conclusion

The Kelvin modes decomposition has proved efficient to define a full elasto-(visco-)plasticity model for FCC superalloys that has been identified and validated in several loading cases. The coupling with anisotropic damage, insured by a cubic effective stress, has been successfully established and carried out to describe tertiary creep.

Acknowledgments The authors thank Snecma (Safran group) that supported this study.

References

1. Barlat, F., Lege, D.J., Brem, J.C.: A six-component yield function for anisotropic materials. Int. J. Plast. **7**, 693–712 (1991)
2. Cailletaud, G.: Une approche micromécanique phénoménologique du comportement inélastique des métaux. Thèse d'État, Université Paris VI (1987)
3. Delautre, J., Lautridou, J.-C., Guédou, J.-Y.: Compréhension des mécanismes de déformation plastique et viscoplastique monotone et cyclique des monocristaux en alliage AM1, vol. YKOM1/60066. Note technique Snecma (1988)
4. Desmorat, R.: Décomposition de Kelvin et concept de contraintes effectives multiples pour les matériaux anisotropes. C.R. Mécanique, **337**, 733–738 (2009)
5. Desmorat, R., Marull, R.: Non quadratic Kelvin modes based plasticity criteria for anisotropic materials. Int. J. Plast. **27**, 328–351 (2011)
6. Fedelich, B.: A microstructure based constitutive model for the mechanical behavior at high temperatures of Nickel-base single crystal superalloys. Comput. Mater. Sci. **16**, 248–258 (1999)
7. François, M.: Identification des symétries matérielles de matériaux anisotropes. Ph.D., Université Paris VI, Cachan (1995)
8. Hosford, W.F.: On the crystallographic basis of yield criteria. Textures Microstruct. **26–27**, 479–493 (1996)
9. Johnson, G.R., Cook, W.H.: A constitutive model and data for metals subjected to large strains, high strain rates and high temperatures. In: Proceedings of the 7th International Symposium on Ballistics, pp. 541–547 (1983)
10. Lemaitre, J.: Evaluation of dissipation and damage in metals. In: Proceedings of I.C.M. Kyoto, Japan (1971)
11. Lemaitre, J.: Sur la détermination des lois de comportement des matériaux élasto-viscoplastiques. Thèse d'État, Université Paris XI, Orsay (1971)
12. Lemaitre, J., Desmorat, R., Sauzay, M.: Anisotropic damage law of evolution. Eur. J. Mech. A/Solids **19**, 197–208 (2000)
13. Lemaitre, J., Chaboche, J.-L.: Mécanique des matériaux solides. Dunod, Paris (1985)
14. Marull, R.: Plasticités cubiques et endommagement anisotrope induit pour les superalliages monocristallins sous chargement complexe. Ph.D., ENS Cachan, Cachan (2011)
15. Méric, L., Poubanne, Ph, Cailletaud, G.: Single crystal modelling for structural calculations: part 1—model presentation. J. Eng. Mater. Technol. **113**, 162–170 (1991)

16. Murakami, S., Ohno, N.: A continuum theory of creep and creep damage. In: Ponter, A.R.S., Hayhurst, D.R. (eds.) 3rd Creep in Structures Symposium, Leicester, IUTAM, pp. 422–443. Springer, Heidelberg (1980)
17. Nouailhas, D.: Anisotropic constitutive equations for cyclic viscoplasticity: application to the case of materials with cubic symmetry. Rech. Aerosp. **3**, 11–28 (1990)
18. Nouailhas, D., Cailletaud, G.: Tension-torsion behavior of single crystal superalloys: experiment and finite element analysis. Int. J. Plast. **11**, 451–470 (1995)
19. Ostrosablin, N.I.: On the structure of the elasticity moduli tensor: elastic eigenstates. In: Dynamics of Continuous Media (in Russian), vol. 66, pp. 113–125. Acad. Sci. USSR (1984)
20. Poubanne, Ph: Étude et modélisation du comportement mécanique d'un superalliage monocristallin pour aube de turbine. Ph.D., École Centrale Paris, Chatillon (1989)
21. Rychlewski, J.: On Hooke's law. Prikl. Matem. Mekhan. **48**, 303–314 (1984)
22. Thomson, W.K. (Lord Kelvin): Elements of a mathematical theory of elasticity. Phil. Trans. R. Soc. **166**, 481 (1856)
23. Thomson, W.K. (Lord Kelvin): Elasticity, Encyclopaedia Britannica. Adam and Charles Black, Edinburgh (1878)
24. Walker, K.P., Jordan, E.H.: Constitutive modelling of superalloy single crystals and directionally solidified materials, p. 65. Research center nonlinear constitutive relations for high temperature applications. NASA-CP-2369 (1984)

A Grand Master Curve Approach for Off-Axis Creep Rupture Behavior of Orthotropic Fiber Composites at Different Temperatures

Masamichi Kawai

Abstract A new time-temperature extrapolation method is proposed for the off-axis creep rupture behavior of unidirectional polymer matrix composites at different stress levels over a range of temperature. It is developed using the framework of the classic Kachanov-Rabotnov damage model in conjunction with a modified temperature shift factor of the Arrhenius type that takes into account a rapid degradation in the strength of a polymer in the vicinity of its glass transition temperature. A particular emphasis is placed on establishment of an analytical formula for extrapolating creep rupture data that depend not only on temperature but also on the direction of creep loading. Validity of the proposed master curve approach to prediction of anisotropic creep life of a unidirectional polymer matrix composite is evaluated by comparing calculated and experimental results. It is also shown that the time-temperature extrapolation method suggests a new and general form of multiaxial creep failure criterion for orthotropic polymer matrix composites.

1 Introduction

Matrix dominated creep rupture is the key for accurate evaluation of the durability of polymer matrix composite (PMC) laminates [1]. To understand and model the matrix dominated creep rupture of PMC laminates, it is necessary to observe the off-axis creep rupture behavior of unidirectional PMC laminates for various fiber orientations over a range of stress and temperature. For a class of unidirectional PMC laminates, the off-axis creep rupture behavior has already been observed [2, 3]. In addition to these studies, the present author also examined the short-term off-axis creep rupture behavior of a unidirectional T800H/2500 carbon/epoxy laminate for

M. Kawai (✉)
Department of Engineering Mechanics and Energy,
Univeristy of Tsukuba, Ibaraki, Tsukuba 305-8573, Japan
e-mail: mkawai@kz.tsukuba.ac.jp

H. Altenbach and S. Kruch (eds.), *Advanced Materials Modelling for Structures*,
Advanced Structured Materials 19, DOI: 10.1007/978-3-642-35167-9_21,

various fiber orientations at 100 °C [4]. A power-law relationship was observed in the experimental data [4] for the unidirectional composite, regardless of fiber orientation. The creep rupture time was inversely proportional to the minimum creep rate for all the fiber orientations. The Monkman-Grant plots [5] of the off-axis creep rupture data did not fall in a single curve, but they were almost parallel with each other. The normalized master rupture curve approach developed in the previous study [4] was successful in coping with the fiber orientation dependence of the off-axis creep rupture data obtained from the short-term tests at the test temperature of 100 °C.

Only a limited amount of data was available for the creep rupture behavior of unidirectional PMC laminates under off-axis loading conditions over a wide range of temperature. Thus, the temperature dependence of off-axis creep rupture behavior in unidirectional PMC laminates has not sufficiently been understood, and an efficient procedure for extrapolating off-axis creep rupture data to a range of different temperatures and longer periods of lifetime has not been established. These facts suggest that further basic investigations on the matrix dominated creep fracture behavior of unidirectional PMC laminates is required with a view to developing an engineering creep rupture life prediction method that takes account of their temperature and fiber orientation dependence.

In an earlier study [6], therefore, the tensile creep rupture behavior of unidirectional carbon/epoxy T800H/2500 laminate under off-axis loading conditions [4] was further examined at different temperatures. Development of a phenomenological creep rupture model that takes into account the temperature and fiber orientation dependence of the off-axis creep rupture behavior of the unidirectional CFRP laminate was also attempted. In this attempt, the Larson-Miller (LM) parameter [7] was successfully used to identify a master curve for the off-axis creep rupture behavior of the unidirectional composite. The master curve identified was described by means of a linear relationship of the non-dimensional effective stress [8] and the LM parameter. The use of such a linear relationship in the previous study [6] for describing a master creep rupture curve, however, implicitly assumes that the slope of creep rupture curve is proportional to temperature; i.e. $\partial \sigma_C^* / \partial \ln t_R \propto T$. The assumption that was implicitly made in the formulation in the previous study [6] was in fact inconsistent with the nonlinear temperature dependence that was observed in experiments [6].

In the present study, a new time-temperature extrapolation method is proposed for the off-axis creep rupture behavior of a unidirectional polymer matrix composite at different stress levels over a range of temperature. It is developed using the classic Kachanov-Rabotnov damage model [9, 10] in conjunction with a new temperature shift factor of the Arrhenius type that takes into account a rapid degradation in strength of a polymer in the vicinity of its glass transition temperature. A particular emphasis is placed on establishing an analytical formula for extrapolating creep rupture data for polymer matrix composites that depend not only on temperature but also on the orientation of reinforcing fibers. The validity of the proposed master curve approach to prediction of anisotropic creep life of a unidirectional polymer matrix composite is evaluated through comparison with the experimental results obtained in a previous study [6]. It is also shown that the time-temperature extrapolation method developed

in this study suggests a more general form of multiaxial creep failure criterion for orthotropic polymer matrix composites.

2 Off-Axis Creep Rupture Behavior of Unidirectional Composites

The characteristic features of the off-axis creep rupture behavior of a unidirectional carbon/epoxy laminate that were observed in the previous study [6] are briefly reviewed below.

2.1 Off-Axis Creep Rupture Curves

The off-axis creep rupture data that were obtained at 130 °C for the different fiber orientations of $\theta = 10, 30, 45$ and 90 ° are shown in Fig. 1, as log-log plots of creep stress σ_C against rupture time t_R. In Fig. 1, the static tensile strengths are plotted by symbols on the vertical axis crossing at the rupture time $t_R = 10^{-3}$ h, since the time to static tensile fracture at the constant displacement rate of 1.0 mm/min was in the order of 10^{-3} h regardless of test temperature. It is obvious that the off-axis creep rupture strength becomes lower as the fiber orientation angle increases, demonstrating a strong fiber orientation dependence of the off-axis creep rupture time. All the off-axis creep rupture data for the different fiber orientations approximately fall on a single straight line in the log-log plot over the range of creep rupture time up to 10 h. This feature is common to all the results that were obtained at different test temperatures.

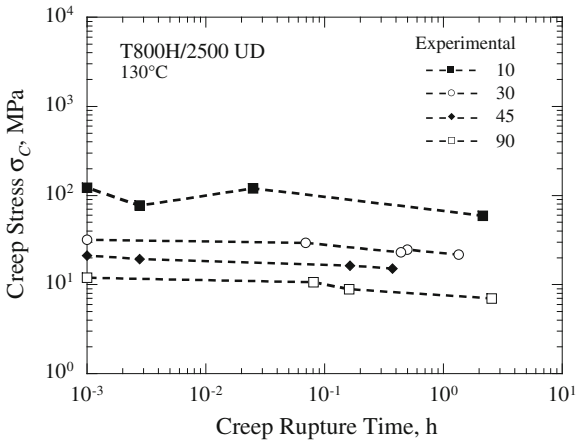

Fig. 1 Off-axis creep rupture data at 130 °C

The power-law relationships that were fitted to the plotted data for different fiber orientations are almost parallel with each other. Therefore, the off-axis creep rupture data for these fiber orientations can be described using a power-law relationship

$$\sigma_C^{q_1} t_R = C_1 \tag{1}$$

where the stress exponent q_1 and the coefficient C_1 stand for the slope and intercept of the straight line fitted to the log-log plot of creep rupture data, respectively.

2.2 Normalized Off-Axis Creep Rupture Curves

The off-axis creep rupture data are re-plotted using the creep stress levels, $\sigma_C/\sigma_{B(\exp)}$, in which σ_C and $\sigma_{B(\exp)}$ are the creep stresses and the static tensile strength, respectively. The results are shown in Fig. 2 for the test temperature of 130 °C. It can clearly be observed that the normalized off-axis creep rupture data are distributed within a narrow range for all the fiber orientations. It is also seen that the normalized creep rupture data can approximately be represented by a single straight line over the range of rupture time. This feature is common to the normalized plots of the creep rupture data for all test temperatures. This observation demonstrates that the fiber orientation dependence of off-axis creep rupture strength can approximately be removed using normalized creep stress level, regardless of the test temperature. In other words, the use of normalized creep stress level allows construction of a master rupture curve (MRC) for off-axis creep data that is independent of off-axis fiber orientation at each of the test temperatures. These facts justify that the normalized creep stress level becomes a useful measure to cope with the anisotropic creep rupture behavior of the unidirectional CFRP laminate over the range of test temperature below 130 °C.

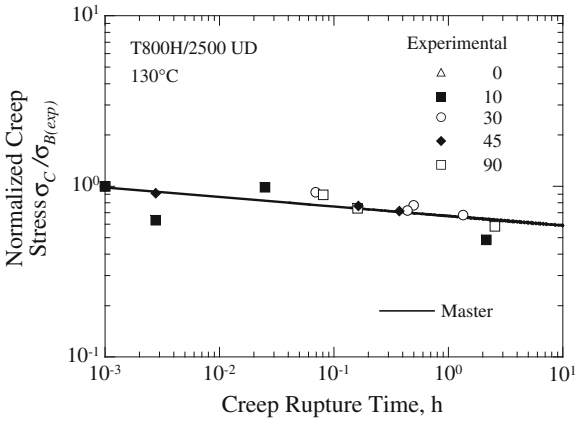

Fig. 2 Normalized off-axis creep rupture data at 130 °C

The straight line fitted to the normalized creep rupture data at a given test temperature, which represents a master creep rupture curve for the temperature that is independent of off-axis fiber orientation, can be described by the following formula:

$$\left(\frac{\sigma_C}{\sigma_{B(\exp)}}\right)^n t_R = t_R^0 \tag{2}$$

where the stress exponent n stands for the slope of the fitted straight line, and t_R^0 is a reference time associated with the condition $\sigma_C = \sigma_{B(\exp)}$.

The slope of the normalized creep rupture curve depends on temperature, and the temperature dependence of the slope can be described by means of a power-law relationship

$$\frac{1}{n(T)} = AT^m \tag{3}$$

where A and m are material constants.

3 Creep Rupture Life Extrapolation Method Based on Larson-Miller Parameter

The off-axis creep rupture data for the unidirectional composite depend not only on temperature but also on fiber orientation. Therefore, we need simultaneous scaling of stress and rupture time, in general, to identify a single master relationship that is approximately independent of temperature as well as of fiber orientation in a specified temperature range.

3.1 Stress Scaling

A theoretical counterpart of the experimental creep strength ratio $\sigma_C/\sigma_{B(\exp)}$ may be identified with the non-dimensional effective stress σ^* [8] that is based on the Tsai-Hill static failure criterion [11]. For the case of plane stress, it can be expressed as

$$\sigma^* = \sqrt{\left(\frac{\sigma_{11}}{X}\right)^2 - \frac{\sigma_{11}\sigma_{22}}{X^2} + \left(\frac{\sigma_{22}}{Y}\right)^2 + \left(\frac{\tau_{12}}{S}\right)^2} \tag{4}$$

where the stress components involved are taken with respect to the in-plane principal axes of material anisotropy, and X and Y represent the longitudinal and transverse strengths and S denotes the shear strength related to the principal fiber coordinate system. Note that $0 \leq \sigma^* \leq 1$, and the static failure occurs when $\sigma^* = 1$.

3.2 Time Scaling

In order to build a grand master curve for off-axis creep rupture data at different temperatures, a time-temperature extrapolation parameter is required. One of the commonly used time-temperature parameters (TTPs) is the Larson-Miller (LM) parameter [7] defined as

$$P_{LM} = T(C + \log t_R) \tag{5}$$

where T is test temperature in K, t_R is time to rupture in hours, and C is a material constant called the Larson-Miller constant.

3.3 An Extrapolation Formula

A master rupture curve for off-axis creep may be formulated by means of the non-dimensional effective stress and the Larson-Miller parameter in the functional form

$$\sigma_C^* = f(P_{LM}) \tag{6}$$

In the previous study [6], the linear relationship of the following form

$$\sigma_{C(RT)}^* = a + bP_{LM} \tag{7}$$

was used to extrapolate the off-axis creep rupture data. The solid line in Fig. 3 indicates the master creep rupture curve identified by fitting Eq. (7) to the normalized creep rupture data for all fiber orientations at different temperatures. It is seen that a

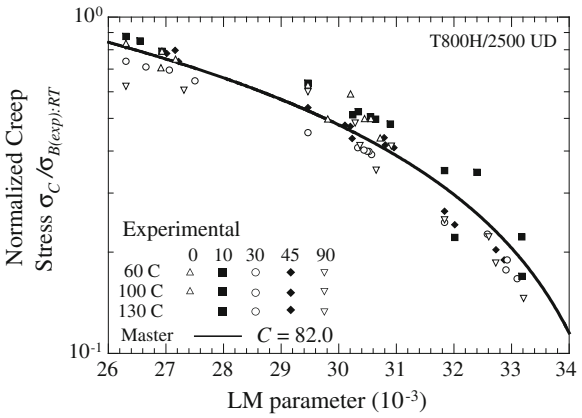

Fig. 3 A normalized grand master creep rupture curve based on the Larson-Miller parameter

good agreement between the theoretical and experimental grand master creep rupture behaviors has been achieved.

4 A Damage Mechanics Based Time-Temperature Extrapolation Method

A more general procedure for extrapolating short-term off-axis creep rupture data is developed on the basis of the classic Kachanov-Rabotnov damage mechanics model for creep failure [9, 10]. It is formulated using a modified temperature shift factor of the Arrhenius type.

4.1 Temperature-Dependent Damage Evolution

Temperature affects the scale of time. To define an engineering creep parameter that is consistent with damage mechanics modelling of creep failure and to establish the associated extrapolation method, it is assumed that similar to thermorheologically simple materials, the effect of temperature on time is described by means of a temperature shift factor $a_{T_{ref}}(T)$, defined as

$$dt_{T=T_{ref}} = \frac{1}{a_{T_{ref}}(T)} dt_{T=T} \tag{8}$$

where dt is a time increment, and T and T_{ref} denote the current temperature and a reference temperature, respectively. The temperature shift factor meets the condition $a_{T_{ref}}(T_{ref}) = 1$.

A representative form of temperature shift factor that meets the condition $a_{T_{ref}}(T_{ref}) = 1$ can be given as

$$a_{T_{ref}}(T) = \exp\left[\frac{H}{R}\left(\frac{1}{T} - \frac{1}{T_{ref}}\right)\right] \tag{9}$$

Assuming the temperature-time transformation given by Eq. (8) with Eq. (9), we can describe a temperature-dependent damage evolution law of the Kachanov-Rabotnov type in the following form:

$$\frac{d\omega}{dt} = K\left(\frac{1}{1-\omega}\right)^k f(\sigma^*_{T_{ref}}) \frac{1}{a_{T_{ref}}(T)} \tag{10}$$

where $\sigma^*_{T_{ref}}$ is the non-dimensional effective stress defined as

$$\sigma^*_{(T_{ref})} = \sqrt{\left(\frac{\sigma_1}{X_{(T_{ref})}}\right)^2 - \frac{\sigma_1\sigma_2}{X^2_{(T_{ref})}} + \left(\frac{\sigma_2}{Y_{(T_{ref})}}\right)^2 + \left(\frac{\tau_{12}}{S_{(T_{ref})}}\right)^2} \tag{11}$$

where $X_{(T_{ref})}$, $Y_{(T_{ref})}$, and $S_{(T_{ref})}$ are the in-plane principal strengths at a reference temperature.

Integrating Eq. (10) under a constant state of stress and temperature with the initial condition ($t = 0, \omega = 0$) and assuming the creep rupture condition $\omega = 1$, we can derive the following expression of creep rupture time t_R:

$$\log(1+k)K + \log t_R = -\left[\log f(\sigma^*_{T_{ref}}) + \log \frac{1}{a_{T_{ref}}}\right] \tag{12}$$

Substitution of the temperature shift factor given by Eq. (9) yields

$$\log f(\sigma^*_{T_{ref}}) = -\frac{1}{T}\left[\left(\frac{T}{T_{ref}} - 1\right)a + P_{LM}\right] \tag{13}$$

where $a = (H/R)\log e$ and $C = \log\{(1+k)K\}$.

The experimental results [6] suggest assuming the power-law stress dependence of creep rupture time

$$f(\sigma^*_{T_{\mathrm{ref}}}) = \sigma^{*n(T)}_{T_{\mathrm{ref}}} \tag{14}$$

Then, we can obtain the following master curve for off-axis creep rupture

$$\log \sigma^*_{T_{ref}} = -P^*_0 \tag{15}$$

where

$$P^*_0 = \frac{1}{Tn(T)}\left[P_{LM} + \left(\frac{T}{T_{ref}} - 1\right)a\right] \tag{16}$$

Note that P^*_0 defines a new temperature-time extrapolation parameter.

4.2 Consideration of Glass Transition Temperature

A rapid change in temperature dependence in the vicinity of the glass transition temperature T_g can be taken into account by assuming a modified temperature shift factor of the following form:

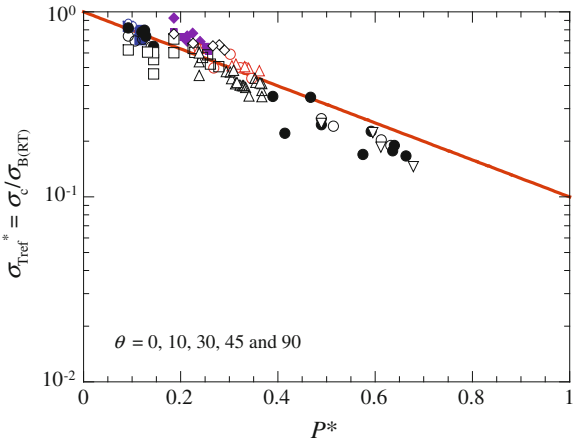

Fig. 4 A normalized grand master creep rupture curve based on a new temperature-time parameter P^*

$$a_T = \exp\left[\frac{H}{R}\left(\frac{1}{T} - \frac{1}{T_{ref}}\right)\frac{1}{L(T)}\right] \tag{17}$$

where

$$L(T) = -\left(1 - \frac{T}{T_M}\right)^c \left\{1 - \left(\frac{T}{T_M}\right)^d\right\} \tag{18}$$

In Eq. (18), T_M stands for a maximum temperature at which a given composite loses its load bearing capability, and it may be expressed as $T_M = T_\gamma + \beta$. Then, the temperature-time extrapolation formula can be generalized into the following form:

$$\log \sigma^*_{T_{ref}} = -P^* \tag{19}$$

where P^* is a generalized temperature-time extrapolation parameter, and it is defined as

$$P^* = \frac{1}{Tn(T)}\left[P_{LM} + \frac{1}{L(T)}\left(\frac{T}{T_{ref}} - 1\right)a\right] \tag{20}$$

Note that by elimination of $L(T)$, Eq. (20) can be reduced to Eq. (16).

Figure 4 shows a master curve for off-axis creep rupture plotted using the generalized temperature-time extrapolation parameter. It is seen that a single master relationship can be identified over a range of temperature below T_g.

5 A Multiaxial Creep Failure Criterion

The temperature-time extrapolation formula, Eq. (19), developed in this study suggests the principal creep strengths

$$X(P^*) = X_{(T_{ref})}10^{-P^*} \tag{21}$$

$$Y(P^*) = Y_{(T_{ref})}10^{-P^*} \tag{22}$$

$$S(P^*) = S_{(T_{ref})}10^{-P^*} \tag{23}$$

Replacing the principal static strengths in the Tsai-Hill static failure criterion with these principal isochronous strengths that are functions of the temperature-time parameter P^*, we can define the following creep failure criterion:

$$f = \left(\frac{\sigma_1}{X(P^*)}\right)^2 - \frac{\sigma_1\sigma_2}{X(P^*)^2} + \left(\frac{\sigma_2}{Y(P^*)}\right)^2 + \left(\frac{\tau_{12}}{S(P^*)}\right)^2 = 1 \tag{24}$$

Note that Eq. (19) can be derived from this creep failure criterion for the case of simple off-axis loading of coupon specimens.

6 Conclusions

A procedure for establishing an enginerring creep data extrapolation formula by means of a simple damage law of the Kachanov-Rabotnov type was proposed. Following this procedure, we developed a new engineering time-temperature extrapolation formula for the off-axis creep rupture behavior of unidirectional polymer matrix composites at different stress levels over a range of temperature. It can cope not only with the temperature dependence but also with the fiber orientation dependence of the off-axis creep rupture behavior of unidirectional CFRP laminates. It was proved that the use of the time-temperature extrapolation formula developed in the present study is equivalent to the use of a multiaxial creep failure criterion for orthotropic polymer matrix composites that is based on the principal isochronous strengths.

References

1. Brinson, H.F.: Matrix dominated time dependent failure predictions in polymer matrix composites. Compos. Struct. **47**, 445–456 (1999)
2. Dillard, D.A., Morris, D.H., Brinson, H.F.: Predicting viscoelastic response and delayed failures in general laminated composites. In: Daniel I.M. (ed) Composite Materials: testing and design (sixth conference). ASTM STP **787**, 357–370 (1982)

3. Raghavan, J., Meshii, M.: Creep rupture of polymer composites. Compos. Sci. Technol. **57**, 375–388 (1997)
4. Kawai, M., Masuko, Y., Sagawa, T.: Off-axis tensile creep rupture of unidirectional CFRP laminates at elevated temperature. Compos. A **37**, 257–269 (2006)
5. Monkman, F.C., Grant, N.J.: An empirical relationship between rupture life and minimum creep rate in creep-rupture test. Proc. ASTM **56**, 593–620 (1956)
6. Kawai, M., Sagawa, T.: Temperature dependence of off-axis tensile creep rupture behavior of a unidirectional carbon/epoxy laminate. Compos. A **39**, 523–539 (2008)
7. Larson, F.R., Miller, A.: A time temperature relationship for rupture and creep stresses. Trans. ASME **74**, 765–771 (1952)
8. Kawai, M.: Damage mechanics model for off-axis fatigue behavior of unidirectional carbon fiber-reinforced composites at room and high temperatures. In: Massard, T., Vautrin, A. (eds) Proceedings of the 12th International Conference on Composite Materials (ICCM12), p. 322. Paris, France, 5–9 July 1999
9. Kachanov, L.M.: On the rupture time under the condition of creep. Izv. Akad. Nauk SSSR, Otd. Tekh. Nauk, (in Russian). **8**, 26–31 (1958)
10. Rabotnov, Y.N.: Creep Problems of Structural Members. North-Holland, Amsterdam (1969)
11. Azzi, V.D., Tsai, S.W.: Anisotropic strength of composites. Exp. Mech. **5**, 283–288 (1965)

Recent Advances in the Processing and Properties of Ultrafine-Grained Metals Prepared Using Severe Plastic Deformation

Terence G. Langdon

Abstract Conventional thermo-mechanical processing provides the potential for producing materials with very small grain sizes, typically of the order of ~5–10 μm. However, recent experiments have demonstrated that much smaller grain sizes may be attained, within the submicrometer or nanometer range, through the application to the material of severe plastic deformation (SPD). In processing by SPD, the material is deformed to a high strain in the presence of a hydrostatic pressure and this introduces a high density of dislocations which re-arrange into a low energy configuration and thereby produce arrays of grain boundaries. Typical SPD processes include equal-channel angular pressing (ECAP) and high-pressure torsion (HPT). Materials processed using SPD have numerous advantages over coarse-grained materials including exceptionally high strength and a potential for use in rapid superplastic forming operations at elevated temperatures. Accordingly, processing by SPD has become a major research area within the field of Materials Science over the last decade. This paper examines some of these more recent developments with an emphasis on processing using HPT.

1 Introduction

In polycrystalline metals, the grain size plays a major role in dictating the properties of the material. Specifically, materials become stronger when the grain size is reduced and, in addition, materials with small grain sizes exhibit high superplastic

T. G. Langdon (✉)
Departments of Aerospace & Mechanical Engineering and Materials Science,
University of Southern California, Los Angeles, CA 90089-1453, USA
e-mail: langdon@usc.edu; langdon@soton.ac.uk

T. G. Langdon
Materials Research Group, Faculty of Engineering and the Environment,
University of Southampton, Southampton SO17 1BJ, UK

H. Altenbach and S. Kruch (eds.), *Advanced Materials Modelling for Structures*,
Advanced Structured Materials 19, DOI: 10.1007/978-3-642-35167-9_22,

ductilities when deformed at elevated temperatures. This trend forms the basis for the commercial superplastic forming industry in which complex shapes and curved parts are easily formed from superplastic sheet metals [1]. The superplastic forming industry is now more than forty years old and it processes thousands of tons of metallic parts every year for a range of applications including in the aerospace and automotive sectors. The materials used in superplastic forming are obtained through thermo-mechanical processing in which the metals are subjected to straining and heat treatments in order to produce grain sizes that are typically in the range of ~5–10 μm. In practice, thermo-mechanical processing is generally not capable of producing materials with grains sizes smaller than 1 μm.

There are two basic procedures for producing metals having grain sizes of <1 μm [2]. The first procedure, known as the "bottom-up" approach, assembles polycrystalline metals from individual atoms using deposition techniques or from nanoscale building blocks produced, for example, by high-energy ball milling. However, these techniques have the disadvantage that the samples are very small, they are suitable only for use in micro-devices and they contain at least a small amount of residual porosity. The second procedure is the "top-down" approach in which bulk fully-dense coarse-grained polycrystalline solids are processed by severe plastic deformation (SPD) to introduce a high dislocation density without any concomitant change in the cross-sectional dimensions of the specimens. Using this approach, the dislocations are able to re-arrange into arrays of high-angle grain boundaries and the grain sizes are typically in the submicrometer range of 100–1000 nm or even in the true nanometer range of <100 nm. Several different SPD procedures are now available [3, 4] but most attention has been devoted to date to the procedures of equal-channel angular pressing (ECAP) [5] and high-pressure torsion (HPT) [6]. Of these two procedures, HPT processing is especially attractive because it introduces grains which are smaller than those produced using ECAP [7].

Processing by HPT has a long history dating back to the work of Nobel Laureate Professor P.W. Bridgman conducted at Harvard University in the 1930s and 1940s [8, 9]. However, it was only much later, with the advent of sophisticated instruments for analytical microscopy, that HPT processing was recognized as a tool that may be used to introduce exceptional grain refinement into polycrystalline solids [10–12]. Accordingly, there is a considerable current interest in the effects of HPT processing and many investigations of HPT materials are now underway at various laboratories around the world. The objective of this paper is to provide a description of the HPT process and to examine some of the more recent developments.

2 Principles of Processing by HPT

The principle of HPT processing is to subject a specimen to a high applied pressure, P, and concurrent torsional straining. A typical HPT facility is shown in Fig. 1 [13]. Samples are generally in the form of thin disks, typically with diameters of 10 or 20 mm, although there are some recent experiments describing HPT processing using

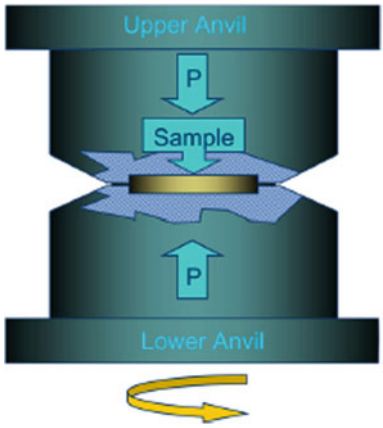

Fig. 1 In HPT processing, a sample, in the form of a disk, is subjected to a pressure P and concurrent torsional straining [13]

small cylindrical samples [14–16]. The disk is then placed in a depression on the lower anvil, the two anvils are brought in to position, the pressure is applied, and one anvil is rotated to provide the torsional straining. This type of processing is generally termed quasi-constrained HPT because the sample is held between two anvils but there is a small gap between the anvils so that there is some limited outflow of material during processing [17, 18]. This contrasts with constrained HPT where the sample is held rigidly within the anvil without any outward flow and unconstrained HPT where the sample is free to flow outwards at all points during processing [19].

When a disk is processed by HPT, it can be shown that the imposed strain is proportional to (Nr/h) where N is the total number of revolutions in HPT, r is the radius of the disk and h is the disk height or thickness [20, 21]. It follows directly from this relationship that the strain varies with the radial distance from the center of the disk and at the center, where $r = 0$, the strain is zero. This calculation suggests that the strain imposed in HPT will be very inhomogeneous, with a high strain around the edge of the disk and an absence of any strain at the center. Based on this calculation, there have been several attempts to evaluate the degree of inhomogeneity after HPT processing. Generally, these evaluations are based on taking measurements of the hardness values across the disks after HPT processing. As will shown in the following section, these measurements reveal a potential for achieving an exceptionally high level of homogeneity in HPT.

3 Potential for Achieving Homogeneity After Processing by HPT

The degree of homogeneity occurring in samples of Ni after processing by HPT was explored in 2003 and the results are shown in Figs. 2 and 3 [7]. These plots show the values of the microhardness in a three-dimensional display where the lower axes denote the positions on the disks having diameters of 10 mm. In Fig. 2 the results are

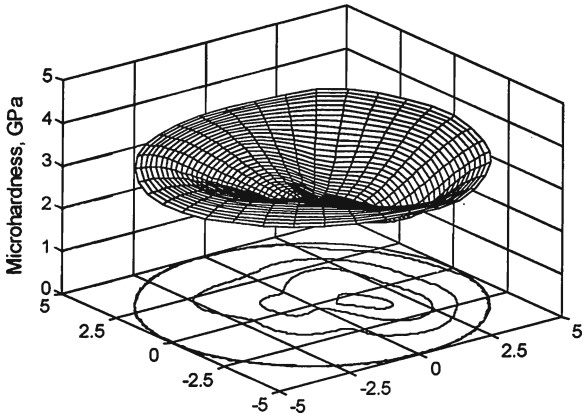

Fig. 2 Hardness values in Ni processed by HPT through 5 turns at $P = 1.0$ GPa [7]

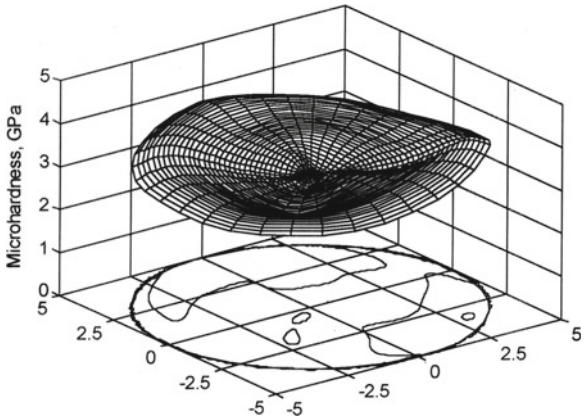

Fig. 3 Hardness values in Ni processed by HPT through 5 turns at $P = 9.0$ GPa [7]

shown for an applied pressure of 1.0 GPa after 5 turns and in Fig. 3 the results are again for 5 turns but with an applied pressure of 9.0 GPa. In Fig. 2 there is a clear depression in the center so that the hardness levels are high around the edge whereas in Fig. 3 there is a much higher level of homogeneity across the disk.

The important result from these early experiments was that the level of homogeneity increases with increasing pressure and/or with increasing numbers of turns. Contrary to expectations based on the simple relationship for the imposed strain in HPT, there is a potential for achieving a reasonably high level of homogeneity provided the pressure is sufficiently high and the torsional straining is applied through a sufficient number of turns. This unexpected result was subsequently confirmed in a theoretical analysis of HPT using strain gradient plasticity [22].

An important contribution followed shortly thereafter in experiments conducted in 2004 on an austenitic steel processed by HPT [23]. In general, these experiments

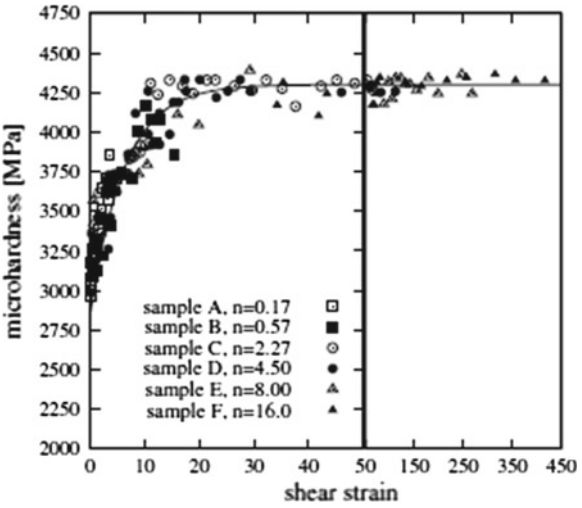

Fig. 4 Plot of microhardness against shear strain for disks of an austenitic steel processed under a pressure of 5.3 GPa through 0.17 to 16.0 turns [23]

recorded similar data to the results presented earlier in Figs. 2 and 3 for pure Ni but the analysis was extended by showing that all of the datum points may be reasonably correlated in a single plot of microhardness against the shear strain. This plot is given in Fig. 4 and it shows data recorded under a pressure, P, of 5.3 GPa for various numbers of turns from 0.17 to 16.0 [23]. All results fall on a single line and there is an initial sharp increase and then, after a shear strain of ~50, a horizontal portion where the results have achieved a steady-state condition.

The data in Fig. 4 suggest there will be a saturation in the grain size produced by HPT processing such that, for any selected processing conditions, the grain size will be refined to a well-defined value. There have been several discussions on the parameters influencing this saturation condition [24, 25] and there is good experimental evidence that it is dependent upon the stacking fault energy of the material [26, 27]. This suggests it may be of a similar form to the model developed for the minimum grain size that may be achieved by the synthesis of bulk nanocrystalline materials by ball milling [28].

4 Experimental Examples of Hardness Variations in HPT

Examples are shown in Figs. 5 and 6 for hardness data obtained using an Al-6061 alloy processed by HPT. In Fig. 5, the hardness values are shown as a function of the position on the disk with the lower line representing the unprocessed condition and the points for $N = 0$ representing the application of an applied stress of 4.0 GPa

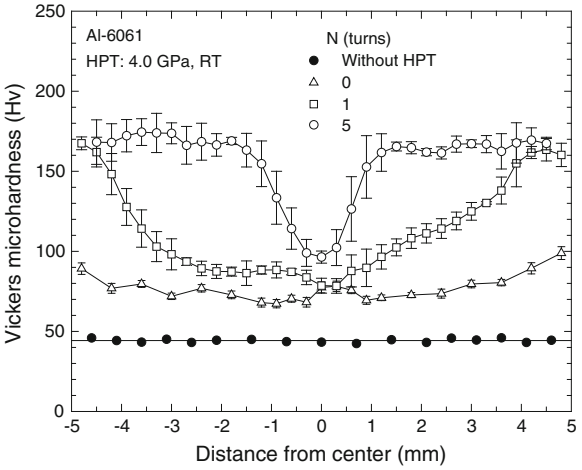

Fig. 5 Values of microhardness versus positions on the disk of an Al-6061 alloy processed by HPT at 4.0 GPa [29]

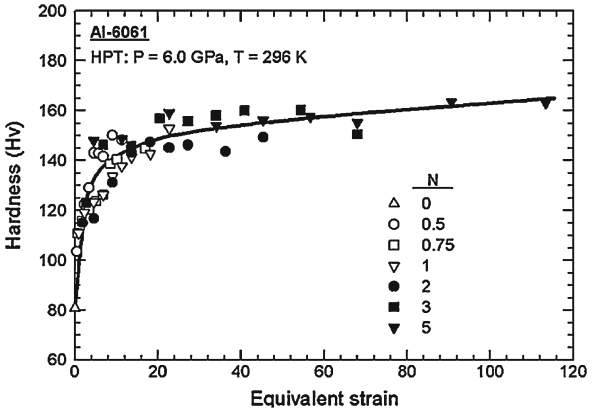

Fig. 6 Hardness versus equivalent strain for an Al-6061 alloy processed by HPT [30]

for 1 min without any torsional straining [29]. In Fig. 6, individual hardness values are plotted against the equivalent strain for an Al-6061 alloy tested under an applied pressure of 6.0 GPa [30].

The important result from Fig. 5 is that the hardness increases under the applied pressure even when there is no torsional straining. There is a further increase with torsional straining especially around the edge of the disk and thereafter these higher values at the edge gradually sweep inwards so that the sample begins to display a reasonably uniform distribution of hardness values. In Fig. 6 the hardness data obtained from an Al-6061 alloy with $P = 6.0$ GPa are plotted against the equivalent strain and it is apparent that all points cluster on or about a single line. This is

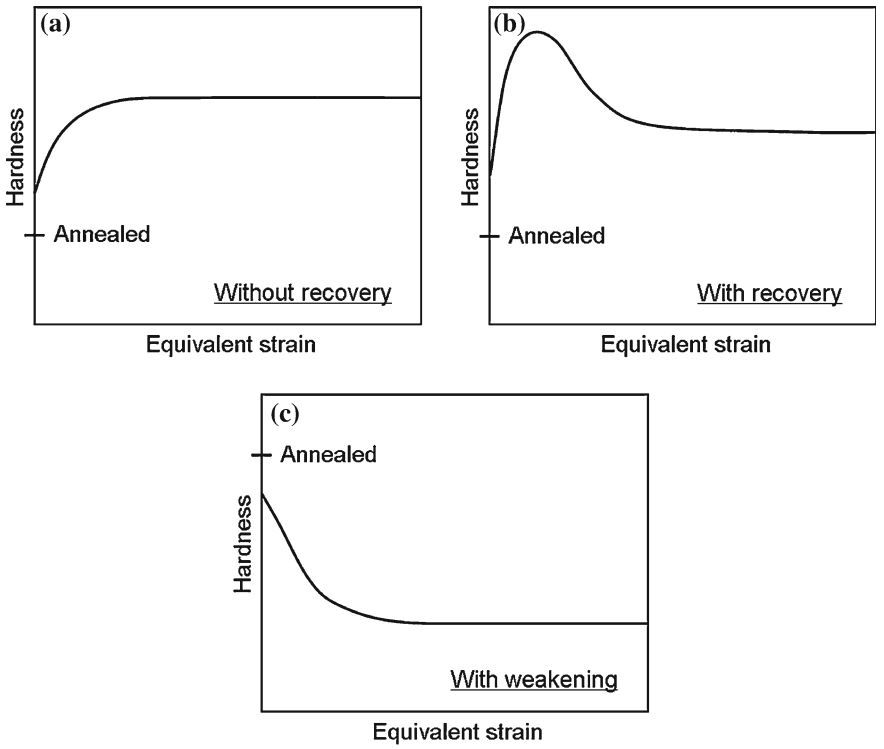

Fig. 7 Examples of three types of variation of hardness with equivalent strain: **a** without recovery, **b** with recovery and **c** with a weakening [31]

consistent with the earlier result shown in Fig. 4 and it suggests that hardness values gradually increase in HPT processing and then saturate at a well-defined value.

Extensive measurements conducted on a number of different materials has shown that this conclusion is an over-simplification. In practice, the variation of hardness with equivalent strain is dependent upon the nature of the material. In many face-centered cubic metals the behaviour will follow the trend in Fig. 6, as depicted schematically in Fig. 7a, but in some other materials the trend will be different: these variations are depicted as Fig. 7b, c [31]. Figure 7b occurs in a material such as high-purity aluminium where there is a very high stacking-fault energy so that recovery by cross-slip is relatively easy. In high-purity Al, hardness measurements give higher, rather than lower, hardness values in the centers of the disks in the initial stages of HPT processing because of the rapid recovery occurring around the disk peripheries [32]. Figure 7c occurs in materials such as the two-phase Zn-22 % Al eutectoid alloy where there is a weakening effect due to the high pressure imposed in HPT [33]: for this alloy the weakening is due to a reduction in the distribution of Zn precipitates within the Al-rich grains.

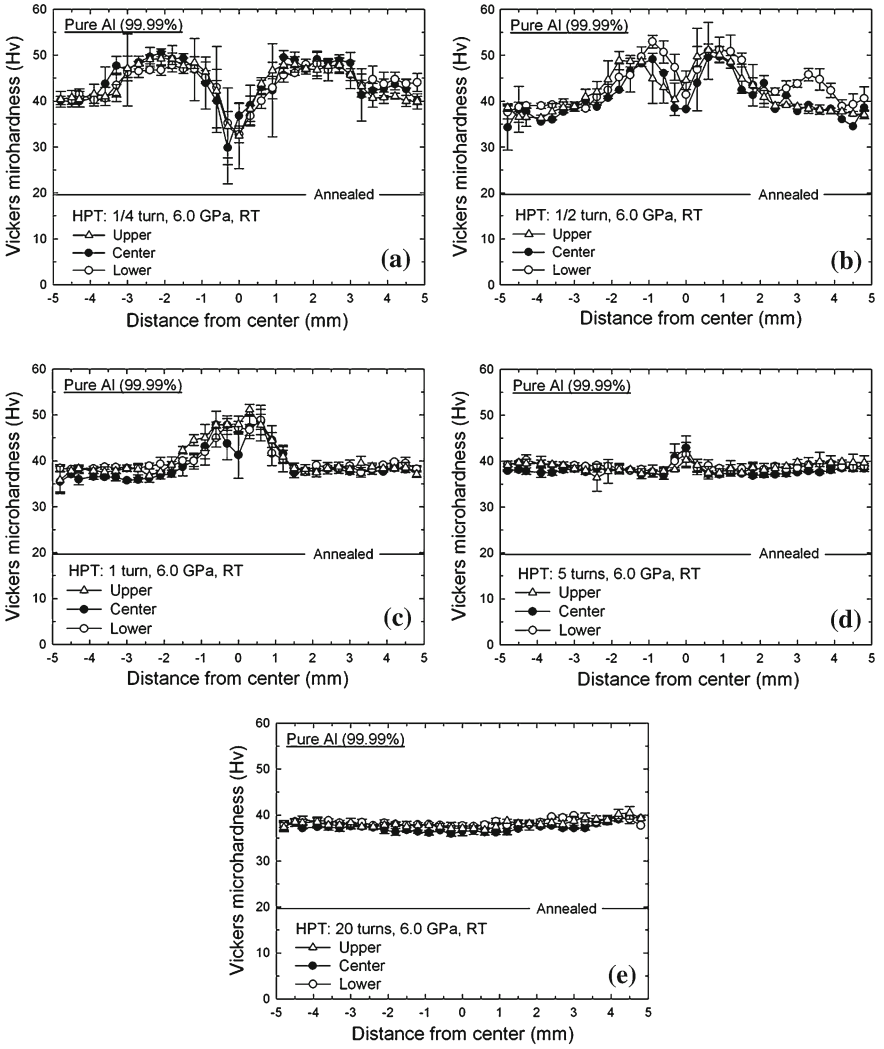

Fig. 8 The variation of hardness across disks of pure Al at the center and at upper and lower positions after (**a**) 1/4 turn, (**b**) 1/2 turn, (**c**) 1 turn, (**d**) 5 turns and (**e**) 20 turns

The hardness data described so far relate to measurements taken on the surfaces of disks processed by HPT. However, these results give no information on the hardness values in the cross-sections of the HPT disks. To overcome this problem, hardness measurements have been taken also on different sections within the disks [34]. Figure 8 shows results for high purity aluminium where hardness measurements were taken in the central cross-sectional plane of each disk and at planes located ~200 μm from the upper and lower surfaces. These results demonstrate that

high purity Al exhibits excellent homogeneity after processing by HPT through 5 or more turns.

Acknowledgments This work was supported by the National Science Foundation of the United States under Grant No. DMR-0855009 and the European Research Council under ERC Grant Agreement No. 267464-SPDMETALS.

References

1. Barnes, A.J.: Superplastic forming: 40 years and still growing. J. Mater. Eng. Perform. **16**, 440 (2007)
2. Zhu, Y.T., Lowe, T.C., Langdon, T.G.: Performance and applications of nanostructured materials produced by severe plastic deformation. Scripta Mater. **51**, 825 (2004)
3. Valiev, R.Z., Estrin, Y., Horita, Z., Langdon, T.G., Zehetbauer, M.J., Zhu, Y.T.: Producing bulk ultrafine-grained materials by severe plastic deformation. JOM **58**(4), 33 (2006)
4. Zhu, Y., Valiev, R.Z., Langdon, T.G., Tsuji, N., Lu, K.: Processing of nanostructured metals and alloys via severe plastic deformation. MRS Bull. **35**, 977 (2010)
5. Valiev, R.Z., Langdon, T.G.: Principles of equal-channel angular pressing: a processing tool for grain refinement. Prog. Mater. Sci. **51**, 881 (2006)
6. Zhilyaev, A.P., Langdon, T.G.: Using high-pressure torsion for metal processing: Fundamentals and applications. Prog. Mater. Sci. **53**, 893 (2008)
7. Zhilyaev, A.P., Nurislamova, G.V., Kim, B.K., Baró, M.D., Szpunar, J.A., Langdon, T.G.: Experimental parameters influencing grain refinement and microstructural evolution during high-pressure torsion. Acta Mater. **51**, 753 (2003)
8. Bridgman, P.W.: Effects of high shearing stress combined with high hydrostatic pressure. Phys. Rev. **48**, 825 (1935)
9. Bridgman, P.W.: On torsion combined with compression. J. Appl. Phys. **14**, 273 (1943)
10. Valiev, R.Z., Krasilnikov, N.A., Tsenev, N.K.: Plastic deformation of alloys with submicron-grained structure. Mater. Sci. Eng. **A137**, 35 (1991)
11. Valiev, R.Z., Korznikov, A.V., Mulyukov, R.R.: Structure and properties of ultrafine-grained materials produced by severe plastic deformation. Mater. Sci. Eng. **A168**, 141 (1993)
12. Valiev, R.Z., Islamgaliev, R.K., Alexandrov, I.V.: Bulk nanostructured materials from severe plastic deformation. Prog. Mater. Sci. **45**, 103 (2000)
13. Xu, C., Horita, Z., Langdon, T.G.: The evolution of homogeneity in an aluminium alloy processed using high-pressure torsion. Acta Mater. **56**, 5168 (2008)
14. Sakai, G., Nakamura, K., Horita, Z., Langdon, T.G.: Developing high-pressure torsion for use with bulk samples. Mater. Sci. Eng. **A406**, 268 (2005)
15. Pippan, R., Scheriau, S., Hohenwarter, A., Hafok, M.: Advantages and limitations of HPT: a review. Mater. Sci. Forum **584–586**, 16 (2008)
16. Hohenwarter, A., Bachmaier, A., Gludovatz, B., Scheriau, S., Pippan, R.: Technical parameters affecting grain refinement by high pressure torsion. Int. J. Mater. Res. **100**, 1653 (2009)
17. Figueiredo, R.B., Cetlin, P.R., Langdon, T.G.: Using finite element modelling to examine the flow processes in quasi-constrained high-pressure torsion. Mater. Sci. Eng. **A528**, 8198 (2011)
18. Figueiredo, R.B., Pereira, P.H.R., Aguilar, M.T.P., Cetlin, P.R., Langdon, T.G.: Using finite element modelling to examine the temperature distribution in quasi-constrained high-pressure torsion. Acta Mater. **60**, 3190 (2012)
19. Zhilyaev, A.P., Oh-ishi, K., Langdon, T.G., McNelley, T.R.: Microstructural evolution in commercial purity aluminium during high-pressure torsion. Mater. Sci. Eng. **A410–411**, 277 (2005)
20. Valiev, R.Z., Ivanisenko, YuV, Rauch, E.F., Baudelet, B.: Structure and deformation behaviour of armco iron subjected to severe plastic deformation. Acta Mater. **44**, 4705 (1996)

21. Wetscher, F., Vorhauer, A., Stock, R., Pippan, R.: Structural refinement of low alloyed steels during severe plastic deformation. Mater. Sci. Eng. **A387–389**, 809 (2004)
22. Estrin, Y., Molotnikov, A., Davies, C.H.J., Lapovok, R.: Strain gradient plasticity modelling of high pressure torsion. J. Mech. Phys. Solids **56**, 1186 (2008)
23. Vorhauer, A., Pippan, R.: On the homogeneity of deformation in high pressure torsion. Scripta Mater. **51**, 921 (2004)
24. Pippan, R., Wetscher, F., Hafok, M., Vorhauer, A., Sabirov, I.: The limits of refinement by severe plastic deformation. Adv. Eng. Mater. **8**, 1046 (2006)
25. Pippan, R., Scheriau, S., Taylor, A., Hafok, M., Hohenwarter, A., Bachmaier, A.: Saturation of fragmentation during severe plastic deformation. Ann. Rev. Mater. Res. **40**, 319 (2010)
26. Zhao, Y.H., Liao, X.Z., Zhu, Y.T., Horita, Z., Langdon, T.G.: Influence of stacking fault energy on nanostructure formation under high pressure torsion. Mater. Sci. Eng. **A410–411**, 188 (2005)
27. Zhao, Y.H., Zhu, Y.T., Liao, X.Z., Horita, Z., Langdon, T.G.: Influence of stacking fault energy on the minimum grain size achieved in severe plastic deformation. Mater. Sci. Eng. **A463**, 22 (2007)
28. Mohamed, F.A.: A dislocation model for the minimum grain size obtainable by milling. Acta Mater. **51**, 4107 (2003)
29. Xu, C., Horita, Z., Langdon, T.G.: Evaluating the influence of pressure and torsional strain on processing by high-pressure torsion. J. Mater. Sci. **43**, 7286 (2008)
30. Loucif, A., Figueiredo, R.B., Baudin, T., Brisset, F., Langdon, T.G.: Microstructural evolution in an Al-6061 alloy processed by high-pressure-torsion. Mater. Sci. Eng. **A527**, 4864 (2010)
31. Kawasaki, M., Ahn, B., Langdon, T.G.: Significance of strain reversals in a two-phase alloy processed by high-pressure torsion. Mater. Sci. Eng. **A527**, 7008 (2010)
32. Xu, C., Horita, Z., Langdon, T.G.: The evolution of homogeneity in processing by high-pressure torsion. Acta Mater. **55**, 203 (2007)
33. Kawasaki, M., Ahn, B., Langdon, T.G.: Microstructural evolution in a two-phase alloy processed by high-pressure torsion. Acta Mater. **58**, 818 (2010)
34. Kawasaki, M., Figueiredo, R.B., Langdon, T.G.: An investigation of hardness homogeneity throughout disks processed by high-pressure torsion. Acta Mater. **59**, 308 (2011)

Macro/Micro Elastic-Viscoplastic Analysis of Woven Composite Laminates with Misaligned Woven Fabrics

Tetsuya Matsuda, Shinya Kanamaru, Naoya Honda and Nobutada Ohno

Abstract The elastic-viscoplastic behavior of woven composite laminates in which woven fabrics are stacked with misalignment is analyzed both macroscopically and microscopically using a homogenization theory. For this, a novel boundary condition for unit cell analysis is proposed based on the point-symmetry and periodicity of internal structures in woven composite laminates. Using the boundary condition, the homogenization theory for nonlinear time-dependent composites developed by the authors is rebuilt for woven composite laminates with misaligned woven fabrics. The theory rebuilt is able to deal with any laminate misalignment of woven fabrics using the same analysis domain, avoiding not only geometry and mesh generation of an analysis domain for every misalignment, but also the influence of mesh dependence. The present theory is then applied to the elastic-viscoplastic analysis of glass fiber/epoxy woven composite laminates with misaligned woven fabrics. It is shown that the misalignment significantly affects the macro/micro elastic-viscoplastic properties of the laminates.

T. Matsuda (✉) · S. Kanamaru · N. Honda
Department of Engineering Mechanics and Energy, University of Tsukuba,
1-1-1 Tennodai, Tsukuba 305-8573, Japan
e-mail: matsuda@kz.tsukuba.ac.jp

S. Kanamaru
e-mail: s-kanamaru@edu.esys.tsukuba.ac.jp

N. Honda
e-mail: s1120976@u.tsukuba.ac.jp

N. Ohno
Department of Mechanical Science and Engineering, Nagoya University, Chikusa-ku,
Nagoya 464-8603, Japan

H. Altenbach and S. Kruch (eds.), *Advanced Materials Modelling for Structures*,
Advanced Structured Materials 19, DOI: 10.1007/978-3-642-35167-9_23,

1 Introduction

Plain-woven composite laminates made of plain-woven fabrics and matrix materials as shown in Fig. 1 possess high specific strength, high specific stiffness and excellent formability. Thus, they are used in many industrial sectors such as aerospace, transportation and energy-related industries, meaning that they can encounter severe situation including high stress and high temperature. It is therefore of great importance to analyze not only elastic but also inelastic properties of plain-woven composite laminates. In such analysis, misalignment of woven fabrics in laminates as illustrated in Fig. 1b, which will be referred to as "laminate misalignment" hereafter, becomes an important issue because they can affect mechanical properties of the laminates. Therefore, it is worth developing a theory to analyze inelastic behavior of plain-woven laminates with laminate misalignment.

The mathematical homogenization theory [1] is one of the most useful theories for inelastic analysis of plain-woven composite laminates. Thus, some researches have already applied this theory to such analysis. Takano et al. [2] conducted a microscopic damage analysis of plain-woven glass fiber-reinforced plastic (GFRP) laminates with "in-phase" or "out-of-phase" laminate configuration. Here, the in-phase and out-of-phase mean that plain-woven fabrics in laminates possess no misalignment and half a unit cell misalignment, respectively. Zeman and Šejnoha [3] further adopted quasi-quarter of a cell misalignment in addition to the two above-mentioned laminate configurations in a statistical investigation of the elastic properties of plain-woven carbon fiber-reinforced plastic (CFRP) laminates. Results of these analyses revealed significant influence of misalignment on the mechanical properties of plain-woven laminates. In the analyses, however, the misalignment was restricted to half or quasi-quarter of unit cells. In addition, the analyses for the misaligned cases required twice the volume of unit cells defined for aligned cases.

The authors [4–7], on the other hand, have performed elastic-viscoplastic and creep analyses of fiber-reinforced composites using a homogenization theory for nonlinear time-dependent composites [8, 9]. In one of these studies [6], the authors proposed a theory which was able to deal plain-woven composite laminates with

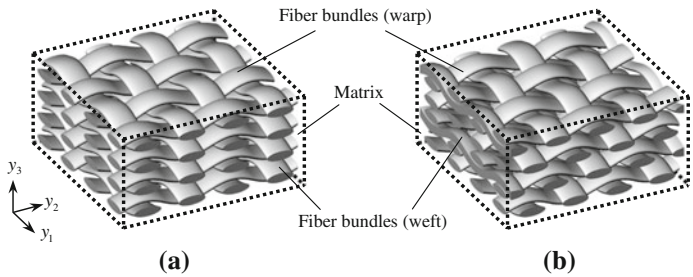

Fig. 1 Plain-woven composite laminates: **a** without laminate misalignment, **b** with laminate misalignment

both the in-phase and out-of-phase laminate configurations using the same basic cell, which was based on a point-symmetric boundary condition for unit cell analysis [10]. Here, the basic cell means a quarter of a unit cell for the in-phase case, which will be described in the subsequent section, resulting in significant improvement of computational efficiency. This method, however, was also limited to the half a cell misalignment, and was not able to deal with arbitrary misalignment of the type shown in Fig. 1b. More recently, the authors [11] developed a homogenization theory for nonlinear time-dependent periodic materials with laminate misalignment. Though this theory was considerably useful because it was able to deal with arbitrary misalignment in periodic materials, it was not able to analyze the mechanical properties of plain-woven composite laminates with misalignment using the basic cell.

In this study, the homogenization theory applicable to the elastic-viscoplastic analysis of plain-woven composite laminates with arbitrary laminate misalignment is developed by employing the basic cell as an analysis domain. This theory is able to deal with any laminate misalignment using the same basic cell. Using the present theory, the elastic-viscoplastic analysis of plain-woven glass fiber/epoxy laminates with misaligned plain-woven fabrics is analyzed both macroscopically and microscopically to examine the effects of misalignment on the elastic-viscoplastic behavior of the laminates.

2 Homogenization Theory for Plain-Woven Composite Laminates with Misaligned Plain-Woven Fabrics

2.1 Point-Symmetry and Periodicity of Perturbed Velocity Fields

A plain-woven composite laminate with misaligned plain-woven fabrics is considered as illustrated in Fig. 2, in which each fabric is assumed to possess the same amount of arbitrary misalignment in the y_2-direction. The laminate is subjected to a uniform load and exhibits infinitesimal deformation both macroscopically and microscopically. Then, a cuboid cell A shown in the figure, which will henceforth be called "basic cell", is defined as an analysis domain, and its boundary is denoted as Γ. It should be noted that this A is a quarter of a usual unit cell for the plain-woven laminate without misalignment depicted in Fig. 1a. Microscopic stress and strain fields in A are denoted as $\sigma_{ij}(\boldsymbol{y}, t)$ and $\varepsilon_{ij}(\boldsymbol{y}, t)$, respectively, where t represents time.

According to the conventional homogenization theory [1], the microscopic velocity field $\dot{u}_i(\boldsymbol{y}, t)$ in Y is expressed as

$$\dot{u}_i(\boldsymbol{y}, t) = \dot{F}_{ij}(t) y_j + \dot{u}_i^{\#}(\boldsymbol{y}, t), \tag{1}$$

where $(\dot{})$ indicates differentiation with respect to t, $F_{ij}(t)$ denotes the macroscopic deformation gradient, and $\dot{u}_i^{\#}$ stands for the perturbed velocity from the macroscopic one $\dot{F}_{ij}(t) y_j$. Then the microscopic strain rate has the following expression:

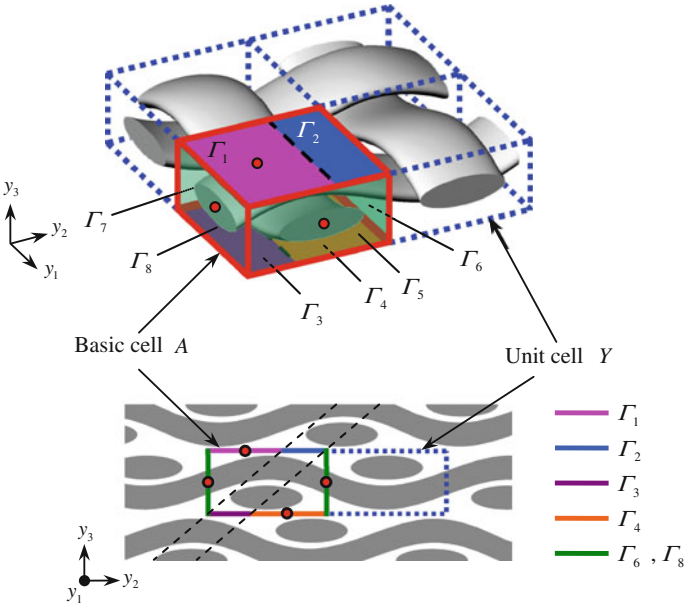

Fig. 2 Plain-woven laminate with laminate misalignment and its basic cell A

$$\dot{\varepsilon}_{ij}(\boldsymbol{y}, t) = \dot{E}_{ij}(t) + \dot{\varepsilon}^{\#}_{ij}(\boldsymbol{y}, t), \tag{2}$$

where $\dot{E}_{ij}$ and $\dot{\varepsilon}^{\#}_{ij}$ indicate respectively the macroscopic strain rate and the perturbed strain rate described as $\dot{E}_{ij} = (\dot{F}_{ij} + \dot{F}_{ji})/2$ and $\dot{\varepsilon}^{\#}_{ij} = (\dot{u}^{\#}_{i,j} + \dot{u}^{\#}_{j,i})/2$, in which $(\,)_{,j}$ represents the differentiation with respect to y_j.

Here, let us discuss the property of the distribution of $\dot{u}^{\#}_i$ in the laminate. First, we divide Γ into eight parts as shown in Fig. 2, i.e. $\Gamma_\alpha (\alpha = 1, 2, \ldots, 8)$. It is noted that Γ_1 and Γ_2, Γ_3 and Γ_4, and Γ_5–Γ_8 respectively belong to the top, bottom and lateral boundary surfaces of the cell. Then, it is found from the cross-sectional view in Fig. 2 that the internal structure of the laminate possesses point-symmetry with respect to the centers of Γ_1 and Γ_4. In addition, one can find that such point-symmetry is also satisfied with respect to the centers of Γ_5–Γ_8. Thus, the distribution of $\dot{u}^{\#}_i$ must possess the point-symmetry with respect to these points. The internal structure, on the other hand, possesses periodicity in the direction indicated by the dashed line in the cross-sectional view in Fig. 2. This suggests that the distribution of $\dot{u}^{\#}_i$ on Γ_2 and Γ_3 must be periodic. These point-symmetry and periodicity of $\dot{u}^{\#}_i$ on Γ can be used as a boundary condition to rebuild the homogenization theory, the process of which will be described in the following subsections. It should be noted that the same point-symmetry and periodicity exist with respect to the microscopic stress σ_{ij} and its rate $\dot{\sigma}_{ij}$.

2.2 Weak Form of Equilibrium of Microscopic Stress and Its Boundary Integral Term

The equilibrium of σ_{ij} is expressed in a rate form as

$$\dot{\sigma}_{ij,j} = 0. \tag{3}$$

Now, let $v_i(\boldsymbol{y}, t)$ be an arbitrary variation of the perturbed velocity field $\dot{u}_i^{\#}$ defined in A at t. Then, the integration by parts and the divergence theorem allow Eq. (3) to be transformed to a weak form:

$$\int_A \dot{\sigma}_{ij} v_{i,j} dA - \int_\Gamma \dot{\sigma}_{ij} n_j v_i d\Gamma = 0, \tag{4}$$

where n_j indicates the unit vector outward normal to Γ. It is noted here that the integral term in the above equation can be expressed as

$$\int_\Gamma \dot{\sigma}_{ij} n_j v_i d\Gamma = \sum_\alpha \int_{\Gamma_\alpha} \dot{\sigma}_{ij} n_j v_i d\Gamma_\alpha. \tag{5}$$

As discussed in the previous subsection, distributions of $\dot{u}_i^{\#}$, i.e. v_i, and $\dot{\sigma}_{ij}$ are point-symmetric on Γ_1, Γ_4 and Γ_5–Γ_8 with respect to their centers, whereas, n_j keeps the same direction on each boundary surface. Thus, we obtain

$$\int_{\Gamma_\alpha} \dot{\sigma}_{ij} n_j v_i d\Gamma_\alpha = 0, \quad (\alpha = 1, 4, 5, 6, 7, 8). \tag{6}$$

In contrast, distributions of v_i and $\dot{\sigma}_{ij}$ are periodic on Γ_2 and Γ_3, whereas, n_j takes the opposite directions on these boundary surfaces. Consequently, the following relation is obtained:

$$\int_{\Gamma_2} \dot{\sigma}_{ij} n_j v_i d\Gamma_2 + \int_{\Gamma_3} \dot{\sigma}_{ij} n_j v_i d\Gamma_3 = 0. \tag{7}$$

From Eqs. (6) and (7), Eq. (5) vanishes, which allows Eq. (4) to be written as

$$\int_A \dot{\sigma}_{ij} v_{i,j} dA = 0. \tag{8}$$

This resulting equation has the same form as that obtained in the original work by Wu and Ohno [8], and Ohno et al. [9], which enables us to rebuild the homogenization theory of time-dependent composites as briefly described in the following subsection.

2.3 Homogenization Theory

Constituents of the laminate are assumed to exhibit linear elasticity and nonlinear viscoplasticity as characterized by

$$\dot{\sigma}_{ij} = c_{ijkl}(\dot{\varepsilon}_{kl} - \beta_{kl}), \tag{9}$$

where c_{ijkl} and β_{kl} represent the elastic stiffness and viscoplastic strain rate of the constituents, satisfying $c_{ijkl} = c_{jikl} = c_{ijlk} = c_{klij}$ and $\beta_{kl} = \beta_{lk}$. Using the above equation, Eqs. (2) and (8), the evolution equation of microscopic stress σ_{ij} and the relation between macroscopic stress rate $\dot{\Sigma}_{ij}$ and strain rate $\dot{E}_{kl}$ are derived [8, 9]:

$$\dot{\sigma}_{ij} = c_{ijpq}\left(\delta_{pk}\delta_{ql} + \chi^{kl}_{p,q}\right)\dot{E}_{kl} - c_{ijkl}\left(\beta_{kl} - \varphi_{k,l}\right), \tag{10}$$

$$\dot{\Sigma}_{ij} = \left\langle c_{ijpq}\left(\delta_{pk}\delta_{ql} + \chi^{kl}_{p,q}\right)\right\rangle \dot{E}_{kl} - \left\langle c_{ijkl}\left(\beta_{kl} - \varphi_{k,l}\right)\right\rangle, \tag{11}$$

where δ_{ij} indicates Kronecker's delta, $\langle\rangle$ stands for the volume average in A defined as $\langle \# \rangle = |A|^{-1}\int_A \# dA$, in which $|A|$ signifies the volume of A. Moreover, χ^{kl}_i and φ_i in the above equations are functions which are determined by solving the following boundary value problems for A, respectively:

$$\int_A c_{ijpq}\chi^{kl}_{p,q}v_{i,j}dA = -\int_A c_{ijkl}v_{i,j}dA, \tag{12}$$

$$\int_A c_{ijpq}\varphi_{p,q}v_{i,j}dA = \int_A c_{ijkl}\beta_{kl}v_{i,j}dA. \tag{13}$$

In general, the boundary value problems (12) and (13) are solved numerically for finding χ^{kl}_i and φ_i using the finite element method (FEM). In this analysis, the boundary condition described in the previous subsections, instead of the original Y-periodic boundary condition [1], is applied. The obtained χ^{kl}_i and φ_i allow Eqs. (10) and (11) to determine the microscopic and macroscopic elastic-viscoplastic behavior of plain-woven composite laminates with laminate misalignment. It is emphasized that the present theory enables only one basic cell to be sufficient to deal with arbitrary misalignment in the y_2-direction by changing the ratio of Γ_1 and Γ_2, and Γ_4 and Γ_3.

3 Elastic-Viscoplastic Analysis of Plain-Woven Composite Laminates with Laminate Misalignment

3.1 Analysis Conditions

In the present analysis, elastic-viscoplastic behavior of plain-woven glass fiber/epoxy composite laminates with laminate misalignment is analyzed using the theory

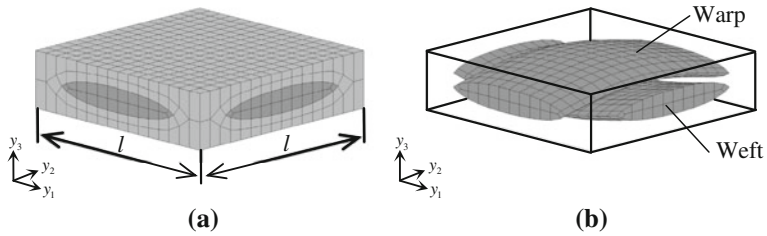

Fig. 3 Basic cell of the plain-woven GFRP laminates and its finite element mesh: **a** full view and **b** fiber bundles in the basic cell

developed. As shown in Fig. 3, a basic cell A of the plain-woven GFRP laminates was defined, and divided into eight-node isoparametric elements (2048 elements, 2499 nodes). The geometry of A was determined by referring to the previous study [6]. Then, the laminate misalignment in the y_2-direction (warp direction) was considered as illustrated in Fig. 4. The amount of laminate misalignment and the length of the basic cell were denoted as d and l, respectively, and five cases of d were selected from 0 to l in increments of $l/4$, i.e. $d = 0, l/4, l/2, 3l/4$ and l. It is noted that $d = 0$ and l correspond respectively to the in-phase and out-of-phase mentioned in Sect. 1.

The laminates were subjected to macroscopic uniaxial tension at a constant strain rate of $10^{-5}\ \mathrm{s}^{-1}$ at room temperature. The loading direction was selected to be 45° off-axis because viscoplastic behavior of the laminates became most significant at the angle [6].

The material constants of the fiber bundles were the same as those in the previous study [6], which had been determined from the elastic constants of the fibers and the epoxy listed in Table 1, by regarding the bundles as glass fiber/epoxy unidirectional composites and as linear elastic materials. For the determination, the homogenization theory [1] was used on the assumption that the fiber volume fraction in the bundles was 75 % in accordance with microscope observation, and that the bundles had a hexagonal fiber array. The epoxy matrix, on the other hand, was regarded as an isotropic elastic-viscoplastic material which obeyed the following constitutive equation [6]:

$$\dot{\varepsilon}_{ij} = \frac{1+\nu_m}{E_m}\dot{\sigma}_{ij} - \frac{\nu_m}{E_m}\dot{\sigma}_{kk}\delta_{ij} + \frac{3}{2}\dot{\varepsilon}_0^p\left[\frac{\sigma_{eq}}{g(\bar{\varepsilon}^p)}\right]^n \frac{s_{ij}}{\sigma_{eq}}, \tag{14}$$

where E_m, ν_m and n signify the material constants, $g(\bar{\varepsilon}^p)$ stands for a hardening function depending on equivalent viscoplastic strain $\bar{\varepsilon}^p$, $\dot{\varepsilon}_0^p$ indicates reference strain rate, s_{ij} denotes the deviatoric part of σ_{ij}, and $\sigma_{eq} = \left[(3/2)s_{ij}s_{ij}\right]^{1/2}$. These material constants are shown in Table 1, which were determined by referring to the previous study [6]. The constitutive equation (14) has been shown to be valid as far as monotonic loading is concerned [4–7]. Incidentally, no failure was assumed to occur in the glass fibers and epoxy.

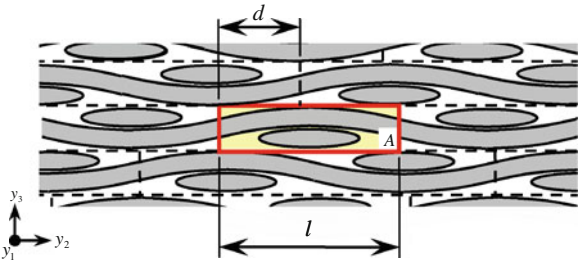

Fig. 4 Misalignment of plain-woven fabrics in the plain-woven GFRP laminates

Table 1 Material constants of the glass fibers and epoxy

Glass fiber	$E_f = 80 \times 10^3$	$\nu_f = 0.30$		
Epoxy	$E_m = 5.0 \times 10^3$	$\nu_m = 0.35$	$\dot{\bar{\varepsilon}}_0^p = 10^{-5}$	
	$n = 20$	$g(\bar{\varepsilon}^p) = 31.7 \times (\bar{\varepsilon}^p)^{0.14} + 9.50$		

MPa (stress), mm/mm (strain), s (time)

3.2 Results of Analysis: Macroscopic Stress-Strain Relations

Figure 5 shows the macroscopic stress-strain relations of the plain-woven laminates subjected to the uniaxial tension in the 45°-direction. As seen from the figure, the influence of laminate misalignment on the behavior of laminates is clearly observed especially at the viscoplastic region. The viscoplastic flow stress decreases as the laminate misalignment increases, i.e. the flow stress for $d = l$ is about 13 % lower than that for $d = 0$ at $E_{11} = 0.02$. The cause of this result is discussed from a microscopic point of view in the next subsection.

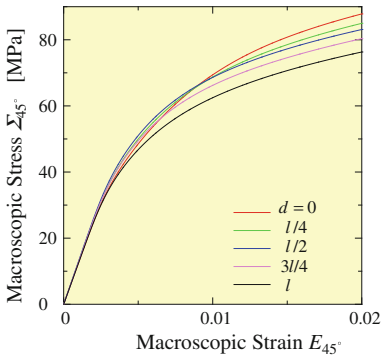

Fig. 5 Macroscopic stress-strain relations of the plain-woven GFRP laminates with laminate misalignment subjected to uniaxial tension in the 45°-direction

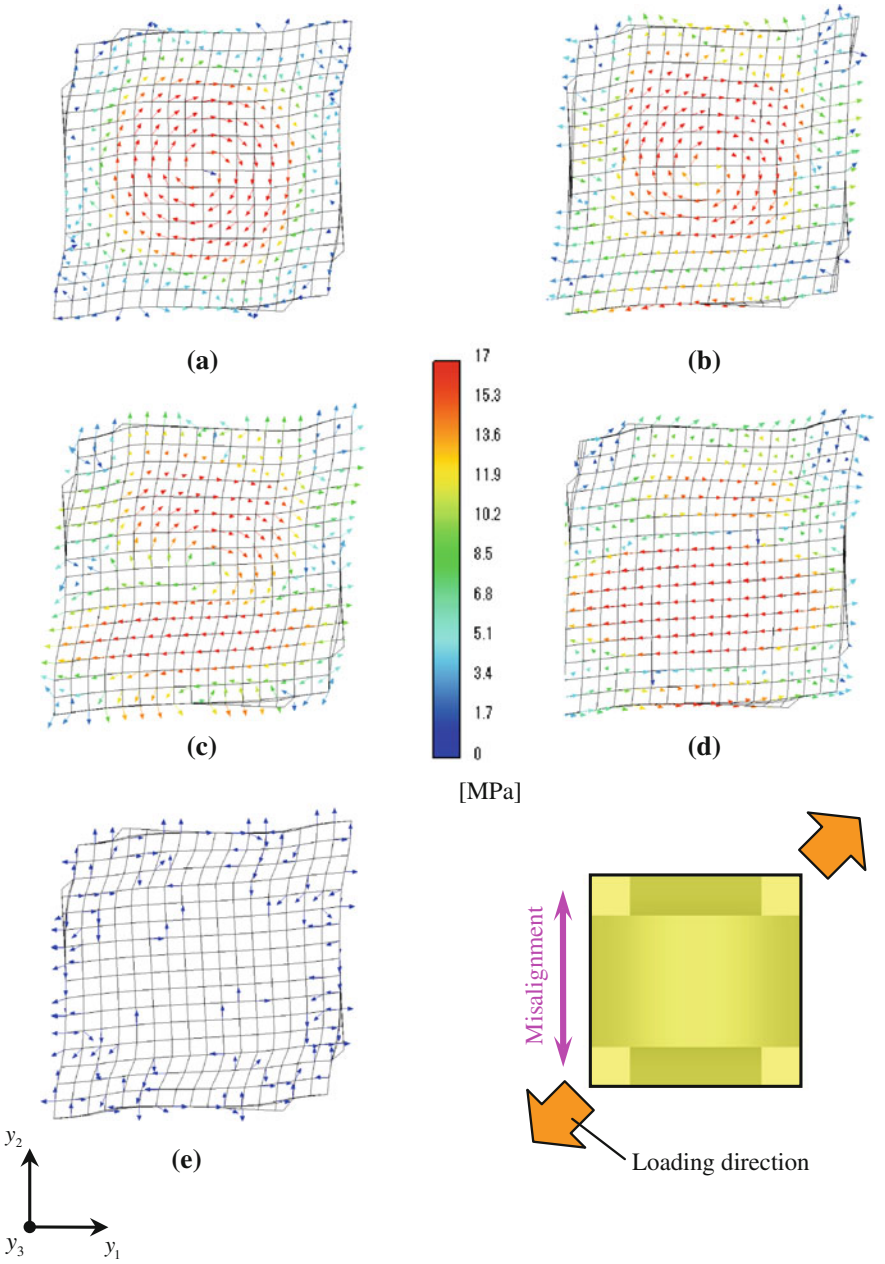

Fig. 6 Deformed shapes of the basic cell and the distributions of resultant shear stress for the 45°-direction loading ($E_{45^\circ} = 0.02$, displacement × 5): **a** d=0, **b** d=l/4, **c** d=l/2, **d** d=3l/4 and **e** d=l

3.3 Results of Analysis: Microscopic Behavior

Figure 6 shows the deformed shapes of the basic cell and the distributions of resultant shear stress on their upper boundary surfaces for the 45°-direction loading. In these figures, the magnitude of vectors represents $(\sigma_{31}^2 + \sigma_{32}^2)^{1/2}$. It is seen from the figures that the distribution of resultant shear stress markedly varies depending on the laminate misalignment. Figure 6a shows that, when $d = 0$, high shear stress occurs around the cell center, which was caused by the rotation of the adjacent warp and weft toward the loading direction. Such high shear stress regions move along the y_2-direction due to the increase of laminate misalignment as depicted in Figs. 6b–d. Moreover, with $d = l$, the shear stress drastically decreases and almost disappears as shown in Fig. 6e, because the warp and warp or the weft and weft are neighboring across the upper boundary facet of the unit cell. These results can explain the decrease of macroscopic flow stress with the increase of laminate misalignment shown in Fig. 5.

4 Conclusions

In the present study, the homogenization theory applicable to the elastic-viscoplastic analysis of plain-woven composite laminates with arbitrary laminate misalignment is developed by employing a basic cell as an analysis domain. The theory developed enables one basic cell to be sufficient to deal with arbitrary laminate misalignment. Then, elastic-viscoplastic behavior of plain-woven glass fiber/epoxy composite laminates with misaligned plain-woven fabrics was analyzed using a basic cell. Five cases of misalignment including no misalignment were considered, and the laminates with such misalignment were subjected to 45°-off-axis tension at a constant strain rate. It was shown that macroscopic flow stress of the laminates varied depending on the misalignment, and that microscopic deformation and stress distribution in the basic cell were significantly affected by the misalignment.

It is emphasized that the present theory is able to avoid not only the generation of basic cell geometry and its finite element mesh for every misalignment, but also the influence of mesh dependence caused by different meshes for different misalignment. The present theory is therefore useful for analyzing properties of plain-woven composite laminates with laminate misalignment.

References

1. Sanchez-Palencia, E.: Non-Homogeneous Media and Vibration Theory. Lecture Notes in Physics,vol. 127. Springer-Verlag, Berlin (1980)
2. Takano, N., Zako, M., Sakata, S.: Three-dimensional microstructural design of woven fabric composite materials by the homogenization method: 1st report, effect of mismatched lay-up of

woven fabrics on the strength. Trans. Jpn Soc. Mech. Eng. Ser. A **61**, 1038–1043 (in Japanese) (1995)
3. Zeman, J., Šejnoha, M.: Homogenization of balanced plain weave composites with imperfect microstructure: part I—theoretical formulation. Int. J. Solids Struct. **41**, 6549–6571 (2004)
4. Matsuda, T., Ohno, N., Tanaka, H., Shimizu, T.: Homogenized in-plane elastic-viscoplastic behavior of long fiber-reinforced laminates. JSME Int. J. Ser. A **45**, 538–544 (2002)
5. Matsuda, T., Ohno, N., Tanaka, H., Shimizu, T.: Effects of fiber distribution on elastic-viscoplastic behavior of long fiber-reinforced laminates. Int. J. Mech. Sci. **45**, 1583–1598 (2003)
6. Matsuda, T., Nimiya, Y., Ohno, N., Tokuda, M.: Elastic-viscoplastic behavior of plain-woven GFRP laminates: homogenization using a reduced domain of analysis. Compos. Struct. **79**, 493–500 (2007)
7. Matsuda, T., Fukuta, Y.: Multi-scale creep analysis of angle-ply CFRP laminates based on a homogenization theory. J. Solid Mech. Mater. Eng. **4**, 1664–1672 (2010)
8. Wu, X., Ohno, N.: A homogenization theory for time-dependent nonlinear composites with periodic internal structures. Int. J. Solids Struct. **36**, 4991–5012 (1999)
9. Ohno, N., Wu, X., Matsuda, T.: Homogenized properties of elastic-viscoplastic composites with periodic internal structures. Int. J. Mech. Sci. **42**, 1519–1536 (2000)
10. Ohno, N., Matsuda, T., Wu, X.: A homogenization theory for elastic-viscoplastic composites with point symmetry of internal distribution. Int. J. Solids Struct. **38**, 2867–2878 (2001)
11. Matsuda, T., Kanamaru, S., Yamamoto, N., Fukuda, Y.: A homogenization theory for elastic-viscoplastic materials with misaligned internal structures. Int. J. Plast. **27**, 2056–2067 (2011)

A Masing-Type Modelling Concept for Cyclic Plasticity at Elevated Temperature

Thomas Mayer, Edoardo Mazza and Stuart R. Holdsworth

Abstract Classical plasticity models commonly apply a yield surface concept for the formulation of elastic-plastic constitutive behaviour. This inherently implies a discontinuous transition between the elastic and plastic deformation regime. In the absence of a direct physical interpretation, the identification of the model parameters is further strongly affected by the adopted elastic modulus and yield stress. A continuous Masing-type model formulation is suggested that effectively represents the continuous elastic-plastic behaviour of a low-alloy steel (2CrMoNiWV). The small number of four model parameters allows for a straight-forward parameter identification due to their direct interpretability both in the stress–strain characteristic and on the physical basis of the Masing approach. In particular, a significant correlation has been found between three of the model parameters and the sub-grain size and dislocation density evolutions upon low-cycle fatigue loading. The adopted approach suggests potential for a future physically motivated modelling concept for the simulation of cyclic plasticity.

T. Mayer (✉) · S. R. Holdsworth
Empa—Swiss Federal Laboratories for Materials Science and Technology,
Ueberlandstrasse 129, 8600 Duebendorf, Switzerland
e-mail: thomas.mayer@empa.ch

S. R. Holdsworth
e-mail: stuart.holdsworth@empa.ch

E. Mazza
ETH Zurich—Swiss Federal Institute of Technology Zurich, Leonhardstrasse 27,
8092 Zurich, Switzerland
e-mail: edoardo.mazza@imes.mavt.ethz.ch

H. Altenbach and S. Kruch (eds.), *Advanced Materials Modelling for Structures*,
Advanced Structured Materials 19, DOI: 10.1007/978-3-642-35167-9_24,

1 Introduction

Low-cycle fatigue (LCF) loading of metallic materials generally leads to changing mechanical properties. These include both cyclic hardening and/or softening of the material strength at a given strain and an evolution of the elastic-plastic flow characteristics of the material. It is well known that a complex interplay between dislocation formation, annihilation and their rearrangement is responsible for an evolution of the dislocation microstructure which causes changes of the mechanical properties. The formation of characteristic heterogeneous dislocation arrangements, such as walls and channels, dislocation cells or sub-grains, has commonly been observed to occur in cyclically loaded metallic materials [1].

Effective constitutive models need to account for this cyclic mechanical evolution. It is a basic principle of constitutive modelling to maximise the application range of a model while minimising its complexity to as practical a level as possible. A great variety of model approaches has been developed that aim to describe cyclic elastic-plastic constitutive material behaviour ranging from simple phenomenological models (e.g. [2]) to complex multi-scale approaches (e.g. [3]). While the former models show difficulties to accurately represent the observed complex material behaviour due to the absence of physical consideration, the latter approaches are sounder in their background but are applicable for special cases only due to their high level of complexity.

A widely accepted phenomenological approach is the yield surface concept. Plastic deformation only occurs when an equivalent stress exceeds the discrete yield stress. The following stress state is then determined by the isotropic and kinematic hardening laws of the respective model (e.g. [4]). Without special measures this approach can imply a discontinuous transition between the elastic and plastic deformation regime, generally causing an inaccurate representation of the constitutive behaviour at small strains. Additional parameters can be included to overcome this problem, e.g. by consideration of additional backstress terms. Over-parameterisation, however, can lead to ill-posed parameter identification problems that result from the lack of physical background of the parameters. As appropriate evolution laws are required for the model parameters in order to describe the cyclic constitutive material behaviour, it is further advantageous to minimise the number of parameters. Advanced model formulations should therefore aim at a small number of physically interpretable parameters.

A more general approach was introduced in 1923 by Masing [5] to explain the Bauschinger effect. He assumed that any macroscopically isotropic metallic material volume can be subdivided into a discrete amount of basic volume elements (BVE). Each of these BVEs features an elastic-ideally plastic constitutive behaviour with identical *elastic modulus* E but different *element yield stresses* $\sigma_{y,i}$. It was further assumed that the BVEs are loaded in parallel such that every BVE experiences a microscopic strain identical to the macroscopically applied strain ε, Fig. 1. As every BVE was attributed the same cross-sectional area, they contributed to the macroscopic stress to the same extent. Further development of this originally discrete

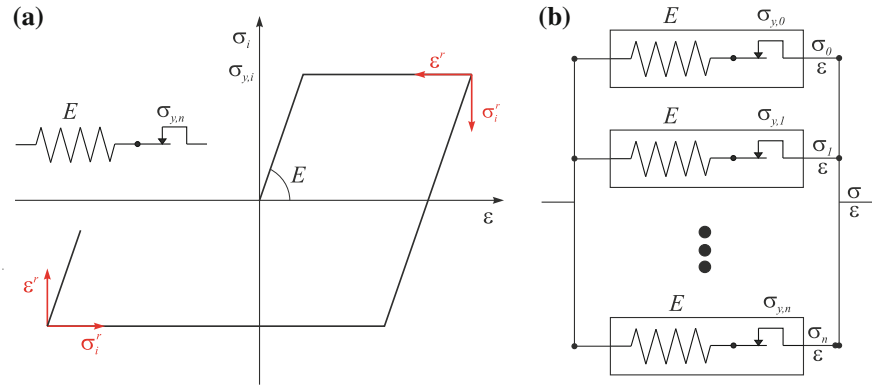

Fig. 1 **a** Elastic-perfectly plastic characteristic of a basic volume element and its rheological model representation with a spring-dry friction element (Prandtl element). **b** Masing model: representation of a macroscopic volume with n parallely loaded Prandtl elements

Masing model by Afanas'ev [6] and Iwan [7] considers a distribution of element yield stresses which assigns different weights to the contributions of the BVEs. This continuous Masing model has been widely applied to study and interpret the cyclic constitutive behaviour of different materials, e.g. Polák et al. [8] and Christ et al. [9]. It was Chiang [10] that first suggested a modelling scheme to describe the mechanical response upon multi-axial loading on the basis of the continuous Masing approach using a Rayleigh-type element yield stress distribution. Skelton et al. [11] also recognised the possibility to model the elastic-plastic constitutive behaviour with a continuous Masing-type model by relating the Ramberg-Osgood approach to the element yield stress distribution.

In the following, we propose a continuous Masing-type modelling approach on the basis of a modified Cauchy element yield strain distribution function. It is shown that the constitutive behaviour of a bainitic low-alloy steam turbine rotor steel (2CrMoNiWV) is very well represented. The evolution of the four model parameters is determined from sequential fitting of the model to a LCF test and it is shown that there is a significant correlation between three of the parameters and the sub-grain size and dislocation density evolutions. The adopted approach suggests potential for a future physically motivated modelling concept for the simulation of cyclic plasticity. A more detailed treatment of the presented model can be found in [12, 13].

2 Model Formulation

In his original formulation, Masing only assumed a discrete number of BVEs, all contributing to the same extent to the macroscopic stress [5]. Afanas'ev [6] and Iwan [7] further developed this approach by assuming a distribution of element yield

stresses $\psi[(E\varepsilon^r]$ that accounts for the frequency of appearance of an element yield stress in the macroscopic volume. This implies the consideration of an infinite amount of BVEs that make up the macroscopic volume.

The fundamental relationship of the continuous Masing model is derived in the following as a starting point for constitutive modelling. More detailed elaborations can be found in Christ [9] and Mayer [12].

2.1 Continuous Masing Model

Relative stress–strain coordinates are used for a formulation that allows both monotonic and cyclic loading, Fig. 1.

$$\begin{aligned} \varepsilon^r &= \kappa(\varepsilon - \varepsilon_0) \\ \sigma^r &= \kappa(\sigma - \sigma_0) \end{aligned} \tag{1}$$

$\kappa = \text{sign}[\text{d}\varepsilon]$ defines the loading direction, i.e. $+1$ for tension going and -1 for compression going loading. ε_0 and σ_0 are the total strain and stress, respectively, at the start of the corresponding loading branch.

The elastic-ideally plastic element stress response of the i-th BVE, σ_i^r can thus be formulated in relative stress–strain coordinates.

$$\sigma_i^r = \begin{cases} E\varepsilon^r, \ \sigma_y^r \leq \sigma_{y,i}^r \\ \sigma_{y,i}^r, \ \sigma_y^r > \sigma_{y,i}^r \end{cases} \tag{2}$$

As long as the pseudo-elastic stress $\sigma_y^r = E\varepsilon^r$ is smaller than the element yield stress $\sigma_{y,i}^r$ of a BVE, it deforms elastically. If it is larger, the BVE deforms plastically with $\sigma_i^r = \sigma_{y,i}^r$. The macroscopic stress response is thus made up of stress contributions originating from elastic and plastic elements. The consideration of an *element yield stress distribution* $\psi[E\varepsilon^r]$ allows to account for the different stress contributions of the BVEs. It gives the relative frequency of BVEs that possess an element yield stress $\sigma_{y,i}^r$ equal to the pseudo-elastic stress $\sigma_y^r = E\varepsilon^r$.

With this, the macroscopic stress–strain relationship is obtained by summing up the respective contributions of the elastic and plastic BVEs weighted by the element yield stress distribution function.

$$\sigma = \sigma_0 + \kappa\sigma^r[\varepsilon^r] = \sigma_0 + \kappa \left[\underbrace{E\varepsilon^r \left[1 - \int_0^{E\varepsilon^r} \psi(\sigma_y^r)\text{d}\sigma_y^r \right]}_{\text{elastic}} + \underbrace{\int_0^{E\varepsilon^r} \sigma_y^r \psi[\sigma_y^r]\text{d}\sigma_y^r}_{\text{plastic}} \right] \tag{3}$$

The tangent modulus is obtained from Eq. (3) by derivation using a variable substitution and the fundamental theorem of differential and integral calculus.

$$\frac{\mathrm{d}\sigma}{\mathrm{d}\varepsilon} = E\left[1 - \int_0^{E\varepsilon^r} \psi[\sigma_y^r]\sigma_y^r\right] = E(1-\chi) \tag{4}$$

It is apparent from Eq. (4) that the tangent modulus is proportional to the share of elastically deformed BVEs, i.e. $1-\chi$. χ thereby describes the cumulative density function of $\psi[E\varepsilon^r]$, i.e. the relative number of BVEs that feature an element yield stress $\sigma_{y,i}^r \leq E\varepsilon^r$. Finally, the second derivative of Eq. (3) yields the fundamental relationship between the element yield stress distribution and the second derivative of the stress–strain hysteresis, i.e. its curvature.

$$\psi[E\varepsilon^r] = -\frac{\kappa}{E^2}\frac{\mathrm{d}^2\sigma}{\mathrm{d}\varepsilon^2} \tag{5}$$

With the choice of an appropriate element yield stress distribution function, a closed form stress–strain relationship can be derived by two-fold integration of Eq. (5).

2.2 Element Yield Strain Distribution

It appears relatively reasonable to subdivide a material volume into BVEs with different element yield stresses on the basis of an element yield stress distribution function. The question may arise, however, whether this is founded on a physical basis.

Various materials have been investigated on the basis of the relationship given in Eq. (5). Originally, Masing reasoned that different orientations of the crystallites with respect to the loading direction are responsible for the element yield stress distribution in polycrystalline material [5]. Christ, however, pointed out that this is likely to form a minor contribution only [9]. It is Mughrabi's comprehensive work on different cyclically deformed poly- and single crystalline metals that identifies heterogeneous dislocation structures, such as walls and channels, cells or sub-grains as the origin of internal long-range stresses, e.g. [1]. To mobilise the dislocations that are subjected to the internal stress fields of heterogeneous dislocation structures, the local internal stresses have to be overcome by the externally applied load to initiate plastic deformation. This gives rise to the interpretation of the element yield stress distribution as a distribution of internal stresses in a macroscopic volume. Polák [14] further pointed out that an additional effective short-range stress affects the element yield stress distribution causing its shift to higher stresses. This is of importance for temperatures $T < 0.1 - 0.2T_m$ where short-range interactions between dislocations and e.g. interstitial atoms, precipitates or other dislocations lack the thermal activation to overcome these obstacles. The shape of the element yield stress distribution is further significantly influenced by the presence of different phases. Precipitation

hardening and dynamic strain ageing considerably change the types of dislocation structures that form during low-cycle fatigue loading [9]. Thereby, also the shape of the element yield stress distribution is affected. At elevated temperatures, the strong thermal activation is expected to generally increase the frequency of plastic deformation occurring at a certain element yield stress due to the activation of dislocation climb mechanisms.

In order to accurately describe the experimentally observed element yield stress distribution, the performance of different formulations has been examined. A modified Cauchy distribution appeared to be the best choice for the representation of the monotonic and cyclic elevated temperature behaviour of a bainitic 2CrMoNiWV steam turbine rotor steel.

$$\psi[E\varepsilon^r] = \frac{\beta}{\pi}\frac{\Gamma}{\Gamma^2 + [E\varepsilon^r - H]^2} \tag{6}$$

H denotes the mode of the element yield stress and Γ the half width at half the maximum of $\psi[E\varepsilon^r]$. Both parameters have the dimension of stress. Reformulation of Eq. (6) to derive the corresponding *element yield strain distribution* $\varphi[\varepsilon]$ facilitates the further steps of constitutive modelling.

$$\varphi[\varepsilon] = \frac{\beta}{\pi}\frac{\gamma}{\gamma^2 + [\varepsilon - [\varepsilon_0 + \kappa\eta]]^2} \tag{7}$$

The *location parameter* $\eta = H/E$ describes the mode of the distribution, while $\gamma = \Gamma/E$ denotes the *scale parameter*, i.e. the half width at half maximum, Fig. 2. Both parameters have the dimension of strain. Parameter β is used to normalise the area of $\varphi[\varepsilon]$ to unity.

$$\beta = \left[\int_0^\infty \varphi[\varepsilon]\mathrm{d}\varepsilon\right]^{-1} = \frac{1}{\frac{1}{2} + \frac{1}{\pi}\arctan\left[\frac{\eta}{\gamma}\right]} \tag{8}$$

With this the tangent modulus can be derived according to [12].

$$\frac{\mathrm{d}\sigma}{\mathrm{d}\varepsilon} = E\left[\alpha - \kappa\frac{\beta}{\pi}\left[\arctan\left[\frac{\varepsilon - [\varepsilon_0 + \kappa\eta]}{\gamma}\right] + \arctan\left[\kappa\frac{\eta}{\gamma}\right]\right]\right] \tag{9}$$

Equation (9) considers an *apparent elastic modulus* $E_{app} = \alpha E$ smaller than the representative elastic modulus E of the BVEs due to relaxation effects at the strain reversal points at elevated temperatures. The *modulus relaxation parameter* α is used to account for these viscous effects at the strain reversal points, Fig. 2. Further integration of Eq. (9) yields a closed form stress–strain relationship on the basis of the modified Cauchy distribution.

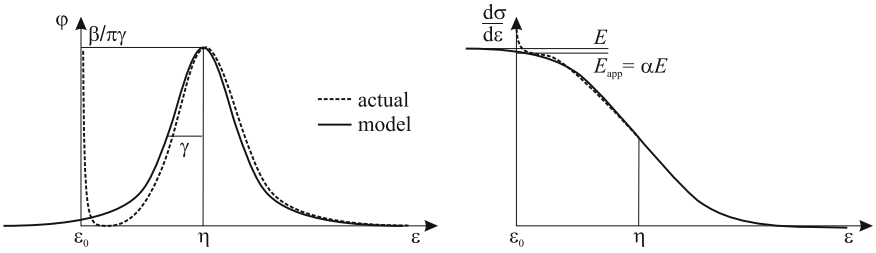

Fig. 2 Schematic of element yield strain distribution (*left*) and tangent modulus (*right*). Interpretation of the four model parameters E, α, γ and η

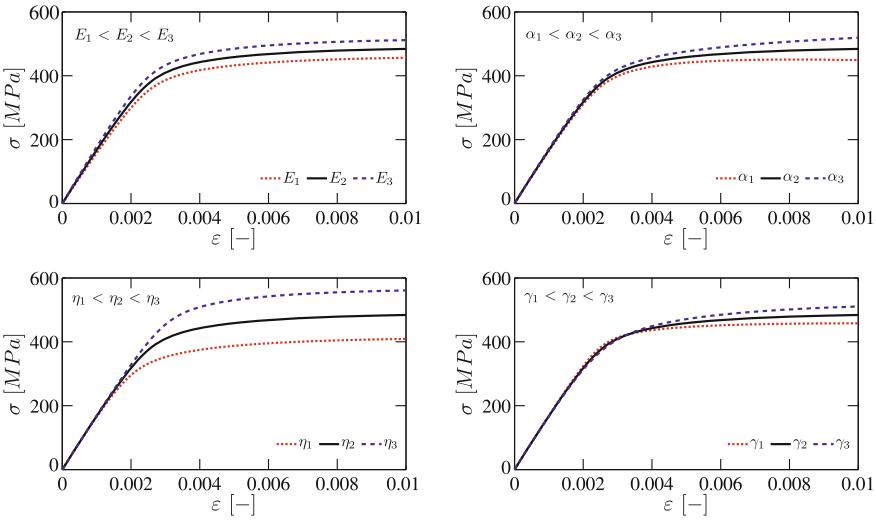

Fig. 3 Influence of model parameters on the stress–strain characteristics

$$\sigma = \sigma_0 + E\left[\alpha[\varepsilon - \varepsilon_0] - \kappa\frac{\beta}{\pi}\left[[\varepsilon - [\varepsilon_0 + \kappa\eta]]\right.\right.$$
$$\times\left[\arctan\left[\frac{[\varepsilon - [\varepsilon_0 + \kappa\eta]]}{\gamma}\right] + \arctan\left[\kappa\frac{\eta}{\gamma}\right]\right]\Bigg]$$
$$\left.\left. - \kappa\frac{\gamma\beta}{2\pi}\left[\ln\left[1 + \left[\frac{\varepsilon - [\varepsilon_0 + \kappa\eta]}{\gamma}\right]^2\right] - \ln\left[1 + \left[\frac{\eta}{\gamma}\right]^2\right]\right]\right] \tag{10}$$

As apparent from Eqs. (9) and (10), the transition from the elastic to the plastic loading regime is continuous and based on four parameters E, α, η and γ. Their influence on the stress–strain characteristics is shown in Fig. 3.

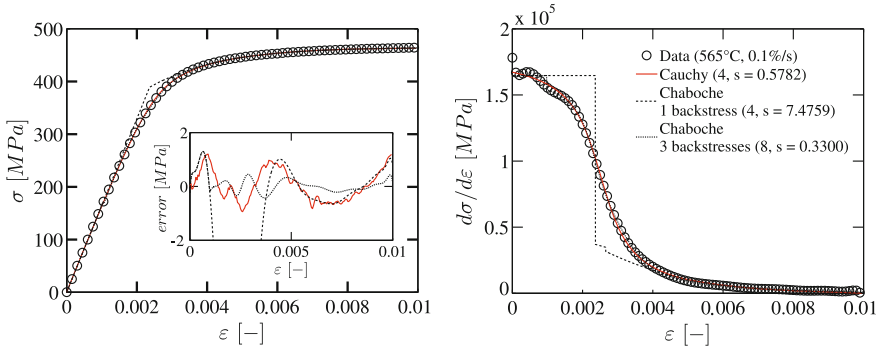

Fig. 4 Comparison of the suggested continuous Masing-type approach with a Chaboche approach with one and three backstress terms (2CrMoNiWV: 565 °C, 0.1 %/s)

3 Model Performance

The model presented in Eq. (10) has several features providing potential advantages over the classical yield surface approach: (i) It describes a continuous transition from the elastic to the plastic loading regime; (ii) The model only involves four parameters facilitating both model calibration and potentially their evolutionary formulation; (iii) There is a physical motivation based on the continuous Masing concept.

Figure 4 shows a comparison between the suggested Cauchy approach for the element yield strain distribution and a classical Chaboche model with one and three backstress terms. It is apparent from the tangent modulus that with the classic yield stress approach there is a discontinuous transition between the elastic and plastic loading regimes. This can cause problems to accurately represent the actual mechanical behaviour at low plastic strains. Only by including more backstress terms significant improvement can be obtained. This is, however, to the cost of the number of parameters. A four parameter Masing-Cauchy approach yields comparable results to a three-term backstress approach with eight parameters.

The small number of parameters in the suggested Masing-type approach allows for a straight-forward model calibration. As the four model parameters feature a direct interpretation in the stress–strain characteristic, Fig. 2, initial values can be easily found for the actual optimisation. In addition, an over-parameterisation leading to an ill-posed optimisation problem is avoided. With this, it is possible to carry out a fast sequential model calibration for successive loading branches of e.g. a LCF test as shown in Fig. 5 for 2CrMoNiWV. The model very well represents both monotonic and cyclic constitutive behaviour. Figure 6 shows the evolution of the model parameters. It is apparent that the evolutions of tension and compression going loading branches differs, indicating a tensile-compressive asymmetry of the material. While the tension going elastic modulus E remains relatively constant, the compression going modulus drops potentially due to the presence of macroscopic damage. The location and scale parameters η and γ, respectively, are both decreasing, indicating a general cyclic

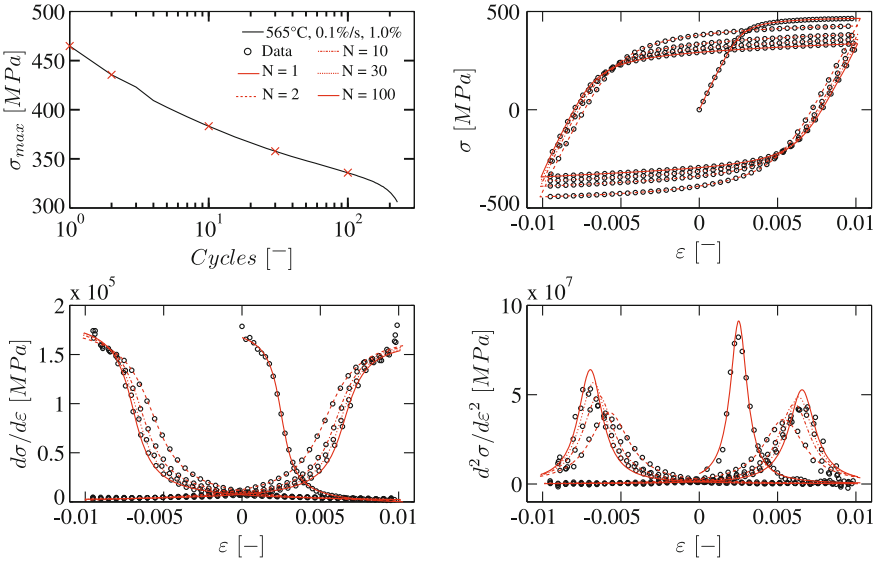

Fig. 5 Cyclic stress–strain curve for 2CrMoNiWV (565 °C, 0.1 %/s, ±1 %) (*top*). Comparison between model fits and stress–strain data and its first and second derivative (*bottom*)

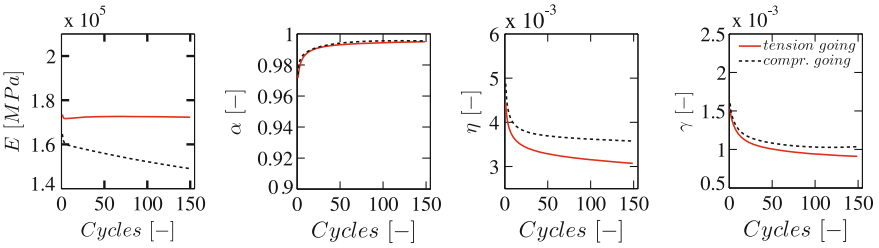

Fig. 6 Cyclic evolution of model parameters corresponding to Fig. 5 for tension (*solid*) and compression (*dashed*) going loading

softening of the material and a reduced variability of the element yield strains due to ongoing recovery of the microstructure during cyclic loading.

As already discussed in Sects. 2.1 and 2.2, the continuous Masing approach is based on the idea that a material volume can be subdivided into basic volume elements that feature different yield stresses. The distribution of yield stresses (or strains) is a fingerprint of the strength determining mechanisms at different strains. Dynamic recovery (i.e. the annihilation and re-arrangement of dislocations and the formation and growth of sub-grains) is responsible for the dislocation density reduction and the sub-grain growth in 2CrMoNiWV [15]. Figure 7 shows the relationship between the four model parameters and the sub-grain size as determined in a multi-specimen LCF approach. Correlations between α, η and γ with the sub-grain size D and the dislocation density are found to be significant and high. As expected, the elastic

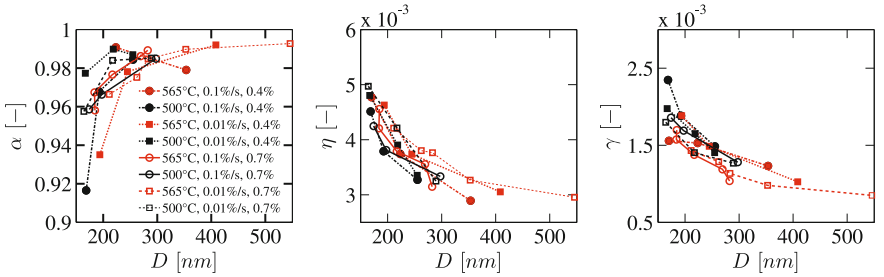

Fig. 7 Scatter plots for analysis of the correlation between the tension going model parameters and the sub-grain size evolution as determined for 2CrMoNiWV in [15]

modulus E is not influenced by these microstructural parameters and it states a representative parameter for the whole entity of BVEs. It can thus be concluded that the model parameters well reflect the evolving state of the material and that the model appropriately represents its constitutive behaviour. A detailed treatment of the proposed approach is given in [12, 13]. Ongoing research focuses on the formulation of the parameter evolution.

4 Conclusion

A new continuous Masing approach based on a Cauchy element yield strain distribution has been proposed and shown to provide a promising foundation for future physically motivated evolutionary cyclic plasticity models.

Acknowledgments The financial support by the Swiss Competence Centre for Materials Science and Technology (CCMX-MERU), ABB Turbo-Generators, ALSTOM and Swissnuclear is gratefully acknowledged.

References

1. Mughrabi, H.: Dislocation wall and cell structures and long-range internal stresses in deformed metal crystals. Acta Metall Mater. **31**(9), 1367–1379 (1983)
2. Chaboche, J.-L.: A review of some plasticity and viscoplasticity constitutive theories. Int. J. Plast. **11**(8), 991–1005 (2008)
3. Roters, F., Eisenlohr, P., Hantcherli, L., Tjahjanto, D.D., Bieler, T.R., Raabe, D.: Overview of constitutive laws, kinematics, homogenization and multiscale methods in crystal plasticity finite-element modelling: theory, experiments, applications. Acta Mater. **58**, 1152–1211 (2010)
4. Ottoson, N.S., Ristinmaa, M.: The Mechanics of Constitutive Modelling. Elsevier Ltd, Oxford (2005)
5. Masing, G.: Zur Heyn'schen Theorie der Verfestigung der Metalle durch verborgene elastische Spannungen. Wiss Veröffentlichung aus dem Siemens-Konzern **3**, 231–239 (1923)

6. Afanas'ev, N.N.: Statistical theory of fatigue strength of metals (in Russian: Statisticheskaia teoriia ustalostnoi prochnosti metallov). Azv Akad Nauk SSSR (1953)
7. Iwan, W.D.: A distributed element model for hysteresis and its steady-state dynamic response. ASME J. Appl. Mech. **33**(4), 893–900 (1966)
8. Polák, J., Fardoun, F., Degallaix, S.: Analysis of the hysteresis loop in stainless steels—I. Austenitic and ferritic steels. Mater. Sci. Eng. A **297**, 144–153 (2001)
9. Christ, H.-J.: Wechselverformung von Metallen—Zyklisches Spannungs-Dehnungs-Verhalten und Mikrostruktur. In: Ilschner, B. (ed.) Werkstoff-Forschung und -Technik. Springer, Berlin (1991)
10. Chiang, D.-Y., Beck, J.L.: A new class of distributed-element models for cyclic plasticity—I. Theory and application. Int. J. Solids Struct. **31**(4), 469–484 (1994)
11. Skelton, R., Maier, H., Christ, H.-J.: The Bauschinger effect, masing model and the Ramberg-Osgood relation for cyclic deformation in metals. Mater. Sci. Eng. A **238**(2), 377–390 (1997)
12. Mayer, T., Mazza, E., Holdsworth, S.R.: A continuous Masing approach for a physically motivated formulation of temperature and strain rate dependent plasticity. Int. J. Pres. Ves. Pip. doi:10.1016/j.ijpvp.2012.11.001 (2012)
13. Mayer, T., Mazza, E., Holdsworth, S.R.: Parameter evolution in a continuous masing approach for cyclic plasticity and its physical interpretation. Mech. Mater. doi:10.1016/j.mechmat.2012.10.014 (2012)
14. Polák, J., Klesnil, M.: The hysteresis loop—1. A statistical theory. Fatigue Eng. Mater. **5**, 19–32 (1982)
15. Mayer, T., Balogh, L., Solenthaler, C., Müller-Gubler, E., Holdsworth, S.R.: Dislocation density and sub-grain size evolution of 2CrMoNiWV during low cycle fatigue at elevated temperatures. Acta Mater. **60**, 2485–2496 (2012)

Phase-Field Simulation of Microstructural Evolution in Nickel-Based Superalloys During Creep and in Low Carbon Steels During Martensite Transformation

Yoshinori Murata, Yuhki Tsukada and Toshiyuki Koyama

Abstract Phase-field simulation was applied to both microstructural simulation of nickel-based superalloys and lath martensite phase formed in heat resistant steels. In nickel-based superalloys, in order to simulate comprehensively from the formation to collapse processes of the rafted structure by the phase-field method, an idea that the anisotropy increases with simulation time was employed in the calculation of the elastic strain energy in alloy. This idea corresponds to the phenomenon that creep strain increases with creep time. The results were in good agreement with the microstructural change observed in practical Ni-based alloys. In lath martensite phase, an elasto-plastic phase-field model was constructed for Fe-0.1 mass%C steel on the basis of the two types of slip deformation (TTSD) model. The simulation results demonstrate that the morphology of the six variants in a packet of the lath martensite phase can be well predicted.

1 Introduction

Ni-based superalloys have excellent creep strength at high temperatures and are used for gas turbines. The superior mechanical property of the superalloys originates from the γ' strengthening phase precipitating in the γ phase, and depends on the γ' volume fraction, morphology and size distribution of the $(\gamma + \gamma')$ two-phase

Y. Murata (✉)
Department of Materials, Physics and Energy Engineering,
Graduate School of Engineering,
Nagoya University, Nagoya 464-8603, Japan
e-mail: murata@numse.nagoya-u.ac.jp

Y. Tsukada · T. Koyama
Department of Materials Science and Engineering,
Graduate School of Engineering,
Nagoya Institute of Technology, Nagoya 466-8555, Japan

H. Altenbach and S. Kruch (eds.), *Advanced Materials Modelling for Structures*,
Advanced Structured Materials 19, DOI: 10.1007/978-3-642-35167-9_25,

microstructure. During the aging heat treatment without external stress, the cuboidal γ' phase precipitates and arranges along the ⟨100⟩ crystallographic directions in the γ phase. During creep tests, on the other hand, the cuboidal γ' phase evolves into the rafted structure, in which plate like γ and γ' phases are stacked alternately in the direction perpendicular to the tensile stress in practical superalloys. The rafted structure collapses especially in the late stage of long term creep, and the creep strength of the superalloys is related to the stability of the rafted structure [1]. It is useful to determine contributing factors in the morphological evolution during both aging heat treatment and high temperature creep for stabilizing the $(\gamma + \gamma')$ microstructure.

It is well known that the mechanical properties of steels are strongly affected by the morphology of the incorporated martensite phase. In ferrous alloys, various morphologies of the martensite phase, such as thin plate, lenticular, and lath martensite, can be observed with different chemical compositions [2, 3]. Among them, lath martensite is important for heat-resistant steels because the carbon content in recent heat-resistant steels is about 0.1 mass% and the martensite phase formed in such steels is lath martensite. Lath martensite has a hierarchical structure consisting of packets, blocks, and laths containing densely packed complex and tangled dislocations without twins.

In recent years, the phase-field method has been applied to simulating microstructural evolution in materials [4–8]. The phase-field approach describes a microstructure using a set of conserved and non-conserved field variables which change continuously across the interface regions. By solving a set of equations governing the evolution of the fields, the microstructural evolution can be simulated driven by the minimization of the total free energy of the system, which includes chemical free energy, interfacial energy and elastic strain energy.

The purposes of this study are to investigate the contributing factors in microstructural evolution in Ni-based superalloys and to present the morphology of lath martensite with a sub-block microstructure in Fe-0.1 mass% C steel using a series of phase-field simulations based on TTSD model [9].

2 Calculation Method

2.1 Ni-Based Superalloy

We consider the $(\gamma + \gamma')$ two-phase model, and the volume fraction of the γ' phase, f $(\mathbf{r}, t)$, and four artificial order parameters, ϕ_i $(\mathbf{r}, t)$ $(i = 1, 2, 3, 4)$, which describe the four types of ordered domains of the γ' phase [2], are employed as field variables. These field variables vary spatially $(\mathbf{r})$ and temporally (t). The temporal evolution of the field variables is given by solving the Cahn-Hilliard and Allen-Cahn equations,

$$\frac{\partial f(\mathbf{r},t)}{\partial t} = M\nabla^2 \frac{\delta G_{\text{sys}}}{\delta f(\mathbf{r},t)}, \tag{1}$$

$$\frac{\partial \phi_i(\mathbf{r},t)}{\partial t} = -L\frac{\delta G_{\text{sys}}}{\delta \phi_i(\mathbf{r},t)} (i = 1,2,3,4), \tag{2}$$

where G_{sys} is the total free energy of the system, M is the diffusion mobility and L is the structural relaxation coefficient. The total free energy is given by

$$G_{\text{sys}} = \int_{\mathbf{r}} \left[G_{\text{chem}}(f,\phi_i) + E_{\text{grad}}(\phi_i) + E_{\text{str}}(\phi_i) \right] d\mathbf{r}, \tag{3}$$

where G_{chem} is the chemical free energy density, E_{grad} is the gradient energy density and E_{str} is the elastic strain energy density. The chemical free energy density is expressed as

$$G_{\text{chem}} = \{1 - h(\phi_i)\} G^{\text{m}}_{\text{chem}}(f^{\text{m}}) + h(\phi_i) G^{\text{p}}_{\text{chem}}(f^{\text{p}}) + wg(\phi_i), \tag{4}$$

where w is the double-well potential height [7, 8]. In Eq. (4), $G^{\text{m}}_{\text{chem}}$ and $G^{\text{p}}_{\text{chem}}$ are the chemical free energy density of the γ matrix and the γ' precipitate, respectively. The functions $h\ (\phi_i)$ and $g\ (\phi_i)$ are selected as [8]

$$h(\phi_i) = \sum_{i=1}^{4} [\phi_i^3 (10 - 15\phi_i + 6\phi_i^2)], \tag{5}$$

$$g(\phi_i) = \sum_{i=1}^{4} [\phi_i^2 (1 - \phi_i)^2] + \alpha \sum_{i=1}^{4} \sum_{j \neq i}^{4} \phi_i^2 \phi_j^2. \tag{6}$$

Here, α is a coefficient that depends on the definition of interfacial thickness. Employing the description by Kim et al. [10], the interface region is regarded as a mixture of the γ and γ' phases with different volume fractions of the γ' phase but with equal chemical potentials:

$$f = \{1 - h(\phi_i)\} f^{\text{m}} + h(\phi_i) f^{\text{p}}, \tag{7}$$

$$\left(\frac{\partial G^{\text{m}}_{\text{chem}}}{\partial f} \right)_{f=f^{\text{m}}} = \left(\frac{\partial G^{\text{p}}_{\text{chem}}}{\partial f} \right)_{f=f^{\text{p}}}. \tag{8}$$

The gradient energy density is estimated from the artificial order parameters as

$$E_{\text{grad}} = \frac{1}{2} \kappa_\phi \sum_{i=1}^{4} (\nabla \phi_i)^2, \tag{9}$$

where κ_ϕ is the gradient energy coefficient of the order parameter [11]. The gradient energy in the phase-field model is correlated with the interfacial energy, and the parameter, w, in Eq. (4) and κ_ϕ in Eq. (9) are related to both the interfacial energy density, γ_s, and the interface width, 2λ.

The elastic strain energy density, E_{str}, arising from the lattice misfit between the γ and γ' phases is calculated on the basis of micromechanics [12, 13]:

$$E_{\mathrm{str}} = \frac{1}{2} C_{ijkl} \varepsilon^{\mathrm{el}}_{ij}(\mathbf{r}, t) \varepsilon^{\mathrm{el}}_{kl}(\mathbf{r}, t) - \sigma^{\mathrm{appl}}_{ij} \bar{\varepsilon}_{ij}, \tag{10}$$

where ${\sigma^{\mathrm{appl}}}_{ij}$ and $\bar{\varepsilon}_{ij}$ represent the external stress and the macroscopic strain, respectively. The elastic strain ${\varepsilon^{\mathrm{el}}}_{kl}$ is expressed as

$$\varepsilon^{\mathrm{el}}_{kl}(\mathbf{r}, t) = \varepsilon_{kl}(\mathbf{r}, t) - \varepsilon^{0}_{kl}(\mathbf{r}, t), \tag{11}$$

where ε_{kl} and ${\varepsilon^{0}}_{kl}$ represent the total strain and eigenstrain, respectively. The eigenstrain is expressed as

$$\varepsilon^{0}_{kl}(\mathbf{r}, t) = \varepsilon_0 \delta_{kl} h(\phi_i), \tag{12}$$

and

$$\varepsilon_0 = \frac{a_{\mathrm{m}} - a_{\mathrm{p}}}{a_{\mathrm{m}}}, \tag{13}$$

where ε_0 represents the lattice misfit and δ_{kl} is the Kronecher delta function. In Eq. (13), a_{m} and a_{p} are the lattice parameters of the γ matrix and the γ' precipitate, respectively. The total strain ε_{kl} is represented as the sum of the homogeneous strain ($\bar{\varepsilon}_{kl}$) and heterogeneous strain ($\delta\varepsilon_{kl}$ ($\mathbf{r}$)):

$$\varepsilon_{kl}(\mathbf{r}) = \bar{\varepsilon}_{kl} + \delta\varepsilon_{kl}(\mathbf{r}), \tag{14}$$

and heterogeneous strain can be expressed as

$$\delta\varepsilon_{kl}(\mathbf{r}) = \frac{1}{2} \left\{ \frac{\partial u_k(\mathbf{r})}{\partial r_l} + \frac{\partial u_l(\mathbf{r})}{\partial r_k} \right\}, \tag{15}$$

where u_i ($\mathbf{r}$) represents the ith displacement component. The Hooke's law gives the local elastic stress as ${\sigma^{\mathrm{el}}}_{ij}$ ($\mathbf{r}$) = $C_{ijkl}{\varepsilon^{\mathrm{el}}}_{kl}$ ($\mathbf{r}$), where C_{ijkl} denotes the elastic constants. Assuming homogeneous elasticity (C_{ijkl} = constant), the local displacement field is evaluated by solving the local mechanical equilibrium equation ($\partial {\sigma^{\mathrm{el}}}_{ij}/\partial r_j = 0$) in Fourier space, and then the elastic strain energy density is calculated from Eq. (10).

2.2 Low Carbon Steel

Based on the TTSD model [10], an elasto-plastic phase-field model is developed by considering both of the Bain deformation and plastic deformation. For the phase-field model, a field variable $\phi_i(\mathbf{r})(i = 1, 2, 3)$ is introduced to describe the Bain deformation. $i = 1, 2, 3$ is used to distinguish the three cases of coordinate coincidences and $\mathbf{r}$ is the coordinate vector. The eigenstrain caused by the Bain deformation $\varepsilon_{kl}^{B}(i)(i = 1, 2, 3)$ is listed in matrix form as

$$\varepsilon_{kl}^{B}(1) = \begin{pmatrix} \sqrt{2}a_{\alpha'}/a_{\gamma} - 1 & 0 & 0 \\ 0 & \sqrt{2}a_{\alpha'}/a_{\gamma} - 1 & 0 \\ 0 & 0 & c_{\alpha'}/a_{\gamma} - 1 \end{pmatrix}, \tag{16}$$

$$\varepsilon_{kl}^{B}(2) = \begin{pmatrix} c_{\alpha'}/a_{\gamma} - 1 & 0 & 0 \\ 0 & \sqrt{2}a_{\alpha'}/a_{\gamma} - 1 & 0 \\ 0 & 0 & \sqrt{2}a_{\alpha'}/a_{\gamma} - 1 \end{pmatrix}, \tag{17}$$

$$\varepsilon_{kl}^{B}(3) = \begin{pmatrix} \sqrt{2}a_{\alpha'}/a_{\gamma} - 1 & 0 & 0 \\ 0 & c_{\alpha'}/a_{\gamma} - 1 & 0 \\ 0 & 0 & \sqrt{2}a_{\alpha'}/a_{\gamma} - 1 \end{pmatrix}, \tag{18}$$

where a_{γ} is the lattice parameter of the austenite phase, $a_{\alpha'}$ and $c_{\alpha'}$ are the lattice parameters of the martensite phase, respectively. With respect to plastic deformation, the other field variable $p_i^{\alpha}(\mathbf{r})(i = 1, 2, 3)$ is introduced to characterize the values of local plastic strain produced by dislocations from a specific slip system, where α is the number of slip systems. When α is equal to 1 or 2, it corresponds to the slip system $[101](\bar{1}01)_{\alpha'}$ or $\left[\bar{1}01\right](101)_{\alpha'}$, respectively. p_i^{α} is defined as [14]

$$p_i^{\alpha} = \frac{|\mathbf{b}_i|}{m_i^{\alpha} \cdot d_{hkl}}(i = 1, 2, 3). \tag{19}$$

Here, $|\mathbf{b}_i|$ is the absolute value of the Burgers vector, m_i^{α} is the number of lattice planes between two adjacent slip planes in each slip system, and d_{hkl} is the distance between $(hkl)_{\alpha'}$ planes.

The eigenstrain tensor ε_{kl}^{P}, caused by plastic deformation can be written as [14]

$$\varepsilon_{kl}^{P} = \sum_{\alpha} \frac{\mathbf{b}_i^{\alpha} \otimes \mathbf{n}_i^{\alpha} + \mathbf{n}_i^{\alpha} \otimes \mathbf{b}_i^{\alpha}}{2\left|\mathbf{b}_i^{\alpha}\right|} \cdot p_i^{\alpha}(\mathbf{r})(i = 1, 2, 3), \tag{20}$$

where $\mathbf{b}_i^{\alpha}$ is the Burgers vector, $\mathbf{n}_i^{\alpha}$ is the unit vector of the slip plane normal, and $\otimes$ represents the dyadic product.

The martensitic transformation is a minimization process of the total free energy, which is defined as the sum of the chemical free energy E_{chem}, gradient energy E_{grad}, and elastic strain energy E_{el} [15]:

$$E_{\mathrm{total}} = E_{\mathrm{chem}}(\{\phi_i(\mathbf{r})\}) + E_{\mathrm{grad}}(\{p_i^a(\mathbf{r})\}) + E_{\mathrm{el}}(\{\phi_i(\mathbf{r})\}, \{p_i^a(\mathbf{r})\}). \tag{21}$$

Equation (21) indicates that the chemical free energy is involved in Bain deformation, the gradient energy is involved in plastic deformation, and the elastic strain energy is related both with Bain deformation and dislocation slip.

The dynamics of the martensitic transformation is controlled by the Allen-Cahn equation:

$$\frac{\partial M(\mathbf{r}, t)}{\partial t} = -L_M \frac{\delta E_{\mathrm{total}}}{\delta M(\mathbf{r}, t)}, \tag{22}$$

where $M(\mathbf{r}, t)(M = \phi_i, p_i^\alpha)$ are the field variables and L_M is the kinetic parameter of each field variable.

3 Results and Discussion

3.1 Ni-Based Superalloy

We perform the simulation of microstructural evolution of the γ' phase during creep under a tensile stress along [001] crystallographic direction. Under the assumption that only the γ phase is uniformly deformed, the total transformation strain is calculated as

$$\varepsilon_0^{\mathrm{total}} = \begin{pmatrix} \varepsilon_0 & 0 & 0 \\ 0 & \varepsilon_0 & 0 \\ 0 & 0 & \varepsilon_0 \end{pmatrix} + \begin{pmatrix} \varepsilon_{\mathrm{p}}/2 & 0 & 0 \\ 0 & \varepsilon_{\mathrm{p}}/2 & 0 \\ 0 & 0 & -\varepsilon_{\mathrm{p}} \end{pmatrix}, \tag{23}$$

where ε_p represents the plastic strain of the matrix along the [001] tensile axis. Then, the eigenstrain is expressed as

$$\varepsilon_{kl}^0(\mathbf{r}, t) = \varepsilon_0^{\mathrm{total}} h(\phi_i). \tag{24}$$

3D phase-field simulation at 1193 K was carried out under the periodic boundary conditions. The system size is $384 \times 384 \times 384\,\mathrm{nm}^3$. The double-well potential height and the gradient energy coefficient are set to be $w = 3.6 \times 10^7\,\mathrm{J\,m^{-3}}$ and $\kappa_\phi = 1.0 \times 10^{-10}\,\mathrm{J\,m}$, respectively. Elastic inhomogeneity is ignored for efficient computation, and the elastic constants of pure Ni ($C_{11} = 250$, $C_{12} = 150$ and $C_{44} = 123\,\mathrm{GPa}$) [16] are employed for the entire system. The volume fraction of the γ' phase in the

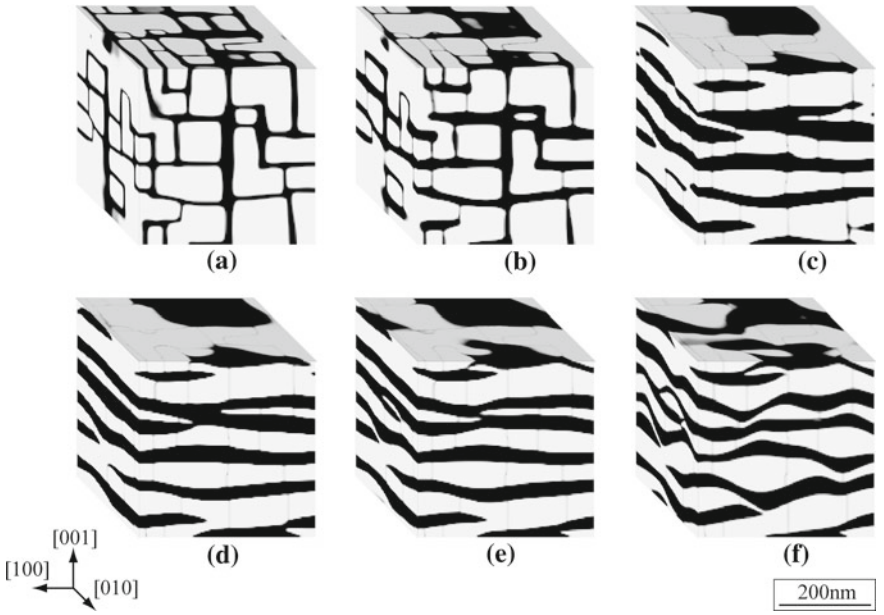

Fig. 1 Morphological evolution of the γ' phase during creep at 1193 K under 130 MPa tension along [001] calculated from 3D phase-field simulation. **a** t = 0, **b** t = 5000, **c** t = 10000, **d** t = 20000, **e** t = 30000 and **f** t = 40000. All time expressed here are dimensionless time steps

equilibrium state is set to be 60 % and the lattice misfit is assumed to be $\varepsilon_0 = -0.004$ [1]. The external tensile stress along [001] direction is set to be 130 MPa.

Figure 1a shows initial configuration of the $(\gamma + \gamma')$ microstructure, which was prepared using the phase-field simulation without incorporating external stress and plastic strain. The cuboidal γ' precipitates aligned along the $\langle 100 \rangle$ direction of the γ matrix is observed. In Fig. 1, the plastic strain (creep strain) is increased at a constant rate of $d\varepsilon_p / dt = 4.0 \times 10^{-7}$, where t represents the simulation time step. This corresponds to the fact that the creep strain increases with creep time. During $t = 0$–20000, it is observed that the γ' phase evolves toward the direction normal to the applied tension axis and (001) rafted structure is produced. After $t = 20000$, the (001) rafted structure gradually transforms into wavy morphology as shown in Fig. 1d–f. This morphological change coincides with the result reported previously that the lamellar structure collapses in the late stage of long term creep [1].

The formation and collapse of the rafted structure are attributed to the change in the stable shape of the γ' phase during creep; the habit plane of plate-like structure deviates from (001) with increasing the creep strain. This can be specifically understood by considering the habit plane and orientation relations of a tetragonal precipitate in a cubic parent phase, because the γ' phase can be regarded as a tetragonal phase with eigenstrain calculated by Eqs. (23) and (24). During long term creep at high temperatures, the microstructure is subject to the morphological evolution with the

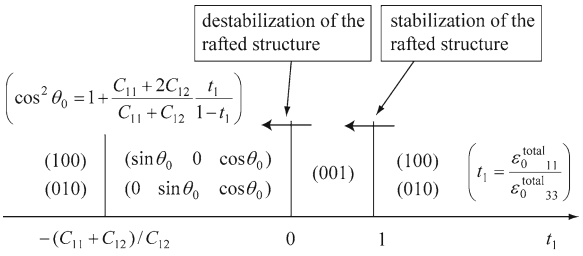

Fig. 2 Schematic interpretation of the relation between the Miller indices of the habit plane of the γ' phase and the tetragonal ratio of the total transformation strain $t_1 = \varepsilon_0^{\text{total}}{}_{11}/\varepsilon_0^{\text{total}}{}_{33}$

help of atomic diffusion. Hence, the stability of the rafted structure is closely related to the change in the energetically favorable structure arising from the introduction of the creep strain.

Figure 2 shows the relation between the Miller indices of the habit plane of the γ' phase and the tetragonal ratio of the total transformation strain $t_1 = \varepsilon_0^{\text{total}}{}_{11}/\varepsilon_0^{\text{total}}{}_{33}$ [11]. When the creep strain is introduced, t_1 is between 0 and 1 and the habit plane of the γ' phase is (001). This is the reason that the (001) plate-like structure (rafted structure) is formed, which is consistent with the simulation results shown in Fig. 1a–d. Furthermore, continuing increase in the creep strain leads to the negative value of t_1 and make the habit plane of the γ' phase deviate from (001). As a result, the destabilization of the (001) plate-like structure occurs, resulting in the collapse of the rafted structure as shown in Fig. 1d–f.

3.2 Low Carbon Steel

The martensitic transformation in Fe-0.1C mass% steel was simulated at 300 K in three-dimensional space. The simulation was carried out in a cubic with N^3 ($N = 64$) meshes and the mesh size is 4 nm, and therefore the computational domain is $256 \times 256 \times 256$ nm. For the initial state, it is assumed that there is a single pre-martensite nucleus in the center of the austenite cubic. The lattice parameters both in austenite matrix and martensite phase are chosen as: $a_\gamma = 3.599 \times 10^{-10}$ m, $a_{\alpha'} = 2.867 \times 10^{-10}$ m, $c_{\alpha'} = 2.880 \times 10^{-10}$ m. The elastic constants in pure iron are referred in this simulation, which are $C_{11} = 2.3310 \times 10^{11}$, $C_{12} = 1.3544 \times 10^{11}$ and $C_{44} = 1.1783 \times 10^{11}$ Pa, respectively. The driving force of martensitic transformation, in 0.1C mass% steel at 300 K is estimated to be 5085 J/mol. The gradient energy coefficients are determined to be $\kappa_\phi = 1.0 \times 10^{-13}$, $\kappa_{u,w} = 3.0 \times 10^{-13}$ J m^2/mol to obtain a smooth interface of austenite/martensite phase. The kinetic parameters are set to be $L_\phi = L_u = L_w = 1$. By inserting such parameters into Eq. (22), the martensitic transformation was performed with a time step of $\Delta t^* = 0.001$, and $*$ represents a dimensionless physical quantity.

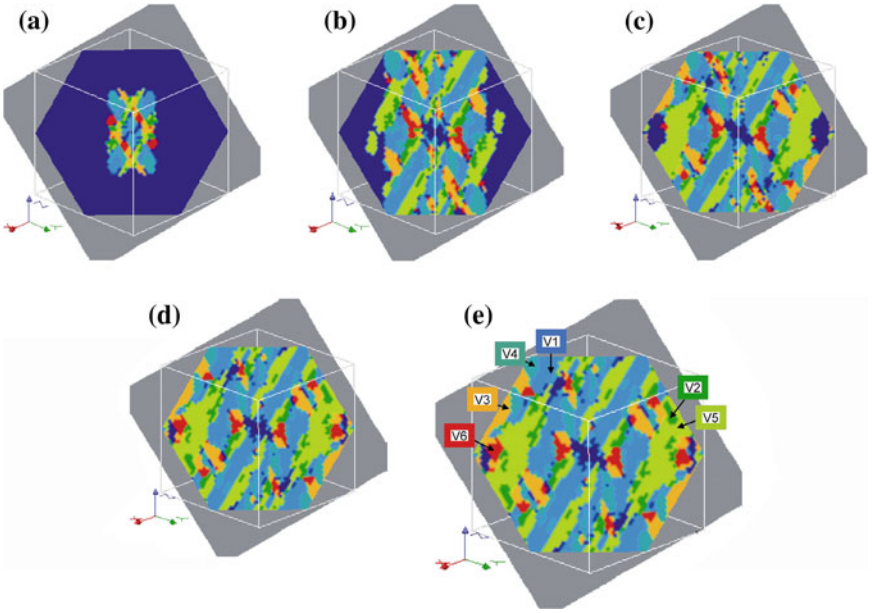

Fig. 3 Variants distribution in a packet with time t. **a** $t* = 4$, **b** $t* = 8$, **c** $t* = 15$ and **d** $t* = 30$. Each colour represents a martensite variant, which is explained in **e**. There are three combinations of variants, i.e., V1 ∼V4, V2∼V5 and V3∼V6, representing three blocks

Figure 3 shows the variant distribution in a packet on the ⟨111⟩ plane and the six colored areas represent the six variants illustrated explicitly in Fig. 3e. As shown in Fig. 3e, each combination of variants, i.e., V1∼V4, V2∼V5, and V3∼V6 represent the sub-block morphology in lath martensite. A domain composed of the two martensitic variants defined by the KS relationship is ideal for the adjustment of the plastic deformations via the two slip systems.

4 Summary

Phase-field simulations have been carried out to investigate the role of elastic strain induced by the lattice coherency between the γ and γ' phases in microstructural evolution in Ni-based superalloys and to simulate the formation of lath-martensite phase in a low carbon steel. As a result, the formation and collapse of the (001) rafted structure in Ni-based superalloys has been reproduced. It is found that this morphological evolution is attributed to the change in the energetically stable structure during creep. Furthermore, the martensitic transformation in a Fe-0.1 mass%C steel was simulated by elasto-plastic phase-field model. It is considered that this result gives a substantive formation mechanism of the hierarchical microstructure of lath martensite, although elastic constants of the martensite phase itself are not available at the present time.

Acknowledgments The authors would like to express their appreciation to JFE 21st Century Foundation for the financial support.

References

1. Murata, Y., Hashizume, R., Yoshinari, A., Aoki, N., Morinaga, M., Fukui, Y.: Superalloys **2000**, 285 (2000)
2. Shibata, A., Morito, S., Furuhara, T., Maki, T.: Scripta Mater. **53**, 597 (2005)
3. Morito, S., Huang, X., Furuhara, T., Maki, T., Hansen, N.: Acta Mater. **54**, 5323 (2006)
4. Wang, Y., Banerjee, D., Su, C.C., Khachaturyan, A. G.: Acta Mater. **46**, 2983 (1998)
5. Hu S.Y., Chen L.Q.: Acta Mater. **49**, 1879 (2001)
6. Vaithyanathan V., Chen L.Q.: Acta Mater. **50**, 4061 (2002)
7. Zhu J.Z., Wang T., Zhou S.H., Liu Z.K., Chen L.Q.: Acta Mater. **52**, 833 (2004)
8. Zhu J.Z., Wang T., Ardell A.J., Zhou S.H., Liu Z.K., Chen L.Q.: Acta Mater. **52**, 2837 (2004)
9. Iwashita, K., Murata, Y., Tsukada, Y., Koyama, T.: Philos. Mag. **91**, 4495 (2011)
10. Kim S.G., Kim W.T., Suzuki T.: Phys. Rev. E **60**, 7186 (1999)
11. Cahn J.W., Hilliard J.E.: J. Chem. Phys. **28**, 258 (1958)
12. Khachaturyan A.G.: Theory of Structural Transformations in Solids. Wiley, New York (1983)
13. Mura, T.: Micromechanics of Defects in Solids, Second, Revised Edition . Kluwer Academic, Dordrecht (1987)
14. Zhou, N., Shen, C., Mills, M., Wang, Y.: Philos. Mag. **90**, 405 (2010)
15. Wang, Y., Khachaturyan, A.G.: Acta Mater. **45**, 759 (1997)
16. Kinzoku data book, Second revised edition. The Japan Inst. Metals (1984)

Viscoplastic Constitutive Model to Divide Inelastic Strain into Time-Independent and Time-Dependent Strains

Ken-ichi Ohguchi and Katsuhiko Sasaki

Abstract This paper proposes a viscoplastic constitutive model for solder alloys. The model is a type of so-called elasto-plastic-creep model in which the inelastic strain is divided into the time-independent plastic strain and the time-dependent creep strain. Especially in the proposed model, the creep strain is characteristically divided into the transient part and the steady-state part. An experimental method which we termed "stepped ramp wave (SW) loading test" is also shown. The SW test can quantify both the plastic strain and the creep strain generated under a loading. The parameters used in the proposed model can be estimated systematically during the quantification process. In addition, the development behaviours of the plastic and creep strains can be clarified by the quantification, and they are useful for constructing the model for each strain with high precision.

1 Introduction

Solder joints in electronic packaging connect chips and substrate which have different coefficient thermal expansion (CTE) value. Then, the mismatch in CTE causes cyclic inelastic deformation of the solder joints when cyclic change in temperature occurs at usage environment of electronic equipment. The cyclic deformation causes fatigue failure of the solder joints and therefore the fatigue strength of the solder joints must be evaluated by conducting finite element analysis (FEA). To conduct the evaluation accurately, the FEA must employ a constitutive model which can precisely describe

K. Ohguchi(✉)
Department of Materials Science and Engineering, Akita University, Akita, Japan
e-mail: ken@ipc.akita-u.ac.jp

K. Sasaki
Division of Human Mechanical Systems and Design, Hokkaido University, Sapporo, Japan
e-mail: katsu@eng.hokudai.ac.jp

H. Altenbach and S. Kruch (eds.), *Advanced Materials Modelling for Structures*, Advanced Structured Materials 19, DOI: 10.1007/978-3-642-35167-9_26,

the deformation behavior of solder alloys. Especially, the deformation behavior of solder alloys shows significant time dependency even at room temperature, and therefore the model must be able to describe time-dependent deformations such as strain rate effect on the stress-strain relation, creep and stress relaxation. Then, there have been many studies for constructing the constitutive model for solder alloys e.g., [1–4] and those for applying the existing constitutive model to solder alloys e.g., [5, 6].

We also have constructed a constitutive model for solder alloys [7]. The model is so-called elasto-plastic-creep model in which the inelastic strain is separated into the time-independent plastic strain and the time-dependent creep strain. To give this type of model a high ability for describing the deformation of solder alloys, detail information of the development behavior of plastic and creep strains during loadings is needed. In addition, since the development period for recent electronic equipment should be shortened, the constitutive model used in the FEA of solder joints is required to be able to estimate the parameters for the model without complicated procedure in a short term. Then, considering these things, we have proposed an experimental method termed "stepped ramp wave (SW) loading test" [8]. By conducting this test once at an arbitrary temperature, the material parameters used in our model at the temperature can be estimated systematically. Also, both the plastic strain and the creep strain generated under a loading can be quantified by conducting the SW loading test, and therefore the development behaviors of these strains are clarified. This paper shows the constructed model and demonstrates the availability of the SW loading test for the parameter estimation and the inelastic strain development behavior analysis.

2 Viscoplastic Constitutive Model

We employ an elasto-plastic-creep model as a viscoplastic constitutive model for solder alloys. In the model, the total strain $\boldsymbol{\varepsilon}$ consists of three strains of the elastic strain $\boldsymbol{\varepsilon}^{\mathrm{e}}$, the plastic strain $\boldsymbol{\varepsilon}^{\mathrm{p}}$, and the creep strain $\boldsymbol{\varepsilon}^{\mathrm{c}}$. The elastic strain $\boldsymbol{\varepsilon}^{\mathrm{e}}$ can be expressed using Hooke's law:

$$\boldsymbol{\varepsilon}^{\mathrm{e}} = (\boldsymbol{D}^{\mathrm{e}})^{-1} : \boldsymbol{\sigma}, \tag{1}$$

where $\boldsymbol{\sigma}$ is the stress tensor and $\boldsymbol{D}^{\mathrm{e}}$ is the elastic tensor.

The plastic strain $\boldsymbol{\varepsilon}^{\mathrm{p}}$ and the creep strain $\boldsymbol{\varepsilon}^{\mathrm{c}}$ are expressed in the following discrete form using the backward Euler's method with consideration for employing the constitutive model into FEM analysis:

$$\begin{aligned} \boldsymbol{\varepsilon}^{\mathrm{p}}_{i+1} &= \boldsymbol{\varepsilon}^{\mathrm{p}}_{i} + \Delta\boldsymbol{\varepsilon}^{\mathrm{p}} \\ \boldsymbol{\varepsilon}^{\mathrm{c}}_{i+1} &= \boldsymbol{\varepsilon}^{\mathrm{c}}_{i} + \Delta\boldsymbol{\varepsilon}^{\mathrm{c}}, \end{aligned} \tag{2}$$

where the subscripts i and $i+1$ respectively denote the start and end of a calculation step. $\Delta\boldsymbol{\varepsilon}^{\mathrm{p}}$ and $\Delta\boldsymbol{\varepsilon}^{\mathrm{c}}$ are the plastic strain increment and the creep strain increment in the current calculation step, respectively.

The plastic strain increment $\Delta\boldsymbol{\varepsilon}^{\mathrm{p}}$ is calculated by using the following equation derived by the associate flow rule considering kinematic hardening:

$$\Delta\boldsymbol{\varepsilon}^{\mathrm{p}} = \frac{3}{2\bar{\sigma}^{\mathrm{p}}_{i+1}} \frac{\Delta\bar{\sigma}^{\mathrm{p}}}{H} (\boldsymbol{s}_{i+1} - \boldsymbol{b}_{i+1}), \tag{3}$$

where H is the plastic tangent modulus and $\bar{\sigma}^{\mathrm{p}}$ is the scalar expressed by the following equation:

$$\bar{\sigma}^{\mathrm{p}}_{i} = \sqrt{3/2(\boldsymbol{s}_i - \boldsymbol{b}_i) : (\boldsymbol{s}_i - \boldsymbol{b}_i)}, \tag{4}$$

where $\boldsymbol{s}$ and $\boldsymbol{b}$ are the deviatoric stress and the deviatoric back stress, respectively. The deviatoric back stress $\boldsymbol{b}$ which represents the center position of the yield surface is obtained by using the following linear kinematic hardening rule:

$$\boldsymbol{b}_{i+1} = \boldsymbol{b}_i + 2/3H\Delta\boldsymbol{\varepsilon}^{\mathrm{p}}. \tag{5}$$

The creep strain increment $\Delta\boldsymbol{\varepsilon}^{\mathrm{c}}$ is expressed as:

$$\Delta\boldsymbol{\varepsilon}^{\mathrm{c}} = \frac{3\boldsymbol{s}_{i+1}}{2\bar{\sigma}_{i+1}} \bar{\dot{\varepsilon}}^{\mathrm{c}}_{i+1} \, \Delta t, \tag{6}$$

where $\bar{\sigma}$ is the von Mises type equivalent stress and Δt is the time increment in the current calculation step. $\bar{\dot{\varepsilon}}^{\mathrm{c}}$ is the equivalent creep strain rate expressed as the sum of the two equivalent creep strain rates of the transient part and the steady-state part as follows:

$$\bar{\dot{\varepsilon}}^{\mathrm{c}}_{i} = (\bar{\dot{\varepsilon}}^{\mathrm{c}}_{i})_{\mathrm{I}} + (\bar{\dot{\varepsilon}}^{\mathrm{c}}_{i})_{\mathrm{II}}, \tag{7}$$

where $(\bar{\dot{\varepsilon}}^{\mathrm{c}}_{i})_{\mathrm{I}}$ and $(\bar{\dot{\varepsilon}}^{\mathrm{c}}_{i})_{\mathrm{II}}$ are respectively the equivalent transient creep strain rate and the equivalent steady-state creep strain rate. $(\bar{\dot{\varepsilon}}^{\mathrm{c}}_{i})_{\mathrm{I}}$ is expressed by the following equation which means $(\bar{\dot{\varepsilon}}^{\mathrm{c}}_{i})_{\mathrm{I}}$ is proportional to $(\bar{\dot{\varepsilon}}^{\mathrm{c}}_{i})_{\mathrm{II}}$ [9]:

$$(\bar{\dot{\varepsilon}}^{\mathrm{c}}_{i})_{\mathrm{I}} = \left\{ C_1 \exp\left(-\frac{(\bar{\varepsilon}^{\mathrm{c}}_{i})_{\mathrm{H}}}{C_2} \right) \right\} (\bar{\dot{\varepsilon}}^{\mathrm{c}}_{i})_{\mathrm{II}}, \tag{8}$$

where C_1 and C_2 are the material constants of positive values. $(\bar{\varepsilon}^{c}_{i})_{\mathrm{H}}$ is the creep hardening parameter, and then Eq. (8) means that the transient creep strain rate approaches zero with increase in the value of $(\bar{\varepsilon}^{c}_{i})_{\mathrm{H}}$.

The equivalent steady-state creep strain rate $(\bar{\dot{\varepsilon}}^{c}_{i})_{\mathrm{II}}$ employs the following Norton's law:

$$(\bar{\dot{\varepsilon}}^{c}_{i})_{\mathrm{II}} = A\bar{\sigma}^{n}_{i}, \tag{9}$$

where A and n are the material constants.

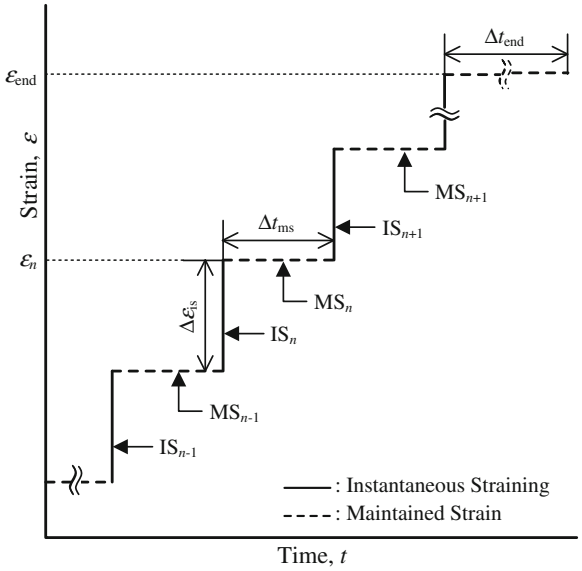

Fig. 1 Schematic outline of the stepped ramp wave (SW) loading

3 Parameter Estimation by SW Loading Test

3.1 SW Loading Test

Figure 1 shows a schematic outline of the stepped ramp wave (SW) loading. The stepped ramp wave consists of an instantaneous straining part expressed as IS and a maintained strain part expressed as MS as shown in Fig. 1. The instantaneous straining (IS) and maintained strain (MS) parts were repeatedly stepped until the strain reached at ε_{end} as shown in Fig. 1. The strain rate for IS should be set in the maximum speed that testing machine can supply, to prevent the development of the creep strain during the straining. The subscripts n of IS and MS in Fig. 1 denote the number of repeated steps during the loading. When the strain is ε_n in Fig. 1, the strain is maintained for a time period Δt_{ms}, and after that the strain is increased by the instantaneous loading until $\Delta\varepsilon_{is}$. Finally, the strain ε_{end} is maintained for a time period Δt_{end}.

Figure 2 shows a stress-strain relation of Sn-3.0Ag-0.5Cu solder subjected to the SW loading in which $\Delta\varepsilon_{is}$,Δt_{ms}, ε_{end} and Δt_{end} were respectively set to 2.75×10^{-4}, 0.5 s, 4.4×10^{-2}, 600 s. In Fig. 2, the stress increases and decreases cyclically until the strain reaches ε_{end}. The small graph in Fig. 2 shows the cyclic stress relaxation curve which corresponds to the stress-strain relation in the circled region. The stresses increase at the instantaneous strained parts, while stress relaxation occurred at the strain maintained parts.

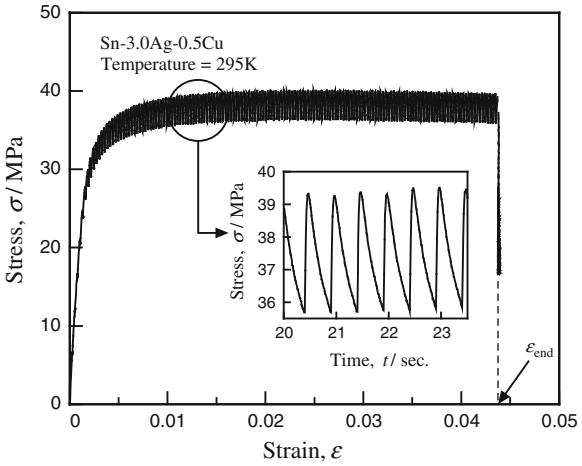

Fig. 2 Stress-strain relation under the stepped ramp wave (SW) loading

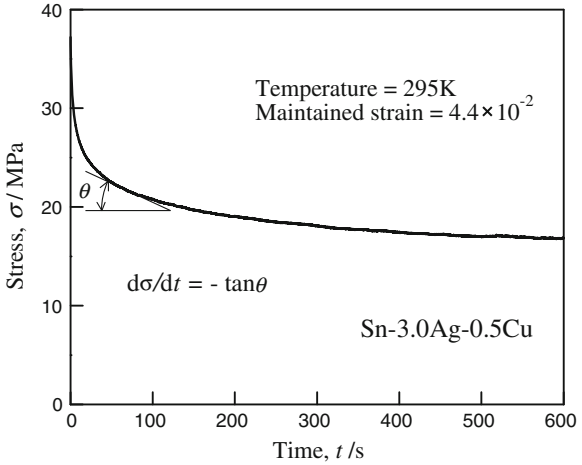

Fig. 3 Stress relaxation curve by maintaining the ε_{end} strain

Figure 3 shows the stress relaxation curve obtained by maintaining the ε_{end} strain of 600 s, here the stress decreases rapidly for about 50 s, while it decreases more gradually after 50 s. Namely, the stress relaxation rate $d\sigma/dt$ given as shown in Fig. 3 becomes lower with time and decrease in the stress.

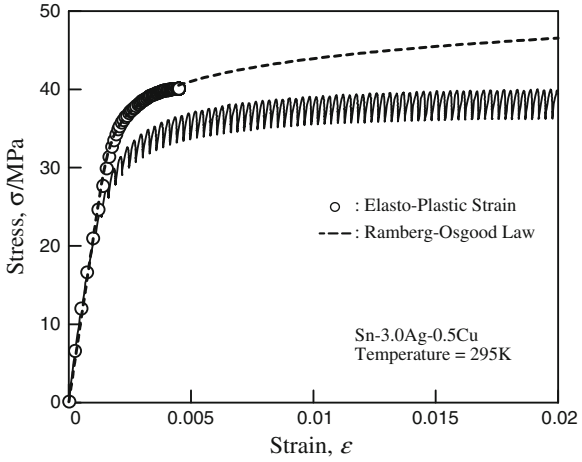

Fig. 4 Relationship between stress and elasto-plastic strain with stress-strain relation of Fig. 2

3.2 Parameter Estimation Method

3.2.1 Parameters for Elastic and Plastic Strains

In the constitutive model shown in the previous chapter, the elastic and plastic strains are treated as the time-independent strains, while the creep strain is treated as the time-dependent strain. Then, the parameters for the elastic and plastic strains should be estimated by using the stress-strain relation which does not include the time-dependent creep strains. To obtain such a stress-strain relation, the stress-strain relations which correspond to each IS process in Fig. 2 are connected. This is because the deformation at the IS part does not include the creep deformation because of the instantaneous loading [8].

The open circles in Fig. 4 show the relationship between the stress and the time-independent elasto-plastic strain obtained by the above-mentioned connection. Meanwhile, the dashed line in Fig. 4 shows the approximated curve of the stress-elasto-plastic strain relation by the following Ramberg-Osgood law:

$$\varepsilon_{\mathrm{t}}^{\mathrm{ep}} = \frac{\sigma_{\mathrm{t}}}{E} + \varepsilon_0 \left(\frac{\sigma_{\mathrm{t}}}{D}\right)^m, \tag{10}$$

where the subscript t denotes uniaxial condition, $\varepsilon_{\mathrm{t}}^{\mathrm{ep}}$ is the elasto-plastic strain, E is Young's modulus, D is the reference stress at the plastic strain ε_0 of 5.00×10^{-4}, and m is the hardening exponent.

The first and second terms on the right-hand side in Eq. (10) respectively represent the elastic and plastic strains. Therefore, the parameters for the elastic and plastic strains can be estimated from the approximate curve using Eq. (10). Namely, Young's

modulus for the elastic strain can be estimated from the first term of Eq. (10). Also the plastic tangent modulus for the plastic strain can be obtained by differentiating the second term of Eq. (10). Therefore, considering the correspondence between the uniaxial stress and the equivalent stress, the plastic tangent modulus is expressed as follows:

$$H = \frac{D}{m\varepsilon_0}\left(\frac{\sigma_t}{D}\right)^{1-m} = \frac{D}{m\varepsilon_0}\left(\frac{\bar{\sigma}}{D}\right)^{1-m}. \tag{11}$$

For the approximation in Fig. 4, the parameters in Eq. (10) were respectively set to $E = 21.0\,\mathrm{GPa}$, $D = 36.1\,\mathrm{MPa}$, and $m = 14.0$.

3.2.2 Parameters for Creep Strain

The parameters for the creep strain are estimated from the stress relaxation curves shown in Figs. 2 and 3. At first, assuming that the stress relaxation shown in Fig. 3 is caused by only the steady-state creep deformation, the parameters for Norton's law of Eq. (9) are estimated. To do that, the following relationship between the axial creep strain rate $\dot{\varepsilon}_t^c$ and the axial stress relaxation rate $\dot{\sigma}_t$ by maintaining strain is employed [8, 9]:

$$\dot{\varepsilon}_t^c = -\dot{\sigma}_t / E, \tag{12}$$

$\dot{\sigma}_t$ in Eq. (12) means the $d\sigma/dt$ shown in Fig. 3. Then, the relationship between the creep strain rate and the stress which is necessary for deriving creep laws can be obtained by evaluating a number of stress relaxation rates at arbitrary stress levels and applying them into Eq. (12) [8, 9].

Figure 5a shows the relationship between the creep strain rate and the stress obtained by the above–mentioned method. The open circles indicate creep strain

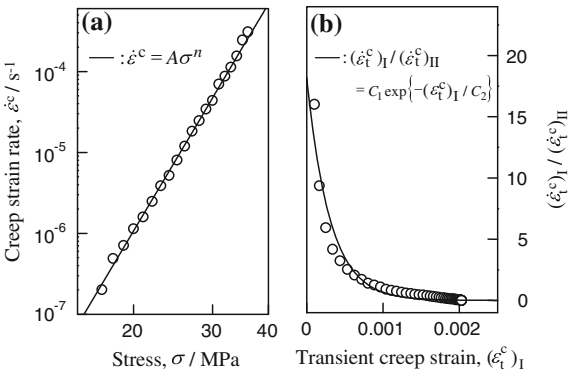

Fig. 5 **a** Relationship between creep strain rate and stress. **b** Relationship between the ratio $(\dot{\varepsilon}_t^c)_I/(\dot{\varepsilon}_t^c)_{II}$ and transient creep strain

rates at a number of stress levels, while the solid line is the approximation of those by Norton's law of Eq. (9). By this approximation, the parameters of A and n for Norton's law were respectively estimated as $A = 8.10 \times 10^{-19}$ and $n = 9.32$.

Using the estimated A and n, and the cyclic stress relaxation curve shown in Fig. 2, the parameters of C_1 and C_2 in Eq. (8) for the transient creep strains are estimated as follows:

(i) Calculate the creep strain increment $\Delta\varepsilon_t^c$ and creep strain rate $\dot{\varepsilon}_t^c$ at each MS process by using Eq. (12).
(ii) Calculate the steady-state creep strain increment $(\Delta\varepsilon_t^c)_{II}$ and steady-state creep strain rate $(\dot{\varepsilon}_t^c)_{II}$ at each MS process by using Norton's law with the estimated A and n.
(iii) Subtract $(\Delta\varepsilon_t^c)_{II}$ from $\Delta\varepsilon_t^c$ to determine the transient creep strain increment $(\Delta\varepsilon_t^c)_I$ at each MS process. Also, subtract $(\dot{\varepsilon}_t^c)_{II}$ from $\dot{\varepsilon}_t^c$ to determine the transient creep strain rate $(\dot{\varepsilon}_t^c)_I$.
(iv) Calculate the ratio of $(\dot{\varepsilon}_t^c)_I/(\dot{\varepsilon}_t^c)_{II}$ at each MS process. Then, plot the relationship between $(\dot{\varepsilon}_t^c)_I/(\dot{\varepsilon}_t^c)_{II}$ and the transient creep strain $(\varepsilon_t^c)_I$ as shown in Fig. 5b.
(v) Regarding the $(\varepsilon_t^c)_I$ as the creep hardening parameter $(\bar{\varepsilon}_i^c)_H$ in Eq. (8), approximate the plotted relation in the step (iv) by using an equation obtained by dividing both side of Eq. (8) by $(\dot{\bar{\varepsilon}}_i^c)_{II}$.

The solid line in Fig. 5b shows the approximation result in the step (v). As a result of the approximation, the parameters of C_1 and C_2 were respectively estimated as 18.2 and 3.03×10^{-4}.

As explained above, we have estimated the parameters for creep strain without conducting long-time creep tests under a number of stress levels.

4 Simulations and Discussions

Numerical simulations of the viscoplastic deformations of Sn-3.0Ag-0.5Cu solder were conducted using the proposed constitutive model with the parameters estimated by the SW test.

Figure 6 shows the stress–strain relations obtained by the tensile loadings under 3 different strain rates at 295 K. There are some differences between the simulations and the experiments, especially in the transient region of the stress-strain relation. However, the strain rate effect in which the stress level of the stress-strain relation becomes larger with increase in the strain rate is reproduced very well by the simulations.

Figure 7 shows the creep curve which is obtained by maintaining a stress of 24.4 MPa at 295 K. In Fig. 7, the transient creep region can be observed in both the experimental creep curve and the simulation. Comparing the creep strain of the experiment with that of the simulation at 600 s, these values are approximately equal. Namely, the simulation almost expresses the characteristics of the experimental creep curve.

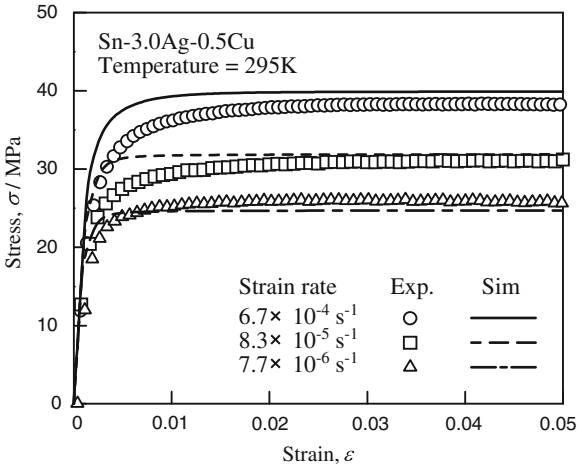

Fig. 6 Calculated stress–strain relations with experimental results

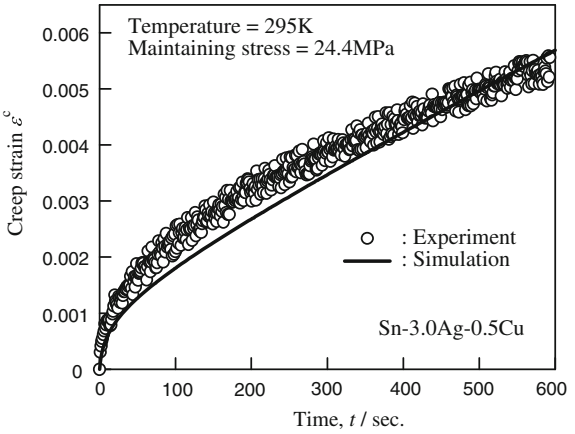

Fig. 7 Calculated creep curve with experimental result

The constitutive model for solders must be able to describe the cyclic deformation because the model is employed to predict the deformation behavior of solder joints subjected to cyclic thermal stress. In the proposed constitutive model, whereas the plastic model is applicable to the cyclic deformation, the creep model is not. Namely, although there is a possibility that the recovery of the strain hardening due to accumulation of transient creep strains occurs when the loading direction changes during the cyclic loading, the creep model shown as Eqs. (6)–(9) does not consider it.

Then, we have investigated the development behavior of the creep strain under cyclic loading by applying the SW loading to a cyclic tension-compression loading of Sn-3.0Ag-0.5Cu solder, and have discussed whether there is such a possibility

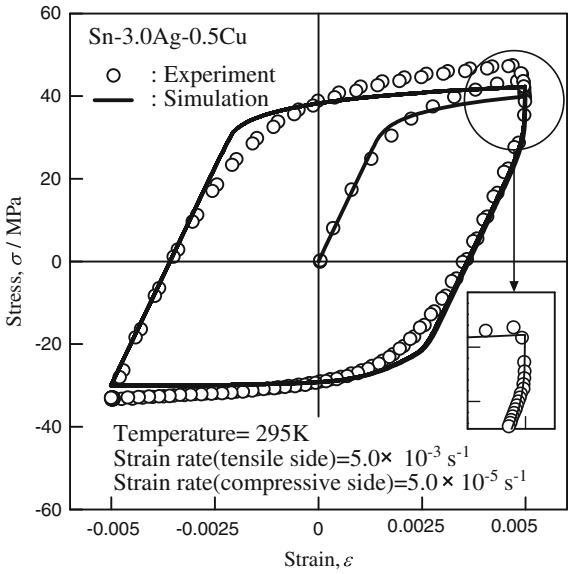

Fig. 8 Calculated cyclic tension-compression loading with experimental result under strain rate of $5.0 \times 10^{-3}\,\mathrm{s}^{-1}$ on the tensile side and $5.0 \times 10^{-5}\,\mathrm{s}^{-1}$ on the compressive side

in the cyclic loading of solder [10]. The result of the investigation suggested that strain hardening due to the accumulation of transient creep strain is recovered when the loading direction changes from being tension to being compressive or vice versa. Consequently, the creep model for cyclic loading of solders must have considered the strain hardening recovery. Therefore, the creep hardening parameter $(\bar{\varepsilon}_i^{\mathrm{c}})_{\mathrm{H}}$ in Eq. (8) (of which we employed $(\bar{\varepsilon}_i^{\mathrm{c}})_{\mathrm{I}}$ as a substitution) was set to zero when the sign of the stress changes in the simulation of cyclic loadings.

Figure 8 shows the stress-strain relation due to the cyclic loading under the $5.0 \times 10^{-3}\,\mathrm{s}^{-1}$ strain rate on the tensile side $5.0 \times 10^{-5}\,\mathrm{s}^{-1}$ on the compressive side. The experimental result expressed by open circles in Fig. 8 shows that the absolute stress level on the tensile side is higher than that on the compressive side because the strain rates on the tensile side are higher than that on the compressive side, and the hysteresis loop is unsymmetrical. Comparing the experimental result with the simulation expressed by the solid line in Fig. 8, there are some differences between the experiment and the simulation. However, the unsymmetrical shape of the hysteresis loop is described by the simulation. Particularly, the characteristic rapid stress decrease with decrease in the strain rate at the maximum strain, which is shown in the inset graph in Fig. 8, is well predicted by the simulation.

5 Conclusions

This paper presented a viscoplastic constitutive model for solders and an experimental method of the SW test for estimating the parameters in the model. The model and the experimental method were applied to Sn-3.0Ag-0.5Cu lead-free solder. The results are summarized as follow.

(1) A viscoplastic constitutive model in which the inelastic strain was divided into the time-independent plastic strain and the time-dependent creep strain was presented. In the model, the creep strain was characteristically divided into the transient part and the steady-state part.
(2) An experimental method which we termed the SW test was presented. The test employs a stepped ramp wave loading which consists of an instantaneous straining (IS) part and short-time maintained strain (MS) part, and the IS and MS parts are repeatedly stepped until the strain reaches a value. When the strain reaches the value, the strain is maintained for a time period.
(3) The parameters for the elastic and plastic strains in the presented model can be estimated by using the stress-elasto-plastic strain relation obtained by connecting the stress-strain relation at IS part.
(4) By using the stress relaxation curve obtained at strain maintenance part, the parameters for creep strain in the presented model can be estimated without conducting long-time creep tests.
(5) The presented constitutive model can describe the viscoplastic deformations of Sn-3.0Ag-0.5Cu lead-free solder although the model employs the parameters estimated by conducting the SW loading test only once. Therefore, the constitutive model and the parameter estimation method employing the SW test would be an efficient tool to develop electronic equipment.

References

1. Kobayashi, M., Mukai, M., Takahashi, H., Ohno, N., Kawakami, T.: Implicit integration and consistent tangent modulus of a time-dependent non-unified constitutive model. Int. J. Numer. Method Eng. **58**, 1523–1543 (2003)
2. Maciucescu, L., Sham, T.-L., Krempl, E.: Modelling the deformation behavior of a Sn-Pb solder alloy using the simplified viscoplasticity theory based on overstress (VBO). ASME J. Electron. Packag. **121**, 92–98 (1999)
3. Whitelaw, R.S., Neu, R.W., Scott, D.T.: Deformation behavior of two lead-free solders: indalloy 227 and castin alloy. ASME J. Electron. Packag. **121**, 99–107 (1999)
4. Ishikawa, H., Sasaki, K., Ohguchi, K.: Prediction of fatigue failure of 60Sn–40Pb solder using constitutive model for cyclic viscoplasticity. ASME J. Electron. Packag. **118**, 164–169 (1996)
5. Woodmansee, M.W., Neu, R.W.: The influence of prior strain rate on stress relaxation in solder alloys. Mater. Sci. Eng. **A322**, 79–88 (2002)
6. Amagai, M., Watanabe, M., Omiya, M., Kishimoto, K., Shibuya, T.: Mechanical characterization of Sn-Ag-based lead-free solders. Microelectron. Reliab. **42**, 951–966 (2002)
7. Ohguchi, K., Sasaki, K.: Elastic-plastic-creep simulation of Pb/Sn solder alloys by separation of plastic and creep. JSME Intl. J. Ser. A **46**, 559–566 (2003)

8. Ohguchi, K., Sasaki, K., Aso, S.: Evaluation of time-independent and time-dependent strains of lead-free solder by stepped ramp loading test. ASME J. Electron. Packag. **131**, 021003-1–021003-7 (2009)
9. Ohguchi, K., Sasaki, K., Ishibashi, M.: A quantitative evaluation of time-independent and time-dependent deformations of lead-free and lead-containing solder alloys. J. Electron. Mater. **35**, 132–139 (2006)
10. Ohguchi, K., Sasaki, K.: Time-independent and time-dependent inelastic strains analysis of lead-free solder by cyclic stepped ramp wave loading test. ASME J. Electron. Packag. **132**, 041003-1–041003-7 (2010)

Multiaxial Low Cycle Fatigue for Ni-Base Single Crystal Super Alloy at High Temperature

Masao Sakane, Shengde Zhang, Akira Yoshinari, Noriaki Matsuda and Nobuhiro Isobe

Abstract This paper presents multiaxial low cycle fatigue lives of YH61 Ni-base single crystal superalloy at elevated temperature. Tension-torsion low cycle fatigue tests were performed using hollow cylinder specimens with aligning the specimen axis to [100] direction at 1173 K. Biaxial tension-compression low cycle fatigue tests were also performed using cruciform specimens whose x and y axes were aligned to ⟨110⟩ directions. The effect of strain multiaxiality on the multiaxial low cycle fatigue lives was discussed. Couples of multiaxial stress and strain parameters were applied to the experimental data for correlating the multiaxial low cycle fatigue lives of both types of the specimens. The strain parameters yielded a large scatter in the correlation and Mises equivalent stress was only the parameter to give a satisfactory correlation of multiaxial low cycle fatigue lives of the superalloy.

1 Introduction

Nickel base superalloys have been widely used in high temperature applications because of their superior mechanical properties and resistance to high temperature corrosion and oxidation [1]. Especially, single crystal (SC) superalloys have been

M. Sakane (✉) · S. Zhang
Ritsumeikan University, 1-1-1, Nojihigashi Kusatsu, Shiga 525-8577, Japan
e-mail: sakanem@se.ritsumei.ac.jp

S. Zhang
e-mail: zhangsd@se.ritsumei.ac.jp

A. Yoshinari · N. Isobe
Hitachi Research Laboratory, Hitachi Ltd., 3-1-1, Saiwai-cho, Hitachi, Ibaraki 317-8511, Japan
e-mail: akira.yoshinari.jz@hitachi.com

N. Isobe
e-mail: nobuhiro.isobe.jk@hitachi.com

N. Matsuda
Hitachi Engineering & Services Co., Ltd., 3-1-1, Saiwai-cho, Hitachi, Ibaraki 317-8511, Japan

H. Altenbach and S. Kruch (eds.), *Advanced Materials Modelling for Structures*, Advanced Structured Materials 19, DOI: 10.1007/978-3-642-35167-9_27,

initially used as a blade material of aircraft gas turbines and they also have been recently introduced to a blade material of power generation gas turbines [2].

SC turbine blades undergo not only creep damage caused by centrifugal forces but also low cycle fatigue (LCF) damage caused by the variation of temperature during start up and shutdown of turbines. Advanced gas turbine blades are cooled internally and by air film covering over the outer surface of blades to lower SC blade temperature, so the blades undergo complex multiaxial LCF damage in the combination of mechanical and thermal loading. In addition, SC superalloys have strong anisotropic deformation and fracture characteristics due to their crystallographic texture, so developing an accurate multiaxial LCF damage evaluation method taking account of the anisotropy of SC superalloys is essential for a safe design and operation of power generation gas turbines.

Many studies [3–10] reported creep and LCF characteristics of SC superalloys under uniaxial stress state and only a few studies [11–13] discussed those under multiaxial stress states. Meric et al. [11] proposed a model of describing the deformation behavior of SC superalloy based on the crystal plasticity under tension and torsion loadings and found the soft zone occurred in torsion loading. Kanda et al. [12] performed tension-torsion multiaxial LCF tests using CMSX-2 SC superalloy and applied several multiaxial strain and stress parameters for discussing the suitability of the parameters for correlating the multiaxial LCF lives. Yorikawa et al. [13] proposed a new strain parameter, taking account of the anisotropy of the elastic constants, and demonstrated that the parameter is suitable for correlating the tension-torsion multiaxial LCF lives of YH61 SC superalloy. However, LCF studies for SC superalloys under multiaxial stress states are still insufficient and are limited in a specific case of CMSX-2 [14].

The objective of this paper is to discuss the LCF lives of YH61 nickel base SC superalloy in two types of multiaxial testings. One is the tension-torsion LCF testing using hollow cylinder specimens aligned the specimen axis to [100] crystallographic direction at 1173 K. The other is the biaxial tension-compression LCF testing using cruciform specimens whose x and y axes were aligned to ⟨110⟩ directions. The effect of strain multiaxiality on the multiaxial LCF lives was discussed. Couples of multiaxial stress and strain parameters were applied for correlating the LCF lives in both types of testings and the suitability of the parameters was discussed.

2 Experimental Procedure

The material tested was YH61 nickel base SC superalloy with a FCC crystallographic structure of which the chemical composition and heat treatment are listed in Tables 1 and 2.

Figure 1a is a hollow cylinder specimen used in tension-torsion LCF tests with 16 mm I.D., 19 mm O.D. and 25 mm gage length. The axis of the specimen was aligned to [100] crystallographic direction. Solid cylinder specimens were partly used in push-pull uniaxial LCF tests whose illustration is not presented in this paper.

Table 1 Chemical composition of the material tested (wt %)

C	Cr	Co	Mo	W	Re	Ta	Nb	Al	Hf	B	Ni
0.07	7.1	1.0	0.8	8.8	1.4	8.9	0.8	5.1	0.25	0.02	Bal.

Table 2 Heat treatment condition

Solution treatment	1250 °C/4h + 1260 °C/4h + 1270 °C/4h + 1280 °C/4h, GFC
Aging	1080 °C/4h, GFC + 871 °C/20h, GFC

GFC: Gas flow cooling

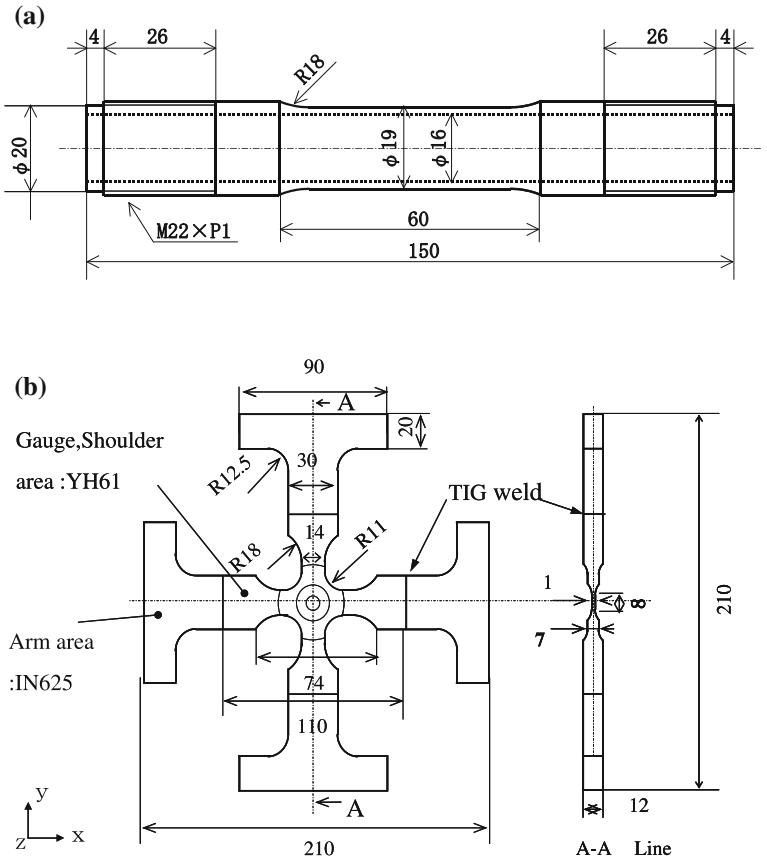

Fig. 1 Shape and dimensions of the specimens tested (mm). **a** Hollow cylinder specimen. **b** Cruciform specimen

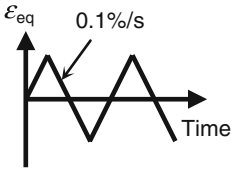

Fig. 2 Strain waveform used in multiaxial LCF tests

Figure 1b is a cruciform specimen used in biaxial tension-compression LCF tests whose x axis was aligned to the [110] and the y axis to $[1\bar{1}0]$ crystallographic directions. Since casting of a large SC plate for providing specimen is difficult technically and costly, only a square plate of YH61 SC superalloy was cast with dimensions of 110×110 mm and 12 mm in thickness. IN625 superalloy plates were TIG welded to the edges of the YH61 plate. The shape of the cruciform specimen was determined by a finite element analysis to distribute the stress and strain uniformly in the gage part [15].

A tension-torsion electric-hydraulic servo machine with load capacity of 245 kN and torque capacity of 2.82 kNm was used in tension-torsion LCF tests for hollow cylinder specimens. Axial displacement and twist angle were measured with a tension-torsion extensometer. A biaxial tension-compression electric-hydraulic servo machine with load capacity of 50 kN, that has four actuators and four servo controllers to generate widely ranged biaxial strain states [16], was used in tension-compression LCF tests for cruciform specimens. Two extensometers were attached to the gage part of cruciform specimen to measure the strains in directions of x and y. Each type of the specimens was heated by a high frequency induction heater and the temperature variation along the gage length was within ± 10 K during test.

Strain controlled tension-torsion LCF tests were performed using hollow cylinder specimens in the range of principal strain ratio (ϕ) of $-1 \leq \phi \leq -0.5$ at 1173 K. The principal strain ratio is the ratio of minimum principal strain (ε_3) to maximum principal strain (ε_1), i.e., $\phi = \varepsilon_3/\varepsilon_1$ for the case of hollow cylinder specimens. The $\phi = -0.5$ test corresponds to a uniaxial push-pull test assuming that the Poisson's ratio is 0.5, and the $\phi = -1.0$ test is a torsion test. Biaxial tension-compression LCF tests using cruciform specimens were also performed in the principal strain range of $-1 \leq \phi \leq 1.0$. The principal strain ratio is defined as $\phi = \varepsilon_x/\varepsilon_y$ that is somewhat different definition from that in the tension-torsion case but the definition has the same physical meaning.

Figure 2 shows a strain waveform used in this study, where the ordinate of the figure is Mises equivalent strain. The strain waveform used was a fully reversed triangular strain waveform with a Mises strain rate of 0.1 %/s. The number of cycles to failure (N_f) was defined as the cycles with a 25 % axial or shear stress amplitude drop from the stable value in tension-torsion tests, while as the cycles with a 5 % load drop for biaxial tension-compression tests.

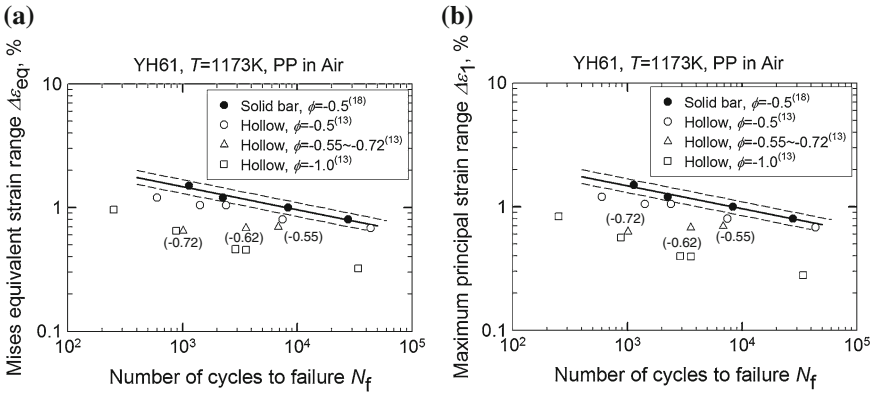

Fig. 3 Correlation of fatigue lives with strain parameters at 1173 K. **a** Mises strain range. **b** Maximum principal strain range

3 Experimental Results and Discussion

3.1 Multiaxial LCF Life Under Tension-Torsion Loading

Figure 3 correlates tension-torsion LCF lives of hollow cylinder and solid bar specimens whose specimen axis is [100] direction with (a) Mises strain range and (b) maximum principal strain range. In the figures, the solid line represents the push-pull LCF lives of solid bar specimens. The uniaxial LCF lives of hollow cylinder specimens are slightly smaller than those of the solid bar specimens in the $\phi = -0.5$ tests, which may result from smaller crack propagation path in the cylinder specimen than in the solid bar specimen. The LCF lives with smaller ϕ show smaller lives in the correlation with the two strain parameters, that is, introducing the torsion loading reduces LCF lives in the tension-torsion LCF tests. The two parameters give a large scatter in the data correlation.

Figure 4a, b correlate the tension-torsion LCF lives with Mises stress and maximum principal stress, respectively. On the contrary to the correlation with the strain parameters shown in Fig. 3, Mises stress correlates successfully the tension-torsion LCF lives within a factor of two scatter band whereas a couple of data are out of the band, Fig. 4a. The correlation with maximum principal stress gives a slightly larger scatter than with Mises stress, where the LCF lives with smaller ϕ are underestimated from the push-pull LCF lives than Mises stress, but maximum principal stress gives a far better correlation than the two strain parameters shown in Fig. 3a, b.

The results in Figs. 3 and 4 showed that the two strain parameters yielded a large scatter but Mises stress gave a successful correlation. To discuss the difference in the correlation of the tension-torsion LCF lives between Mises strain and Mises stress, LCF lives and Mises stress ranges at Mises strain range of 0.68 % are compared against the principal strain ratio in Fig. 5. The LCF life increases with the principal

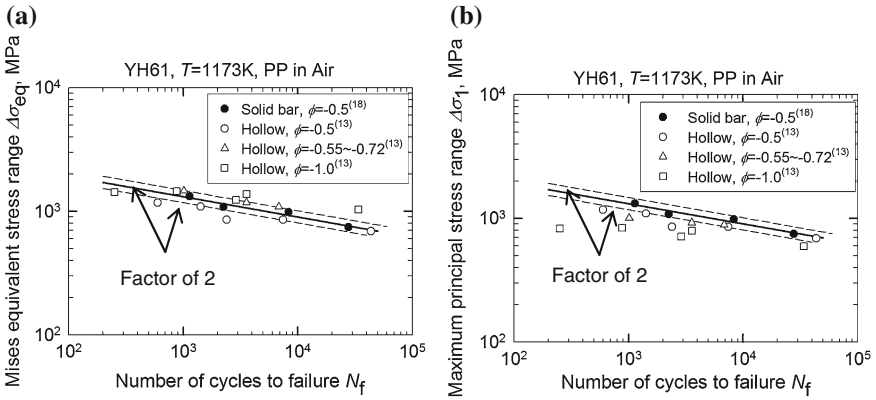

Fig. 4 Correlation of fatigue lives with stress parameters at 1173 K. **a** Mises stress range. **b** Maximum principal stress range

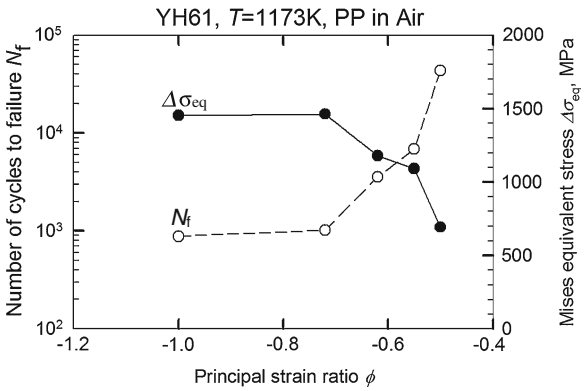

Fig. 5 Variations of number of cycles to failure and Mises stress range with principal strain ratio for hollow cylinder specimens

strain ratio but Mises stress range, on the contrary, decreases with the principal strain ratio. The trend of LCF lives well corresponds with that of Mises stress. LCF test in which larger Mises stress range occurs shows smaller LCF life.

3.2 Multiaxial LCF Life Under Biaxial Tension-Compression Loading

Figure 6 shows the variation of biaxial tension-compression LCF lives of cruciform specimens with the principal strain ratio in the y directional strain range constant tests. In multiaxial LCF tests using cruciform specimens, multiaxial LCF lives in

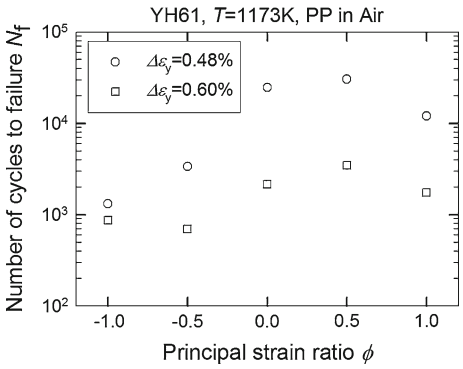

Fig. 6 Variation of number of cycles to failure with principal strain ratio for cruciform specimen

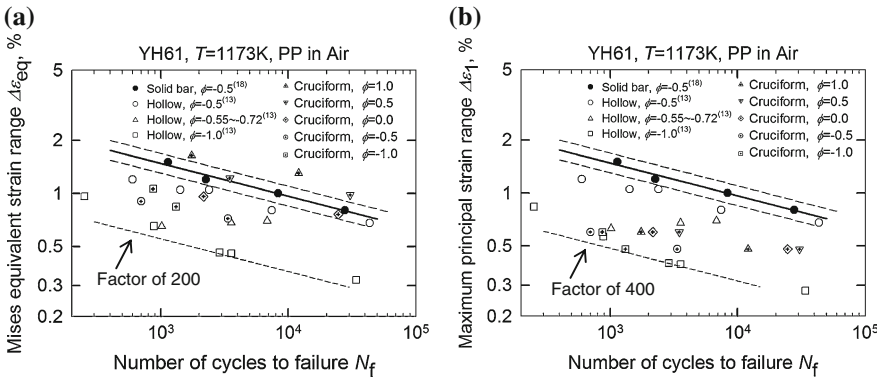

Fig. 7 Correlation of multiaxial LCF lives of hollow cylinder and cruciform specimens with Mises strain and maximum principal strain. **a** Mises strain range. **b** Maximum principal strain range

the full range of the principal strain ratio of $-1 \leq \phi \leq 1$ are obtainable. The LCF lives increased with the principal strain ratio range of $-1.0 \leq \phi \leq 0.5$, while they decreased in the range of $0.5 \leq \phi \leq 1$. In the tension-torsion LCF tests using the hollow cylinder specimens, the LCF lives increased with the principal strain ratio range of $-1.0 \leq \phi \leq -0.5$ as shown in Fig. 5. The trend of the tension-torsion tests using hollow cylinder specimens in Fig. 5 well agrees with the results shown in Fig. 6 using cruciform specimens in the principal strain ratio range of $-1.0 \leq \phi \leq -0.5$.

Figure 7a, b correlate the tension-torsion and biaxial tension-compression LCF lives with Mises strain range and maximum principal strain range. These strain parameters give a large scatter of the data depending on the principal strain ratio for both types of the specimens. Mises strain range underestimates most of the lives by a factor of 200 at maximum, Fig. 7a. Maximum principal strain range gives almost the same results as Mises strain range but the degree of the underestimation becomes somewhat larger.

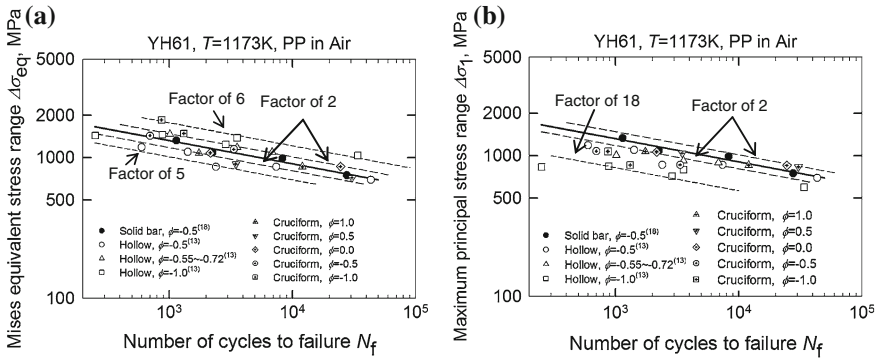

Fig. 8 Correlation of multiaxial LCF lives of hollow cylinder and cruciform specimens with Mises stress and maximum principal stress. **a** Mises strain range. **b** Maximum principal strain range

Figure 8a, b correlate the multiaxial LCF lives in the two types of tests with Mises stress and maximum principal stress. The correlation of the LCF lives with the stress parameters are quite improved from that with the strain parameters shown in Fig. 7. Mises stress range correlates most of the lives within a factor of 2 although it has a trend to give an unconservative estimate for the $\phi = -0.5$ data of hollow cylinder specimens and conversely a conservative estimate for $\phi = -1.0$ data. Maximum principal stress underestimates most of the lives more than a factor of 2 and some of the data locate outside a factor of 18. The results in Fig. 8 clearly indicate that the multiaxial LCF lives in the principal strain ratio range of $-1.0 \leq \phi \leq 1.0$ are estimatable from the uniaxial push-pull LCF lives using Mises stress.

4 Conclusions

(1) Tension-torsion LCF lives using hollow cylinder specimens increased with principal strain ratio range of $-1.0 \leq \phi \leq -0.5$. Biaxial tension-compression LCF lives using cruciform specimens increased with the principal strain ratio range of $-1.0 \leq \phi \leq 0.5$ but decreased in the range of $0.5 \leq \phi \leq 1.0$. The results using the hollow cylinder specimens agreed with those using the cruciform specimens.

(2) Mises strain and maximum principal strain ranges gave a lager scatter in the correlation of tension-torsion and biaxial tension-compression LCF lives depending on the principal strain ratio.

(3) Mises stress and maximum principal stress correlated the multiaxial LCF lives of the two types of the specimens mostly within a factor of two scatter and Mises stress gave the better correlation than maximum principal stress. The successful correlation of multiaxial LCF lives with Mises stress indicated that multiaxial LCF lives in a full range of the principal strain ratio are estimatable by using Mises stress range based on the LCF lives in uniaxial push-pull tests.

References

1. Fu, S.H., Dong, J.X., Zhang, M.C., Xie, X.S.: Mater. Sci. Eng. A **499**, 215–220 (2009)
2. Harada, H.: Ni-base superalloys and new materials: present status and possibilities in future. J. Gas Turbine Soc, Japan **28**, 14–20 (2000)
3. MacKay, R.A., Maier, R.D.: The influence of orientation on the stress rupture properties of nickel-base superalloy single crystal. Metall. Trans. **A13**, 1747–1754 (1982)
4. Hopgood, A.A., Martin, J.W.: The creep behavior of a Nickel-based single-crystal superalloy. Mater. Sci. Eng. **82**, 27–36 (1986)
5. Ghosh, R.N., Curtis, R.V., McLean, M.: Creep deformation of single crystal superalloys-modelling the crystallographic anisotropy. Acta Metall. Mater. **38**, 1977–1992 (1990)
6. Gabb, T.P., Gayda, J., Miner, R.V.: Orientation and temperature dependence of some mechanical properties of the single-crystal nickel-base superalloy rene N4: Part II. Low Cycle Fatigue Behav. Metall. Trans. **17A**, 497–505 (1986)
7. Martinez, J.M., Martin, A., Affildt, E.E., Bennett, A., Fuentes, M.: High temperature fatigue in single crystal superalloys. Fatigue Frac. Eng. Mater. Struct. **20**, 771–788 (1997)
8. Sakaguchi, M., Takashima, H., Hayashi, H., Okazaki, M.: γ/γ' Microstructural changes induced by monotonic and cyclic loadings in a single crystal Ni-base superalloys. J. Eng. Mater. Tech. **56**, 121–128 (2007)
9. Tada, N., Ohtani, R., Wada, A.: Mechanism of crack initiation induced by oxide-layer cracking in high temperature fatigue of the nickel base single crystal superalloy CMSX-2. J. Eng. Mater. Tech. **52**, 132–138 (2003)
10. Matsuda, N., Ichikawa, K., Fukuda, Y., Yoshinari, S., Toriya, H.: Evaluation of fatigue-creep interaction life using total strain energy criterion for superalloys and application for life evaluation of air cooled-blade of gas turbine. J. Gas Turbine Soc. Japan **23**, 84–91 (1995)
11. Meric, L., Cailletaud, G.: Single crystal modelling for structural calculations: Part2-Finite element implementation. Trans. ASME J. Eng. Mater. Tech. **113**, 171–182 (1991)
12. Kanda, M., Sakane, M., Ohnami, M., Hasebe, T.: High temperature multiaxial low cycle fatigue of CMSX-2 Ni-base single crystal superalloy. Trans. ASME J. Eng. Mater. Tech. **119**, 153–160 (1997)
13. Yorikawa, M., Matsuda, N., Sakane, M., Isobe, N., Tsuruki, M., Yoshinari, A.: Multiaxial low cycle fatigue of nickel base single crystal superalloy. J. Soc. Mater. Sci. Japan **58**, 149–154 (2009)
14. Hiyoshi, N., Sakane, M.: Tension-torsion multiaxial creep-fatigue for CMSX-2 nickel base single crystal superalloy. J. Soc. Mater. Sci. Japan **50**, 137–143 (2001)
15. Tsuruki, M., Matsuda, N., Sakane, M., Ohata, Y., Isobe, N., Yoshinari, A., Yorikawa, M., Masuno, K.: Development of inelastic analysis for Ni base single crystal superalloy under multiaxial stress states. J. Soc. Mater. Sci. Japan **60**, 94–101 (2011)
16. Itoh, T., Sakane, M., Ohnami, M.: High temperature multiaxial low cycle fatigue of cruciform specimen. Trans. ASME J. Eng. Mater. Tech. **116**, 90–98 (1994)

Mechanics of Materials for Microelectronic Components and Packages

Vadim V. Silberschmidt

Abstract Modern microelectronic packages are multi-material structures containing miniaturised components with dimensions in a micrometre range. This, together with their specific in-service conditions, defines main features of realisation of deformation processes in them. The latter need special approaches and techniques both in characterisation and modelling. The chapter deals with some examples of materials used in microelectronic components and packages, namely, lead-free and indium solders. The former is used in many microelectronic devices while the latter is employed predominantly in low-temperature applications. Respective features and deformation mechanisms are presented together with discussion of their implementation in numerical (finite-element) modelling.

1 Introduction

Microelectronic devices have become an important part of nearly all the aspects of our life; they surround us everywhere. The main drive in their development for many years was miniaturisation in order, on the one hand, to enhance their performance and, on the other hand, to decrease their manufacturing costs. As a result of miniaturisation characteristic dimensions of components in microelectronic packages are now in a micrometre range, so that solder bumps contain only a few grains. This makes a use of macroscopic parameters as well as models at best questionable and should be considered in simulation strategies.

The main regime of loading for microelectronic devices is thermal cycling that is defined by changes in external temperature and/or powering of devices. The former results in a predominantly spatially uniform temperature distribution while the latter

V. V. Silberschmidt (✉)
Wolfson School of Mechanical and Manufacturing Engineering, Loughborough University, Ashby Road, Loughborough, Leics LE11 3TU, UK
e-mail: V.Silberschmidt@lboro.ac.uk

H. Altenbach and S. Kruch (eds.), *Advanced Materials Modelling for Structures*, Advanced Structured Materials 19, DOI: 10.1007/978-3-642-35167-9_28,

can cause thermal gradients even in small-sized components [1, 2]. The mismatch in thermo-mechanical properties of constituent materials, especially in magnitude of their coefficients of thermal extension, is the source of thermal stresses and/or strains that can cause accumulation of irreversible deformation and failure of the component at some stage of its loading history. Thermal fatigue can take a form of creep-fatigue since many traditional solder materials are specifically chosen for their low melting point, moving their operational conditions into the area of high homologous temperatures. Indium, used as a solder for low-temperature microelectronics, is prone to creep even at low homologous temperatures [3].

A presence of interfaces between dissimilar materials in the package is another important feature in assessment of performance and reliability of microelectronic packages. Two major points should be considered: (i) stress concentration at the edges of interfaces that in many cases act as loci for the onset of fracture process and (ii) processes at interfaces initiated by manufacturing and affected by post-manufacturing storage and/or service. The latter are not limited to some manufacturing defects of areas of decohesion but also comprises initiation and growth of intermetallic compounds (IMCs). IMCs have non-trivial spatio-thermal realisation [4, 5] and are affected by manufacturing parameters [6–9]. They are much more brittle, and in small solder joints and/or after long aging can occupy a significant part of the joint making it a composite structure that should be adequately modelled. This topic is outside the scope of the current paper and would not be treated below.

Apart of the factors mentioned above, even at such small a length scale the shape and dimensions of constituents in multi-material packages are as important as for macroscopic structures and should be considered when dealing with specific systems. This paper describes effects of main mentioned factors on deformation processes in electronic devices. Obviously, it is impossible to cover such a vast field within a single work hence the discussion is limited to behaviour of solder joints in multi-material packages, covering arrays of bumps in flip-chip joints as well as surface-mount devices. Two types of solders—lead-free and indium—are considered: lead-free solder for both cases, and indium only for the former one.

2 Joints and Materials

Modern microelectronic devices employ various types of joining its components. In this chapter two main types will be considered: flip chip connection, consisting of many joints, and surface mounting (see Fig. 1). Both schemes can use the same type of a solder material. As immediately apparent from these schematics, even in the case of a post-manufacturing stress-free state, the components are prone to thermal stresses and strains due to the difference in their coefficients of thermal expansion. Since solders are much softer than most of other components in packages (i.e. with lower values of the Young's modulus and yield points), their deformation will be largest, and, as a result, they will be exposed to large-amplitude thermal fatigue and, possibly, to creep-fatigue as well.

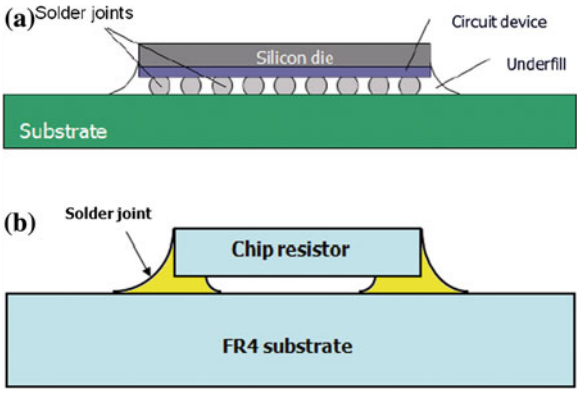

Fig. 1 Schematics of flip chip connection (**a**) and surface mounting (**b**)

But before dealing with material-specific response of the packages some important features should also be considered.

2.1 Structural Features

Though being at a scale of tens of microns, components of microelectronic devices can demonstrate 'architecture'-related features. Their response is by no means spatially uniform even when the devices are exposed to uniformly distributed temperatures. The factors such as the effect of the shape and stress concentrators can play a significant part at this scale as well. For instance, consider the case of the eutectic Sn3.5Ag solder connecting two Cu pads with fixed distance between two pads and diameters of pad/joint interfaces (80 μm in each case). For the three possible shapes of joints, varying in the diameter of their middle section (Fig. 2), different distributions of stresses and sizes of coarsened Ag_3Sn particles, affecting the softening behaviour under purely thermal cycling, were found [10]. For instance, the shape with the smallest diameter demonstrates not only the shift of the areas with the highest coarsening rate away from the edges of interfaces, but also a formation of another one just in the centre of the joint.

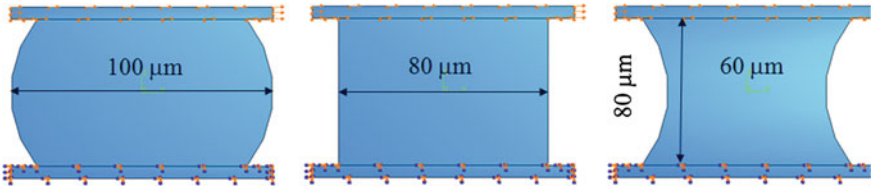

Fig. 2 Shapes of solder joints with different diameters for the same distance between pads in flip chip connection

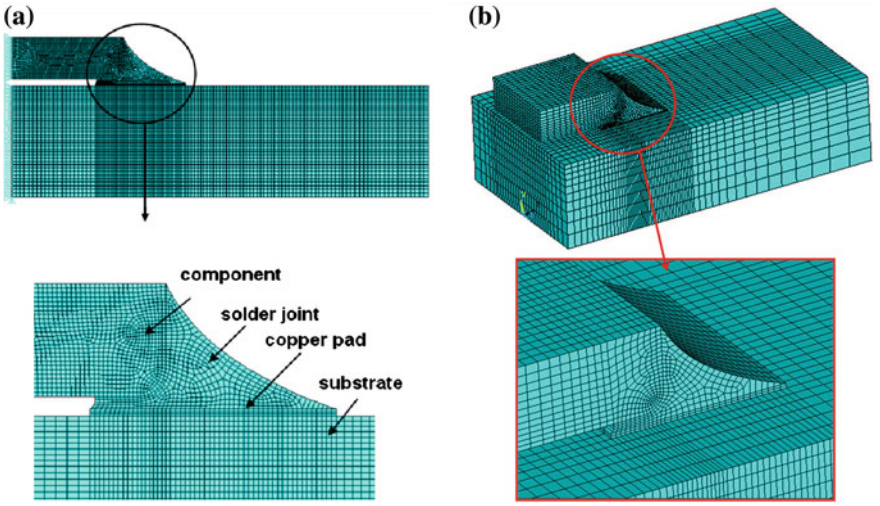

Fig. 3 Two-dimensional (**a**) and three-dimensional (**b**) models of surface mount assembly

This example demonstrates a need for careful introduction of the geometric features even for rather small elements of microelectronic packages in order to capture main deformation and/or fracture mechanisms. In some cases simplifications, e.g. a decrease in problem's dimensional can be considered, as it is the case in the large-scale multi-component structures. For instance, solder joints in surface mount assemblies can take a rather non-trivial shape (see Fig. 3). Still, a comparison of full three-dimensional simulations with two-dimensional ones allowed the use of the latter. Both the maximum temperature excursions and the maximum shear stresses were observed in the same location in both formulations, and the distribution patterns were similar [1].

2.2 Intrinsic Spatial Non-Uniformity

Still, specific structural features (e.g. shape), discussed above, are automatically captured in a (detailed-enough) finite-element model. Another feature—a spatially non-uniform distribution of temperatures—should be taken care of explicitly, and many works disregard it. It is based on a misconception that due to minuscule dimensions of (mainly well-conducting) components the temperature in all parts of the package is the same. Experiments prove that it is not the case (Fig. 4).

Powering of microelectronic devices can cause spatially non-uniform distributions of temperature [1]. Direct measurements with a high-precision infrared camera demonstrate differences of several degrees (Fig. 4). Considering the small scale of the base—several millimetres—the resulting magnitudes reach to 10^3–10^4 K/m, and should be accounted for in the analysis.

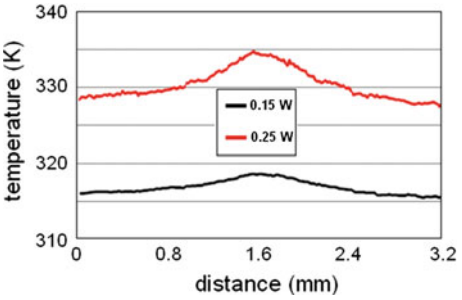

Fig. 4 Temperature distribution over chip resistor for two levels of power (The maximum rated power of operation is 0.25 W)

2.3 Material Properties at Microscale

Another important problem is determining respective material properties to be employed in finite-element simulations of microelectronic devices. The use of properties obtained at the macro-scale for bulk specimens is, in many cases, a poor approximation of reality. Hence, a special emphasis is on obtaining mechanical properties at the micro-scale. For soft solders, there is an additional challenge linked to their gripping. As a result, a solder is usually attached to copper plates (Fig. 5a), which are much stiffer.

But even in this case of a relatively simple geometry of the tested solder its stress state under conditions of uniform tension along the longitudinal direction of the specimen is rather non-uniform. Thus, loading of such a specimen will produce the

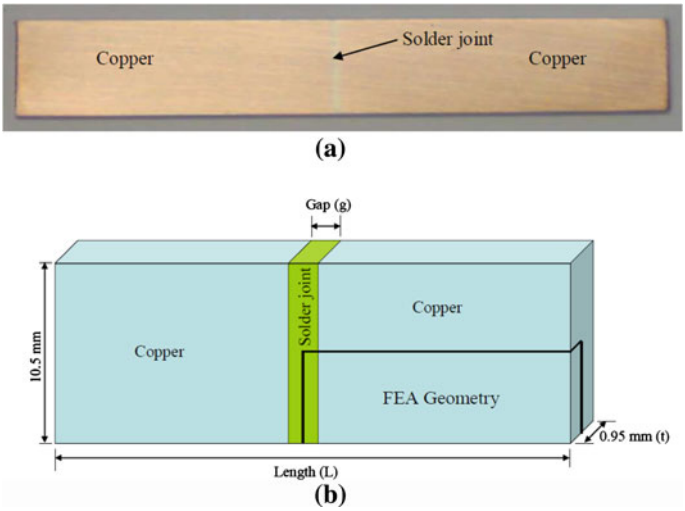

Fig. 5 **a** Specimen with solder joint; **b** geometry of specimen with solder joint and its octant used in FE analysis (both gap and length can vary)

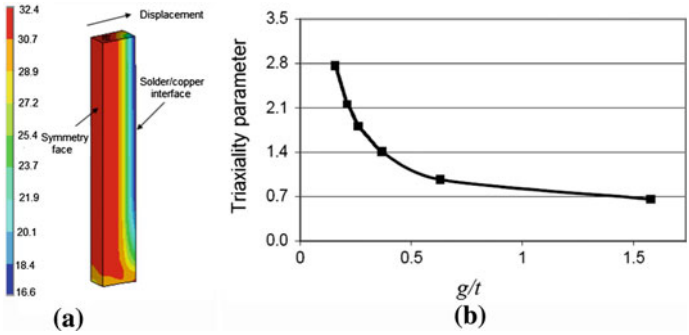

Fig. 6 **a** Distribution of equivalent stresses in solder joint with 1 mm gap length. **b** Effect of solder shape on triaxiality factor

response not of a studied material but rather of a structure. This presupposes a use of supporting FE simulations (see Fig. 5b) to extract the material's data from the 'structural' response. The results of the simulations (Fig. 6a) vividly demonstrate non-uniformity of the stress distribution. To quantify the effect of the solder's size, a triaxiality parameter is introduced as the ratio of volume averages (for the solder part of the specimen) of the hydrostatic stress and von Mises (equivalent) stress σ_e:

$$R = \frac{\sigma_h}{\sigma_e}. \tag{1}$$

Apparently, for a given thickness of the entire specimen, a decrease in the characteristic size of the solder joint (its gap length) will cause a significant increase in triaxiality of the stress state, affecting the solder's response to the applied load.

Additionally, with decrease in dimensions polycrystallinity starts playing a more prominent part since fewer grains will occupy the solder—down to 3–5 for a SAC solder with thickness of 100 μm [11]. Obviously, in this case different modelling approaches are necessary, as discussed below.

3 Numerical Models and Constitutive Equations

A discussed interaction between structural ('architecture') and material features in microelectronic packages needs analysis at least at two different scale levels: of the entire device and of its critical component. The former is used to obtain a global response of all the elements of the device (albeit, usually, with a coarser mesh and simplified mechanical models of its parts) in order to obtain boundary conditions for the lower-scale simulations. Such mapping allows a significantly finer meshes and/or more complex material formulations for the modelled component.

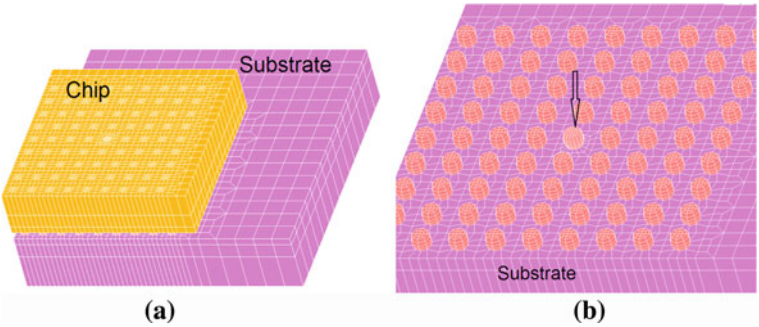

Fig. 7 **a** Model of one quarter of package. **b** Substrate and solder bumps (chip removed; *arrow* indicates solder with finer mesh)

One of the obvious examples is a use of a quarter or an octant of the flip-chip interconnection (based on its symmetry) in three-dimensional finite-element simulations. But even this approach for a case of a square grid array does not allow sufficient resolution of a single solder bump. Hence, a general solution can be used to define, for instance, displacement fields at its interfaces with other components and use them in a single-bump model with a higher spatial resolution. An alternative to this two-stage approach was suggested in [11, 12]. In this approach, one of the solder bumps in a model of a quarter of a flip-chip (shown by an arrow in Fig. 7) was discretised with a finer mesh than all the other bumps.

Such an approach allows obtaining both a global response as well as a refined local one in a single run of simulations. This is possible thanks to a significant rigidity of a chip that prevents large global deformations in a case of purely thermal cyclic loading in a temperature range defined by the device's usability envelope (between 253 and 353 K in that case). The refined model, e.g. for a single bump loaded as a part of a package, provides an opportunity to assess not only the effect of different material formulations of various mechanisms, underpinning its deformational behaviour, but also to include directly some elements of its microstructure into consideration.

SnAgCu grains are composed predominantly of β-Sn that defines their mechanical behaviour. It has a body-centred tetragonal unit cell, with one side longer than two other sides, thus resulting in orientation-dependence of its properties. To study the effect of this structure, four different modelling schemes were used to model a solder bump in [11]: (i) macroscopically isotropic; (ii) single-crystal; (iii) bi-crystal and (iv) multi-crystal (two last cases are presented in Fig. 8).

Though the obtained results for the same loading history in terms of von Mises stress does not differ much for different formulations or different orientations for the same formulation (e.g. various orientations of a single grain in models (ii))—some 5 % for the maximum level, the differences in shear stresses due to different orientations are much larger (Fig. 9).

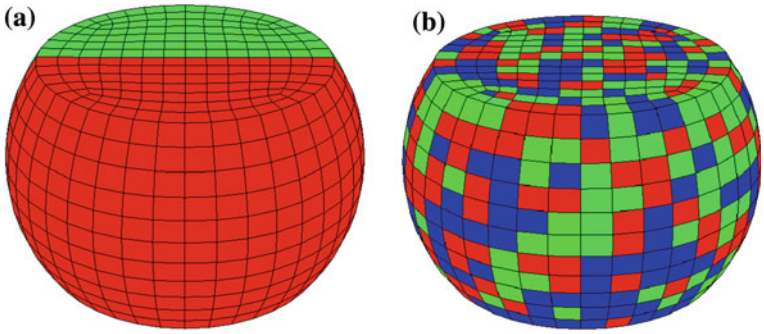

Fig. 8 Bi-crystal (**a**) and multi-crystal (**b**) models of solder joints (different colours correspond to different orientations of BCT unit cells; only orientations along three principal axes of co-ordinate systems are used)

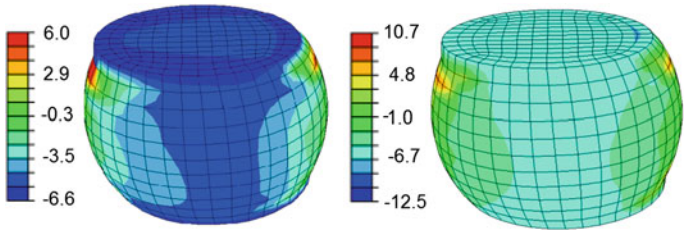

Fig. 9 Distributions of out-of-plane shear stresses (in MPa) for two cases of orientation of crystalline lattice along two different orthogonal orientations in single-grain model of solder bump

3.1 Constitutive Equations

Apparently, each constituent material in a multi-material package should be described with its own set of constitutive equations. In many cases not all the constituents demonstrate a complex type of material performance within the usability envelope of the device. For instance, silicon and ceramics in many cases can be described in terms of elastic (albeit, anisotropic) behaviour. Solders, in contrast, demonstrate a thermo-elasto-visco-plastic behaviour in many cases thanks to their low melting point. This continuous description is, where necessary, expanded to incorporate additional deformational mechanisms, usually linked to crystalline plasticity. A discussion below is limited to solders only.

At the macroscopic (continuous) level, thermo-elasticity is dealt with using a traditional scheme—isotropic or anisotropic, depending mostly on the type of manufacturing process. Plasticity is usually described with a Johnson-Cook model, capable to account for effects of temperature and strain-rate sensitivity [13] that are prominent due to high homologous temperatures of traditional in-service conditions for solders. Description of creep contribution involves normally a hyperbolic sine equation:

$$\dot{\varepsilon_{ss}} = A[\mathrm{Sinh}(\alpha\sigma)]^n \exp\left(-\frac{Q}{RT}\right), \tag{2}$$

where A, α and n are material parameters, σ is the applied stress, Q is the activation energy. R is the gas constant and T is the absolute temperature. This form can need modification to incorporate effects of main deformation mechanisms, responsible for creep at different temperatures. This is especially important in case of low-temperature (cryogenic) application, where In is used as a solder (the coefficient of thermal expansion of indium also changes significantly in the temperature range characteristic for such applications) [3].

At the microscopic level, mechanism-specific constitutive relationships can be introduced to accommodate the effect of main mechanisms such as dislocation mobility, void diffusion etc. An example of such model descriptions for thermal cyclic loading of SnAgCu solder can be found, e.g. in [11, 12]. A benefit of numerical schemes incorporating such mechanisms (at a price of developing user-defined subroutines) is a possibility of quantification of the effects caused by single mechanisms that can be hardly achieved in tests where many mechanisms interact in a complex way.

4 Conclusions

Mechanics of materials for microelectronic devices is characterised, as have been shown, by additional levels of complexity. As in structural mechanics, it needs to incorporate a precise (and in many cases, especially of 3d integration, intricate) geometry of packages and interconnections together with non-trivial boundary conditions that in many cases include thermal exchanges with environment. The stage of introduction of material's properties should take consideration both of the characteristic length scale of material as well as manufacturing-induced anisotropy (and, in many cases—heterogeneity due to presence of IMCs, voids and interfaces). Most properties should be obtained not only for a specific length scale and realisation of manufacture, but also for a large range of temperatures and, in case of solders, various strain rates.

In many cases, especially when dealing with critical and post-critical behaviours (onset and development of damage and fracture), the macroscopic approach is not sufficient. It should be accomplished by two main features: (i) direct introduction of microstructure (its morphology and main features with specific mechanical properties) and (ii) an additional set of mechanism-specific constitutive equations. Numerical models for microelectronic packages should incorporate all the complicating factors mentioned above; some of them can be found in commercial software packages but some need development of subroutines. Realisation of statistical simulations based on such models in many cases should be fully three-dimensional and accommodate at least two interacting scale levels—of the entire device and of the critical component.

Acknowledgments The author is grateful to his current and former colleagues, Prof. Changqing Liu, Dr David Whalley, Dr Jicheng Gong, Dr Pradeep Hegde, Dr Hui Xu and Dr Natalie Cheng for their contribution to this research.

References

1. Hegde, P.: Mechanical behaviour and reliability of Sn3.8Ag0.7Cu solder for a surface mount assembly. Ph.D. Thesis, Loughborough University, UK (2009)
2. Hegde, P., Ochana, A.R., Whalley, D.C., Silberschmidt, V.V.: Finite element analysis of lead-free surface mount devices. Comput. Mater. Sci. **43**, 12–220 (2008)
3. Cheng, X.: A study on indium joints for low-temperature microelectronics interconnections. Ph.D. Thesis, Loughborough University, UK (2011)
4. Gong, J., Liu, C., Conway, P.P., Silberschmidt, V.V.: Evolution of CuSn intermetallics between molten SnAgCu solder and Cu substrate. Acta Mater. **56**, 4291–4297 (2008)
5. Gong, J., Liu, C., Conway, P.P., Silberschmidt, V.V.: Initial formation of CuSn intermetallic compounds between molten SnAgCu solder and Cu substrate. Scripta Mater. **60**, 333–335 (2009)
6. Xu, H., Liu, C., Silberschmidt, V.V., Chen, Z.: Growth of intermetallic compounds in thermosonic copper wire bonding on aluminum metallization. J. Electron. Mater. **39**, 124–131 (2010)
7. Xu, H., Liu, C., Silberschmidt, V.V., Pramana, S.S., White, T.J., Chen, Z., Acoff, V.L.: Behavior of aluminum oxide, intermetallics and voids in Cu-Al wire bonds. Acta Mater. **59**, 5661–5673 (2011)
8. Xu, H., Liu, C., Silberschmidt, V.V., Pramana, S.S., White, T.J., Chen, Z., Acoff, V.L.: Intermetallic phase transformations in Au-Al wire bonds. Intermetallics **19**, 1808–1816 (2011)
9. Xu, H., Acoff, V.L., Liu, C., Silberschmidt, V.V., Chen, Z.: Facilitating intermetallic formation in wire bonding by applying a pre-ultrasonic energy. Microelectron. Eng. **88**, 3155–3157 (2011)
10. Gong, J., Liu, C., Conway, P.P., Silberschmidt, V.V.: Modelling of Ag3Sn coarsening and its effect on creep of Sn-Ag eutectics. Mater. Sci. Eng. A **427**, 60–68 (2006)
11. Gong, J.: Microstructural feature and mechanical behaviour of lead-free solders for microelectronic packaging. Ph.D. Thesis, Loughborough University, UK (2007)
12. Gong, J., Liu, C., Conway, P.P., Silberschmidt, V.V.: Mesomechanical modelling of SnAgCu solder joints in flip chip. Comput. Mater. Sci. **43**, 199–211 (2008)
13. Johnson, G.R., Cook, W.H.: Fracture characteristics of three metals subjected to various strains, strain rates, temperatures and pressures. Eng. Fract. Mech. **21**, 31–48 (1985)

Constitutive Models for the Description of Creep and Plasticity of Cast and Wrought Mg-Al and Mg-Zn Alloys

Stefano Spigarelli, Mohamad El Mehtedi and A. Di Salvia

Abstract Investigations on the microstructural aspects of creep in Mg-Al alloys resulted in the development of a constitutive model, describing the strain rate dependence on applied stress and temperature. The model was used to describe the behaviour of the single-phase AZ31 alloy, as well as of the more complex materials. These analyses demonstrated that the behaviour of hcp Mg-Al alloys follows, in general terms, the same well known scheme typical of fcc Al-Mg alloys, also in respect to the existence of two regimes, the first characterized by an $n = 3$ stress exponent, and the second described by the modified form of the Garofalo equation. A low stress regime dominated by grain boundary sliding was also observed in fine-grained alloys. A similar approach was used to analyse creep and plasticity of Mg-Zn alloys.

1 Introduction: The Constitutive Model

The creep model here presented is based on two traditional constitutive equations, i.e. the Garofalo relationship

$$\dot{\varepsilon}_d = A\,\{\sinh\,[\alpha(\sigma/G)]\}^{\mathrm{n}}\exp(-Q/RT) \tag{1}$$

and the Norton equation

$$\dot{\varepsilon}_d = A'(\sigma/G)^n\exp(-Q/RT) \tag{2}$$

S. Spigarelli (✉) · M. El Mehtedi · A. Di Salvia
DIISM, Università Politecnica delle Marche, via Brecce Bianche, 60131 Ancona, Italy
e-mail: s.spigarelli@univpm.it

M. El Mehtedi
e-mail: elmehtedi@univpm.it

H. Altenbach and S. Kruch (eds.), *Advanced Materials Modelling for Structures*,
Advanced Structured Materials 19, DOI: 10.1007/978-3-642-35167-9_29,

where $\dot{\varepsilon}_d$ is the minimum creep rate (or the testing strain rate in case of constant strain rate tests) associated with dislocation motion, σ is the applied stress, T is the absolute temperature, n is the stress exponent, α, A and A' are material parameters, Q is the creep activation energy, G is the shear modulus and R is the gas constant. While Eq. 2 is valid in the low strain rate/high temperature regimes typical of creep, Eq. 1 is more general, and can be used also above the power-law breakdown which usually characterizes the experiments carried out in the intermediate temperature regime (100–150 °C in the case of Magnesium alloys). Equation (1) reduces to Eq. (2) when the applied stress is low.

The model takes into account the class A behaviour [1] observed in Mg alloys [2], i.e. the existence of two different creep regimes: (i) a low strain-rate regime, with $n = 3$ stress exponent, typical of alloys where deformation is controlled by viscous glide of dislocations in an atmosphere of solute atoms; (ii) a high strain rate regime, where creep is climb controlled, and $n = 5$. In addition, the role of grain boundary sliding is also quantified. Each regime will be described separately in the following.

In the high-strain rate regime, creep is controlled by climb, $n = 5$, Q is equivalent to the activation energy for lattice self diffusion in Mg (Q_l); in many cases, the creep experiments were carried out at relatively low temperature (100–150 °C), and, as a result, most of the data lie above the power-law breakdown. Thus, the model is based on the use of Eq. (1) [3], properly modified to take into account the effects of chemical composition and of the grain size [4]. Major alloying elements considered in the present study are Al and Zn in Mg-Al and Mg-Zn alloys respectively. These alloying elements play two major roles, namely: (i) a solid solution strengthening effect; (ii) a particle strengthening effect in those cases where precipitation of secondary phase particles occurs. The particle-strengthening effect has been neglected in this study, which considers data obtained above 200 °C, where particle coarsening or even dissolution occur.

The most obvious effect of the elements in solid solution is to reduce the strain rate, for a given stress, even in the climb-controlled creep regime. In this respect the behaviour of the Mg-Al alloys is formally similar to that of the materials belonging to the Al-Mg system [1]. The stress exponent in climb-controlled creep remains constant, but the strain rate versus applied stress curve shifts toward lower values of the strain rate as the content of elements in solid solution increases. This behaviour can be modelled by supposing that either A or α change with the content of element in solid solution. Preliminary studies on Al-alloys [5, 6] seem to suggest that α is particularly sensitive to variations in chemical composition. The analysis of the data obtained by Sato and co-workers for Mg-Al [7] (Fig. 1a) and of a collection of literature results for Mg-Zn (see [8] for a detailed description) thus gave

$$\alpha = 69.6/c_{Al}^{0.37} \tag{3}$$

and

$$\alpha = 85/c_{Zn}^{0.3} \tag{4}$$

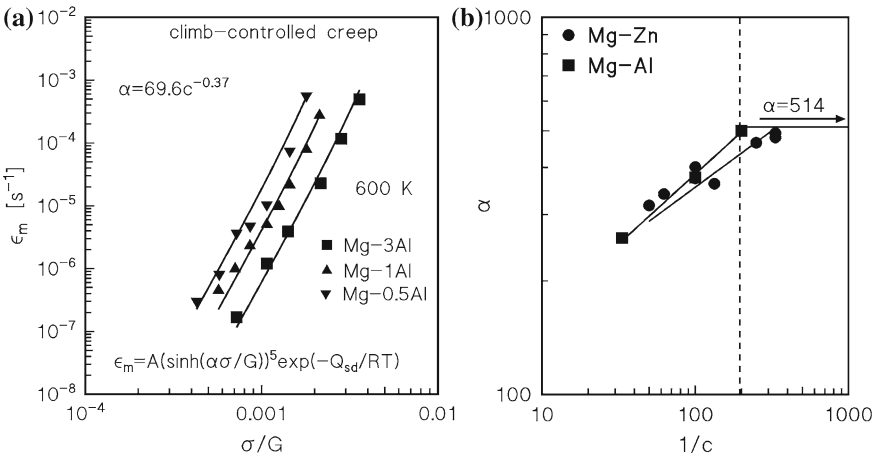

Fig. 1 **a** Strain rate versus stress for Mg-Al coarse-grained dilute alloys tested at high temperature [7] (the grain size was 170 μm); **b** variation of α with the concentration of the major alloying element (Al or Zn) in solid solution [8]

where c_{Al} and c_{Zn} were the concentration of Al and Zn in solid solution (Fig. 1b).

The grain size effect on the dislocation-creep properties of the AZ31 magnesium alloy has been investigated by comparing data obtained by testing materials of similar chemical compositions but different initial microstructures [9–12]. The results of this analysis confirmed the presence of a weak but not negligible effect of the grain size in the climb-controlled regime. The Eq. (1) was thus modified as follows:

$$\dot{\varepsilon}_d = A(b/d)^p \{\sinh[\alpha(\sigma/G)]\}^5 \exp(-Q_l/RT) \tag{5}$$

where d is the grain size and b is the Burgers vector, with $p = 0.6$ [4]. The model Eq. 5 was successfully used to describe the high temperature response of an Mg-4Al-1Ca alloy [13, 14].

The existence of a low stress regime where the creep data can de described by a power law with $n = 3$ (see Ref. [2] for a review of the literature data), suggested that, in Mg-Al alloys, deformation could be controlled by viscous glide of dislocations in atmospheres of Al-solute atoms, a behaviour which is intrinsically similar to that of Al-Mg dilute alloys [1, 7]. Combination of the traditional models with the findings of several studies on AZ31 [2] led to an equation in the form:

$$\dot{\varepsilon}_d = A^*(c_{Al})^{-1}(b/d)^{p*}(\sigma/G)^3 \exp(-Q^*/RT) \tag{6}$$

which takes into account both the effects of the content of Al in solid solution and of the grain size. In this regime $p = 0.4$ and $Q^* = 101$ kJ/mol [2]. This value of the activation energy Q^*, which was calculated by interpolating data from both strain

rate changes (SRC) experiments and continuous tests, is substantially lower than the theoretical value, i.e. the activation energy for diffusion of Al in Mg (143 kJ/mol).

Strain rate changes (SRC) experiments [11, 12], which present the advantage of obtaining different data from a single experiment, with a limited grain growth, led some authors [12] to suggest that at sufficiently high temperature, grain boundary sliding (GBS) substantially contributes to the deformation of the sample. The resulting creep model equations should be thus rewritten in the form

$$\dot{\varepsilon} = \dot{\varepsilon}_{GBS} + \dot{\varepsilon}_{disl} = A_{GBS}\,(b/d)^{p'}\,(\sigma/G)^2 \exp(-Q_{GBS}/RT) + \dot{\varepsilon}_d \qquad (7)$$

where p' is 2 or 3, Q_{GBS} is equivalent to Q_l or to the activation energy or grain boundary diffusion (Q_{GB}), which, in Mg, is close to 92 kJ/mol [15], while the $\dot{\varepsilon}_d$ term assumes the form of Eq. (5) or (6). It can be here observed that the anomalously low Q^* value computed by interpolating constant stress, constant strain rate and SRC experiments, can be the result of the parallel actions of viscous glide (characterized by a value of the activation energy similar to that of self diffusion) and GBS.

2 Description of Creep Data for Mg-Al and Mg-Zn Alloys

This section analyses the accuracy of the model in describing the creep response of different Mg alloys. In all these cases the same A, A^* and A_{GBS} values were used.

2.1 The AZ31 Alloy

The AZ31 alloy contains a low amount of Al, and can be considered a single-phase material, since only limited precipitation of $Mg_{17}Al_{12}$ in form of coarse particles occurs during cooling from rolling or extrusion temperature (typical initial conditions for creep testing). Figure 2 plots the data obtained by del Valle et al. [12] by SRC and continuous experiments, and the model curves calculated by Eq. (7) with $c_{Al} = 2.2\,\%$ (at.). The values of the activation energies Q_l, Q^* and Q_{GBS} were the theoretical 135, 143 and 92 kJ/mol respectively. The agreement between the SCR data and the model curves is excellent, even though the only free parameters were the A, A^* and A_{GBS} constants. The deviation between the curves and the constant strain rate experiments, as clearly suggested by del Valle et al., can be attributed to the marked grain coarsening which occurs during the low-strain rate experiments, an effect that will be later discussed.

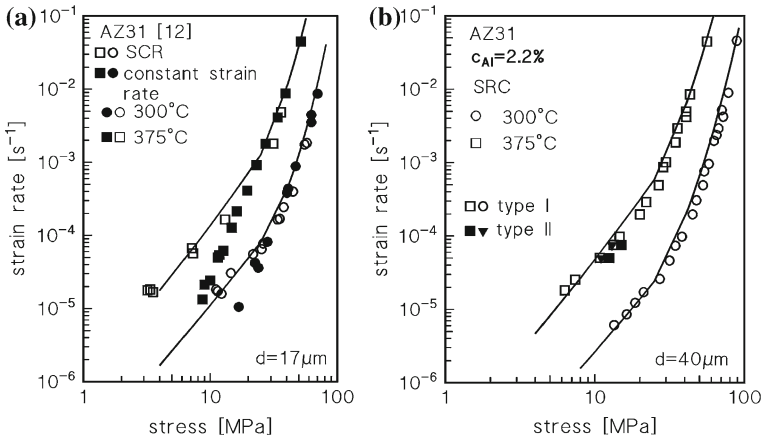

Fig. 2 Strain rate as a function of applied stress for SCR and constant strain rate tests [12]. Concentration of Al in solid solution in at.%

2.2 The AM60 and AZ61 Alloys

Recent investigations analysed the high temperature response of the AM60 [15] and AZ61 [16] alloys with fine grain sizes, tested by the SRC technique. A common feature of these investigations is the existence of a low-stress regime at temperatures above 300 °C, characterised by a stress exponent close to 2 (Fig. 3), an indication of the possible role of GBS as rate-controlling mechanism. The limited intergranular precipitation of $Mg_{17}Al_{12}$, in these cases, is thought to have a beneficial effect in retarding or even suppressing grain growth, thus maintaining the fine grain size which is a prerequisite for the occurrence of GBS [16]. The analysis of the data obtained by del Valle and Ruano [15] suggests that GBS assumes a significant role, and can be described with $p' \cong 2$ and $Q_{GBS} = Q_{GB}$. Figure 3 shows the model curves obtained by assuming that $c_{Al} = 3\,\%$, i.e. that a minor but non negligible fraction of Al is combined with Mg, to form the intermetallic precipitates which retard grain growth. The values of the different parameters were those calculated to obtain the plots in Fig. 2. The correlation between model curves and experimental data is in both cases very good.

2.3 The ZK60 Alloy

Only few data on the high temperature response of Mg-Zn alloys are available, and in most cases they apply to the ZK60 [17–19] (Fig. 4). In these alloys the existence of a regime of viscous-glide controlled deformation has been not unambiguously ascertained, being the amount of Zn in solid solution ($c_{Zn} \cong 0.023$) relatively low.

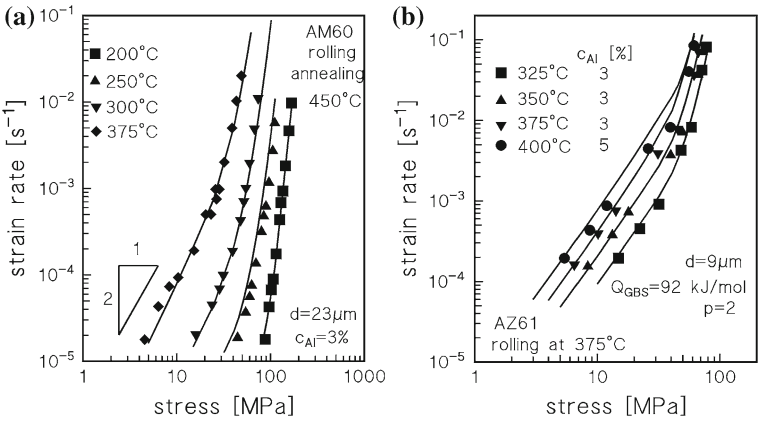

Fig. 3 Strain rate versus stress for an AM60 ($d = 23\,\mu$m) [15] (**a**) and an AZ61 ($d = 9\,\mu$m) [16] (**b**). All these data were obtained by the strain rate change technique (SRC)

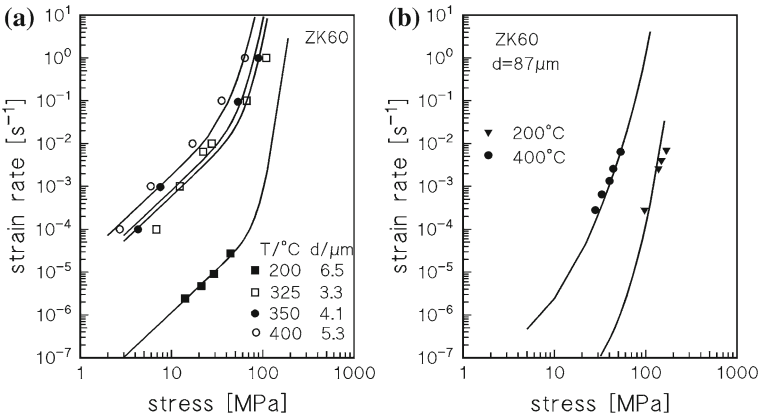

Fig. 4 Strain rate versus stress for ZK60 with different grain sizes: **a** data from [17]; **b** data from [18]

At temperatures above 200 °C, Zn is completely in solid solution; Zr acts as a grain refiner, and for this reason the ZK60 exhibits a fine grain size [20]. Again, Eq. (7) with the same values of the parameters was used. The simple substitution of the relevant grain size results in an excellent description of the experimental data. Figure 5 shows an additional dataset obtained by Watanabe et al. [21] by testing a ZK60 with ultra-fine grain sizes. All the data in the figure were obtained by using continuous tests under constant strain rate or constant load. The analysis of Fig. 5 confirms that the use of a p' exponent of 2 is more than adequate to quantify the grain size dependence of the strain rate at 200 °C.

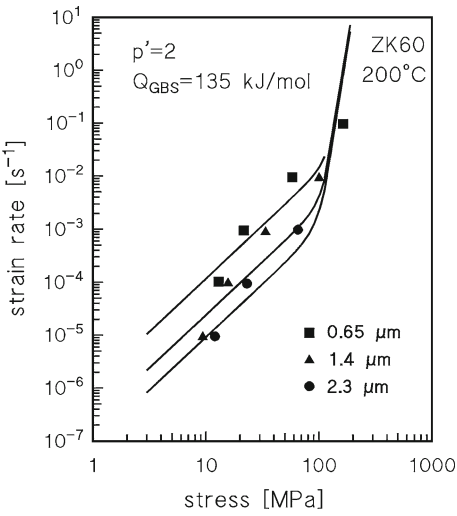

Fig. 5 Strain rate versus stress for ZK60 with different grain sizes at 200 °C

3 Effect of Grain Growth

The model Eq. (7), in combination with Eqs. (5) and (6), gives an excellent description of the SRC data obtained by different authors on different materials. Yet, two major features still need to be clarified: (i) the relevance of the $n = 3$ regime; viscous glide in many cases, in particular for fine-grained metals, is obscured by the concurring effect of GBS, which results in higher strain rates; (ii) the quantification of the effect of grain growth during continuous tests.

The first issue is analysed in Fig. 6a, which plots the data obtained by Kitazono et al. [9], by Kim et al. [16], and by Mukai et al. [22] by testing AZ31 alloys with coarse grain size ($d = 85$–$130\,\mu m$). The initial grain size was large enough to substantially reduce the potential effect of grain growth. The model Eq. (7) describes very well the experimental data; the figure also reports the transitions stresses from viscous glide to dislocation climb, and from GBS to viscous glide, i.e. the applied stress corresponding to $\dot{\varepsilon}_{GBS} = \dot{\varepsilon}_d$. It can be easily observed that viscous glide is rate controlling in a relatively large range of applied stresses. This observation in turns demonstrates that high temperature deformation is controlled by viscous glide of dislocations in all those cases in which a relatively coarse-grained alloy is tested in the low-stress regime.

The second issue, i.e. the effect of grain growth during continuous tests, is addressed in Fig. 6b. Del Valle et al. measured the grain growth during a test at 375 °C, under a strain rate of $5 \times 10^{-5}\,s^{-1}$ [12]. These data permit to estimate the growth law, i.e. the dependence of the grain size on testing time t, which assumed the form:

$$d^4 = d_0^4 + K \cdot t \tag{8}$$

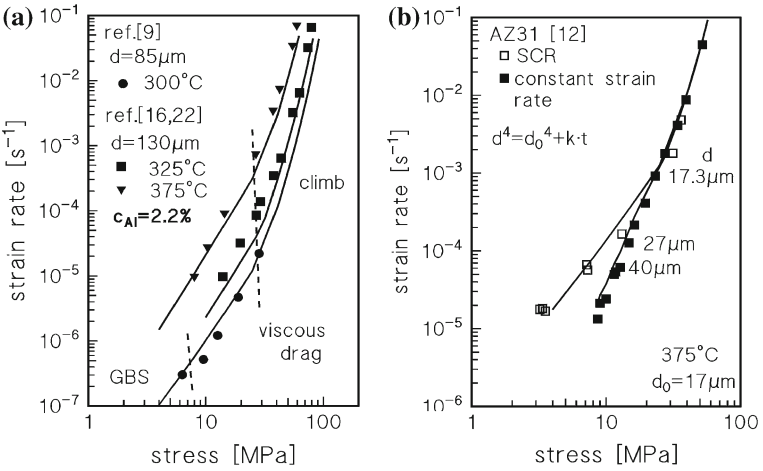

Fig. 6 **a** Strain rate versus stress for the creep experiments on coarse grained AZ31 [9, 16, 22], and model curve; **b** grain-growth corrected curve describing the AZ31 data obtained by continuous tests by del Valle et al. [12]. The figure also reports the value of the grain size in correspondence of the peak flow stress in some of the experimental conditions

where d_0 was the initial grain size (17 μm), and K a temperature-dependent constant. This relationship allows the estimation of the grain size in correspondence of the peak flow stress for the continuous curves carried out at this temperature. Substitution of the calculated d values into Eq. (7) gives the model curve illustrated in the figure. Again, the correlation is excellent; this simple analysis unambiguously confirms that the combination of constitutive Eqs. (5), (6) and (7) is able to describe, in a wide range of temperature and applied stresses, the high temperature behaviour of magnesium alloys, once the grain size instability is properly taken into account. The use of Eq. (7) also allows to quantify the grain growth occurring during a standard SCR test at 375 °C. A SRC experiment, in the form used by del Valle and co-workers and described in [12, 15], typically consists in an initial deformation under a high strain rate (10^{-3} s^{-1}), followed by a jump down to 10^{-5} s^{-1}. Subsequently, the strain rate is increased in successive jumps; at the end of the test, the grain size calculated by Eq. (7) increases from 17 to 18.4 μm, i.e. grain growth is almost negligible.

The above discussion demonstrates that a rationalization of the different experimental behaviour observed by testing Mg alloy is possible, once the different microstructural parameters (grain size and concentration of elements in solid solution) are considered and quantified. Moreover, a deformation mechanisms map can be drawn by combining the constitutive equations for the various mechanisms (Fig. 7). The figure is only a representative example, which was obtained for Mg-Al alloys at 300 °C.

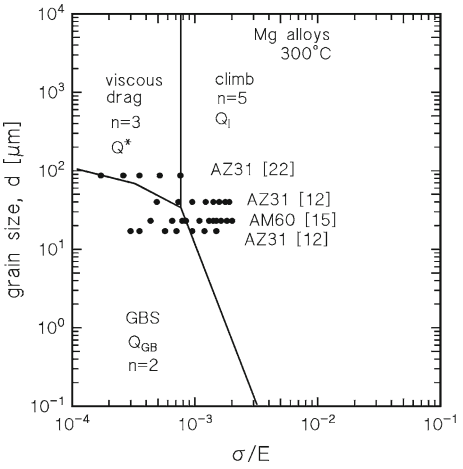

Fig. 7 Deformation mechanisms map for Mg-Al alloys at 300 °C by Eqs. (5)–(7)

4 Conclusions

The high temperature mechanical behaviour of Mg-Zn and Mg-Al alloys has been considered in the present study. The experimental data has been successfully described by a constitutive model which takes into account the different rate-controlling mechanisms, i.e. climb, viscous glide of dislocations and grain boundary sliding. The use of the theoretical values for the activation energy, i.e. the activation energy for self diffusion, for diffusion of Al in Mg, and for grain boundary diffusion, resulted in an excellent description of the data, provided that microstructural parameters, such as the grain size and the amount of elements in solid solution, are considered.

References

1. Yavari, P., Langdon, T.G.: An examination of the breakdown in creep by viscous glide in solid solution alloys at high stresses. Acta Metall. **30**, 2181–2196 (1982)
2. Spigarelli, S., El Mehtedi, M.: Creep as an extension of cold working: a unified approach to high temperature deformation of AZ31 magnesium alloy. Mater. Sci. Eng. **A527**, 5708–5714 (2010)
3. Spigarelli, S.: Constitutive equations in creep of Mg-Al alloys. Mater. Sci. Eng. **A492**, 153–160 (2008)
4. Spigarelli, S., et al.: Effect of grain size on high temperature deformation of AZ31 alloy. Mater. Sci. Eng. **A528**, 6819–6826 (2011)
5. Bardi, F., et al.: An analysis of hot deformation of an Al-Cu-Mg alloy produced by powder metallurgy. Mater. Sci. Eng. **A339**, 43–52 (2003)
6. Spigarelli, S., et al.: A study of the hot formability of an Al-Cu-Mg-Zr alloy. J. Mater. Sci. **38**, 81–88 (2003)

7. Sato, H., Oikawa, H.: Transition of creep characteristics of HCP Mg-Al solid solutions at 600–650 K. In: Brandon, D.G., et al. (eds) Strength of Metals and Alloys, pp. 463–470. Freund, London (1991)
8. Spigarelli, S., El Mehtedi, M.: Constitutive equations in creep of wrought Mg-Zn alloys. Mater. Sci. Eng. **A527**, 126–131 (2009)
9. Kitazono, K., et al.: Internal stress superplasticity in polycrystalline AZ31 magnesium alloy. Scripta Mater. **44**, 2695–2702 (2001)
10. Somekawa, H., et al.: Dislocation creep behavior in Mg-Al-Zn alloys. Mater. Sci. Eng. **A407**, 53–61 (2005)
11. Kim, H.-K., Kim, W.-J.: Creep behavior of AZ31 magnesium alloy in low temperature range between 423 K and 473 K. J. Mater. Sci. **42**, 6171–6176 (2007)
12. Del Valle, J.A., et al.: Deformation mechanisms responsible for the high ductility in a Mg AZ31 alloy analyzed by electron backscattered diffraction. Metall. Mater. Trans. **36A**, 1427–1438 (2005)
13. Milicka, K.: Creep threshold of a Mg-4Al-1Ca alloy. Kovove Mater. **46**, 323–329 (2008)
14. Spigarelli, S., El Mehtedi, M.: Microstructure-related equations for the constitutive analysis of creep in magnesium alloys. Scripta Mater. **61**, 729–733 (2009)
15. del Valle, J.A., Ruano, O.A.: Separate contribution of texture and grain size on the creep mechanisms in a fine-grained magnesium alloy. Acta Mater. **55**, 455–466 (2007)
16. Kim, W.J., et al.: Superplasticity in thin magnesium alloy sheets and deformation mechanisms maps for magnesium alloys at elevated temperatures. Acta Mater. **49**, 3337–3343 (2001)
17. Watanabe, H., Mukai, T.: Superplasticity in a ZK60 magnesium alloy at low temperature. Scripta Mater. **40**, 477–484 (1999)
18. Galiyev, A., et al.: Correlation of plastic deformation and dynamic recrystallization in magnesium alloy ZK60. Acta Mater. **49**, 1199–1207 (2001)
19. Spigarelli, S., et al.: Enhanced plasticity and creep in an extruded Mg-Zn-Zr alloy. Scripta Mater. **63**, 617–620 (2010)
20. Lee, Y.C., et al.: The role of solute in grain refinement of magnesium. Metall. Mater. Trans. **33A**, 2895–2906 (2000)
21. Watanabe, H., et al.: Realization of high-strain rate superplasticity at low temperatures in a Mg-Zn-Zr alloy. Mater. Sci. Eng. **A307**, 119–128 (2001)
22. Mukai, T., et al.: Experimental study of the mechanical properties at elevated temperatures in commercial Mg-Al-Zn alloys for superplastic forming. Key Eng. Mater. **171–174**, 337–342 (2000)

Deformation and Failure of Various Alloys Under Creep-Fatigue Loading and Their Modelling

Yukio Takahashi

Abstract Plant components often undergo the loading which have both aspects of fatigue and creep, by experiencing steady-state operation intermitted by repeated start-up/shut-downs and other transients. In such a case, material shows inelastic deformation and failure characteristics that are different from those observed under pure fatigue or pure creep conditions. In this paper, some recent progresses made in both deformation and failure modelling under such a circumstance are outlined. In the first part, an attempt to improve the capability of the inelastic constitutive model is described with an example on modified 9Cr-1Mo steel. In the second part, efforts made for improving the accuracy and reliability of failure prediction under creep-fatigue loading are described.

1 Introduction

When the components are used at high temperatures where time-dependent inelastic deformation, creep, cannot be ignored, failure due to its accumulation or interaction with fatigue should be considered. It is known that inelastic deformation is closely related with these phenomena in metallic materials which have high ductility so that the accurate estimation of both inelastic deformation and resulting damage is essential in order to precisely address the possibility of failure.

In general, inelastic deformation mainly controlled by dislocation movement is known to be sensitive to microstructure of material which changes with inelastic deformation itself as well as thermal effect at high temperature, causing substantial history-dependency even in the originally same materials. These observations prompted the development of "unified" constitutive models in which cyclic and creep deformations are treated as inelastic deformation in a unified way. This type of models

Y. Takahashi (✉)
Central Research Institute of Electric Power Industry, Tokyo, Japan
e-mail: yukio@criepi.denken.or.jp

H. Altenbach and S. Kruch (eds.), *Advanced Materials Modelling for Structures*,
Advanced Structured Materials 19, DOI: 10.1007/978-3-642-35167-9_30,

shows a larger advantage over the conventional "non-unified" approach treating plastic and creep deformation separately even with some ad-hoc rules representing their interaction, especially for the materials which show significant rate-dependency of tensile curve as this phenomenon itself is not easy to express by the latter. Modified 9Cr-1Mo steel widely used in recent fossil power plants and also considered as a promising candidate of structural materials in the future nuclear power plants is the case so that efforts have been made for the development of a unified model which can describe the behaviour of this steel [1–4] with a reasonably high accuracy. The latest model [5] which is able to describe deformation behaviour under more critical conditions including tertiary creep stage and its acceleration by cyclic loading will be described in the paper.

In addition to deformation analysis, choice of methods to estimate damage and resulting failure may also have a significant effect on the assessment of components, as they often supply very different values of damage and consequently failure lives. In order to find the most reliable approach to estimate creep damage under creep-fatigue loading, systematic study has been performed using the data on various alloys employed in high-temperature components in power generation plants [8]. An outline of the results obtained by this study will be described in a latter half of the paper.

2 Modelling of Inelastic Deformation Under Creep-Fatigue Interaction

2.1 Outline of Constitutive Model

Inelastic strain rate is governed by a complex law including history-dependency. It was assumed in our model to be a function of deviatoric stress tensor, s_{ij}, and back stress tensor, α_{ij}, as

$$\dot{\varepsilon}_{ij}^{in} = \left\{ \frac{3}{2} \frac{s_{ij} - \alpha_{ij}}{\sqrt{3(s_{kl} - \alpha_{kl})(s_{kl} - \alpha_{kl})/2}} + l\eta \frac{|\sigma_{kk}|^l}{\sigma_{kk}} \delta_{ij} \right\} \dot{p} \tag{1}$$

where $\dot{p}$ denotes the equivalent inelastic strain rate calculated by

$$\dot{p} = \left\langle \frac{\sqrt{3(s_{kl} - \alpha_{kl})(s_{kl} - \alpha_{kl})/2} + \eta \frac{|\sigma_{kk}|^{l+1}}{\sigma_{kk}} - Z}{D} \right\rangle^n \tag{2}$$

with Z being the drag stress increasing with decreasing inelastic strain rate for representing the dynamic aging effect observed in many materials by and large. Difference between tensile and compressive behaviours is generalized as the effect of mean stress and expressed by the term including the hydrostatic stress, σ_{kk} and

materials constants, l and η. D and n are additional material constants giving a flow property. In both equations, α_{ij} plays a dominant role, as a back stress tensor describing a kinematic nature of hardening. Variation of α_{ij} is assumed to be given by sum of several elements changing with the deviatric components of inelastic strain rate, $\dot{e}_{ij}^{in}$ as

$$\alpha_{ij} = \sum_{k=1}^{N} \left[\begin{array}{l} \varsigma_k \left\{ \frac{2}{3} r_k \dot{e}_{ij}^{in} - H(\bar{\alpha}^{(k)} - r_k) \left\langle \dot{e}_{ij}^{in} \frac{\alpha_{ij}^{(k)}}{r_k} - \mu \dot{p} \right\rangle \alpha_{ij}^{(k)} - \mu \alpha_{ij}^{(k)} \dot{p} \right\} \\ -\gamma_k (\bar{\alpha}^{(k)})^{m-1} \alpha_{ij}^{(k)} \end{array} \right] \tag{3}$$

according to the proposal by [6] and its modification [7] with an additional term representing static recovery for expressing continuous deformation observed at high-temperature. Here r_k represents the maximum value which the norm of each back stress component, $\bar{\alpha}^{(k)} = (3\alpha_{ij}^{(k)} \alpha_{ij}^{(k)}/2)^{0.5}$ can take. ς_k, μ and γ_k are constants related to hardening, dynamic recovery and static recovery, respectively. Cyclic hardening or softening can be described by changing the value of r_k with the cyclical change of inelastic strain from the initial value, r_k^0. Furthermore, in the latest development [5], acceleration of strain rate in constant-load tests observed as tertiary creep is able to be expressed by assuming that the rate of static recovery increases with the accumulation of inelastic strain and/or cyclic hardening/softening according to

$$\gamma_k = \gamma_k^0 \left\{ 1 + (\bar{\varepsilon}_{in}/\bar{\varepsilon}_0)^{\phi} (r_k^0/r_k)^{\varphi} \right\} \tag{4}$$

with the equivalent inelastic strain given by $\bar{\varepsilon}_{in} = \sqrt{2\varepsilon_{ij}^{in} \varepsilon_{ij}^{in}/3}$ and constants, $\bar{\varepsilon}_0$, ϕ and φ.

2.2 Comparison with Test Records on Modified 9Cr-1Mo Steel

Detailed modelling for Modified 9Cr-1Mo steel has been performed according to the above equations and other complimentary equations [5]. Examples of simulations by the model for several loading conditions are shown in Figs. 1, 2, 3 and 4 in comparison with the corresponding experimental data. In Fig. 1 comparing creep deformation under constant load, effectiveness of the present model can be clearly seen by a comparison with the result obtained by the old model which does not incorporate the change in static recovery rate through Eq. (4). Figure 2 then shows the capability of the model in terms of describing the effect of prior cyclic loading on creep deformation behaviour. It can be seen that the acceleration of creep deformation induced by cyclic softening is expressed properly and naturally. Applicability of the model to the conventional strain-controlled creep-fatigue loading condition can be also seen in Figs. 3 and 4 where predicted hysteresis loops and stress relaxation behaviours show a good agreement with the test data, although the mean stress

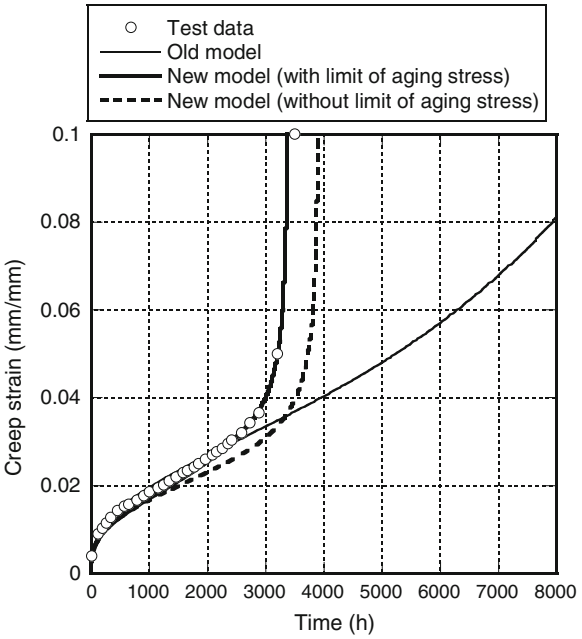

Fig. 1 Comparison of test data and simulations on creep curve (600C, 200 Mpa)

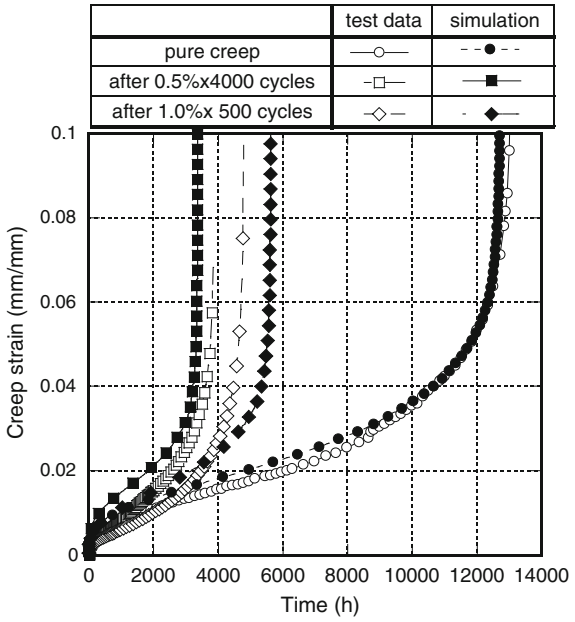

Fig. 2 Comparison of test data and simulations on creep curves with and without prior cyclic loading (600C, 180 Mpa)

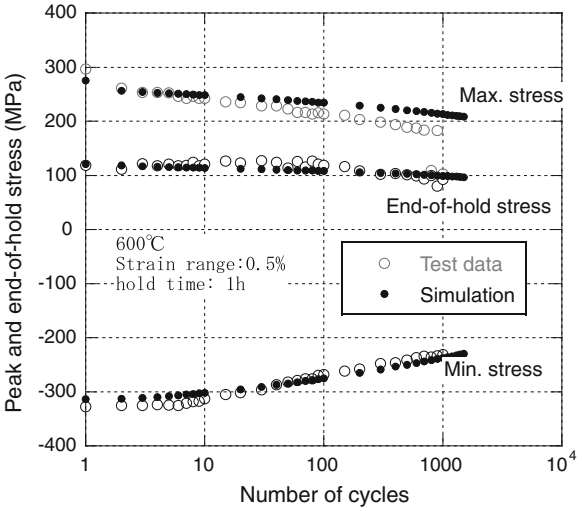

Fig. 3 Comparison of test data and simulation on the variation of peak and end-of-hold stress during creep-fatigue test

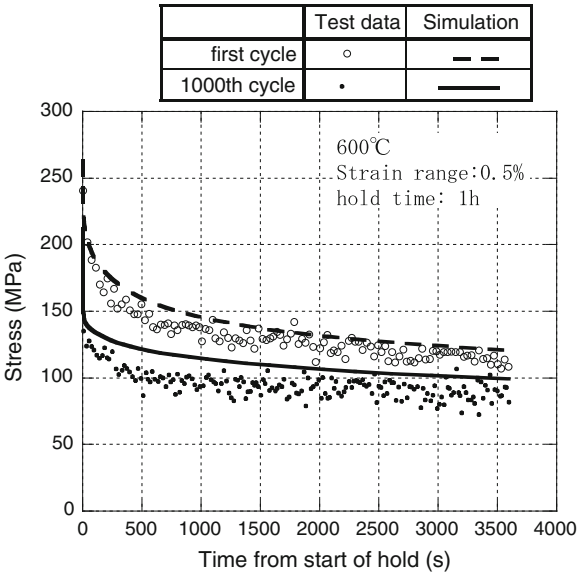

Fig. 4 Comparison of test data and simulation on the stress relaxation in creep-fatigue test

developing in the direction opposite to the strain hold side tends to be larger in the test than that in the simulation and a room for the improvement of the model seems to still exist in this regard.

3 Comparison of Creep Damage Models

3.1 Outline of Models

Tests for examining the material behaviour under creep-fatigue loading are usually performed under strain-control, as an extension of low-cycle fatigue tests. Strain is fixed for a certain period at a certain point on triangular waveform, usually at the tensile peak strain. Stress relaxes during this period with the accumulation of inelastic strain, causing some reduction in number of cycles to failure. The amount of life reduction cannot be explained only by the increase in inelastic strain range, suggesting the activation of different damage mechanism. The change in fracture morphology, typically from transgranular to intergranular, is often observed. These observations clearly suggest the need of introducing a parameter which is responsible for representing this type of damage, usually called "creep damage" in addition to the conventional fatigue damage.

In order to evaluate their characteristics in a systematic manner, four models for the calculation of creep damage have been applied to creep-fatigue tests carried out on various materials including ferritic and austenitic steels as well as superalloys [8]. They include the conventional approaches called time fraction and ductility exhaustion methods, respectively. The former regards the stress as a parameter governing creep damage and it is based on the assumption that the stress of the same value brings about an equal amount of creep damage both in creep and creep-fatigue conditions, in which creep damage per a hold time of t_H is simply estimated by

$$d_c = \int_0^{t_H} \frac{dt}{t_R(\sigma)} \tag{5}$$

where t_R denotes the time to rupture expected in the constant-load creep test conducted at the stress of σ. On the other hand, the following equation is used in the ductility exhaustion approach to calculate creep damage:

$$d_c = \int_0^{t_H} \frac{\dot{\varepsilon}_{in}}{\delta(\dot{\varepsilon}_{in})} dt \tag{6}$$

where δ denotes the rupture elongation in the creep test where the average creep strain rate is $\dot{\varepsilon}_{in}$.

Two additional approaches have also been applied in order to look for the possibility of improved estimation of damage. Both of them are based on the idea that creep damage in creep-fatigue condition without a gloss accumulation of inelastic strain should be evaluated only in terms of the effect of reducing ductility. In an earlier approach, creep damage was estimated as

$$d_c = \int_0^{t_H} \left(\frac{1}{\min\left[\delta(\dot{\varepsilon}_{in}), \delta_0\right]} - \frac{1}{\delta_0} \right) \dot{\varepsilon}_{in} dt \tag{7}$$

where δ_0 denotes the upper-bound rupture elongation under the absence of creep damage (elongation in short-term tensile tests). On the other hand, a more recent approach employs inelastic energy density instead of inelastic strain, as a parameter governing the accumulation of creep damage as

$$d_c = \int_0^{t_H} \left(\frac{1}{W_f(\dot{W}_{in})} - \frac{1}{W_{f0}} \right) \dot{W}_{in} dt \tag{8}$$

where W_f denotes the inelastic strain energy density at creep rupture when the inelastic energy is applied at the rate of $\dot{W}_{in}$ bounded by W_{f0} obtained by short-term tensile tests. It should be noted that the use of strain energy density, rather than inelastic strain, tends to give larger creep damage because of the consideration of the stress as well as inelastic strain rate.

3.2 Results of Evaluation on Many Materials

The above four procedures have been applied to many creep-fatigue tests performed on various alloys used in power generation and other high-temperature plants. Figures 5, 6, 7, and 8 plot the accumulated creep damage calculated by the four approaches against accumulated fatigue damage at failure obtained using inelastic strain range, constituting so call "interaction diagram". It should be noted that the

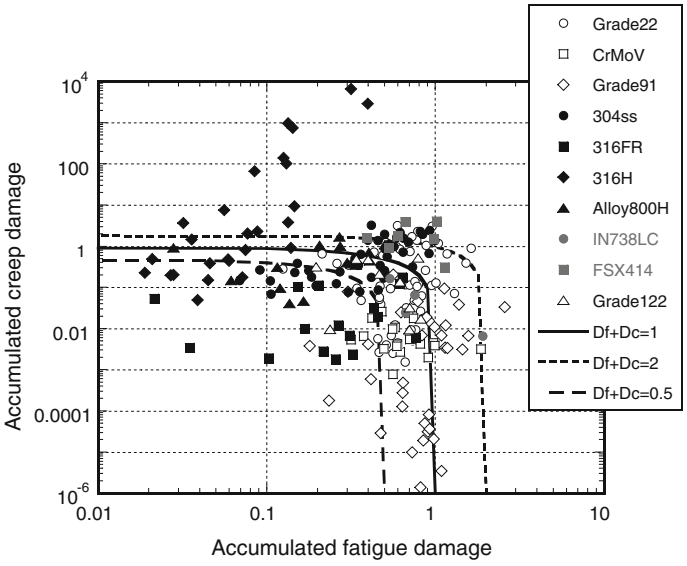

Fig. 5 Accumulated fatigue damage versus creep damage by time fraction approach

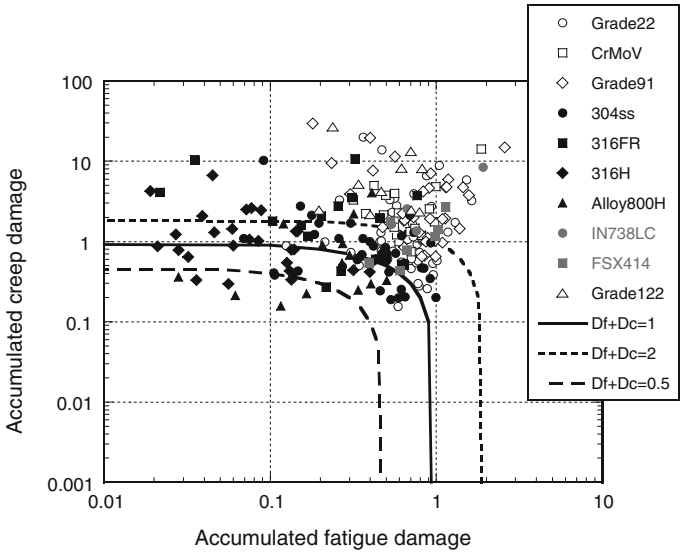

Fig. 6 Accumulated fatigue damage versus creep damage by ductility exhaustion approach

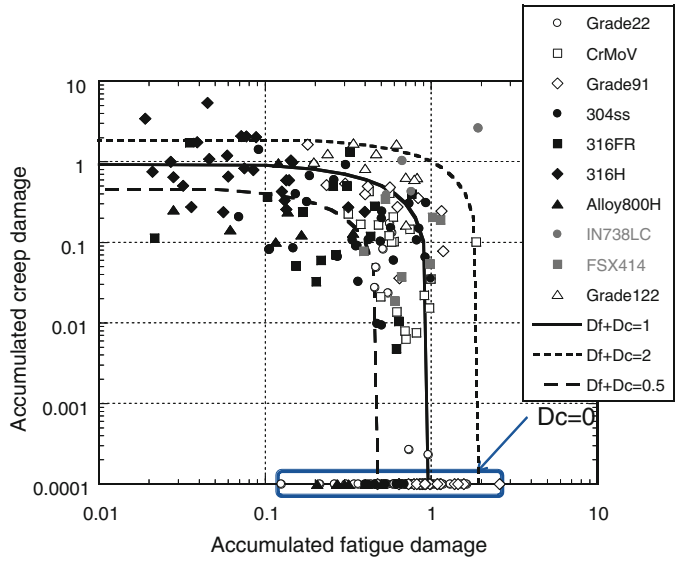

Fig. 7 Accumulated fatigue damage versus creep damage by modified ductility exhaustion approach

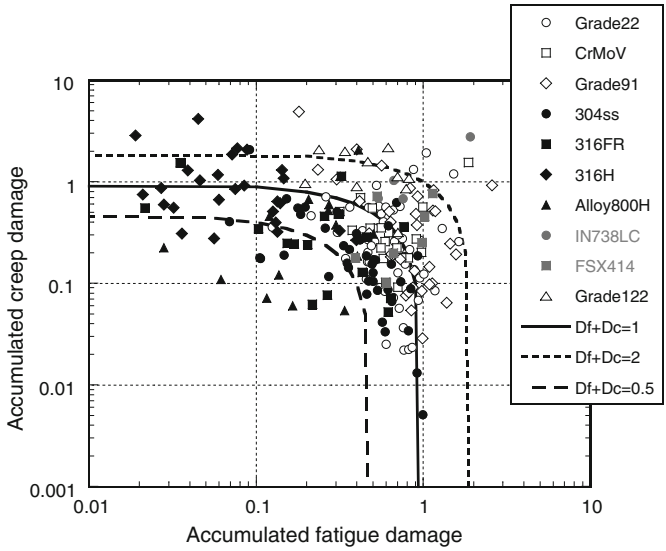

Fig. 8 Accumulated fatigue damage versus creep damage by energy-based approach

values of accumulated fatigue damage are common in all these figures and only those of creep damage differ depending on the approach taken. It can be firstly seen that the values of creep damage can change significantly with a choice of the procedure. In particular, stress-based time fraction approach provided a very wide range of creep damage, depending on materials and loading conditions, which is sometime very small and in other cases excessively large. Such a large variation, even in the same materials, renders determining a failure criterion as a function of accumulated creep and fatigue damage quite difficult. The other three approaches using inelastic strain or inelastic strain energy density do not show such an extremely large scatter, providing more stable estimation of creep damage.

In comparing the two approaches using the inelastic strain as a damage indicator in detail, a tendency to overestimate the damage observed in the classical ductility exhaustion approach is improved by the additional term in the modified approach given by Eq. (7). Benefit of using inelastic strain energy instead of strain can be also seen from the comparison of Figs. 7 and 8, although its effect is not as magnificent as those obtained when changing from stress-based to strain-based evaluation and when adding the second term within the latter framework. The values of total accumulated damage in the energy-based approach range from 0.2 to 5, which means that failure lives can be predicted with an error within this range when a simple linear damage summation rule is applied. There appears some tendency depending on the material type, suggesting a possibility of further improvement of the model.

4 Concluding Remarks

In order to make reliable assessment of integrity against the failure due to creep-fatigue interaction, accurate evaluation of inelastic deformation and resulting damage is indispensable. Some of the results obtained from recent works by the author have been briefly described. A combination of a unified constitutive model with en extended capability and a creep damage model based on inelastic strain energy density appears to be a most promising tool for accurate estimation of failure lives under a wide range of loading including creep-fatigue interaction. The current constitutive model is much more complicated than the damage model and an effort needs to be continued to find a procedure for identifying material parameters in a systematic way.

References

1. Yaguchi, M., Takahashi, Y.: Unified inelastic constitutive model for modified 9Cr-1Mo steel incorporating dynamic strain aging effect. JSME Int. J. (A). **42**, 1–10 (1999)
2. Yaguchi, M., Takahashi, Y.: A viscoplastic constitutive model incorporating strain aging effect during cyclic deformation conditions, Int. J. Plasticity **16**, 241–262 (2000)
3. Yaguchi, M., Takahashi, Y.: Ratchetting of viscoplastic material with cyclic softening. Part 1: experiments on modified 9Cr-1Mo steel. Int. J. Plasticity **21**, 43–65 (2005)
4. Yaguchi, M., Takahashi, Y.: Ratchetting of viscoplastic material with cyclic softening. Part 2: application of constitutive models. Int. J. Plasticity **21**, 835–860 (2005)
5. Takahashi, Y.: Development of unified constitutive and life prediction models for grade 91 steel including load history effect. Mater High Temp (2012)
6. Ohno, N., Wang, J.D.: Kinematic hardening rules with critical state of dynamic recovery. Part 1: formulation and basic features for ratcheting behavior. Int. J. Plasticity **9**, 375–390 (1993)
7. Ohno, N., Abdel-Karim, M.: Uniaxial ratchetting of 316FR steel at room temperature—Part 2: constitutive modelling and simulation. Trans. ASME. J. Eng. Mater. Technol. **122**, 35–41 (2000)
8. Takahashi, Y., Dogan, B., Gandy, D.: Systematic evaluation of creep-fatigue life prediction methods for various alloys. In: Proceedings of PVP2009, PVP2009-77990 (2009)

The Effect of Temperature on Interfacial Gradient Plasticity in Metallic Thin Films

George Z. Voyiadjis and Danial Faghihi

Abstract The material microstructural interfaces have a profound impact on the scale-dependent yield strength and strain hardening when the surface-to-volume ratio of the medium increases such as in micro and nanosystems. In this paper, the framework of higher-order strain gradient plasticity with interfacial energy effect is used to investigate the coupling of thermal and mechanical responses of materials in small scales and fast transient processes. In addition to the nonlocal yield condition for the material bulk, a temperature and rate dependent microscopic yield condition for the interface is presented, which determines the stress at which the interface begins to deform plastically and harden. In order to address the strengthening and hardening mechanisms, the theory is developed based on the decomposition of the mechanical state variables into energetic and dissipative counterparts. This, consecutively, provides the constitutive equations to have both energetic and dissipative gradient length scales ℓ_{en} and ℓ_{dis} respectively. Hence four material length scales are introduced: two for the bulk and the other two for the interface. In addition, the effect of temperature on the yield strength and hardening of the interface is included in the formulation by postulating that the interfacial energy decreases as temperature increases. Finally the developed framework is solved numerically to investigate the size effect of unaxial loading of a film substrate system.

1 Introduction

Thermoplastic modelling of metallic components becomes more complex when their size reduces to the order of a few hundreds of nanometers and they are subjected to inhomogeneous plastic flow under short elapsed time during a transient.

G. Z. Voyiadjis (✉) · D. Faghihi
Computational Solid Mechanics Laboratory,
Department of Civil and Environmental Engineering,
Louisiana State University, Baton Rouge, LA 70803, USA
e-mail: voyiadjis@eng.lsu.edu

H. Altenbach and S. Kruch (eds.), *Advanced Materials Modelling for Structures*,
Advanced Structured Materials 19, DOI: 10.1007/978-3-642-35167-9_31,

Since conventional continuum plasticity theories, based on the local thermodynamic equilibrium, do not account for the microstructural characteristics of materials, they cannot be used to adequately address the following problems:

(i) Size dependency of the macroscopic yield strength and strain-hardening rate during the inelastic deformation observed from micro-mechanical experiments including those from nano/micro-indentation, torsion of micron-dimensioned wires, and bending of micron-dimensioned thin films (see e.g., [28]).
(ii) The classical (macro-mechanical) test results such as increase in the macroscopic yield strength and strain-hardening rate of polycrystalline metals with decrease of the particle size and the grain diameter (i.e. the Hall–Petch behavior) (see e.g., [10]).
(ii) Heat transport responses under both short time and spatial scales such as very high transient thermal loads on microelectronic devices and pulsed-laser processing of materials (see e.g., [24, 29]).

It is known that the observed size effect is mainly due to the interaction between statistically stored dislocations (SSDs) which increases with the plastic strain and density of geometrically necessary dislocations (GNDs), that are generated by inhomogeneous plastic flow attributable to gradients of plastic strain (e.g., [25]). Over the size scale range in which most of the experiments have been conducted, the number of dislocations is generally so large that a continuum formulation such as strain gradient plasticity (e.g., [2, 12, 13, 20, 26, 33, 34]) is required to describe the deformation. Moreover, when the phonon mean free path is of the order of or larger than the medium size, the heat transport is not purely diffusive (as opposed to the Fourier law) and is partly ballistic. This is caused by the activation of microstructural effects due to the small depth of the heat-affected zone or the smallness of the structures (e.g., [22, 31]). On the other hand, if the response time in the small volume components reduces to the range comparable to the thermalization time, it leads to nonequilibrium transition of thermodynamics between electrons and phonons (e.g., [4, 9, 18, 30, 32]). Therefore, the continuum theory of heat transfer needs to be extended to incorporate the effect of microscopic (i.e. phonon–electron) interactions.

In the implementation of the higher-order gradient theories, higher-order boundary conditions naturally arise via the work principle, and in this sense the theories are well-posed. These conditions are required at the external boundary of a region in which plastic-flow occurs as well as at the internal boundary of the plastic region and are motivated from the physical understanding of the dislocation mechanics at the interface between the two phases. Free surfaces and interfaces of a material confined in a small volume can strongly affect the mechanical properties of the material. Free surfaces in submicron and nano-systems can be sources for development of defects and its propagation towards the interior. Hard, soft, or intermediate interfaces between distinct phase regions can also be locations for dislocations' blocking and pile-ups that give rise to strain gradients to accommodate the GNDs. The increase in the initial yield stress with decreasing thickness observed in tensile tests of various thin films are the experimental evidences in this direction. The free surfaces of the thin film and the interface between the film and substrate, therefore, can have a significant effect

on the strength of the thin film. In this regard, careful modelling of the interface will supply critical information in the continued development of strain gradient plasticity theories.

In this work a coupled thermo-mechanical framework of higher-order strain gradient plasticity theory is used to investigate the behavior of small-scale metallic volumes in fast transient times. In order to incorporate the multiple sources of thermodynamic processes into higher order strain gradient-dependent theory, the state variables are decomposed into energetic and dissipative components. Furthermore, the effect of temperature change due to the plastic work along with the generalized heat equation is incorporated into the formulation. The main focus of this paper is laid on investigating the coupling of interfacial energy with temperature and how the yield strength and the strain hardening are affected by the temperature change in the interface. In this regard, the application of the developed theory is considered to investigate the thermal and mechanical behavior of a metallic thin film on a silicon substrate under uniaxial loading.

2 Thermodynamic Framework

A thermodynamic consistent formulation to address the thermomechanical behavior of metals is derived in this section utilizing the thermodynamic principles, internal state variables, and thermodynamic and dissipation potentials. In order to include the micromechanical evolution, for the mechanical part, the enhanced strain gradient theory is considered, however, a micromorphic model is taken into account for the thermal counterpart of the formulation.

As it is mentioned in the introduction section, interface plays an important role for the plastic deformation at the micron scale where there exists relatively high ratio of surface area to volume ratio. Therefore it is further assumed that if internal work develops in the region occupied by the elastic-plastic continuum, an additional contribution to the internal virtual work should be considered [16, 17]. The principles of virtual power should therefore include the contributions of the interface surface energy that depends on the plastic strain state at the interface of the plastically deforming phase (i.e. $M^I_{ij}\dot{\varepsilon}^{pI}_{ij}$). This interface energy introduces resistance against dislocation movements (emission/transmission). The principal of virtual power is then obtained by equating the external power to the principle of internal power as $P_{ext} = P_{int}$ follows:

$$\begin{aligned}\int_V (\sigma_{ij}\dot{\varepsilon}^e_{ij} + X_{ij}\dot{\varepsilon}^p_{ij} + S_{ijk}\dot{\varepsilon}^p_{ij,k} + \mathcal{A}\dot{T} + \mathcal{B}_i\dot{T}_{,I})dV + \int_{s^I}(M^I_{ij}\dot{\varepsilon}^{pI}_{ij})dS^I \\ = \int_S t_i v_i dS + \int_S (m_{ij}\dot{\varepsilon}^{pI}_{ij})dS\end{aligned} \tag{1}$$

where σ_{ij} is the Cauchy stress tensor, $\dot{\varepsilon}^e_{ij}$ is the rate of elastic strain, $\dot{\varepsilon}^p_{ij}$ is the local plastic strain rate, X_{ij} and S_{ijk} are the microforces conjugate to the plastic strain and its gradient respectively. The terms $\mathcal{A}$ and $\mathcal{B}_i$ are generalized stresses, or the so called microforces according to Gurtin's terminology [19]. From Eq. (1) the nonlocal microforce balance and nonlocal microtraction condition can be given, respectively, as follows:

$$\tau_{ij} = X_{ij} - S_{ijk,k}; \quad m_{ij} = S_{ijk} N_k \tag{2}$$

The microscopic boundary conditions in Eq. $(2)_2$ are related to the interfacial energy at the free surfaces or interfaces. This interfacial energy introduces an interfacial resistance against dislocation emission/transmission. A consideration of arbitrary variations of the plastic strain at the interface defines conditions for the moment tractions, M^I_{ij} given the following interface nonstandard moment traction conditions

$$M^I_{ij} + S_{ijk} N^I_k = 0 \tag{3}$$

where N^I_k denotes the unit normal vectors of the surface S^I pointing outwards from the interface. If interface properties should be included in the analysis then the constitutive relations must be defined for the moment and the force tractions.

2.1 Thermodynamic Formulation with Higher Order Gradients of Stress and Temperature

The second law of thermodynamics is used in order to derive the constitutive equations and the first law is considered to derive the generalized heat equation. By introducing the Helmotz free energy such that $\Psi = e - Ts$, followed by taking the time derivative of this relation and substituting in the entropy production inequalities, the following Clausius-Duhem inequality for the bulk and the interface are obtained respectively [35]:

$$\sigma_{ij}\dot{\varepsilon}^e_{ij} + X_{ij}\dot{\varepsilon}^p_{ij} + S_{ijk}\dot{\varepsilon}^p_{ij,k} + \mathcal{A}\dot{T} + \mathcal{B}_i, T_{,i} - \rho\dot{\Psi} - \rho s\dot{T} - (q_i \frac{T_{,i}}{T}) \geq 0 \tag{4}$$

$$M^I_{ij}\dot{\varepsilon}^{pI}_{ij} - \dot{\Psi}^I - s^I\dot{T}^I \geq 0 \tag{5}$$

The term s is the specific entropy where s^I is the surface density of the entropy at the interface. In order to model the small-scale phenomena, such as the effect of size on the material mechanical properties and the width of the localization zones in the softening media with variation in temperature in the localized region, an attempt is made in this work to account for the effect of nonuniform distribution of microdefects with temperature on the homogenized response of the material. Furthermore,

decomposition of the thermodynamic forces into energetic and dissipative components give:

$$X_{ij} = X_{ij}^{en} + X_{ij}^{dis} = \rho \frac{\partial \Psi}{\partial \varepsilon_{ij}^{p}} + \frac{\partial \mathcal{D}}{\partial \dot{\varepsilon}_{ij}^{p}}; \; S_{ijk} = S_{ijk}^{en} + S_{ijk}^{dis} = \rho \frac{\partial \Psi}{\partial \varepsilon_{ij,\,k}^{p}} + \frac{\partial \mathcal{D}}{\partial \dot{\varepsilon}_{ij,\,k}^{p}} \quad (6)$$

$$M_{ij}^{I} = M_{ij}^{Ien} + M_{ij}^{Ien} = \rho \frac{\partial \Psi^{I}}{\partial \varepsilon_{ij}^{pI}} + \frac{\partial \mathcal{D}^{I}}{\partial \dot{\varepsilon}_{ij}^{pI}} \quad (7)$$

where $\mathcal{D}$ and $\mathcal{D}^{I}$ are the complementary part of the dissipation potentials.

2.1.1 Definition of the Thermodynamic Admissible Potentials

The choice of the form of the Helmholtz free energy function Ψ is very important since it constitutes the bases in deriving the constitutive equations. The complexity of any model is directly determined by the form of the Helmholtz free energy and by the number of conjugate pair of variables. In this work, however, one postulates the following general definition of energy:

$$\Psi = \frac{1}{2\rho}\varepsilon_{ij}^{e} E_{ijkl} \varepsilon_{kl}^{e} + \frac{1}{2\rho}\left(h\left(1 - \left(\frac{T}{T_m}\right)^{n}\right)\varepsilon_{ij}^{p}\varepsilon_{ij}^{p} + G\ell_{en}^{2}\varepsilon_{ij,\,k}^{p}\varepsilon_{ij,\,k}^{p}\right) - \frac{1}{2}\frac{c_{\varepsilon}}{T_r}(T - T_r)^{2} + \frac{1}{2\rho}\alpha T_{,ii} \quad (8)$$

where T_m is the melting temperature (m is not a tensorial subscript) and n is the temperature softening component which might be assumed different for each hardening mechanism. In the above equation c_{ε} (ε is not a tensorial subscript) is the specific heat coefficient at constant stress, a is an additional material parameter for an isotropic heat conduction and T_r (r is not a tensorial subscript) is the reference temperature [14]. The interface is characterized by a surface energy that depends on the plastic strain at the interface. The distinct feature of the present formulation is to introduce an interfacial yield stress that allows the interface to follow its own yield behavior. This interfacial yield stress is then described via dislocation transfer phenomena where its physical justification is made from observations obtained by nanoindentation tests near the grain boundaries of body centered cubic (bcc) metals [3, 8, 11, 27, 36]. The interface Helmholtz free energy is postulated as follows:

$$\Psi^{I} = \frac{1}{2} G \varepsilon_{ij}^{pI} \varepsilon_{ij}^{pI} \quad (9)$$

where ℓ_{en}^{I} is the interfacial energetic length scale which characterizes the back-stresses at a dislocation pile-up near the interface.

In this proposed work, one assumes the following functional forms for dissipation potentials of the bulk:

$$\mathcal{D} = \frac{1}{2}\left(\frac{\dot{\wp}}{\dot{\wp}_0}\right)^m \left(1 - \left(\frac{T}{T_m}\right)^n\right)\left[\frac{\sigma_Y \dot{\varepsilon}^p_{ij}\dot{\varepsilon}^p_{ij} + \sigma_Y \ell^2_{dis}\left(\dot{\varepsilon}^p_{ij,k}\dot{\varepsilon}^p_{ij,k}\right)}{\dot{\wp}}\right] + \frac{1}{2g}\mathcal{A}^2 - \frac{1}{2}kT_{,ii} \geq 0 \tag{10}$$

where $\dot{\wp} = \sqrt{(\dot{p})^2 + \ell^2_{dis}\dot{p}_{,k}\dot{p}_{,k}}$ is the effective nonlocal flow rate, σ_Y is a constant for the initial coarse grain yield strength [21] g and is a material parameter [15]. The interface the dissipation potential is given by:

$$\mathcal{D}^I = \left(\sigma^I_Y \ell^I_{dis}\right)\left(1 - \frac{T^I}{T_Y}\right)^{n^I}\left(\frac{\dot{\varepsilon}^{pI}_{ij}}{\dot{p}^I_0}\right)^{m^I} \geq 0 \tag{11}$$

where σ^I_Y is a constant representing the initial yield stress of the interface, $\dot{p}^I_0$ is a constant for interfacial flow rate and has the unit of (1/s) and m is a constant for rate sensitivity parameter. The temperature-dependency of the interfacial energy is provided here phenomenologically where T_Y is the bulk scale-independent temperature at the onset of yield and $0 \leq n^I < 1$ is the thermal exponent [1]. Equation (9) implies that the interfacial energy decreases as the temperature increases and when $T^I = T_Y$, the interface behaves like a free surface with zero interfacial energy. This corresponds to the condition that dislocations are nucleated within the bulk and did not yet reach the interface. The functional dependence of the interfacial energy in Eq. (9) is analogous to that proposed by Cahn [5] and Cahn and Hilliard [6] for heterogeneous domains in which T_Y is interpreted as the critical temperature at which the thickness of the interface becomes infinite. This function implies that the interfacial properties may be a function of the thermo-mechanical properties of the adjacent materials along with additional parameters that characterize the distinct thermo-mechanical behavior of the interface. One might select another temperature other than T_Y to normalize the temperature-dependency term in Eq. (9) that depends on the material properties of the joined materials at the interfaces. In the case of polycrystalline materials the interface represents a grain boundary. The grain boundaries act as strong obstacles to dislocation motion at low temperature while, at high temperatures, the grain boundaries function as sites of weakness and grain boundary sliding may occur leading to plastic flow or opening up voids along the boundaries [23]. In this regard, one may assume the interfacial yield temperature as a fraction of the material melting point, T_m, such as $T_Y = \alpha^I T_m$ where $0.3 < \alpha^I < 0.6$ according to Chung [7]. However, this argument needs to be verified through novel experimental setups for extracting the thermo-mechanical properties of the interfaces.

Making use of the above equations and substituting into the micro balance momentum and interface nonstandard moment traction, the following expressions for the nonlocal form of the yield criterion for the grain core region and interface can be obtained:

$$\tau = h\left(1-\left(\frac{T}{T_m}\right)^n\right)\varepsilon_{ij}^p + \sigma_Y\left(\frac{\dot{\wp}}{\dot{\wp}_0}\right)^m\left(1-\left(\frac{T}{T_m}\right)^n\right)\frac{\dot{\varepsilon}_{ij}^p}{\dot{\wp}} - G\ell_{en}^2\varepsilon_{ij,\,kk}^p$$
$$-\sigma_Y\ell_{dis}^2\left(1-\left(\frac{T}{T_m}\right)^n\right)\left(\frac{\dot{\wp}}{\dot{\wp}_0}\right)^m\frac{\dot{\varepsilon}_{ij,\,kk}^p}{\dot{\wp}} \tag{12}$$

$$\left(1-\frac{T^I}{T_Y}\right)^{n^I}\left(\ell_{en}^I G\varepsilon_{ij}^{pI} + \ell_{dis}^I\sigma_Y^I\left(\frac{\dot{\varepsilon}_{ij}^{pI}}{\dot{p}_0^I}\right)^m\right)$$
$$= \left(G\ell_{en}^2\varepsilon_{ij,\,k}^p\left(1-\left(\frac{T}{T_m}\right)^n\right) + \sigma_Y\ell_{dis}^2\left(\frac{\dot{\wp}}{\dot{\wp}_0}\right)^m\left(1-\left(\frac{T}{T_m}\right)^n\right)\frac{\dot{\varepsilon}_{ij,\,k}^p}{\dot{\wp}}\right)N_k^I \tag{13}$$

2.2 Evolution Equation of Temperature

Viscoplastic adiabatic deformation of metals is not only influenced by the rate of loading but also by the initial testing temperature as well as its evolution due to conversion of the plastic work into heat. According to the aforementioned thermodynamic forces one can postulate the conservation of energy as follows:

$$\rho\dot{e} = \sigma_{ij}\dot{\varepsilon}_{ij}^e + X_{ij}\dot{\varepsilon}_{ij}^p + S_{ijk}\dot{\varepsilon}_{ij,\,k}^p + \mathcal{A}\dot{T} + \mathcal{B}_i\dot{T},i - q_{i,\,i} \tag{14}$$

Substituting for the internal energy density rate e after taking the time rate of $\Psi = e - T_s$ into the first law of thermodynamics, the heat equation in the presence of a viscous generalized stress $\mathcal{A}^v$ is obtained as follows:

$$X_{ij}^{dis}\dot{\varepsilon}_{ij}^p + S_{ijk}^{dis}\dot{\varepsilon}_{ij,\,k}^p + \mathcal{A}^v\dot{T} - \mathrm{div}q_i = \rho\dot{\&}T \tag{15}$$

By solving for the entropy rate and substituting into Eq. (15), along with assuming $\gamma = \frac{k}{\rho c_\varepsilon}$, $\tau_T = -\frac{T_r a}{k}$, and $\tau_q = \frac{T_r\ell}{\rho c_\varepsilon}$ (all these are scalar relations), the following thermodynamic heat balance equation which accounts for the effect of microstructural interaction (microscale in space) in fast-transient (microscale in time) can be obtained as follows:

$$\dot{T} = \frac{1}{\rho c_\varepsilon}\left(X_{ij}^{dis}\dot{\varepsilon}_{ij}^p + S_{ijk}^{dis}\dot{\varepsilon}_{ij,\,k}^p\right) + (\gamma T_{,ii} + \gamma\tau_T\dot{T}_{,ii} - \tau_q\ddot{T}) \tag{16}$$

where γ is the effective thermal diffusivity in the phonon–electron or pure-phonon system and τ_T and τ_q are two positive intrinsic time scales (scalar quantities) characterizing the effect of the microstructural interactions and the fast transient response respectively (e.g., [32]). The values of τ_T and τ_q (scalar quantities) have to be determined by the transient response of temperature measured in the laboratory.

3 Numerical Example: Uniaxial Loading of a Thin Film on a Substrate

A thin film of thickness L constrained on a thick elastic substrate at $z = 0$ and subjected to uniaxial uniform tension at high rates is considered. Since the film is infinitely long in the x-direction and initially homogeneous, the solution depends only on z such that by assuming a plane strain problem in the y-direction, the non-vanishing components can be written for the stress tensor as $\sigma_{xx} = \sigma_0$, where the stress field σ_0 is the uniform applied stress. Due to the symmetry and because the strain components do not depend on x, the total strain $\varepsilon_{xx} = \varepsilon_0$ must be uniform throughout the film length such that the effective plastic strain and its Laplacian in this case can be assumed as $\varepsilon^p_{ij} = \varepsilon^p_0$ and $\varepsilon^p_{ij,kk} = \varepsilon^p_{0,zz}$.

The results analyzed for the case of biaxial loading of a 1 μm thick aluminum film on a silicon substrate during 1 μs is presented here. Typical properties of aluminum are adopted such as: $E = 70$ GPa, $\nu = 0.33$, $\sigma_Y = 36$ MPa and $h = 100$ MPA. The thermal exponent for the bulk and the interface are assumed as $n = 0.3$ and $n^I = 0.5$ respectively. It is possible to obtain the numerical solution by solving the nonlinear differential equation, Eq. (12), with the boundary condition, Eq. (13). Moreover, a three point fourth order compact finite difference scheme suggested by Zhang and Zhao (see e.g., [37]) is taken into account for solving the one-dimensional generalized heat equation presented in Eq. (16).

Figure 1 shows the distribution of normalized plastic strain and temperature through the film thickness at the last stage of loading for different values of energetic and dissipative length scales. Figure 2 also shows the variation of interfacial plastic strain and temperature with different values of the normalized length scales (ℓ_{en}/L and ℓ_{dis}/L). From these figure one can realize that the energetic length scale gives rise to the strain hardening. However, considering the compliant interface leads to higher plastic strain and consequently higher temperature through the thickness while the boundary layer formation is more pronounced when fewer dislocations are allowed to transmit through the interface (stiff interface). The variation of interfacial plastic strain and temperature in both cases are qualitatively the same with different energetic length scale values which for larger values of the length scale they approach constant values. Contrary to the case with varying energetic length scales which gives rise to strain-hardening, the higher amount of dissipative length scale increases the yield strength but no additional strain hardening is observed in this case.

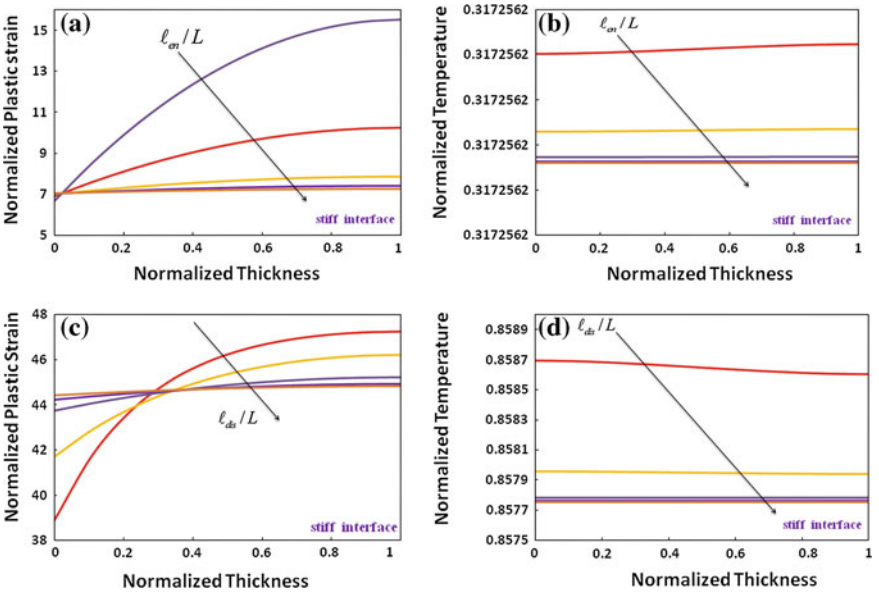

Fig. 1 Size effects due to energetic and dissipative length scales. Distribution of the normalized plastic strain [plots (**a**) and (**c**)] and normalized temperature [plots (**b**) and (**d**)] across the normalized film thickness. In all cases $\ell_{en}^I/L = \ell_{dis}^I/L = 0.1$

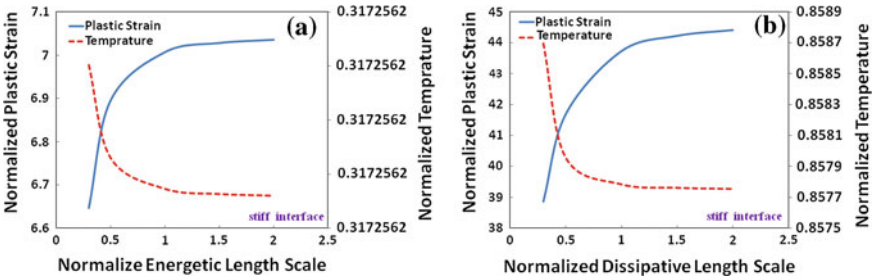

Fig. 2 Variation of interfacial plastic strain and temperature with energetic and dissipative length scales

The effect of different values of the interfacial length scales are investigated in Fig. 3. From this figure one can conclude that the interfacial energetic length scale only affects the plastic strain and temperature at the interface while the plastic strain and the temperature profiles though the thickness are the same for different length scales. Although lower interfacial strains and temperatures are indicated in stiff interfaces, their variation with ℓ_{en}^I/L is more pronounced for such stiff interface. On the other hand, the variation of interfacial plastic strain and temperature with interfacial length scale is quite different in each of ℓ_{en}^I/L and ℓ_{dis}^I/L as shown in Fig. 4. In both cases, temperature and plastic strain at the interface decreases with increasing the

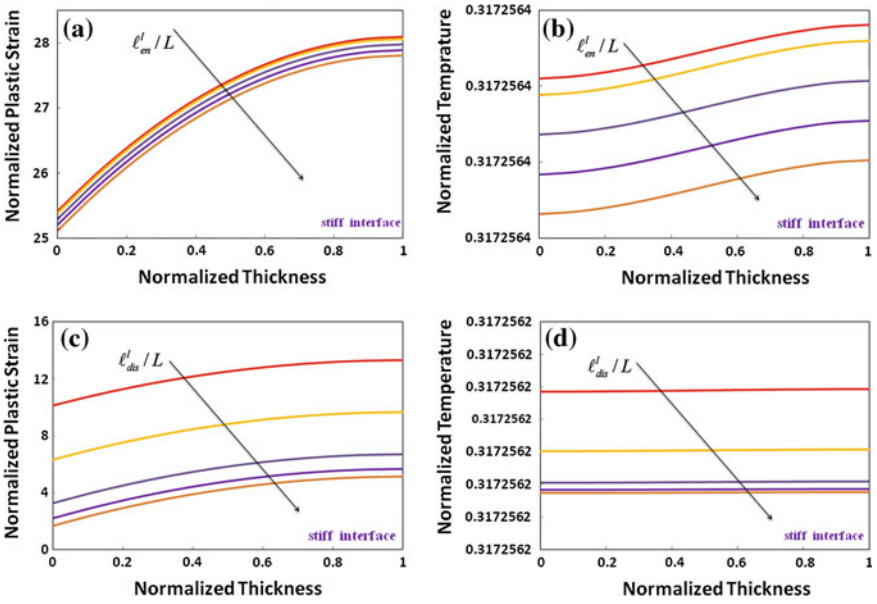

Fig. 3 Size effects due to interfacial energetic and dissipative length scales. Distribution of the normalized plastic strain [plots (**a**) and (**c**)] and normalized temperature [plots (**b**) and (**d**)] across the normalized film thickness. In all cases $\ell^I_{en}/L = \ell^I_{dis}/L = 0.5$

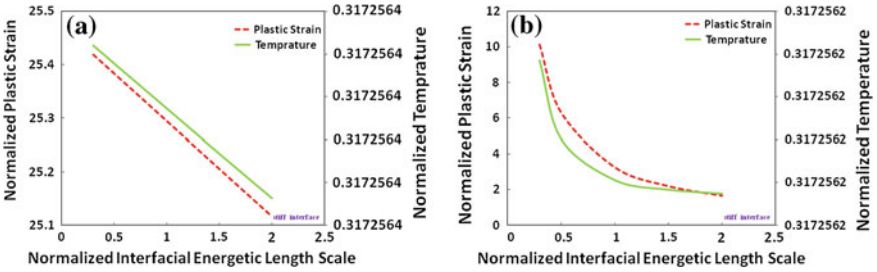

Fig. 4 The variation of interfacial plastic strain and temperature with ℓ^I_{en}/L and ℓ^I_{dis}/L

normalized interfacial length scales. However, the variation is quite linear for the case of ℓ^I_{en}/L and parabolic for ℓ^I_{dis}/L.

4 Conclusion

Free surfaces and interfaces of a material confined in a small volume or structure can strongly affect the mechanical and thermal properties of micro and nanosystems. In this work a coupled thermo-mechanical formulation within the framework of

higher-order strain gradient plasticity and the application of micromorphic approach to the temperature variable is used to investigate the behavior of small-scale metallic volumes in fast transient times. The higher-order boundary conditions that result from the mathematical consistency of strain gradient plasticity theory are interpreted as microtraction forces that are related to the interfacial energy at the interface. The interfacial energy is a measure of the interface resistance to dislocation motion, transmission, and emission. The proposed interfacial condition in this paper allows the interfaces to be able to follow their own yield behavior as well as being rate and temperature dependent. It is postulated that the interfacial energy decreases as the temperature increases. This implies that size effect on the yield strength and strain hardening rate decreases as temperature increases. In order to address the strengthening and hardening mechanisms, the theory is developed based on the decomposition of the mechanical state variables into energetic and dissipative counterparts. This, consecutively, provides the constitutive equations to have both energetic and dissipative gradient length scales ℓ_{en} and ℓ_{dis} respectively. Hence four material length scales are introduced: two for the bulk and the other two for the interface.

The proposed framework is applied to solve uniaxial loading of a film-substrate system with two different interface properties (hard and soft). It is concluded that the postulated interfacial energy expression provides the size dependency of the yield strength and strain hardening rates. Furthermore, it is concluded that the yield stress (corresponding to the dissipative counterpart) is more temperature sensitive as the film thickness decreases.

References

1. Abu Al-Rub, R.K., Faruk, A.N.M.: Coupled interfacial energy and temperature effects on size-dependent yield strength and strain hardening of small metallic volumes. J. Eng. Mater. Technol. Trans. ASME **133**(1), (2011). doi:Artn011017, Doi 10.1115/1.4002651
2. Aifantis, E.C.: On the role of gradients in the localization of deformation and fracture. Int. J. Eng. Sci. **30**(10), 1279–1299 (1992)
3. Aifantis, K.E., Soer, W.A., De Hosson, J.T.M., Willis, J.R.: Interfaces within strain gradient plasticity: theory and experiments. Acta Materialia **54**(19), 5077–5085 (2006). doi:10.1016/j.actamat.2006.06.040
4. Brorson, S.D., Kazeroonian, A., Moodera, J.S., Face, D.W., Cheng, T.K., Ippen, E.P., Dresselhaus, M.S., Dresselhaus, G.: Femtosecond room-temperature measurement of the electron-phonon coupling constant-lambda in metallic superconductors. Phys. Rev. Lett. **64**(18), 2172–2175 (1990)
5. Cahn, J.W.: Free energy of a nonuniform system. 2. Thermodynamic basis. J. Chem. Phys. **30**(5), 1121–1124 (1959)
6. Cahn, J.W., Hilliard, J.E.: Free energy of a nonuniform system. 1. Interfacial free energy. J. Chem. Phys. **28**(2), 258–267 (1958)
7. Chung, Y.-w.: Introduction to Materials Science and Engineering. CRC, Boca Raton (2007)
8. De Hosson, J.T.M., Aifantis, K.E., Soer, W.A., Willis, J.R.: Interfaces within strain gradient plasticity: theory and experiments. Acta Materialia **54**(19), 5077–5085 (2006). doi:10.1016/j.actamat.2006.06.040

9. Elsayed-Ali, H.E., Juhasz, T., Smith, G.O., Bron, W.E.: Femtosecond thermoreflectivity and thermotransmissivity of polycrystalline and single-crystalline gold-films. Phys. Rev. B **43**(5), 4488–4491 (1991)
10. Espinosa, H.D., Prorok, B.C., Peng, B.: Plasticity size effects in free-standing submicron polycrystalline FCC films subjected to pure tension. J. Mech. Phys. Solids **52**(3), 667–689 (2004). doi:10.1016/j.jmps.2003.07.001
11. Faghihi, D., Voyiadjis, G.Z.: Determination of nanoindentation size effects and variable material intrinsic length scale for body-centered cubic metals. Mech. Mater. (2011, in press, corrected proof). doi:10.1016/j.mechmat.2011.07.002
12. Fleck, N.A., Willis, J.R.: A mathematical basis for strain-gradient plasticity theory—part I: scalar plastic multiplier. J. Mech. Phys. Solids **57**(1), 161–177 (2009a). doi:10.1016/j.jmps.2008.09.010
13. Fleck, N.A., Willis, J.R.: A mathematical basis for strain-gradient plasticity theory. Part II: tensorial plastic multiplier. J. Mech. Phys. Solids **57**(7), 1045–1057 (2009). doi:10.1016/j.jmps.2009.03.007
14. Forest, S., Aifantis, E.C.: Some links between recent gradient thermo-elasto-plasticity theories and the thermomechanics of generalized continua. Int. J. Solids Struct. **47**(25–26), 3367–3376 (2010). doi:10.1016/j.ijsolstr.2010.07.009
15. Forest, S., Amestoy, M.: Hypertemperature in thermoelastic solids. Comptes Rendus Mecanique **336**(4), 347–353 (2008). doi:10.1016/j.crme.2008.01.007
16. Fredriksson, P., Gudmundson, P.: Size-dependent yield strength and surface energies of thin films. Mater. Sci. Eng. Struct. Mater. Prop. Microstruct. Process. **400**, 448–450 (2005). doi:10.1016/j.msea.2005.02.090
17. Fredriksson, P., Gudmundson, P.: Competition between interface and bulk dominated plastic deformation in strain gradient plasticity. Model. Simul. Mater. Sci. Eng. **15**(1), S61–S69 (2007). doi:10.1088/0965-0393/15/1/S06
18. Fujimoto, J.G., Liu, J.M., Ippen, E.P., Bloembergen, N.: Femtosecond laser interaction with metallic tungsten and nonequilibrium electron and lattice temperatures. Phys. Rev. Lett. **53**(19), 1837–1840 (1984)
19. Gurtin, M.E.: Generalized Ginzburg-Landau and Cahn-Hilliard equations based on a microforce balance. Physica D **92**(3–4), 178–192 (1996)
20. Gurtin, M.E., Anand, L.: Thermodynamics applied to gradient theories involving the accumulated plastic strain: the theories of Aifantis and Fleck and Hutchinson and their generalization. J. Mech. Phys. Solids **57**(3), 405–421 (2009). doi:10.1016/j.jmps.2008.12.002
21. Gurtin, M.E., Fried, E., Anand, L.: The Mechanics and Thermodynamics of Continua. Cambridge University Press, New York (2010)
22. Joshi, A.A., Majumdar, A.: Transient ballistic and diffusive phonon heat-transport in thin-films. J. Appl. Phys. **74**(1), 31–39 (1993)
23. Meyers, M.A., Chawla, K.K.: Mechanical Behavior of Materials, 2nd edn. Cambridge University Press, Cambridge (2009)
24. Narayan, J., Godbole, V.P., White, C.W.: Laser method for synthesis and processing of continuous diamond films on nondiamond substrates. Science **252**(5004), 416–418 (1991)
25. Niordson, C.F., Hutchinson, J.W.: Non-uniform plastic deformation of micron scale objects. Int. J. Numer. Methods Eng. **56**(7), 961–975 (2003). doi:10.1002/Nme.593
26. Polizzotto, C.: A nonlocal strain gradient plasticity theory for finite deformations. Int. J. Plast. **25**(7), 1280–1300 (2009). doi:10.1016/j.ijplas.2008.09.009
27. Soer, W.A., Aifantis, K.E., De Hosson, J.T.M.: Incipient plasticity during nanoindentation at grain boundaries in body-centered cubic metals. Acta Materialia **53**(17), 4665–4676 (2005). doi:10.1016/j.actamat.2005.07.001
28. Stolken, J.S., Evans, A.G.: A microbend test method for measuring the plasticity length scale. Acta Materialia **46**(14), 5109–5115 (1998)
29. Sze, S.M., Ng, K.K.: Physics of Semiconductor Devices, 3rd edn. Wiley-Interscience, Hoboken (2007)

30. Tzou, D.Y.: Experimental support for the lagging behavior in heat propagation. J. Thermophys. Heat Transf. **9**(4), 686–693 (1995a)
31. Tzou, D.Y.: The generalized lagging response in small-scale and high-rate heating. Int. J. Heat Mass Transf. **38**(17), 3231–3240 (1995b)
32. Tzou, D.Y., Zhang, Y.S.: An analytical study on the fast-transient process in small scales. Int. J. Eng. Sci. **33**(10), 1449–1463 (1995)
33. Voyiadjis, G.Z., Deliktas, B.: Formulation of strain gradient plasticity with interface energy in a consistent thermodynamic framework. Int. J. Plast. **25**(10), 1997–2024 (2009a). doi:10.1016/j.ijplas.2008.12.014
34. Voyiadjis, G.Z., Deliktas, B.: Mechanics of strain gradient plasticity with particular reference to decomposition of the state variables into energetic and dissipative components. Int. J. Eng. Sci. **47**(11–12), 1405–1423 (2009). doi:10.1016/j.ijengsci.2009.05.013
35. Voyiadjis, G.Z., Faghihi, D.: Thermo-mechanical strain gradient plasticity with energetic and dissipative length scales. Int. J. Plast. (2011a) doi:10.1016/j.ijplas.2011.10.007
36. Voyiadjis, G.Z., Faghihi, D.: Variable (intrinsic) material length scale for face-centred cubic metals using nano-indentation. Proc. Inst. Mech. Eng. Part N J. Nanoeng. Nanosyst. (2011b). doi:10.1177/1740349911413647
37. Zhang, J., Zhao, J.J.: Unconditionally stable finite difference scheme and iterative solution of 2D microscale heat transport equation. J. Comput. Phys. **170**(1), 261–275 (2001)

A Cyclic Crystal Viscoplastic Model Considering Both Dislocation Slip and Twinning

Chao Yu, Guozheng Kang, Qianhua Kan, Otto T. Bruhns and Chuanzeng Zhang

Abstract Based on the framework of crystal visco-plasticity, a new single crystal cyclic constitutive model is first constructed to describe the cyclic plastic deformation of single crystal metal by considering both the dislocation slip and twinning. The new orientation of the slip system in the twinned region can be obtained only by a rotation of the original one, and then, a rotation tensor is introduced in the proposed model. Also, a nonlinear kinematic hardening rule is employed to describe the evolution of resolved shear back stress in each active slip system and twinning system. Then, an explicit scale-transition rule is adopted to extend the proposed single crystal model to the polycrystalline version. Finally, the capability of the proposed model to describe the uniaxial ratchetting is verified by comparing the simulations with the corresponding experiments of polycrystalline Ti-6Al-4V alloy, a dual-phase material consisting of a primary hexagonal close packed (HCP) phase α and secondary body-centered cubic (BCC) phase β.

C. Yu · G. Kang (✉) · Q. Kan
State Key Laboratory of Traction Power, Southwest Jiaotong University,
Chengdu, 610031 Sichuan , Peoples's Republic of China
e-mail: guozhengkang@yahoo.com.cn

C. Yu
e-mail: yuchao5045@163.com

Q. Kan
e-mail: qianhuakan@yahoo.com.cn

O. T. Bruhns
Institute of Continuum Mechanics, Ruhr-University Bochum,
44801 Bochum, Germany
e-mail: otto.bruhns@rub.ge

C. Zhang
Department of Civil Engineering, University of Siegen, 57068 Siegen, Germany
e-mail: c.zhang@uni-siegen.de

H. Altenbach and S. Kruch (eds.), *Advanced Materials Modelling for Structures*,
Advanced Structured Materials 19, DOI: 10.1007/978-3-642-35167-9_32,

1 Introduction

In the last decades, many constitutive models were proposed to describe the cyclic deformation of metallic materials as reviewed by [1–4]. Most of the existing models were derived directly from the macroscopic experimental results, and did not consider the physical nature of plastic deformation reasonably. Recently, based on the crystal plasticity, several micromechanical constitutive models were constructed to capture the microscopic physical nature of plastic deformation. The typical models are presented in [5–10] and so on. However, the ratchetting of metallic materials occurring in the asymmetrical stress-controlled cyclic loading as reviewed by [1–4] is not reasonably considered in the above-mentioned models. More recently, Ref. [11] presented a cyclic polycrystalline visco-plastic constitutive model to describe the uniaxial ratchetting of 316L stainless steel (a FCC polycrystalline metal) by considering only the dislocation slip and referring to the work done by [12]. However, for some materials such as Titanium alloys, twinning has been proved to be also a cause of plastic deformation by [13, 14]. It is necessary to introduce the twinning mechanism into the cyclic constitutive model to describe the ratchetting of polycrystalline metals reasonably.

Therefore, in this work, a cyclic polycrystalline visco-plastic constitutive model is proposed in the framework of thermodynamics and crystal plasticity to describe the ratchetting of polycrystalline material at room temperature. In the model, both dislocation slip and twinning are considered. An explicit scale-transition rule considering the plastic accommodation of grains is employed to transit the single crystal model into its polycrystalline version. The capability of the developed model to predict the ratchetting is verified by comparing the simulations with the experiments of a commercial Ti-6Al-4V alloy made in China.

2 Cyclic Polycrystalline Visco-Plastic Constitutive Model

2.1 Cyclic Single Crystal Constitutive Model

2.1.1 Assumptions for Elastic and Plastic Strains

Based on the hypothesis of small deformation, the total strain can be decomposed into two parts, i.e., elastic strain $\boldsymbol{\varepsilon}^e$, and plastic strain $\boldsymbol{\varepsilon}^p_{twin}$caused by twinning and $\boldsymbol{\varepsilon}^p_{slip}$by dislocation slip:

$$\boldsymbol{\varepsilon} = \boldsymbol{\varepsilon}^e + \boldsymbol{\varepsilon}^p_{twin} + \boldsymbol{\varepsilon}^p_{slip} \tag{1}$$

It is well-known that polycrystalline Ti-6Al-4V alloy is aggregated by the single-phase grains of a primary α (HCP) and the dual-phase ones of primary α (HCP)

and secondary β (BCC) phases. In the dual-phase single crystal grain, the volume fraction of secondary β phase is represented by the parameter ξ; while in the single-phase grain of a primary α (HCP), the parameter ξ is set to be zero. The details of microstructure and the length-scale effect in a single crystal are not considered in this work.

In this work, it is assumed that the twinning just occurs in the primary α (HCP) phase, and then three types of twinning, i.e., tension twinning $\{10\bar{1}2\}\langle\bar{1}011\rangle$ with maximum shear strain of 16.7 %, compression one $\{10\bar{1}1\}\langle\bar{1}012\rangle$ with maximum shear strain of 22.5 %, and compression one $\{11\bar{2}2\}\langle\bar{1}\bar{1}23\rangle$ with maximum shear strain of 63.8 % are considered by referring to [14]. Therefore, the plastic strain caused by the twinning occurring in the primary α (HCP) phase is a sum of the contributions by all the twinning systems, i.e.,

$$\dot{\boldsymbol{\varepsilon}}^{p}_{twin} = (1-\xi)\sum_{i=1}^{ntwin} \dot{f}^{i} g^{i} \Lambda^{i} \tag{2}$$

$$\Lambda^{i} = \frac{1}{2}(\mathbf{m}^{i} \otimes \mathbf{n}^{i} + \mathbf{n}^{i} \otimes \mathbf{m}^{i}) \tag{3}$$

$$f = \sum_{i=1}^{ntwin} f^{i} \tag{4}$$

Here, f is the total volume fraction of all twinning systems for the contribution to the plastic deformation of the primary α (HCP) phase; *ntwin* is the number of twinning systems; f^{i} and Λ^{i} are the volume fraction and orientation tensor of the ith twinning system; g^{i} is the maximum shear strain caused by the ith twinning system which is listed in the previous context; $\mathbf{m}^{i}$ and $\mathbf{n}^{i}$ are the twinning direction and habit plane normal vectors, respectively.

Concerning the dislocation slip occurring in the Ti-6Al-4V dual-phase single crystal grain under the cyclic loading, two contributions are considered in this work, i.e., one comes from the slip in the primary α (HCP) phase, and the other from that in the secondary β (BCC) phase. There are four types of slip systems in the primary α phase: basal slip system $3\langle 11\bar{2}0\rangle(0001)$, prismatic one $3\langle 11\bar{2}0\rangle(10\bar{1}0)$, first-order pyramidal one $6\langle 11\bar{2}0\rangle(10\bar{1}1)$ and second-order pyramidal one $12\langle 11\bar{2}3\rangle(10\bar{1}1)$are considered by referring to [10]. In this work, the contribution of the second-order pyramidal slip system to the plastic deformation is neglected, because its critically resolved shear stress is much higher than those of basal, prismatic, and first-order pyramidal slip systems.

With respect to the dislocation slip occurring in the secondary β (BCC) phase, it is assumed that only the 12 primary slip systems $\langle 111\rangle\{110\}$ will be activated under the cyclic loading for simplicity. In the Ti-6Al-4V dual-phase single crystal, the orientations of α and β phases are not arbitrary, but satisfy the Burgers' orientation relation [15, 16], i.e., $(0001)_{\alpha}//\{101\}_{\beta}$ and $(11\bar{2}0)_{\alpha}//\{111\}_{\beta}$. So, if the orientation

of the α phase in a dual-phased single crystal is determined, that of the β phase can be readily obtained by the Burgers' orientation relation.

Considering the further dislocation slip occurring in the twinned crystal structure, the total plastic strain caused by the dislocation slip can be obtained from the following formula

$$\dot{\boldsymbol{\varepsilon}}^{p}_{slip} = (1-\xi)\left[(1-f)\sum_{j=1}^{HCP\_nslip}\dot{\gamma}_0^j\mathbf{P}_0^j + \sum_{i=1}^{ntwin} f^i\left(\sum_{j=1}^{HCP\_nslip}\dot{\gamma}_i^j\mathbf{P}_i^j\right)\right] + \xi\sum_{i=1}^{BCC\_nslip}\dot{\lambda}^i\mathbf{M}^i \tag{5}$$

Here, the first term represents the plastic strain caused by the dislocation slip in the un-twinned and twinned α phases and the second one in the β phase; $\sum_{j=1}^{HCP\_nslip}\dot{\gamma}_0^j\mathbf{P}_0^j$ is the plastic strain caused by the dislocation slip in un-twinned α phase, $\mathbf{P}_0^j$ is the orientation tensor of the jth slip system, $\dot{\gamma}_0^j$ is the slipping rate related to $\mathbf{P}_0^j$; $\sum_{j=1}^{HCP\_nslip}\dot{\gamma}_i^j\mathbf{P}_i^j$ is the plastic strain caused by the dislocation slip in the ith twinned α phase, $\mathbf{P}_i^j$ is the orientation tensor of the jth slip system in the ith twinned region, and $\dot{\gamma}_i^j$ is the slipping rate related to $\mathbf{P}_i^j$; $\sum_{i=1}^{BCC\_nslip}\dot{\lambda}^i\mathbf{M}^i$ is the plastic strain caused by the dislocation slip in β phase, $\mathbf{M}^i$ is the orientation tensor of the ith slip system, and $\dot{\lambda}^i$ is the slipping rate related to $\mathbf{M}^i$.

The orientation tensors $\mathbf{P}_0^j$ and $\mathbf{M}^i$ can be easily obtained by the slip direction and the slip plane normal vectors using

$$\mathbf{P}_0^j = \frac{1}{2}(\mathbf{s}_{HCP}^j \otimes \mathbf{l}_{HCP}^j + \mathbf{l}_{HCP}^j \otimes \mathbf{s}_{HCP}^j) \tag{6}$$

$$\mathbf{M}^i = \frac{1}{2}(\mathbf{s}_{BCC}^i \otimes \mathbf{l}_{BCC}^i + \mathbf{l}_{BCC}^i \otimes \mathbf{s}_{BCC}^i) \tag{7}$$

where $\mathbf{s}_{HCP}^j$ is the slip direction and $\mathbf{l}_{HCP}^j$ is the slip plane normal vector of the jth slip system in the primary HCP α phase, and $\mathbf{s}_{BCC}^i$ is the slip direction and $\mathbf{l}_{BCC}^i$ is the slip plane normal vector of the ith slip system in secondary BCC β phase. It is well known that the orientation of the slip system in the twinned region of the α phase is different from that in the un-twinned one. However, the crystal structure remains unchanged during the twinning. The new orientation of the slip system in the twinned region can be obtained by rotating the original one. So, a rotation tensor is introduced similar to the work done in [11], i.e.,

$$\mathbf{R}^i = 2\mathbf{n}^i \otimes \mathbf{n}^i - \mathbf{I} \tag{8}$$

where $\mathbf{R}^i$ the rotation tensor acting on the slip system in the ith twinned region. The new orientation tensor of the jth slip system in the ith twinned region is formulated as

$$\mathbf{P}_i^j = \mathbf{R}^i \mathbf{P}_0^j (\mathbf{R}^{i)^T} \tag{9}$$

2.1.2 Thermodynamics Description

Considering a representative volume element (RVE) of a dual-phase single crystal, the Helmholtz free energy can be written as

$$\psi = \psi^e + \psi_{twin}^p + \psi_{slip}^p \tag{10}$$

The explicit expressions of each energy part can be obtained as follows

$$\psi^e(\boldsymbol{\varepsilon}^e) = \frac{1}{2}\boldsymbol{\varepsilon}^e : \mathbf{C} : \boldsymbol{\varepsilon}^e \tag{11}$$

$$\psi_{twin}^p(t) = \int_0^t \sum_{i=1}^{ntwin} X_{twin}^i g^i \dot{f}^i d\tau \tag{12}$$

$$\psi_{slip}^p(t) = (1-\xi)\int_0^t \sum_{i=1}^{HCC\_nslip} X^i \dot{\bar{\gamma}}^i d\tau + \xi \int_0^t \sum_{i=1}^{BCC\_nslip} T^i \dot{\lambda}^i d\tau \tag{13}$$

$$\dot{\bar{\gamma}}^i = (1-f)\dot{\gamma}_0^i + \sum_{j=1}^{ntwin} f^j \dot{\gamma}_j^i \tag{14}$$

Here, $\mathbf{C}$ is a fourth-order elastic tensor which for simplification can be set as an isotropic tensor; $\psi_{twin}^p(t)$ describes the strain hardening caused by the twinning, while $\psi_{slip}^p(t)$ represents the strain hardening caused by the dislocation slip; X_{twin}^i is the resolved shear back stress of ith twinning system which is a dual variable of the weighted volume fraction rate $g^i \dot{f}^i$; $\sum_{i=1}^{HCP\_nslip} X^i \dot{\bar{\gamma}}^i$ is the strain hardening caused by the dislocation slip, X^i and $\dot{\bar{\gamma}}^i$ are the resolved shear back stress and the effective slipping rate of the ith slip system in the primary HCP α phase, respectively. Also, $\sum_{i=1}^{BCC\_nslip} T^i \dot{\lambda}^i$ is the hardening caused by the dislocation slip, T^i and $\dot{\lambda}^i$ are the back stress and the slipping rate of the ith slip system in the secondary BCC β phase. In the isothermal case, the dissipative inequality can be written as

$$\boldsymbol{\sigma} : \dot{\boldsymbol{\varepsilon}} - \dot{\psi} \geq 0 \tag{15}$$

Since the dissipation of the elastic deformation is zero, and no interaction between the dislocation slip and the twinning is considered, the dissipative inequality can be rewritten as

$$\boldsymbol{\sigma} = \mathbf{C} : \boldsymbol{\varepsilon}^e \tag{16}$$

$$\sum_{i=1}^{ntwin} (\boldsymbol{\sigma} : \Lambda^i - X^i_{twin}) g^i \dot{f}^i \geq 0 \tag{17}$$

$$(1-\xi)[(1-f) \sum_{j=1}^{HCP\_nslip} (\boldsymbol{\sigma} : \mathbf{P}_0^j - X^j)\dot{\gamma}_0^j + \sum_{i=1}^{ntwin} \sum_{j=1}^{HCP\_nslip} f^i (\boldsymbol{\sigma} : \mathbf{P}_i^j - X^j)\dot{\gamma}_i^j] + \xi \sum_{i=1}^{BCC\_nslip} (\boldsymbol{\sigma} : \mathbf{M}^i - T^i)\dot{\lambda} \tag{18}$$

By Eqs. (17) and (18) the thermodynamic driving force of each internal variable can be written as

$$F^j_{twin} = (\boldsymbol{\sigma} : \Lambda^i - X^i_{twin}) g^i \tag{19}$$

$$F^j_i = \boldsymbol{\sigma} : \mathbf{P}^j_i - X^j \tag{20}$$

$$Q^j = \boldsymbol{\sigma} : \mathbf{M}^i - T^i \tag{21}$$

If the thermodynamic driving force F^i_{twin} is positive and larger than a critical value, then twinning occurs. However, a negative thermodynamic driving force can recover a part of the twinning deformation. So, a criterion should be constructed to distinguish the twinning from its recovery. It can be stated as

$$\dot{\boldsymbol{\sigma}} : \boldsymbol{\varepsilon}^i \geq 0; \quad f^i \leq 1; \quad f \leq 1 \quad \text{for twinning of } i\text{th twinning system} \tag{22}$$

$$\dot{\boldsymbol{\sigma}} : \boldsymbol{\varepsilon}^i < 0; \quad f^i \geq 0; \quad f \geq 0 \quad \text{for recovery of } i\text{th twinning system} \tag{23}$$

2.1.3 Evolution of Internal Variables

The evolution rule of the volume fraction of the twinning can be obtained in the framework of visco-plasticity as

$$\dot{f}^i = \left\langle \frac{F^i_{twin}}{g^i K_{twin}} \right\rangle^n \quad \text{for twinning of } i\text{th twinning system} \tag{24}$$

$$\dot{f}^i = -\left\langle \frac{-F^i_{twin}}{g^i K_{twin}} \right\rangle^n \quad \text{for recovery of } i\text{th twinning system} \tag{25}$$

where $g^i K_{twin}$ is the resistance to twinning deformation, g^i is a weighting factor introduced to reflect a higher potential barrier encountered in the shear deformation with larger magnitude, and n represents the rate sensitivity of the twinning deformation. The evolution rules of the dislocation slip occurring in both the primary α and the secondary β phase can be also obtained in the framework of visco-plasticity as

$$\dot{\gamma}_i^j = \left(\frac{\left| F_i^j \right|}{K_{HCPslip}} \right)^n sign(F_i^j) \tag{26}$$

$$\dot{\lambda}^i = \left(\frac{|Q^i|}{K_{BCCslip}} \right)^n sign(Q^i) \tag{27}$$

where$K_{HCPslip}$ is the viscosity resistance to the dislocation slip occurring in the primary α phase and $K_{BCCslip}$ is that in the secondary β phase.

2.1.4 Hardening Rules

Due to the low symmetrical of HCP crystal lattice, it is difficult to obtain the interaction matrix for each slip and twin system. Thus, following the previous work done by [10], only the self-hardening in each slip system or twinning system is considered in formulating the evolution equations of the resistances X_{twin}^i, X^i and T^i during the cyclic deformation of Ti-6Al-4V single crystal. Referring to the nonlinear kinematic hardening rule proposed by [17], the following evolution rules are constructed

$$\dot{X}_{twin}^i = B_{twin}\dot{f}^i - C_{twin}X_{twin}\left|\dot{f}^i\right| \tag{28}$$

$$\dot{X}^i = B_{HCP\_slip}\dot{\bar{\gamma}}^i - C_{HCP\_slip}X^i\left|\dot{\bar{\gamma}}^i\right| \tag{29}$$

$$\dot{T}^i = B_{BCC\_slip}\dot{\lambda}^i - C_{BCC\_slip}T^i\left|\dot{\lambda}^i\right| \tag{30}$$

where $B_{twin}, B_{HCP\_slip}, B_{BCC\_slip}$ and $C_{twin}, C_{HCP\_slip}, C_{BCC\_slip}$ are the coefficients of the strain hardening and the dynamic recovery terms for the resistances, respectively. However, further work should be done in order to obtain the interaction matrix for each slip and twin system.

2.2 Explicit Scale-Transition Rule

To obtain the stress-strain responses of polycrystalline aggregates from that of a single crystal, an effective scale-transition rule is required. The explicit β-rule has already been used in [11, 12] to develop a cyclic polycrystalline plastic model to describe

the ratchetting behavior of some face-centered cubic (FCC) and body-centered cubic (BCC) polycrystalline materials. So, the β-rule is also employed in this work and outlined in the following parts.

With the assumption of homogeneous isotropic elasticity for polycrystalline aggregates, the local stress tensor $\boldsymbol{\sigma}^g$ can be obtained from the applied uniform stress tensor $\boldsymbol{\sigma}$ by using following formulae

$$\boldsymbol{\sigma}^g = \boldsymbol{\sigma} + C(\boldsymbol{\beta} - \boldsymbol{\beta}^g) \tag{31}$$

$$\dot{\boldsymbol{\beta}}^g = \dot{\boldsymbol{\varepsilon}}^g - D\boldsymbol{\beta}^g \left\| \boldsymbol{\varepsilon}^g \right\| \tag{32}$$

where $\boldsymbol{\beta} = [\boldsymbol{\beta}^g]$, the symbol $[\bullet]$ denotes the volume average for the polycrystalline aggregates, and C and D are material parameters.

3 Verification and Discussion

For the verification purpose, 50 isometric randomly oriented single crystal grains are used to represent the polycrystalline Ti-6Al-4V alloy, which consist of 30 single-phase α (HCP) grains and 20 dual-phase ($\alpha + \beta$) ones. Thus, the total volume fraction of the β phase is 3.2 %, when the parameter ξ is set to be 0.08. The proposed model is verified at the macroscopic scale. Since the experimental data of cyclic deformation for Ti-6Al-4V single-phase and dual-phase single crystal grains have not been obtained yet in microscopic scale, all the material parameters can be just determined by a trial-and-error method from the macroscopic experimental data of a commercial Ti-6Al-4V alloy made in China (its chemical compositions are as follows: C 0.06, Al 6.2, Fe 0.12, V 4.1, N 0.02, H 0.009, O 0.15, and the remained Ti), and they are listed in Table 1. The experimental observation showed that the twinning occurs during the ratchetting deformation of the Ti-6Al-4V alloy after certain cycles.

Firstly, the proposed model is verified by comparing the simulations and the experiments under the monotonic tension. It can be seen from Fig. 1 that the simulated results are in good agreement with the experimental ones.

Then, the proposed model is used to simulate the ratchetting of Ti-6Al-4V alloy occurring under the uniaxial stress-controlled cyclic loading. The ratchetting strain

Table 1 Material parameters used in the proposed model

Elastic constants: E = 100 GPa; $\nu = 0.3$
Flow rule: n = 25; $K_{twin} = 335$ MPa; $K_{HCPslip} = 485$ MPa; $K_{BCCslip} = 385$ MPa
Kinematic hardening rule: $B_{twin} = 6$ GPa; $C_{twin} = 4$; $B_{HCP-slip} = 0.4$ GPa; $C_{HCP-slip} = 10$; $B_{BCC-slip} = 0.4$ GPa; $C_{BCC-slip} = 10$
β-rule: C = 5 GPa; D = 80
Volume fraction: $\xi = 0.08$

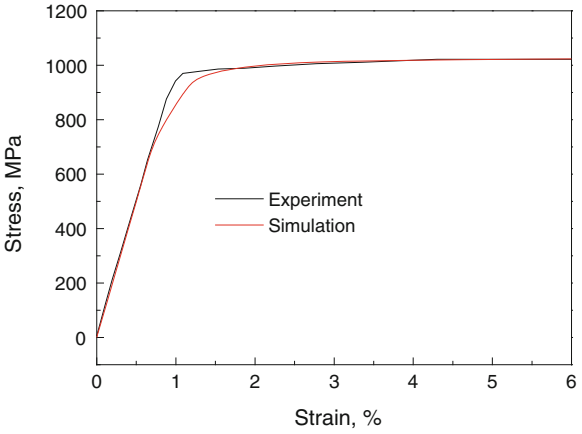

Fig. 1 Simulated and experimental monotonic tensile stress-strain curves

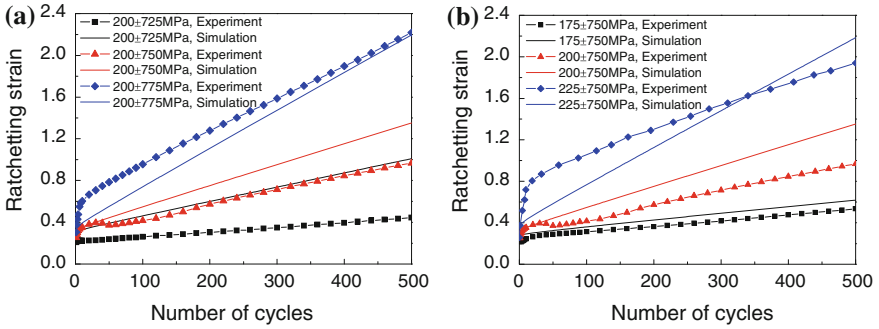

Fig. 2 Ratchetting behavior of Ti-6Al-4V polycrystalline alloy: **a** Ratchetting strain versus number of cycles with various stress amplitudes; **b** Ratchetting strain versus number of cycles with various mean stresses

is defined as $\varepsilon_r = (\varepsilon_{\max} + \varepsilon_{\min})/2$, where $\varepsilon_{\max}$ and $\varepsilon_{\min}$ are the maximum and minimum strains of each cycle, respectively. The results are shown in Fig. 2.

It can be seen from Fig. 2 that the simulated results are in fairly good agreement with the corresponding experimental ones, and the dependences of the ratchetting on the applied mean stress and stress amplitude observed in the experiments are also reasonably described by the proposed model. It should be noted that the proposed model just provides a constant rate of ratchetting strain due to the employment of kinematic hardening rules similar to Armstrong-Frederick model [17]. Although the decreased rate of ratcheting strain occurring at the beginning of the cyclic loading test cannot be reasonably predicted, the capability of the proposed model to predict the ratchetting behavior of the material can be improved by using more advanced nonlinear kinematic hardening rules [4].

4 Conclusions

A new cyclic polycrystalline visco-plastic constitutive model is proposed in the framework of thermodynamics and crystal plasticity by considering the contributions of both dislocation slip and twinning to the plastic deformation of a single crystal. The polycrystalline version of the proposed model is obtained by extending the cyclic single crystal plastic constitutive model with the help of an explicit scale-transition rule (i.e., β-rule). It is shown that the simulated results of uniaxial ratchetting by the proposed model are in fairly good agreement with the corresponding experimental ones for polycrystalline Ti-6Al-4V alloy. As future research works, much effort is necessary to verify the capability of the proposed model to describe the multiaxial ratchetting of polycrystalline aggregates and the ratchetting of single crystals, where the corresponding experimental studies are also needed.

Acknowledgments The work was financially supported by the National Natural Science Foundation of China (11025210), and GZ Kang appreciates the AvH Foundation for supporting his visit in Germany from October 2009 to October 2010 at the Ruhr-University Bochum and from March 2012 to September 2012 at the University of Siegen.

References

1. Ohno, N.: Recent progress in constitutive modelling for ratchetting. Mater. Sci. Res. Int. **3**, 1–10 (1997)
2. Kang, G.Z.: Progresses in ratcheting and its constitutive modelling. Int. J. Fatigue **30**, 1448–1472 (2008)
3. Chaboche, J.: A review of some plasticity and viscoplasticity constitutive theories. Int. J. Plast. **24**, 1642–1693 (2008)
4. Sai, K.: Multi-mechanism models: present state and future trends. Int. J. Plast. **27**, 250–281 (2011)
5. Goh, C.-H., Wallace, J.M., Neu, R.W., McDowell, D.L.: Polycrystal plasticity simulations of fretting fatigue. Int. J. Fatigue **23**, 423–435 (2001)
6. Goh, C.-H., Neu, R.W., McDowell, D.L.: Crystallographic plasticity in fretting of Ti-6Al-4V. Int. J. Plast. **19**, 1627–1650 (2003)
7. Mayeur, J.R.: M.S. Thesis, Georgia Institute of Technology (2004)
8. Vikas, H., Ghosh, S., Mills, M.J., Joseph, D.S.: A size-dependent crystal plasticity finite-element model for creep and load shedding in polycrystalline titanium alloys. Acta Materialia **50**, 4533–4549 (2003)
9. Staroselsky, A., Anand, L.: A constitutive model for hcp materials deforming by slip and twinning: application to magnesium alloy AZ31B. Int. J. Plast. **19**, 1843–1864 (2003)
10. Zhang, M., Zhang, J., McDowell, D.L.: Microstructure-based crystal plasticity modelling of cyclic deformation of Ti-6Al-4V. Int. J. Plast. **23**, 1328–1348 (2007)
11. Kang, G.Z., Bruhns, O.T., Sai, K.: Cyclic polycrystalline visco-plastic model for ratchetting of 316L stainless steel. Comput. Mater. Sci. **50**, 1399–1405 (2011)
12. Cailletaud, G., Sai, K.: A polycrystalline model for the description of ratchetting: effect of intergranular and intragranular hardening. Mater. Sci. Eng. A **480**, 24–39 (2008)
13. Leo Prakasha, D.G., Dingb, R., Moata, R.J., Jonesb, I., Withersa, P.J., Quinta da Fonsecaa, J., Preussa, M.: Deformation twinning in Ti-6Al-4V during low strain rate deformation to moderate strains at room temperature. Mater. Sci. Eng. A **527**, 5734–5744 (2010)

14. Yapici, G.G., Karaman, I., Luo, Z.P., Rack, H.: Mechanical twinning and texture evolution in severely deformed Ti-6Al-4V at high temperatures. Acta Materialia **54**, 3755–3771 (2006)
15. Ankem, S., Margolin, H.: The role of elastic interaction stresses on the onset of plastic flow for oriented two ductile phase structures. Metall. Mater. Trans. A **11**, 963–972 (1980)
16. Lutjering, G., Williams, J.C.: Titanium. Springer, Berlin (2003)
17. Armstrong, P., Frederick, C.: A mathematical representation of multiaxial Bauschinger effect. CEGB Report rd/b/n731, Berkeley Nuclear Laboratories, Berkeley (1996)